P
2mit

NASA TECHNICAL TRANSLATION

NASA TT F-752

NASA TT F-752

(NASA-TT-F-752) SIMULATION OF THERMAL SYSTEMS OF A SPACE VEHICLE AND ITS ENVIRONMENT (Scientific Translation Service) 396 p HC $8 00 CSCL 22B

N74-14531

Unclas

H1/31 25479

JAN 1974
RECEIVED
NASA STI FACILITY
INPUT BRANCH

SIMULATION OF THERMAL SYSTEMS OF A SPACE VEHICLE AND ITS ENVIRONMENT

by L. V. Kozlov and M. D. Nusinov et al.

"Mashinostroyeniye" Press, Moscow, 1971

NATIONAL AERONAUTICS AND SPACE ADMINISTRATION • WASHINGTON, D. C. • NOVEMBER 1973

1. Report No. NASA TT F-752	2. Government Accession No.	3. Recipient's Catalog No.
4. Title and Subtitle SIMULATION OF THERMAL SYSTEMS OF A SPACE VEHICLE AND ITS ENVIRONMENT		5. Report Date November 1973 6. Performing Organization Code
7. Author(s) L. V. Kozlov, M. D. Nusinov et al.		8. Performing Organization Report No. 10. Work Unit No. 11. Contract or Grant No. NASW-2035
9. Performing Organization Name and Address Scitran Santa Barbara, CA		13. Type of Report and Period Covered Translation
12. Sponsoring Agency Name and Address National Aeronautics and Space Administration Washington, D.C. 20546		14. Sponsoring Agency Code

15. Supplementary Notes

Translation of "Modelirovaniye teplovykh rezhimov kosmicheskogo apparata i okruzhayushchey ego sredy," Edited by G. I. Petrov, Moscow, "Mashinostroyeniye" Press, 1971, 382 pages

16. Abstract

This book investigates the methods and equipment for simulating spacecraft thermal regimes in equipment on the Earth. The primary and secondary physical characteristics of space are distinguished, which can directly or indirectly affect the thermal condition of the spacecraft. The different methods of simulating thermal regimes which are studied in the book take into account the heat exchange between the spacecraft and the surrounding medium, and also the action of a vacuum, space radiation, and meteorites on the structural materials. A simulation technique is presented which uses vacuum chambers, radiant flux simulators, and different laboratory equipment.

17. Key Words (Selected by Author(s))	18. Distribution Statement Unclassified - Unlimited		
19. Security Classif. (of this report) Unclassified	20. Security Classif. (of this page) Unclassified	21. No. of Pages 396 ~~395~~	22. Price* Domestic, $8.00 Foreign, $10.50

*For sale by the National Technical Information Service, Springfield, Virginia 22151

ANNOTATION

This book investigates the methods and equipment for simulating spacecraft thermal regimes in equipment on the Earth. The primary and secondary physical characteristics of space are distinguished, which can directly or indirectly affect the thermal condition of the spacecraft. The different methods of simulating thermal regimes which are studied in the book take into account the heat exchange between the spacecraft and the surrounding medium, and also the action of a vacuum, space radiation, and meteorites on the structural materials. A simulation technique is presented which uses vacuum chambers, radiant flux simulators, and different laboratory equipment.

The book is designed for scientific researchers and engineers working in the field of rocket construction and cosmonautics. It will also be useful to students in higher education in the appropriate disciplines. The sections of the book describing experiments on equipment simulating physical conditions of space (vacuum, corpuscular and roentgen radiation, micrometeorite matter, etc.) may be of interest for readers studying the behaviour of materials in space. 223 illustrations, 54 tables, 274 references.

PRECEDING PAGE BLANK NOT FILMED

PRECEDING PAGE BLANK NOT FILMED

FOREWORD

The problem of simulating the thermal conditions of a spacecraft and its surrounding medium arose even during the initial stage of development of cosmonautics. Special theoretical and experimental investigations were required to solve it. Since then the methods and techniques for simulation have achieved great success, but the problems of ground testing the thermal conditions of spacecraft launched into space have not only not become simpler, but have become more complicated due to the complexity of spacecraft design as a whole and to an increase in the dimensions of spacecraft. In most cases, analytical methods of calculating the thermal state of a spacecraft do not provide the desired accuracy. /3*

Practice has shown that thorough checking and adjusting of a spacecraft and its on-board systems under ground conditions lead to an appreciable increase in flight reliability. This may be explained by special attention given to problems of developing simulators in the United States, France, England, West Germany, Japan and other countries.

Special devices which simulate the conditions in space have been created to investigate spacecraft behavior under the proposed conditions. Development of such devices requires a knowledge of various branches of science and technology: space physics, optics, vacuum and cryogenic technology, low-temperature physics, nuclear physics, molecular physics, solid-state physics, electronics, automation, light engineering, study of space materials, etc. The diverse information on many problems in these fields may be obtained from various books and journals, but there are not yet enough papers either in Soviet or foreign literature which are devoted especially to the creation of simulators and the development of procedures for

(*) Numbers in the margin indicate pagination in the original foreign text.

investigating the efficiency of spacecraft on the ground under conditions which simulate natural ones to the maximum extent possible.

This book is the first attempt to generalize the numerous foreign publications which have appeared during the past decade on simulation of the thermal conditions of spacecraft.

A great deal of attention is devoted in the book to methods and procedures for investigating the effects of vacuum, solar, electromagnetic and corpuscular radiation, micrometeorite particles and other factors on the spacecraft hull materials, /4 since these effects are the indirect factors which affect the thermal conditions of the spacecraft.

Many of the problems touched on in the book are still far from a final solution. However, the authors felt that it was possible to mention them in order to show the importance and necessity of conducting further investigations in these directions.

The book was written by a collective of authors:

L.V. Kozlov — Introduction, Ch. 1, secs. 3 and 5; Ch. 2, sec. 6; Ch. 3, secs. 1-9, 12 and 14; Ch. 4, secs. 5, 8, 9, 10, 12 and Ch. 5;

M.D. Nusinov — Ch. 1, sec. 1; Ch. 2, sec. 1; Ch. 3, sec. 13; and Ch. 4, secs. 1-4;

A.I. Akishin — Ch. 1, sec. 4; Ch. 2, secs. 4 and 5; Ch. 3, sec. 10; and Ch. 4, sec. 11;

V.M. Zaletayev — Ch. 2, sec. 2;

V.V. Kozelkin — Ch. 2, sec. 3; Ch. 3, sec. 11;

V.V. Koselkin and L.V. Kozlov — Ch. 1, sec. 2; Ch. 4, secs. 6 and 7;

M.D. Nusinov and Ye.N. Yevlanov — Ch. 3, sec. 13 and Ch. 4, sec. 2.

The authors express their gratitude to Academician S.N. Vernov, Associate Member of the USSR Acad. of Sci., A.I. Shal'nikov, Prof. S.S. Vasil'yev, Cand. of Tech. Sci., Yu.D. Poskacheyev, S.B. Novikov, P.B. Kuznetsov and L.I. Kuz'minskiy and Cand. of Phys.-Math. Sci., Ye.V. Gorchakov, L.N. Isayev and L.I. Tseplyayev for useful and valuable advice given when reading certain sections of the manuscript.

The authors will gratefully accept all comments of readers of the book. Responses and critical comments should be sent to "Mashinostroyeniye" Press at: Moscow, B-66, 1-y Basmannyy per., 3.

PRECEDING PAGE BLANK NOT FILMED

NOTATION

A — albedo;

a — probability of wall capture of gas molecules;

b — probability of return of molecule reflected from wall of simulator to object;

C — coefficient of evacuation; coefficient of adhesion;

C_c — coefficient of condensation; contamination factor;

C_e — effective coefficient of evacuation;

C_i — coefficient of evaporation;

$C_{i/j}$ — coefficient of cryocapture;

C_s — self-contamination factor;

D — absorbed radiation dose;

d — coefficient of evacuation related to desorption;

E — energy of molecular interaction; irradiation;

E_d — energy of displacement of atoms in crystal lattice;

E_0 — radiant flux density emitted from surface of planet;

E_0^n — natural radiant flux density emitted from surface of planet;

E_0^r — solar radiation flux density reflected from planet;

F_0, F^* — regions on surface of planet delineated by solid angles Ω^0 and Ω^*, respectively;

H — heat flux density of radiant energy;

H_0 — distance from surface being considered along upper boundary of the layer of its atmosphere effectively radiating toward spacecraft;

H_a — distance from surface of planet to upper boundary of layer of its atmosphere effectively radiating toward spacecraft;

I — intensity of radiation;

G — rate of evaporation (sublimation) of matter;

j — particle flux density;

k — overload factor;

K — fraction of evacuating surface of inner walls of vacuum chamber;

L — parameter corresponding to distance (in earth radii) from magnetic center of earth to intersection with the plane of equator of the line of force passing through this point;

$\bar{m}$ — mass of gas particle;

N_a — number of atoms vaporized from 1 cm^2 of surface;

N_λ — spectral refractive index;

N_t — concentration of color centers;

n_λ — active component of spectral refractive index;

n_2 — unit normal to element of planet surface;

$\vec{n}_1$ — outer unit normal to element of surface;

P — polarization factor;

Q_Σ — energy flux received by a surface per unit time;

q — outgassing; gas load; /6

R — light reflection coefficient; gas constant per mole of matter;

R_0 — average radius of planet;

$R°$ — universal gas constant;

R_e — relaxation length;

R_λ — spectral reflection coefficient;

$\vec{r}$ $\vec{l}$ — unit vectors determining direction;

S — cathode sputtering factor; specific evacuation rate or volume output of vacuum pump;

$S_\odot$ — solar constant;

$S°$, $S*$ — zones on sphere of unit radius, surrounding surface under consideration, intersected by solid angles, respectively;

s — zone on sphere of unit radius;

T_e — electron gas temperature;

W — probability of chemical reaction;

w — probability of gas molecule penetration through screen;

Z — collision coefficient;

α — helium ion symbol;

α_c — heat transfer coefficient;

α_i — thermal accomodation coefficient;

β — thermal radiation screening factor;

γ_s — angle between direction toward surface under consideration and direction toward Sun from center of planet;

δ_s — angle between vertical plane passing through normal to surface element and vertical plane passing parallel to solar flux;

ε_λ — spectral absorption coefficient, spectral emissivity;

θ — degree of surface saturation by adsorbed gas particles;

κ — coefficient of friction losses during flow of gas in pipes;

κ_λ — spectral radiation absorption coefficient in matter;

λ_0 — radiation wavelength;

ν — gas flow;

ρ — coefficient of absorption;

σ_0 — force of surface tension;

τ^* — duration of monolayer formation; duration of existence ("lifetime") of molecule on surface;

Φ — density of radiation flux impinging on spacecraft;

Φ_λ — spectral radiant flux density;

$\Phi_{\lambda\omega}$ — spectral energy brightness;

Φ_ω — energy brightness;

φ_{1-2} — irradiation ratio between body "1" and body "2";

φ_1 — angular coefficient (or irradiation ratio) between surface under consideration and planet (for surface element — local angular coefficient);

φ_2 — combined angular coefficient (local combined angular coefficient for surface element) between surface under consideration and planet;

ψ — angle between outer normal to surface element and vertical to it;

ψ_0 — zenith angle of Sun for surface element of planet;

Ω — solid angle of planet (angle within the limits of which the planet emits energy toward the surface under consideration);

Ω^* — portion of solid angle of planet within the limits of which the portion of the planet illuminated by the Sun is visible from the surface under consideration;

ω — unit solid angle.

ABBREVIATIONS

/7

SC — spacecraft;

TCS — temperature control system;

TSS — thermostat system;

TS — thermal simulator;

EC — electronic computer;

UV — ultraviolet;

IF — infrared;

AU — astronomical unit;

TCC — temperature controlling covering;

AIAA — American Institute of Aeronautics and Astronautics;

IES — Institute of Environmental Sciences;

ASTM — American Society for Testing Materials.

TABLE OF CONTENTS

Annotation iii
Foreword v
Notation ix
Abbreviations xii
Introduction 1
Chapter I. THE PHYSICAL CHARACTERISTICS OF SPACE 8
1. The Interplanetary Medium. The Atmospheres of the Planets and the Moon. 8
2. Solar Radiation 11
3. Radiation of the Planets and Moon 15
4. Corpuscular Radiation in Circumterrestrial and Interplanetary Space and Meteor Material 36
5. The "Darkness" and "Cold" of Space 43

Chapter II. INFLUENCE OF THE SURROUNDING MEDIUM ON A SPACECRAFT 45
1. Space Vacuum 45
2. Flux of Radiant Planetary Energy Falling on a Spacecraft 49
3. Action of Short-Wave Solar Radiation on Spacecraft Materials 79
4. Mechanism by Which Temperature Controlling Coverings Are Damaged by Charged and Micrometeorite Particles 81
5. Stability of Temperature Controlling Coverings During the Simulation of the Interaction Between Corpuscular Fluxes and Ultraviolet Radiation 93
6. Influence of Weightlessness 104

Chapter III. SIMULATION OF A SPACECRAFT THERMAL REGIME IN GROUND-BASED EQUIPMENT 110
1. Characteristics of Heat Exchange Between a Spacecraft and the Surrounding Medium 110
2. Basic Problems of Testing and Developing a Spacecraft Thermal Regime 111
3. Methods of Simulating Spacecraft Thermal Conditions 114
4. Classification of Spacecraft (Fig. 3.1.). 115
5. Simulation of the Radiant Flux Field Impinging on the Spacecraft 118
6. Approximate Simulation 122
7. Method of Reproducing Thermal Boundary Conditions 128

8. Scale Modelling of Spacecraft Thermal Conditions 138
9. Mathematical Modelling of Spacecraft Thermal Conditions 150
10. Simulating the Effects of Cosmic Corpuscular Radiation on the Temperature Controlling Covering of the Spacecraft 164
11. Methods of Simulating the Effects of Short-Wave Solar Radiation on the Temperature Controlling Coverings of Spacecraft 181
12. Simulation of the Interaction of Atmospheric Molecules with the Spacecraft Surface 186
13. Requirements for Simulation of a Space Vacuum 189
14. Thermal Testing of the Cosmonaut's Spacesuit 211
Chapter 4. FACILITIES WHICH SIMULATE CONDITIONS OF SPACE 214
1. Vacuum Systems 214
2. Cryogenic Systems 218
3. Cryogenic Pumping 221
4. Design Characteristics of Vacuum Facilities 241
5. Solar Radiation Simulators 259
6. Radiation Sources for Solar Spectrum Simulation 279
7. Measuring the Radiant Flux Characteristics of a Solar Simulator 302
8. Planetary Radiation Simulator for Orbital Spacecraft 307
9. Radiation Simulators for a Spacecraft Located on the Surface of the Moon 311
10. Methodical Errors in Simulation of Radiant Fluxes Impinging on a Spacecraft 321
11. Equipment for Simulating Corpuscular Streams and Micrometeor Showers 338
12. Facilities for Investigating the Effect of Weightlessness 350
Chapter 5. FOREIGN DEVELOPMENT OF SPACECRAFT GROUND TEST FACILITIES 354
Appendix 361
References 367

INTRODUCTION /8

The problem of ensuring spacecraft reliability acquires special importance with the development of space technology. One of the main factors which determine the reliability and lifetime of a spacecraft is the stability of its thermal conditions. Modern electronic equipment installed on board satellites and spacecraft operates within a limited temperature range. Deviation of temperature from permissible limits may lead to a variation of the electrical characteristics of the equipment, a reduction of its service life, and to various functional breakdowns.

Especially severe temperature requirements are placed on manned spacecraft and on the cosmonaut life-support system, in particular, on the spacesuit.

Most existing spacecraft designs have special temperature control systems (TCS) or thermostat systems (TSS), whose weight is sometimes 30% of the weight of the spacecraft. Orbital injection of every kilogram of payload requires very high energy expenditures. Hence, it is obvious that the problem of reducing the weight of temperature control systems with a simultaneous increase of their operational reliability is extremely important. This is one of the reasons for the increasing interest in the problems of thermal stabilization of the spacecraft and in the means of providing it.

Rigid weight limitations induce designers to create temperature control systems without significant reserves of cold or heat capacity. In this case, even slight errors in thermal calculations may lead to the fact that the thermal conditions of the spacecraft will not be maintained within given limits. Spacecraft design is usually too complex for a precise theoretical calculation of thermal conditions. Therefore, experimental methods are employed to check and refine approximate calculations.

The essence of these methods is that spacecraft operating conditions are reproduced in ground laboratory devices with the aid of a physical model. It is obvious that the effectiveness of applying experimental investigation methods depends to a great extent on the accuracy of simulating the internal and external processes. Investigation of the thermal conditions of objects in scale models is /9 employed widely in aviation, machine building and other branches of technology. However, extending these methods to spacecraft entails difficulties due to an inadequate knowledge of external conditions affecting the spacecraft. The science of the conditions surrounding the spacecraft (environics) is only now beginning to be developed. Processes of interaction of the external parts of the spacecraft with space radiation or vacuum are very complex and have been studied very inadequately. As a result, the thermal state of a spacecraft does not yield to mathematical modeling with the same degree of reliability as, for example, in aerodynamics, gas dynamics or heat engineering.

Scale modeling may be of great assistance in this case. By investigating the thermal state of a reduced spacecraft model, the temperature distribution pattern on the full-scale spacecraft may be obtained. Scale modeling methods are suitable, but not always applicable. It is more complicated to prepare a scale model similar to a spacecraft when it is complex than to prepare a model of the spacecraft in full scale. Temperature errors inevitably occur when simplifications and schematization are introduced into the model.

Therefore, of all the experimental methods, those for comprehensive investigation of spacecraft thermal conditions are especially important. Special vacuum devices, equipped with space radiation simulators, are created for this. Simulation of thermal conditions may be conducted in complex* tests of the spacecraft as a whole. Economic calculations show that the considerable financial and technical difficulties of creating simulators for complex testing of full-scale spacecraft under conditions simulating those in space are justified completely, because such tests appreciably reduce the periods required for finishing the spacecraft and the /9 total material expenditures for development of the various on-board systems and equipment as a whole. What is more important, they increase the reliability of space flights and at the same time reduce the number of unsuccessful flights.

*Complex is understood to be tests of spacecraft completely supplied with all instrumentation operating according to the flight program.

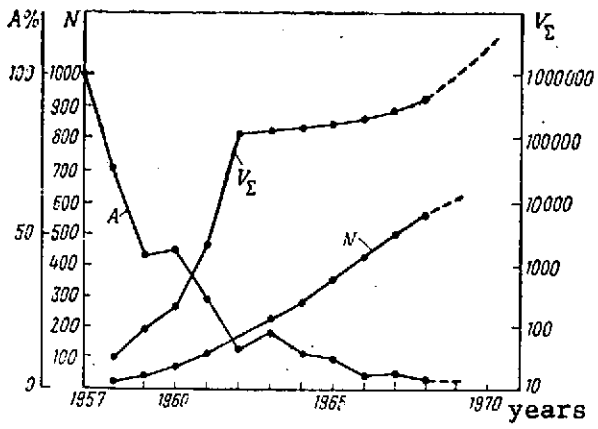

Variation in number of spacecraft launched (N), percentage of unsuccessful launches (A) and total volume of simulator vacuum chambers (V_Σ m^3) in the United States as a whole.

The unsuccessful launches in the United States during the early years of the space program forced American technical leaders to reconsider the methods of testing space material. The relative number of unsuccessful launches has begun to decline as a result of several organizational and technical measures (see diagram).

Some of the main reasons for the decrease in the rate of failure of spacecraft launches in the United States are the following:

— extensive use of the latest systems and designs;
— introduction of new technology; /10
— high level of operations organization;
— a great deal of attention to ground testing of different systems and of the spacecraft as a whole.

Unlike the methods of testing the first ballistic missiles in the United States, a new principle was adopted for testing space technology, consisting of the fact that all on-board and ground systems must be tested in the most careful manner and adjusted on the ground, and only those systems are flight tested which cannot be checked on the ground at the current level of technology.

This approach predetermined the considerable capital investments in construction of test centers. Appropriations for these purposes have increased continuously and have presently reached hundreds of millions of dollars annually. Thus, for example, investments to create new simulators exceeded 800 million dollars in 1963. The cost of constructing the experimental base for testing the Saturn-Apollo system is estimated at 3 - 4 billion dollars. And the total expended on this program for ground testing of systems was 16 out of 24 billion dollars, comprising the total expenditures. In future space programs the Americans plan an even greater increase in the expenditures for ground testing of systems, scientific investigations and ground testing and construction of experimental installations. During a ten-year period (1958 - 1968) more than 400 different simulators were introduced in the /11

United States, with a total volume of more than 350,000 m^3.

Two methods are possible in creating a complex of experimental installations for heat and vacuum testing of spacecraft. The first method assumes construction of many chambers with radiant flux simulators which are equipped for testing some specific type of apparatus. Such specialization of chambers and simulators provides a simpler design and more economical operation, but the number of chambers becomes very great. The second method is to create a limited number of more universal chambers having radiant flux simulators which test various types of apparatus in the same installation, regardless of their configuration and orientation with respect to the Sun and planets. An almost full-scale radiant flux field must be created in the working zone of the vacuum chamber for this.

The advantages of a certain method of developing simulators are presently being discussed both from the point of view of engineering and technical problems, and maximum return of investments. There are as yet no set generally accepted views on this. Therefore, descriptions of both narrowly specialized and universal simulators are presented in the book. The desire to obtain the closest possible approximation of conditions in the chamber to real space conditions encounters extremely great difficulties of a technical and economic nature. Each new stage in achieving more perfect simulation of space conditions which affect spacecraft thermal conditions is achieved at a cost which may be unjustified, if the additional precision obtained is taken into account.

In connection with this, when designing ground installations to simulate space conditions or spacecraft thermal conditions, the question always arises of the maximum permissible error in reproducing external radiant fluxes and the vacuum of space. The answer to this question cannot be formulated in a general form, because the effect of variations of external conditions for each specific apparatus on its thermal conditions is different.

In some cases corrections may be introduced into the results of approximate thermal testing of spacecraft with the aid of theoretical methods of calculating errors. Unfortunately, this approach is possible only when investigating the thermal conditions of bodies of the simplest shapes. Solutions of the problem of unsteady thermal states for most spacecraft having a complex configuration may be obtained only with the aid of a procedurally and correctly run experiment which provides rather high accuracy.

When creating space simulators, it is necessary to determine: /12

a) what conditions (or parameters) of the space environment may have a decisive effect on spacecraft elements and may affect its thermal conditions;

b) with what accuracy these parameters must be simulated for different types of spacecraft;

c) what the practical possibilities are of simulating space parameters which determine the thermal conditions of the spacecraft.

These problems are closely related to the characteristic features of spacecraft design and its temperature regulating systems.

The numerous existing methods of temperature control may be divided into two essentially different classes.

The first class may include methods of active temperature control using circulating heat carriers, adjustable louvers, movable valves, etc.

The second class combines methods of passive temperature control, the basis of which is calculation of previously balanced radiant exchange of the spacecraft and the surrounding medium, without using any kind of movable elements to alter the thermal resistance of the system.

Active temperature control is employed in those cases when spacecraft temperature must be maintained within a very narrow range or when the temperature of the spacecraft hull is higher than the permissible temperature inside the instruments and equipment. In most cases pressurized spacecraft compartments, equipped with active TCS have a relatively simple shape and good thermal insulation. The requirements for accuracy of reproduction in the simulator chamber of all characteristics of incident radiant fluxes are considerably less rigid for such objects than for those of complex shapes with a passive temperature control system.

Passive methods of temperature control are employed in those cases when a wider range of temperature variations of spacecraft assemblies is permitted. These methods are promising, because electric power sources and control systems are not

required. However, successful use of passive temperature control requires that the optical characteristics of the surfaces participating in heat exchange do not vary during prolonged flights of the spacecraft in space. When testing spacecraft with a passive temperature control system, increased accuracy of reproducing the incident radiant fluxes is required. This refers primarily to the spectrum, the uniformity of radiation density in terms of volume and angular distribution. A deviation of these characteristics from real values leads to distortion of the structural temperature field.

Data on the stability (or variation) of the radiation factors of different /13
materials may be obtained both from flight experiments with the aid of artificial earth satellites and on the ground in special installations equipped with space radiation simulators. Ground experiments are more inexpensive and yield numerous quantitative interrelationships of the parameters, which is difficult to achieve at present using automatic space laboratories. However, creation of an installation in which all space parameters could be simulated simultaneously without exception, or which indirectly affect spacecraft thermal conditions, remains an unsolved problem. Therefore, a series of experiments must be conducted, simulating in them separately certain determining parameters. Then mathematically or with the aid of special experiments, the results must be synthesized or generalized with respect to real conditions. Accurate simulation of spacecraft thermal conditions may be rather closely approximated in this manner. Present technology permits such experiments by combining:

— moderate vacuum (i.e., $p = 10^{-4}$ to 10^{-5} torr) with the radiant fluxes of the Sun and planets;

— high vacuum (i.e., $p = 10^{-7}$ to 10^{-8} torr) with ultraviolet and corpuscular radiation;

— moderate vacuum with micrometeorite particles, particles of planetary origin etc.

The installations in which corpuscular radiation and micrometeorites are investigated are still too complex and small in size. The entire spacecraft cannot be irradiated. Such installations are employed mainly for exposure of samples of materials subject to the effects of space during flight.

During the first stages of testing a spacecraft or its systems and assemblies,

the tightness of the compartments is checked in the presence of temperature gradients and under conditions of unsteady heating; the efficiency of the on-board temperature control systems is investigated; and service life tests are conducted and the efficiency of movable assemblies is checked in a high vacuum under real temperature conditions (movable assemblies may include those with sliding and rolling bearing surfaces, the sliding parts of spacesuit pressure seals, flexible hoses, undulated pipes, membranes, films, elastic visors and the soft components of spacesuits). During these stages the following are investigated: the effective irradiation coefficients of complex structures; the stability of temperature controlling coverings and optical elements under the combined effects of vacuum, ultraviolet radiation and X-rays and corpuscular radiation; the effect of vibration on the strength of supporting structures and the stability of electronic equipment; gas distribution in the ventilating devices of the life-support system; and spacecraft /14 temperature fields on scale models or thermal mock-ups in full scale and other problems.

Thorough investigation of the thermal conditions of full-scale spacecraft with functioning equipment is carried out during the final stage at low ambient pressure under conditions of radiant exchange, close to that which occurs during a circumterrestrial or interplanetary trajectory, or on the surface of a planet (for example, on the Moon). In this case three types of experiments are usually conducted: 1) tests under extreme (most severe) anticipated thermal conditions; 2) tests according to the nominal flight program; and 3) tests under emergency conditions.

Correct selection of measures for making thermal conditions severe, whether overheating or overcooling, is very important in the first type of testing. Too rigid, irrationally selected and maximum severe temperature conditions may ultimately lead to both overloading of the temperature control system and to overloading of the supporting structure.

Tests according to the nominal program provide information on the thermal parameters of the object being tested. These data are employed for theoretical prediction of the temperature variation of the spacecraft under conditions differing from (but similar to) those for conducting the experiment.

Testing under conditions simulating emergency situations envisions combinations of breakdowns whose probability actually amounts to a few percents or fractions of a percent.

CHAPTER 1

THE PHYSICAL CHARACTERISTICS OF SPACE

1. The Interplanetary Medium. The Atmospheres of the Planets and the Moon.

The interplanetary medium is filled with gaseous particles of mainly solar origin. /15

The Sun consists (in terms of mass) primarily of hydrogen (~90%) and helium (~9%) [13]. The gas particles are ejected at velocities from 300 to 800 km/sec (an average of 500 km/sec) from the active regions of the Sun into circumsolar space and form steady plasma flows (the "solar wind"). The solar wind, consisting mainly of hydrogen and helium ions, is characterized by an average concentration of ionized hydrogen atoms of 1 cm^3 ($n_{avg} < 10$) and temperature of $T \approx 10^5$ K [240].

The conditions in the interplanetary medium vary rather strongly as a function of solar activity (11-year cycle, 27-day variations and flares) [13], [168]. During the period of increased solar activity after chromospheric flares appear on the Sun, average particle velocities may increase to ~1000 km/s and concentrations — to ~100 particles/cm^3.

A shock wave develops as a result of the interaction of supersonic particle flows of the solar wind and the geomagnetic field at distances from the Earth's surface approximately equal to ten earth radii.

The Earth's Atmosphere

Approximate data are presented in Table 1 on the concentrations, pressures

TABLE 1. DEPENDENCE OF CONCENTRATIONS, TEMPERATURES, PRESSURES, AVERAGE MOLECULAR WEIGHT AND GAS COMPOSITION (NEUTRAL PARTICLES) ON DISTANCE TO EARTH'S SURFACE* [48].

Distance to Earth's surface, km	Pressure, torr	Temperature, °K	Average molecular weight, G/mole	Neutral particle concentration, cm^{-3}			Approximate composition of gas
				total	molecular	atomic	
0	$760 \approx 10^3$	300	29	$2{,}7 \cdot 10^{19}$			N_2 (~78%); O_2 (~21%) Ar (~1%) H_2; He; Ne; Kr ($2{,}5 \cdot 10^{-3}$%)
30	$\sim 10^2$	243	29	$4 \cdot 10^{17}$			N_2; O_2; O_3; Ar
50	$5 \cdot 10^{-1}$	270					N_2; O_2; O_3
100	$2{,}2 \cdot 10^{-4}$	200	29				N_2; O_2; O
150	$3{,}8 \cdot 10^{-6}$	800					N_2; O; O_2.
200	$1{,}0 \cdot 10^{-6}$	1200	25	$2 \cdot 10^{10}$	$1 \cdot 10^{10}$	$1{,}3 \cdot 10^7$	N_2; O; O_2; Ar; He; H
300	$1{,}5 \cdot 10^{-7}$	1300	21	$2 \cdot 10^9$	10^9	$2{,}2 \cdot 10^6$	O; N_2; O_2; He; Ar; H
500	$7 \cdot 10^{-9}$	1300	17	$7{,}6 \cdot 10^7$	$5{,}1 \cdot 10^6$	10^7	O; N_2; He; O_2; H
800	$5 \cdot 10^{-10}$	1300	14	$3{,}5 \cdot 10^6$	10^4	$3{,}4 \cdot 10^6$	O; He; H; N_2; O_2
1 000	$\sim 10^{-10}$	1300	9	$2{,}6 \cdot 10^5$	10^2	$2{,}5 \cdot 10^5$	O; He; H; N_2; O_2
2 000	$\sim 10^{-11}$	1300	3	$2{,}1 \cdot 10^4$	—	$2{,}1 \cdot 10^4$	H; He; O
5 000	$\sim 10^{-12}$	$\sim 10^3$	2	$3 \cdot 10^3$	—	$3 \cdot 10^3$	H; He;
10 000	$\sim 10^{-13}$	$\sim 10^3$	2	$\sim 10^3$	—	$\sim 10^3$	H; He
20 000	$\sim 10^{-14}$	$\sim 10^3$	2	$\sim 10^2$	—	$\sim 10^2$	H; He

*Commas represent decimal points.

and temperatures of neutral particles at various distances from the Earth's surface [207] (conditions of average solar activity).

The Earth's atmosphere is in continuous motion and change, which is due to many causes, in particular to solar activity [168], [179], [180].

The mean free path of residual gas particles at a distance of 100 - 150 km /17
from the Earth becomes equal to several tens of meters, i.e., it becomes comparable to the characteristic linear dimensions of the spacecraft. These conditions are identical to those of a high vacuum in accordance with the classification accepted in vacuum technology [43].

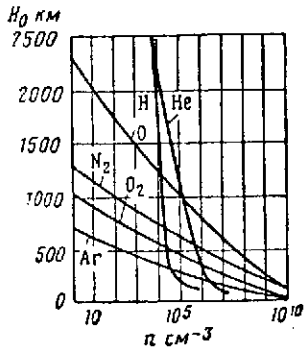

Fig. 1.1. Dependence of neutral gas concentration in Earth's atmosphere on height above sea level.

The Earth's atmosphere is not uniform. Gas composition at distances equal to or exceeding 100 km from the Earth's surface are essentially different both in terms of the chemical and physical state of the particles (molecules, atoms, ions). However, at distances up to 100 km the atmosphere is almost uniform (an exception is ozone and water vapor).

Gas exists essentially only in the form of neutral molecules at short distances (up to 60 km) from the Earth's surface [168], [180], [247]. Beginning at distances above 60 km, electron and ion concentration increases and at distances greater then 700 - 800 km gas exists primarily in the form of atoms. At a distance of several thousand kilometers from the Earth's surface, gas particles are found primarily in an ionized stage (Figure 1.1).

The Moon's Atmosphere

The Moon has a mass approximately 81 times less than that of the Earth. Because of this, it has expended the main portion of its initial atmosphere. Xe, Kr, Ar and other components are presumably present in the lunar atmosphere.

The concentration of neutral particles near the lunar surface, according to present concepts [40], [179], [240], comprises ~10^5 to 10^7 cm^{-3} (see note on page 189). The dependence of neutral particle concentration in the lunar atmosphere on the distance to the lunar surface is presented in Figure 1.2. A model with a gas concentration near the surface equal to /18 ~10^6 cm^{-3}, temperature of T = 400°K and average molecular weight equal to 20, was assumed.

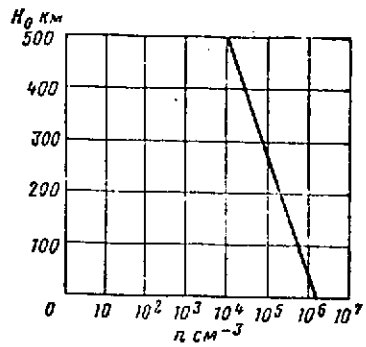

Fig. 1.2. Dependence of neutral particle concentration in lunar atmosphere on distance to its surface.

The Atmosphere of Mars [240], [270]

The mass of Mars is approximately 9 times less than that of earth. The dependence of neutral gas particle concentration in the atmosphere of Mars on the distance to its surface is presented in Figure 1.3. A model

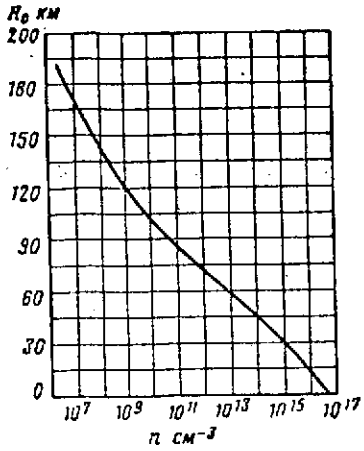

Fig. 1.3. Dependence of neutral gas concentrations in atmosphere of Mars on distance to its surface.

with 100% surface concentration of CO_2, n = $2.78 \cdot 10^{17}$ cm^{-3} and T = 210°K was adopted. As the data obtained by Mariner-6 and Mariner-7 show, the surface temperature of Mars varies from +24° to -210°C and pressure — from 6 to 10 mb (1 mb equal to 0.75 torr).

The Atmosphere of Venus*

Venus, as shown by experimental investigations, carried out with the aid of Venera-4, Venera-5, Venera-6, Venera-7 and Mariner-5 [35], [240], has an extremely dense atmosphere. Estimates of the pressure near the surface yield a value equal to ~90 atm and a temperature of ~500°C. The atmosphere near the surface of the planet contains a large amount (95%) of CO_2, less then 7% N_2 and small amounts of O_2 (~0.4% < O_2 < 1.5%) and H_2O (< 1.0%).

The concentration of atomic hydrogen at a iistance of about 1000 km from the surface of Venus is equal to ~10^3 atoms/cm^3, at a distance of ~6000 km is ~10^2 atoms/cm^3 and at a distance of 20,000 km is ~10 atoms/cm^3.

2. Solar Radiation [8], [60], [92], [117], [123], [130], [212] /19

General Information

The Sun is the only powerful source of radiant energy in our planetary system. Every second it emits radiation into space whose total output comprises $3.86 \cdot 10^{23}$ kW. This comprises 64,000 kW when converted to 1 square meter of the visible surface of the Sun. A unit of solar surface shines approximately 10,000 times brighter than melted platinum. Solar radiant flux density at a distance of 150,000,000 km (i.e., on the Earth's orbit) in accordance with a square law diminishes to a value of 1396 W/m^2, which is called the "solar constant" and which is

*Refined data on the atmosphere of Venus are presented in the investigation of V. S. Avduyevskiy, M. Ya. Marov and M..K. Rozhdestvenskiy "Space Research" (Kosmicheskiye issledovaniya), AN SSSR, Vol. 2, No. 2, 1969; Vol. 8, No. 6, 1970.

denoted by $S_{\odot}$. At present this value is calculated with an accuracy of $\pm$ 2%. As subsequent investigations showed, the solar constant does not fully justify its name, because it varies by approximately 2% from time to time, which is related to a variation of solar activity. Besides these variations, there are also seasonal variations of $S_{\odot}$ by $\pm$ 3.5%, caused by the elliptical nature of the Earth's orbit. In January (perihelion) the solar constant is equal to 1444 W/m^2 and in July (aphelion) it decreases to 1349 W/m^2. At an average distance from the Earth to the Sun, its disk is visible at an angle of 32', or 0.0093048 radians (solid angle is $\sim 6.8 \cdot 10^{-5}$ steradians). Solar flux intensity for the other planets and the corresponding dimensions of the Sun are given in the appendix.

It is generally assumed in calculating spacecraft thermal conditions that the average energy brightness of the sun is equal to 2020 $W/cm^2 \cdot$steradian, and its radiation temperature (i.e., the temperature of an absolutely black body, which, having the angular dimensions of the Sun, creates energy illumination equal to that of the Sun in a vacuum on a surface perpendicular to incident rays) is 5785°K. It is assumed that the radiating capacity of the Sun is equal to 0.99.

This concept may be inaccurate in a number of cases. In fact the solar spectrum differs from that of an absolutely black body at a temperature of 5785°K (see Figure 1.14), and brightness distribution over the solar disk is non-uniform Visual brightness in the center is 1.22 times greater than average. The brightness of the solar disk decreases closer to the edge, and wavelength varies. This dependence, which is more strongly manifested near the edge of the solar disk, is depicted graphically in Figure 1.4. The specific weight of red rays increases as the distance from the center of the solar disk to its edge increases. Color temperature along the edges is lower than that in the center, as a result of which the edges seem redder than the central portion.

There is a continuously varying luminescent corona around the Sun. Its temperature is about 1,000,000°K and its diameter sometimes exceeds that of the Sun two- or threefold. Radiant flux from the corona is approximately 900,000 times /20 weaker than that from the Sun itself and is approximately twice as weak as the light of the full Moon. Therefore, when solving problems related to spacecraft thermal conditions, the radiation of the corona may always be ignored. However, the corona emits radiation in the ultraviolet band (20 - 100 Å), which is important when investigating the effect of short-wave radiation on the optical characteristics

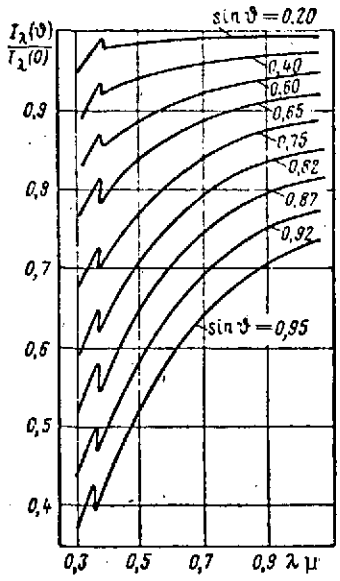

Fig. 1.4. Dependence of solar disk brightness on wavelength for various distances from the center.

of the temperature controlling coverings of the spacecraft, although the energy contribution of the corona to the ultraviolet component of the spectrum of the Sun itself is slight and comprises less than 2%.

Long-Wave Radiation

The main contribution to the heat of spacecraft is made by the long-wave region of the spectrum — from 0.3 to 3 microns, where 92% of all the radiant energy of the Sun is concentrated. About 6% of the Sun's energy is located in the region of wavelengths from 0.3 to 0.38 μm, and approximately 1.4% is located in the region from 0.2 to 0.3 micron.

Nevertheless, it is this short-wave portion of the spectrum which deserves special attention, because ultraviolet radiation is one of the causes of changes in the radiation coefficients of the external surfaces of spacecraft which determine their thermal conditions.

Short-Wave Radiation

The upper limit of the short-wave region of the solar spectrum is conditionally assumed to be the ultraviolet limit of the visible portion of the spectrum with a radiation wavelength of 0.38 micron (3800 Å). The spectrum of short-wave radiation with a quiet sun goes down to a few angstroms, and during flares — to approximately tenths of an angstrom. The greater portion of the radiation energy in this region (about 75%) is contained in the portion of the spectrum from 3800 to 2000 Å.

The spectral distribution of solar radiation intensity in the ultraviolet and /20
X-ray regions is shown in Figures 1.5 and 1.6. As can be seen from Figure 1.5, a number of emission lines is superimposed on the continuous radiation spectrum in /21
the short-wave portion, beginning at approximately 1800 Å. The most intensive of them is the emission line of atomic hydrogen — the so-called Lyman alpha L_α (λ = 1216 Å) with an average intensity of about $0.5 \cdot 10^{-6}$ W/cm^2, and the second in

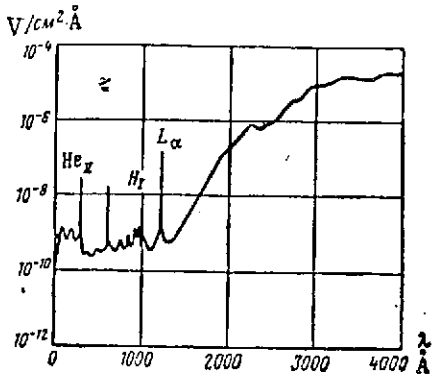

Fig. 1.5. Spectrum of solar ultraviolet radiation for a Sun spot maximum.

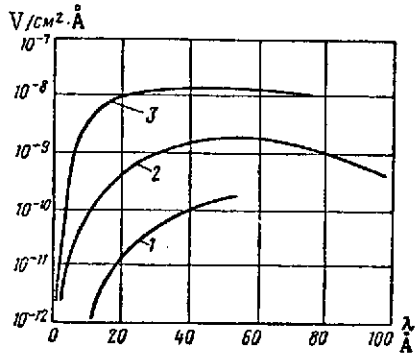

Fig. 1.6. Solar X-ray spectrum:
1 — quiet sun at minimum activity;
2 — quiet sun at maximum activity;
3 — flare of 2^+ intensity.

intensity is the line of ionized helium He_{II} (λ = 304 Å) with an intensity of ~$0.03 \cdot 10^{-6}$ W/cm^2. The energy of continuous radiation, including background radiation in the shorter wave portion of the spectrum, usually exceeds that contained in the emission lines (with the exception of individual brighter lines).

The average absolute values of radiation intensities for different regions of the short-wave solar spectrum may be found from H. Hinteregger [130], [190]; for the range of λ > 3000 Å — from Johnson [212]; and for X-rays — from S.L. Mandel'shtam [224]. Radiation intensity in the X-ray region of the spectrum depends on solar activity. One of the manifestations of solar activity are Sun spots, the appearance of which has an 11-year cycle.

The X-ray spectrum during flares becomes harder and radiation intensity increases (see Figure 1.6). The spectrum boundary during 2 - 3 class flares shifts to 1 Å and the flux of photons with λ < 10 Å increases by an order of magnitude. Total radiation intensity at λ < 100 Å increases more than twofold compared to a quiet sun. Radiation at wavelengths shorter than 1 Å during flares is not usually observed, although there are indications of the possibility of such radiation during the first several minutes after the beginning of the flare [92]. It is noted that even with considerable variations in X-ray intensity, the intensity of the hydrogen emission line L_α during flares hardly increases [67]. Variations in the intensi- /22
ties of other emission lines become apparent as wavelength decreases. Continuous solar radiation in the region of λ > 1300 - 1500 Å barely changes with time. The concentration of γ-rays in solar radiation is negligible, and their effect on the spacecraft may be ignored.

3. Radiation of the Planets and Moon [144]

The radiation emitted from a planet may be arbitrarily divided into two components. First, there is natural infrared radiation, the source of which is mainly the absorbed portion of solar energy, re-emitted by the planet in the long-wave band of the spectrum. (The internal heat liberation of the planet also contributes to the given type of radiation. However, for small planets the heat supply to the surface from hot interiors is neglibible and may be ignored in a number of cases). Secondly, there is solar radiation reflected from the planet, which depends on reflectivity, the simplest quantitative characteristic of which is spherical albedo*.

By definition, the value of the spherical albedo is numerically equal to the ratio of the total amount of solar energy scattered by the planet in all directions (Φ) to the total radiation energy flux from the Sun ($S_{\odot}F_n$), incident on the surface of the planet, namely:

$$A_{sf} = \frac{\Phi}{S_{\odot}F_n}.$$

For an ideal diffuse** and white surface $A_{sf} = 1$. Such a surface has the same brightness for any direction. Therefore, spherical albedo may also be expressed by the relation

$$A_{sf} = \Phi/\Phi_0,$$

where Φ_0 is the radiant flux scattered by an absolutely white sphere. The term "albedo" is also used for bodies of arbitrary configuration, for example, plane bodies, as well as for spheres.

Since absolutely grey ideal diffuse surfaces are not found in nature, albedo depends on the wavelength of incident radiation and the angle of incidence of the rays.

For some materials, the dependence of albedo on the angle of illumination is very great. Thus, for example, for water the value of A varies from 0.45 to 0.03.

---

*This value is sometimes called whiteness, luminosity, or the coefficient of diffuse reflection.

**An ideal diffuse surface is one in which radiation intensity varies as a function of the direction according to Lambert's Law: $E = E_0 \cos \gamma$.

Therefore, the direction of illumination or the limits of possible variations of albedo are usually indicated in tables of the reflectivity of different materials.

The brightness coefficient $r = \frac{E}{E_0}$, where E is the surface brightness in a given /23 direction and E_0 is illumination, is employed for the characteristics of brightness of individual formations on the Moon or other planets. In the general case the coefficient r depends on the wavelength of radiation λ and the direction toward the light source (for example, toward the Sun), determined by azimuthal (δ_s) and polar (γ_s) angles, as well as by two angles (δ and γ), which determine the direction of the reflected beam $\vec{N}$ (Figure 1.7).

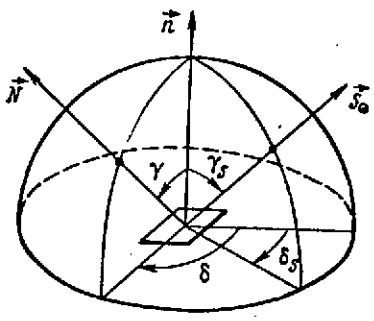

Fig. 1.7. Azimuthal and polar angles which determine the orientation of a surface with respect to direction toward Sun.

When the angle of vision changes, the visual brightness of an object located under invariable conditions of illumination may vary. On the contrary, a constant brightness of an object for a given direction also does not indicate that its albedo remains constant upon variation of the angle of incidence of beams on the object.

Only those properties of radiant fluxes from the planets and the Moon will be considered below which the spacecraft designer must know in order to calculate their thermal state.

The data presented below describe the radiation of different planets in varying detail, which is caused by two reasons: first, by the non-uniform level of knowledge in the corresponding fields and, secondly, by the impending investigations of certain planets of the solar system in the next few years.

Terrestrial Radiation [52], [63], [68], [78], [85], [181], [182]

The Earth is an optically very non-uniform and variable surface for solar rays. The continuously changing cloud cover, which almost completely conceals the land and sea surfaces, can be seen in long-range photographs of our planet. The visual brightness of different regions of the globe varies over a wide range, both in the visible and invisible regions of the spectrum. Reflected solar radiation

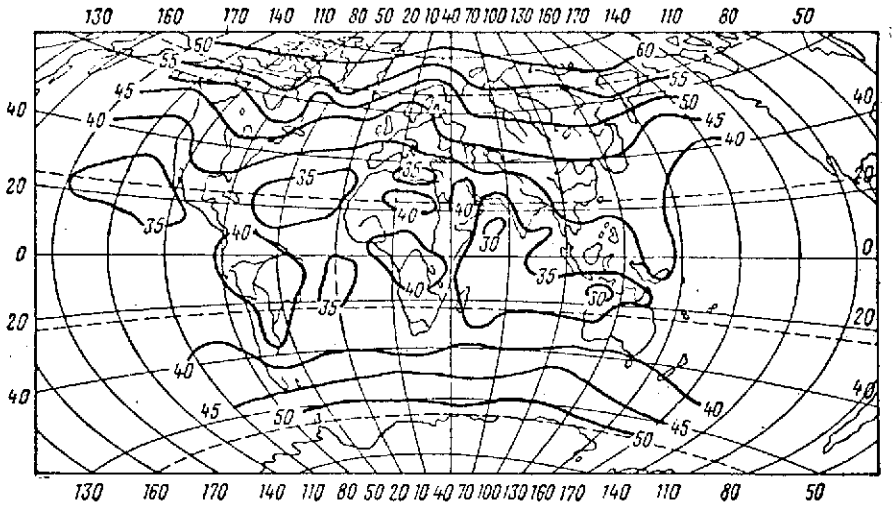

Fig. 1.8. Distribution of mean annual values of albedo over the Earth's surface.

consists of radiation reflected from the cloud cover, radiation reflected from the underlying surface and also of radiation reflected by the atmosphere.

Moving in low orbits above the Earth's surface, a spacecraft is irradiated at any moment only on some small area, for which local albedo may differ from average /24 planetary spherical albedo (Figure 1.8). The reason for the difference in local and average spherical albedo is that different regions of the Earth have different reflectivities, as well as that the reflection coefficient for most regions of the Earth's surface depends on the angle of incidence of rays. Flashing and reflecting surfaces at large angles reflect rays in a completely different manner than do diffuse scattering ("Lambert") surfaces, even if their coefficients are similar during normal radiation. Deviation of radiation according to a cosine law (Lambert's law) leads to the fact that sections of the Earth at the subsolar point (solar zenith) are brighter than those near the terminator. From the side, the Earth looks like a sphere rather than like a flat disk like the Moon.

Experimental investigations of the reflectivity of snow, sand, soil, water, etc. have showed that the range of variation of albedo in different regions of the Earth's surface is always extensive.

VALUES OF ALBEDO FOR DIFFERENT REGIONS OF THE EARTH'S SURFACE

Surface	Albedo	Surface	Albedo
Grass.	0.14 - 0.37	Snow (old). . .	0.45 - 0.70
Dry Soil	0.08 - 0.14	Ice	0.37

Surface	Albedo	Surface	Albedo
Damp soil	0.08 - 0.09	Granite	0.24
Sand (desert)	0.24 - 0.28	Forest	0.03 - 0.10
Snow (fresh)	0.80 - 0.90	Sea water	0.04 - 0.45

Clouds, like various regions of the earth's surface, depending on their structure, also reflect solar rays. /25

VALUES OF ALBEDO FOR VARIOUS TYPES OF CLOUDS

Types of clouds	Albedo
Very large and dense	0.78
Dense stratocumulus	0.56 - 0.81
Dense and completely opaque	0.44
Alto-stratus with occasional breaks	0.17 - 0.36
Compact alto-stratus	0.39 - 0.59
Cirrostratus	0.44 - 0.50
Stratus thicker than 300 m	0.60 - 0.85
Stratus 150 - 300 m thick	0.40 - 0.70
Stratus less than 150 m thick	0.10 - 0.50

The nature of clouds, their density and distribution over the Earth's surface, and consequently, their albedo vary continuously. The dependence of the mean annual albedo has been plotted as a function of the geographical coordinate (latitude) under different meteorological conditions: for compact overcast, absence of overcast and average conditions, according to data of albedo distribution in various regions of the Earth (Figure 1.9).

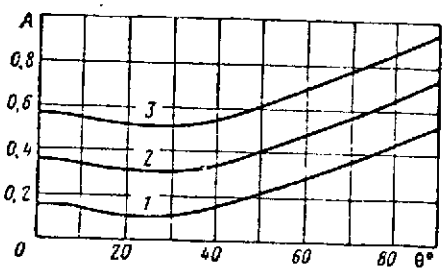

Fig. 1.9. Average latitude albedo of Earth for different meteorological conditions: 1 — clear sky; 2 — average overcast; 3 — heavy overcast.

Let us assume that all types of clouds are equally probable, and average albedo for the clouds is equal to 0.5. If the clouds occupy 50% of the Earth's surface, the radiation reflected from them comprises 25%. Average albedo for water is 0.09, and for dry land it is 0.12. We obtain an average albedo of 0.1 for the Earth's surface not covered by clouds. Together with the clouds, this comprises 0.35.

Such estimates and calculations are approximate. They do not take the fact into account that the reflection of clouds, water and ice are highly dependent on the angle of incidence of solar rays. They also do not take into account scattering

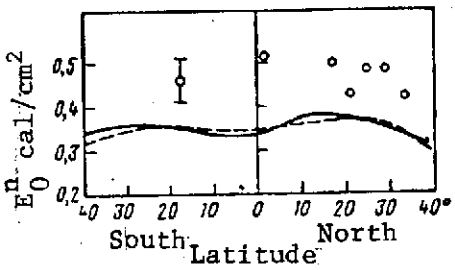

Fig. 1.10. Natural radiation of the Earth: 0 — data obtained from OSO-1, March-May 1962; ——— data obtained from Tiros-4, average latitudinal values for February-April 1962; — — — — — average theoretical latitudinal values, according to London [85].

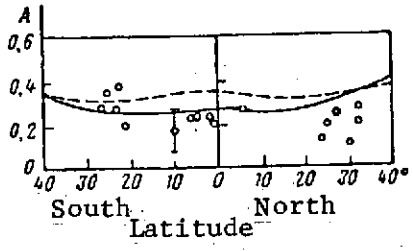

Fig. 1.11. Earth's albedo: 0 — data obtained from OSO-1, March-May, 1962; ——— data obtained from Tiros-4, average latitudinal values, February-March 1962; — — — — — average theoretical latitudinal values, according to London [85].

of light in dust, ice and water particles in the atmosphere and on the molecules of air themselves. This is the main reason that the angular distribution of reflected radiation for indirect rays of the Sun is not subject to Lambert's law.

The most precise distribution of albedo over the planet is derived with the aid of direct measurements from an artificial Earth satellite. There have been /26 attempts at such measurements, for example, with the aid of the Orbital Solar Observatory (OSO-1) in 1962, the Tiros series of satellites from 1960 - 1962, and other satellites. Some data of these measurements, together with mean latitudinal values of albedo, are presented in Tables 2 and 3 and in Figures 1.10 and 1.11.

TABLE 2. EXPERIMENTAL VALUES OF ALBEDO.*

Date (1962)	Geographical coordinates of satellite in deg.		Albedo	Date (1962)	Geographical coordinates of satellite in deg.		Albedo
	latitude	longitude			latitude	longitude	
March 8	—6	—75	0,23	March 19	—23	—73	0,38
March 9	5	—74	0,26	April 3	—26	—67	0,34
March 10	23	—86	0,12	April 16	—27	—88	0,23
March 11	—2	—78	0,23	April 16	32	—83	0,20
March 11	—22	—69	0,20	April 19	32	—84	0,25
March 12	—5	—81	0,23	April 21	30	—87	0,10
March 12	—24	—71	0,27	April 23	25	—82	0,19
March 13	—10	—80	0,17	May 3	—1	—82	0,20
March 13	—27	—71	0,28				

*Commas represent decimal points.

TABLE 3. NATURAL RADIATION OF THE EARTH.

Date (1962)	Geographical coordinates of satellite in deg.		Q_E, W/m^2	Date (1962)	Geographical coordinates of satellite in deg.		Q_E, W/m^2
	latitude	longitude			latitute	longitude	
March 11	—17	—78	320	May 3	1	—81	354
March 23	17	—84	340	May 15	29	—85	334
April 3	25	—85	334	May 15	33	—85	292
April 5	21	—89	292				

The data from OSO-1 were obtained from an orbital altitude of 560 km [85]. The angle of inclination of the orbital plane to the equator was approximately 33°. The /27 regions falling within the field of vision of the radiation sensors are presented in Figure 1.12. They begin on the southeastern coast of North America and extend along the estern coast of South America. All the albedo values measured from the satellite are within the range from 0.1 to 0.38. Due to the absence of sufficiently complete meteorological data at the time of the experiments, the results of measurements were not compared with the state of the cloud cover in the zone of measurement.

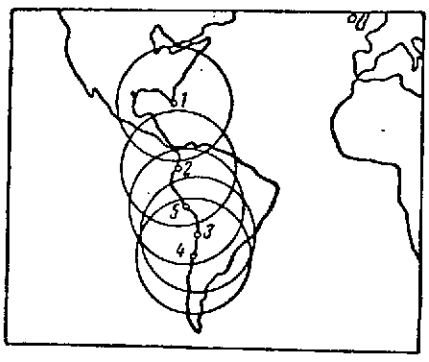

Fig. 1.12. Regions falling within the field of vision of the OSO-1 satellite during measurement of albedo and reflected radiation of the Earth: 1 — Fort Myers; 2 — Quito; 3 — Antofagasta; 4 — Santiago; 5 — Lima.

The experiments on OSO-1 and Tiros-4 cannot be considered complete and systematic. They only established that the Earth's albedo values, averaged over large regions of its surface, may vary within a broad range of values, and the average values for the regions investigated differ from the Earth's average spherical albedo. Seasonal variations of mean latitudinal distribution of albedo are presented in Figure 1.13.

The Earth's albedo also depends on wavelength, since the reflectivity of clouds and the ground cover have a spectral selective nature. Waves in the blue-green portion of the spectrum are scattered and reflected best of all, (up to 50%), somewhat /28 worse in the visible region (up to 40%) and even less in the infrared region (28%). The far ultraviolet region ($\lambda < 0.03$ micron) is almost completely absorbed by ozone in the upper layers of the atmosphere. Since, as indicated above, the cloud cover is the dominant factor in the albedo factor, the spectral composition of reflected radiation is determined to a significant extent by meteorological conditions.

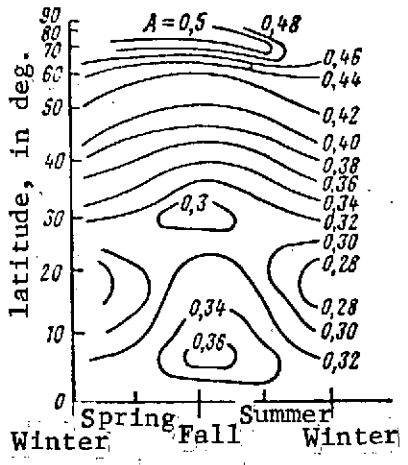

Fig. 1.13. Mean latitudinal distribution of albedo during different seasons for the northern hemisphere of the Earth.

Investigation of the spectrum of reflected radiation is much more complex than obtaining data on average albedo value. There are as yet few published papers in this area.

Two curves of spectral distribution radiation reflected from the Earth for a clear and cloudy sky are presented in Figure 1.14.

In view of the fact that clouds at various altitudes above the Earth's surface make the maximum contribution to the reflected flux, a correction for the Earth's radius for the value of the optically active layer H_0, which is approximately 12 - 15 km, must be introduced into energy calculations. /29

The natural thermal radiation of the Earth consists of the surface radiation of dry land, the seas, and the atmosphere. The Earth's surface temperature varies from 190°K (the Antarctic) to 340°K (rocky deserts). According to Planck's law, the maximum radiation of a black body having such temperatures is in the infrared portion of the spectrum at wavelengths from 14.5 to 8.7 microns. Moreover, more

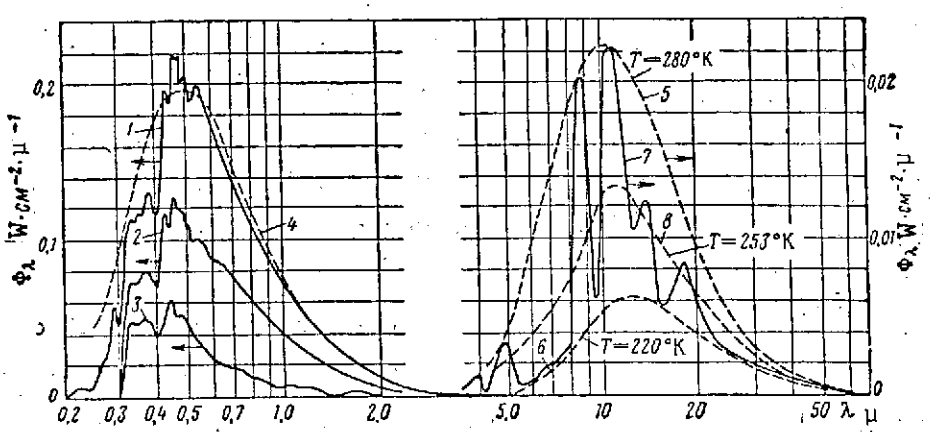

/28

Fig. 1.14. Spectral distribution of radiation from Sun and Earth: 1 — solar radiation beyond atmosphere; 2 — radiation reflected from Earth (cloudy sky); 3 — radiation reflected from Earth (clear sky); 4 — black body radiation at T = 5785°K; 5 — black body radiation at T = 280°K; 6 — minimum radiation from cloudy sky, T = 220°K; 7 — natural radiation of Earth; 8 — black body radiation with effective temperature of T = 253°K.

than 90% of the energy of infrared radiation is in the portion of the spectrum with a wavelength greater than 5 microns. The emissivity of dry land, water and vegetation is this infrared portion of the spectrum is very high and is equal to approximately 0.93 on the average for the entire Earth.

VALUES OF THE COEFFICIENT OF EMISSIVITY FOR DIFFERENT PORTIONS OF EARTH'S SURFACE

Surface	Emissivity (absorption)
Grass	0.96
Dry soil	0.9 - 0.95
Wet soil	0.98
Desert	0.89 - 0.91
Snow	0.995
Water	0.92 - 0.93
Entire surface of Earth (average)	0.93

A considerable portion of the Earth's surface radiation is retained by the clouds. Only about 2.5% of radiation is emitted directly from the Earth's surface through the so-called transparent windows, mainly at wavelengths of 8 and 11 microns. These bursts of radiation intensity are easily seen in Figure 1.14, where the spectrum of thermal radiation for the Earth as a whole is presented.

The peaks of the two more clearly expressed maxima are located on the curve, corresponding to black body radiation at 280°K or of a gray body with $\varepsilon = 0.93$ at 310°K. This temperature is close to the average temperature of the Earth's surface. On the whole, the Earth and its atmosphere emit 230 W from one square meter, which is equivalent to black body radiation at 253°K. The curve for an equivalent black body is also shown in Figure 1.14.

The interior portions of the Earth are strongly heated. Measurements show that the temperature of the Earth's core increases by 30°C for every kilometer. However, the thermal flux toward the surface, caused by this temperature gradient, is small compared to the heat received by the Earth from the Sun. Ignoring internal heat, the above-indicated average value of the Earth's natural radiation may be calculated in the following manner.

Absorbed solar energy, equal to $(1 - A)\, S_{\odot}\pi\overline{R}^2$ (where $\overline{R} = R_0 + H_0$ is the Earth's effective radius), is re-emitted uniformly from the entire area of the

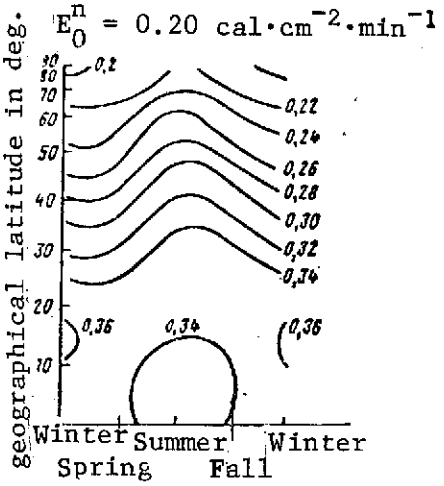

Fig. 1.15. Mean latitudinal values for Earth's natural radiation during different seasons.

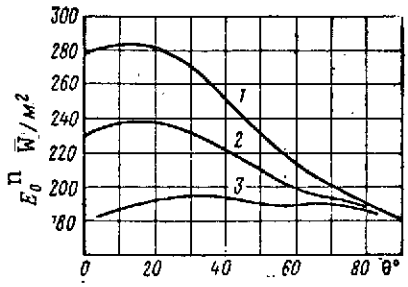

Fig. 1.16. Dependence of average intensity of Earth's infrared radiation on geographical latitude θ for different meteorological conditions: 1 — clear sky; 2 — average overcast; 3 — heavy overcast.

Earth's surface $4\pi R^2$. The Earth emits an average of $E_0^n = \frac{1 - A}{4} S_\odot$ per unit of its surface. For A = 0.35, E_0^n = 230 W/m^2.

In fact, the average intensity of the Earth's infrared radiation depends on geographical latitude, the season, and meteorological conditions. There are presently no reliable data on the actual distribution of the Earth's natural radiation for its different regions. Approximate functions of the distribution of mean latitudinal values of the Earth's natural radiation E_0^n during different seasons are presented in Figure 1.15. The effect of meteorological conditions on a variation of E_0^n is shown in Figure 1.16.

The Radiation of Venus [68], [87], [89], [92], [125], [132], [133]

The average distance of Venus from the Sun is 0.62 times less than that from the Sun to the Earth. Solar flux intensity for Venus comprises an average of 2698 W/m^2 annually. The orbital eccentricity is very slight (0.007), as a result of which seasonal variations of solar flux do not exceed ± 36 W/m^2 (i.e., less than 1.5%). A year on Venus lasts for 226 Earth days. Venus is surrounded by a uniform and dense atmosphere, completely opaque to rays in the visible portion of the spectrum. The albedo of Venus, according to data of various authors, is equal to 0.73 to 0.80. The atmosphere of Venus is a good reflector of visible rays. A decrease of reflectivity is noted in the violet and ultraviolet portions of the /31

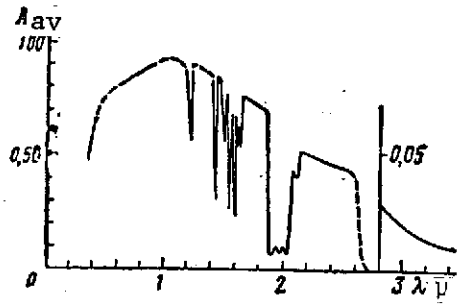

Fig. 1.17. Spectral albedo of Venus.

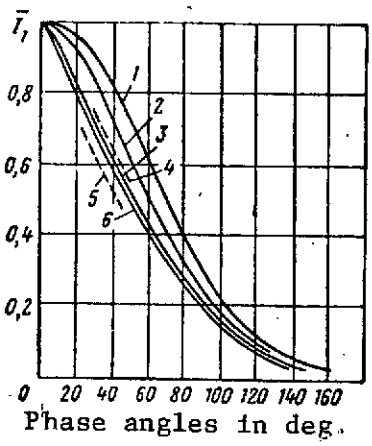

Fig. 1.18. Angular distribution of reflected radiation (in relative values) for the Earth, Mars and Venus: 1 — Lambert sphere; 2 — Venus; 3 — Earth; 4 — Mars (λ > 0.63 micron); 5 — Mars (λ > 0.5 micron); 6 — Mars (λ > 0.55 micron).

spectrum (Figure 1.17). Observations show that the optical homogeneity of the cloud cover of Venus is very high. The angular distribution of reflected radiation is close to Lambert's law (Figure 1.18).

It is assumed that the radiation absorbed by the planet is uniformly distributed over its entire surface and is emitted in the infrared spectrum by the upper layers of clouds at an effective temperature of about 234°K*. The average flux density of radiant energy in the infrared region is estimated at approximately 173 W/m^2.

Direct measurements of the temperature and density of the atmosphere of Venus, made by the first Soviet space station Venera-4, showed that the temperature of its atmosphere near the surface of the planet is approximately equal to 490°C. However, this radiation cannot pass directly through the thickness of the atmosphere, which creates a type of greenhouse effect.

The Radiation of Mars [14], [27], [36], [68], [80], [87], [89], [112], [125]

The average distance of Mars from the Sun is 1.52 times more than that from the Sun to the Earth, and therefore, the average annual solar flux intensity for it is considerably less than that for the Earth and is equal to 620 W/m^2. Somewhat greater than that of the Earth, the elongation of the orbit of Mars (eccentricity 0.093) leads to seasonal variations of the solar flux, comprising $\pm$ 117 W/m^2. The mean planetary spherical albedo of Mars is equal to 0.15. Since the atmosphere of Mars is less dense than that of Earth, the effect of atmospheric opacity and /32

*If we assume that the darkness of Venus in the infrared band is $\varepsilon = 1$.

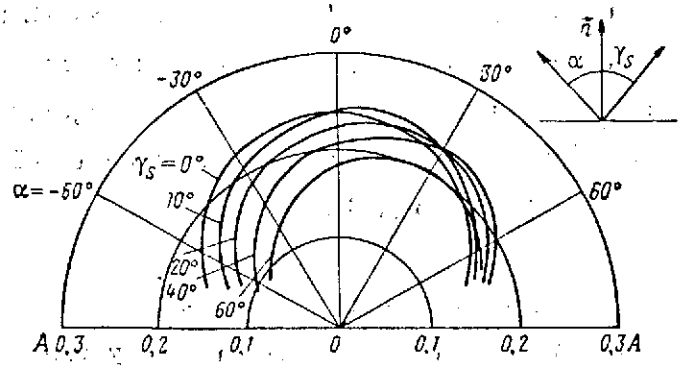

Fig. 1.19. Angular distribution of reflectivity (in the plane of incidence) of the light regions of the Martian surface for rays with a wavelength of $\lambda = 0.62$ micron.

seasonality of its variation on albedo are much more weakly expressed, but even so they exist.

The Lambert radiation of the underlying layer (soil) is distorted by diffuse scattering in the atmosphere of Mars. Because of this, through a telescope Mars appears as a sphere rather than as a disk, like the Moon [14]. This is especially discernible in photographs taken through a blue filter. The dependence of reflection on the angle of incidence for red rays, for which the atmosphere of Mars is transparent, is close to Lambert (Figures 1.18 and 1.19), at least up to a distance from the center of 0.85 of the radius, although during individual periods of observation the curves go higher than a Lambert curve. Most authors explain this by the increased dustiness of the Martian atmosphere at the moment of observation.

Knowing the albedo of the underlying surface and scattering in the atmosphere, the brightness of the planet's disk may be calculated for different wavelengths. The data of I.K. Koval' [80], [125] on the reflectivity for land masses in the center of the Martian disk (see table) may be presented as an example of such calculations.

REFLECTIVITY OF "CONTINENTS" IN CENTER OF MARTIAN DISK

λ, microns	A
0.360	0.06
0.429	0.11
0.53	0.175
0.647	0.252
0.75	0.33
0.84	0.41

Polar caps, apparently consisting of frozen CO_2 or snow crystals, are visible on the surface of Mars. The albedo of these locations may reach 0.7. Since the axis of rotation of Mars is inclined toward the plane of its orbit at almost the same angle as the Earth's axis, a /33 change of seasons is observed on it, which is manifested in a variation of the dimensions of the polar caps and the brightness of other portions of the planet.

The average temperature of the Martian surface is approximately equal to 260°K. The average temperature of the polar regions is 213°K, and in the equatorial

TABLE 4. SURFACE TEMPERATURE (°C) OF MARS FOR DIFFERENT LATITUDES AND TIMES OF MARTIAN DAYS

Latitude, deg	Hours, Mars time					
	7	8	11	12	13	14
+14	−78	−21	+10	+16	+14	+8
+10	−64	−19	+13	+26	+28	+15
+8	−54	−11	+18	+26	+23	+20
−2	−64	−16	+16	+22	+22	+7
−8	−55	−10	+19	+20	+20	+14
−12	−42	−6	+18	+18	+18	+8

regions it is 290°K. The temperature in the polar regions during the course of the year varies by 100 - 200°, and in the equatorial — by 30°. The observations of Sinton and Strong led to a calculation of the surface temperature (°C) of Mars for different latitudes and times of Martian days (Table 4).

The dark regions on the surface of Mars are approximately 20° hotter than the light regions. No small-scale temperature irregularities were observed. The infrared spectrum of Mars, obtained by F. Low with the aid of radiometric observations, indicates the presence of selective absorption. On the whole, it is similar to the radiation spectrum of an absolutely black body (Figure 1.20).

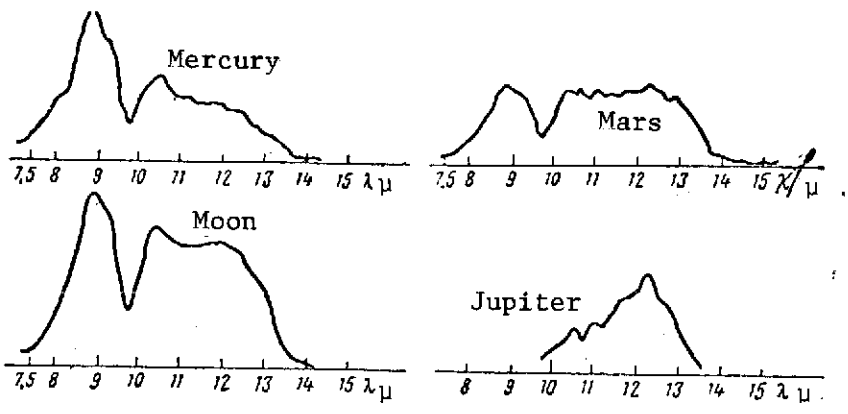

Fig. 1.20. Infrared spectra of Mercury, the Moon, Mars and Jupiter. The deep dip at 10 microns is the ozone absorption line of the Earth's atmosphere.

TABLE 5. ALBEDO FOR CERTAIN LUNAR FORMATIONS.*

Object	Coordinates: Selenographic latitude (deg)	Coordinates: Selenographic longitude (deg)	Albedo	Object	Coordinates: Selenographic latitude (deg)	Coordinates: Selenographic longitude (deg)	Albedo
Sinus Medium	+7	—8	0,054	Ptolemy Crater	—44	—53	0,108
Sea of Clouds	—23	—14	0,062	Aristotle Crater	+50	+17	0,110
Sea of Serenity	+28	+15	0,070	Copernicus Crater	+10	—20	0,120
Sea of Nectar	—15	+33	0,080	Tycho Crater	—43	—12	0,137
Sea of Nectar	—7	+26	0,089	Ray of Tycho Crater	—23	+25	0,163
Palus Somnii	+13	+43	0,095	Aristarchus Crater	+23	—47	0,176
Continent	0	+70	0,100				

*Commas represent decimal points.

Lunar Radiation [16], [19], [68], [76], [81], [110], [113], [125], [242]

Investigations of lunar surface brightness during various phases lead to a calculation of the spherical albedo of the Moon. It was found that the lunar sphere as a whole reflects approximately 7.3% of the solar radiation impinging on it. However, even simple visual observations of the brightness of different components of the lunar surface indicate that there are brighter and darker regions on the Moon for which albedo may differ considerably from average values. The brightest formations reflect about 18% of the radiation and the darkest spots (usually the "seas") — about 5% (Table 5).

The brightest point on the Moon is the bottom of Aristarchus Crater and its central ridge. They are almost 3.5 times brighter than the bottom of the seas.

If we compare the reflectivity of Aristarchus Crater with that of the most common rocks of Earth, it turns out that most Earth rocks are much brighter (see p. 28 and the data given below). /34

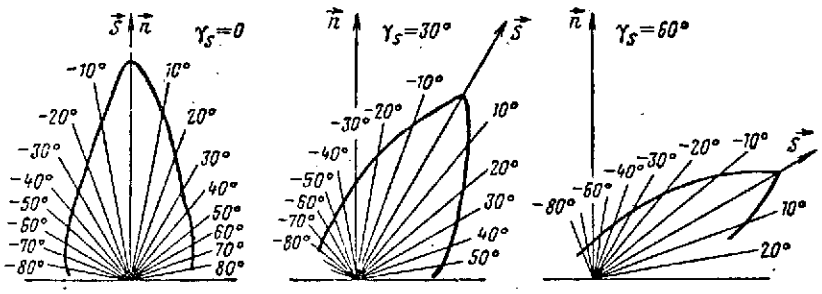

Fig. 1.21. Angular distribution of solar radiation reflected from Moon for three positions of the Sun above the lunar horizon (γ_s = 0°, 30° and 60°).

ALBEDO FOR SURFACES OF TERRESTRIAL OBJECTS

Object	Albedo
Sandstone	0.22
Clays and schists	0.25
Limestone	0.56
Trachytic lava	0.10
Basaltic lava	0.06
Granite	0.24
Basalt	0.14
Rock meteorites	0.18
Melted meteorite core	0.05
Chernozem	0.05-0.07

The lunar surface has a very remarkable and important characteristic, which distinguishes it considerably from even those Earth analogs for which albedo has close values. Precise photometric observations showed that solar radiation reflected by the lunar surface is distributed extremely irregularly in terms of direction, namely, that at any value of the angle of incidence of radiation the greater portion of light is reflected back toward the Sun (Figure 1.21). This follows from the experimental fact that maximum brightness of the lunar surface visible from the Earth begins when the directions toward the Sun and Earth coincide. During full Moon this condition is almost fulfilled. It is at this moment that any lunar formation seems brighter from the Earth. The increase in brightness toward full Moon begins simultaneously for all observed portions of the Moon, regardless of whether they are in the center of the lunar disk or on its edge. For this reason, a spherical Moon seems to be a flat, uniformly illuminated disk to the observer. This effect is absent in observations of Mars, Jupiter, Venus and the other planets having an atmosphere. The indicated properties of lunar reflectivity are the result of the extreme pitted nature, unevenness and porosity of the material of its surface. Investigations of lunar soil samples brought back to Earth by the Apollo crews and /36 by the Luna-16 probe showed that the lunar surface is actually covered with dark, extremely porous scoriaceous material.

The data averaged for the equator and presented in Tables 4 - 7 of the

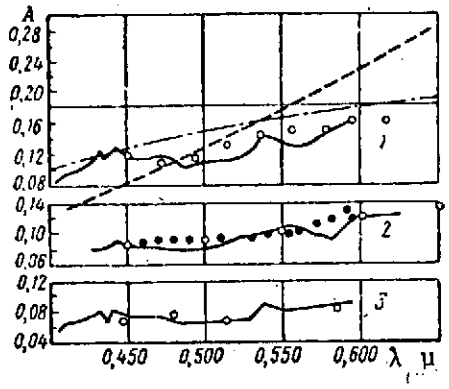

Fig. 1.22. Spectral reflectivity of sections of lunar and Martian surface: 1 — bottom of Schickard Crater; o — rhyolitic pechstein, broken line — "continents of Mars," dot-dash line — "seas of Mars"; 2 — embankment of Alphonsus Crater, o — brown scoria, • — tufaceous lava; 3 — Ocean of Storms, o — pechstein porphyry.

Appendix may be used in a quantitative calculation of the reflected radiation on the spacecraft, due to the absence of detailed photometric observations for each sector of the Moon. The values of reflected radiation in these tables refer to two cases: when incident radiation and the direction of observation are in the same plane and when incident radiation and the direction of observation are in two mutually perpendicular regions.

Not only albedo, averaged for the entire spectrum, but the spectral distribution of reflectivity must be known for the complete characteristics of the radiant flux reflected from the Moon.

Analysis of color photographs of the Moon showed that its surface is rich in varied shades encompassing the different regions of the spectrum. The Sea of Crises is greenish in the southern portion and reddish in the northern portion. The Sea of Tranquility and the mountain regions adjacent to it are bluish. The Sea of Serenity is reddish in the middle and has greenish strips near its southern and northern shores. The Sea of Rains has a mottled structure with reddish greenish and rust-colored regions. The strips around Tycho Crater and some mountain regions in the southern hemisphere are reddish. There are rather large spots of greenish color in the center of the lunar disk. It is assumed that the greenish tones are inherent to young formations and the reddish ones — to more ancient ones. Despite the richness of the color tones, on the whole, the color contrast of the lunar sectors is slight and comprises an average of 1 - 8%, although for individual sectors it reaches 20 - 25%. The spectral distribution of relative intensity for some lunar objects and the apparent albedo are presented in Table 6.

It is obvious from this table that the color gradation of the lunar surface is considerably less than that of the albedo. This is also confirmed by the course of the curves showing the dependence of albedo on wavelength for the continents and seas, both according to old observations made at the Potsdam Astrophysical Observatory as early as 1909 and according to new data [125] (Figure 1.22).

TABLE 6. SPECTRAL DISTRIBUTION AND ALBEDO OF LUNAR OBJECTS.*

Object	Spectral distribution of relative intensity in % of intensity at λ=0.5 microns				Albedo
	λ=0.45μ	λ=0.48μ	λ=0.50μ	λ=0.64μ	
Light spot in northwestern portion of Sea of Tranquility	88	95	100	136	0,095
Dark region in Sea of Serenity north of Menelaus Crater	90,5	90,5	100	116	0.069
Northern portion of embankment of Proclus Crater	102	92	100	142	0,163
Bottom of Copernicus Crater	115	105	100	144	0,120
Dark region in Sea of Crises	66	88	100	97	0,062
Bottom of Grimaldi Crater	106	84	100	96	0,062
Dark region in Sea of Rains between Archimedes and Carlini	96	102	100	118	0,064
Light region between Proclus and Macrobius Craters.	94	99	100	130	0,123

*Commas represent decimal points.

The surface relief of the back side of the Moon differs considerably from that on the side of the Moon facing the Earth. Photographs indicate that the seas on the opposite side of the Moon occupy approximately 10% of the entire surface, whereas they reach 25% on the visible side. This must be reflected in the average albedo. Based on the data of Table 5, we may assume that the albedo of the back side of the Moon is somewhat higher than that of the visible side. There are hardly any reliable data on the emissivity of the portions of the lunar surface in the infrared region. One of the averaged curves is presented in Figure 1.20. /37

Investigations of the polarization of the light reflected by the Moon indicated that the degree of polarization (P) depends on the phase angle (Figure 1.23) and is different for different sections of the lunar surface.*

Comparing the maximum values of the degree of polarization to the albedo of those same objects, the specific interrelationship of these values can be seen. The data presented in Figure 1.24 (with the exception of certain points) confirm /38

*See Section 9 of Chapter 4 for more details on polarization.

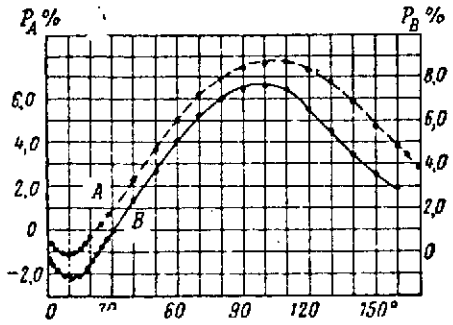

Fig. 1.23. Dependence of polarization of integral light (A) and volcanic ash (B) on phase angle.

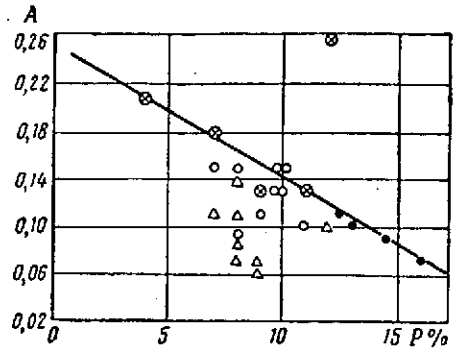

Fig. 1.24. Dependence of maximum value of positive polarization P of lunar objects on albedo: Craters: ⊗ — radiating; o — continental; Seas: • — large; Δ — crater.

that there is a general tendency for an increase in the degree of polarization as albedo decreases. Aristarchus Crater and the crater seas are an exception to the general rule. It is assumed [16] that the seas are related to ancient formations.

POLARIZATION OF LIGHT REFLECTED FROM MOON

Object	Degree of polarization in %
Bright spot in Furnerius	+ 4.8
Bay of Rainbows	+12.6
Sea of Nectar, northern portion	+12.1
Sea of Fertility west of Messier	+14.0
Sea of Rains northwest of Le Verrier	+15.5
Sea of Serenity north of Maskelyne	+16.0
Very dark spot between Eratosthenes and Mesting	+17.0

The Sun is the main source which determines lunar temperature. The temperature of the lunar surface illuminated by the Sun depends mainly on radiation coefficients and on the angle between the normal to the surface and the direction toward the Sun. Let us assume that the lunar surface is smooth and non-heat conducting. Then, ignoring the small angle between the plane of the lunar equator and the ecliptic plane (this angle is $\approx 1.5°$), we may express the dependence of lunar surface temperature on the zenith angle of the Sun (γ_s) and the latitude of /39
the locality (β) in the following manner:

$$T=\sqrt[4]{\frac{A_s}{\varepsilon}\frac{S_\odot}{\sigma}\cos\beta\cos\gamma_s}.$$

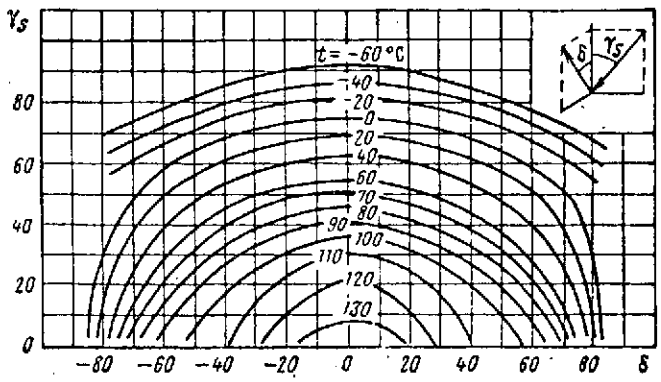

Fig. 1.25. Effective temperatures of thermal radiation of illuminated side of Moon. The plane of observation is perpendicular to the plane of incident radiation:
γ_s — angle of incidence in deg,
δ — angle of observation.

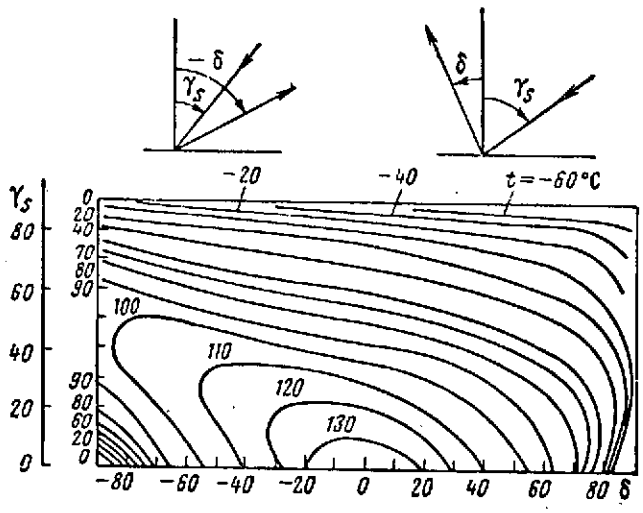

Fig. 1.26. Effective temperatures of thermal radiation of illuminated side of Moon. The plane of observation coincides with the plane of incident radiation:
γ_s — angle of incidence in deg,
δ — angle of observation in deg.

However, this dependence differs considerably from the observed distribution of effective temperatures. Observational data, averaged for the entire lunar disk, are presented in Figures 1.25 and 1.26. It is obvious from Figures 1.26 and 1.27 that the thermal radiation of the Moon has a discernible anisotropy in the plane of incidence of radiation, and the indicatrices of the thermal radiation of the Moon differ considerably from those of reflected radiation.

The asymmetry of the natural radiation of the moon was noted by Petit and Nicholson, when they measured the temperature of the subsolar point and discovered that the temperature (358°K) for the Moon during the last quarter is almost 50°K lower than that at the same point for a full Moon. In other words, lunar surface temperature was a function of the angle of vision. This difference was explained by the unevenness of the surface and by the very low heat conductivity, which prevented equalization of temperatures.

Anisotropy is observed for reflected radiation as well. When the Sun is at its zenith, reflected radiation is maximum and impinges on the spacecraft uniformly on all sides. However, for any other angles of inclination of the Sun ($\gamma_s \neq 0$), anisotropy of reflected radiation is disrupted. Standing with our backs toward the Sun, we see a considerably brighter landscape than we do when we

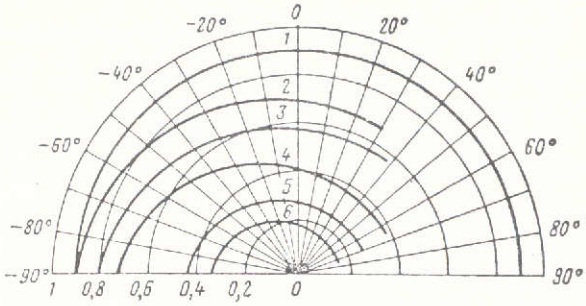

Fig. 1.27. Angular distribution of thermal radiation of lunar surface: curve 1 — $0 < \gamma_s < 30°$; curve 2 — $30° < \gamma_s < 40°$; curve 3 — $40° < \gamma_s < 50°$; curve 4 — $50° < \gamma_s < 60°$; curve 5 — $60° < \gamma_s < 70°$; curve 6 — $70° < \gamma_s < 80°$.

turn our face toward the Sun (Figure 1.28).

An analysis of photographs of the lunar surface, obtained with the aid of the Luna-9, Luna-13 and Ranger-7 spacecraft, indicates that for every 100 m^2 of lunar surface there is an average of one object measuring 1 - 2 m; 19 objects measuring 0.2 - 0.4 m; 64 objects measuring 0.1 - 0.2 m, etc. /41

According to A. Gurshteyn [19], the relationship between the number of rocks or clumps (N) and their dimensions (d) may be described by the mathematical formula

$$N = 3 \cdot 10^5 d^{-1.77}$$

These data may be taken as the reference data in a calculation of the anisotropy of reflected radiation as a function of angle γ_s.

The effect of radiation anisotropy may be found not only by being on the Moon,

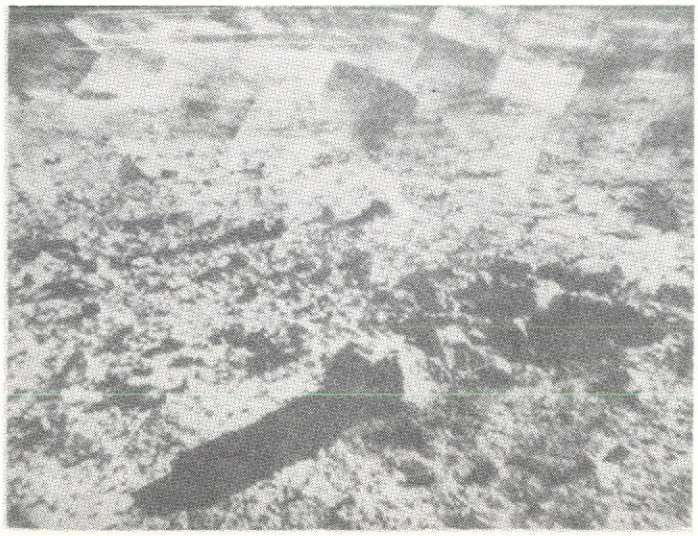

Fig. 1.28. Photograph of lunar surface from a distance of several meters.

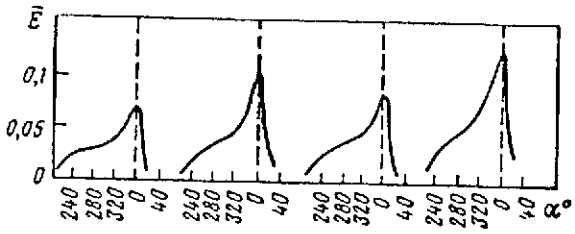

Fig. 1.29. Variation of brightness of various sections of lunar surface as a function of phase angle.

but also by observing the Moon from Earth. It is well known that the full Moon is approximately 9 times brighter than a quarter Moon, although the areas of the illuminated portions are related in a 2:1 ratio. This is mainly caused by the fact that near the terminator solar radiation impinges on the surface at a very sloping angle. Mountains, rocks and particles of sand throw long shadows, which reduce the average brightness of the surface.

The effect of a variation in intensity of reflected radiant flux from the lunar surface as a function of the angle of vision finds quantitative confirmation in the curves of lunar brightness variation from new Moon to new Moon, obtained by /42
N.N. Sytinskaya and V.V. Sharonov [19]. Referring to Figure 1.29, we see that the brightness initially changes slowly up to a maximum at full Moon, and then decreases rapidly. This asymmetry of the curves was found for all sections of the lunar surface independently of the absolute albedo.

The variation of lunar surface temperature during lunar eclipses is very similar to the temperature pattern of a body having extremely low thermal conductivity. We may assume that surface temperature for any solar zenith angle (angle γ_s) coincides with its equilibrium value. Temperature variations of the Moon during lunar eclipses indicate that the course of the temperature curve for rapid transitions from light to shadow during approximately one hour is close to equilibrium. The surface temperature of the Moon from the moment of total darkening of the Sun by the Earth rapidly approaches a minimum constant value $T^*_{min} \approx 173°K$. This temperature may occur if the flux, equal to approximately 30 - 40 kcal/m^2 hr, impinges on the surface from without, which corresponds to the temperature gradient of 1.5 deg/m in the upper layers of lunar soil [116]. Calculations of other authors do not differ greatly from the values presented.

Spectral values of albedo, temperature, polarization and degree of darkness, measured from the Earth, refer to sections of the lunar surface, whose dimensions are calculated by the resolving power of the optical instruments and comprise not less than several tens of kilometers (about 22 km in the best case and usually 100 - 200 km). It is assumed that there are outcrops of bedrock on the Moon which

have not yet been broken down by cosmic effects. However, the area of exposed rocks probably does not exceed 5% of the lunar surface [19], and their dimensions are no greater than 3 - 5 km, which is beyond the resolving power of optical instruments during observation from Earth. Such outcrops may be anticipated in the region of the steeper slopes of the lunar Apennines, Alps, on the 41-degree slope of the /43 Straight Range, on the steeper walls of ridges and on the inner steep slopes of the walls of young cirques. The surface structure of the Moon, which can be seen from photographs, obtained with the aid of automatic lunar probes (see Figure 1.28), leads to the assumption that temperature, albedo, polarization and color contrast at close range probably have a wider range of values than indicated above.

The temperature field of the Earth from the flight altitude of a satellite also seems more uniform than the actual value.

The Radiation of Mercury [8], [87], [125], [132]

Mercury is the planet nearest to the Sun. Its period of rotation around its own axis is equal to 59 $\pm$ 5 Earth days. The period of rotation around the Sun is 87.97 days. Maximum temperature on the illuminated side reaches +413°C. The probable temperature on the shaded side is -130°C. Temperature does not equalize, because the planet is devoid of an atmosphere. The surface of Mercury, devoid of any gaseous protection, has been subjected for a long period of time to the effects of cosmic rays and micrometeorites. The albedo of Mercury, like that of the Moon, is approximately equal to 0.07. However, the infrared spectrum of Mercury differs from that of the Moon. This difference is greatest of all at wavelengths from 10 to 13 microns (see Figure 1.20).

Because of the elongation of its orbit, the intensity of solar radiant flux for Mercury varies almost twofold — from 6240 to 12,560 W/m^2.

The Radiation of Jupiter, Saturn, Uranus, Neptune and Pluto [87], [125], [132]

Solar flux intensity on the orbit of Jupiter is almost 26 times less than that of Earth and comprises 52.8 W/m^2. This is very low energy. As an example, we may point out that a black body under solar radiation in the orbit of Jupiter is heated only to a temperature of -100°C, whereas on Earth it would reach an equilibrium temperature of +121°C.

As a result of internal heat liberation, the natural radiation of Jupiter exceeds the heat which it receives from the Sun threefold.

Solar radiation in the orbits of Saturn, Uranus, Neptune and Pluto is weaker than that in the Earth's orbit by 90, 360, 900 and 1500 times, respectively.

The albedo of Jupiter, Saturn, Uranus and Neptune is almost the same as that of Venus and the albedo of Pluto — as that of Mars (see Table 2 of Appendix).

4. Corpuscular Radiation in Circumterrestrial and Interplanetary Space and Meteor Material /44

Interplanetary space is permeated by corpuscular and electromagnetic radiation, generated by the Sun and galactic cosmic rays, and accumulations of micrometeorite particles and particles of planetary origin are encountered.

Due to the presence of a magnetic field near the Earth, there are relatively stationary radiation zones around it (Figure 1.30) [67], [115], the so-called radiation belts of the Earth. The inner and outer radiation belts were discovered during the launch of the first satellites and spacecraft [32]. There is a region of low-energy transient electron flows beyond the outer radiation belt.

Combined data on corpuscular flows in circumterrestrial and interplanetary space, which permit comparison of the energy, flux density and type of particles in the different regions of space, are presented in Figure 1.31 [48].

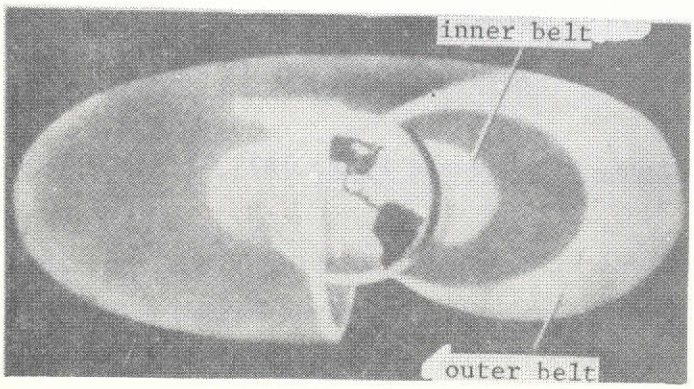

Fig. 1.30. Diagram of Earth's radiation belts.

Region 1 refers to the interaction of the external surface of spacecraft and particles of the upper layers of the Earth's atmosphere and the atmospheres of other planets at orbital and superorbital flight speeds, as well as in the presence of ion and plasma engines on-board spacecraft. These particles consist mainly of molecules, atoms

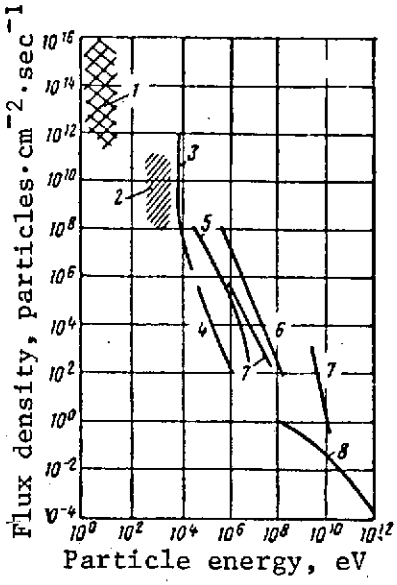

Fig. 1.31. Dependence of corpuscular flux density on the energy of particles in circumterrestrial and interplanetary space (combined data): 1 — corresponds to interaction of the outer surface of an artificial Earth satellite and particles of upper atmosphere of the Earth and other planets (depending on the orbit and speed of the satellite); 2 — solar plasma protons; 3 — electrons in zone of auroras; 5 — electrons captured in radiation belts of Earth; 6 — protons of Earth's radiation belts; 7 — solar flare protons; 8 — galactic cosmic rays.

and ions of oxygen, nitrogen, helium, hydrogen and carbon dioxide.

The flux density of low-energy solar corpuscular radiation (the solar wind) is characterized by region 2. Steady flows of solar wind beyond the limits of the Earth's magnetosphere, or rather beyond the limits of the shock wave, have an average flux density of 3.10^8 protons/ /45
$cm^2 \cdot sec$ at an average particle energy of about 1.5 KeV at the level of the Earth's orbit. Unsteady flows of solar plasma, especially during active Sun years, may reach values of 10^{10} to 10^{11} protons/ $cm^2 \cdot sec$ at a particle energy of 5 - 10 keV.

Corpuscular flows, which cause the auroras, correspond to curves 3 — electrons, and 4 — protons. These particle flows are observed mainly at high latitudes at distances of 100 - 500 km from the Earth's surface.

Curves 5 and 6 correspond to electrons of the outer and protons of the inner radiation belts of the Earth. The inner radiation belt consists of high-energy protons with an energy up to several hundred MeV. The flux density of protons with an energy greater than 40 MeV is equal to $\sim 10^4$ protons/$cm^2 \cdot sec$ at the center of the inner zone of the radiation belt and the flux density of protons in the range of 0.1 - 4 MeV comprises $\sim 10^8$ protons/$cm^2 \cdot sec$.

The outer radiation belt consists primarily of electrons with an energy up to several MeV: flux density at E > 1.6 MeV comprises $\sim 10^4$ el/$cm^2 \cdot sec$ and at E > 40 keV comprises $\sim 10^8$ el/$cm^2 \cdot sec$. Protons having an energy of several tens of megaelectron volts are essentially absent in the outer radiation belt, but proton flows with an energy up to several MeV may reach $\sim 10^8$ protons/$cm^2 \cdot sec$.

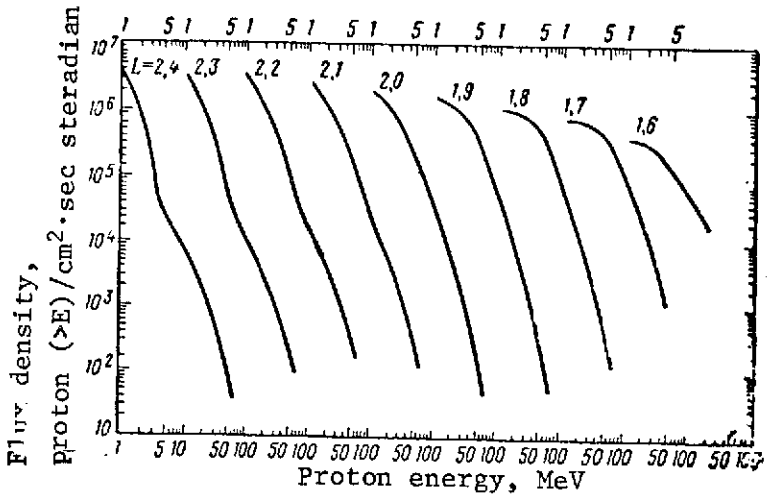

Fig. 1.32. Energy spectra of captured protons in the equatorial plane for different values of parameters L (L characterizes the magnetic envelope. The numerical value of L is equal to the distance in units of the Earth's radius in the equatorial plane of the magnetic dipole from the center of the magnetic envelope).

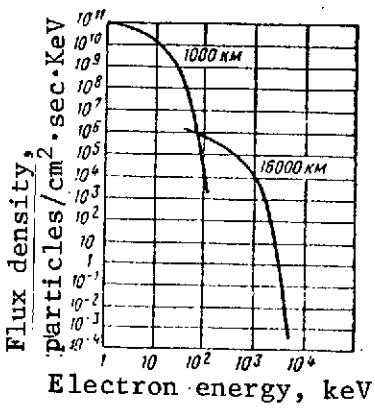

Fig. 1.33. Comparison of electron energy spectrum, typical for the center of the outer zone of the radiation belt at an altitude of 15,000-20,000 km, with a spectrum of more intensive electron flows than those known up to the present, discovered at an altitude of 1000 km near the zone of the auroras.

Typical energy spectra of protons and electrons in the natural radiation belt of the Earth are presented in Figures 1.32 and 1.33. Figure 1.34 shows the spatial distribution of protons near the Earth. The central region of the inner radiation belt is located at a distance of approximately 3500 km from the Earth's surface in the plane of the geomagnetic equator. The central zone of the inner radiation belt is filled with electrons having an energy from fractions up to several MeV, and is located at a distance of 15,000-20,000 km from the Earth's surface in the plane of the Earth's geomagnetic equator. /46 The Earth's outer radiation belt, unlike the inner belt, is unstable, and its parameters depend on the geomagnetic situation. One should not think that the radiation situation near the Earth is determined only by captured radiation. In particular, particle flows are observed in the polar regions. Their energy is considerably lower than that of particles captured by the geomagnetic field.

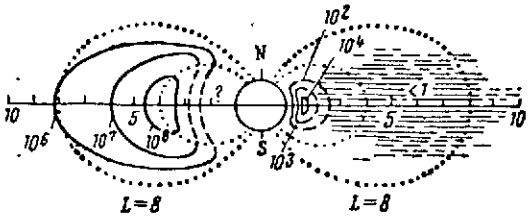

Low-energy $0.1<E_p<4$ MeV High-energy $E_p>40$ MeV

Fig. 1.34. Proton flux density (proton·cm^{-2}·sec^{-1}) of comparatively low ($0.1<E_p<4$ MeV) and comparatively high ($E_p>40$ MeV) energies. High-energy proton flux densities in the cross-hatched zone vary with time.

The main portion (~99%) of positively charged particles in the Earth's inner radiation belt consists of protons. The injection mechanism of particles into the inner radiation belt has not yet been completely determined. It is assumed that it is related mainly to radioactive decay of neutrons, formed as a result of nuclear interactions of cosmic rays and particles of the Earth's atmosphere.

The nature of charged particle flows in the outer radiation belt in the auroral zone is determined mainly by penetration of particles from the solar plasma. The presence of high-energy particles in these regions indicates the existence of certain acceleration processes. Along with continuous inflow of new particles into the Earth's magnetosphere, there is a reverse process — decay of charged particles due to interaction with particles of the Earth's upper atmosphere.

Artificial radiation belts of electrons, the average energy and intensity of which may exceed similar parameters in the natural radiation belt, develop as a result of detonation of atomic and thermonuclear devices in the upper layers of the atmosphere. The main source of electrons in the artificial belts are radioactive fission fragments and neutrons. Several nuclear explosions have been conducted since 1959 in the upper layers of the atmosphere, as a result of which artificial radiation belts have developed [92], [93]. The artificial electron belt, formed on 9 July 1962 after a thermonuclear blast with a TNT equivalent of 1.4 megaton, conducted by the United States under the codename "Starfish" above Johnston Island at an altitude of 400 km, has been studied best of all [93]. The Earth's magnetic field captured 10^{25} to 10^{26} electrons, formed as a result of this detonation. Radiation intensity in the artificial belt is gradually decreasing /48 due to interaction of the electrons with the upper layers of the atmosphere. The lifetime of the artificial belt is measured in several years [92], [115].

Intensive particle flows, which affect the parameters of the upper layers of the atmosphere (so-called "geoactive particle flows"), are observed in the region of the auroral zone and more rarely at lower altitudes. These flows consist of

electrons and protons having an energy up to several hundreds keV. One of the causes of such flows is ejection of charged particles from the Earth's radiation belt. Powerful particle flows of comparatively low energy, unrelated to the presence of the radiation belt, are the cause of the auroras.

Particle flows with an energy up to a thousand erg/cm^2·sec were recorded during rocket investigations in the auroral zone, which corresponds in recalculations to monoenergetic particle flows having a maximum particle flux density with an energy of about 1 keV of approximately 10^{11} to 10^{12} particles/cm^2·sec. Both protons and electrons were discovered. /49

Due to hydrodynamic expansion of the solar corona, the Sun steadily emits particle flows with an energy on the order of 1.5 keV — the solar wind.

The positive component of solar corpuscular radiation consists mainly of protons. About 10% of the particles are helium ions.

Protons with an energy up to 1000 MeV are generated during chromospheric flares on the Sun. The duration of a solar flare is several hours, but the increase of total corpuscular radiation intensity as a result of the flare may be longer. Solar flares are conditionally divided into several classes. It is assumed that the integral flow of particles having an energy greater than 30 MeV in large flares exceeds 10^8 particles/cm^2 during the entire period of the flare. The concentration of helium ions in the total flow of particles, generated during solar flares, comprises approximately 10%. The fraction of heavier ions does not exceed one percent.

Composite data characterizing the various types of corpuscular radiation in circumterrestrial and interplanetary space are presented in Table 7.

Micrometeorite Particles

Along with the elementary particles in circumterrestrial and interplanetary space, there are micrometeorite particles and particles of planetary origin having a mass from 10^{-14} to 10^{-8} g. These particles do not present a direct danger to the vitally important spacecraft parts, but may cause surface erosion of materials, which is reflected in the heat balance or operation of optical systems.

TABLE 7

Main radiation zones	Type of particles*	Particle energy	Maximum observable flux densities, particle/ $cm^2 \cdot sec$
Earth's protonosphere	p	~1 keV	10^9
Earth's electronosphere	e	~1 keV	10^9
Earth's inner radiation belt	p	>0.1 MeV	10^8
		>30 MeV	10^5
		>40 MeV	10^4
Earth's outer radiation belt	e	>0.1 MeV	10^8
		>0.6 MeV	10^7
		>1.5 MeV	10^5
Earth's artificial radiation belt of Starfish type	e	>40 keV	10^9
		>1.0 MeV	10^8
		>5 MeV	10^7
Particle flows causing auroras	e	1-10 keV	$10^{11} - 10^{12}$
	p	~100 keV	10^6
Solar cosmic rays	p	>5 MeV	$10^5 - 10^6$
	α	>5 MeV	$10^4 - 10^5$
Solar wind	p	~1.5 keV	$3 \cdot 10^8$
	α	~5 keV	$5 \cdot 10^7$
Solar low-energy transient corpuscular flows	p	~5-10 keV	$10^{10} - 10^{11}$
	α	~5-20 keV	$10^9 - 10^{10}$

*p — protons; α — helium ions; e — electrons.

The main data on micrometeorite particles have been derived from observations of zodiacal light and by direct recording with piezoelectric and other instruments mounted on rockets and satellites by Soviet and American investigators.

Micrometeorite particles may consist of rocks and iron-nickel compounds with a density of $\rho \approx 3$ and $\rho = 7.8$ g/cm^3, respectively. Brittle micrometeorite particles of conglomerate dust particles with a density of $\rho \approx 0.5$ g/cm^3 are found. The velocities of micrometeorites with respect to Earth are within the range of 12 - 72 km/sec. Interaction of the spacecraft with particles of planetary origin is determined by the speed of the spacecraft and particle concentration.

A generalized dependence of flux density $j_m^{\cdot}$ of micrometeorites on their mass m, derived on the basis of numerous investigations at a distance of several hundred kilometers from the Earth's surface [67], is presented in Figure 1.35. If we /50

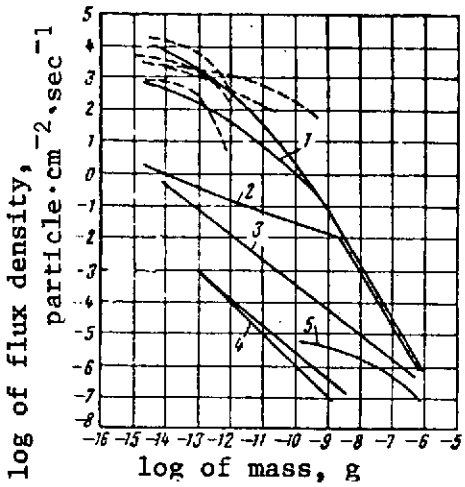

Fig. 1.35. Generalized data showing the dependence of flux density of micrometeorites and particles of planetary origin on mass in circumterrestrial and interplanetary space.

assume an average velocity of micrometeorites equal to 30 km/sec, the dependence of $j_m(m)$ (curve 1) in the range of masses from 10^{-6} to 10^{-10} g may be described by the equation $\log j_m = -17.0 - 1.70 \log m$. The increment of flux density in the range of micrometeorite masses less than 10^{12} g decreases appreciably. This fact is apparently caused by the circumstance that particles with a mass less than 10^{-12} g are "swept out" by solar light pressure beyond the limits of the solar system, since the ratio between the gravitational forces and force of light pressure for particles of such small dispersion varies toward an excess of light pressure.

As a result of recent application of various methods of recording micrometeorites and direct sampling of particles of planetary origin in circumterrestrial space [258], data have appeared which indicate that the flux density of micrometeorites having a mass below 10^{-8} g in the region of the Earth is several orders lower (curve 2).

The relation $j_m(m)$ (curve 1) is not very reliable, because the experimental data from which it is constructed were obtained by microphone and acoustical sensors having high noise levels [258]. In connection with this, the data represented by curve 1 should be regarded only as the upper limit of total flux density of micrometeorites and particles of planetary origin in circumterrestrial and circumlunar space in the calculation of spacecraft surface erosion.

Curve 2 characterizes $j_m(m)$, obtained in the region of masses less than 10^{-8} g during the flight of the Gemini S-10 spacecraft. Curve 3 is a compromise between the readings of S-10 and the Pegasus artificial satellite (curve 5). The dashed curves correspond to experiments on sampling cosmic dust with the aid of rockets launched during passage of the Earth through micrometeorite flows. Curves 4 were derived from data on calculation of the luminescence of zodiacal light.

There is reason to assume that there is an increased coneentration of dust particles of lunar origin near the lunar surface, compared to interplanetary space. /51 This dusty atmosphere is apparently continuously replenished by fragments of lunar soil as a result of interaction of primary meteor particles with the lunar surface. The basic mass of such particles should have a velocity up to 1 - 2 km/sec. The concentration of dust particles near the Moon may exceed by several orders the concentration of primary micrometeorites, which is related to the fact that hundreds and thousands of fragments occur upon impact of a primary meteor on the lunar surface.

5. The "Darkness" and "Cold" of Space

Various types of radiation, which, impinging on the spacecraft surface in space, may directly or indirectly lead to changes in its thermal conditions, were considered in the preceding sections.

If we disregard the radiation of the Sun and the nearby planets, the total remaining energy of the so-called background radiation of the stars, galaxies and cosmic rays is negligible. The density of this energy is estimated at approximately 10^{-5} W/m^2 in any direction. A black body at a temperature of about 4°K emits such energy. The term "cold" space is sometimes used in this sense.

Of course, this value in no way characterizes the kinetic temperature of the particles of interstellar and interplanetary medium.

The temperature acquired by a body devoid of internal heat sources in space depends on its emissivity (extent of darkness) and capacity to absorb incident radiation. Theoretically, the equilibrium temperature of a body may become very close to the kinetic temperature of even a strongly rarified medium, if the ratio of radiation and absorption coefficients is rather small. Such a hypothetical body could be used as a thermometer of the space medium. However, without going into the details of this problem, we note that the generally accepted concept of temperature for space has no meaning, because the particles penetrating it from all possible directions are not in thermodynamic equilibrium (at least on scales of the solar system).

Another important characteristic of radiant exchange for space is its "darkness." The dimensions of spacecraft flying in space are too small and the distances to the planets and stars are too great to calculate reflection and return of the rays emitted by spacecraft surfaces. We can assume with very great accuracy /52 that space absorbs all radiation emitted by the spacecraft surface, as an ideal black body. However, if the dimensions of bodies are comparable to the distances between them, mutual radiant exchange must be taken into account, for example, in those cases when the mutual heat exchange by radiation of two or more spacecraft a short distance from each other is being investigated or when a spacecraft is located on the Moon, or during consideration of the radiant exchange between the Earth and Moon, etc.

CHAPTER 2
INFLUENCE OF THE SURROUNDING MEDIUM ON A SPACECRAFT

1. Space Vacuum

Loss of materials. The low pressures in space cause accelerated sublimation /53
(evaporation) of the surface layers of the materials used in spacecraft (metals, nonmetals, etc.) [68], [207].

Sublimation leads to loss of the mass of materials, disturbs its surface properties, and produces other effects.

The state of the surface (surface stress, contamination) may change the sublimation rate. Approximate estimates of the sublimation rates may be made with formulas (3.122) — (3.125), which only give the order of magnitude of the phenomenon occurring in actuality in space. When a more precise value of the sublimation rate is required, this rate must be verified experimentally under conditions which simulate space conditions.

Electromagnetic and corpuscular radiation are also in effect in a spacecraft simultaneously with a vacuum. Since the binding energy of atoms (molecules) in the material may be lower than the energy of the corresponding forms of radiation (quanta or particles), the combined action of the vacuum and the radiation may intensify the sublimation effect. This is particularly important for those materials which vigorously absorb radiation (for example, for Fe_2O_3 and ZnO, which vigorously absorb ultraviolet radiation).

Sublimation of temperature controlling coverings has been studied in a vacuum ($\sim 10^{-7}$ torr) during the simultaneous action of ultraviolet radiation, with a strength equal to a 10-fold strength of solar radiation. When exposure lasts for several days, only certain pigment substances, which contain ethylene propylene fluoride, do not indicate significant sublimation. The majority of coverings revealed a significant weight loss during tests in a vacuum for one week at a temperature of 20°C.

Change in optical radiation characteristics. The optical radiation characteristics of surfaces will change when the protective gas and oxide films are removed, /54 and also when there is sublimation of the surface layers having a thickness which is a multiple of the radiation wavelength.

The results of studies on the concurrent action of a superhigh vacuum ($\sim 10^{-8}$ torr) and ultraviolet radiation ($\geq$2200 Å) on certain temperature controlling coverings have indicated that in white coverings the reflectivity usually increases as a result of such action. Organic paints usually change more than inorganic paints.

The optical radiation characteristics of materials at rather low temperatures cannot change greatly, due to the low sublimation rates and the fact that there is no change in the composition. However, very small losses of O_2, and also possibly N_2 and H_2O, in a vacuum at high temperatures may cause significant changes in the reflectivity of certain types of ceramics.

Deterioration of heat transfer. There is practically no convective heat exchange or thermal conductivity of the medium in a vacuum, and the transfer of heat only occurs due to radiation exchange. In addition, in a vacuum it is difficult for heat to pass through parts of the spacecraft which are statically contiguous, due to the presence of micro-nonuniformities of the surface and vacuum areas between them.

Heat transfer in a space vacuum, under the condition that the flow of molecules to the spacecraft surface is small (i.e., when the spacecraft moves not in dense, but in rarified layers of the atmosphere, or in interplanetary space), takes place practically entirely due to radiation.

There are three regimes for gas flow, and in accordance with this there are

three regimes for heat transfer in a gas: viscous, molecular-viscous, and molecular.

The boundaries between the regimes are approximately determined by the values of the dimensionless Knudsen criterion (Kn). The Knudsen criterion equals the ratio of the mean free path l of gas particles to the characteristic linear dimension of this system L_0 ($Kn = \frac{l}{L_0}$).

The regime boundaries are as follows: $Kn < 0.005$ — for a viscous regime; $0.005 < Kn < 5$ — for a molecular-viscous regime; and $Kn > 5$ for a molecular regime [43].

Heat transfer in a gas depends greatly on the gas flow regime. With a viscous and molecular-viscous regime, the heat transfer is comprised of the transfer of heat by thermal conductivity, convection, and radiation. In a molecular regime, convection and thermal conductivity are negligibly small, and heat is transfered primarily due to radiation exchange.

It is known from the kinetic theory of gases that thermal conductivity of a gas in a wide range does not depend on pressure. When the mean free path of gas molecules becomes greater than the characteristic dimensions of the system, the thermal conductivity coefficient begins to decrease in proportion to the pressure. With a change to the molecular regime, the gas thermal conductivity becomes negligibly small. For example, at $p \sim 10^{-4}$ the thermal conductivity of air is 0.01% of the thermal conductivity of air at atmospheric pressure [43]. /55

Change in the accommodation coefficient. The coefficient for energy exchange between a gas and a solid surface — the coefficient of thermal accommodation α_t — depends essentially on the state of the spacecraft surface. The presence or absence of surface films (absorbed, oxide) may change greatly the accommodation coefficient.

Thus, the accommodation coefficient for helium on "pure" tungsten is $\alpha_t \approx 0.017$, and on tunsten with an adsorption film — $\alpha_t \approx 0.5$ [268]. The accommodation coefficient may have a great influence on the spacecraft thermal regime when it moves in dense atmospheric layers.

Change in thermal conductivity and electroconductivity. As a result of the gas separation of materials and the loss of highly volatile components when the materials remain for a long period of time in a space vacuum, the properties of the materials, which are connected with the thermophysical and dielectric characteristics (thermal conductivity, electroconductivity, etc.) may change.

Pulverization of material. When a spacecraft moves in dense atmospheric layers, and is also bombarded by charged particles in space, the material of the spacecraft surface may become pulverized. This process has the greatest influence on the leading (in the direction of motion) parts of the spacecraft. The layer of pulverized material is usually small (at the maximum up to 50 - 100 Å per year). In addition, when the spacecraft moves in the "solar wind" or in the hydrogen corona of the earth diffusion of hydrogen ions in the surface layers of the material may occur, as a result of which they are enriched with hydrogen (saturation up to ~10%). This may change the optical characteristics of the materials.

Change in the mechanical (surface and volumetric) properties. At extremely low pressures in space, the external or internal dividing surfaces in the materials may be disturbed, as a result of which the mechanical properties of the materials change. This may be a result of microscopic surface cracks, or intergranular corrosion. The absence of oxide or other surface protective films may have an appreciable influence on the mechanical properties of materials, particularly when areas of the greatest stresses are being considered.

In addition, due to a change in the properties of the surface layers, the volumetric-mechanical properties of the materials may change also (creep strength, fatigue stress, etc.). /56

Change in the surface electrical conductivity, and the development of discharges. Significant electrical charges may be applied to the surfaces of dielectrics in space, and discharges may occur between the current-carrying parts. In addition, the electrical conductivity of surface layers, which depends on their physical condition, may lead to the development of current leakages on the surface. The propagation of high-frequency electromagnetic signals along the conductor surface (the so-called "skin-effect") in a space vacuum will also change.

Increase of adhesion (cohesion) in a vacuum, intensification of friction, and wear. Under normal atmospheric conditions, the surfaces of materials are protected with oxide films. In their turn, these films are covered by adsorption gas layers. In a vacuum, the adsorption surface gas layers are volatilized, and the oxide films may be disturbed. Due to this, adhesion (cohesion), i.e., adhesion of materials, increases and friction is intensified.

This pertains to the negative influence of a vacuum.

At the present time, studies are being conducted on the beneficial use of a space vacuum:

a) to form inflated and frothing structures in space;

b) to control the position and stabilization of spacecraft by means of diffusion and sublimation surfaces [248];

c) to create sublimation microengines [263], etc.

2. Flux of Radiant Planetary Energy Falling on a Spacecraft

Models of planets for calculating the radiant flux falling on a spacecraft

The density of planetary radiation flux Φ impacting on a spacecraft is a function of the radiation characteristics of the region on the planet which is visible from the surface of the spacecraft.

As has already been indicated, the planetary radiation characteristics depend on the properties of its surface and atmosphere, if it exists, and also on the distribution over the surface of the density of the flux of solar radiation falling on it. Consequently, nonuniformity of radiation characteristics may be either regular in nature, which is due to the nonuniformity of the illumination of the planet by the Sun or it may have random variations caused by the condition of the atmosphere in that region of the planet above which the spacecraft is located, the properties of the surface, etc. (See Section 3, Chapter 1). /57

Due to the fact that at each moment of time radiation from a relatively large region on the planet impacts on the spacecraft, and also due to the thermal inertia of the spacecraft, local nonuniformity of the planetary radiation characteristics

has only a slight influence on its thermal regime. Thus, for example, if it is assumed that the density of radiation impacting the spacecraft fluctuates with respect to a certain average value, which changes monotonically, with the amplitude ± 30% and a frequency of one oscillation per ten minutes (at an altitude of 200 - 250 km the artificial Earth satellite passes over an area with a diameter of ~2500 km), then the oscillation amplitude of the temperature of an absolutely black, aluminum shell with a thickness of 2 mm does not exceed 1% of a certain average value, corresponding to the average value of the incident flux.

Therefore, the simplest model of a planet provides the basis for calculating and simulating the planetary radiation impacting on a spacecraft. This model is based on averaging its radiation characteristics over a large region or even over the entire surface. The planet is thus regarded as a spherical body which radiates and reflects in a diffuse manner, and has an effective radius of $\overline{R}$. The planet effective radius is introduced to calculate the atmospheric radiation, if it exists. The planetary radiation impacting on the spacecraft is comprised of the radiation from its surface and the atmospheric radiation. Therefore, to determine the thermal influence on a spacecraft it is assumed that the distance between the spacecraft and the planet equals the distance from the spacecraft to the upper boundary of the effective radiation layer of its atmosphere, i.e., it is assumed that the effective radius of the planet is

$$\overline{R}=R_0+H_a,$$

where R_0 is the average radius of the planet; H_a — upper boundary of the emitting layer of the atmosphere.

Table 8 gives the values of $\overline{R}$ assumed for different planets.

TABLE 8. VALUES OF THE COEFFICIENTS C_1 AND C_2 FOR CERTAIN PLANETS OF DIFFERENT TYPES AND THE MOON

Planet	$\overline{R}$ km	C_1 W/m^2	C_2 W/m^2	Model type	H_a km
Venus	6230 - 6280			1	30 - 80
Earth	6383			1	12
Moon	1736	5	1300	2 – 3	0
Mars	3380 - 3390	46	310	3	0 - 10

It is necessary to know the albedo, density, and strength of the planetary and /58 reflected solar radiation in order to calculate and simulate the planetary radiation impacting on a spacecraft.

The planetary albedo is averaged, and it is assumed to be constant over the entire surface of the planet.

The strength of the radiation, in view of the assumed diffuse law of radiation, is π times less than the radiation density:

$$J_0 = \frac{1}{\pi} E_0. \tag{2.1}$$

The density of reflected solar radiation for all planets is assumed to be proportional to the albedo and the density of the incident solar radiation:

$$E_0^r = A_{av} S_\odot \frac{\cos\psi_0 + |\cos\psi_0|}{2}. \tag{2.2}$$

Here ψ_0 is the zenith distance of the Sun for an element on the surface of the planet, from which the radiation is established, i.e., the angle between its external normal and the direction of the Sun;

$S_\odot$ — solar constant, i.e., the quantity of energy in the solar radiation passing per unit time through a unit area which is normal to the solar rays.

(Using the form (2.2) eliminates the necessity of indicating that on the shadow side of the planet, where $\psi_0 \geq \frac{\pi}{2}$, the density of reflected solar radiation equals zero).

The density of self radiation for different planets is approximated in a different manner. Depending on the distribution over the surface of the planet of the density of self radiation (see Chapter 1, Section 3), all planets may be divided into three types.

The first type pertains to planets with the most uniform distribution of self radiation density. For them, it is assumed to be constant over the surface, and is determined from the thermal balance of the planet as a whole

$$\pi R^2 (1 - A_{av}) S_\odot = 4\pi R^2 E_0^e, \quad E_0^e = \frac{1 - A_{av}}{4} S_\odot. \tag{2.3}$$

The second type pertains to a planet with a clearly expressed nonuniformity over the surface of the self radiation density, caused primarily by rarefaction of the atmosphere or its complete absence, and also by a relatively large period of rotation around its axis. For these planets, the density of the emitted thermal flux, just like the density of the reflected solar flux, is assumed to be proportional to the density of the incident solar flux

$$E_0^e = (1 - A_{av}) S_\odot \frac{\cos\psi_0 + |\cos\psi_0|}{2} \tag{2.4}$$

The third type pertains to planets which, in terms of the distribution of the self radiation density over the surface, are located midway between the two planets indicated above. On the side of these planets illuminated by the Sun, the self radiation depends on the zenith distance of the sun, and on the shadow side — it is almost constant over the surface of the planet and is much lower than the maximum value on the illuminated side. In order to describe the radiant thermal effect on a spacecraft, mathematically the density of the self radiation of these planets is satisfactorily described by the expression /59

$$E_0^e = C_1 + C_2 \frac{\cos\psi_0 + |\cos\psi_0|}{2}, \tag{2.5}$$

where C_1 and $(C_1 + C_2)$ are the density of radiation from the shadow and from a region on the planet with a zero zenith distance of the Sun, $C_1 \ll C_2$.

One model corresponds to each type of planet. This model is characterized by the effective radius $\bar{R}$, the average albedo which is constant over the surface, the diffuse law of radiation and reflection, and one of the three laws indicated above governing the distribution of the self radiation density over the surface.

The first model is used to calculate and simulate the thermal effect of the Earth and Venus on a spacecraft. The second model is used to calculate and simulate the thermal effect of the Moon on a spacecraft. In actuality, the radiation density from the surface on the shadow side of the Moon does not exceed 10 W/m^2, which comprises no less then 1% of the maximum density on the illuminated side, and has barely any influence on the thermal regime of the spacecraft. Therefore, for the overwhelming majority of satellites and spacecraft, it is permissible to disregard the thermal effect from the shadow side of the Moon when simulating the surrounding medium, in which the spacecraft moves. Data on the temperature distribution over the surface of the illuminated side of the Moon are satisfactorily

approximated by the expression (2.4) with an average albedo of $A_{av} = 0.07$.

The third model is used to calculate and simulate the thermal influence on a spacecraft of Mars. Daily oscillations in the temperature on Mars may amount to 80 - 100°C. Thus, the maximum temperature on the side of the planet illuminated by the Sun may range between 0 – + 30°C; the minimal temperature — 85 – — 100°C. We shall assume $C_1 = 46$, $C_2 = 310$ W/m^2, which corresponds to the following temperatures: minimum temperature — 100°C, maximum temperature + 9°C; average value of the solar constant is $S_{\odot} = 600$ W/m^2. Thus, to maintain the thermal balance of the planet as a whole, the average albedo of the planet must be assumed to equal $A_{av} = 0.17$. As was shown above, the albedo of Mars ranges between $A_{av} = 0.15 - 0.26$, so that the model assumed for Mars corresponds to existing concepts regarding the /60 physical conditions on this planet.

It is much more difficult to relate the other planets of the solar system to a certain type, due to the lack of information on their radiation characteristics. Since the period of rotation of a planet around its axis is one of the main factors which influences the distribution of temperature over the surface, and along with it the density of the planetary long-wave radiation, then, with respect to Mercury whose period of rotation is 88 days, it must belong to the second type. The other planets with a period of rotation around their axis which does not exceed 10 - 11 hours must belong to the first type.

Relationship between the radiation density E_0 from the surface of the planet and the flux Φ of this radiation which falls on the surface F

In accordance with the definition of the radiation strength, the amount of radiant energy impacting per unit time in the direction of the unit vector $\vec{r}$ on the surface F, within the limits of an elementary solid angle $d\omega(\vec{r})$, equals the product of the strength of radiation $J_0(\vec{r})$ in this direction in the area F_n which is normal to this direction by the elementary solid angle $d\omega(\vec{r})$:

$$dQ = J_0(\vec{r}) F_n d\omega(\vec{r}).$$

Consequently, the flux of planetary radiation on the surface is

$$\Phi = \frac{1}{F} \int_{\Omega} dQ = \frac{1}{F} \int_{\Omega} J_0(\vec{r}) F_n d\omega(\vec{r}), \qquad (2.6)$$

where Ω is the solid angle, within whose limits the planet emits energy on the surface F (from now on, we shall call this angle the solid angle of the planet).

For the majority of calculations, it is more advantageous to replace integration with respect to the solid angle by integration with respect to a sphere of unit radius. In the case of real relationships between the dimensions of the spacecraft and the planet, the center of the unit sphere may be located at any point of the spacecraft.

Distinguishing on the sphere the region S^0, which is delineated by the solid angle Ω of the planet, and taking the fact into account that for a unit sphere $d\omega = ds$, after substituting variables and the integration limits we arrive at the basic equation for calculating and simulating the planetary radiation impacting on the spacecraft: /61

$$\Phi = \frac{1}{\pi}\int_{\Omega} E_0 \frac{F_n}{F} d\omega = \frac{1}{\pi}\iint_{S^0} E_0 \frac{F_n}{F} ds. \tag{2.7}$$

Here we have

$$E_0 \equiv E_0(\vec{r}),\ F_n \equiv F_n(\vec{r}),$$
$$d\omega \equiv d\omega(\vec{r}),\ ds \equiv ds(\vec{r}).$$

The amount of radiant energy incident per unit time on its entire surface F is:

$$Q_\Sigma = \Phi F. \tag{2.8}$$

The amount of radiant energy incident on a surface of definite configuration is determined by equation (2.7). The final form of the formulas depends on the type of planet, in whose field of radiant flux the surface is being studied.

Infared radiation from planets of the first type

For the first type of planet $E_0^e = \frac{1-A_{av}}{4} S_\odot$ according to the model assumed the radiant field is isotropic.

Therefore, we have

$$\Phi = \frac{1-A_{av}}{4} S_\odot \frac{1}{\pi}\iint_{S} \frac{F_n}{F} ds. \tag{2.9}$$

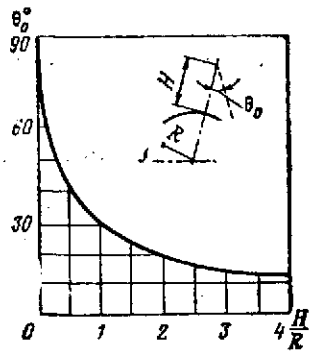

Fig. 2.1. Dependence of θ_0° on the relative altitude H/R.

The factor $\frac{1}{\pi}\iint\limits_S \frac{F_n}{F}\,ds$ represents the relative magnitude of the flux from the planet to the spacecraft. It coincides with the angular coefficient between the spacecraft and the planet, and is a purely geometric characteristic of this system.

Thus, calculating the self radiation from a planet of the first type falling on the spacecraft reduces to calculating the angular coefficient

$$\varphi_1 = \frac{1}{\pi}\iint\limits_S \frac{F_n}{F}\,ds. \tag{2.10}$$

With a certain value of φ_1, the flux may be calculated from the following formula

$$\Phi = \frac{1 - A_{av}}{4} S_{\odot}\varphi_1. \tag{2.11}$$

/62

Angular coefficient φ_1 for a sphere

A sphere is frequently used as a reference when developing a method for simulating the external flux falling on a spacecraft. To standardize and control the radiant field, which simulates the external thermal influence on the spacecraft, it is useful to know both the flux on the sphere as a whole, and a diagram of its distribution over the surface.

For a spherical surface in any direction, we have

$$\frac{F_n}{F} = \frac{1}{4}.$$

The average angular coefficient for the sphere is

$$\varphi_1 = \frac{S^\circ}{4\pi} = \frac{1 - \cos\theta_0}{2} = \sin^2\frac{\theta_0}{2}, \tag{2.12}$$

where $\theta_0 = \arcsin\frac{R}{R+H}$ is the angle between the vertical direction and tangent direction to the planet from the center of the sphere (Figure 2.1).

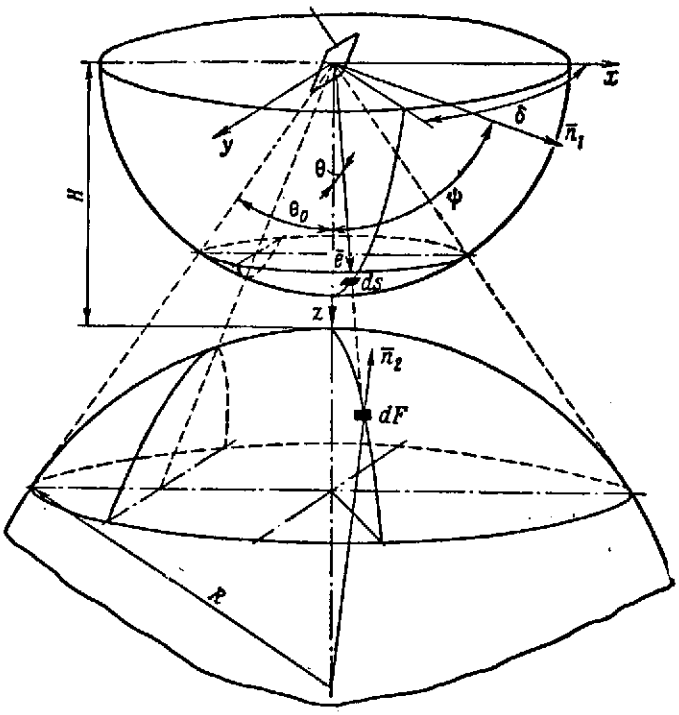

Fig. 2.2. Calculation of the density of self radiation from planets of the first type.

In order to obtain the distribution of flux over the surface of the sphere, it is necessary to know the angular coefficient between any element on its surface and the planet (the local angular coefficient for any element which is given beforehand).

Angular coefficient φ_1 for a surface element

Let us assume a unit normal $\vec{n}_1$ to the side of the element surface being studied makes an angle ψ with the vertical direction (direction to the center of the planet), and $0 \leq \psi \leq \frac{\pi}{2} + \theta_0$ is the unit vector $\vec{e}$ with the spherical coordinates θ and δ on a unit sphere (Figure 2.2) which determines a certain direction to the planet (the vector $\vec{r} = -\vec{e}$ which is opposite to it determines the direction of the incident radiation). For this direction $\frac{F_n}{F} = \cos(\vec{n}_1, \vec{e}) = (\vec{n}_1, \vec{e})$, where $(\vec{n}_1, \vec{e})$ is the scalar product of the vectors $\vec{n}_1$ and $\vec{e}$. In the xyz coordinate system in Figure 2.2

$$\vec{e} = \{\sin\theta\cos\delta,\ \sin\theta\sin\delta,\ \cos\theta\},\quad \vec{n}_1 = \{\sin\psi,\ 0,\ \cos\psi\}. \tag{2.13}$$

Consequently,

$$\frac{F_n}{F} = \sin\psi\sin\theta\cos\delta + \cos\psi\cos\theta. \tag{2.14}$$

Noting that $ds = \sin\theta d\theta d\delta$, we finally obtain the expression for the local angular coefficient φ_1: /63

$$\varphi_1 = \frac{1}{\pi}\iint\limits_{\theta\delta}(\sin\psi\sin\theta\cos\delta + \cos\psi\cos\theta)\sin\theta\, d\theta d\delta. \tag{2.15}$$

The integration limits in this expression are different for different cases:

a) If the plane of the element does not intersect the planet, i.e., if

$$\psi \leqslant \frac{\pi}{2} - \theta_0, \text{ then } -\pi \leqslant \delta \leqslant \pi \quad \text{for } 0 \leqslant \theta \leqslant \theta_0;$$

and

$$\varphi_1 = \frac{1}{\pi} \int_0^{\theta_0} \sin\theta d\theta \int_{-\pi}^{\pi} (\sin\psi \sin\theta \cos\delta + \cos\psi \cos\theta) d\delta = \cos\psi \sin^2\theta_0; \tag{2.16}$$

b) If the plane of the element intersects the planet and $\psi \leq \frac{\pi}{2}$, then /64

$$\text{for } 0 \leqslant \theta \leqslant \frac{\pi}{2} - \psi \qquad -\pi \leqslant \delta \leqslant \pi,$$

$$\text{for } \frac{\pi}{2} - \psi \leqslant \theta \leqslant \theta_0 \qquad -\delta_i \leqslant \delta \leqslant \delta_i; \text{ if } \quad \psi > \frac{\pi}{2}, \text{ then for}$$

$$0 \leqslant \theta \leqslant \psi - \frac{\pi}{2} \quad \delta = 0, \quad \text{for } \quad \psi - \frac{\pi}{2} \leqslant \theta \leqslant \theta_0 \quad -\delta_i \leqslant \delta \leqslant \delta_i.$$

The angle δ_i determines the line of intersection of the element plane with the surface of the unit sphere, i.e., one of the boundaries of the planet from the side of the element surface being considered. At this boundary we have

$$\frac{F_n}{F} = \sin\psi \sin\theta \cos\delta + \cos\psi \cos\theta = 0, \quad \delta = \delta_i,$$

Consequently, we have

$$\delta_i = \pi - \arccos(\operatorname{ctg}\theta \cdot \operatorname{ctg}\psi),$$

$$\varphi_1 = \frac{1}{\pi} \int_0^{\pi/2-\psi} \sin\vartheta d\theta \int_{-\pi}^{\pi} (\sin\psi \sin\theta \cos\delta + \cos\psi \cos\theta) d\delta + \tag{2.17}$$

$$+ \frac{1}{\pi} \int_{\pi/2-\psi}^{\theta_0} \sin\theta d\theta \int_{-\delta_i}^{\delta_i} (\sin\psi \sin\theta \cos\delta + \cos\psi \cos\theta) d\delta.$$

As a result of integration with allowance for (2.16), we obtain the following expression for the local angular coefficient φ_1:

$$\varphi_1 = \begin{cases} \cos\psi \sin^2\theta_0 \ldots \text{ for } 0 \leqslant \psi \leqslant \frac{\pi}{2} - \theta_0, \\ \frac{\cos\psi \sin^2\theta_0}{\pi} \left[\frac{\pi}{2} + \arcsin(\operatorname{ctg}\theta_0 \operatorname{ctg}\psi)\right] + \\ \quad + \frac{1}{\pi} \arcsin \frac{\sqrt{\sin^2\theta_0 - \cos^2\psi}}{\sin\psi} - \\ \quad - \frac{1}{\pi} \cos\theta_0 \sqrt{\sin^2\theta_0 - \cos^2\psi} \ldots \end{cases} \tag{2.18}$$

$$\varphi_1 = \begin{cases} \ldots \text{for } \frac{\pi}{2} - \theta_0 \leqslant \psi \leqslant \frac{\pi}{2} + \theta_0, \\ 0 \ldots\ldots\ldots\ldots\ldots \\ \ldots \text{for } \frac{\pi}{2} + \theta_0 \leqslant \psi \leqslant \pi. \end{cases} \tag{2.18}$$

In particular, for an element located in the vertical plane /65

$$\left(\psi = \frac{\pi}{2}\right), \quad \varphi_1 = \frac{\theta_0 - \sin\theta_0 \cos\theta_0}{\pi} = \frac{2\theta_0 - \sin 2\theta_0}{2\pi}. \tag{2.19}$$

(Here and below, we use the term vertical plane at a given point in space around the planet to designate the plane passing through this point and the center of the planet. The plane passing through the same point normal to the vertical direction is called the horizontal plane).

Figure 2.3 shows the dependence of the local angular coefficient φ_1 on the angles ψ and θ_0.

Angular coefficient φ_1 for an arbitrary body

Formula (2.18) may be used to give an analytical description of the distribution of incident flux over any curved surface, if its equalization and orientation with respect to the planet are given. To do this, it is necessary to express the angle ψ by the parameters which characterize the given surface and its orientation with respect to the planet.

By way of an example, let us examine a conical surface. Let us assume β is the angle of taper, α — angle between the vertical direction and the direction passing along the axis of the cone from its apex to the base (Figure 2.4). Then, for an element of the side surface of the cone with the angular coordinate φ we have:

$$\psi = \arccos(\cos\beta \cos\varphi \sin\alpha - \sin\beta \cos\alpha). \tag{2.20}$$

The average angular coefficient φ_{1_c} between the side surface of the cone and /66
the planet is determined by numerical integration:

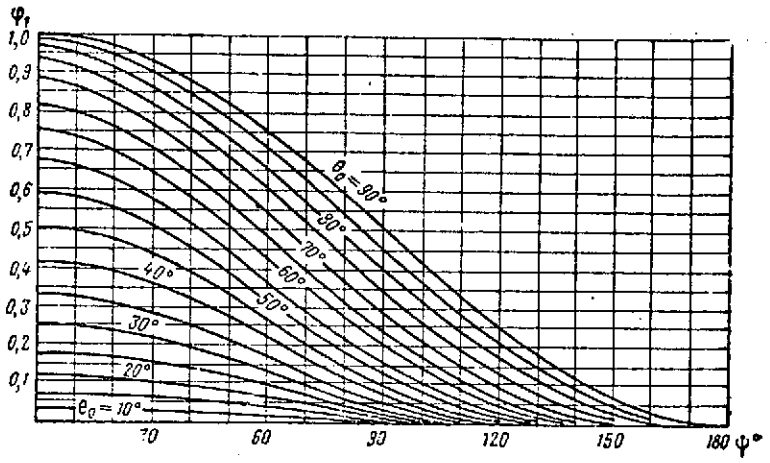

Fig. 2.3. Local angular coefficient φ_1.

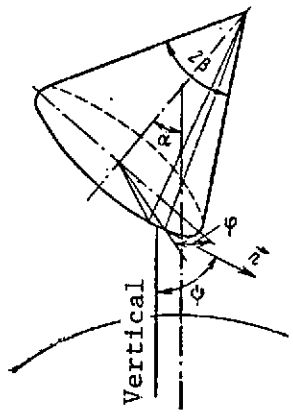

Fig. 2.4. Determination of the radiant flux on a conical surface.

$$\varphi_{1_c} = \frac{1}{\pi}\int_0^{\pi} \varphi_1(\theta_0, \psi(\alpha, \beta, \varphi))\, d\varphi.$$

The computational results are given in Figure 2.5.

If the axis of the cone is located vertically ($\alpha = 0$ or $\alpha = \pi$), then as follows from (2.20), the angle ψ does not depend on φ. Consequently, in this case the flux on the outer side of the lateral surface of the cone equals the flux on an elementary area with the angle $\psi = \frac{\pi}{2} - \beta$ for $\alpha = 0$ and $\psi = \frac{\pi}{2} + \beta$ for $\alpha = \pi$. In a similar way, we may calculate the relative magnitude of the flux on any circular surface, which is given analytically in space.

If an arbitrary body rotates randomly and rapidly in space, then its average (in a certain time interval) projection in any direction is the same. For a curved body, in this case the flux may be assumed to equal the flux on a sphere. By way of an example, Figure 2.6 shows the dependence of the relative magnitude of the flux falling on a sphere and a cylindrical shell rapidly rotating in a vertical plane around one of its transverse axes. A comparison of the computational results shows that even in the case of random rotation the flux on a cylindrical surface is very close to the flux on a sphere.

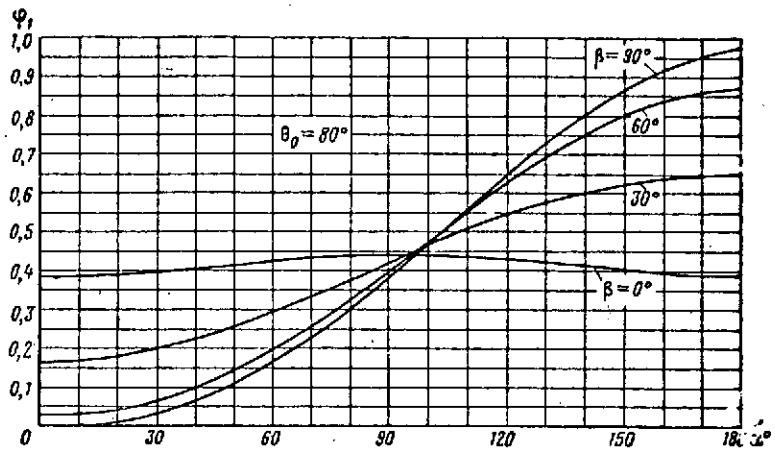

Fig. 2.5. Relative radiant flux on a conical surface.

Infared radiation from planets of the second type

The density of self radiation leaving a surface of planets of the second type, as was shown above, may be described by the following relationship:

$$E_0^e = (1 - A_{av}) S_\odot \frac{\cos\psi_0 + |\cos\psi_0|}{2}.$$

Thus, on the basis of (2.7) it follows that the flux of this radiation falling on the surface F equals:

$$\Phi = (1 - A_{av}) S_\odot \frac{1}{\pi} \int_\Omega \frac{F_n}{F} \frac{\cos\psi_0 + |\cos\psi_0|}{2} d\omega.$$

Just as for planets of the first type, here it is more advantageous to obtain /68 the analytical expression for the flux falling on a spherical surface, and to find the diagram showing the distribution of this flux over the surface of the sphere. The solution of this problem will be used later in simulating the planetary self radiation, and also to determine the necessary magnitude of the radiant flux when adjusting the simulator. The diagram for the flux distribution over the sphere will be determined, if we obtain the analytical expression for the flux falling on a surface element which is oriented arbitrarily in space.

If only a part (Ω^*) of the solid planetary angle Ω, within whose limits the illuminated part of the planet is visible from the surface under consideration, is used as the integration region, then we may write:

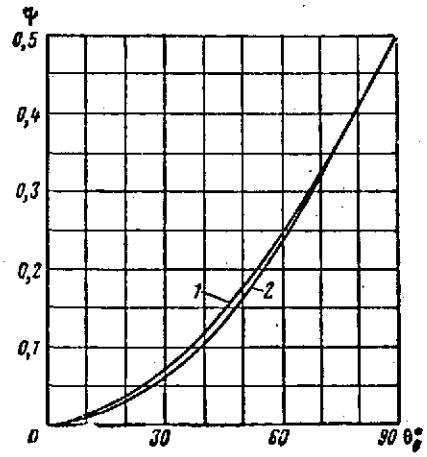

Fig. 2.6. Angular coefficient φ_1 for a sphere (curve 1) and a rotating cylinder (curve 2).

$$\Phi=(1-A_{av})S_{\odot}\frac{1}{\pi}\int_{\Omega^*}\frac{F_n}{F}\cos\psi_0 d\omega. \quad (2.21)$$

In order to determine the flux from planets of the second type, two conditions must be imposed on the integration region: the planet must be visible from the surface being considered, and the visible part of the planet must be illuminated by the Sun. This complicates the calculation and the simulation of the flux on a spacecraft from planets of the second type, as compared with calculating and simulating the flux from planets of the first type. The possibility of simplifying both the calculation and the simulation of flux on the spacecraft in this case is shown below.

We should note that calculating the flux from planets of the second type reduces to calculating the expression $\varphi_2=\frac{1}{\pi}\int_{\Omega^*}\frac{F_n}{F}\cos\psi_0 d\omega$, which in this case is the analog of the angular coefficient φ_1. The coefficient φ_2 is called below the combined angular coefficient (for an element on the surface — the local combined angular coefficient). If the value of φ_2 is known, then the flux may be determined from the formula

$$\Phi=(1-A_{av})S_{\odot}\varphi_2. \quad (2.22)$$

Combined angular coefficient φ_2 for a sphere

Let us assume the Sun-sphere-planet system (Figure 2.7) is characterized by the parameters θ_0 and γ_s (the angle between the directions to the surface being studied and to the Sun from the center of the planet).

It is simplest to determine φ_2 by integrating over the sphere of unit radius: $\frac{F_n}{F}=\frac{1}{4}$ in any direction. For example, $\cos\psi_0$, by using the scalar product of the vectors $\vec{n}_2$ (unit normal to the element dF on the planet's surface) and $\vec{s}$ (unit vector, directed toward the Sun), may be readily expressed by the angles γ, δ and /69

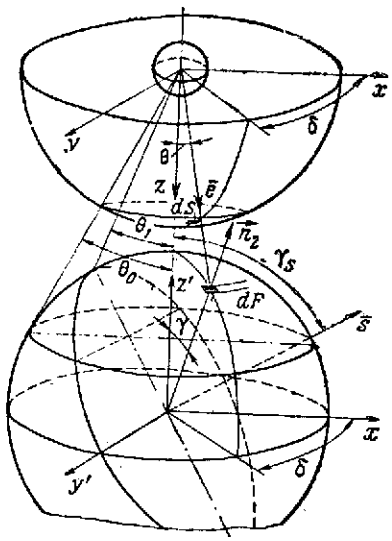

Fig. 2.7. Determination of φ_2 for a sphere.

γ_s in the x'y'z' coordinate system, with the origin at the center of the planet:

$$\cos\psi_0 = \cos\delta\sin\gamma\sin\gamma_s + \cos\gamma\cos\gamma_s. \qquad (2.23)$$

The transition from the coordinates γ, δ on the surface of the planet to the coordinates θ, δ on the surface of the unit sphere (see Figure 2.8) is done by means of the formulas:

$$\gamma = \arcsin(\sin\theta/\sin\theta_0) - \theta; \qquad (2.24)$$

$$ds = \sin\theta d\theta d\delta. \qquad (2.25)$$

The integration region is determined as follows:

a) If the entire visible surface of the planet is illuminated by the Sun, i.e., if $\gamma_s \leq \theta_0$, if $-\pi \leq \delta \leq \pi$ for $0 \leq \theta \leq \theta_0$;

b) If a small part of the visible surface is located in the shade, i.e., if $\theta_0 \leqslant \gamma_s \leqslant \frac{\pi}{2}$, then when $0 \leqslant \theta \leqslant \theta_1$ $-\pi \leqslant \delta \leqslant \pi$, when $\theta_1 \leqslant \theta \leqslant \theta_0$ $-\delta_m \leqslant \delta \leqslant \delta_m$;

c) If a large part of the visible surface is in the shade, i.e., if $\frac{\pi}{2} \leqslant \gamma_s \leqslant \pi - \theta_0$, then integration is performed only in the interval (θ_1, θ_0), i.e.,

for $0 \leqslant \theta \leqslant \theta_1$ $\quad \delta = 0$,

for $\theta_1 \leqslant \theta \leqslant \theta_0$ $\quad -\delta_m \leqslant \delta \leqslant \delta_m$;

and δ_m is determined from the condition $\cos\psi_0(\delta_m) = 0$:

$$\delta_m = \pi - \arccos(\operatorname{ctg}\gamma\operatorname{ctg}\gamma_s); \qquad (2.26)$$

θ_1 is determined from the condition $\delta_m(\gamma(\theta_1)) = \pi$:

$$\theta_1 = \arccos\frac{1 - \sin\theta_0\sin\gamma_s}{\sqrt{1 - 2\sin\theta_0\sin\gamma_s + \sin^2\theta_0}}. \qquad (2.27)$$

Taking the above into consideration and integrating over δ, we obtain

$$\varphi_{2s} = \frac{1}{2\pi}\int_0^{\theta_0}(\sin\gamma_s\sin\gamma\sin\delta^* + \delta^*\cos\gamma_s\cos\gamma)\sin\theta d\theta. \qquad (2.28)$$

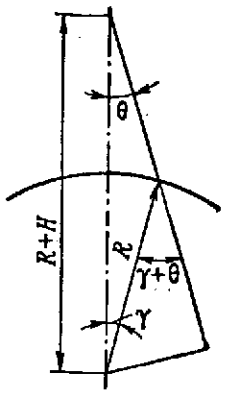

Fig. 2.8. Relation between the parameters θ and γ.

If $\gamma_s \leqslant \theta_0$, then $\delta^* = \pi$ for $0 \leqslant \theta \leqslant \theta_0$; if $\theta_0 \leqslant \gamma_s \leqslant \frac{\pi}{2}$, then $\delta^* = \begin{cases} \pi \text{ for } 0 \leqslant \theta \leqslant \theta_1 \\ \pi - \arccos(\operatorname{ctg}\gamma_s \operatorname{ctg}\gamma) \text{ for } \theta_1 \leqslant \theta \leqslant \theta_0; \end{cases}$

$$\text{if } \frac{\pi}{2} \leqslant \gamma_s \leqslant \pi - \theta_0, \text{ then } \delta^* = \begin{cases} 0 \text{ for } 0 \leqslant \theta \leqslant \theta_1; \\ \arccos(-\operatorname{ctg}\gamma_s \operatorname{ctg}\gamma) \\ \text{for } \theta_1 \leqslant \theta \leqslant \theta_0. \end{cases} \tag{2.29}$$

In the most important case, when $\gamma_s \leqslant \theta_0$ (this case encompasses those positions of the planet-Sun-surface F system when the radiation flux from the planet on the surface F is maximum) the expression for φ_{2_S} may be written in the final form:

$$\varphi_{2_S} = f_1(\theta_0)\cos\gamma_s, \tag{2.30}$$

where the function

$$f_1(\theta_0) = (2 - 3\cos\theta_0 + \cos^3\theta_0 + \sin^3\theta_0)/6\sin\theta_0, \tag{2.31}$$

diagrammed by Figure 2.9 shows how the relative incident flux changes in this case with a change in altitude. The expression for φ_{2_S} is also obtained in a final form when the sphere is located in the plane of the terminator, i.e., when $\gamma_s = \frac{\pi}{2}$:

$$\varphi_{2_S} = \frac{1}{6\pi}\left[\sin^2\theta_0 - \sin\theta_0 E(\theta_0) + 2\cos^2\theta_0 \frac{K(\theta_0) - E(\theta_0)}{\sin\theta_0}\right], \tag{2.32}$$

where $K(\theta_0) = \int_0^{\pi/2} \frac{d\theta}{\sqrt{1 - \sin^2\theta_0 \sin^2\theta}}$, $E(\theta_0) = \int_0^{\pi/2} \sqrt{1 - \sin^2\theta_0 \sin^2\theta}\, d\theta$ —

are complete elliptical integrals of the first and second kind.

Figure 2.10 graphically shows the relative flux on a sphere located in the plane of the terminator. Figure 2.11 (solid line) shows the result of a numerical /71 calculation of the combined angular coefficient for a sphere φ_{2_S}. Formula (2.30) is valid in the region above the dashed line, which corresponds to the condition $\gamma_s = \theta_0$. The dot-dashed line shows the computational results of using this formula when $\gamma_s \geqslant 0$. In the region $0 \leqslant \gamma_s \leqslant 70°$ they practically coincide with the exact values. When $\gamma_s > 70°$ formula (2.30) gives values which are too low. The maximum error is produced when $\gamma_s = 90°$ in the range $\theta_0 = 50—60°$, and is ~3% of the maximum

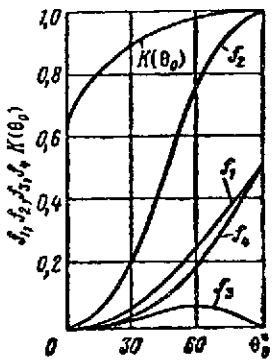

Fig. 2.9. Auxiliary functions for determining the effect of planetary radiation on the spacecraft.

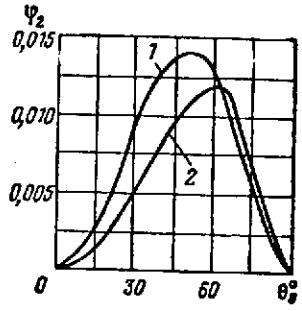

Fig. 2.10. Combined angular coefficient φ_2 for a sphere (curve 1) and a vertical cylinder (curve 2) above the terminator.

flux on the sphere, which does not exceed the error produced as a result of averaging the albedo of the planet. Representing the incident fluxes in the form of the product of two functions, one of which depends only on the altitude, and the other only on the mutual angular position of the Sun and the spacecraft, greatly simplifies the method of simulating the incident fluxes. Therefore, it is assumed that in the entire range of angles γ_s the flux on a sphere of planets of the second type equals

$$\Phi = (1 - A_{av}) S_{\odot} f_1(\theta_0) \frac{\cos\gamma_s + |\cos\gamma_s|}{2}. \tag{2.33}$$

Combined angular coefficient φ_2 for a surface element

Let us assume the surface element-Sun-planet system (Figure 2.12) is characterized by the parameters θ_0, γ_s, δ_s, ψ, where δ_s — angle between the vertical plane passing through the normal to the surface element, and the vertical plane parallel to the solar flux.

In Figure 2.12 ψ is the angle between the normal $\vec{n}_1$ to the surface element and /73 the vertical direction

$$\left(0 \leqslant \delta_s \leqslant \pi,\ \ 0 \leqslant \psi \leqslant \frac{\pi}{2} + \theta_0,\ \ 0 \leqslant \gamma_s \leqslant \pi - \theta_0\right).$$

When calculating the local combined angular coefficient, it is advantageous to perform integration over a sphere of unit radius with the surface element F being considered in the center:

$$\varphi_2 = \frac{1}{\pi} \iint_{S_\odot} \frac{F_n}{F} \cos\psi_0 ds.$$

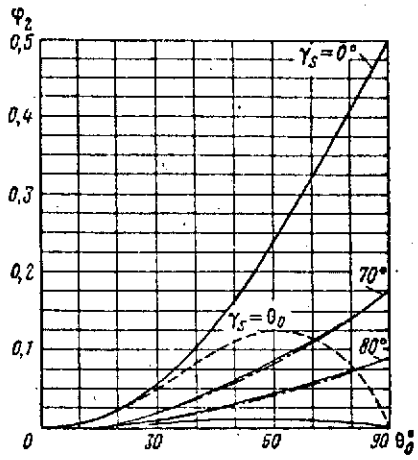

Fig. 2.11. Combined angular coefficient φ_2 for a sphere. Solid line — exact calculations; dashed line — calculations using an approximate method.

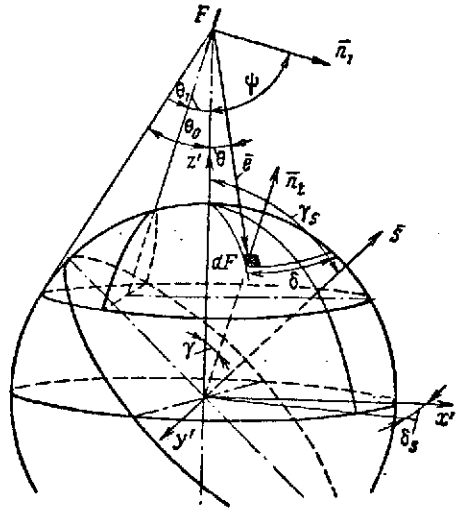

Fig. 2.12. General position in space of the planet-Sun-surface element system.

Let us first study the most important case, when the entire part of the planet, which is visible from the side of the element F, is illuminated by the sun. In this case, the integrand in formula (2.34) with only the factor cos ψ_0 differs from the integrand in formula (2.15) obtained when calculating the local angular coefficient φ_1. The integration limits remain the same with respect to θ and δ.

We may use the scalar product of the vectors $\vec{n}$ (unit normal to the element dF on the surface of the planet) and $\vec{s}$ (unit vector directed toward the Sun) to express cos ψ_0 by means of the parameters θ_0, γ_s, δ_s and the coordinates θ and δ:

$$\begin{gathered}\vec{n}_2=\{\sin\gamma\cos\delta,\ \sin\gamma\sin\delta,\ \cos\gamma\};\\ \vec{s}=\{\sin\gamma_s\cos\delta_s,\ \sin\gamma_s\sin\delta_s,\ \cos\gamma_s\};\\ \cos\psi_0=(\vec{n}_2\vec{s})=\sin\gamma\sin\gamma_s\cos(\delta-\delta_s)+\cos\gamma\cos\gamma_s,\end{gathered}\tag{2.35}$$

where according to (2.24) γ = arc sin (sin θ/sin θ_0) — θ.

After integrating with respect to δ, the expression for φ_2 in this case may be represented in the following form:

$$\varphi_2=f_2^*(\theta_0,\ \psi)\cos\gamma_s+f_3^*(\theta_0,\ \psi)\sin\psi\sin\gamma_s\cos\delta_s,\tag{2.36}$$

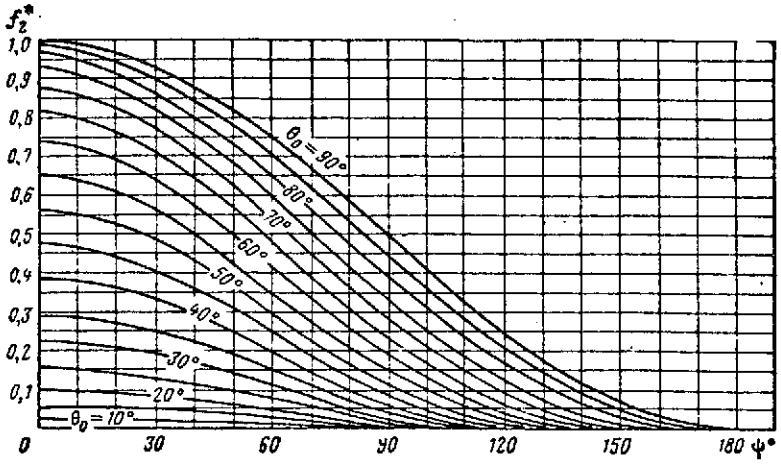

Fig. 2.13. Function $f_2^*(\theta_0, \psi)$

where

$$f_2^*(\theta_0, \psi)=\frac{2}{\pi}\int_0^{\theta_0}(\sin\psi\sin\theta\sin\delta^*+\delta^*\cos\psi\cos\theta)\cos\gamma\sin\theta d\theta \tag{2.37}$$

$$f_3^*(\theta_0, \psi)=\frac{1}{\pi}\int_0^{\theta_0}[\sin\theta(\delta^*+\sin\delta^*\cos\delta^*)+$$
$$+2\sin\delta^*\operatorname{ctg}\psi\cos\theta]\sin\gamma\sin\theta d\theta, \tag{2.38}$$

and the function δ^* is determined as follows: /74

$$\text{if } 0\leqslant\psi\leqslant\frac{\pi}{2}-\theta_0, \text{ then } \delta^*=\pi \text{ for } 0\leqslant\theta\leqslant\theta_0;$$

$$\text{if } \frac{\pi}{2}-\theta_0\leqslant\psi\leqslant\frac{\pi}{2}, \text{then } \delta^*=\begin{cases}\pi \text{ for } 0\leqslant\theta\leqslant\frac{\pi}{2}-\psi,\\ \pi-\arccos(\operatorname{ctg}\theta\operatorname{ctg}\psi)\\ \text{for } \frac{\pi}{2}-\psi\leqslant\theta\leqslant\theta_0;\end{cases}$$

$$\text{if } \frac{\pi}{2}\leqslant\psi\leqslant\frac{\pi}{2}+\theta_0, \text{ then } \delta^*=\begin{cases}0 \text{ for } 0\leqslant\theta\leqslant\frac{\pi}{2}-\psi,\\ \arccos(-\operatorname{ctg}\psi\operatorname{ctg}\theta)\\ \text{for } \frac{\pi}{2}-\psi\leqslant\theta\leqslant\theta_0.\end{cases}$$

Figures 2.13, 2.14 and 2.15 give the results of numerically calculating the functions $f_2^*(\theta_0, \psi)$ and $f_3^*(\theta_0, \psi)$. In some of the most particular cases, integration in formulas (2.37) and (2.38) is performed in elementary functions. For example,

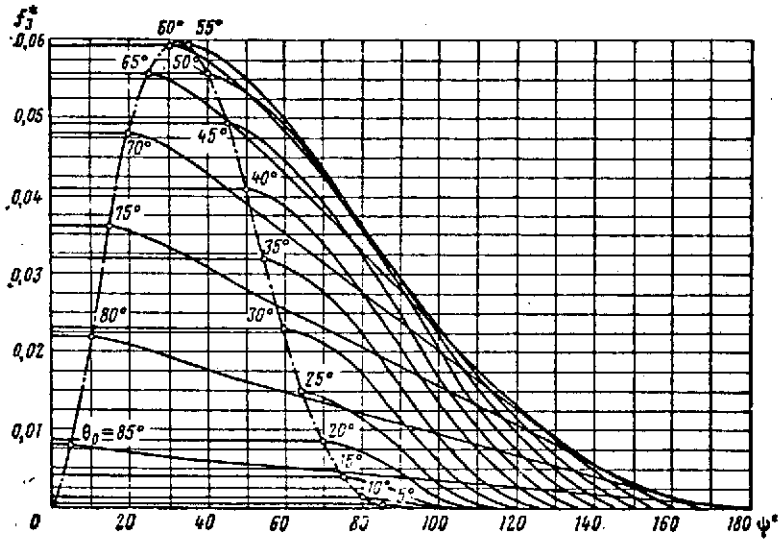

Fig. 2.14. Function $f_3^*(\theta_0, \psi)$

when

$$0 \leqslant \psi \leqslant \frac{\pi}{2} - \theta_0$$

(a surface element does not intersect the planet)

$$\varphi_2 = f_2(\theta_0)\cos\psi\cos\gamma_s + f_3(\theta_0)\sin\psi\sin\gamma_s\cos\delta_s, \tag{2.39}$$

where /75

$$f_2(\theta_0) = \frac{1}{4}\left(1 + \sin^2\theta_0 + 2\sin^3\theta_0 + \frac{\cos^4\theta_0}{2\sin\theta_0}\ln\frac{1-\sin\theta_0}{1+\sin\theta_0}\right), \tag{2.40}$$

$$f_3(\theta_0) = \frac{\cos^2\theta_0(3+\sin^2\theta_0)}{16\sin\theta_0}\ln\frac{1+\sin\theta_0}{1-\sin\theta_0} - \frac{(1-\sin\theta_0)(3+3\sin\theta_0+2\sin^2\theta_0)}{8}; \tag{2.41}$$

when $\psi = \frac{\pi}{2}$ (a surface element is located vertically)

$$\varphi_2 = f_4(\theta_0)\cos\gamma_s + \frac{1}{2}f_3(\theta_0)\sin\gamma_s\cos\delta_s, \tag{2.42}$$

where

$$f_4(\theta_0) = \frac{1}{8\pi}\left[6\left(\frac{\theta_0}{\sin\theta_0} - \cos\theta_0\right) + \pi\sin^3\theta_0 - 4\cos\theta_0\sin^2\theta_0\right]. \tag{2.43}$$

The functions $f_2(\theta_0)$, $f_3(\theta_0)$, $f_4\theta_0$ are represented graphically in Figure 2.9.

Let us now turn our attention to the great similarity between the set of curves $f_2^*(\theta_0, \psi)$ in Figure 2.13 and the set of curves $\varphi_1(\theta_0, \psi)$ in Figure 2.3. These curves were obtained in an investigation of the incident flux on planets of the first type, and represent the dependence of the local angular coefficient φ_1 on the parameters θ_0 and ψ.

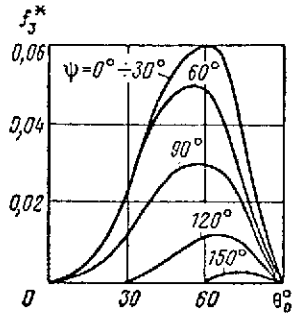

Fig. 2.15. Function $f_2^*(\theta_0, \psi)$

In actuality, these two sets are practically identical, and the set of curves $f_2^*(\theta_0, \psi)$ with an absolute error of no less than 1% may be obtained from the set $\varphi_1(\theta_0, \psi)$, by multiplying it by the similarity coefficient $k(\theta_0)=\frac{f_2^*(\theta_0, 0)}{\varphi_1(\theta_0, 0)}$. /76

It follows from equations (2.36) and (2.39) that when $\psi=0$ $f_2^*(\theta_0, \psi)\equiv f_2(\theta_0)$, and it follows from equation (2.16) that $\varphi_1(\theta_0, 0)=\sin^2\theta_0$.

Consequently,

$$k(\theta_0)=\frac{f_2(\theta_0)}{\sin^2\theta_0}, \tag{2.44}$$

$$f_2^*(\theta_0, \psi)\approx k(\theta_0)\varphi_1(\theta_0, \psi). \tag{2.45}$$

In the range $0\leqslant\psi\leqslant\frac{\pi}{2}-\theta_0$ the sets $f_2^*(\theta_0, \psi)$ и $k(\theta_0)\varphi_1(\theta_0, \psi)$ identically coincide.

With respect to the function $f_3^*(\theta_0, \psi)$, we may say that in the range $0\leqslant\psi\leqslant\frac{\pi}{2}-\theta_0$ it identically equals $f_3(\theta_0)$.

In the range $\frac{\pi}{2}-\theta_0\leqslant\psi\leqslant\frac{\pi}{2}+\theta_0$ for all θ_0 a linear dependence of $f_3^*(\theta_0, \psi)$ on ψ is assumed:

$$f_3^*(\theta_0, \psi)=\begin{cases} f_3(\theta_0) \;\ldots\ldots\ldots \text{for } 0\leqslant\psi\leqslant\frac{\pi}{2}-\theta_0, \\ f_3(\theta_0)\dfrac{\theta_0+\frac{\pi}{2}-\psi}{2\theta_0} \;\ldots \text{for } \frac{\pi}{2}-\theta_0\leqslant\psi\leqslant\frac{\pi}{2}+\theta_0. \end{cases} \tag{2.46}$$

(The absolute error in determining the flux for any approximation does not exceed $\pm 0{,}0035\,(1-A_{av})\,S_\odot$ w/м², , which is much less than the error assumed when averaging the albedo of the planet). Thus, if the entire part of the surface of the planet, which is visible from the side of the element F, is illuminated by the Sun, formulas (2.36), (2.45), (2.46) are sufficiently accurate with respect to a simple and analytical description of the incident flux.

This case encompasses all possible orientations of the element with respect to the planet in the range $0\leqslant\gamma_s\leqslant\theta_0$, i.e., in the range where the incident flux

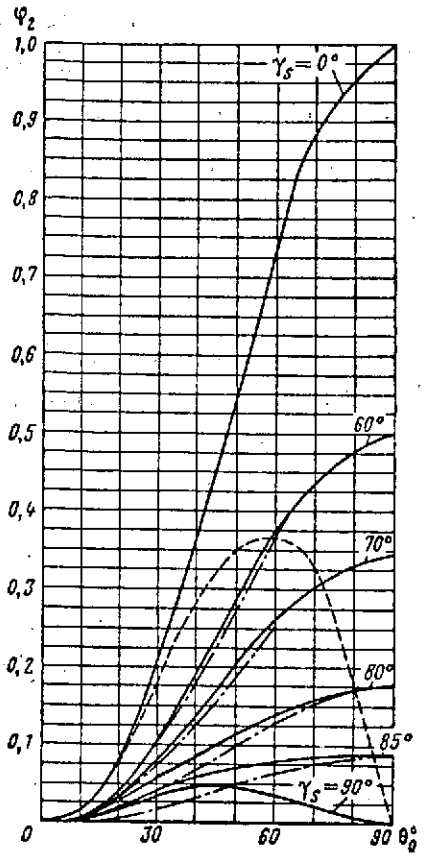

Fig. 2.16. Combined angular coefficient φ_2 for a horizontal element.

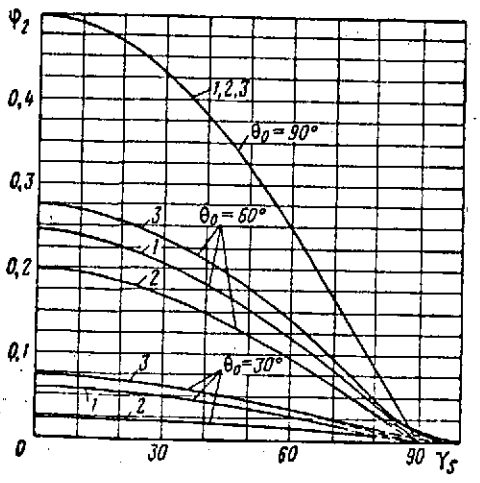

Fig. 2.17. Combined angular coefficient for a sphere, and cylinders oriented vertically and horizontally (curves 1, 2 and 3, respectively).

is maximum. In addition, if $\gamma_s>\theta_0$, and the plane of the element F intersects the planet, i.e., $\frac{\pi}{2}-\theta_0\leqslant\psi\leqslant\frac{\pi}{2}+\theta_0$, then formula (2.36) holds up to the angles

$$0\leqslant\delta_s\leqslant\arccos(\operatorname{ctg}\theta_0\operatorname{ctg}\psi)-\arccos(\operatorname{tg}\theta_0/\operatorname{tg}\gamma_s)$$

under the condition that $\operatorname{tg}\gamma_s\operatorname{ctg}\psi<\operatorname{tg}^2\theta_0$ /77
(it may be readily established that under these conditions $\frac{F_n}{F}\geqslant 0$ and $\cos\psi_0\geqslant 0$ simultaneously, i.e., the entire part of the planet, which is visible from the side of the element F, is illuminated by the Sun).

For example, if $\psi=\frac{\pi}{2}$, then formula (2.36) is valid in the range $0\leqslant\delta_s\leqslant\arcsin\left(\frac{\operatorname{tg}\theta_0}{\operatorname{tg}\gamma_s}\right)$. If $\psi=\frac{\pi}{2}+\Delta\psi$, then when $\delta_s=0$ formula (2.36) is valid in the range

$$0\leqslant\gamma_s\leqslant\frac{\pi}{2}+\arcsin\left(\frac{\sin\Delta\psi}{\sin\theta_0}\right)-\Delta\psi,$$

i.e., it encompasses the region lying beyond the terminator.

Figure 2.16 shows the results of numerically calculating φ_2 for a surface element located horizontally (solid line). The dashed line outlines the region above which formula (2.36) holds. The dot-dashed line shows the computational results using this formula when $\gamma_s>\theta_0$, for purposes of comparison. In the range $\theta_0=75$—$90°$ (the range of altitudes $H_0\leqslant 220$ км for the Earth) for all γ_s formula (2.36) is assumed to be accurate.

In the range $\theta_0<75°$, it gives results which are too low. The error is maximal when $\theta_0=40°$—$50°$, and is ~2% of the maximum flux on the element when $\gamma_s=70°$, 2.5% for γ_s and 4.5% for $\gamma_s=90°$. Since

it does not exceed the error obtained by averaging the albedo of the planet, in order to simplify the computational method and simulate the incident flux, we assume that the combined angular coefficient φ_2 for a surface element may be represented in the form (2.36) in the entire range of angles $0 \leqslant \gamma_s \leqslant \pi - \theta_0$.

In formal terms, for large values of γ_s and $\delta_s > \frac{\pi}{2}$ formula (2.36) may give small negative values of the flux. In these cases, we must assume the flux equals zero.

Thus, the diagram of the distribution of the relative incident flux over the surface of a sphere may be described by the equation

$$\overline{\Phi} = \frac{\Phi}{(1 - A_{av}) S_{\odot}} = k(\theta_0) \cos \gamma_s \varphi_1(\theta_0, \psi) + \\ + f_3^*(\theta_0, \psi) \sin \psi \sin \gamma_s \cos \delta_s, \tag{2.36a}$$

where $\varphi_1(\theta_0, \psi)$ and $f_3^*(\theta_0, \psi)$ is determined by relationships (2.18) and (2.46).

Formula (2.36) or (2.36a) with respect to the angle δ_s represents the equation of the cosine curve A + B cos δ_s which passes near the average $A = f_2^*(\theta_0, \psi) \cos \gamma_s \approx k(\theta_0) \varphi_1(\theta_0, \psi) \cos \gamma_s$ with the amplitude $B = f_3^*(\theta_0, \psi) \sin \psi \sin \gamma_s$. Consequently, for an /79
elementary spherical horizontal region or, which is the same thing, for a surface element rotating around the vertical, we have

$$\varphi_2 = f_2^*(\theta_0, \psi) \cos \gamma_s \approx k(\theta_0) \varphi_1(\theta_0, \psi) \cos \gamma_s.$$

Combined angular coefficient φ_2 for an arbitrary body

For any circular body having the vertical axis of symmetry (in any horizontal section of this body the angle ψ does not depend on δ_s), the combined angular coefficient differs from the angular coefficient in the usual sense only by the factor

$$k(\theta_0) \cos \gamma_s, \text{ i. e. } \varphi_2(F) \approx k(\theta_0) \cos \gamma_s \varphi_1(F) \tag{2.47}$$

or

$$\varphi_2(F) \approx k(\theta_0) \cos \gamma_s \frac{1}{\pi} \int_{\Omega} \frac{F_n}{F} d\omega. \tag{2.48}$$

For purposes of comparison, Figure 2.17 gives the results of a numerical calculation and a calculation using formula (2.47) for a sphere and a cylinder located vertically and horizontally. The exact calculations (solid line) practically coincide with the values calculated with the formula (2.47) (dashed line). The error up to 3% only occurs in the region of the terminator.

It is extremely important to note that in the region $\gamma_s = 0 \div 60°$, i.e., in the region in which the flux falling on the planet reaches the greatest values, the amplitude of B is much less than the average value A, near which the cosine curve passes. This means that in this region the rotation of a surface element around the vertical axis has an insignificant effect on the incident flux, and therefore relationship (2.47) will be absolutely valid for a body of any configuration.

Thus, to develop a simulation method, the flux falling on the spacecraft from planets of the second type may be represented in the following form:

$$\Phi = (1 - A_{av}) S_{\odot} \cos \gamma_s k(\theta_0) \frac{1}{\pi} \int_{\Omega} \frac{F_n}{F} d\omega, \tag{2.49}$$

$$0 \leqslant \gamma_s \leqslant \frac{\pi}{2}.$$

It may thus be seen that simulating the flux falling on the spacecraft from planets of the second type methodically differs from simulating the incident flux from planets of the first type only in the fact that the radiation intensity of an infrared emitter must additionally change in time, in accordance with the flight program of the spacecraft, proportionally to the change in the function of the altitude $k(\theta_0)$ and the cosine of the angle between the directions to the spacecraft /80
and the Sun from the center of the planet. The function of the altitude $k(\theta_0)$ is shown in Figure 2.9.

Infrared radiation from planets of the third type

For the third type of planets, we have

$$E_0 = C_1 + C_2 \frac{\cos \psi_0 + |\cos \psi_0|}{2}, \tag{2.50}$$

Therefore, in accordance with (2.7), we have

$$\Phi = C_1 \frac{1}{\pi} \int_{\Omega} \frac{F_2}{F} d\omega + C_2 \frac{1}{\pi} \int_{\Omega^*} \frac{F_n}{F} \cos\psi_0 d\omega,$$

where the factor for C_1 represents the angular coefficient φ_1, for C_2 — the combined angular coefficient φ_2, i.e.,

$$\Phi = C_1\varphi_1 + C_2\varphi_2. \tag{2.51}$$

Consequently, when calculating the infrared radiation from planets of the third type we may use the results of calculating the coefficients φ_1 and φ_2 obtained when examining the infrared radiation from planets of the first and second type.

Thus, the flux of infrared radiation from planets of the third type falling on a finite body may be represented in the following form:

$$\Phi = (C_1 + k(\theta_0)\cos\gamma_s C_2) \frac{1}{\pi} \int_{\Omega} \frac{F_n}{F} d\omega. \tag{2.52}$$

If the body is circular, the diagram showing the distribution of this flux over its surface may be described by the equation

$$\Phi = [C_1 + C_2 k(\theta_0)\cos\gamma_s]\varphi_1(\theta_0, \psi) + C_2 f_3^*(\theta_0, \psi)\sin\psi\sin\gamma_s\cos\delta_s, \tag{2.53}$$

obtained from (2.51) with allowance for (2.36).

Reflected solar radiation

Within the framework of the assumed diffusion law of reflection, the method of calculating the solar radiation falling on the spacecraft and reflected from the planet coincides with the method of calculating the infrared radiation on the spacecraft from planets of the second type.

In actuality, the density of the reflected solar radiation coming from the planet, as was indicated above, may be represented in the following form:

$$E_0 = A_{av} S_{\odot} \frac{\cos\psi_0 + |\cos\psi_0|}{2}$$

In this case, the flux of this radiation falling on the spacecraft surface, /81
by analogy with the flux of self radiation from planets of the second type, may

be expressed by the combined angular coefficient

$$\Phi = A_{av} S_{\odot} \frac{1}{\pi} \int_{\Omega} \frac{F_n}{F} \cos \psi_0 d\omega = A_{av} S_{\odot} \varphi_2. \tag{2.54}$$

Thus, all the results obtained above when analyzing the coefficient φ_2 may be used in calculating the reflected flux falling on the spacecraft.

Taking (2.48) into account, we may describe the reflected flux on the spacecraft by the following analytical expression:

$$\Phi = A_{av} S_{\odot} k(\theta_0) \cos \gamma_s \frac{1}{\pi} \int_{\Omega} \frac{F_n}{F} d\omega, \quad 0 \leqslant \gamma_s \leqslant \frac{\pi}{2}. \tag{2.55}$$

Here the factor $\frac{1}{\pi} A_{av} S_{\odot} k(\theta_0) \cos \gamma_s$ determines the law governing the change, in accordance with the spacecraft flight program, in the radiation intensity of the simulator when simulating reflected solar fluxes emitted by the planet on the spacecraft.

The diagram of the distribution of the incident reflected flux over a circular surface of the spacecraft may be described by the equation

$$\Phi = A_{av} S_{\odot} \varphi_2(\theta_0, \psi, \gamma_s, \delta_s),$$

where $\varphi_2(\theta_0, \psi, \gamma_s, \delta_s)$ is the local combined angular coefficient determined by relationships (2.36) or (2.36a).

The formulas for calculating the radiation from the planet on the spacecraft are given in Tables 9 - 11.

TABLE 9. DENSITY E_0 OF RADIATION FROM PLANET'S SURFACE AND THE FLUX Φ OF RADIATION FROM THE PLANET ON THE SPACECRAFT

Form of radiation		Type of planet		
		1	2	3
Eigen	E_0	$\frac{1 - A_{av}}{4} S_{\odot}$	$(1 - A_{av}) S_{\odot} \times \frac{\cos \psi_0 + \lvert \cos \psi_0 \rvert}{2}$	$C_1 + C_2 \frac{\cos \psi_0 + \lvert \cos \psi_0 \rvert}{2}$

(Continued on next page.)

Table 9 (Continued)

Form of radiation		Type of planet 1	2	3
Eigen	Φ	$\frac{1-A_{av}}{4} S_{\odot}\varphi_1$	$(1-A_{cp}) S_{\odot}\varphi_2$	$C_1\varphi_1 + C_2\varphi_2$
Reflected	E_0	$A_{av} S_{\odot} \frac{\cos\psi_0 + \lvert\cos\psi_0\rvert}{2}$		
	Φ	$A_{av} S_{\odot}\varphi_2$		

TABLE 10. ANGULAR COEFFICIENT ϕ_1

/82

Surface	Computational scheme	Angular coefficient
Sphere	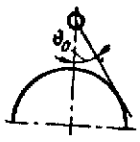	$\sin^2 \frac{\theta_0}{2}$
Surface element	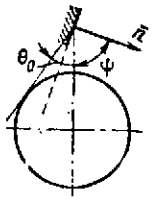	$\cos\psi \sin^2\theta_0 \ldots \text{for } 0 \leqslant \psi \leqslant \frac{\pi}{2} - \theta_0$ $\frac{\cos\psi \sin^2\theta_0}{\pi}\left[\frac{\pi}{2} + \arcsin(\operatorname{ctg}\theta \operatorname{ctg}\psi)\right] +$ $+ \frac{1}{\pi}\arcsin\frac{\sqrt{\sin^2\theta_0 - \cos^2\psi}}{\sin\psi} -$ $- \frac{1}{\pi}\cos\theta_0\sqrt{\sin^2\theta_0 - \cos^2\varphi} \ldots$ $\ldots \text{for } \frac{\pi}{2} - \theta_0 \leqslant \psi \leqslant \frac{\pi}{2} + \theta_0$ $0 \ldots \text{for } \frac{\pi}{2} + \theta_0 \leqslant \psi \leqslant \pi$
Arbitrary body	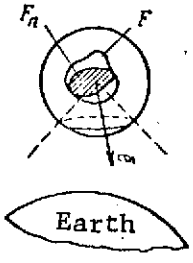	$\varphi_1 = \frac{1}{\pi}\int_{\Omega}\frac{F_n}{F}\,d\omega = \frac{1}{\pi}\iint_{S^\circ}\frac{F_n}{F}\,ds$ Ω — solid angle at which the planet is visible from the surface F F_n — projection of the surface on the plane normal to the variable direction $\vec{e}$ to the planet S° — region on a unit sphere around the surface F located within the limits of the solid angle Ω

TABLE 11. COMBINED ANGULAR COEFFICIENT ϕ_1 /83

Surface	Computational scheme	Combined angular coefficient
Sphere $\gamma_s < \theta_0$ (the entire visible part of the planet illuminated by the Sun)	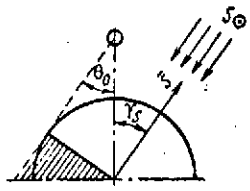	$\varphi_2 = f_1(\theta_0)\cos\gamma_s$ $f_1(\theta_0) = (2 - 3\cos\theta_0 + \cos^3\theta_0 + \sin^3\theta_0)/6\sin\theta_0$
/82 Sphere $\gamma_s = \frac{\pi}{2}$ (the sphere is located in the plane of the terminator	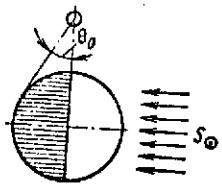	$\varphi_2 = \frac{1}{6\pi}\left[\sin^2\theta_0 - \sin\theta_0 E(\theta_0) + 2\cos^2\theta_0 \frac{K(\theta_0) - E(\theta_0)}{\sin\theta_0}\right]$ $K(\theta_0) = \int_0^{\pi/2} \frac{d\theta}{\sqrt{1 - \sin^2\theta_0 \sin^2\theta}}$, $E(\theta_0) = \int_0^{\pi/2} \sqrt{1 - \sin^2\theta_0 \sin^2\theta}\, d\theta$
Surface element $\gamma_s < \theta_0$, $0 < \psi < \frac{\pi}{2} - \theta_0$ (the plane of the element does not intersect the planet)	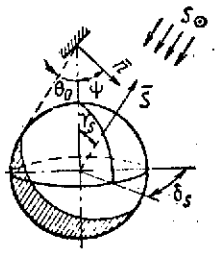	$\varphi_2 = f_2(\theta_0)\cos\psi\cos\gamma_s + f_3(\theta_0)\sin\psi\sin\gamma_s\cos\delta_s$, $f_2(\theta_0) = \frac{1}{4}\left(1 + \sin^2\theta_0 + 2\sin^3\theta_0 + \frac{\cos^4\theta_0}{2\sin\theta_0}\ln\frac{1 - \sin\theta_0}{1 + \sin\theta_0}\right)$ /84 $f_3(\theta_0) = \frac{\cos^2\theta_0(3 + \sin^2\theta_0)}{16\sin\theta_0}\ln\frac{1 + \sin\theta_0}{1 - \sin\theta_0} -$ $- \frac{(1 - \sin\theta_0)(3 + 3\sin\theta_0 + 2\sin^2\theta_0)}{8}$
Surface element, $\psi > \frac{\pi}{2} - \theta_0$ the entire part of the planet, visible from the side of the element surface, is illuminated by the Sun	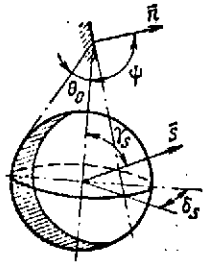	$\varphi_2 = f_2^*(\theta_0, \psi)\cos\gamma_s + f_3^*(\theta_0, \psi)\sin\psi\sin\gamma_s\cos\delta_s$ $f_2^*(\theta_0, \psi) = k(\theta_0)\varphi_1(\theta_0, \psi)$ $k(\theta_0) = f_2(\theta_0)/\sin^2\theta_0$ $f_3^*(\theta_0, \psi) = \begin{cases} f_3(\theta_0) & \text{for } 0 < \psi < \frac{\pi}{2} - \theta_0 \\ f_3(\theta_0)\frac{\theta_0 + \frac{\pi}{2} - \psi}{2\theta_0} \ldots & \text{for } \frac{\pi}{2} - \theta_0 < \psi < \frac{\pi}{2} + \theta_0 \end{cases}$ $\varphi_1(\theta_0, \psi)$ (see Table 10)

(Continued on next page.)

Table 11 (Continued)

Surface	Computational scheme	Combined angular coefficient
Arbitrary surface which has a vertical axis of symmetry $\gamma_s < \theta_0$	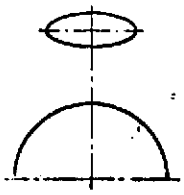	$\varphi_2 = k(\theta_0)\cos\gamma_s\varphi_1$
Arbitrary curved surface		$\varphi_2 \approx k(\theta_0)\dfrac{\cos\gamma_s + \lvert\cos\gamma_s\rvert}{2}\varphi_1$

/85

The spacecraft approaches the shadow of the planet /86

At certain angles α_0 (see Figure 3.4) and flight altitudes H_0 the spacecraft may approach the shadow of the planet. The transition from the zone of complete illumination to complete shadow does not occur at once, but gradually. The time the spacecraft remains in the shadow and the semi-shadow, and consequently the rate of change in the illumination in this zone, depends on the flight altitude, the time of year, the distance of the planet from the Sun, its radius, the presence of an atmosphere, its optical characteristics, and also the brightness distribution over the disk of the Sun. As shown in Section 2, Chapter 1, this distribution depends on the radiation wavelength. In the simplest case, when the spacecraft orbit is circular and the planet has no atmosphere, the time the spacecraft remains in complete shade may be determined from the approximate formula

$$t_{sh} = \frac{1}{\sqrt{g}}\frac{(R_0+H_0)^{3/2}}{R_0}\left(\pi - 2\arccos\frac{\cos\alpha}{\sin\alpha_0}\right), \tag{2.56}$$

where $\alpha = \arccos\dfrac{R_0}{R_0+H_0}$, R_0 is the radius of the planet, g — acceleration of gravity on the surface of the planet. Taking the fact into account that the time of one revolution of the spacecraft along a circular orbit is determined from the formula

$$t_r = \frac{2\pi}{\sqrt{g}}\frac{(R_0+H_0)^{3/2}}{R_0}, \tag{2.57}$$

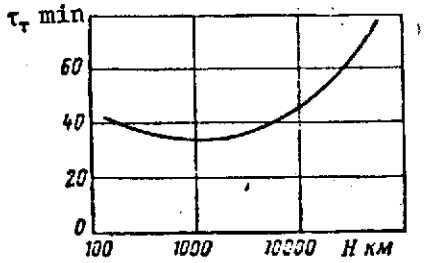

Fig. 2.18. Length of time the spacecraft remains in the shadow of the Earth as a function of the altitude of the circular orbit for $\alpha_0 = \pi/2$ (see Figure 3.4).

we may find the expression for the time the spacecraft remains in the shade, with respect to the time of one revolution:

$$t_{sh}/t_T = \bar{t} = \frac{1}{2} - \frac{\arccos \frac{\cos \alpha}{\sin \alpha_0}}{\pi}. \qquad (2.58)$$

Figure 2.18 shows the dependence of the time the spacecraft remains in the shade on the flight altitude along a circular orbit for $\alpha_0 = \pi/2$. The curve $\tau = \tau(H)$ has a minimum for an altitude of 8 - 10 thousand kilometers. This may be explained by the fact that, as the altitude increases, the spacecraft velocity along the orbit decreases:

$$V = R_0 \sqrt{\frac{g}{R_0 + H_0}}.$$

Thus, for a 24-hour orbit $t_{sh} \approx 69$ min. For very high altitudes (for the Earth $H_0 \approx 1.5 \cdot 10^6$ km) the spacecraft sometimes does not approach the complete shade (Figure 2.19). To the observer located in the penumbra of the Earth at a distance greater than 1.5 million kilometers, it would appear that over the bright disk of the Sun there is a small dark circle of the planet, which hides part of the solar disk. /87

The time the spacecraft remains in the complete shade (or penumbra) may be found by solving the problem of the intersection of the cone with an arbitrary plane of the orbit, and calculating the time required for the spacecraft to pass along one of the symmetrical halves of the so-called "shade ellipse".

In a precise formulation of the problem, determining the strength of the solar radiant flux in the penumbra requires that we take into account not only the angular dimension of the Sun and the parameters of the spacecraft orbit, but also other, no less important factors, such as:

a) Non-uniformity of the solar disk surface brightness (see Section 2, Chapter I);

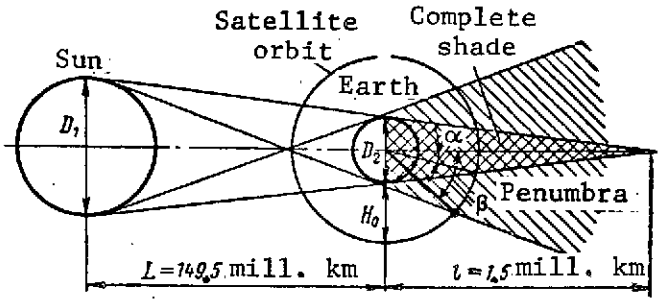

Fig. 2.19. Diagram showing a spacecraft approaching the shadow of the Earth for $\alpha_0 = \pi/2$ (Mill.=Million).

b) Non-uniformity of the spectral distribution over the solar disk surface;

c) Refraction attenuation of the solar flux in the atmosphere of the planet;

d) Scattering and selective absorption in the atmosphere;

e) Geographic position and actual blurring of the terminator on the planet, which has an atmosphere;*

f) Activity of the Sun, etc.

As a result of the concurrent action of these factors, the spectrum of solar radiation in the penumbra is shifted considerably toward the "red" side. A graphic example may be copper-red, brick red, dark red, and other lunar eclipses visible from the Earth with the naked eye.

An examination of these phenomena and the ability to calculate all of the parameters of radiant solar flux falling on a spacecraft in the penumbra is important in developing methods of simulation and in constructing solar simulators. However, this problem falls outside the framework of this book. Therefore, the authors refer the readers who are interested in these problems to the monograph of the well-known Czech astronomer F. Link [73], devoted to a study of the lunar eclipses and the photometric and physical phenomena connected with them. /88

*The width of the terrestrial terminator is approximately 900 km.

3. Action of Short-Wave Solar Radiation on Spacecraft Materials

Radiation from the Sun in the ultraviolet and x-ray regions of the spectrum may cause radiation damage to certain materials, and change the optical properties of coverings designed for active and passive temperature control of the spacecraft.

As is known, radiation damage to materials is primarily due to ionization or displacement of atoms in the material, and in many nonmetallic materials their physical properties may change as a result of dissociation of chemical bonds in the molecules. The nature of the processes taking place when material is subjected to solar radiation depends on the wavelength and the radiation strength. The energy of a photon with a wavelength of $\lambda|\mathring{A}|$ is

$$E_p = h\nu = \frac{hc}{\lambda} = \frac{19.8 \cdot 10^{-16}}{\lambda} \text{ J} = \frac{12.395}{\lambda} \text{ eV}, \tag{2.59}$$

i.e., a photon of ultraviolet radiation with a wavelength of 3000 Å has an energy of 4.1 eV, a photon with a wavelength of 1500 Å — 8.2 eV, etc. This energy is not sufficient to displace atoms* or to separate an electron from an atom of the material. However, electron excitation is possible during the absorption of photons by the material, i.e., the transition of electrons to higher energy levels.

In metals and alloys, solar radiation cannot cause radiation damage, since metallic materials are not influenced by ionization and excitation. The energy of protons of short-wave solar radiation is insufficient to displace the atoms, as may be seen from formulas (2.59) and (2.60).

In inorganic insulating materials, their optical characteristics may change due to the formation of the so-called "color centers". These color centers are formed due to the accumulation of electrons which have left the equilibrium position in the crystal lattice during excitation or ionization. The trapped elec- /89
88 trons and holes form sections which absorb light in the visible spectral region. As a result of this absorption, the color of the material changes, and becomes generally dark.

---

*The minimum (limiting) energy of a photon which is necessary to displace atoms in material [44] is:

$$E_{p.d} = 8000 \text{ A eV} \tag{2.60}$$

where A is the atomic weight of the material.

The formation of color centers changes the color of the pigments used to prepare painted temperature controlling coverings. Thus, for example, after ultraviolet radiation titanium dioxide changes from white to yellow; zirconium dioxide and aluminum dioxide become darker, etc. Therefore, when preparing paints with specific optical characteristics for passive temperature control, they must be checked for resistance to short-wave solar radiation.

Photochemical processes of two basic types are possible under the action of short-wave solar radiation on polymer materials: disturbance of the polymer chains (destruction) and formation of crosslinks between them. The disturbance of the chains may cause a weight loss and an increase in porosity, a decrease in mechanical strength and elasticity, and deterioration of electrical properties. The development of crosslinks may be useful for certain materials, since mechanical strength thus increases. However, the development of crosslinks leads to a loss of elasticity, which is undesirable for elastomers. For rigid plates, the development of crosslinks leads to disintegration and rupture of the material due to development of internal stress.

To initiate photochemical processes, radiation quanta must have sufficient energy to disturb the chemical bonds. The dissociation energy of the majority of chemical bonds does not exceed 100 - 150 kcal/mole. Since 1 eV = 23.05 kcal/mole, with allowance for relationship (2.59) radiation with wavelengths shorter than 2500 - 3000 Å may initiate chemical processes in several organic materials.

The rate at which the majority of chemical processes occur, which arise when materials are irradiated with photons, increases with a temperature increase.

The nature of the disturbance of the materials under the effect of short-wave solar radiation greatly depends on the absorbed dose of radiation connected with the depth to which the radiation penetrates into the material. The depth of penetration is characterized by the relaxation length R_e — the distance (or the distance corresponding to this of the specific mass per 1 cm^2) at which the radiation strength decreases by a factor of e. The relaxation length is inverse to the absorption coefficient τ:

$$R_e = \frac{1}{\tau}. \tag{2.61}$$

The relaxation length depends on the spectral composition of the radiation and/90 the properties of the material. Based on data in [44], the penetration depth of radiation with wavelengths of 100 - 1000 Å is ~0.001 - 1 micron, and with a decrease in the wavelength the penetration depth increases. However, for the overwhelming majority of materials, the changes produced by short-wave solar radiation will take place primarily in the thin surface layers. This is explained by the fact that significant changes in the material properties will occur only for a large radiation absorption coefficient, and in this case the depth of radiation penetration will be small.

Thus, short-wave solar radiation in space may primarily harm the outer surfaces of spacecraft elements: temperature controlling coverings, polymer films and wires, optical elements, etc. It is apparent that when selecting non-metallic materials and coverings, which — depending upon the operational conditions in space — may be subjected to the prolonged influence of solar radiation, the radiation stability of these materials must be first checked in devices with sources of radiation which simulate solar radiation.

4. Mechanism by Which Temperature Controlling Coverings Are Damaged by Charged and Micrometeorite Particles [202], [282], [291]

Different physico-chemical processes, which change the optical and other characteristics of the coverings, take place under the influence of corpuscular radiation in space and micrometeorite particles impacting on the material of temperature controlling coverings. We shall first be interested in the change in the absorption coefficient of solar radiation A_s and the radiation blackness coefficient ε of the coverings, which influence the normal temperature regime of the spacecraft. The coefficient ε barely changes during the absorption of large doses of radiation by the temperature controlling coverings. We shall examine the influence of ionizing radiation primarily on the change in the coefficients A_s or R_λ of different types of temperature controlling coverings [28], [291].

Micrometeorite erosion of the covering surfaces leads to a change both in the coefficients A_s and R_λ and the coefficients ε.

The spectral reflection coefficient R_λ of the temperature controlling covering, in the case of normal incidence of a plane electromagnetic wave on a rough

surface, is determined by the Fresnel equation [46]:

$$R_\lambda = \frac{(n_\lambda - 1)^2 + \varkappa_\lambda^2}{(n_\lambda + 1)^2 + \varkappa_\lambda^2}, \tag{2.62}$$

where n_λ is the actual component of the spectral coefficient of light refraction in the covering material; $\varkappa_\lambda$ — spectral absorption coefficient of light radiation in the covering. /91

The complex expression for the index of refraction has the form

$$N_\lambda = n_\lambda - i\varkappa_\lambda. \tag{2.63}$$

It is known [46] from the theory of light reflection that N_λ, and consequently n_λ and $\varkappa_\lambda$, depend on several constants which are characteristic for the given material.

Under the influence of ionizing radiation and micrometeorite particles with components which comprise the temperature controlling covering, n_λ and $\varkappa_\lambda$ may change, which in turn causes a change in R_λ and ε_λ.

Since the propagation of light in the material of most temperature controlling coverings must be regarded from the viewpoint of the optics of turbid media, the use of formula (2.62) is limited for R_λ.

An extensive class of materials may be used as temperature controlling coverings: pure metals, anodized metallic surfaces, enamels, ceramics, polymer coverings, specular coverings, etc.

A change in the optical characteristics of temperature controlling coverings is determined by different processes occurring in the covering material:

1) A disturbance of the crystal lattice due to the formation of radiation defects;

2) Formation of color centers;

3) Radiation-chemical changes;

4) Pulverization of material and a change in the surface properties;

5) Micrometeorite erosion of the surface.

Many of these phenomena in metals, polymers, glasses, and ion crystalls, have been described in detail in numerous monographs [1], [9], [32], [36], [103], [114], [115]. The overall interaction of different types of radiation with material is shown in Figure 2.20.

The mechanism of radiation damage to temperature controlling coverings has been discussed in much less detail, due to the fact that there has only been particular interest in such materials in the last ten years due to the conquest of space. We shall now give a brief description of the basic processes connected with bombardment of the coverings by corpuscular fluxes. The change in optical characteristics of the temperature controlling coverings depends primarily on the fluxes.

/92

Disturbance of the order in the crystal lattice

The main result produced by the action of charged particles on materials with a crystal lattice is connected with the formation of defects in them. As a result of the elastic interaction of charged particles with atoms of the lattice, the

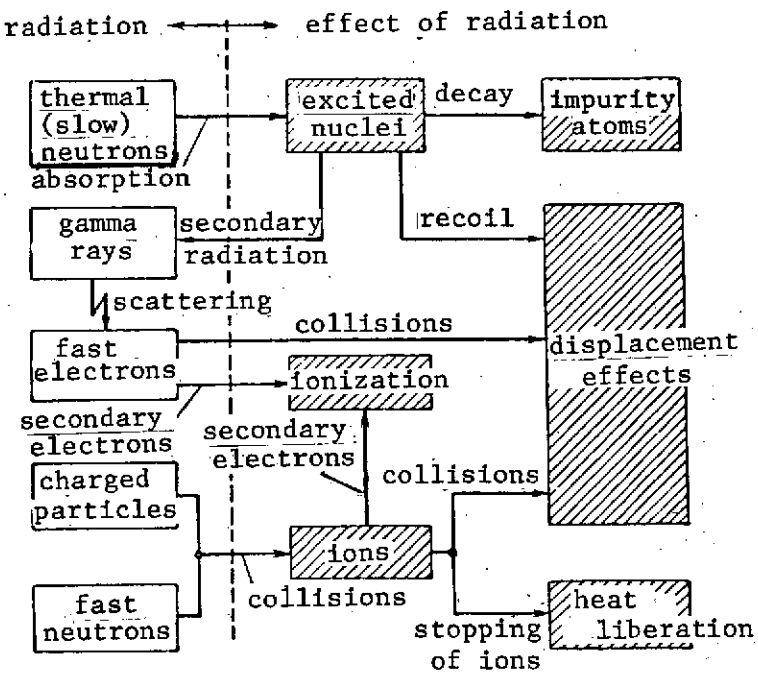

Fig. 2.20. Characteristics of ionizing radiation interaction with a material.

latter are displaced from their equilibrium positions. The simplest radiation defects, the so-called Fresnel defects [9], [54], characterize the resultant displaced atoms and vacancies in the lattice. Thus, to displace an atom of silicon from the crystal lattice, it must be given an energy of $E_d \approx 25$ eV. The number of displaced atoms v(E) in the lattice depends on the binding energy of the atoms in the lattice, the energy, and the form of particles interacting with the material:

$$\nu(E) \approx \frac{E_y}{2E_d},$$

where E_y is the energy expended by an interacting particle on elastic interactions; E_d — threshold displacement energy of an atom in the lattice.

However, for ion crystals and several other compounds, the effects of the displacement of atoms and the formation of vacancies may even be observed if the energy of interacting radiation is insufficient to displace the particles as a result of the direct action. In order to explain the high effectiveness of the formation of optical defects in ion crystals, Varly [219], [220] proposed a mechanism for atom displacement in the case of multiple ionization of a negative ion in a lattice site. With this ionization, the position of the atom becomes unstable, and it may be rejected from its position by Coulomb forces of the positive ions located at adjacent lattice sites. After the capture of the deficient electrons, the atom changes to a stable, displaced atom. Varly did not discover the end of this mechanism. /93

Heavy charged particles with sufficient energy can produce a large amount of secondary and tertiary displaced atoms along their track. These atoms will comprise a significant proportion of the total amount of displaced atoms. Recently, the dynamics of the formation of radiation defects in the crystal lattice has been successfully studied by means of computers.

More complex radiation defects of the lattice, such as thermal wedge, displacement wedge, etc., are characterized by the interaction of numerous particles covering the zone with hundreds and thousands of atoms.

The excited region along the track of a primary ejected atom, if its energy is adequate to excite a large number of secondary particles, is heated to a very high temperature in the time 10^{-10}—10^{-11} sec. The heated local region which is formed is called the thermal wedge.

If the energy of the ejected atom is sufficiently large to displace a large number of atoms in the lattice, then such a region is usually called the displacement wedge. The thermal wedges and the displacement wedges are characteristic for interaction of charged particles and neutrons with matter. The electrons primarily form point defects, which fill the radiated volume more or less uniformly.

The radiation defects in the crystal lattice are not stable formations. They may be displaced over the lattice, and recombine when encountering defects of the opposite sign. Adsorption of the radiation defects occurs at the dislocations and at the grain boundaries. Some types of radiation defects, combining together, form complexes of defects.

After the radiated material is heated, the radiation defects acquire great mobility, and recombination and annealing of the radiation defects are accelerated. The formation of solid bodies and more complex radiation defects in the crystal /94 lattice influences the optical, electrical, mechanical, and other properties of the material.

Formation of color centers [26], [219], [220]

When charged particles pass through dielectric and semiconductive pigments, which comprise the main part of temperature controlling coverings, secondary electrons and holes are produced as a result of the ionization processes. A large portion of the electrons and holes recombine with each other in a very short period of time. Others are captured by defects in the structure and impurity atoms. In pigments of temperature controlling coverings (ZnO, TiO_2, etc.) the impurity atoms, particularly aluminum atoms and alkaline metal atoms, play an important role in the formation of the color centers. Different types of color centers are formed, depending on the type of defect which captures an electron or a hole. The color centers in ion crystals have been studied particularly carefully. The color center is a defect in the crystal lattice, which is formed due to the capture of an electron or a hole in the zone of the vacant node. The coloration centers determine the level of light absorption in transparent optical materials, and may influence the increase in the solar radiation absorption coefficient in the temperature controlling coverings. The effectiveness of the formation of color centers in the majority of optical materials, in the case of an absorbed dose of radiation up to 10^6--10^7 rad, depends slightly on the type of radiation, since

secondary electrons and holes are primarily captured by defects existing in the material and by foreign atoms [26]. When the material absorbs large doses of radiation, during the process when additional color centers are formed, the formation of new defects in the crystal lattice plays an important role.

At low temperatures, the equilibrium concentration of color centers increases, since the recombination of captured electrons and holes is slowed down. In the case of heating and irradiation of crystals with light, which were previously subjected to the action of radiation, the color centers concentration sharply decreases due to their intensified recombination.

Radiation-chemical conversions [30], [104]

When charged particles pass through a substance, if their energy exceeds some tens of electron volts, they cause ionization and excitation of molecules along the track of the interacting particle. The ionization and excitation molecules are chemically active products. The state of these particles depends slightly on the type of radiation. Differences are observed only in the relationship of the products formed, due to a differing intensity of the ionization and excitation products in the track of the particles. The maximum density of energy losses by ions in a /95 substance is observed at the end of their path. The number of excited and ionized molecules is proportional to the strength of the absorbed dose of radiation.

An excited molecule is formed, either immediately during interaction of radiation with a molecule, or as a result of neutralization of the ionized molecule. The lifetime of excited molecules is $\sim 10^{-8}$ sec. The excited molecule can return to an unexcited state as a result of the following : a) fluorescence, b) transfer of energy to adjacent molecules, c) dissociation of the excited molecule, and d) chemical reaction with the adjacent molecule.

The probability of molecule dissociation depends on the binding energy of the molecule. During the dissociation of molecules, they are decomposed into atoms, radicals, and ions. During the decomposition of excited molecules, or as a result of ion reactions, free radicals are produced which have one or several unfilled chemical bonds. The presence of free radicals determines the course of certain radiation-chemical reactions in a solid body. The remaining free radicals recombine, and the lifetime of certain types of free radicals may be counted in hours and days.

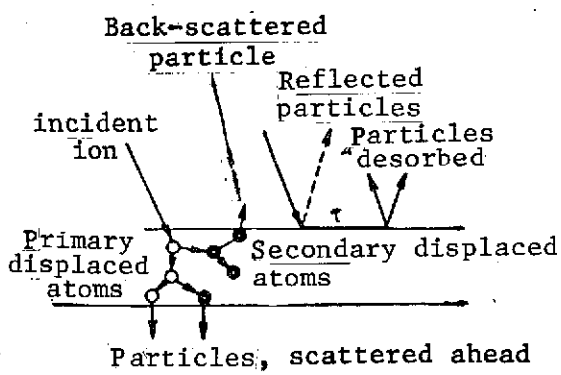

Fig. 2.21. Schematic representation of certain phenomena occurring during the collision of ions and the surface of the metal. τ — average time the incident particle remains on the surface in the adsorbed state.

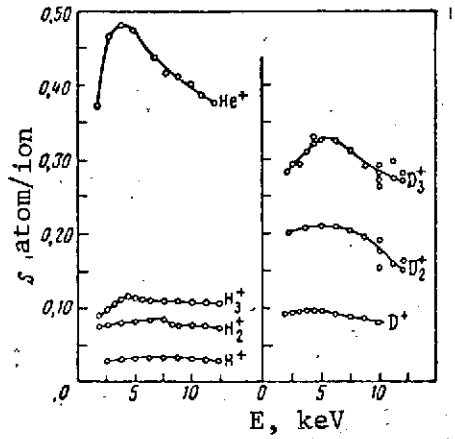

Fig. 2.22. Dependence of the cathode puttering coefficient S of a silver target on the energy of the bombarding ions.

In polymer materials, as a result of radiation-chemical reactions, destruction processes may occur, i.e., the formation of more simple molecules, or else crosslinking processes, when complex crosslinks are produced between molecules. In the case of crosslinking, there is an increase in the molecular weight, the formation of an insoluble lattice, and strengthening of the polymer. Simpler compounds are produced, and the mechanical properties of the polymers deteriorate in the case of destruction, due to a breakoff of the molecular bonds.

Pulverization of material and change of its surface properties [1], [54], [94]

The pulverization of the surface layers of a material occurs when the surfaces which are of different materials are bombarded with ions of hydrogen, helium, and other elements having a wide range of energies. This phenomenon has been described in detail in several studies as pulverization of matter under the influence of ion bombardment. We shall briefly discuss its most important features in connection with the interaction of the outer surface of a spacecraft with particles of the upper atmosphere of the Earth and other planets, with corpuscular radiation of the Sun and the radiation belts of the Earth [2].

At the present time, there are two predominant hypotheses regarding the mechanism of pulverization of material with ion bombardment. With the formation of rapid displaced atoms in the surface layers of a material, as a result of ion bombardment

part of them may penetrate the surface due to cascade transfer of energy (Figure 2.21). According to another hypothesis, the pulverization of material in the case of ion bombardment may be explained by strong local heating of the surface in the region where the ion impacts, and, as a result, sublimation of the material. Under real conditions, another pulverization mechanism may occur. /96

The coefficient of cathode sputtering of material S greatly depends on the energy and mass of the interacting ion, the angle of incidence of the ion beam, the state of the surface, and many other factors. Figure 2.22 shows the dependence of the sputtering coefficient S of silver on the energy of hydrogen and helium ions. The energy dependence of the coefficient S has a mildly sloping maximum for these ions in the region of several kiloelectron volts.

In comparison with pure metals, the oxide layers have a much lower sputter-ing coefficient. The energy of atoms in the pulverized material may change to several kiloelectron volts.

If we assume the maximum coefficient of cathode sputtering for protons is $S \approx 2 \cdot 10^{-2}$ atom/proton, then the amount of pulverized material per year when artificial Earth satellites remain in the radiation belts of the Earth, or in the zone of the aurora polaris, will be $\Phi_a \approx S\Phi_p \approx 2 \cdot 10^{14}$ atom/cm$^2 \cdot$gr, i.e., it comprises about one monolayer of material.

Protons and ions of helium, interacting with the materials, may also enter into chemical reactions with the material of the target and with the layers of gas molecules and other compounds adsorbed on its surface. The chemical activity of /97 accelerated ions is much greater than particles with thermal energy, since the activation energy of chemical processes amounts to only tenths of an electron volt. Exciting the surface atoms of the covering material and the gases adsorbed upon it, the bombarding ions have a very catalytic effect during certain chemical processes. The volatile chemical compounds produced as a result of the surface reactions may penetrate the target, increasing the effective coefficient of cathode sputtering [27].

When thin metal films, which are deposited on the surface of a solid body by vacuum spraying or by chemical means, are bombarded by hydrogen ions, small bubbles may be observed under the film of metal, which also leads to a change in

the optical properties of the surface being bombarded.

During the flight of spacecraft around the Earth or other planets, the surface layers of the temperature controlling coverings and other elements on the outer body of the spacecraft interact with particles of the upper atmosphere of the planets. As was shown in Chapter I, the upper atmosphere of the Earth at altitudes above 200 km is primarily composed of molecules, atoms, and ions of oxygen, nitrogen, helium, and hydrogen. The maximum concentration of ions in the upper atmosphere of the Earth is $n_i \approx 5 \cdot 10^5$ ion/cm^3 at an altitude of 250 - 300 km. According to recent data, the upper atmosphere of Venus and Mars is primarily composed of carbon dioxide.

For artificial satellites of the Earth, Mars, or Venus the collision energy of particles in the upper atmosphere with the temperature controlling coverings is 5 - 10 eV. The negative potential of the satellite at altitudes of 200 - 500 km with respect to the ionosphere is tenths of an electron volt [67]. Its contribution to the energy of interaction between ions and surface elements of the artificial Earth satellite may be disregarded when such processes are simulated.

When there are ion or plasma engines on board the spacecraft, the satellite potential with respect to the surrounding medium may increase. In this case, the energy of interaction for ions of the upper atmosphere of the planets with the outer surface of the artificial Earth satellite may exceed the energy range given above.

The pulverization of temperature controlling coverings with bombarding ions and atoms due to the kinetic collision energy is not important. In actuality, the sputtering coefficient, for example of glass, with ions of argon having an energy of ~5 eV is $S \approx 10^{-10}$ atom/ion according to estimates and [94]. The maximum pulverization rate of a satellite surface at an altitude of 250 - 300 km per unit of time by ionosphere particles, with an artificial Earth satellite velocity of $v \approx 8 \cdot 10^5$ cm/sec, will be $\Phi_a = Svn_i \approx 40$ *ат/см*^{2}sec, and in one year $\Phi_a \approx 10^9$ *ат/см*^{2}. If we /98
assume that the coefficient for pulverization of a surface by ions and atoms of equal energy is the same, then the amount of pulverized material per year is $\sim 10^{14}$ *ат/см*^{2} for interaction with particles of the upper atmosphere at these orbits. The pulverization rate for silver, obtained by a direct measurement on an artificial earth satellite by means of a quartz resonator, is ~50 Å/year. Since ions and atoms interacting with the surface of temperature controlling coverings have a very great chemical activity, the pulverization rate will primarily be determined by the

electrochemical pulverization [126], [134], [270].

An ion and atomic gaseous flux impacting on temperature controlling coverings has the same thermal energy $kT > E_a$. For many chemical processes E_a does not exceed 0.3 - 0.4 eV. New branches of chemistry are studying the chemical interaction with matter of atomic and ionized particles with an energy greater than E_a: high energy chemistry and plasma chemistry. The basic constants of the chemical reactions are not available for these branches of chemistry in the majority of cases. The kinetics of chemical processes of particles with Boltzmann distribution cannot be used for high energy chemistry [270], [272]. It is well-known that atoms and ions with an energy exceeding E_a have very great chemical activity. When these particles interact with a surface, many types of chemical processes may take place, which as a rule do not occur under ordinary conditions.

Thus, for example, the diffusion rate of a gas with an energy of 5 - 10 eV must be greater than for a gas at room temperature [153]. The saturation of metal surface layers with a gas may change its optical characteristics.

The interaction of free oxygen atoms with the surface of polymers leads to a high oxidation rate, which is much greater than the oxidation rate during contact with molecular oxygen.

Micrometeorite erosion

When spacecraft operate for a long period of time in circumterrestrial or interplanetary space, the erosion of temperature controlling coverings, coated optics, and specular surfaces may be observed as a result of the interaction of micrometeorite fluxes and particles of planetary origin. The erosion rate may sharply increase when the spacecraft enters a region of high concentration of micrometeorite particles, for example, during a flight to Jupiter through the asteroid belt, etc. Micrometeorite erosion may change the coefficient of solar radiation absorption A_s and the radiation blackness coefficient ε of the temperature controlling coverings.

There is a reduction of the light reflection coefficient R on the specular surfaces. Micrometeorite erosion of optical surfaces will primarily be determined /99 by micrometeorite particles with masses of $m < 10^{-8}$ g, since the density of

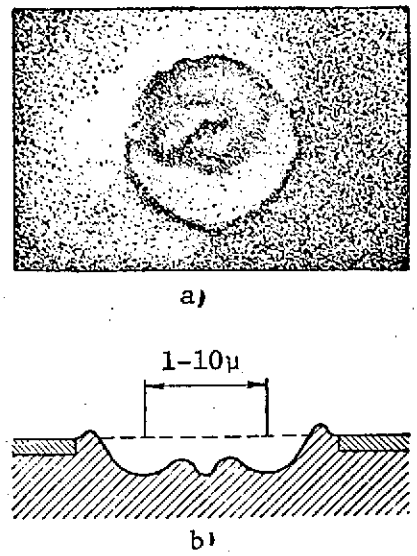

Fig. 2.23. Photograph of a crater formed by the impact of a high speed particle (a). Profile of the crater transverse cross section (b).

micrometeorite particles in circumterrestrial and interplanetary space, as was indicated above in Section 4, Chapter I, increases with a decrease in the particle mass.

For a precise calculation of the influence of micrometeorite erosion in space upon the change in the characteristics of temperature controlling coverings, it is necessary to know, on the one hand, the manner in which the form and dimensions of the crater for different types of materials depends on the mass and velocity of micrometeorite particles. On the other hand, the precise value is necessary for the dependence of the density of micrometeorite particle fluxes on their mass for different regions of circumterrestrial and interplanetary space.

To answer the first question, we have more or less reliable experimental data obtained under laboratory conditions by means of microparticles accelerated up to space velocities. The relationship $j_m(m)$ for $m < 10^{-8}$ g in different regions of space is very uncertain (see Figure 1.35), and represents the primary inaccuracy involved in calculating the area of micrometeorite erosion of different materials.

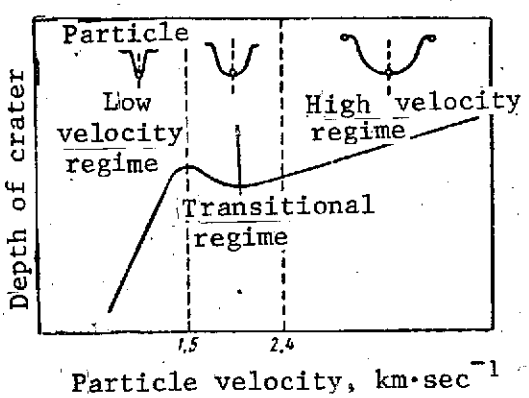

Fig. 2.24. Dependence of the crater depth in relative units and its form on the particle impact velocity.

The mechanism of the interaction of accelerated microparticles up to $v < 10$ km/sec with solid bodies has been adequately studied [38], [48]. There are much fewer data on the interaction with materials of particles with higher velocities. This may be explained by the experimental difficulties in accelerating microparticles up to $v > 10$ km/sec.

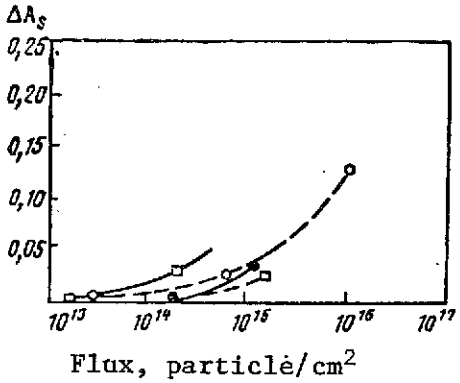

Fig. 2.25. Dependence ΔA_s of a white, temperature controlling covering ($ZnO + K_2SiO_3$) on the flux of charged particles: curve 1-α (5 MeV); curve 2-p (8 KeV); curve 3-α (8 KeV); curve 4-p (2.5 MeV).

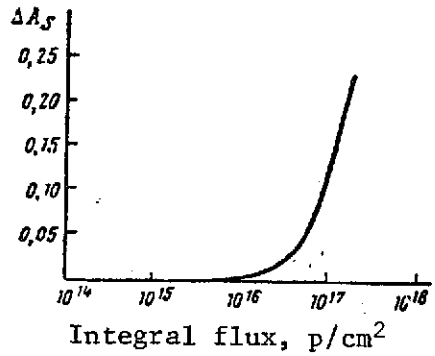

Fig. 2.26. Dependence ΔA_s of anode covering with low ε on a flux of low energy protons.

In the region where the micrometeorite particle impacts on the target, a shockwave is propagated, a crater is formed (Figure 2.23), the temperature increases, and luminescence is observed. The energy of the colliding particle is primarily expended on ejecting the target material from the crater, deformation of the material in the region of the crater, and propagation of the shockwave throughout the material, radiation of light, formation of a bulge around the crater, etc.

The pressure on the front of the shockwave may reach millions of bars [79], [100]. In the case of a hypersonic impact, when the velocity of the particle exceeds 15 - 20 km/sec, a significant portion of the energy of the particle is expended on fusion, vaporization of the particle and the target, and creation of a plasmoid. The pressure of a shockwave may thus reach tens of millions of bars.

The size and form of the crater depend on the velocity of the particle and on the form of the particle material and the target (Figure 2.24). At particle velocities of 5 - 10 km/sec, the crater has a semi-spherical form. At greater velocities, the interaction of the particle with the target has an "explosive" nature. For different metallic targets, the threshold velocity of the "explosive" interaction of accelerated particles ranges between 14 - 20 km/sec.

As a result of micrometeorite erosion, polished and specular surfaces become /101
turbid, the R coefficient decreases, and there is a change in the ratio A_s/ε on the temperature controlling coverings [79].

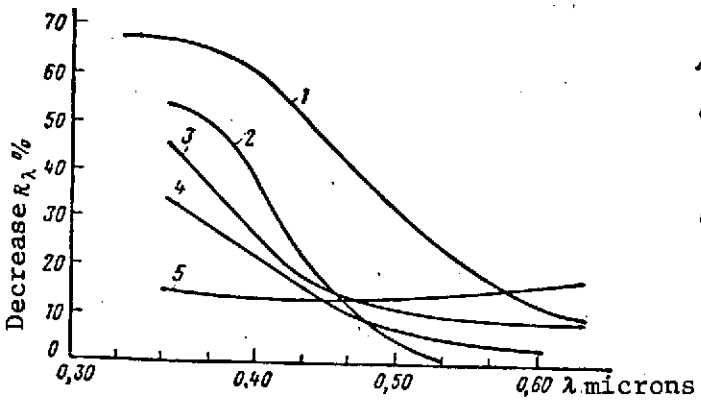

Fig. 2.27. Influence of proton bombardment (E_p = 50 KeV) $\Phi_p = 8 \cdot 10^{14}$ proton/cm^2; $j_p = 2 \cdot 10^{12}$ proton/cm^2·sec on the change in the spectral dependence of the reflection coefficient of different white coverings: 1 — ZnS + epoxy resin; 2 — ZnO + silicon binder; 3 — TiO_2 + silicon binder; 4 — ZnO + K_2SiO_3; 5 — TiO_2 + + K_2SiO_3.

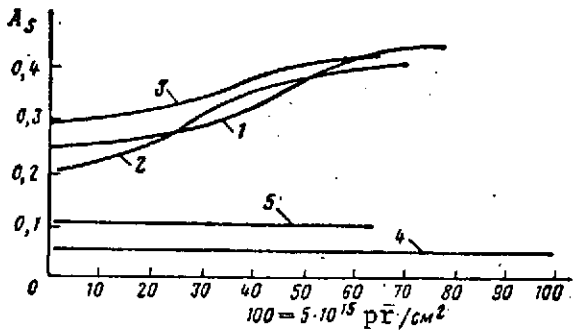

Fig. 2.28. Influence of proton bombardment (E_p = 130 KeV) on a change in A_s of different coverings: 1 — TiO_2 on aryl resin; 2 — TiO_2 on silicon binder; 3 — white covering; 4 — optical solar reflector; 5 — optical solar reflector, pr=protons.

5. Stability of Temperature Controlling Coverings During the Simulation of the Interaction Between Corpuscular Fluxes and Ultraviolet Radiation

Both beams of charged particles and other types of nuclear radiation are used when studying the radiation stability of temperature controlling coverings.

Studies of the radiation stability of temperature controlling coverings to the action of charged particles have been carried out by using beams of protons with energies of 2 - 9 keV; 50 - 400 keV, 2 MeV, and also beams of helium ions with energies of 2 - 16 keV, 5 MeV, and beams of electrons with an energy of 1 MeV (Figure 2.25 - 2.30). The integral fluxes of the particles change between 10^{13} — 10^{16} part/cm^2.

Tables 12 and 13 give data on the change in the absorption coefficient A_s of coverings before and after radiation with protons having an energy of 130 keV, electrons with an energy of 1 MeV, and ultraviolet radiation from a xenon lamp of the AN-6 type, with a power of 1 kW [145], [155], [156], [157].

It follows from these studies (Figures 2.25 - 2.30 and Tables 12 and 13) that

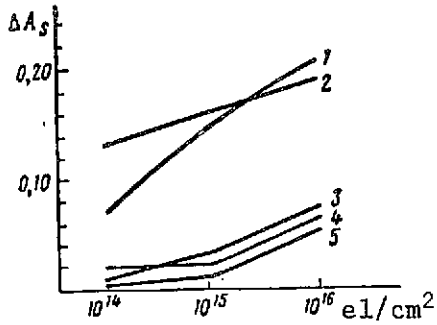

Fig. 2.29. Change in absorption coefficient A_s after irradiation in a vacuum of different coverings with electrons having an energy of 1 MeV:
1 — LiAl x SiO_4; 2 — LiAl = SiO_3; 3 — TiO_2 on epoxy resin; 4 — TiO_2 on aryl resin; 5 — TiO_2 on silicon binder.

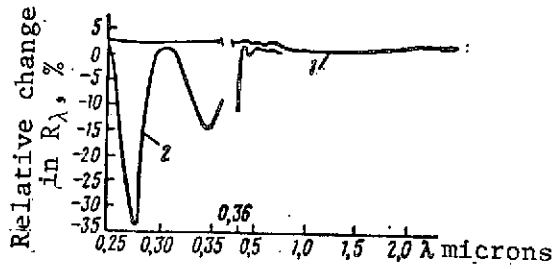

Fig. 2.30. Influence of irradiation protons having an energy of E_p = 7.7 KeV on the change in the reflection coefficient R_λ of anodized aluminum:
1 — control specimen; 2 — after irradiation with $1 \cdot 10^{16}$ proton/cm^2.

fluxes of charged particles

$$\Phi_p \approx 10^{16} \text{ proton/cm}^2, \ 1 \text{ keV} < E_p < 10 \text{ keV},$$

$$\Phi_p \approx 10^{14} \text{ proton/cm}^2, \ 10 \text{ keV} < E_p < 1 \text{ MeV},$$

$$\Phi e \approx 10^{15} \text{ electron/cm}^2, \ 1 \text{ keV} < E_e < 0.1 \text{ MeV}$$

produce significant changes in the absorption coefficients of different types of /103 white temperature controlling coverings. With these fluxes, the anodized metallic surfaces with thin metallic layers barely change their optical characteristics, and to damage them fluxes of 10^{16} — 10^{17} proton/cm^2 are required [200], [201].

The data given in Figures 2.25 - 2.30 and Tables 12 - 14 were obtained by /104 measuring the A_s and R_λ coefficients of irradiated samples of coverings, after the coverings were removed from the experimental vacuum chambers into the air. Irradiated coverings with a high A_s coefficient "become white" during contact with oxygen from the air, i.e., the A_s coefficient decreases. Therefore, the results obtained from these studies on the radiation stability of temperature controlling coverings may be regarded as too high and not sufficiently reliable.

In a study of the dependence of a change in the A_s coefficient on the absorbed/105 dose of radiation D, saturation is observed for absorbed doses of radiation higher than 10^8 - 10^9 rad [200] - [203]. The spectral relationships ε have the same form

TABLE 12.*

Type of covering	Integral flux proton/cm^2	A_{s_0} before irradiation	A_s** after irradiation
TiO_2 on aryl resin	$3{,}9\cdot10^{15}$ $2\cdot10^{15}$ $2\cdot10^{15}$ $3{,}9\cdot10^{15}$	0,24 0,24 0,24 0,24	0,44 0,33 0,35 0,44
TiO_2 on silicon binder	$3{,}5\cdot10^{15}$ $1{,}5\cdot10^{15}$ $1{,}0\cdot10^{15}$ $3{,}5\cdot10^{15}$	0,19 0,19 0,19 0,19	0,42 0,32 0,25 0,42
Brilliant white covering (TiO_2 + silicon resin)	$>10^{15}$ $3{,}2\cdot10^{15}$ $2\cdot10^{15}$	0,29 0,29 0,29	0,54 0,42 0,38
Optical solar reflector	$2\cdot10^{15}$ $>10^{15}$	0,05 0,05	0,05 0,05
Gilded surface	$1{,}5\cdot10^{15}$ $1{,}0\cdot10^{15}$	0,33 0,34	0,33 0,34

*Commas represent decimal points.

**A_s was measured in the air.

TABLE 13.

Type of covering	Before irradiation A_{s_0}	U.V. of 436 solar hours, $\lambda = 0.2$ — 0.4 μ A_s	Electrons $6\cdot10^{14}$ electron/cm^2 A_s	Combination of electrons $6\cdot10^{14}$ el/cm^2 + U.V. of 436 solar hours, A_s
TiO_2 on silicon binder	0.19	0.22	0.20	0.24
TiO_2 on aryl resin	0.24	0.33	0.25	0.43
Brilliant white covering (TiO_2 + silicon resin)	0.29	0.38	0.30	0.38
Optical solar reflector	0.044	0.044	0.044	0.044

U.V. = Ultraviolet radiation of 436 solar hours.

TABLE 14.

Covering		Solar absorption coefficient			
Pigment	Binder	Initial value As_0	ΔA_s dose of gamma radiation		ΔA_s 300 equivalent solar hours
			77 Mrad	385 Mrad	
Zinc oxide	K_2SiO_3	0.14	0.04	0.04	0.01
Zinc oxide	Organo silicon	0.17	0.04	0.04	0.04
Titanium dioxide	Organo silicon	0.25	0.12	0.18	0.03
Antimony trioxide	K_2SiO_3	0.26	0.10	0.26	0.07
Titanium dioxide	Epoxy	0.20	0.22	0.27	0.19

for many types of coverings after being subjected to charged particles and ultraviolet radiation. This points to similar radiation processes in the coverings irradiated.

Particularly rigid requirements for radiation stability are imposed on temperature controlling coverings which are used on spacecraft with a nuclear reactor on board [170]. The test conditions of the temperature controlling coverings were determined, on the one hand, by the presence on the spacecraft of a nuclear source SNAP-10A and, on the other hand, by the flight duration (8000 hours) along a polar orbit at an altitude of 1300 km.

Table 15 gives the results of experiments when simulating the radiation effect of a reactor and of bundles of charged particles on certain types of coverings. These experiments showed that protons have a greater influence on increasing the A_s coefficient than do electrons. The coefficient ε decreases slightly under the influence of radiation from the reactor.

There is still no final solution to the problem of selecting the most radiation resistant covering for radiation in space. Studies of different types of temperature controlling coverings have shown that a covering based on $ZnO + K_2SiO_3$ has the

TABLE 15.*

Pigment	Binder	Protons (proton/cm^2) E_p = 150 keV	Electrons (electron/cm^2) E_e = 2 MeV	Neutrons (neutron/cm^2) rapid	Gamma radiation R (roentgen)	T°C	Vacuum, torr	A_{s_0}	A_s	ΔA_s %	ε_0	ε
ZnO	K_2SiO_3	$1,2 \cdot 10^{16}$	—	—	—	—	10^{-6}	0,17	0,33	94	—	—
ZnO	K_2SiO_3	$1,0 \cdot 10^{16}$	—	—	—	50	10^{-6}	0,17	0,27	59	—	—
ZnO	K_2SiO_3	$1,0 \cdot 10^{16}$	—	—	—		10^{-6}	0,17	0,30	77	—	—
ZnO	K_2SiO_3	$1,0 \cdot 10^{15}$	—	—	—		10^{-6}	0,17	0,21	24	—	—
ZnO	K_2SiO_3	$1,0 \cdot 10^{14}$	—	—	—		10^{-6}	0,17	0,19	12	—	—
ZnO	K_2SiO_3	—	$1,0 \cdot 10^{16}$	—	—		10^{-6}	0,17	0,20	18	—	—
ZnO	K_2SiO_3	—	$1,0 \cdot 10^{15}$	—	—		10^{-6}	0,17	0,18	6	—	—
ZnO	K_2SiO_3	—	$1,0 \cdot 10^{14}$	—	—		10^{-6}	0,17	0,18	6	—	—
SnO_2	Al phosphate	$1,0 \cdot 10^{16}$	—	—	—		10^{-6}	0,35	0,50	43	—	—
SnO_2	Al phosphate	$1,0 \cdot 10^{15}$	—	—	—		10^{-6}	0,35	0,42	20	—	—
SnO_2	Al phosphate	—	—	$3 \cdot 10^{18}$	$1,9 \cdot 10^{10}$	315	10^{-5}	—	—	—	0,91	0,90
SnO_2	Al phosphate	—	$3 \cdot 10^{18}$	—	—	315	10^{-5}	—	—	—	0,90	0,88
SnO_2	Al phosphate	—	$3 \cdot 10^{18}$	—	—	315	10^{-5}	—	—	—	0,90	0,89
Cr_2O_3	deposited with plasma	—	—	$3 \cdot 10^{18}$	$1,9 \cdot 10^{10}$	315	10^{-5}	—	—	—	0,84	0,81

*Commas represent decimal points.

greatest radiation resistance.

The following general recommendations may be followed to increase the radiation resistance of coverings.

The type of binder has a great influence on the resistance of coverings to

corpuscular and ultraviolet radiation. White, ceramic temperature controlling coverings have great radiation stability as compared with white enamels on a base of organic binders. When white enamel coverings are used, it is advantageous to employ silicon binders which have greater radiation resistance, as compared with other organic binders. When the grains of the pigment powder increase, the radiation resistance of the coverings increases, since thus there is a reduction in the number of surface defects, which are traps for electrons and holes when color centers are formed. It is advantageous to use pigments with a maximum degree of chemical purity, since foreign admixtures in their lattice lead to the development of additional color centers. It is expedient to expose the pigments to heat treatment in order to reduce the concentration of surface defects, which form due to mechanical stresses when they are applied. Special forms of protective additives which are introduced into the binder may contribute to the absorption and scattering of the energy of excitation, which is introduced by the radiation, thus increasing the radiation resistance of the coverings.

Micrometeorite erosion of the surface of temperature controlling coverings /107
changes the coefficients A_s, R_λ, ε. A great number of experimental studies on the influence of micrometeorite erosion upon the coefficients A_s, R_λ and ε have been carried out with metallic surfaces.

The studies [38], [79], [227], [231] have investigated the influence of the bombardment by accelerated microparticles upon the optical properties of metallic surfaces. Particles of silicon carbide with a diameter of 100 microns have been accelerated in a gas gun up to $v \approx 6$ km/sec. After the particles impacted on the metallic surfaces, the spectral relationships R_λ were recorded in the wavelength region $\lambda \approx 2-25$ microns (Figures 2.31 - 2.33). The coefficients A_s and ε were measured by the calorimetric method. As a rule, a change in the optical properties of the coverings appeared in the infrared region, since the dimensions of the craters were comparable with the wavelengths of light in the infrared region. As the calculations showed, carried out on the basis of data given in Figure 1.35, when spacecraft remain for one year in circumterrestrial space the maximum damage to the metallic surfaces, caused by erosion during the interaction of micrometeorites with particles of planetary aerosol, may amount to several tens of percents (Figure 2.34). This may have a great influence on the ratio A_s/ε on their surface.

Figure 2.35 shows the experimental relationship $\bar{R}_f/\bar{R}_0(E)$ obtained when polished

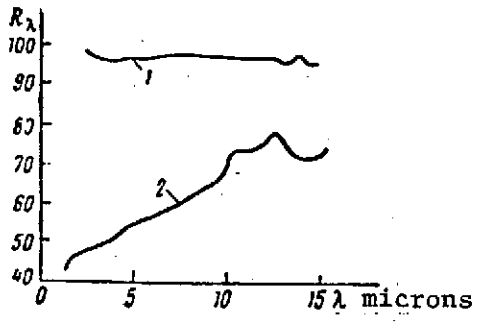

Fig. 2.31. Spectral dependence of the reflection coefficient of an aluminum disk before (curve 1) and after (curve 2) bombardment by particles with diameters from 2 to 14 microns of silicon carbide, with a velocity of M ≈ 8.4 (M — Mach number).

aluminum was bombarded with accelerated microparticles. With a total impact energy of $E=\sum\frac{1}{2}m_i v_i^2$, which amounts to on the order of 1 J/cm^2, $\tilde{R}$ decreases from $\overline{R}_0$ = 0.95 to $\overline{R}_f$ = 0.76 and the coefficient ε changes under these conditions from 0.05 to 0.24, i.e., by approximately a factor of 5 in the λ = 1.5 ÷ 15 microns wavelength range. If it is assumed that the upper limit for the total kinetic energy $\sum\frac{1}{2}m_i v_i^2$ of the fluxes of micrometeorite particles and planetary particles, when the mass ranges from $10^{-12} \div 10^{-6}$ g per year, corresponds to approximately 1,5 J/ /109
1.5 J/cm^2 or 1 J/cm^2 in eight months, we then have

$$\overline{R}_f/\overline{R}_0 \approx 0{,}8.$$

The empirical relationship R(E) has the form

$$\overline{R}_f/\overline{R}_0(E)=\left\{1-\left(1-\frac{\overline{R}_\infty}{\overline{R}_f}\right)(1-e^{-\delta E})\right\},$$

where $\overline{R}_\infty$ is the reflection coefficient after prolonged bombardment;
δ — constant equal to 0.211 J$^{-1}\cdot$cm^2.

If we assume that $\overline{R}_\infty$ = 0, then the time necessary for $\overline{R}_0$ to double is approximately three years.

The data given in Figures 2.34 and 2.35 on the influence of micrometeorite erosion upon the degree to which metallic surfaces become dull and the change in their reflection coefficient were obtained on the assumption that the density of the micrometeorite fluxes and planetary particles of the mass j(m) is distributed along the curve 1 (see Figure 1.35). Therefore, keeping in mind the comments made above regarding the possible errors in measurements of the density of solid particle fluxes in space, these data may be regarded as only the upper limit for the influence of erosion on optical properties of metals.

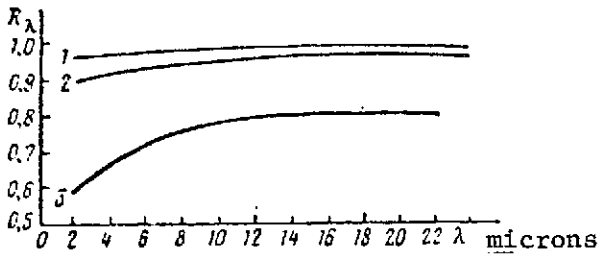

Fig. 2.32. Spectral reflection coefficient R_λ in the infrared spectral region for an aluminum target before and after bombardment by microparticles:
1 — smooth target; 2 — target bombarded with particles with v = 1.5 km·sec^{-1}; 3 — target bombarded by particles with v = 6.0 km·sec^{-1}.

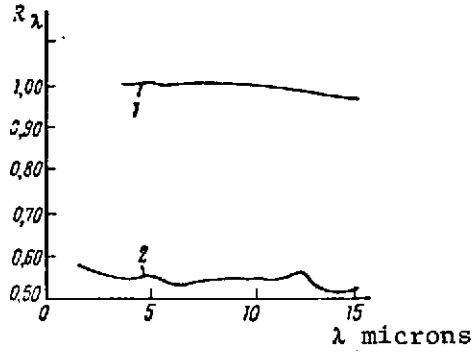

Fig. 2.33. Spectral dependence of the reflection coefficient R_λ of film made from mylar with a thickness of 12 microns with a sprayed layer of aluminum 2200° A, placed on a metallic disk before (curve 1) and after (curve 2) bombardment by microparticles of silicon carbide with a diameter of 2 to 14 microns and a velocity of M = 8.98.

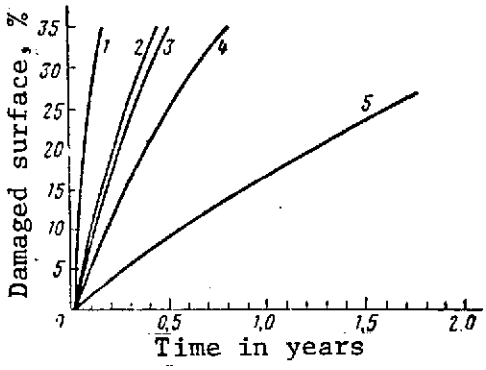

Fig. 2.34. Computational dependence of the damaged area on the time different metals remain on the surface of spacecraft:
1 — lead; 2 — cadmium; 3 — aluminum; 4 — copper; 5 — steel.

To obtain the absolute values of the change in the thermo-radiation properties of coverings, as a result of different factors in space, real tests must be carried out. A study of the behavior of the coverings under space conditions makes it possible to refine the methods of laboratory simulation of the action of different types of radiation in space and fluxes of micrometeorite particles on the most important characteristics of temperature controlling coverings.

American researchers have drawn up a program of real tests determining the resistance of temperature controlling coverings to the action of the space medium on artificial satellites of the Earth such as the OSO, the "Pegasus", and the interplanetary spacecraft "Mariner". /110

About 15 different types of temperature controlling coverings [221], [235], [236], [241], [252], [253] have been tested.

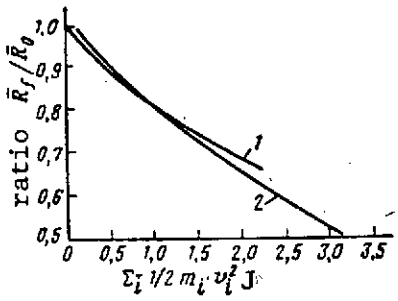

Fig. 2.35. Ratio $\bar{R}_f/\bar{R}_0$ as a function of the total energy $\sum \frac{1}{2} m_i v_i^2$ of interaction of a flux of accelerated microparticles of SiC with dimensions of 2 - 14 microns, bombarding an aluminum disk:
1 — experiment; 2 — calculated curve, $\bar{R}_f$ — average reflection coefficient of surface after bombardment, $\bar{R}_0$ — average reflection coefficient before bombardment.

The coverings on the artificial Earth satellites of the OSO and "Pegasus" type were subjected to the action of only three types of fluxes: a flux of ultraviolet solar radiation, a flux of particles from the upper atmosphere of the Earth, and a flux of micrometeorite particles. There was practically no bombardment of the coverings by charged particles with higher energies, since the artificial Earth satellite orbits were below the radiation belts of the Earth. The coverings on "Mariner-IV", apart from the action of ultraviolet solar radiation and micrometeorite particles, were subjected to the influence of solar corpuscular radiation.

Both on satellites such as OSO and "Pegasus", and also on "Mariner-IV", a change in the coefficient A_s of the coverings was determined by calorimetric methods by measuring the temperatures of samples of coverings on the outer surface of the spacecraft, which were insulated from the main mass of the spacecraft. For purposes of illustration, Figure 2.36 gives the time dependence of a change in the surface temperature of two types of coverings in one revolution around the Earth by the satellite OSO-I. A detailed description of the method used to measure A_s on the artificial Earth satellite OSO-I is given in [235], [236].

Figure 2.37 shows the dependence of a change in the coefficient A_s of a white covering (TiO_2 + silicon binder) on the duration of radiation in the laboratory and under space conditions. For this type of covering, there was a good agreement of the relationship $A_s(t)$ for real tests and radiation by an AN-6 Mercury arc lamp.

Figure 2.38 shows the dependence of a change in the coefficient A_s of white temperature controlling coverings (eight different types) on the time they remained on the outer surface of the OSO-II artificial Earth satellite (h = 600 km, φ = 33°) [241].

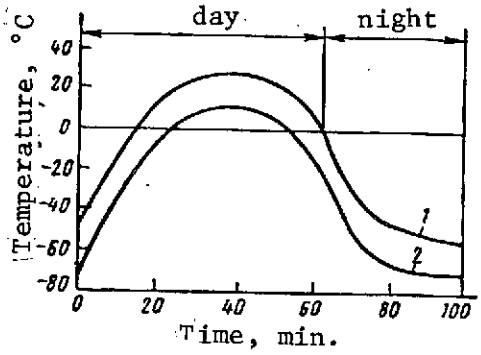

Fig. 2.36. Observed changes in the surface temperature of temperature controlling coverings on the OSO-I satellite:
1 — TiO_2 with epoxy binder;
2 — TiO_2 with silicon binder.

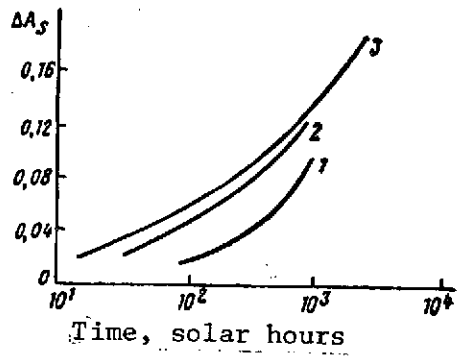

Fig. 2.37. Increase in the solar radiation absorption coefficient ΔA_s of a temperature controlling covering with a silicon binder when irradiated with a light flux from an A-N6 lamp (curve 1), B-N6 lamp (curve 2), and on the satellite OSO-1 (curve 3).

Figure 2.39 compares the results of laboratory tests when simulating the action of electromagnetic solar radiation on the covering with the data obtained during the flight of OSO-II. Under laboratory /111 conditions, the coverings were irradiated with a B-N6 lamp, whose radiation intensity was 5 times greater than solar radiation in the ultraviolet spectral region. The pressure in the experimental chamber was $\sim 10^{-7}$ torr.

An analysis of the flight and laboratory tests shows that coverings with an /112 inorganic binder are more resistant to ultraviolet radiation than coverings with an organic binder. The covering TiO_2 + silicon binder has the least resistance; $ZnO + K_2SiO_3$ has the maximum resistance.

Laboratory tests still cannot reliably predict the change in the coefficient A_s of coverings under space conditions. In actuality, the covering ZrK_2SiO_3, based on laboratory tests, has a relatively low resistance to ultraviolet radiation. In real tests, this covering had a higher resistance. On the other hand, the covering ZnO + silicon binder during flights had low resistance, while in laboratory tests it was quite stable.

Figure 2.40 shows the relationships of the change A_s/A_{s0} during the flight of "Mariner-IV" toward Mars in seven and a half months [3500 equivalent solar hours) [221].

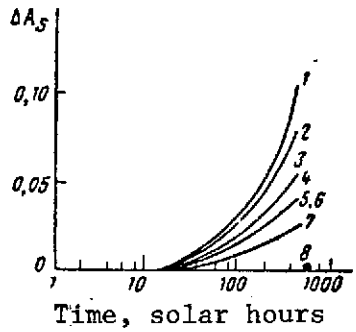

Fig. 2.38. Change in the coefficient A_s of certain temperature controlling coverings as a function of the flight duration of OSO-II:
1 — TiO_2 + silicon binder;
2 — ZnO + silicon binder;
3 — ZnO + silicon binder;
4 — LiO x Al_2O_3 x $4SiO_2$ + Na_2SiO_3;
5 — $ZrSiO_4$ + K_2SiO_3;
6 — Zr + K_2SiO_3;
7 — ZnO + silicon binder;
8 — ZnO + K_2SiO_3.

Experimental data on a change in the coefficient A_s of white temperature controlling coverings in space were obtained under real and laboratory conditions. They were not identical [241], [252], which indicates that the laboratory methods of simulating the action of different factors in space on temperature controlling coverings are not reliable. The reasons for these discrepancies may be varied. For example, no composite irradiations were used when obtaining the major portion of the experimental data on a change in the coefficient A_s of coverings, and a higher density of fluxes of corpuscular and /113 electromagnetic radiation was used under laboratory conditions as compared with real conditions. There is not always reliable control of the temperature of the sample irradiated in laboratory tests.

It is very difficult to reproduce exactly the characteristic energy spectra of corpuscular and electromagnetic radiation in space; these spectra are used under laboratory conditions to irradiate coverings. As recent studies have shown [223], with a decrease in the wavelength of light λ in the ultraviolet region of the

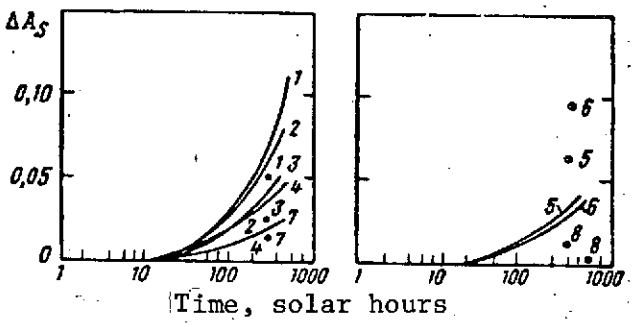

Fig. 2.39. Comparative data from laboratory and flight (on OSO-II) tests of temperature controlling coverings of eight different types: Points — laboratory tests; curves — flight data; remaining notation is the same as in Figure 2.38.

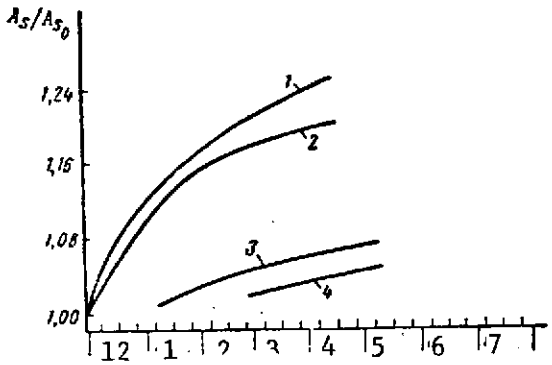

Fig. 2.40. Time dependence of a change in the ratio A_s/A_{s0} of temperature controlling coverings of four different types, on "Mariner-IV": 1 — white covering ARF-2; 2 — polished aluminum; 3 — aluminum powder in silicon binder; 4 — dark color with high values of A_s and ε.

spectrum, the effectiveness of temperature controlling coverings increases. There are specific technical difficulties entailed in a correct reproduction of ultraviolet radiation fluxes in the wavelength range <3000 Å with laboratory simulation. Thus, for example, due to the line structure of the radiation spectrum of mercury-quartz lamps, they cannot be used for predicting a change in the coefficients A_s of the coverings.

As a rule, the coefficients A_s of irradiated coverings are measured at atmospheric pressure, and not in an experimental vacuum chamber during or immediately after irradiation. This yields values which are too low for the influence of radiation on the coefficients A_s, due to partial whitening of the white temperature controlling coverings which have become darker during the irradiation [164], [223], [273].

In the case of laboratory simulation, the irradiated coverings may become contaminated due to inadequate sterilization of the vacuum conditions in the experimental chambers [58].

The effects of thermo- and photo-annealing of radiation defects in irradiated coverings, etc. are not always taken into account.

6. Influence of Weightlessness [18], [137]

One of the characteristic features of spacecraft operation is a very small or zero acceleration of gravity. Weightlessness may influence the spacecraft thermal regime indirectly by influencing the following:

a) Hydrodynamics of the heat carriers, fuel, oxidants;

b) Hydrostatics of the fuel and oxidants (particularly, cryogenic) in the tanks;

c) Boiling and condensation of coolants.

The designer checking the operation of the life support systems or the active temperature control, under the ordinary conditions of gravitation on the Earth, must establish what the thermal processes will be under conditions of weightlessness. In the future, when electric propulsion engines are widely used which produce very small accelerations ($\sim 10^{-3}$ g) over a long period of time, it will be important to /114 study the thermal processes not only at zero, but at very small gravitation*.

Liquids which do not completely fill the tanks under conditions of weightlessness attempt to take on the form at which the free surface energy assumes a minimum value. If the liquid does not contact the solid surface and has a temperature which is constant over the volume, it takes on the form of a sphere in the absence of perturbing forces. The presence of gravitational or inertial accelerations which are equivalent to them may greatly distort the equilibrium form of the free surface. For each specific case, there is a definite critical value of the acceleration of gravity, $g_* = kg_0$ (where $g_0 = 9.8$ m/sec^2, k — load factor), above which capillary action has a very small influence on the form of the free liquid surface. To determine the order of magnitude of g_*, let us write the ratio of the intensity of capillary forces acting on the liquid to the inertial forces:

$$N = \frac{\sigma L}{\varrho g_* L^3} = \frac{\sigma}{\varrho k g_0 L^2}. \tag{2.64}$$

Here L designates the characteristic linear dimension of the volume occupied by the liquid, σ — coefficient of surface tension**.

---

*Brief accelerations on the order of 10^{-2} - 10^{-3} g may arise during the operation of the attitude control engine.

**The coefficient of surface tension σ depends on the type of liquid and its temperature. According to the Ramsay and Shield law

$$\sigma = \frac{K}{v^{2/3}} (T - T_* - C),$$

where v is the molecular volume of the liquid, T_* — critical temperature at which σ and the surface energy of the liquid simultaneously decrease to zero, K and C — constants which characterize the given liquid, $K \approx 2$-2.23 erg/mole, C — between 6 and 9°C. For low temperatures and cases when great accuracy is not required, the Ramsay and Shield law may be replaced by the Eötvös formula:

$$\sigma = \frac{K}{v^{2/3}} (T - T_*).$$

As calculations of certain particular cases have shown [18], capillary action begins to predominate if $N \gg 1$, i.e., when $g_* = kg_0 \ll \frac{\sigma}{\varrho L^2}$.

Let us assume that at a certain moment of time weightlessness suddenly occurs for the spacecraft. Under the action of surface tension, the liquid with the free surface is set in motion, and tries to reach a new stable position. We may estimate the time necessary for the liquid to leave the state, when gravitational forces are decisive, and change to the state when surface forces prevail. The mass forces acting on a volume of liquid with the characteristic dimension L have the order of /115 magnitude ρL^3. The surface forces causing the acceleration of the liquid, $\sim\sigma L$.

The deformation of the liquid will occur with the acceleration

$$a = \frac{\sigma L}{\varrho L^3} = \frac{\sigma}{\varrho L^2}. \tag{2.65}$$

We shall assume that the difference between the initial form of the liquid surface and the equilibrium form is of the order of magnitude L. Then the time t_* necessary for this deformation will be on the order of

$$\sqrt{\frac{L}{a}} = \sqrt{\frac{\varrho L^3}{\sigma}}.$$

In order to determine the braking influence of viscosity, let us compare the energy dissipation rate

$$\dot{W} \sim \nu\varrho V_l^2 L \tag{2.66}$$

with the rate at which the forces of surface tension complete their work:

$$\dot{V}_\sigma \sim \frac{d(\sigma L^2)}{dt} \approx \sigma L V_l. \tag{2.67}$$

With allowance for equation (2.65), we may write the velocity of the liquid, which is included in (2.66) and (2.67), under the action of the surface tension forces in the following form

$$V_l \sim \sqrt{aL} \sim \sqrt{\frac{\sigma}{\varrho L}}. \tag{2.68}$$

We thus obtain

$$q = \frac{V_\sigma}{W} \approx \sqrt{\frac{\sigma L}{\rho \nu^2}}. \tag{2.69}$$

The numerical values in formula (2.69) show that we may disregard the viscosity when examining the motion arising under the influence of surface tension only for liquids whose masses are very small, or almost microscopic in size.

Retaining the quantities N, q and t^*, we may study the influence of reduced gravitation on the behavior of real liquids by means of models and specially selected liquids. /115

In the absence of strong gravitational fields, we must take into account all the forces which are of one order of magnitude with intermolecular forces. In addition to those indicated above, these forces may also be forces of electrostatic charges and forces of gravitational attraction of liquid insulated masses. Estimates [18] have shown that for spacecraft which are smaller than 10 m the inherent gravitational attraction of isolated liquid masses may be disregarded.

Hydrodynamics of heat carriers /116

The stationary flow of a single phase heat carrier through the channels and compartments of a spacecraft may be described by the equation

$$\mathrm{Nu} = A\,\mathrm{Re}^a \mathrm{Gr}^b \mathrm{Pr}^c. \tag{2.70}$$

The acceleration of gravity is included in this equation by means of the Grashof number $\mathrm{Gr} = \frac{k g_0 L^3 \rho^2 \beta \Delta T}{\mu^2}$ For small Re numbers, the Nu number depends only on Gr and Pr, namely: $\mathrm{Nu} \sim \sqrt[4]{\mathrm{GrPr}} \sim (k g_0)^{1/4}$. and the heat transfer is determined only by the thermal conductivity of the medium.

Experimental relationships of the (2.70) type are usually derived for k = 1, since it is difficult to carry out experimental studies when $g < g_0$ under terrestrial conditions. The experiments can only be carried out in a very short period of time, amounting to several seconds. For this purpose, flying laboratories and falling models are used (see Section 10, Chapter IV). However, scaling theory

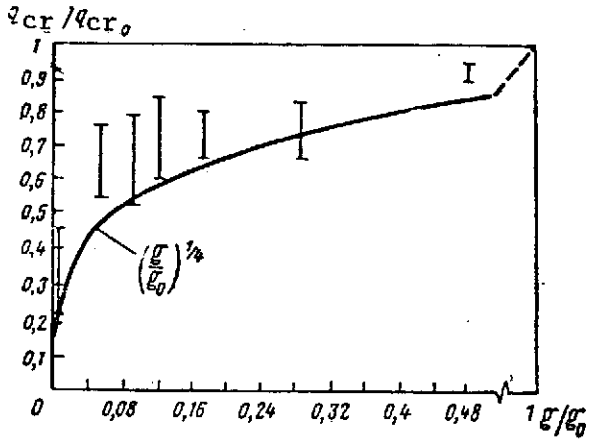

Fig. 2.41. Influence of a decrease in the gravitational field on the ratio of the critical thermal flux (when a wire is burned) to the critical thermal flux when g = 9.8 m/sec^2.

can be used to study the influence of the Gr number by changing any parameter which it includes.

Direct measurements of g may be most readily carried out by studying the boiling processes, and have shown that the load factor $k = g/g_0$ is actually included in the formulas describing the thermal and hydrodynamic processes in the form $k^{1/4}$ (Figure 2.41).

When studying the active systems /117 of temperature control at those locations in the spacecraft where the heat carrier has small Re numbers, the heat exchange due to natural convection $\alpha_{n.c.}$ becomes commensurate with the heat exchange due to forced convection ($\alpha_{f.c.}$). To decrease the ratio $\alpha_{n.c.}/\alpha_{f.c.}$ and to approximate conditions of space flight, we can decrease the Gr number by decreasing the linear size of L (changing to a scale model), using a heat carrier with a small dilation β, or by increasing the kinematic viscosity $\nu = \mu/\rho$. Decreasing the characteristic dimension L is a very effective method of reducing natural convection. It may be used when the spacecraft design makes it possible to establish horizontal deflectors in the flow, which divide the flow into several parallel streams. Decreasing the pressure (or the density, since $p = g\rho RT$) in a compartment also reduces the methodical errors when determining the effectiveness of active TCS. However, the heat exchange coefficient for forced convection $\alpha_{f.c.}$ depends on ρ, and the velocity of the heat carrier must be increased to maintain the thermal fluxes at the previous level. In compartments where the heat carrier is not set in motion by fans, to reduce the Gr number the compartment must be filled with porous, poorly conductive material.

Two-phase flow

The force of the velocity head p acting on a drop or a bubble is determined by an equation having the following form

$$p/F\,\frac{\varrho V^2}{2} = k\,\mathrm{Re}^a\mathrm{Bo}^b\mathrm{We}^c\mathrm{Fr}^d,$$

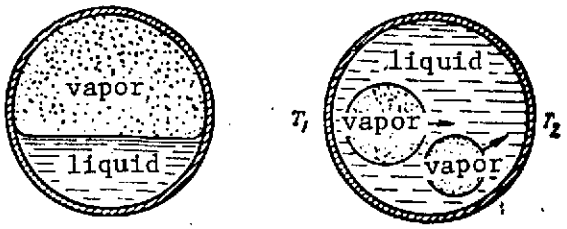

a) b)

Fig. 2.42. Movement of a gas bubble in a non-isothermic field:
a — normal gravitation ($g \geq 1$);
b — weightlessness ($g = 0$).

where

$$\mathrm{Re} = \frac{\varrho V L}{\mu}, \quad \mathrm{Bo} = \frac{\varrho g L^2}{\sigma},$$

$$\mathrm{We} = \frac{\varrho V^2 L}{\sigma}, \quad \mathrm{Fr} = \frac{V}{\sqrt{gL}}$$

are the Reynolds, Bond, Weber, Froude numbers.

As indicated above, for small L the viscous forces may be disregarded as compared with the forces of surface tension.

The forces of surface tension determine the critical thermal flux during boiling, the form and distribution of gas bubbles and liquid drops (globules). With reduced gravitation (or small dimensions) the capillary forces and the gravitation forces are of one order of magnitude. Therefore, it is particularly important here that the similarity of the temperature fields be satisfied. Thus, for example, non-uniform temperatures of the wall of tanks filled with liquid (Figure 2.42) may cause a displacement of gas bubbles to one side. The velocity of the liquid under the action of surface tension forces in this case is also on the order of $V_l \sim \sqrt{\sigma/\varrho L}$. When investigating the motion of two-phase media (particularly /118
boiling and condensation) for the case of small gravitation, the perturbing action of random impulses must be taken into account. These impulses may have a great influence on the transfer velocity when there is no forced motion [18].

CHAPTER 3 /119

SIMULATION OF A SPACECRAFT THERMAL REGIME IN GROUND-BASED EQUIPMENT

1. Characteristics of Heat Exchange Between a Spacecraft and the Surrounding Medium

Due to the extremely rarefied nature of the interplanetary medium, the possibility of the spacecraft cooling by means of external convective heat exchange is excluded. One possible way in which the spacecraft may exchange energy with the surrounding medium is absorption and emission of electromagnetic radiation — for example, in the visible or infrared region of the spectrum. Satellites moving along low orbits in the upper rarefied layers of the atmosphere may be subjected to the influence of aerodynamic heating. The strength of this heating depends greatly on the flight altitude. At altitudes less than 110 km, the aerodynamic heating may exceed the heat received by the spacecraft from the Sun. However, the time that artificial Earth satellites may remain at such altitudes is limited by the natural braking of the air. At altitudes more than 200 km, aerodynamic heating is so small that it may be disregarded. This eliminates the use of external fairings. The design of the outer surface of the spacecraft may therefore be very complex (see Figure 3.1).

The position of a spacecraft and its attitude with respect to the external sources of energy (Sun, planets, etc.) changes in space, and the strength of the incident radiation changes in time within wide limits.

The thermophysical and optical characteristics of a spacecraft surface (for example, contact thermal resistances, heat insulating properties of a screen-vacuum insulation, spectral coefficients of absorption and reflection, degree of polarization, etc.), which determine the energy exchange with the surrounding medium, do

not remain constant. They change under the action of radiation and a high vacuum.

A liquid or a gas heat carrier moves in the hermetic compartments of a spacecraft under conditions of reduced or zero gravitation. This decreases, or completely excludes, natural convection from heat liberating elements (radio tubes, resistors, etc.). /120

Individual sections of the spacecraft surface, which are made out of different materials or have different coverings, may have different optical characteristics (ε, R, A_s) which in the general case are a function of the radiation wavelength, the direction of the rays, and the temperature of the body. In addition, if other surfaces of the spacecraft are "visible" from any section of the surface, the effective degree of blackness of this portion depends on the geometry of the body. In the majority of cases, it is practically impossible to accurately calculate theoretically the effective degree of blackness for spacecraft having a complex form.

It may be seen from this brief description of certain features of spacecraft heat exchange with the surrounding medium that its thermal regime differs greatly from a thermal regime under ordinary terrestrial conditions.

2. Basic Problems of Testing and Developing a Spacecraft Thermal Regime

Before it is launched, a spacecraft must be checked in every way possible. The development of the spacecraft thermal regime plays an important role in the tests carried out. The cycle of this development includes many tests in different areas. In particular, this may include:

1) Checking the operation of the temperature control system (TCS) of the spacecraft under conditions which simulate real conditions as closely as possible;

2) Studying the operation of TCS under conditions of an emergency, i.e., with a partial breakdown of certain units, parts, and sensors, with a random change in the optical properties, a disturbance of the hermeticity, a change in the internal heat liberation, etc.;

3) Studying the temperature fields which may actually exist in a spacecraft, auxilary system for the instrument compartment. It is necessary to

4) Checking the operation of the electron and ion equipment under conditions of real, non-stationary temperature gradients;

5) Establishing the actual temperature limits of the automatic systems, electron units, and other equipment, as well as outer movable elements;

6) Developing an efficient (from the point of view of cooling) arrangement of the heat liberating and non-heat liberating equipment in hermetic containers, and studying their mutual thermal influence;

7) Performing tests on all systems under real temperature conditions;

8) Determining the average thermophysical parameters, such as effective temperature values, heat capacity, heat conductivity, heat conductivity of individual sections of the structure, the equipment, and the spacecraft compartments; /121

9) Checking the theoretical methods of calculating the thermal regime for the spacecraft as a whole, or parts of it in order to clarify the possibility of extrapolating the computational results to conditions which differ from the experimental conditions;

10) Studying the thermal deformations of the spacecraft.

The main problems of testing and developing a spacecraft thermal regime include special studies of materials, which are necessary to determine the stability of materials and coverings during spaceflight, as well as flight experiments.

Experimental method

The method of performing a complex experimental study of a spacecraft thermal regime is determined by structural characteristics, the inner heat liberation, its attitude in flight, requirements on the accuracy of maintaining the thermal regime, etc.

Let us assume that we must test an apparatus with a complex form having movable protuding parts whose temperature is completely determined by the thermal balance with the surrounding bodies and the internal heat sources. There is only an active

temperature control system for the instrument compartment. It is necessary to determine what the spacecraft thermal regime will be during a long flight around a planet (the Earth). A device with regular operating equipment, which is precisely the same as must occur during flight, is used for the test. The device used for the experiment contains temperature sensors at all points, which — in the opinion of the experimenter — must completely characterize the thermal field of the apparatus as a whole. In addition to temperature sensors, there are other sensors on this device (for example, sensors of pressure, voltage of the battery, flow rate of heat carrier, position of movable parts, etc.). Before it is placed into the experimental chamber, the apparatus is carefully purified from all possible contamination, which may be a source of "false" leaks when the chamber is evacuated. Then it is placed in the rotation mechanism. The apparatus is placed in the chamber, along with the rotation mechanism. The operation of the on-board equipment and the system for measuring the spacecraft controlling parameters is also checked.

After a pressure of $\sim 10^{-5}$ torr has been reached in the pressure chamber, the /122
cryogenic shields are cooled to liquid nitrogen temperature, and the experiment begins.

The external radiant flux simulators, the mechanism for rotating the spacecraft, which orients it in the given manner with respect to the Sun and planet, and the on-board equipment are switched on.

The sensor readings of pressure, temperature and other parameters are transmitted along conduits (partially using the on-board telemetry equipment) to the recording apparatus located outside the pressure chamber. A special miniature transmitter, which is installed in the spacecraft being investigated only during tests, may be used for transmission of the sensor readings.

The length of the experiment is determined by flight conditions and by the operational cyclicity of the on-board equipment. If the operating time of the equipment during flight is counted in many months or years, checking of the thermal conditions in the simulator is carried out according to a reduced program. In this case, those conditions which would be more typical or extreme for the given type of equipment are selected for experimental verification.

3. Methods of Simulating Spacecraft Thermal Conditions

There are many methods of simulating spacecraft thermal conditions which find practical application. The following are the most common among them:

1. Simulation of surrounding space conditions, acting on a full-scale spacecraft, to the maximum extent possible.(*)

2. Simulation of the resulting heat flux on the external surface of the spacecraft.

3. Reproduction of the temperature conditions on the external surface of the spacecraft.

4. Scale modelling of the spacecraft in combination with reproduction of almost all analogous surrounding conditions.

5. Scale modelling with modified surrounding conditions.

6. Mathematical modelling of spacecraft heat exchange with the surrounding medium, taking into account experimental data on simulation of individual types of effects of the space environment on the optical characteristics of the spacecraft materials.

Each of the enumerated methods of simulation has its advantages and disadvantages. The methods are distinguished not only by the manner of applying or dissipating heat, but also by the degree of accuracy provided by the experimental devices employed. The specific design of spacecraft must be considered in order to compare the advantages of this or that method. Therefore, for convenience in a further detailed analysis of the methods given above, as well as for systematization of the requirements placed on space simulators, it is expedient to divide all possible types of spacecraft into classes for which the conditions imposed on the accuracy of the simulators are approximately equal. /123

(*) Only the main radiant fluxes from the Sun and planet, vacuum and thermal absorption by "cold, dark" space are usually reproduced simultaneously (see Section 5, Ch. 3).

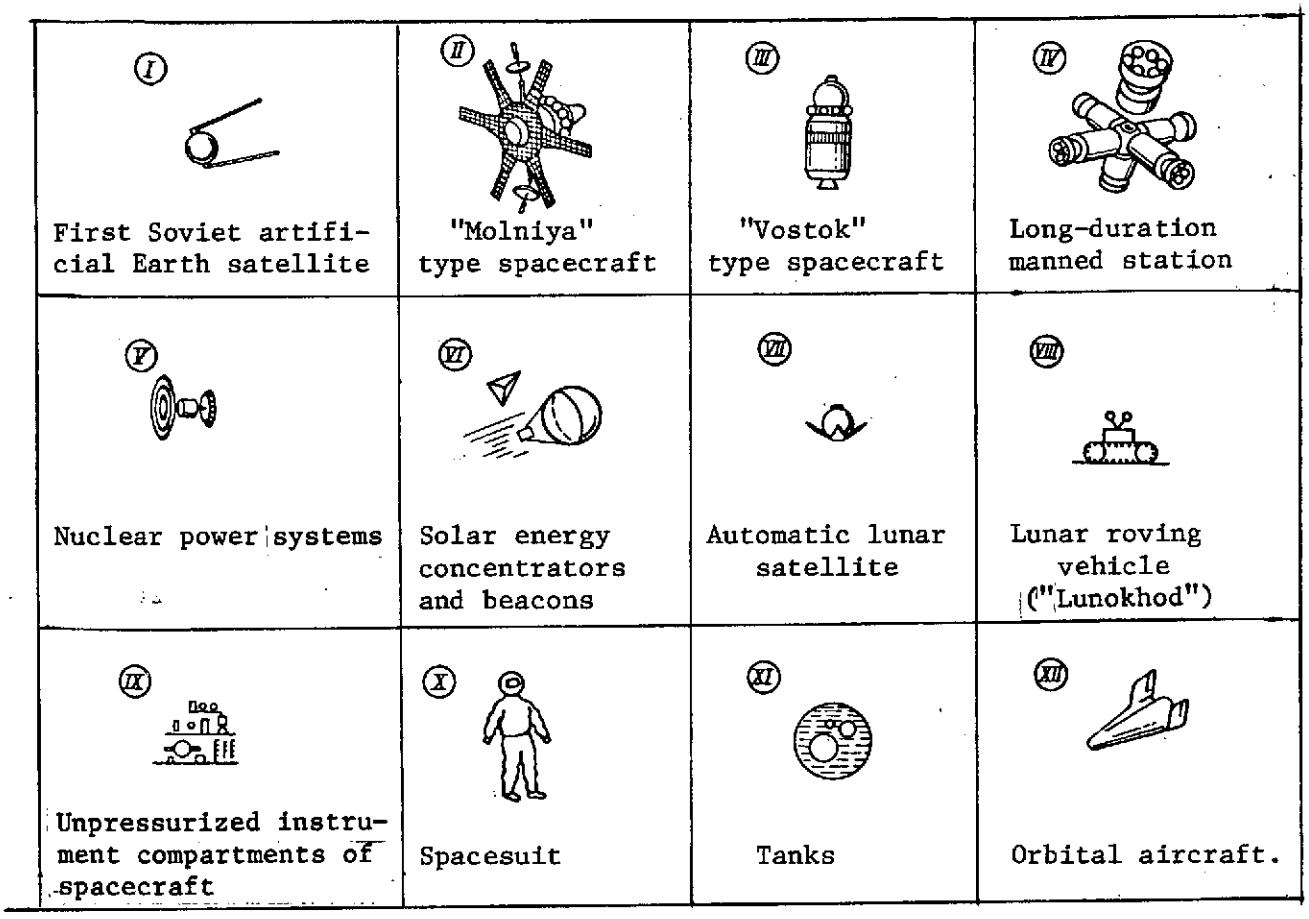

Fig. 3.1. Classification of spacecraft from aspect of thermal conditions.

4. Classification of Spacecraft (Fig. 3.1).

Class I. Unmanned automatic spacecraft with pressurized instrument compartments and an active temperature control system having external radiators. Internal heat dissipation per unit radiator surface is from 50 to 150 W/m^2. The external configuration of the instrument container is a simple convex shape. The container is well heat-insulated from the surrounding medium. The surface is generally uniform and has continuous optical characteristics. The temperature inside the instrument container is maintained within the range of 10 - 50° C. Lifetime is from several weeks to several years. Orientation in space is arbitrary. The incident radiant fluxes of the Sun and planet may vary in both time and direction. The dimensions of the spacecraft are on the order of a meter.

Class II. Unmanned automatic spacecraft with pressurized instrument compartments and an active temperature control system having very low average internal heat dissipation (from 0 to 10 W/m^2) and very long lifetime calculated in years.

Orientation is constant with respect to the Sun or planet. The instrument compartment is well heat-insulated, but there are numerous thermal bridges in the form of protruding parts: solar batteries, antennas, the sensors of the scientific instruments, etc. As a whole the spacecraft is of complex shape, and its external dimensions in the deployed position comprise meters or tens of meters. Individual sections of the spacecraft surface have different spectral characteristics. The temperature requirements of individual sections are different and lie within different ranges. The average volumetric specific heat is low ($0.01 < G_{av} < 0.1$).

Class III. Manned spacecraft of short duration operating near the Earth. Lifetime is several days. The temperature control system is active with evaporative coolers. The specific heat of the spacecraft is high and there is considerable internal heat dissipation with particular peak loads. Orientation is arbitrary, and the incident thermal fluxes of the Sun and planet may vary in both time and direction. The configuration is simple with few protruding parts. The greater part of the external surface has a uniform covering. Permissible cabin temperature varies from +15 to +25° C. The dimensions of the spacecraft are within the range of several meters.

Class IV. Manned spacecraft and stations with prolonged lifetimes from a week /124
to several years. The temperature control system is active. There are sections with different coverings. The shape of the spacecraft is simple and convex. Heat dissipation per unit surface is low (from 5 to 15 W/m^2), and peak loads are possible. Different ranges of operating temperatures are permitted in different sections: from 5 to 50°C in the instrument compartments and from 15 to 25°C in the living quarters. Very rigid requirements within the range of $\pm$ 1 - 2°C are placed on temperature variations in the optical instrument compartments. Orientation is continuous with respect to the planet or the Sun. The spacecraft dimensions are from 10 meters or more, and effective thermal conductivity is low, on the whole.

Class V. Nuclear space power systems (making up more complex spacecraft.) Typical dimensions are from several meters to tens of meters. Radiators of complex configuration are located near the main capsule of simple shape. The average radiator temperature is 300 - 600°C. Some sections of the surface have different spectral characteristics. The temperature control system is an active-passive one. Lifetime is counted in months and years. Orientation in space is arbitrary.

Class VI. Automatic retransmitters, reflecters, beacons, solar concentrators, etc. of inflatable, thin-film, skeleton, etc. designs. These spacecraft are very large (tens of meters) and have good uniform reflecting surfaces. Internal heat dissipation is equal to zero. The temperature control system is passive. The permissible temperature range is from -30 to +60°C. Thermal conductivity is very low. The lifetime is counted in years. Orientation with respect to the Sun or planet is constant or variable. /125

Class VII. Automatic planetary stations with short lifetimes (several hours) and active evaporative or other temperature control systems. The surface configuration of the main instrument capsule is simple, but there are many protruding parts of attached equipment, antennas and scientific instrument sensors. Different sections of the surface may have different spectral characteristics. Internal heat dissipation is within the range from 10 to 50 W/m^2.

Class VIII. Automatic planetary stations with means of locomotion for prolonged activity under conditions of the lunar day and night. External radiant thermal input varies a hundredfold. The temperature control system is active-passive. There are external movable connections and mechanisms (carriers, levers, wheels, friction axles, etc.). Average internal heat dissipation is low. There may be peak loads during the operating schedules of the equipment. The temperature requirements of different parts are different. Individual surface sections have different spectral characteristics.

Class IX. Spacecraft of very complex configuration with passive temperature control systems. The unpressurized instrument compartments may have temperatures which vary over very wide ranges (especially in "closed" electronic circuits.) The temperature requirements of different parts of the spacecraft are different and are strongly delineated both in absolute value and in the permissible range of temperature variation. The spectral characteristics of parts of the spacecraft may be very different. Heat dissipation is low on the average, but is very non-uniform in time for individual sections. The thermal conductivity of the equipment is from 0.05 to 0.12 kcal/kg°C. There are increased requirements for stability of thermal conditions during prolonged spacecraft lifetimes (counted in years). The intensity and angular distribution of external heat fluxes may vary over a wide range.

Class X. The cosmonaut's spacesuit. Any orientation is possible with respect to external radiant fluxes. The temperature control system is active (for example, evaporative.) There are rigid temperature conditions (+18 to +23°C) placed on the life-support system. This system has a complex variable configuration and inhomogeneity of the spectral characteristics of the outer coverings.

Class XI. Tanks for prolonged storage of fuel and oxidizers (in particular, cryogenic) during circumplanetary orbits and while on the surface of planets. /126
Internal heat dissipation is zero or negative. External radiant fluxes may vary over very wide ranges in both value and direction. The geometric shape is simple, the surface is uniform, and thermal conductivity is high. The main requirement on thermal conditions is minimum external thermal input.

Class XII. The aerospace aircraft. The thermal conductivity of the skin is high, and the length of stay in space is comparatively short. A large portion of the surface is convex and smooth with uniform spectral characteristics. Internal heat dissipation is high in the region of the engines. Very high local external heat inputs and temperature gradients on the surface are possible during reentry into the dense layers of the atmosphere.

5. Simulation of the Radiant Flux Field Impinging on the Spacecraft

The term simulation is usually understood to be a method of investigation (most often experimental) in which the specific object of the experiment (or phenomena) is replaced by another object similar to it, i.e., its model. In this sense, the method considered in this section, which is based on maximum approximation of conditions in the chamber to those of space, is not simulation in the generally accepted interpretation of this concept.

It is obvious that if the full-scale transient radiant flux field could be recreated in sufficient volume, and if a full-scale model of the spacecraft with equipment functioning according to the flight program and with the two required degrees of freedom for arbitrary attitude control with respect to the Sun and planet could be placed within this space, the problem of preflight trials and testing of the spacecraft would become comparatively simple. However, artificial reproduction of the simultaneous action of all characteristics of space is an extremely complex task, even when the experimentor has all available means of

modern highly developed experimental technology at his disposal. At the same time, this problem may become completely soluble, if, instead of reproducing all the parameters of space, only those which have (or in principle may have) a specific effect on the thermal conditions of the spacecraft are reproduced. Moreover, with a careful approach to the characteristics of the spacecraft being tested, it becomes possible and expedient in a number of cases to separate the experiments according to types of action, i.e., it becomes possible to test separately the effects of a vacuum, X-rays, ultraviolet, corpuscular and molecular radiation, etc., /127 and then, by using the data obtained, the resulting effect may be synthesized.

Unfortunately, the problem of methodical competence of separate investigation with subsequent summarizing of partial results has not yet progressed beyond the limits of scientific discussions. Many authors assume that the true picture of degradation of the surface properties of materials may be obtained only under the simultaneous action of all types of radiation in combination with an ultrahigh vacuum, but there are others who do not share this opinion.

Since the fact itself of variation in the optical properties of materials under the action of space radiation has been indisputedly established, it must be taken into consideration if the active lifetime of the spacecraft in space exceeds several weeks.

It is generally accepted at present [144], [215], [216] that for complete investigation of spacecraft thermal conditions, it is sufficient to reproduce the following main factors of space:

a) a high vacuum;
b) solar radiation;
c) radiation from the planet
d) the "cold" and "darkness" of space within the limits of solid angles occupied by the planet and Sun.

The remaining factors (corpuscular and micrometeorite flows, ultraviolet radiation, etc.) (see Sect. 4, Ch. 1), which have an indirect effect on spacecraft thermal conditions, as a result of variation of the optical and thermal properties of materials and coverings, are investigated individually in special material

testing devices(*) (see Sects. 2, 3, 4, Ch. 2). Sublimation of materials is investigated, movable assemblies are tested, processes of development and breakdown of surface molecular films, etc., are studied in these same devices, which are usually of very small dimensions. The experimental data, obtained in so-called material testing chambers, are taken into account when conducting experiments according to the basic program in installations with solar and planetary radiant flux simulators, designed to simulate spacecraft thermal conditions(**). The four main parameters of space enumerated above are reproduced with different degrees of precision in most thermal simulators. The reason for this lies not only in technical difficulties, but mainly in the practical necessity which determines the class of the spacecraft being tested and the specifications for its thermal conditions.

Radiant Flux Field Properties in Orbit. /128

Before determining a satisfactory approximation of real conditions in thermal simulation, let us consider the main properties of the radiant fluxes impinging on the spacecraft during its motion in an orbit near a planet.

Let us take an arbitrary point on the mechanical trajectory of a spacecraft passing over the illuminated side of a planet (the Earth), and let us consider some minimum volume of space, within which the described spacecraft is inscribed. We may establish that:

a) the same amount of radiant energy impinges at any point of the volume of space under consideration on an elementary area, the orientation of which remains constant with respect to the Sun - Earth - spacecraft system. The reason for this is that the dimensions of the volume under consideration are much less than the distance to the planet and to the Sun;

b) the planet is visible at any point of the volume considered at the same solid angle, which varies only with flight altitude.

(*) It would be better to call them chambers for simulating operating conditions or physicochemical processes.
(**) Henceforth, we shall abbreviate them TS.

For low orbits this angle may be rather large (for example, when the spacecraft is moving in a circumterrestrial orbit, $2\theta_0 = 160°$ for an altitude of H = 100 km; $2\theta_0 = 152°$ for H = 200 km; $2\theta_0 = 140°$ for H = 400 km, etc.). Because of this, the rays coming from the Earth impinge on a spherical spacecraft or body similar to a sphere over almost the entire external surface ($\overline{F} = \frac{F_{illum}}{4\pi r^2} = 99.2\%$ for H = 100 km; $\overline{F} = 97\%$ for H = 200 km; $\overline{F} = 94\%$ for H = 400 km, etc.);

c) the directions of solar rays reflected from the planet for each flight altitude H at any point of the volume under consideration are included within the limits of the solid angle at which the planet is visible, and their intensity for each direction depends on the type of radiation of the optically active layer (diffuse and uniform; reflecting and mixed);

d) any variations in the radiant flux field in the volume occur simultaneously for all its points;

e) radiation from the spacecraft surface does not alter the value of the incident radiant flux. (The planet is too distant. The angular dimensions of the spacecraft are essentially equal to zero from any point on the planet);

f) the three main components of incident external radiant flux (direct solar radiation, radiation reflected from the planet and the natural (infrared) radiation of the planet) vary non-uniformly in time and space.

The indicatrices of irradiation of a spherical artificial Earth satellite are shown in Figure 3.2 for different positions during its motion in a "shaded" (i.e., located in the umbra) orbit. In these figures the arrows indicate the vectors whose directions coincide with that of incident radiation, and their length is proportional to the incident radiation flux density in the given direction. /129

Let us introduce the concept of the resultant vector of irradiation for radiation from a planet, which we shall assume to be the vector whose value is equal to the radiant flux density on an area with a normal directed toward the center of the planet, and the direction coincides with the direction of maximum radiation for the given type of radiation.

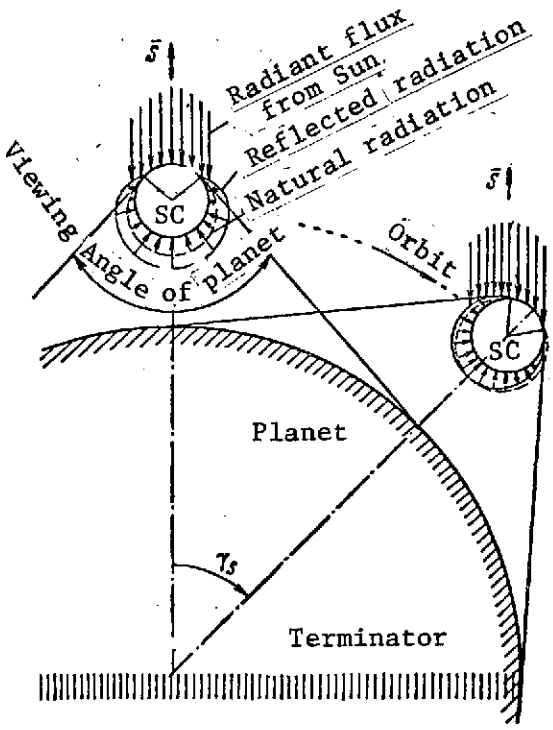

Fig. 3.2. Indicatrices of irradiation of a spherical artificial Earth satellite for different positions during motion in a "shaded" orbit (not to scale).

Thus, the infrared and reflected components of terrestrial radiation will be characterized by two vectors $\vec{\Phi}_e$ and $\vec{\Phi}_s$. The directions of these two vectors are similar, and are coincident at the subsolar point.

In the general case, the mutual disposition of the three vectors $\vec{\Phi}_e$, $\vec{\Phi}_s$ and $\vec{S}_\odot$ may be very different.

When the spacecraft is located at a great distance from the planet, radiant fluxes from the planet become less than the average error of reproduction of solar flux. Thus, the radiant flux from the Earth at an /130 altitude of 10,000 km comprises approximately 4% of the solar flux, and may be disregarded for all practical purposes. A solar simulator alone is required to investigate spacecraft thermal conditions at such distances in vacuum chambers. The effect of the Earth at such altitudes may be manifested for those sections of the spacecraft trajectory which correspond to the spacecraft entering the umbra or penumbra of the planet (see Sect. 3, Ch. 1).

6. Approximate Simulation

In some cases, when the spacecraft being tested has only one degree of freedom, for example, rotation around the vertical axis of the chamber, it becomes necessary to resort to approximate methods of simulating the radiant fluxes impinging on the spacecraft. The approximate simulation is determined to a great extent by the shape and thermal properties of the spacecraft.

Let us assume that the lateral surface of the spacecraft being tested is convex and close to cylindrical, and that the main portion of the thermal flux passes through this surface.

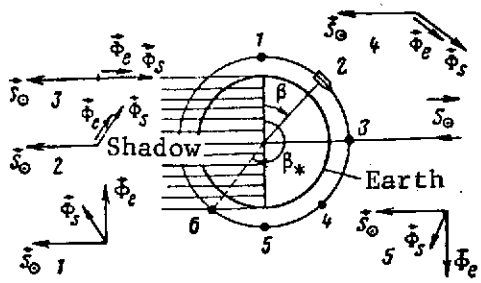

Fig. 3.3. Variation of values and directions of vectors $\vec{S}_{\odot}$, $\vec{\Phi}_s$ and $\vec{\Phi}_e$ during motion of the spacecraft in a circumterrestrial orbit.

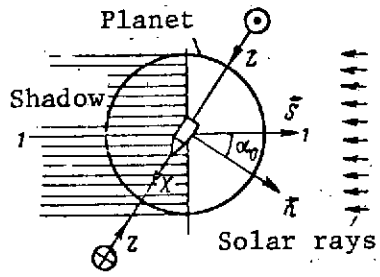

Fig. 3.4. Diagram of artificial Earth satellite motion along an orbit whose plane is inclined toward the plane of the ecliptic.

When a spacecraft moves along a shaded orbit (Figure 3.3) through positions 1 - 2 - 3 - 4 - 5, the directions of vectors $\vec{\Phi}_s$, $\vec{\Phi}_e$ and $\vec{S}_{\odot}$ vary. If a system of coordinates is linked to the spacecraft and if it is assumed that it is constantly oriented toward the Earth, vector $\vec{\Phi}_s$ varies its position by almost 180° with respect to the artificial Earth satellite during the time corresponding to half of a single revolution. In this case, the absolute value of the radiation reflected from the Earth also varies from a maximum at position 3 to zero when the spacecraft approaches position 6. Some thermal simulators are equipped with simplified simulators of radiant flux from the planet, which does not permit reproduction of the dynamics of radiant flux variation, and consequently study of the transient thermal conditions of the spacecraft. This is permissible only for very good heat-conducting space- /131 craft, for which it makes no difference on which side heat arrives or departs. In the majority of cases, the thermal conductivity of spacecraft is not so great that variation of the angular distribution of external fluxes could be disregarded.

Only a single trajectory for a particular orientation of the satellite with respect to the Earth and Sun may be indicated when the resulting vectors of irradiation $\vec{\Phi}_e$, $\vec{\Phi}_s$ and solar flux do not vary their relative arrangement. This case corresponds to satellite motion in an orbit passing above the terminator in a plane perpendicular to the plane of the ecliptic and to the direction toward the Sun. In this case one side of the satellite should be turned toward the Earth at all times, and the other side (along the axis of rotation) — toward the Sun. Calculations show that for such an orbit $\vec{\Phi}_s$ comprises ~1 - 2% of the total radiant flux. This flux may be disregarded, or it may be reproduced with the aid of the simplest simulator, without concern about the precise angle and spectral similarity.

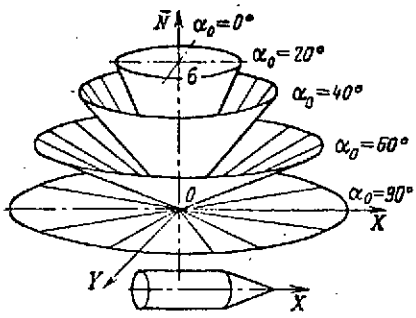

Fig. 3.5. Set of conical surfaces along whose generatrices the solar radiation vector moves: $\alpha_0 = 0°$ is flight above the terminator.

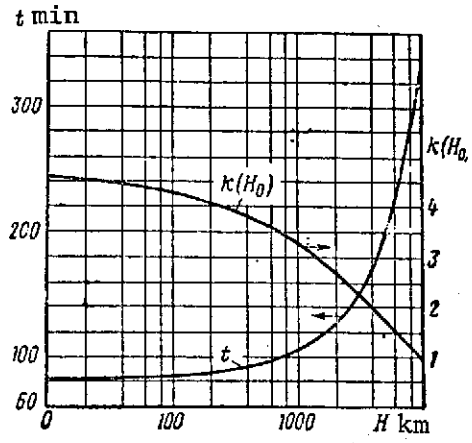

Fig. 3.6. Variation of period of artificial Earth satellite rotation and function $k(H_0)$ as a function of flight altitude in a circular orbit.

Let us consider the motion of a spacecraft around the Earth in an orbit whose plane comprises an arbitrary angle of inclination to the plane of the ecliptic. For simplicity we shall assume that the orbit is circular. The angle between the direction toward the Sun and the normal to the orbital plane shall be denoted by α_0. As can be seen from Figure 3.4, when α_0 is fixed, the rotation of the orbital plane around axis 1 - 1, which coincides with the direction toward the Sun, does not alter the nature of irradiation of the spacecraft from the direction of the Sun nor from the direction of the Earth (with an accuracy up to albedo distribution over the planet). Therefore, it is sufficient to analyze the nature of irradiation of a spacecraft, moving in one of the orbits with an arbitrarily selected angle α_0, in order to apply the result obtained to any other orbits. Let us assume that the orbital plane is perpendicular to the plane of the diagram, coinciding with the plane of the ecliptic. The spacecraft moves in an orbit with constant orientation with respect to the local horizon. Its longitudinal axis X coincides with the direction of motion, while the lateral side (Z-axis) (for example, from the camera hatch) is oriented toward the Earth. When the spacecraft moves in an orbit with an orientation as indicated in Figure 3.4, the vector directed toward the Sun will move along the surface of a circular cone at an angle of $2\alpha_0$ at the apex. The axis of the cone coincides in direction with the normal to the orbital plane (Figure 3.5). The span of the cone will not depend on orbital altitude H. Variation of the direction of irradiation in a simulator with an immobile "Sun" may be achieved by varying the orientation of the spacecraft being tested with respect to vector $\vec{S}_\odot$. If variation of spacecraft orientation in the simulator vacuum chamber is not specified and the spacecraft

may move in it only vertically, it may be rotated around the longitudinal axis X. /132
By accomplishing such rotation at the required angle, a variation in the direction of the solar vector in the NOY plane (plane σ), perpendicular to the spacecraft axis, may be simulated. Mutual variation of spacecraft orientation and the Sun in the NOX plane, which passes through the spacecraft axis, cannot be accomplished in such a chamber. If the spacecraft being tested has a simple geometric shape close to a circular cylinder, the actual motion of vector $\vec{S}_{\odot}$ in planes, differing from plane σ, may be replaced by variation of its normal (to the spacecraft surface) component. Thus, the motion of vector $\vec{S}_{\odot}$ along the conical surface is replaced by its motion in plane σ within the limits of angle $\pm\alpha_0$, the modulus of vector $\vec{S}_{\odot}$ varying cyclically according to the law

$$|\vec{s}^{*}_{\odot}|=|\vec{s}_{\odot}|\cos\alpha_0\left|\sqrt{\mathrm{tg}^2\alpha_0\sin^2\beta(\tau)+1}\right|, \tag{3.1}$$

where β(τ) is the angle which determines the spacecraft position in orbit. It may be calculated from any direction. For example, from the line of the terminator (see Figure 3.3). For a circular orbit

$$\beta(\tau)=\frac{360^\circ}{t}\tau=k(H_0)\tau\ [\tau]=[\mathrm{min}],$$
$$t=\frac{2\pi}{\sqrt{g}}\frac{1}{R_0}(R_0+H_0)^{3/2}, \tag{3.2}$$

where t is the time of a complete revolution of the spacecraft around the Earth, which depends on orbital altitude H_0 (Figure 3.6).

Variation of $\vec{S}^{*}_{\odot}$ is related to cyclic rotation of the spacecraft with respect /133
to its longitudinal axis by the relation

$$\alpha(\tau)=\arccos\left[\pm\sqrt{\mathrm{tg}^2\alpha_0\sin^2\beta(\tau)+1}\right]^{-1}. \tag{3.3}$$

The functions $\vec{S}^{*}_{\odot}=\frac{\vec{S}^{*}_{\odot}}{|\vec{S}_{\odot}|}=f(\tau,\alpha_0)$ and $\alpha=\alpha(\tau,\alpha_0)$ are presented in Figures 3.7 and 3.8. At a certain value $\beta=\beta_{*1}$ the spacecraft moves into the Earth's shadow and the "Sun" must be switched off. At $\beta=\beta_{*2}$ the "Sun" is again switched on. The length of stay in the shadow is calculated beforehand for a specific orbit (see Sect. 2, Ch. 2).

When the spacecraft rotates in the vacuum chamber with respect to the direction $\vec{S}^{*}_{\odot}$, the main vector of irradiation from the Earth must also be rotated simultaneously at the same angle. This refers both to natural (infrared) terrestrial and reflected radiation. If the simulators of infrared radiation and that reflected

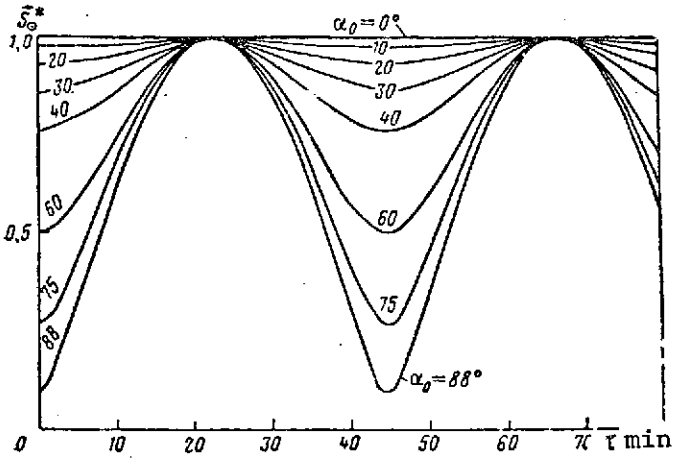

Fig. 3.7. Variation of relative intensity of "solar" energy flux in time for different angles α_0 (H_0 = 200 km, circular orbit).

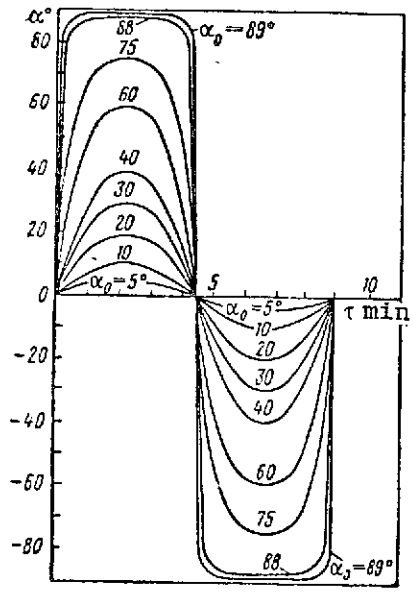

Fig. 3.8. Dependence of angle of spacecraft rotation around X-axis in time for different angles of inclination of the orbital plane to the plane of the ecliptic (H_0 = 200 km).

from the Earth in the chamber do not make it possible to change the angles of irradiation, at least their values should be varied, i.e., the average amount of incident radiant energy on the spacecraft surface at any moment of time should be reproduced, without taking into consideration its angular distribution in this case.

The total amount of radiant energy received by the spacecraft surface from the planet for each moment of time is calculated by the formulas (see Table 9): /134

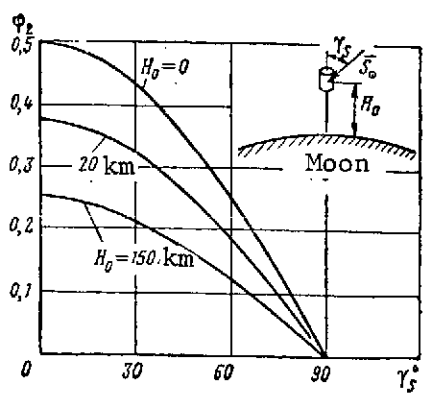

Fig. 3.9. Dependence of angular coefficient φ_2 for vertical cylinder on altitude H_0 and zenith angle of the Sun γ_s.

$$\Phi_s = \frac{1 - A_{av}}{4} S_\odot \varphi_1,$$

$$\Phi_e = A_{av} S_\odot \varphi_2.$$

The angular coefficients φ_1 and φ_2 depend on flight altitude H_0, the radius of the planet R_0, spacecraft orientation and the angle between the local vertical and orientation toward the Sun. If these values are given for each point of the orbit, coefficients φ_1 and φ_2 may be calculated with the aid of the method outlined in Sect. 2, Ch. 2).

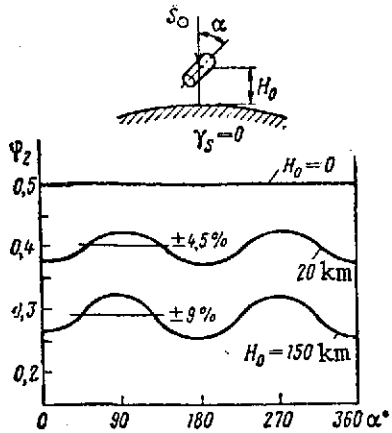

Fig. 3.10. Dependence of coefficient of irradiation of cylinder on angle of rotation α for different altitudes. The zenith angle of the Sun $\gamma_s = 0$.

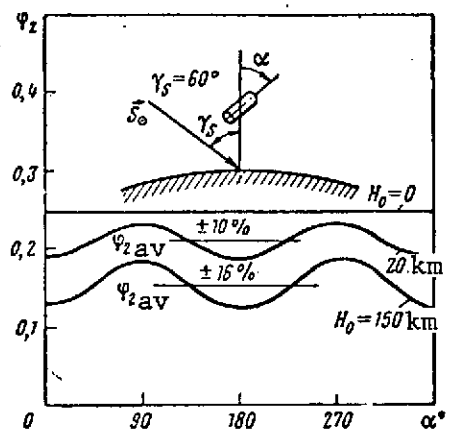

Fig. 3.11. Dependence of coefficient of irradiation of cylinder on angle of rotation α for different altitudes. The zenith angle of the Sun $\gamma_s = 60°$.

The results of calculating φ_2 for the lateral surface of a circular cylinder, rotating around a transverse axis, are presented in Figures 3.9 - 3.11 as an example. It is obvious from these graphs that the effect of the angle of rotation of the cylinder axis (α) decreases rapidly as orbital altitude H_0 decreases and reaches zero at the planet's surface. It is noteworthy that the amplitudes of variations of φ_2 (α) remain unchanged for any altitude as the Sun approaches the local horizon, although the average value of φ_2 decreases as γ_s increases.

In the described method, only thermal fluxes on the lateral surface of the /135
spacecraft are reproduced comparatively accurately. The simulation errors of solar vector motion for the aft and nose portions of the spacecraft will be too great. However, if these portions can be separated from the main hull and if, after their separation, their dimensions do not exceed those of the operating zone (the transverse dimensions of the solar spot of the thermal simulator), very precise reproduction of solar vector motion along a conical surface is possible. This requires that the portion of the spacecraft being tested be secured inside the thermal simulator on the rotatable block with two degrees of freedom.

Two possible schematic diagrams of a rotatable block are shown in Figure 3.12. In diagram a, spacecraft rotation during the experiment is accomplished around axis $\vec{n}$ (see Figure 3.4), which coincides with the normal to the orbital plane. /136
Variation of α_0 as orbital orientation varies may also be accomplished intermittently and arbitrarily during the experiment itself. In diagram b (see Figure 3.12) this

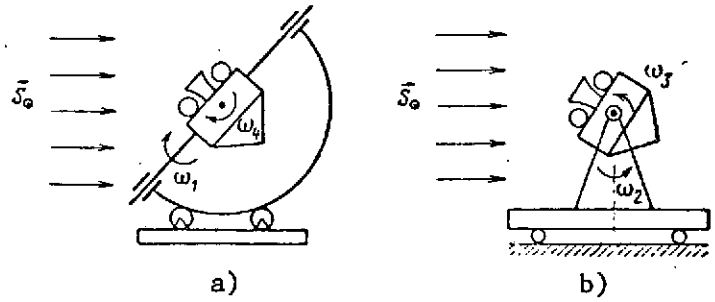

Fig. 3.12. Possible diagrams of rotatable block.

same rotation of the spacecraft around axis $\vec{n}$ is achieved as a result of simultaneous rotation around the vertical Y and the horizontal X axes.

7. Method of Reproducing Thermal Boundary Conditions

The method of reproducing thermal boundary conditions may be conveniently used for testing spacecraft in Classes I and IV (see Sect. 4, Ch. 3), i.e., those spacecraft in which there is an active temperature control system and convex radiation surface, under which the heat carrier circulates. The radiator may be divided into sections having "hot" and "cold" coverings, differing by their spectral radiation capacities.

The optical characteristics of different materials and coverings are presented in Figure 3.13. Depending on the amount of internal heat dissipation and the temperature requirements on the instrument compartment, the radiator emerges beyond the confines of the spacecraft or occupies a portion of its external surface. The heat budget of the section of external surface is usually written in the form

$$Q_i(t)+\sum Q_e(t)-\sum \varepsilon\sigma_0\left(\frac{T_w}{100}\right)^4=(mc)_w\frac{dT_w}{dt}. \tag{3.4}$$

Here ΣQ_e is assumed to be the total thermal input from the Sun and Earth; Q_i is the external thermal input; and $(mc)_w$ is the specific heat of the unit surface of the section of spacecraft covering being considered.

The simple external geometric shape of the spacecraft covering and its radiator using the methods outlined in Sect. 2, Ch. 2, makes it possible to calculate /137
the amount of heat absorbed by the surface $\Sigma Q_e(t)$, which varies in time in accordance with the trajectory of motion and orientation of the spacecraft.

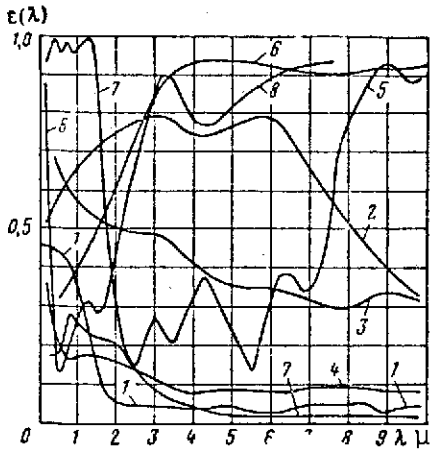

Fig. 3.13. Spectral degree of darkness of different coverings:
1 — polished beryllium; 2 — 1Kh18N9T stainless steel unoxidized at 20°C; 3 — oxidized titanium alloy Ti - 92% and Mn - 8%; 4 — aluminum at 20°C (machine turning); 5 — aluminum oxide; 6 — white enamel; 7 — dark mirror; 8 — white paint.

If $Q_i(t)$ is now calculated, the desired function $T_w(t)$ may be derived from a solution of Equation (3.4). Further, assigning the temperature of the external covering $T_w(t)$ derived by calculation in the experimental installation, the temperature field inside the compartment may be traced. However, the value of Q_i itself depends on the temperature of the covering T_w and, in this case, in a rather complex manner.

The value of Q_i is calculated during the experiment as the difference of the enthalpy of the heat carrier at the input and output from the radiator channel. The experiment itself is conducted in the following sequence. The temperature of each section of the covering, the total number of which is equal to N, is first derived on the thermal model of the spacecraft for the initial level(*) $T^{\circ}_{w1}, T^{\circ}_{w2}, \ldots, T^{\circ}_{wN}$, and these values are kept constant during a certain time interval (for example, $\Delta t = 1$ min). During this time $Q^{\circ}_{i1}, Q^{\circ}_{i2}, \ldots, Q^{\circ}_{iN}$ are calculated experimentally for each section and $\Delta T^{\circ}_{w1}, \Delta T^{\circ}_{w2}, \ldots, \Delta T^{\circ}_{wN}$ are calculated by formula (3.4). All N sections are then heated (or cooled) to new temperatures

$$T'_{w1} = T^{\circ}_{w1} + \Delta T^{\circ}_{w1}, \quad T'_{w2} = T^{\circ}_{w2} + \Delta T^{\circ}_{w2}, \ldots, \quad T'_{wN} = T^{\circ}_{wN} + \Delta T^{\circ}_{wN}$$

and the new values of T'_{wi} are kept constant during the next time segment $\Delta t'$. Further, at the end of this time interval the derived internal heat inputs $Q'_{i1}, Q'_{i2}, \ldots, Q'_{iN}$ to all sections are again measured and $T^{\circ}_{w1}, T^{\circ}_{w2}, \ldots, T^{\circ}_{wN}$ are again calculated for the next moment of time $\Delta t''$. Thus, data on the temperature variation of all sections of the spacecraft covering during a single revolution around the planet are derived step by step.

(*) For example, the temperature at the end of the orbital injection of the spacecraft may be taken as the initial level.

Calculation by formula (3.4) may be conveniently carried out with the aid of an electronic computer. The minimum value of Δt will then be calculated by the inertial method of assigning the temperatures of the spacecraft surface sections.

In the method described, theoretical calculations of external heat fluxes, which may be accomplished comparatively accurately for a given spacecraft, are combined with experimental calculation of internal heat distribution, which it is extremely complex to calculate with sufficient accuracy.

There is also another variant of this method. It can be managed without using an electronic computer, but more time is required for conducting the experiment. This method may be called the method of successive approximations. It is /138 essentially as follows. The temperatures of all sections of the spacecraft during a complete revolution around the Earth are first calculated approximately. These calculated values $T^{\circ}_{w1}(t)$, $T^{\circ}_{w2}(t), \ldots, T^{\circ}_{wN}(t)$ are maintained on the mock-up during the entire period of a single cycle (revolution) and $Q_{i1}(t), Q_{i2}(t), \ldots, Q_{iN}(t)$ are measured simultaneously. The internal heat inputs obtained experimentally permit refining the initial curves of temperature variation of the sections of the covering and make it possible to again conduct an experiment for the entire cycle, but with new functions $T'_{w1}(t), T'_{w2}(t), \ldots, T'_{wN}(t)$. The temperature curves of all sections of the spacecraft begin to be repeated after several cycles with the constantly repeating law of heat dissipation inside the instrument compartment. This serves as the basis for terminating the experiment.

In this method, the time between the first experimental measurement and the moment when corrections must be introduced into the parameters of the experimental simulator increases from 1 minute to approximately 90 minutes (the time of one revolution of the spacecraft). This time is quite adequate to calculate the refined temperature fucntions $T_w(t)$ with the aid of nomograms on all sections of the spacecraft surface for its new cycle.

It is natural that the length of the experiment by the new method increases by the time of the additional cycles. Usually, 3 - 4 cycles are sufficient in order for the thermal process to be repeated completely, i.e., the length of the entire experiment, reproducing a single revolution in orbit, comprises approximately 6 hours.

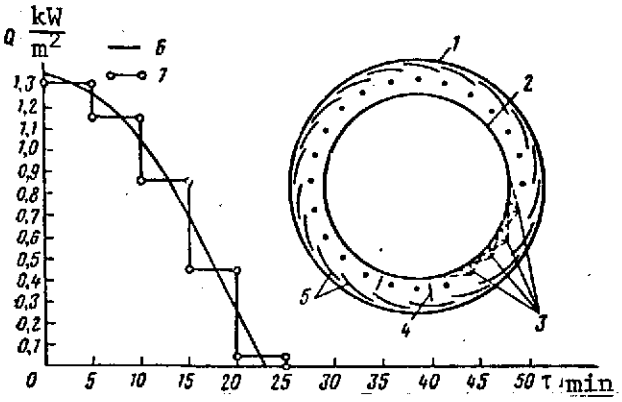

Fig. 3.14. Diagram of simulator of radiant flux from planet with linear sources of radiant energy:
1 — cylindrical chamber wall;
2 — spacecraft profile; 3 — directions of source radiation; 2 lamps per zone, a total of 12 zones every 30°; 4 — reflecting screens mounted at points where required; 5 — panels cooled with liquid nitrogen; 6 — theoretical energy distribution for a daytime polar orbit;
7 — actual energy supplied.

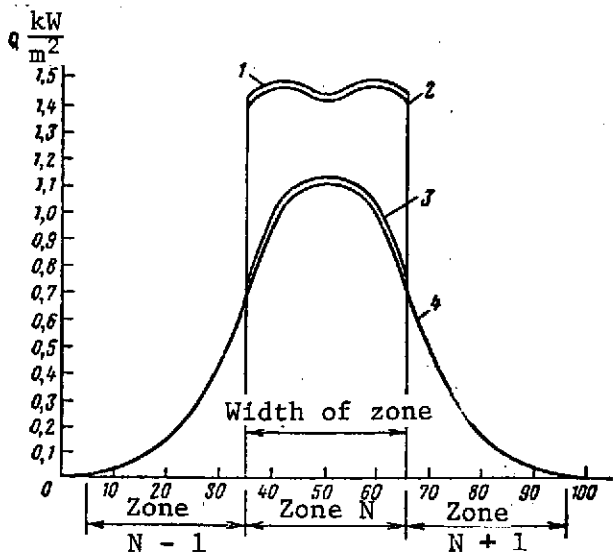

Fig. 3.15. Density distribution of radiant flux on spacecraft surface within limits of zone from a single linear radiator:
1 — total incident energy with consideration of correction for reflection and scattering (average value is equal to 1.454); 2 — incident energy with all lamps switched on; 3 — distribution of irradiation intensity from a single lamp with consideration of reflection of cold walls; 4 — main intensity distribution of a single lamp.

Methods of Setting Surface Temperatures.

The temperatures of the spacecraft surface sections may be varied by different methods. Methods of temperature control with the aid of electric surface heaters in the form of panels, strips, rods, etc. have been extensively developed. The diagrams of two such devices are shown in Figures 3.14 and 3.16 [114], [145], [146]. The accuracy of reproducing boundary conditions depends on the shape of the spacecraft surface and on the number of sections. As a rule, 12 sections are sufficient for smooth spacecraft (Figure 3.16) in order that the curve of temperature distribution approximate the real curve, and the density distribution of radiant flux on the spacecraft surface within the limits of the zone of a single radiator be sufficiently uniform (Figure 3.15). Regulation of $Q_e(t)$ may be smooth or stepped as a function of the method selected.

Another version of the device, meeting the requirements of maximum approximation of calculated temperature distribution, may be a thermostat device in which a gas or liquid, flowing in the space between the skin of the spacecraft model being tested and a special configured jacket, is employed as the working body. A diagram /141 of such a device is shown in Figure 3.17.

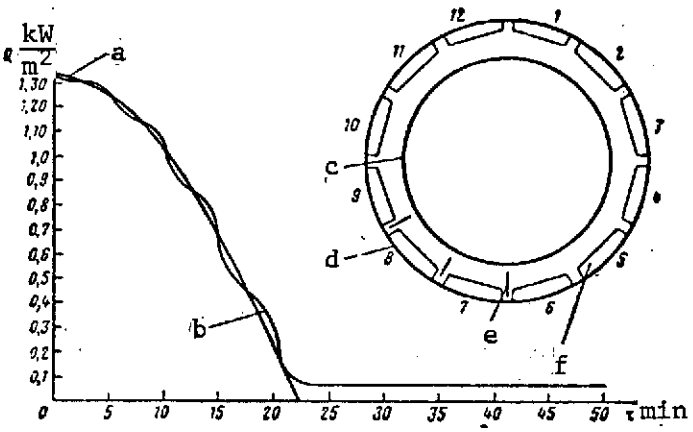

Fig. 3.16. Diagram of device for simulating radiant flux of planet with extended radiation sources: 1 - 12 — panels with heating elements as radiation sources; a — ideal distribution of required energy for a solar polar orbit; b — actual energy emitted by panels; c — spacecraft; d — cylindrical wall of chamber; e — reflecting screens; f — panels for temperature control of spacecraft skin.

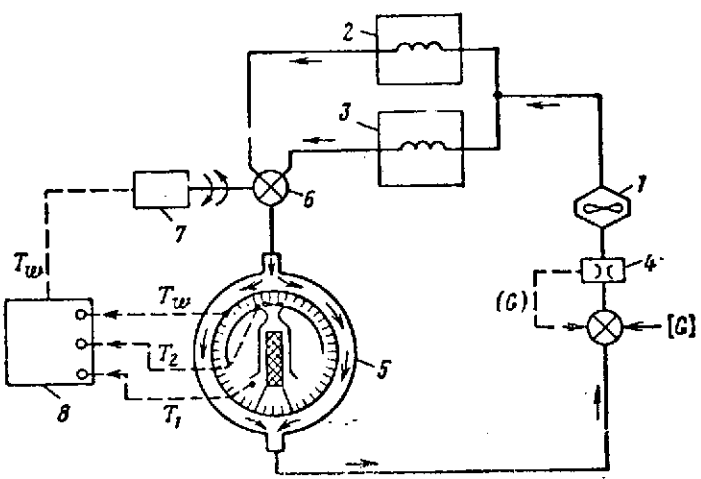

Fig. 3.17. Diagram of experimental device for investigating thermal conditions of spacecraft of simple shape: 1 — blower; 2 — cooler; 3 — heater; 4 — coolant flow rate regulator; 5 — covering; 6 — temperature regulator; 7 — auxiliary mechanism; 8 — computer.

The law governing the variation of the through cross-sectional area of the channel is found from the condition of maintaining a constant temperature at a given wall of the model. A constant temperature of the section of the spacecraft surface indicates that in space the heat flux emitted by this section will be uniform for all of its points. Consequently, the profile of the through cross section of the channel should be selected in order to fulfill the condition

$$q = \alpha(T_w - T_0) = \text{const}, \tag{3.5}$$

where T_0 is the average cross-sectional temperature of the gas (or liquid), dependent on the coordinate along the generatrix of the model.

Calculating the Effective Values of Thermophysical Characteristics.

Experimental verification of the thermal conditions of the spacecraft instrument capsule is usually carried out under nominal and several extreme conditions. Too much time would be required to investigate experimentally all possible thermal conditions which depend on internal and external transient heat fluxes. Therefore, to predict the temperature of spacecraft instrument compartments under conditions which differ from experimental, theoretical methods are employed in which the average effective values of instrument temperature and thermal conductivity, as well as the heat transfer from the instruments to the heat carrier, are employed.

The average effective thermal conductivity of instruments $(mc)_n$ may differ from the average thermal conductivity of instruments due to the fact that $(mc)_n$ depends on the temperature distribution in the instruments and equipment, i.e., on the intensity of the heat dissipation of the instruments Q_n, the temperature of the heat carrier at the input $T_1(t)$, the location of the instruments and cooling conditions, and finally, the directions of the heat flux (i.e., on the fact that the instruments and equipment are heated or cooled at a given moment).

Therefore, we shall denote the thermal conductivity of the instruments and equipment by the symbol $(mc)_n$, which is calculated experimentally for real internal heat dissipation, averaged over a sufficiently long cycle.

Let us consider an instrument compartment with heat-dissipating and non-heat-dissipating equipment located inside it. There are channels between the equipment

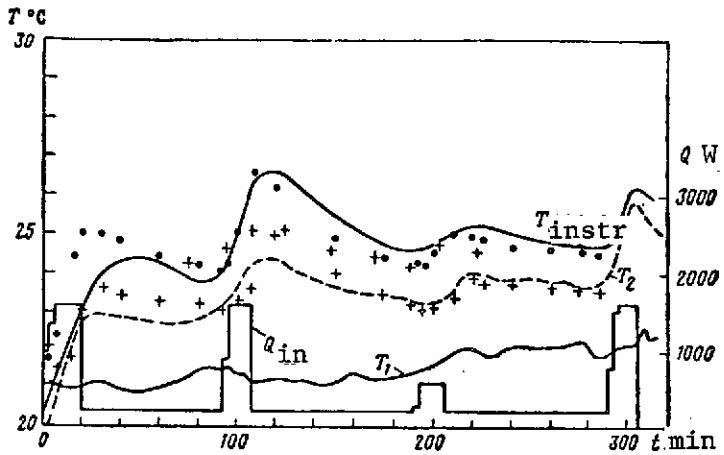

Fig. 3.18. Variation of atmospheric temperature (T_1 and T_2) and instrument temperature (T_{instr}) for the third Soviet artificial Earth satellite: the points indicate the experiment; the lines denote calculation with the aid of experimentally derived effective thermal conductivity of the instrument compartment: Q_{in} — internal heat dissipation.

circuits through which a coolant circulates (gas or liquid). Let us also assume that heat transfer to the external radiator takes place mainly with the aid of the coolant, rather than through the lateral walls of the compartment (Figure 3.18). The instruments may exchange heat among /142 themselves either by irradiation or by convection. There are no limiting assumptions about the structure of the compartment, the law of heat dissipation, etc. Let us denote the temperature of the heat carrier at the input to the compartment by T_1 and that at the output — by T_2. These temperature values are known from the experiment for any moment of time t. The heat balance equation for the instrument compartment as a whole may be written in the form

$$(mc)_n \frac{dT_n}{dt} = Q_n - (mc)_t (b-1)(T_n - T_2), \tag{3.6}$$

where $(mc)_t$ is the product of the second flow rate and the thermal conductivity of the coolant;

$$b = \frac{T_n - T_1}{T_n - T_2} \tag{3.7}$$

is the value dependent only on the flow rate of the coolant, and does not depend on temperatures T_n, T_1 and T_2.

In fact,

$$Q = \alpha \Delta T_{eff} dt = (mc)_t (T_1 - T_2),$$

$$\alpha \frac{T_1 - T_2}{\ln\left(\frac{T_n - T_1}{T_n - T_2}\right)} dt = (mc)_t (T_1 - T_2),$$

i.e., $\alpha \sim \ln(b)$.

Differentiating (3.7), we find that /143

$$\frac{dT_n}{dt}=\frac{\partial T_2}{\partial t}\frac{b}{b-1}-\frac{1}{b-1}\frac{\partial T_1}{\partial t}. \tag{3.8}$$

Any variation of T_1 over a certain time interval may be represented as the linear value $T_1=T^\circ_1+at$, where $a=\frac{\partial T_1}{\partial t}$.

Then Equation (3.6) may be written in the form

$$\frac{\partial T_2}{\partial t}+\frac{(mc)_t}{f}T_2=\frac{Q_n}{f}+\frac{a}{b}+\frac{(mc)_t}{f}T_1^\circ+\frac{(mc)_t}{f}at, \tag{3.9}$$

where

$$f=\frac{b}{b-1}(mc)_a.$$

Integrating this equation within the limits from t = 0 to t and grouping the terms, we obtain

$$[(T_2-T_1)-k]=[(T_2-T_1)_0-k]e^{-n(t_1-t_2)}, \tag{3.10}$$

where

$$k=\frac{Q_n}{(mc)_t}-a\frac{(mc)_n}{(mc)_t}, \tag{3.11}$$

$$n=\frac{(mc)_t}{f}. \tag{3.12}$$

The terms in the brackets of formula (3.10) have the dimensionality of temperature. We shall denote them by ϑ and ϑ_0 and we find that

$$n=\frac{\ln\vartheta_0-\ln\vartheta}{t_1-t_2}. \tag{3.13}$$

The logarithm of excess temperature at constant values of $(mc)_t$ and Q_n is a linear function of time. Formula (3.13) is a generalization of the theorem on regular thermal conditions [59] for the case when the temperature of the heat carrier, flowing around a body, varies with time, and there is a heat source (or flow) inside the body.

It is typical that the temperature of the body (in our case T_n) does not figure in Equation (3.10), which is very important, since it is very difficult to

calculate the average temperature of the instrument compartment experimentally. It is much simpler and more reliable to measure the temperature of the heat carrier (for example, of air) at the input and output of the instrument compartment.

The value of k has a simple physical meaning: this is the temperature drop between cross sections, where temperatures T_1 and T_2 (Figure 3.18) are measured during a steady process. In other words, this is the value of $(T_2 - T_1)$, toward which the drop of $(T_2 - T_1)$ approaches at a given moment at $t \to \infty$.

Setting $T_2 - T_1 = T$, we shall write (3.10) in a different form: /144

$$\Delta T - \Delta T_\infty = (\Delta T_0 - \Delta T_\infty) e^{\frac{(mc)_t}{(mc)_n} \frac{b-1}{b} \Delta t}. \tag{3.14}$$

If we utilize the fact that the dependence of the logarithm of excess temperature on time

$$\ln(\Delta T - \Delta T_\infty) = f(t)$$

is a straight line, i.e., that

$$\frac{\ln \vartheta_1 - \ln \vartheta_2}{t_1 - t_2} = \frac{\ln \vartheta_2 - \ln \vartheta_3}{t_2 - t_3},$$

where

$$\vartheta_1 = \Delta T - \Delta T_\infty,$$

we obtain the expression for k:

$$k = \frac{\Delta T_2^2 - \Delta T_1 \Delta T_3}{2\Delta T_2 - (\Delta T_3 + \Delta T_1)} \equiv \nabla(\Delta T). \tag{3.15}$$

Here $\Delta T_1 = T_2 - T_1$ at moment of time t_1, $\Delta T_2 = T_2 - T_1$ at moment of time t_2, and $\Delta T_3 = T_2 - T_1$ at moment of time t_3.

The relations obtained yield $(mc)_t$, $(mc)_n$, α, and T_n, if $T_1(t)$, $T_2(t)$ and $Q_n(t)$ are known from the experiment.

Calculating $(mc)_t$ of the heat carrier

We find a section on the curve for $T_1(t)$ where $a = \frac{\partial T_1}{\partial t} = 0$. At this moment the instruments must be somewhat overheated or overcooled in order that a variation

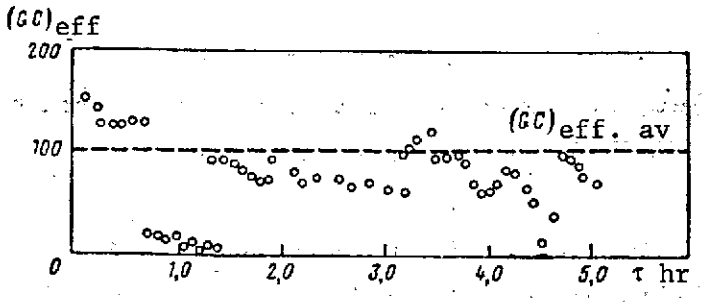

Fig. 3.19. Values of effective thermal conductivity of the instrument compartment derived experimentally for the third Soviet artificial Earth satellite.

of $T_2(t)$ and $Q_n \neq 0$ be noted. It then follows from expression (3.9) that

$$(mc)_t = \frac{Q_n}{\nabla}. \qquad (3.16)$$

The value of ∇ is calculated by formula (3.15).

Calculating $(mc)_n$ of the instruments

Let us find on the curve for $T_1(t)$ another section where $a = \frac{dT_1}{dt} = \text{const}$ and is not equal to zero. In this case $Q_n \neq 0$.

Then

$$(mc)_n = \frac{Q_n - \nabla (mc)_t}{a}. \qquad (3.17)$$

Calculating the value of b

From the derived values of $(mc)_t$ and $(mc)_n$ for section $T_1(t)$, where a = const, we find

$$b = \left[b + \frac{(mc)_t}{(mc)_n} \frac{t_1 - t_2}{\ln(\Delta T_1 - \nabla) - \ln(\Delta T_2 - \nabla)} \right]^{-1}.$$

Calculating the effective temperature of the instrument compartment T_n /145

From the derived value of b, we find

$$T_n = \frac{bT_2 - T_1}{b - 1}.$$

A special case

If $Q_n = 0$ and $T_1(t) = \text{const}$, it is sufficient to measure ΔT_1 and ΔT_2 at moments of time t_1 and t_2 in order to calculate ΔT_3 at moment of time t_3 by the

formula

$$\Delta T_3 = \Delta T_2 \frac{\Delta T_2}{\Delta T_1}.$$

Here

$$t_1 - t_2 = t_3 - t_2.$$

The values of $(mc)_n$ derived by formula (3.17) will be different, depending on whether the instruments are heated or cooled. The least errors in further theoretical calculations will occur if their experimental values are used as $(mc)_n$, taking into account the direction of heat flux — toward or away from the instruments. The error will be compensated for if the average thermal conductivity, obtained during heating and cooling, is taken in the cycle with variable heat dissipation of the instruments. Data obtained for the third Soviet artificial Earth satellite are presented in Figure 3.19 as an example of numerical calculation of $(mc)_n$ by formulas (3.15) - (3.17).

8. Scale Modelling of Spacecraft Thermal Conditions [41], [144], [162], [216]

In a number of cases, the spacecraft dimensions are considerably larger than those of the installations designed to simulate spacecraft thermal conditions. Other complications also arise, for example, if the process being investigated takes place very slowly, but the time of the experiment may not be as long as that /146 under natural conditions. It is sometimes difficult(and in other cases simply impossible) to obtain large volumes of dense molecular or energy beams, an ultra-high vacuum, or to recreate the radiation spectrum with the same accuracy as under natural conditions. All this makes it attractive to conduct experiments on reduced spacecraft models under conditions not identical to real conditions. Variation of the external conditions and spacecraft dimensions is not selected arbitrarily, but in order that all quantitative characteristics of the process, expressed in relative dimensionless form, remain similar for real and experimental conditions. For this it is necessary to select in the appropriate manner the dimensionless criteria of similarity. In this case, the phenomenon itself is not actually studied during the experiment, but the process similar to it. Data, which lead to a prediction of the spacecraft temperature field during flight, may be obtained from the experiment if the similarity criteria are properly selected.

When attempting to establish the conditions of similarity between the

compromise solutions. One of these solutions is based on the fact that not all dimensionless criteria of similarity for the model retain their numerical values. By selecting various combinations of main and secondary similarity criteria, many special methods of scale modelling may be obtained.

Some of these methods may be illustrated on the example of simulating the thermal conditions of a hypothetical spacecraft, which is a pressurized capsule with instruments which dissipate heat. This heat may be transferred to the skin by convection, thermal conductivity and radiation. The radiant flux of the Sun impinges on the skin from without. The material of the skin has a finite thermal conductivity, and therefore, due to non-uniform heating, temperature gradients along the skin are possible. We shall also take into account contact thermal resistance, which determines the heat fluxes at points of contact of various components.

In the general case, the differential equation of thermal conductivity has the form

$$C\rho\frac{\partial T}{\partial t}=\frac{\partial}{\partial x}\left(\lambda\frac{\partial T}{\partial x}\right)+\frac{\partial}{\partial y}\left(\lambda\frac{\partial T}{\partial y}\right)+\frac{\partial}{\partial z}\left(\lambda\frac{\partial T}{\partial z}\right)+Q, \tag{3.18}$$

where Q, C, ρ, and λ are the output of internal heat dissipation in W/m^3, specific heat, density and the coefficient of thermal conductivity, respectively.

This equation may be used to describe heat transfer both inside the spacecraft and in its skin. The characteristics of the specific process of heat transfer are determined by the use of boundary conditions which take into account the initial state of the system, processes of convective, conductive and radiant heat transfer /147 between the internal assemblies of the spacecraft, as well as those on the internal and external surfaces of the skin. It is usually necessary to reduce the differential equations of heat transfer and boundary conditions to dimensionless form to find the similarity criteria of the heat transfer processes of the spacecraft and its model. The dimensionless criteria derived in this manner permit a study of the simulation problem without finding solutions to the generalized boundary value problem.

Let x, y, z and η, ξ, ψ be the spatial coordinates, respectively, inside the spacecraft and in its skin (the coordinate ψ is reckoned along the normal to the

surface of the skin). T_{instr} and Q_c are the instrument temperature in °K and the heat flux through the point of contact of adjacent units, respectively, and α and φ are the coefficient of convective heat transfer and the coefficient of irradiation between units, respectively. Let us introduce characteristic (with the bar) and dimensionless (with the prime) values.

$$
\begin{gathered}
(C\varrho)'=\frac{C\varrho}{\overline{C\varrho}};\quad t'=\frac{t}{\bar{t}};\quad T'=\frac{T}{\bar{T}};\quad \lambda'=\frac{\lambda}{\bar{\lambda}};\quad Q'=\frac{Q}{\bar{Q}};\\
\alpha'=\frac{\alpha_{av}}{\bar{\alpha}_{av}};\quad \varepsilon'=\frac{\varepsilon}{\bar{\varepsilon}};\quad (A_sS_{\odot})'=\frac{A_sS_{\odot}}{\overline{A_sS_{\odot}}};\\
x'=\frac{x}{\bar{L}};\quad y'=\frac{y}{\bar{L}};\quad z'=\frac{z}{\bar{L}};\\
\xi'=\frac{\xi}{\bar{L}};\quad \eta'=\frac{\eta}{\bar{\eta}};\quad \psi'=\frac{\psi}{\bar{D}}.
\end{gathered}
\tag{3.19}
$$

Length L is taken as the characteristic dimension for the coordinate inside the spacecraft, as well as for the longitudinal coordinate of the skin, and skin thickness D — as the characteristic dimension for coordinate ψ. For a narrow temperature range, the functions $C\rho(t)$ and $\lambda(T)$ may be approximated by a power function of the form

$$
\lambda'=(T')^p,\quad (C\varrho)'=(T')^b,
\tag{3.20}
$$

where p and b are dimensionless values.

Then in coordinates x', y' and z', Equation (3.18) assumes the form

$$
\begin{gathered}
\frac{\overline{C\varrho}\bar{L}^2}{\bar{\lambda}\bar{t}}(C\varrho)'\frac{\partial T'}{\partial t'}=\lambda'\left[\frac{\partial^2T'}{(\partial x')^2}+\frac{\partial^2T'}{(\partial y')^2}+\frac{\partial^2T'}{(\partial z')^2}\right]+\\
+\lambda'\frac{p}{T'}\left[\left(\frac{\partial T'}{\partial x'}\right)^2+\left(\frac{\partial T'}{\partial y'}\right)^2+\left(\frac{\partial T'}{\partial z'}\right)^2\right]+\frac{\bar{Q}\bar{L}^2}{\bar{T}\bar{\lambda}}Q'.
\end{gathered}
\tag{3.21}
$$

The dimensionless equations which describe boundary conditions are written in a like manner.

The similarity of the thermal processes of a real spacecraft and its reduced scale model occurs in the case when the corresponding dimensionless complexes of /148 equations, written for the spacecraft (subscript a) and its model (subscript m), are identical. Thus, we arrive at the following criterial equations.

For internal units:

$$\left(\frac{\overline{C\varrho}\bar{L}^2}{\bar{t}\bar{\lambda}}\right)_m=\left(\frac{\overline{C\varrho}\bar{L}^2}{\bar{t}\bar{\lambda}}\right)_a; \tag{3.22}$$

$$\left(\frac{\bar{Q}\bar{L}^2}{\bar{\lambda}\bar{T}}\right)_m=\left(\frac{\bar{Q}\bar{L}^2}{\bar{\lambda}\bar{T}}\right)_a; \tag{3.23}$$

$$\left(\frac{\overline{\varepsilon^*\mathrm{av}\varphi}\bar{T}^3\bar{L}}{\bar{\lambda}}\right)_m=\left(\frac{\overline{\varepsilon^*\mathrm{av}\varphi}\bar{T}^3\bar{L}}{\bar{\lambda}}\right)_a; \tag{3.24}$$

$$\left(\frac{\overline{\alpha^*\mathrm{av}}\bar{L}}{\bar{\lambda}}\right)_m=\left(\frac{\overline{\alpha^*\mathrm{av}}\bar{L}}{\bar{\lambda}}\right)_a; \tag{3.25}$$

$$\left(\frac{\bar{Q}\mathrm{c}\bar{L}}{\bar{\lambda}\bar{T}}\right)_m=\left(\frac{\bar{Q}\mathrm{c}\bar{L}}{\bar{\lambda}\bar{T}}\right)_a. \tag{3.26}$$

For the skin:

$$\left(\frac{\overline{cp}\bar{D}^2}{\bar{t}\bar{\lambda}}\right)_m=\left(\frac{\overline{cp}\bar{D}^2}{\bar{t}\bar{\lambda}}\right)_a; \tag{3.27}$$

$$\left(\frac{\overline{\varepsilon\mathrm{av}\varphi}\bar{T}^3\bar{D}}{\bar{\lambda}}\right)_m=\left(\frac{\overline{\varepsilon\mathrm{av}\varphi}\bar{T}^3\bar{D}}{\bar{\lambda}}\right)_a; \tag{3.28}$$

$$\left(\frac{\overline{\alpha\mathrm{av}}\bar{D}}{\bar{\lambda}}\right)_m=\left(\frac{\overline{\alpha\mathrm{av}}\bar{D}}{\bar{\lambda}}\right)_a; \tag{3.29}$$

$$\left(\frac{\overline{A_s S_\odot}\bar{D}}{\bar{\lambda}\bar{T}}\right)_m=\left(\frac{\overline{A_s S_\odot}\bar{D}}{\bar{\lambda}\bar{T}}\right)_a; \tag{3.30}$$

$$\left(\frac{\overline{\varepsilon\varphi}\bar{T}^3\bar{D}}{\bar{\lambda}}\right)_m=\left(\frac{\overline{\varepsilon\varphi}\bar{T}^3\bar{D}}{\bar{\lambda}}\right)_a. \tag{3.31}$$

For the skin and internal units:

$$p_m=p_a; \tag{3.32}$$

$$\left(\frac{\bar{D}}{\bar{L}}\right)_m=\left(\frac{\bar{D}}{\bar{L}}\right)_a. \tag{3.33}$$

Certain parameters, making up Equations (3.22) - (3.33), may conveniently remain the same for the model and spacecraft when scale modelling. Selecting certain parameters as constant, many possible combinations of conditions may be considered, which are superimposed on the determining parameters. Let us consider /149 five combinations, or as they are often called, methods, which are of greatest practical interest.

First method — equality of spacecraft and model temperatures

Temperatures at similar points of the model and prototype should be identical to $\overline{T}_m = \overline{T}_a$. The material of the model may differ from that of the prototype. We shall assume that the coefficient of thermal conductivity λ_m and λ_a, as well as that of specific heat $(C\rho)_m$ and $(C\rho)_a$, do not depend on temperature.

We shall denote the scale change of linear dimensions by

$$\frac{\overline{L}_a}{\overline{L}_m} = M \text{ and } \frac{\overline{D}_a}{\overline{D}_m} = m.$$

Using these equalities, from Equations (3.22) - (3.33) we obtain the following relations for the internal units:

$$\frac{\overline{t}_m}{\overline{t}_a} = \frac{\overline{\lambda}_a}{\overline{\lambda}_m} \frac{(\overline{C\varrho})_m}{(\overline{C\varrho})_a} \frac{1}{M^2}, \tag{3.34}$$

$$\frac{\overline{Q}_m}{\overline{Q}_a} = \frac{\overline{\lambda}_m}{\overline{\lambda}_a} M^2. \tag{3.35}$$

The equality of irradiation coefficients $\varphi_m = \varphi_a$, follows from geometrical similarity; therefore,

$$\frac{\overline{\varepsilon}^*_m}{\overline{\varepsilon}^*_a} = \frac{\overline{\alpha}^*_m}{\overline{\alpha}^*_a} = \frac{(\overline{Q}_C)_m}{(\overline{Q}_C)_a} = M \frac{\overline{\lambda}_m}{\overline{\lambda}_a}. \tag{3.36}$$

For the skin:

$$\frac{\overline{t}_m}{\overline{t}_a} = \frac{\overline{\lambda}_a}{\overline{\lambda}_m} \frac{(\overline{C\varrho})_m}{(\overline{c\varrho})_a} \frac{1}{m^2}; \tag{3.37}$$

$$\frac{\overline{\varepsilon}_m}{\overline{\varepsilon}_a} = \frac{\overline{\alpha}_m}{\overline{\alpha}_a} = m \frac{\overline{\lambda}^*_m}{\overline{\lambda}^*_a}; \tag{3.38}$$

$$\frac{(\overline{Q}_C)_m}{(\overline{Q}_C)_a} = \frac{(\overline{A_s S_\odot})_m}{(\overline{A_s S_\odot})_a} = m \frac{\overline{\lambda}_m}{\overline{\lambda}_a}. \tag{3.39}$$

Total heat dissipation in the space is:

$$\frac{\overline{N}_m}{\overline{N}_a} = \frac{1}{M} \frac{\overline{\lambda}^*_m}{\overline{\lambda}^*_a}. \tag{3.40}$$

And, finally, the equality of scales M = m. When using the given method, one should take the fact into account that, if ε_a is close to unity, the coefficient of thermal conductivity of the model should be selected such that $\frac{\bar{\lambda}_a}{\bar{\lambda}_m} > m$, /150

because ε_m should always be less than unity. It is convenient to maintain the darkness coefficients of the model and spacecraft as $\varepsilon_m = \varepsilon_a$. For this purpose it is necessary to select material for the model so that the ratio of thermal conductivity coefficients for the spacecraft and model would be equal to the scale of reduction of skin thickness, i.e., $\frac{\lambda_a}{\lambda_m} = m$. The appropriate material for the model is selected almost at the beginning, which clearly determines the scale of m. It is obvious from Equation (3.39) that the condition $m \frac{\lambda_m}{\lambda_a} = 1$ also denotes the equality $(A_s S_\odot)_m = (A_s S_\odot)_a$.

In the case when the degree of darkness of the spacecraft surface is different for its different sections and its values are within broad ranges ($0.01 < \varepsilon_a < 0.9$), it is impossible to select the corresponding coefficient. This circumstance is an essential limitation of the given method. For internal surfaces it is also difficult to vary the relation

$$\frac{\bar{\varepsilon}_m^*}{\bar{\varepsilon}_a^*} = M \frac{\bar{\lambda}_m}{\bar{\lambda}_a}. \tag{3.41}$$

However, it may be kept constant if the coefficient of thermal conductivity of the internal units is varied in proportion to the scale:

$$\frac{\bar{\lambda}_a}{\bar{\lambda}_m} = M = \frac{\bar{L}_a}{\bar{L}_m}.$$

Actually, the coefficients $\bar{\lambda}_m$ and $\bar{\lambda}_a$ depend on temperature in most cases. Therefore, the assumption that λ = inv (T) may lead to errors.

If a material is selected for the model which differs from that of the spacecraft, the dependence of thermal conductivity on the temperature of these materials may, generally speaking, be different.

Let us assume that a material is selected for some point of the model in which the relation (3.41) is fulfilled. But this will not mean that the condition

(3.41) will be fulfilled for other points with different temperatures. For a narrow range of temperature variations of the spacecraft units, we may assume that $\frac{\lambda_m}{\lambda_a} =$ const. In the general case the resulting error must be estimated for each specific temperature distribution.

In this sense the method in which the unambiguity of the material is retained along with the equality of temperatures is more precise.

Second method — equality of temperatures and similarity of material in the model and the spacecraft /151

The main relations for this method may be derived from the preceding method if we assume that $(\overline{C_Q})_m = (\overline{C_Q})$ and $\lambda_m = \lambda_a$.

For the internal units we have:

$$\frac{\bar{t}_m}{\bar{t}_a} = \frac{1}{M^2}; \tag{3.42}$$

$$\frac{\bar{Q}_m}{\bar{Q}_a} = M^2; \tag{3.43}$$

$$\frac{\bar{\varepsilon}^*_m}{\bar{\varepsilon}^*_a} = \frac{\bar{\alpha}^*_{av}}{\bar{\alpha}^*_{av}}\frac{m}{a} = \frac{(\bar{Q}_C)_m}{(\bar{Q}_C)_a} = M = m. \tag{3.44}$$

For the skin:

$$\frac{\bar{t}_m}{\bar{t}_a} = \frac{1}{m^2}; \tag{3.45}$$

$$\frac{\bar{\alpha}_{av}}{\bar{\alpha}_{av}}\frac{m}{a} = \frac{\bar{\varepsilon}_m}{\bar{\varepsilon}_a} = \frac{(\bar{Q}_C)_m}{(\bar{Q}_C)_a} = \frac{(\overline{A_s S_\odot})_m}{(\overline{A_s S_\odot})_a} = m; \tag{3.46}$$

$$\frac{\bar{N}_m}{\bar{N}_a} = \frac{1}{M}. \tag{3.47}$$

The disadvantage of the method is that at $\varepsilon_a \approx 1$ and large values of M and m, equalitites (3.44) and (3.46) are almost impossible to fulfill. This method may be employed if $\bar{\varepsilon}^*_a M < 1$ and $\bar{\varepsilon}_a m \leq 1$. It is sometimes necessary that the relative skin thickness be increased, i.e., the inequality $M \neq m$ is permitted. This leads to the fact that the external dimensions of the spacecraft at a certain selected scale M vary in a different scale M*.

The relative distortion of the scale may be calculated by the formula

$$\frac{M^*}{M}=\frac{1}{1-\frac{D_a}{L_a}\left(\frac{M}{m}-1\right)}. \tag{3.48}$$

We assume

$$\frac{D_a}{L_a}=\frac{0,1}{10}=0,01,\ M=100,\ m=10.$$

Distortion of the scale for the external configuration will then be

$$\frac{M^*}{M}=\frac{1}{1-0,01\left(\frac{100}{10}-1\right)}=\frac{1}{0,91}\approx 10\%.$$

Distortion of the linear scale is undesirable for yet another reason. /152

It is obvious from Equations (3.42) and (3.45) that the inequality m ≠ M leads to the fact that the heat transfer processes for the skin and internal units will take place at different scales of time reduction.

Third method — the equality of the coefficients of irradiation and temperatures of the model and spacecraft

We have the following equalities at similar points of the model and prototype: $\bar{T}_m=\bar{T}_a$, $(\overline{\varepsilon\varphi})_m=(\overline{\varepsilon\varphi})_a$, $(\overline{\varepsilon^*\varphi^*})_m=(\overline{\varepsilon^*\varphi^*})_a$, and $(\overline{A_s})_m=(\overline{A_s})_a$. Using these equalities, we find from expressions (3.22) - (3.26) that for the internal units

$$\frac{\bar{t}_m}{\bar{t}_a}=M^{-1}\frac{(\overline{CU})_m}{(\overline{CU})_a}; \tag{3.49}$$

$$\frac{\bar{Q}_m}{\bar{Q}_a}=M; \tag{3.50}$$

$$\frac{(\bar{Q}_C)_m}{(\bar{Q}_C)_a}=\frac{(\alpha^*_{av})_m}{(\alpha^*_{av})_a}=1; \tag{3.51}$$

$$\frac{\bar{t}_m}{\bar{t}_a}=M^{-1}; \tag{3.52}$$

$$\frac{\bar{N}_m}{\bar{N}_a}=M^{-2}. \tag{3.53}$$

For the skin, from expressions (3.27) - (3.31), we have

$$\frac{\bar{t}_m}{\bar{t}_a} = m^{-1}\frac{(\overline{C\varrho})_m}{(\overline{C\varrho})_a}; \tag{3.54}$$

$$\frac{\bar{\lambda}_m}{\bar{\lambda}_a} = m^{-1}; \tag{3.55}$$

$$\frac{\bar{\varepsilon}_m}{\bar{\varepsilon}_a} = \frac{(\bar{S}_\odot)_m}{(\bar{S}_\odot)_a} = \frac{(\bar{\sigma}_{av})_m}{(\bar{\sigma}_{av})_a} = \frac{(\bar{Q}_c)_m}{(\bar{Q}_c)_a} = 1; \tag{3.56}$$

$$m = M. \tag{3.57}$$

This method does not require special selection of the covering for the model. It remains the same as that on the prototype. Solar flux and heat transfer coefficients also remain unchanged. The disadvantage of the method appears in the case when the equality of scales m = M is not maintained due to the complexity of preparing the model or when the thermal conductivity (λ_a) of the spacecraft skin is very low. For example, the spacecraft is covered from above with vacuum-shielding insulation having an extremely low heat transfer coefficient. According to expression (3.55), another more perfect insulation ($\bar{\lambda}_m = \lambda_a m^{-1}$) must be selected for the model, and its thickness must be reduced simultaneously. It is practically impossible to do this and it must be assumed that the inequality m < M or even the skin thickness must remain unchanged (m = 1). However, retention of the scale for the skin leads to non-uniform variation of the time scale for the skin and internal units. /153

If some connection of an internal unit to the skin of the prototype were made of the same material, different materials would have to be used for the same assembly in the model at M ≠ m, according to (3.52) and (3.55).

The method in which the spacecraft and prototype material is identical is more suitable in some cases.

Fourth method — similarity of material and equality of irradiation coefficients of model and spacecraft

The material is the same at similar points of the model and prototype, but temperatures may have different values. Therefore, the typical values of specific heat and thermal conductivity may be different. Let us assume that we can

approximate the dependence of thermal conductivity and specific heat by the power functions $(\overline{C\varrho}) = (C\varrho)_0 \left(\frac{\overline{T}}{T_0}\right)^b$ and $\lambda = \lambda_0 \left(\frac{\overline{T}}{T_0}\right)^p$, where T_0 = 300°K, and λ_0 and $(C\rho)_0$ are the values of λ and $C\rho$ at T_0 = 300°K. Then, from Equations (3.22) - (3.33), and taking into account (3.20), we obtain complexes for the internal units:

$$\left(\frac{\overline{T}^{b-p}\overline{L}^2 T^p (C\varrho)_0}{\overline{t}T_0^b\lambda_0}\right)_m = \left(\frac{\overline{T}^{b-p}\overline{L}^2 T_0^p (C\varrho)_0}{\overline{t}T_0^b\lambda_0}\right)_a$$

or

$$\left(\frac{\overline{T}^{b-p}\overline{L}^2}{\overline{t}}\right)_m = \left(\frac{\overline{T}^{b-p}\overline{L}^2}{\overline{t}}\right)_a; \tag{3.58}$$

similarly

$$\left(\frac{\overline{Q}\overline{L}^2}{\overline{T}^{p+1}}\right)_m = \left(\frac{\overline{Q}\overline{L}^2}{\overline{T}^{p+1}}\right)_a; \tag{3.59}$$

$$(\overline{\varepsilon}^*_{av}\overline{T}^{3-p}\overline{L})_m = (\overline{\varepsilon}^*_{av}\overline{T}^{3-p}\overline{L})_a; \tag{3.60}$$

$$\left(\frac{\overline{\alpha}^*_{av}\overline{L}}{\overline{T}^p}\right)_m = \left(\frac{\overline{\alpha}^*_{av}\overline{L}}{\overline{T}^p}\right)_a; \tag{3.61}$$

$$\left(\frac{\overline{Q}_c\overline{L}}{\overline{T}^{p+1}}\right)_m = \left(\frac{\overline{Q}_c\overline{L}}{\overline{T}^{p+1}}\right)_a. \tag{3.62}$$

For the skin: /154

$$\left(\frac{\overline{T}^{b-p}\overline{D}^2}{\overline{t}}\right)_m = \left(\frac{\overline{T}^{b-p}\overline{D}^2}{\overline{t}}\right)_a; \tag{3.63}$$

$$(\overline{\varepsilon}_{av}\overline{T}^{3-p}\overline{D})_m = (\overline{\varepsilon}_{av}\overline{T}^{3-p}\overline{D})_a; \tag{3.64}$$

$$\left(\frac{\overline{\alpha}_{av}\overline{D}}{\overline{T}^p}\right)_m = \left(\frac{\overline{\alpha}_{av}\overline{D}}{\overline{T}^p}\right)_a; \tag{3.65}$$

$$\left(\frac{\overline{A_s S_\odot}\overline{D}}{\overline{T}^{p+1}}\right)_m = \left(\frac{\overline{A_s S_\odot}\overline{D}}{\overline{T}^{p+1}}\right)_a; \tag{3.66}$$

$$(\overline{\varepsilon}\overline{T}^{3-p}\overline{D})_m = (\overline{\varepsilon}\overline{T}^{3-p}\overline{D})_a; \tag{3.67}$$

$$\left(\frac{\overline{Q}_c\overline{D}}{\overline{T}^{p+1}}\right)_m = \left(\frac{\overline{Q}_c\overline{D}}{\overline{T}^{p+1}}\right)_a. \tag{3.68}$$

For the skin and internal units:

$$p_m = p_a; \quad b_m = b_a; \tag{3.69}$$

$$M = m. \tag{3.70}$$

Equations (3.58) - (3.68), as well as the conditions of similar external and internal coverings $[\varepsilon_m = \varepsilon_a,\ \varepsilon_m^* = \varepsilon_a^*,\ (A_s)_m = (A_s)_a]$ permit the following relationships to be written for the internal units:

$$\frac{\bar{T}_m}{\bar{T}_a} = M^{\frac{1}{3-p}}; \tag{3.71}$$

$$\frac{\bar{t}_m}{\bar{t}_a} = M^{\frac{p+b-6}{3-p}}; \tag{3.72}$$

$$\frac{\bar{Q}_m}{\bar{Q}_a} = M^{\frac{7-p}{3-p}}; \tag{3.73}$$

$$\frac{(\alpha^*_{av})_m}{(\alpha^*_{av})_a} = M^{\frac{3}{3-p}}; \tag{3.74}$$

$$\frac{(\bar{Q}_c)_m}{(\bar{Q}_c)_a} = M^{\frac{4}{3-p}}; \tag{3.75}$$

$$\frac{N_m}{N_a} = M^{\frac{7-p}{3(3-p)}}. \tag{3.76}$$

For the skin: /155

$$\frac{\bar{T}_m}{\bar{T}_a} = m^{\frac{1}{3-p}}; \tag{3.77}$$

$$\frac{\bar{t}_m}{\bar{t}_a} = m^{\frac{p+b-6}{3-p}}; \tag{3.78}$$

$$\frac{(\bar{\alpha}_{av})_m}{(\bar{\alpha}_{av})_a} = m^{\frac{3}{3-p}}; \tag{3.79}$$

$$\frac{(\bar{S}_\odot)_m}{(\bar{S}_\odot)_a} = \frac{(\bar{Q}_c)_m}{(\bar{Q}_c)_a} = m^{\frac{1}{3-p}}. \tag{3.80}$$

An obvious limitation of the method (when p = 3) may be encountered only for special materials. If $p = b \approx 1$, model temperature will be $\sqrt[2]{M}$ times greater than that of the prototype, characteristic time will decrease by $1/\sqrt{M}$, the output of internal heat dissipation will increase M-fold, the average heat transfer coefficient will increase $M^{2/3}$-fold, and "solar" radiation and heat influx through the contacts will increase M^2-fold.

If M ≠ m, $\frac{\bar{T}_m}{\bar{T}_a}$ for the skin and $\frac{\bar{T}_m}{\bar{T}_a}$ for the internal units will be different. Therefore, it is necessary to make the scales of m and M identical; otherwise, the temperature distribution over the model as a whole will not be similar to that on the spacecraft. When using this method, one must keep in mind that A_s and ε may vary in some coverings as temperature increases (on the model as compared to the prototype), i.e., the main condition of the given method may be disrupted.

Fifth method — equality of irradiation coefficients and volumetric outputs of heat dissipation of the model and spacecraft

Here, in addition to geometric similarity, it is assumed that the following equalities are fulfilled at similar points of the spacecraft and its model:

$$\varepsilon_m=\varepsilon_a;\ \varepsilon_m^*=\varepsilon_a^*;\ (A_s)_m=(A_s)_a;\ Q_m=Q_a.$$

From equations (3.22) - (3.33), we obtain the relations for the internal units:

$$\left(\frac{\bar{L}^2}{\bar{T}\bar{\lambda}}\right)_m=\left(\frac{\bar{L}^2}{\bar{T}\bar{\lambda}}\right)_a; \tag{3.81}$$

$$\left(\frac{\overline{C\varrho}\,\bar{L}^2}{\bar{\lambda}\bar{t}}\right)_m=\left(\frac{\overline{C\varrho}\,\bar{L}^2}{\bar{\lambda}\bar{t}}\right)_a; \tag{3.82}$$

$$\left(\frac{\bar{T}^4}{\bar{L}}\right)_m=\left(\frac{\bar{T}^4}{\bar{L}}\right)_a; \tag{3.83}$$ /156

$$\left(\frac{\bar{T}^3\bar{L}}{\bar{\lambda}}\right)_m=\left(\frac{\bar{T}^3\bar{L}}{\bar{\lambda}}\right)_a; \tag{3.84}$$

$$\left(\frac{\bar{a}^*\bar{L}}{\bar{\lambda}}\right)_m=\left(\frac{\bar{a}^*\bar{L}}{\bar{\lambda}}\right)_a. \tag{3.85}$$

In a like manner, we obtain for the skin:

$$\left(\frac{\bar{Q}_c\bar{L}}{\bar{\lambda}\bar{T}}\right)_m=\left(\frac{\bar{Q}_c\bar{L}}{\bar{\lambda}\bar{T}}\right)_a; \tag{3.86}$$

$$\left(\frac{\overline{A_s S_\odot}\bar{D}}{\bar{\lambda}\bar{T}}\right)_m=\left(\frac{\overline{A_s S_\odot}\bar{D}}{\bar{\lambda}\bar{T}}\right)_a; \tag{3.87}$$

$$\left(\frac{\overline{C\varrho}\,\bar{L}^2}{\bar{\lambda}\bar{t}}\right)_m=\left(\frac{\overline{C\varrho}\,\bar{L}^2}{\bar{\lambda}\bar{t}}\right)_a; \tag{3.88}$$

$$\left(\frac{\bar{\alpha}^*\bar{L}}{\bar{\lambda}}\right)_m = \left(\frac{\bar{\alpha}^*\bar{L}}{\bar{\lambda}}\right)_a. \tag{3.89}$$

For the internal assemblies and skin:

$$m = M.$$

From these criteria, we find the relations for the main parameters of the spacecraft and model:

$$\frac{\bar{\lambda}_m}{\bar{\lambda}_a} = M^{-7/4}; \tag{3.90}$$

$$\frac{\bar{T}_m}{\bar{T}_a} = M^{-1/4}; \tag{3.91}$$

$$\frac{\bar{t}_m}{\bar{t}_a} = M^{-1/4}\frac{(\overline{CQ})_m}{(\overline{CQ})_a}; \tag{3.92}$$

$$\frac{(\bar{S}_\odot)_m}{(\bar{S}_\odot)_a} = \frac{(\bar{Q}_C)_m}{(\bar{Q}_C)_a} = M^{-1}; \tag{3.93}$$

$$\frac{N_m}{N_a} = M^{-3}; \tag{3.94}$$

$$\frac{(\bar{\alpha}_C^*)_m}{(\bar{\alpha}_C^*)_a} = \frac{\bar{\alpha}_m}{\bar{\alpha}_a} = M^{-3/4}. \tag{3.95}$$

The convenience of this method is that it permits the output of the solar radiation simulator to be decreased M-fold ($S_{\odot m} = S_{\odot a} M^{-1}$), which facilitates a simulation of the thermal conditions of a spacecraft flying a short distance from the Sun.

9. Mathematical Modelling of Spacecraft Thermal Conditions

One of the methods of obtaining information about the temperature distribution in a spacecraft is to combine mathematical modelling of spacecraft thermal conditions with the results of temperature measurements at various points (units) on its thermal model. This method was developed in the investigations of M. Toussaint [265]. The method permits refinements to be introduced into the initial mathematical model.

The mathematical model. The inverse problem

The spacecraft being investigated is divided into separate units, within the limits of which the temperature may be considered constant. Such units may be large and small components, for which the Biot criterion $\left(\mathrm{Bi} = \frac{\alpha x}{\lambda}\right)$ is sufficiently small (i.e., Bi $\leq$ 0.1).

The thermal interaction of the units among themselves and with the surrounding medium is described by formulas of elementary energy balance:

$$\begin{aligned} E_0 \varepsilon_i \varphi_{1-i} F_i + S_\odot A_{si} \varphi_{s-i} F_i + S_\odot A_{si} \varphi_{3-i} F_i - \varepsilon_i F_i \sigma T_i^4(t) \varphi_{4-i} - \\ - (C\varrho)_i \dot{T}_i(t) + \sum_{j \neq i}^{N} \alpha_{ij} [T_j(t) - T_i(t)] F_i + \\ + \sum_{m \neq i}^{N} \varepsilon_{m-i} \sigma \left[T_m^4(t) - T_i^4(t)\right] F_i = 0, \end{aligned} \tag{3.96}$$

or, more briefly, $f_i(t) = 0$, where N is the number of units;

$T_i(t)$ is the temperature of the i-th assembly at moment of time t;

$\dot{T}_i(t)$ is the time derivative;

$(C\rho)_i$ is the specific heat of the i-th unit;

φ_{1-i}; φ_{s-i}; φ_{3-i} is the coefficient of irradiation for infrared and solar rays and those reflected from the planet,

α is the heat transfer coefficient.

The first four terms in Equation (3.96) describe heat transfer with the surrounding medium. The last two terms are the interaction between the i-th unit and the remaining units.

We shall call vector $\vec{M}$, the "mathematical model", the components of which are the values

$$\begin{gathered} A_{s1}, A_{s2}, \ldots, A_{sN}; \ (C\varrho)_1, \ldots, (C\varrho)_N; \ \varepsilon_1, \varepsilon_2, \ldots, \varepsilon_N; \\ \alpha_{11}, \alpha_{12}, \ldots, \alpha_{NN}; \ \varepsilon_{11}, \varepsilon_{12}, \ldots, \varepsilon_{NN}. \end{gathered} \tag{3.97}$$

Measurements of specific heat, coefficients of radiant exchange and other components of vector $\vec{M}$ permit the first a priori approximation of the mathematical model to be obtained. Let us denote this first approximation by the symbol $\vec{M}^{o}$. /158 Knowing this approximation, we can calculate the temperature of any unit for conditions corresponding to experimental(*).

If the measured experimental temperatures do not agree with the calculated temperatures, corrections must be introduced into the mathematical model. We denote by $\vec{X}$ the vector whose components are corrections to the elements of first approximation of the mathematical model. Then we may write

$$\vec{M}=\vec{M}^{\circ}+\vec{X}. \tag{3.98}$$

The problem which is included in a calculation of the components of vector $\vec{M}$ from the results of experimental measurement shall be called the "inverse problem." The inverse problem may be solved by the trial-and-error method. Sequentially corrected values are given, and the temperatures corresponding to the mathematical model are calculated.

The trial-and-error operations are repeated until the calculated and measured values of temperature agree.

Let us find the conditions in which the mathematical model may be calculated. Instead of sequential calculation of the temperatures of all units, let us compare the results of the calculation with the experiment.

We construct the function

$$\Psi=\int_{t_0}^{t_f}\sum_{i}^{N}|f_i(t)|^2\,dt,$$

where t_0 and t_f are the initial and final moments of the time of the experiment;

$f_i(t)$ is brief notation for the instantaneous heat balance in unit i.

(*) For this we solve the system of differential equations

$$f_1(t)=0;\ f_2(t)=0;\ \ldots\ldots\ f_N(t)=0.$$

The function Ψ may be regarded as the function of the mathematical model $\vec{M}$ $(\Psi=\Psi(\vec{M}))$ or as the function of corrections $\vec{X}$: $\Psi=\Psi(\vec{X})$.

The function $f_i(t)$ is the linear function of variables ε_l, A_{sl}, $(C\varrho)_l$, α_{lj} and ε_{m-l}, and may be written in the form

$$f_i(t)=\Phi_l(t)+\Delta\varepsilon_l\frac{\partial f_i(t)}{\partial\varepsilon_l}+\Delta A_{sl}\frac{\partial f_i(t)}{\partial A_{sl}}+\Delta(C\varrho)_l\frac{\partial f_i(t)}{\partial(C\varrho)_l}+ \tag{3.99}$$
$$+\sum_{j\neq l}^{N}\Delta\alpha_{lj}\frac{\partial f_i(t)}{\partial\alpha_{lj}}+\sum_{m\neq l}^{N}\Delta\varepsilon_{m-l}\frac{\partial f_i(t)}{\partial\varepsilon_{m-l}},$$

where

$$\Delta\varepsilon_l=\varepsilon_l-\varepsilon_l^0,\ \Delta A_{sl}=A_{sl}-A_{sl}^0,$$

$$\Phi_l(t)=-\varepsilon_l^0F_l\sigma T_l^4(t)\varphi_{4-l}+E_0\varepsilon_l^0\varphi_{1-l}F_l+S_0A_{sl}^0\varphi_{3-l}F_l+$$
$$+S_\odot A_{sl}^0\varphi_{s-l}F_l-(C\varrho)_l^0\dot{T}_l(t)+\sum_{j\neq l}^{N}\alpha_{lj}^0[T_j(t)-T_l(t)]F_l+ \tag{3.100}$$ /159
$$+\sum_{m\neq l}^{N}\varepsilon_{m-l}^0\sigma F_l\left[T_m^4(t)-T_l^4(t)\right].$$

For any values of the components of vector $\vec{X}$, the function $\Psi(\vec{X})$ always assumes positive values. If the components of vector $\vec{X}$ agree precisely with the mathematical model, the function has a minimum value $\Psi(\vec{X})=0$.

Thus, solution of the inverse problem is equivalent to finding the minimum value of the function $\overline{\Psi}(\vec{X})$, i.e., a solution of the following system of equations:

$$\frac{\partial\overline{\Psi}(\vec{X})}{\partial X_1}=0,\ \frac{\partial\overline{\Psi}(\vec{X})}{\partial X_2}=0,\ldots,\frac{\partial\overline{\Psi}(\vec{X})}{\partial X_N}=0. \tag{3.101}$$

These equations are called "normal equations"(*).

Let us consider an example in which the results of calculations are included instead of experimental data. Let us assume that the system being investigated consists of three isothermal units, surrounded by a common spherical covering. The degree of darkness of the unit surface is $\varepsilon_1=\varepsilon_2=\varepsilon_3=0.9$. The surface area of the units (in cm^2) is $F_1=F_3=3000$ and $F_2=40{,}000$. The specific heat of the units is $(C\rho)_1=(C\rho)_3=300$ kcal/°C and $(C\rho)_2=$ kcal/°C. The initial temperatures

(*) This is in essence the least squares method.

of the units are T_1 = 123.74°C; T_2 = 123.06°C; and T_3 = 122.38°C.

Since the unit temperatures in the example considered are not clearly distinguished, the last member in Equation (3.100) may be linearized. This permits ε_{m-i} to be excluded from consideration and their equivalent heat transfer coefficients to be replaced by α_{ij}, which include radiant and convective heat transfer simultaneously. We assume that $\alpha_{1\,2} = \alpha_{2\,1} = \alpha_{1\,3}$ = 0.5 W/°C and $\alpha_{3\,2} = \alpha_{2\,3}$ = 0.2 W/°C. Let us assume that, prior to a specific moment of time, the external heat fluxes are absent, and the energy absorbed by the units is equal to zero: $P_1 = P_2 = P_3 = 0.0$.

The solar simulator was switched on at a certain moment of time (t = 0) and the system began to absorb heat: P_1 = 2.0 W, P_2 = 1.0 W and P_3 = 0.0. Let us assume that the absorption capacity remains constant throughout the entire preceding moment of time (let it be equal to 26 hours). Uisng the Rungs-Kutta method, the temperature values of the units $T_i(t)$ and the time derivatives $\dot{T}_i(t)$ may be calculated. Let us divide the given time interval (26 hours) into N parts (N = 26). /16
Thus, we have at our disposal three systems of 2N values:

$$T_i(t_1),\ T_i(t_2), \ldots,\ T_i(t_N) \quad i = 1,\ 2,\ 3 \ldots$$
$$\dot{T}_i(t_1),\ \dot{T}_i(t_2), \ldots,\ \dot{T}_i(t_N).$$

Let us assume that these values were measured experimentally. Let us now use them as initial data for the inverse problem. The mathematical model includes the system of 12 values:

$$\vec{M} = \vec{M}(P_1, P_2, P_3;\ (C\varrho)_1,\ (C\varrho)_2,\ (C\varrho)_3;\ \varepsilon_1, \varepsilon_2, \varepsilon_3;\ \alpha_{3\,1}, \alpha_{2\,1}, \alpha_{3\,2}).$$

The maximum number of unknowns in the inverse problem is equal to 12. Let us determine which of these unknowns may be regarded as independent values(*). For this the normal equations must first be written.

Let us consider the case in which the unknowns of the inverse problem will be

(*) For simplicity, we shall assume P_1, P_2 and P_3 as unknown instead of A_{s1}, A_{s2}, and A_{s3}.

$$\left.\begin{aligned} X_1 &= \Delta P_1 = P_1 - P_1^0; \\ X_2 &= \Delta \varepsilon_1 = \varepsilon_1 - \varepsilon_1^0; \\ X_3 &= \Delta (C\varrho)_1 = (C\varrho)_1 - (C\varrho)_1^0 \text{ (*)}. \end{aligned}\right\} \tag{3.102}$$

Let us find the members of the first normal equation. This equation is written in the form

$$\frac{\partial \Psi(\vec{X})}{\partial X} = 0, \tag{3.103}$$

or

$$\frac{\partial}{\partial \Delta P_1}\left(\sum_k^N |f_1(t_c)|^2\right) = 0,$$

or

$$\sum_k^N f_1(t_c) \frac{\partial f_1(t_k)}{\partial \Delta P_1} = 0.$$

Since $\frac{\partial f_1(t_k)}{\partial \Delta P_1} = 1$, finally, we may write /161

$$\Delta P_1 \left(\sum_k^N \frac{\partial f_1(t_c)}{\partial P_1}\right) + \Delta \varepsilon_1 \left(\sum_k^N \frac{\partial f_1(t_c)}{\partial \varepsilon_1}\right) + \Delta (C\varrho)_1 \left(\sum_k^N \frac{\partial f_1(t_c)}{\partial (C\varrho)_1}\right) = 0. \tag{3.104}$$

Equation (3.104) may be written in the form

(*) $P_1^0, \varepsilon_1^0 (C\varrho)_1^0$ are the coefficients of the first approximation of the mathematical model $\vec{M}^0 = \vec{M}^0 (P_1^0, P_2, P_3; \varepsilon_1^0, \varepsilon_2, \varepsilon_3; (C\varrho)_1^0, (C\varrho)_2, (C\varrho)_3; \alpha_{31}, \alpha_{21}, \alpha_{32})$;
$P_1, \varepsilon_1, (C\varrho)_1$ are the coefficients of the correct mathematical model
$\vec{M} = \vec{M} (P_1, P_2, P_3; \varepsilon_1, \varepsilon_2, \varepsilon_3; (C\varrho)_1, (C\varrho)_2, (C\varrho)_3, \alpha_{31}, \alpha_{21}, \alpha_{32})$

It is assumed that the coefficients of $P_2, P_3, \varepsilon_2, \varepsilon_3, (C\varrho)_2, (C\varrho)_3; \alpha_{31}, \alpha_{21}, \alpha_{32}$ are precisely known.

$$\sum_{j}^{N} L_{1j}X_j = B_1, \text{ where } B_1 = -\sum_{k}^{N} \Phi_1(t_C),$$

$$\left.\begin{aligned} L_{11} &= \sum_{k}^{N} \frac{\partial f_1(t_C)}{\partial P_1} = M; \\ L_{12} &= \sum_{k}^{N} \frac{\partial f_1(t_C)}{\partial \varepsilon_1} = -\sum_{k} \sigma A_{s1} T_1^4(t_C); \\ L_{13} &= \sum_{k}^{N} \frac{\partial f_1(t_C)}{\partial (C\varrho)_1} = -\sum_{k} \dot{T}_1(t_C). \end{aligned}\right\} \tag{3.105}$$

The complete system of normal equations may be presented in the form of the system: $\{L\}.\vec{X}=\vec{B}$. The components of vector $\vec{B}$ (i.e., the right side of the normal equations) are functions of temperature, the first time derivatives, and the first approximation of the mathematical model. The coefficients of matrix {L} are only functions of temperatures and the derivatives. Normal functions are written in Table 3 of the Appendix for the case when the unknowns of the inverse problem are the following corrections:

$$\begin{array}{llll} X_1 = \Delta P_1, & X_4 = \Delta (C\varrho)_1, & X_7 = \Delta\varepsilon_1, & X_{10} = \Delta\alpha_{31}, \\ X_2 = \Delta P_2, & X_5 = \Delta (C\varrho)_2, & X_8 = \Delta\varepsilon_2, & X_{11} = \Delta\alpha_{21}, \\ X_3 = \Delta P_3, & X_6 = \Delta (C\varrho)_3, & X_9 = \Delta\varepsilon_3, & X_{12} = \Delta\alpha_{32}. \end{array}$$

In this same table, the symbol $\sum_{k}^{N}$, is omitted and the symbol $\dot{T}_1$ should be regarded as $\sum_{k}^{N} \dot{T}_1(t_K)$. It is most convenient to solve normal equations by using an electronic computer. The compiled program permits a numerical calculation of the coefficients of the equations for any combinations of unknowns and determines whether the system has been calculated and whether it may be solved to the end.

The results of calculations, obtained for various combinations of unknowns, indicated the following.

1. The corrections were greater than the corresponding terms of the mathematical model. For example, when a value of 0.5 was taken in calculating the correction $\Delta\varepsilon_1$ as the first approximation, the correct value was equal to 0.9. /162

2. In the case when the system of normal equations may be solved, the results are obtained with an error not exceeding 0.001. (Hereafter, we shall denote as correct results only those in which all corrections have been calculated with the indicated accuracy.)

3. The relationships between the various unknowns may sometimes be found directly. For example, in the considered case, it follows from concepts of symmetry that $\alpha_{3\,1} = \alpha_{2\,1}$. Thus, the minimum value of $f(\vec{X})$ is a limited minimum which is calculated according to the program using the Lagrangian method.

4. In those cases when the results do not correspond to the condition $0 \leq \varepsilon \leq 1$ in a calculation of the minimum of function $f(\vec{X})$, the problem must again be solved with a different combination of unknowns. When calculating the unknown values, the following cases were considered:[1]

1. * ΔP_1, $\Delta\varepsilon_1$.
2. * ΔP_1, $\Delta(C\varrho)_1$.
3. * ΔP_1, $\Delta\varepsilon_1$.
4. ΔP_1, $\Delta(C\varrho)_1$, $\Delta\varepsilon_1$.
5. $\Delta\alpha_{1\,2}$, $\Delta\alpha_{2\,3}$, $\Delta\alpha_{3\,1}$.
6. * $\Delta\alpha_{1\,2}$, $\Delta\alpha_{2\,3}$, $\Delta\alpha_{3\,1}$.[2] ($\Delta\alpha_{1\,2} = \Delta\alpha_{1\,3}$).
7. * ΔP_1, $\Delta\alpha_{1\,2}$.
8. * $\Delta C\varrho_1$, $\Delta\alpha_{1\,2}$.
9. * $\Delta\varepsilon_1$, $\Delta\alpha_{1\,2}$.
10. ΔP_1, ΔP_2, $\Delta\alpha_{1\,2}$.
11. * $\Delta\varepsilon_1$, $\Delta\varepsilon_2$ $\Delta\alpha_{1\,2}$.
12. * $\Delta\varepsilon_1$, $\Delta\varepsilon_2$, $\Delta\alpha_{1\,2}$.
13. ΔP_1, ΔP_2, $\Delta\alpha_{1\,2}$, $\Delta\alpha_{2\,3}$, $\Delta\alpha_{3\,1}$ ($\Delta\alpha_{1\,2} = \Delta\alpha_{3\,1}$).
14. * $\Delta(C\varrho)_1$, $\Delta(C\varrho)_2$, $\Delta(C\varrho)_3$, $\Delta\alpha_{1\,2}$, $\Delta\alpha_{3\,2}$, $\Delta\alpha_{3\,1}$ ($\Delta\alpha_{1\,2} = \Delta\alpha_{3\,1}$).
15. * $\Delta(C\varrho)_1$, $\Delta(C\varrho)_2$, $\Delta(C\varrho)_3$, $\Delta\alpha_{1\,2}$, $\Delta\alpha_{2\,3}$, $\Delta\alpha_{3\,1}$ ($\Delta\alpha_{1\,2} = \Delta\alpha_{3\,1}$).
16. * $\Delta\varepsilon_1$, $\Delta\varepsilon_2$, $\Delta\varepsilon_3$, $\Delta\alpha_{1\,2}$, $\Delta\alpha_{2\,3}$, $\Delta\alpha_{3\,1}$ ($\Delta\alpha_{1\,2} = \Delta\alpha_{3\,1}$).
17. $\Delta(C\varrho)_1$, $\Delta\varepsilon_1$, $\Delta\alpha_{1\,2}$.
18. ΔP_1, $\Delta\Sigma_1$, $\Delta\alpha_{1\,2}$.
19. ΔP_1, ΔP_2, $\Delta(C\varrho)_1$, $\Delta(C\varrho)_2$, $\Delta\alpha_{1\,2}$.
20. ΔP_1 ΔP_2, $\Delta(C\varrho)_1$, $\Delta(C\varrho)_2$, $\Delta\alpha_{1\,2}$.
21. ΔP_1, ΔP_2, $\Delta\varepsilon_1$, $\Delta\varepsilon_2$, $\Delta\alpha_{1\,2}$.
22. $\Delta(C\varrho)_1$, $\Delta(C\varrho)_2$, $\Delta\varepsilon_1$, $\Delta\varepsilon_2$, $\Delta\alpha_{1\,2}$.

---

(1) The asterisk indicates correctly obtained results.

(2) We find from concepts of symmetry that $\alpha_{1\,2} = \alpha_{1\,3}$, if $\alpha^0_{1\,2} = \alpha^0_{1\,3}$ (the first approximation of the mathematical model); then $\Delta\alpha_{1\,2} = \Delta\alpha_{1\,3}$.

Thus, whereas we considered the unknowns of type P_i $(C\rho)_i$ or ε_i (which affect only the heat balance), the maximum number of unknowns which may be calculated for an assembly is two. When calculating P_1, ε_1 and $(C\rho)_1$ (this case comes under No. 4 in the list of unknown values), the system of normal equations was written incorrectly. We note that, if temperatures calculated experimentally do not vary with time, there is only one normal independent equation for each unit. An experimental investigation of transient processes reveals the possibility of calculating several, rather than one, variable. If ΔP_i, $\Delta(C\rho)_i$ or $\Delta\varepsilon_i$, as well as $\Delta\alpha_{ij}$ are taken as variables, a maximum of six values may be calculated, i.e., two each for each unit. When calculating the values of $\Delta\alpha_{3\,1}$, $\Delta\alpha_{2\,1}$ and $\Delta\alpha_{3\,2}$ (case No. 5 on the list), the terms of matrix {L} were: /163

103.0	25.0	26.6
25.0	24.2	-12.9
26.6	-12.9	27.5

and the determinant $|L| = 0$. Since the sum of the heat transfer coefficients is equal to zero, it would be assumed that the normal equations are not independent, if the complete system of heat transfer coefficients is calculated. However, the ambiguity disappears if the symmetry hypothesis is utilized, i.e., the fact is taken into account that $\Delta\alpha_{3\,1} = \Delta\alpha_{2\,1}$ (see case No. 6). Precisely the same type of ambiguity is encountered in calculations of cases Nos. 10 and 13. If none of the experimental errors is taken into account, interpretation of the results of control tests on the mathematical model permits a calculation of two coefficients each per unit. However, it is possible that certain combinations of unknowns lead to ambiguity or to incorrectness of the system of normal equations. In this case, only experiments can indicate whether the selection of unknowns is correct or not.

The Effect of Experimental Errors on the Mathematical Model.

To solve the inverse problem, the coefficients of the mathematical model must be calculated, using measurement data for this. Since these measurements are never absolutely correct, the problem arises about the effect of measurement errors on the results of solving the inverse problem. Let us consider some cases.

1. Errors in measurement of temperature depend on many causes, in particular on the location and attachment of thermocouples. If $T_i(t)$ is the measured

temperature of a unit, and $\vartheta_i(t)$ is its correct temperature, the error of $\Delta T_i(t) = \vartheta_i(t) - T_i(t)$ is a function of time, whose effect on the mathematical model may be calculated with the aid of the Taylor series: /164

$$\Delta T_i(t) = [\vartheta_i(t_0) - T_i(t_0)] + \left[\frac{d\vartheta}{dt} - \frac{dT_i}{dt}\right]_{t=t_0} (t - t_0) + \ldots \tag{3.106}$$

In experiments where there is cooling or heating of the system, the maximum effect of temperature measurement errors may be calculated, assuming that $\Delta T_i(t)$ is a constant value, not dependent on time, and that there exists a maximum difference between $\vartheta_i(t)$ and $T_i(t)$. Hereafter, we shall denote errors in calculation of $T_1(t)$, $T_2(t)$, ... etc. by $E(T_1)$, $E(T_2)$, and shall regard them as components of the vector $\overrightarrow{E(T)}$

2. Since the time derivatives of temperatures were obtained from experiments, it is easy to make great errors in calculating them, since the process of differentiation is not very precise(*). Let us denote by $E(\dot{T}_1)$, $E(\dot{T}_2)$,... the errors in calculating the derivatives of $\dot{T}_1(t)$, $\dot{T}_2(t)$, ..., which are the result of the imperfection of the differentiation technique. The symbol $\overrightarrow{E(\dot{T})}$ is a vector whose components are the values of $E(\dot{T}_1)$, $E(\dot{T}_2)$, ...

3. Let us assume that the total error of calculating the radiant flux of the solar simulator comprises about 5%. The errors resulting in a calculation of the heat fluxes impinging on the external surface of the spacecraft will be regarded as constant in space and not dependent on time throughout the experiment. Let us denote them by $E(P_1)$, $E(P_2)$, ...,$E(P_N)$. Let these values be the components of vector $\overrightarrow{E(P)}$.

Let us consider the effect of experimental errors.

We shall denote by $E(X)_1$, $E(X)_2$, ..., $E(X_{NT})$ the vector $\overrightarrow{E(X)}$ of errors obtained in the calculation of the unknowns for the inverse problem, which occurred due to errors $\overrightarrow{E(T)}$, $\overrightarrow{E(P)}$ and $\overrightarrow{E(\dot{T})}$, calculated above.

(*) Calculating the derivative by the simple method $\dot{T}_i(t_k) = \{T_i(t_{k+1}) - T_i(t_k)\}/(t_{k+1} - t_k)$ we may commit errors exceeding 30%. Use of a more precise method may yield better results.

Let us present the system of normal equations in the form

$$\{L\}\cdot\vec{X}=\vec{B} \quad \text{or} \quad \vec{X}=\{L^{-1}\}\cdot\vec{B}.$$

Thus, we may write

$$E(X_i)=\sum_j E(L_{ij}^{-1})\,B_j+\sum_k L_{ic}^{-1}E(B_c), \tag{3.107}$$

where $E(L_{ij}^{-1})$ is the error, occurring in calculating the term L_{ij}^{-1} of the matrix $\{L^{-1}\}$. $E(B_c)$ is the error arising in a calculation of the components B_c of vector $\vec{B}$. We recall that the components of vector $\vec{B}$ are functions of the main approximation of the mathematical model, used in solving the normal equations. If this approximation is identical to the correct mathematical model, the values of these components are equal to zero. On the other hand, we may show that the error $\overrightarrow{E(X)}$ does not depend on the method of approximation of the mathematical model, used in calculation of the normal equations. Expression (3.107) may be simplified and reduced to the form $E(X_i)=\sum_k L_{ic}^{-1}E(B_c)$, where the errors $E(B_c)$ are those of calculations of the right sides of the normal equations in the correct mathematical model. We may write /165

$$E(B_k)=\sum_i^N\left\{\sum_m^M\frac{\partial B_c}{\partial T_i(t_m)}\right\}E(T_i)+$$
$$+\sum_i^N\left\{\sum_m^M\frac{\partial B_c}{\partial \dot{T}_i(t_m)}\right\}E(\dot{T}_i)+\sum_i^{N'}\frac{\partial B_c}{\partial P_i}E(P_i). \tag{3.108}$$

Finally, the errors $E(X_1)$, $E(X_2)$, ..., committed in calculation of the unknowns of the inverse problem, may be expressed as functions of the experimental errors $\overrightarrow{E(T)}$, $\overrightarrow{E(P)}$ and $\overrightarrow{E(\dot{T})}$.

Thus,

$$\vec{E}(X)=\{MT\}\,\vec{E}(T)+\{MDT\}\,\vec{E}(T)+\{\overrightarrow{MP}\}\,\vec{E}(P)^{*}. \tag{3.109}$$

(*) The matrices {MT}, {MDT} and {MP} are quadrangular matrices with NT rows and N columns (N and NT are the numbers of the units and numbers of the unknowns, respectively. We may write

(continued)

A calculation of the members of matrices {MT}, {MDT} and {MR} makes it possible to determine which coefficients depend most strongly on the various types of errors. In a sense, the members NT of the first row of the matrix {MT} are errors in calculating NT corrections, if the temperature of the first unit $T_1(t)$ is calculated with a constant error $E(T_1) = 1°K$.

For the unknowns ΔC_{Q_1}, ΔC_{Q_2}, ΔC_{Q_3}, $\Delta\alpha_{31}$, $\Delta\alpha_{21}$, $\Delta\alpha_{32}$, using the correct values of the derivatives, we may obtain the following calculated values: /166

$$C_{Q_1} = 300.000 \text{ J}/°\text{K}, \qquad \alpha_{31} = 0.500 \text{ W}/°\text{K},$$
$$C_{Q_2} = 400.000 \text{ J}/°\text{K}, \qquad \alpha_{21} = 0.500 \text{ W}/°\text{K},$$
$$C_{Q_3} = 300.000 \text{ J}/°\text{K}, \qquad \alpha_{32} = 0.200 \text{ W}/°\text{K}.$$

Using for calculation of $\dot{T}_i(t_c)$ the simplest method of differentiation

$$\dot{T}_i(t_c) = \frac{T_i(t_{c+1}) - T_i(t_c)}{t_{c+1} - t_c}$$

we obtain

$$C_{Q_1} = 491 \text{ J}/°\text{K}, \qquad \alpha_{31} = 0.499 \text{ W}/°\text{K},$$
$$C_{Q_2} = 656 \text{ J}/°\text{K}, \qquad \alpha_{21} = 0.499 \text{ W}/°\text{K},$$
$$C_{Q_3} = 491 \text{ J}/°\text{K}, \qquad \alpha_{32} = 0.201 \text{ W}/°\text{K}.$$

On the other hand, calculation of the matrix {MDT} with a constant error $\dot{E}(\dot{T}_1)$ from the derivative of $\dot{T}_1(t)$ yields the following results:

(continued)

$$\{MT\}_{ij} = \sum_{k}^{NT} L_{ic}^{-1} \sum_{j}^{N} \sum_{m}^{M} \frac{\partial B_c}{\partial T_j(t_m)},$$

$$\{MDT\}_{ij} = \sum_{k}^{NT} L_{ic}^{-1} \sum_{j}^{N} \sum_{m}^{M} \frac{\partial B_c}{\partial \dot{T}_j(t_m)},$$

$$\{MP\}_{ij} = \sum_{k}^{NT} L_{ic}^{-1} \sum_{j}^{N} \frac{\partial B_c}{\partial P_j}.$$

(concluded)

$$E(\Delta C\varrho_1)=20.64 \quad J/^\circ K, \qquad E(\Delta\alpha_{31})=-0.013 \quad W/^\circ K,$$
$$E(\Delta C\varrho_2)=4.04 \quad J/^\circ K, \qquad E(\Delta\alpha_{21})=-0.013 \quad W/^\circ K,$$
$$E(\Delta C\varrho_3)=4.03 \quad J/^\circ K, \qquad E(\Delta\alpha_{32})=0.0067 \quad W/^\circ K.$$

It is obvious from these data that the effect of errors in calculating the time derivatives of $\dot{T}_i(t)$ is maximum in a calculation of specific heat $(C\rho)_1$.

Let us assess the effect of errors $\overline{E}(\vec{P})$ on the value of absorbed heat fluxes.

Having calculated the matrix {MP}, we find the error of calculating the flux P_1:$E(P_1)$ = 1 watt.

Calculation of $\Delta\varepsilon_1$, $\Delta\varepsilon_2$, $\Delta\varepsilon_3$, $\Delta\alpha_{31}$, $\Delta\alpha_{21}$, $\Delta\alpha_{32}$ yields:

$$E(\Delta\varepsilon_1)=0.23\,(25\%), \qquad E(\Delta\alpha_{31})=0.30\ (60\%),$$
$$E(\Delta\varepsilon_2)=0.16\,(20\%), \qquad E(\Delta\alpha_{21})=0.30\ (60\%),$$
$$E(\Delta\varepsilon_3)=0.21\,(25\%), \qquad E(\Delta\alpha_{32})=-0.15\,(75\%).$$

Calculation of $\Delta(C\varrho)_1$, $\Delta(C\varrho)_2$, $\Delta(C\varrho)_3$, $\Delta\alpha_{31}$, $\Delta\alpha_{21}$, $\Delta\alpha_{32}$ yields:

$$E(\Delta(C\varrho)_1)=-103, \qquad E(\Delta\alpha_{31})=0.31,$$
$$E(\Delta(C\varrho)_2)=-94, \qquad E(\Delta\alpha_{21})=0.31,$$
$$E(\Delta(C\varrho)_3)=-94, \qquad E(\Delta\alpha_{32})=-0.15.$$

The error in calculating the heat fluxes has a considerable effect not only on calculation of the absorption capacity, but also on calculation of the other coefficients of the mathematical model. This effect may be especially great in calculating thermal conductivity. /167

Let us determine the effect of errors $\overline{E}(\vec{T})$ on calculating temperature. Calculation of the matrix {MT} yields an error of $E(T_1)$ = 1°K in the calculation of $T_1(t)$.

Calculation of $\Delta(C\varrho)_1$, $\Delta(C\varrho)_2$, $\Delta(C\varrho)_3$, $\Delta\alpha_{31}$, $\Delta\alpha_{21}$, $\Delta\alpha_{32}$ yields

$$E(\Delta(C\varrho)_1)=580, \qquad E(\Delta\alpha_{31})=0.431,$$
$$E(\Delta(C\varrho)_2)=-276, \qquad E(\Delta\alpha_{21})=0.431,$$
$$E(\Delta(C\varrho)_3)=-276, \qquad E(\Delta\alpha_{32})=0.215.$$

Calculation of $\Delta\varepsilon_1$, $\Delta\varepsilon_2$, $\Delta\varepsilon_3$, $\Delta\alpha_{31}$, $\Delta\alpha_{21}$, $\Delta\alpha_{32}$ yields

$$E(\Delta\varepsilon_1)=-4.8, \qquad E(\Delta\alpha_{31})=0.31,$$
$$E(\Delta\varepsilon_2)=1.8, \qquad E(\Delta\alpha_{21})=0.31,$$
$$E(\Delta\varepsilon_3)=2.5, \qquad E(\Delta\alpha_{32})=-0.16.$$

Errors in calculation of temperatures are most strongly manifested in the results of calculating external radiation and thermal conductivity. Whereas this error may be disregarded in a calculation of temperature alone, in a calculation of the temperature difference it is easy to commit an error of more than 100%. In this case, calculation of the thermal conductivity loses any meaning. The above analysis permits definite conclusions to be made about which type of data should be obtained in conducting thermal tests, as well as formulation of the requirements placed on experiments of this type. In particular, it follows from this analysis that:

1) every coefficient may not be calculated in the mathematical model, but it is possible to calculate two independent parameters for every unit;

2) experiments should be carried out under conditions of steady thermal conditions, in which time-varying temperature gradients occur in the units of the model; the requirements for ensuring a vacuum are not rigid in the given case. The experimental layout should be simple, the conditions — clearly defined, and the experiment should be performed carefully.

/168

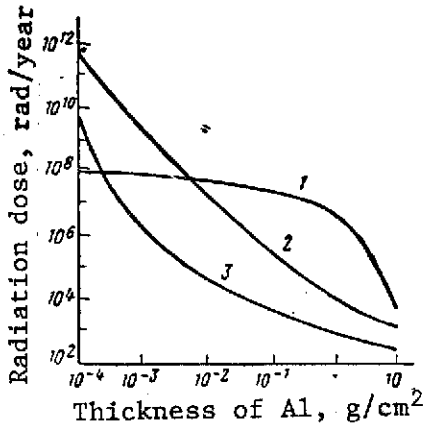

Fig. 3.20. The distribution of the absorbed radiation dose through thickness of aluminum for different orbits during a flight lasting for one year:
1 — equatorial orbit in the center of the artificial electron belt during the first months of its existence; 2 — equatorial orbit in the center of the inner radiation belt; 3 — dose from solar corpuscular radiation during interplanetary flight.

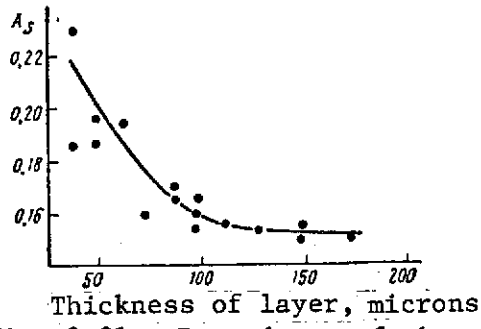

Fig. 3.21. Dependence of the coefficient of solar radiation absorption A_s on the thickness of the covering ($ZnO + K_2SiO_3$).

10. Simulating the Effects of Cosmic Corpuscular Radiation on the Temperature Controlling Covering of the Spacecraft /168

Energy and the Type of Radiation

When selecting the conditions for simulating radiation effects on a certain surface element of a spacecraft, various factors should be kept in mind. The orbit and duration of powered operation of the spacecraft determine the type and integral fluxes of cosmic radiation, acting on the materials and elements of the spacecraft [3], [185], [259], [260],[267].

The relative arrangement of the working area of the element being investigated with respect to the external surface of the spacecraft, as is shown in Figure 3.20, affects the dose of absorbed radiation. Thus, for example, the active zone which affects the main optical characteristics is located directly on the external surface of the covering for white temperature controlling coverings. The thickness of this zone comprises 100 - 150 microns (Figure 3.21) [185], [259].

The type of material from which the investigated element is made affects the selection of the parameters of ionizing radiation. Thus, for example, the type of radiation does not play a primary role for investigating the radiation tolerance of polymers. The important thing here is the absorbed integral dose of radiation

and the distribution of the absorbed dose through the thickness of the material being investigated. On the other hand, the rate of formation of radiation-induced flaws in materials having a crystal lattice is strongly dependent on the type and energy of charged particles.

It is expedient to use proton beams as the main type of penetrating radiation when investigating the radiation processes and tolerance of coverings. This selection is determined by the fact that maximum absorbed radiation doses in the surface layers of a material, as was demonstrated in Figure 3.20, are primarily related to the proton component of the radiation belts of the Earth and to solar corpuscular radiation. /169

At the same time, different types of radiation transformations may be more extensively investigated under the effect of protons compared to the effects of electrons.

When investigating the relative radiation tolerance of pigments and temperature controlling coverings and when determining the reliability of coverings under various conditions of space flight, it is expedient to also employ electron and neutron radiation.

Since the thickness of an optically active zone of most temperature controlling coverings comprises 100 - 150 microns, the energy of proton beams may not exceed several MeV [3], which corresponds to the path of such protons, in this zone of the covering. Protons with higher energies will lose a considerable part of their energy in deeper layers, the state of which has no effect on the main optical parameters of temperature controlling coverings.

An investigation of the radiation tolerance of temperature controlling coverings, as well as of other elements of spacecraft structures, may be carried out in two phases.

During the first phase, the relative tolerance of all types of temperature controlling coverings is investigated.

An attempt is made to obtain absolute data on radiation tolerance during the second phase. In this case the effects of cosmic radiation are simulated in order

to find the dependence of a variation of absorption coefficients A_s of the coverings on the absorbed radiation dose. Taking into account the radiation conditions for specific orbits of the spacecraft, this dependence permits a calculation of the variation of A_s on the duration of the spacecraft under space conditions.

Those brands of coverings which have increased radiation tolerance are selected as a result of laboratory tests. In this case less rigid requirements are placed on the sources of ionizing radiation than in an investigation of the absolute radiation tolerance of coverings. The main requirement placed on such investigations is that identical test conditions must be maintained for different brands of coverings.

The investigation of the radiation tolerance of coverings is an important and complex experimental problem. The further discussion is devoted primarily to problems of simulating radiation effects in order to predict the absolute radiation tolerance of temperature controlling coverings, designed for prolonged operation in different regions of space. /170

Use of Monoenergetic Proton Beams [3], [4], [5], [6], [7], [24]

Since standard proton accelerators available in laboratories generate monoenergetic particle beams, we must discuss the possibility of investigating the radiation tolerance of temperature controlling coverings in such installations. It is quite obvious that, by exposing the coverings of different brands of coverings to proton beams of equal energy and the same integral flux, we may investigate the relative radiation tolerance of the irradiated specimens of coverings and find those which are more radiation-tolerant.

In those cases when the absolute radiation tolerance of coverings, designed for lunar or interplanetary spacecraft, must be evaluated, monoenergetic proton and helium ion beams are used. The maximum absorbed dose in the surface layers of the external surface of such spacecraft is determined by the solar wind (Figure 3.20) with an average proton energy of ~1.5 keV and by steady proton fluxes with an energy of 1 - 10 keV. The annual absorbed surface dose from such fluxes may reach 10^9 - 10^{10} rads. The absorbed surface dose of proton radiation from solar flares is several orders less.

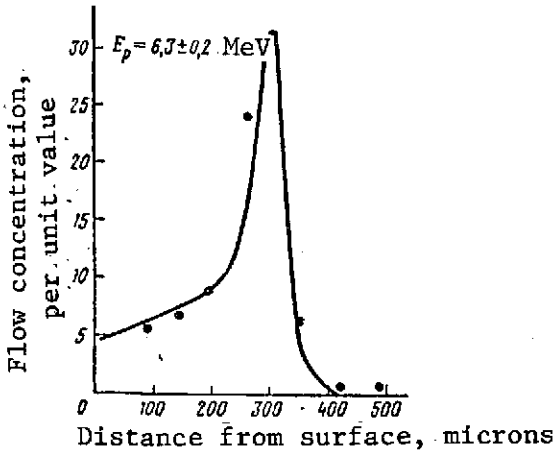

Fig. 3.22. Theoretical and experimental (points) dependence of concentration of radiation defects on depth for silicon exposed to protons with an energy of 6.3 MeV.

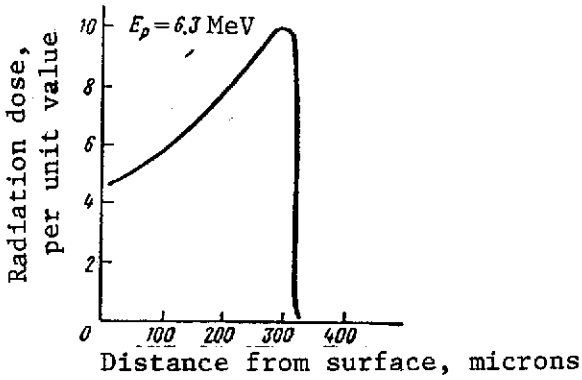

Fig. 3.23. Theoretical dependence of absorbed radiation dose for silicon exposed to protons with an energy of 6.3 MeV.

It is expedient to use standard ion guns with controlled energy when simulating the radiation effects of low-energy solar proton radiation under laboratory conditions. After obtaining the dependence of $A_s(\Phi_p)$ at E_p = 0.5 - 20 keV for different brands of coverings, conclusions may be made about the absolute radiation tolerance of coverings used for lunar and interplanetary spacecraft.

The problem of the conformity of the absorbed dose distribution through the thickness of the covering does not play a significant role in the given case, because the path of the protons and helium ions with an energy up to 20 keV in the covering material comprises tenths of a micron, which is less than the dimensions of the roughness of the outer layer of the covering, and is comparable to the wavelengths of solar light radiation.

The depth distribution of radiation defects and the absorbed radiation dose for monoenergetic proton beams (Figures 3.22 and 3.23) and cosmic rays (see Figure 3.20) has an opposite nature [3], [24]. The dependence of the variation of the coefficient A_s on the dose of gamma and ultraviolet radiation (Figures 3.24 and /171
3.25) approaches saturation. Therefore, the possibility of using monoenergetic proton beams to investigate the absolute radiation tolerance of coverings when simulating the effect of the proton component of the Earth's radiation belts requires more detailed consideration.

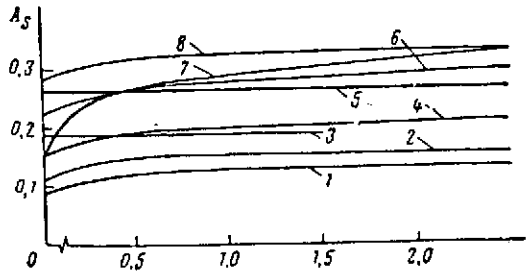

Gamma radiation, 10^8 roentgens

Fig. 3.24. Effect of gamma radiation in a vacuum on variation of solar radiation absorption A_s of different coverings. Measurement of A_s was made in air:
1 — $La_2O_3 + Na_2SiO_3$; 2 — $ZrSiO_4 + KSiO_3$; 3 — TiO_2 + modified organic silicon binder; 4 — $ZnO + Na_2SiO_3$; 5 — TiO_2 + organic silicon binder; 6 — $LiAl \times SiO_4 + Na_2SiO_3$; 7 — TiO_2 + epoxy binder; 8 — white gloss acrylic paint.

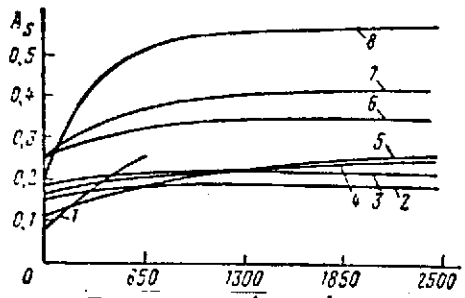

Exposure time, hours

Fig. 3.25. Variation of A_s of several types of temperature controlling coverings under the effects of near ultraviolet radiation in a vacuum (A_s was measured in air):
1 — $La_2O + Na_2SiO_3$; 2 — $ZnO + Na_2SiO_3$; 3 — TiO_2 + organic silicon binder; 4 — $LiAl \cdot SiO_4 + Na_2SiO_3$; 5 — $ZrSiO_4 + K_2SiO_3$; 6 — TiO_2 + modified organic silicon binder; 7 — white glossy acrylic paint, 8 — TiO_2 + epoxy binder.

About 95% of the energy of the proton component of the Earth's radiation belts is determined by protons with an energy up to 0.5 MeV [92]. The path of protons with an energy of 0.5 MeV, for example, in aluminum, comprises about 5 microns [92]. The path of such protons in the covering material is unknown, but, taking into account the atomic number of the elements, comprising the coverings of different brands, we may assume that it will be in the range of 5 - 8 microns.

When artificial Earth satellites are flying in the zone of the radiation belts, their external surface is subject to proton and electron bombardment. The /172
effect of protons is most dangerous, because the radiation dose from them in the surface layers of temperature controlling coverings is higher than that of electrons. The maximum proton flux density in the energy range of $0.1 < E_p < 4$ MeV in the radiation belt comprises $j_0 \approx 10^8$ protons/cm^2·sec. Its integral energy spectrum has the form [92]:

$$j = j_0 e^{-E_p/E_0};$$

where $E_0 \approx L^{-3}$;
for $L = 6{,}1$ $E_0 = 64$ (keV),
for $L = 5$ $E_0 = 120$ (keV),
for $L = 2{,}8$ $E_0 = 400$ (keV).

The energy spectrum of protons in the auroral zone in the energy range of 30 keV < E_p < 500 keV has the form:

$$j = 10^7 e^{-E_p/30\,(\mathrm{keV})}.$$

In the case of an artificial Earth satellite operating, for example, in an equatorial orbit in the center of the radiation belt for a year, its surface is subjected to proton irradiation at a proton radiation flux energy (E_Σ) of:

$$E_\Sigma = t \int_{0.03\,\mathrm{MeV}}^{0.5\,\mathrm{MeV}} E_p \left(\frac{dj}{dE}\right) dE,$$

where t is time equal to one year (~ $3 \cdot 10^7$ sec), and $E_\Sigma \approx 5 \cdot 10^{14}$ MeV/cm^2.

It was shown experimentally during measurement of A_s in air for different brands of temperature controlling coverings the variation of the absorption coefficient $\Delta A_s(E_\Sigma)$ may be presented in the first approximation by an empirical function of the type

$$\Delta A_s = \Delta A_{s\infty}(1 - e^{-bE_\Sigma}),$$

where ΔA_s^∞ is the variation of A_s at sufficiently high total energy of proton radiant flux E_Σ, impinging on the temperature controlling covering; /173

b is a constant typical for the given type of covering.

If we consider the zone $E_\Sigma < 5 \cdot 10^{14}$ MeV/cm^2, we may present $\Delta A_s = kE_\Sigma$, i.e., the linear dependence of ΔA_s on E_Σ will be observed for protons with energy E_p, equal to 8 keV and 2 MeV. The effective damage k_p of coverings by protons of different energies is a linear function of E_p, i.e., $k_p = (A = \alpha E_p)$.

/172 The permissible range of variation in thermophysical engineering calculations for passive temperature control systems for spacecraft usually does not exceed $\Delta A_s \approx 0.1$.

It follows from the foregoing that, if the dependence of ΔA_s (E_Σ) is known, for example, for protons with E_p = 8 keV, the variation of ΔA_s may be found by calculating the corresponding value of E_Σ taking into account the proton energy spectrum, for example, of the type $j(E_p) \sim j_0 e^{-E_p/E_0}$, in the range from E_{min} = 0.008 MeV to E_{max} = 0.5 MeV and taking into account the energy dependence of the

effective damage of coverings by protons of $k_p = (A - \alpha E_p)$.

Let us find the total value of E_Σ:

$$E_\Sigma = t \int_{0{,}008\,\mathrm{MeV}}^{0{,}5\,\mathrm{MeV}} E_p(A - \alpha E_p)\left(\frac{dj}{dE}\right) dE.$$

Since the function was obtained during measurement of A_s in the atmosphere without taking into account the effect of "whitening of radiation damage," the increase in A_s found by this function must be regarded as the lower limit of a variation in A_s.

Let us consider the possibility of using more perfected methods of investigating the radiation tolerance of coverings. Thus, for example, sequential exposure of coverings to monoenergetic proton beams with an energy from several tenths of a keV to 6.3 MeV [3], with corresponding selection of integral fluxes equivalent to those in space, permits a stricter simulation of radiation effects.

In those cases when reproduction of the absorbed dose distribution through the thickness of the structural element being investigated is extremely desirable and when an investigation of the radiation tolerance with the aid of monoenergetic particle beams may lead to undesirable errors, it is expedient to employ methods of converting monoenergetic beams into proton beams having a spectral distribution similar to the energy spectra of protons in the radiation belts.

The idea of one of the possible methods of converting a monoenergetic proton beam of protons into one with a continuous energy spectrum, for example, of the $j(E) \backsim E^{-\gamma}$ type consists of using a shaped foil, the thickness of which varies /174
according to a definite law [3]. When employing such a method, protons with an energy spectrum of the type $E^{-\gamma}$ must impact on every point of the exposed surface simultaneously. When the dimensions of the conversion cells whose parameters are determined mainly by technological capacities are relatively small and when there are many of them, a beam with the given energy distribution may be obtained at some distance from a shaped foil. A theoretical calculation of the shape of aluminum foil when using protons with an energy of $E < 10$ MeV was carried out by

Bulgakov and Kumakhov [3]. The analytical function of the cell profile for the protons is calculated by the expression:

$$X = M\left(\frac{E_{min}}{E_{max}}\right)^{1}\left[\left(1-\frac{t}{R}\right)^{-1/\beta}-1\right],$$

where E_{max} is the initial particle energy;

E_{min} is the lower boundary of the energy spectrum of the beam passing through the foil;

R is the path at $E = E_{max}$;

M is an arbitrary constant which determines the transverse dimensions of the cells on the foil, usually $M \approx R$, $\beta = 1.8$.

Effect of the Strength of the Absorbed Dose of Radiation

When simulating the radiation effects of space on temperature controlling coverings, it is necessary because of economic and technical reasons to increase the intensity of corpuscular beams by several orders of magnitude compared to radiation under real conditions. It is natural that the duration of exposure of coverings is reduced by the same factor in order to maintain the radiation dose unchanged. Under such experimental conditions, the problem arises about the equivalence of a suitable replacement. Due to the difference in the mechanisms of radiation damage, it may be anticipated that the effect of the absorbed radiation dose on the integral effects for different types of materials will be manifested differently. These effects may be related to thermal and cascade processes, to annealing of radiation defects, etc.

When simulating the effect of radiation on temperature controlling coverings by proton beams, accelerated in high-voltage or electrostatic accelerators, it is usually necessary to use particle beams with an intensity on the order of 1 microampere/cm^2. At lower intensities, continuous wave accelerators operate unstably. At accelerating voltages of 0.5 - 2 MeV, the output emitted by a particle beam on the surface of the specimen irradiated lies within the range of 1 W/cm^2. Under these conditions, the temperature of the surface being irradiated may reach 50 - /175
100° C, which may change the rate of radiation-chemical processes in the covering material. The effect of the temperature of the material being irradiated on radiation damage will be considered below.

Cascade processes may occur when the intensity of proton irradiation is high. Thus, for example, a long-lived radical, formed in a polymer bond due to interaction with a primary particle, may interact with the next proton a second time without forming a new chemical bond. Cascade processes may alter the rate that radiation processes take place and the kinetics of chemical reactions [264].

There are few experimental data on the effect of the absorbed radiation dose on the integral effect of radiation damage to temperature controlling coverings during proton irradiation. It was shown in [228] that the variation of A_s of coverings was identical when proton beam density varied from 10^{10} to 10^{12} protons/cm^2•sec at $E_p \approx 50 - 400$ keV and $\Phi_p \approx 10^{15} - 10^{16}$ protons/cm^2 in the case of irradiation of temperature controlling coverings having low A_s.

Similar results were obtained upon exposure of white temperature controlling coverings to electrons having an energy of 1 MeV at a flux density of $2.8 \cdot 10^{11}$ electrons/cm^2 • sec and $56 \cdot 10^{11}$ electrons/cm^2 • sec. However, it is not possible at present to approximate the given data for other classes of materials and for a different range of variation of the absorbed radiation dose.

The annual radiation absorption dose during radiation simulation is usually accumulated by the covering during the course of several hours. The time between exposure of the covering and measurement of its optical parameters may comprise several hours or days. During this period, unstable radiation defects in the exposed covering disappear due to their annealing at room temperature. The radiation dose in the covering under real conditions is accumulated over the entire period of flight, and, consequently, the time of annealing of radiation defects is considerably greater than in the case of laboratory simulation. Therefore, the integral radiation effects on ΔA_s, observed during simulation, may be higher than under real conditions.

The different effects of electron and proton radiation

Electrons and protons, as is already known, comprise the corpuscular radiation of the Earth's radiation belts. During investigations under laboratory conditions, it is important to establish the relative contribution of both the electron and /176
proton components to the total radiation damage of the covering. At the same time,

when investigating the radiation tolerance of coverings, it is useful to know, for example, whether electron radiation may be replaced by proton and vice versa. Such a substitution would simplify radiation simulation of cosmic radiation on coverings.

The difference between the radiation effects of electron and proton radiation on binders of organic origin will be minimum, because radiation-chemical transformations of organic materials essentially do not depend on the type of radiation. Some difference may be manifested only in the fact that, with substitution of electron radiation by proton and vice versa, it is difficult to recreate a monotypic distribution of the radiation absorption dose through the mass of the material.

Pigments, binders of inorganic origin, and consequently, coverings themselves as a whole will react differently to electron and proton bombardment. Let us note some of these differences.

Compared to electrons of corresponding energies, protons have a considerably higher effectiveness of formation of atomic defects in the crystal lattice of pigments and materials of an inorganic binder due to elastic interactions. The types of radiation defects may also be different. When radiation absorption doses are higher than 10^6 - 10^8 rads, the primary electron and hole traps in optical materials, as already noted above, are filled up completely. A certain portion of the crystal lattice defects, newly formed due to the effects of radiation, may be additional energy traps for formation of new color centers.

Unlike electrons, protons may interact chemically with the covering material; in particular, under the effects of protons, processes of gradual reduction of various oxides take place, for example, $2CuO + 2H_1 = Cu_2O + H_2O$; $Cu_2O + 2H_1 = 2Cu + H_2O$. The colloidal metal particles formed as a result of this process become centers for absorption of light radiation [270].

Cathode sputtering of covering materials may be observed under the effects of proton irradiation. There is hardly any sputtering under the effects of high-speed electrons.

When thin metallic films applied to compact substrates are exposed to protons, formation of gas bubbles between the film and substrate is observed [145]. Such gas bubbles cause the metal film to swell and alter the coefficient A_s of the surface. Such effects are not observed during electron irradiation.

An electric charge is accumulated inside the material upon electron irradiation /17 of certain dielectrics having low electrical conductivity. The electrical field gradient which develops inside the dielectric under certain conditions may lead to electrical breakdown of the dielectric. The nature of electric charge distribution in the dielectric in the case of proton and electron irradiation should be different, due to the presence of overcharging effects when the proton beam passes through the material.

This brief analysis of simulation methods indicates that the interchangeability of electron and proton irradiation to obtain data on the absolute tolerance of temperature controlling coverings is unjustified in general form. When investigating the relative radiation tolerance of components and coverings, such a substitution should be carried out with great care. Similar conclusions are also related to the possibility of interchangeability of helium ion and electron beams.

The role of a vacuum

When investigating the radiation tolerance of coverings, irradiation should be carried out in experimental vacuum chambers coupled with charged particle sources. Pressure and the composition of the residual gas in the experimental chamber may affect the radiation damage of temperature controlling coverings being investigated.

Such phenomena as sputtering of materials, desorption of gases from the irradiated surface, thermal and electrical conductivity of the gaseous medium, and the effect of the gaseous medium on the radiation-chemical reactions of the materials being irradiated depend primarily on pressure. However, this effect may be negligible at pressures below 10^{-5} - 10^{-6} torr, and in a number of cases, it may be disregarded.

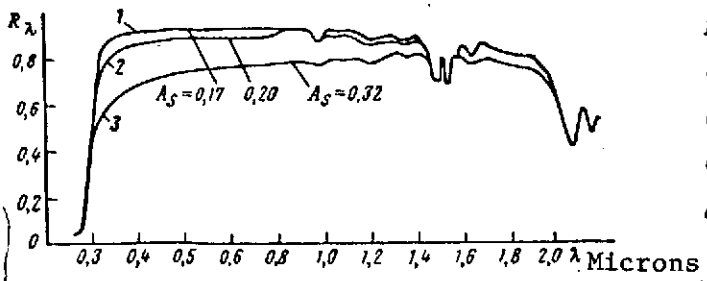

Figure 3.26. Spectral variation of coefficient R_λ of a covering of TiO_2 on a silicon binder after the effects of ultraviolet radiation over a period of 1330 "solar hours." The radiation flux density of the A-H6 lamp at wavelengths of 0.2 - 0.4 microns is twenty-fold greater than natural. Specimen temperature is 40° C, $p \approx 10^{-6}$ torr: 1 - before irradiation; 2 - after measurement in the atmosphere; 3 - after measurement in a vacuum.

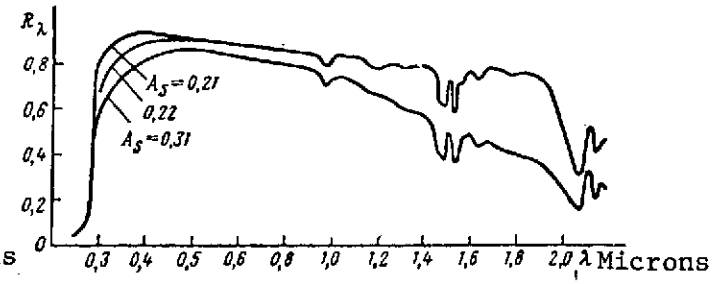

Figure 3.27. Variation of spectral reflection coefficient of a covering of ZnO on a silicon binder after the effects of ultraviolet radiation. The irradiation conditions and notations are the same as those in Figure 3.26.

Another more considerable effect of the vacuum conditions in the experimental chamber is related to the presence of organic vapors in the vacuum. When coverings are exposed to charged particles or ultraviolet radiation, formation of hydrocarbon films on their surface is observed [58]. The formed films have high thermal stability, are poorly soluble in ordinary solvents and are amorphous in structure. Films formed on the surface have a light radiation absorption factor over a wide spectral range and may distort the experimental results due to variation of A_s.

The rate of formation of organic films may be measured by using the interference technique or piezoquartz resonators [5].

In order to decrease the rate of formation of hydrocarbon films, it is necessary to maintain a higher temperature for the irradiated target and a lower temperature /178 for the walls surrounding it. Partial pressure of the organic vapors in the vacuum may be reduced by using "oilless" means of vacuum pumping or by use of cryosorption techniques.

Another important effect of vacuum conditions on the accuracy of measuring the radiation variation of the absorption factor A_s is related to the effects of the residual gas oxygen on reduction of radiation distortions in coverings exposed to ionizing or ultraviolet radiation in a vacuum (Figures 3.26 and 3.27). Similar

effects were observed upon exposure of coverings in a high-frequency gas discharge plasma while simulating the effects of low-energy ions on coverings. /175

It is obvious from the data presented in the figures that especially strong reduction of radiation damage is observed in the infrared region of ε_λ. The effect of reducing radiation damage in irradiated coverings is not yet clear. One of the possible causes of these phenomena may be that the colloidal particles formed in the pigments of the coverings during irradiation or the free radicals in the organic binders alter their state upon contact of the irradiated covering with the oxygen of the atmosphere. Since the main experimental data on variation of ΔA_s of coverings exposed to various types of ionizing radiation have been obtained during measurement of A_s in the atmosphere, they must be treated with specific care since they give results which are too low.

Temperature conditions

Temperature controlling coverings may be applied to both shaded portions and those portions of oriented spacecraft illuminated by the Sun, which fly around the Earth, Moon or in interplanetary space. Therefore, the temperature of temperature controlling coverings may vary over a wide range from -150° to +150° C. When investigating the radiation stability of coverings and for a better understanding of the nature of radiation effects, it is important to investigate the temperature dependence of radiation damage.

Moreover, when simulating the effects of cosmic radiation on coverings, as was already indicated above, exposure time must be reduced, and radiant flux density must be increased. During such investigations, especially in the case when charged particle pulsed accelerators are employed, the temperature of the irradiated coverings may appreciably exceed operating temperature. It is necessary to know within which range the temperature of the coverings being irradiated may vary, without introducing appreciable errors into the rate of formation of radiation defects when the radiation absorption dose is increased.

Data on the effects of temperature on the radiation stability of three types of temperature controlling coverings during reactor irradiation are presented in Table 16. A reduction of radiation stability is observed for enamel when the temperature of the covering being irradiated is increased, which may be explained qualitatively by the following concepts.

TABLE 16 /180

Covering	Approximate temperature during irradiation, °C	A_s^*		Dose of gamma radiation (γ); neutron flux
		Before irradiation	After irradiation	
TiO_2 on epoxy resin	-80	0.22	0.22	$2.2 \cdot 10^6$ roentgens
	-20	0.22	0.22	$0.6 \cdot 10^{13}$ protons/cm^2, E < 0.48 ev
	40	0.22	0.23	$1 \cdot 10^{14}$ protons/cm^2. E > 2.9 MeV
$ZrSiO_4 + K_2SiO_3$	20	0.11	0.13	$2.2 \cdot 10^6$ roentgens
	-196	0.11	0.22	$2.26 \cdot 10^{14}$ protons/cm^2, E < 0.48 ev
				$4.72 \cdot 10^{14}$ protons/cm^2, E > 2.9 MeV
$Na_2O \cdot Al_2O_3 \cdot 4SiO_2 + Na_2SiO_3$	20	0.17	0.24	Same conditions
	-196	0.17	0.34	

*Measurement of A_s occurred at atmospheric pressure; therefore, the given data on variation of A_s are insufficiently reliable.

1. The rate of diffusion of radicals of gas-like molecule fragments, etc., through the irradiated space increases as temperature increases; the output of many radiation-chemical reactions in irradiated polymers increases and thermal destruction of the organic binder may be observed.

2. Since annealing of the color centers in the pigment should be observed and, consequently, there should be a decrease of A_s as temperature increases, the increase in the coefficient A_s for the given type of enamel exposed to radiation is apparently related primarily to variation of the optical properties of the binder and formation of colloidal metal particles as a result of dissociation of the pigment molecules. Obviously, the effect of color centers in the pigment on variation of A_s for a given type of covering is not a determining factor. Figure /181
3.28 illustrates the effect of temperature on the spectral coefficient ε_λ of a covering (TiO_2 + epoxy resin) upon exposure to ultraviolet radiation. In this case, reduction of the stability of the covering as temperature increases is also observed.

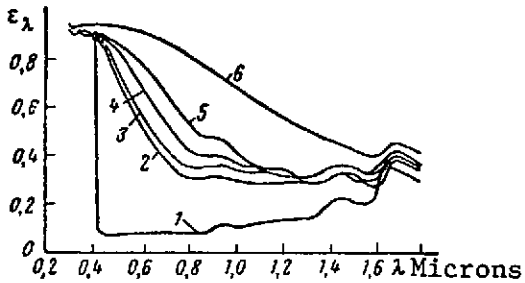

Figure 3.28. Effect of temperature on variation of the spectral absorption coefficient ε_λ during the action of ultraviolet radiation on a temperature controlling covering of TiO_2 on an epoxy binder. Radiant flux density exceeded a natural exposure time of 50 hours by tenfold, and the coefficient ε_λ was measured in air: 1 - control specimen; 2 - 35° C; 3 - 40° C; 4 - 110° C; 5 - 175° C; 6 - 260° C.

There are few data on the effect of temperature on the radiation stability of various types of temperature controlling coverings, and it is presently difficult to make broad generalizations on this problem. When investigating radiation stability, the temperature of the irradiated targets must be strictly controlled and the temperature of the coverings should not be permitted to exceed working temperature.

Complex Tests of Coverings

Temperature controlling coverings in space are subjected to the complex effects of the main factors of space — the effects of vacuum, corpuscular beams, micrometeorite particles, electromagnetic solar radiation, and temperatures over a broad range. Simultaneous reproduction of all the enumerated factors under laboratory conditions entails considerable technical difficulties. Therefore, investigation of the stability of coverings is usually carried out by simulating only some factors, for example, charged particles, vacuum and temperature or ultraviolet radiation, vacuum and temperature, etc.

The necessity of reproducing the multiple effects of various factors of space on temperature controlling coverings has not been completely proved at present. Recent experimental investigations showed that multiple effects on coverings are not equivalent to the sum of individual factors. The effect of multiple factors may not always be obtained by simple addition of the effects of individual factors.

The spectral functions ε_λ of two types of temperature controlling coverings under individual and multiple effects of reactor and ultraviolet irradiation are presented in Figures 3.29 and 3.30 [155, 157, 228, 262]. Thus, for example, the multiple effects of reactor and ultraviolet irradiation increase ε_λ less than the effects of reactor radiation alone. In the case of combined effects, ultraviolet radiation is apparently reduced due to photoannealing of a portion of the radiation defects caused by reactor radiation.

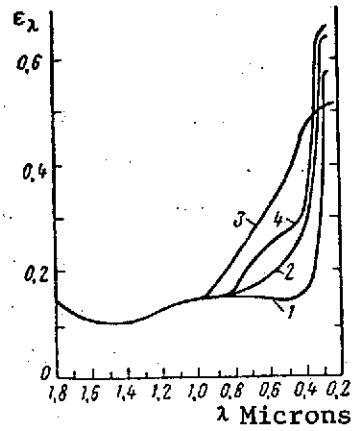

Figure 3.29. Spectral function of absorption coefficient ε_λ of a white covering (1) prior to exposure and after exposure to ultraviolet (2) and neutron (3) radiation. Combined exposure to ultraviolet and neturon irradiation is denoted by (4).

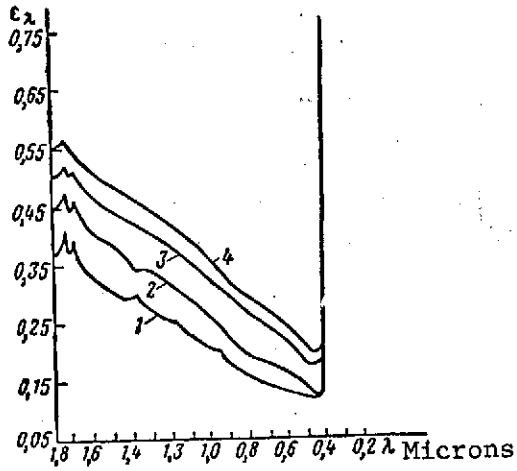

Figure 3.30. The effect of combined and individual irradiation on coefficient ε_λ of a covering of TiO_2 on a silicon binder: 1 - control specimen; 2 - neutron radiation; 3 - UV + neutrons — low intensity UV; 4 - UV + neutrons — high intensity UV.

Simultaneous effects of corpuscular and electromagnetic solar radiation on coverings may also lead to opposite processes: to generation and photoannealing of color centers.

Another reason for the necessity of using multiple tests is related to the fact that the effects of an uncompensated electric charge must be encountered upon irradiation of dielectric materials by like-charged particles. If particle energy is low, the electric charge is concentrated near the dielectric surface. The magnitude of the charge and the potentials created by it on the surface are determined by the energy dependence of secondary emission of the charged particles and by surface conductivity. /182

To compensate for such a charge, it is expedient to simultaneously irradiate the surface of dielectric materials being investigated with charged particles having opposite charges, for example, protons and electrons. If this is not always convenient, a thermoemission cathode is installed near the surface being irradiated in the case of ion bombardment of a dielectric. Electron emission from such a cathode neutralizes the positive surface charge on the dielectric surface.

In other cases, application of a high-frequency accelerating voltage in a plasma to the substrate of the irradiated dielectric target is employed, which permits automatic compensation for the electric charge on the dielectric surface [2, 4, 6, 7, 220]. /18

When investigating the radiation stability of glass or other dielectrics with the aid of electron beams or gamma radiation, an uncompensated electric charge in the material is observed, which may lead under certain conditions to electrical breakdown of the dielectric.

In conclusion, we recall the main conditions for simulating the radiation effects of cosmic radiation on the optical properties of temperature controlling coverings:

1. carrying out the investigations in two phases:

a. obtaining data on the relative radiation stability of temperature controlling coverings for the purpose of selecting the more radiation resistant ones;

b. investigating radiation stability for the purpose of assessing the behavior of temperature controlling coverings under conditions of space;

2. carrying out accelerated tests at least within the range of two or three orders;

3. the feasibility of employing monoenergetic proton beams with an energy of 0.5 - 2 MeV;

4. measurement of coefficients A_s of irradiated coverings in experimental vacuum chambers without bringing them into the atmosphere;

5. maintaining temperature control of the coverings during irradiation of them.

11. Methods of Simulating the Effects of Short-Wave Solar Radiation on the Temperature Controlling Coverings of Spacecraft

When investigating the stability of temperature controlling coverings (TCC), essentially two problems must be encountered: comparative tests of various coverings to determine the more resistant ones and determination of the stability of the technical characteristics of the covering selected. The second task places more rigid requirements on simulation conditions, because in this case, one must have an idea about the processes which take place in specimens upon irradiation, by which the test conditions will be mainly determined. Correct solution of both of the above problems and the cost of the required equipment will depend to a considerable extent on selection of simulation conditions which determine the reliability of the results obtained. In this case, it is necessary to bear in mind that the problem of simulation consists in creating those conditions whose effects on TCC will be similar to those of space conditions rather than in a precise reproduction of space conditions, which is very complicated in a number of cases. This should be justified by both calculation (analytical) procedures and by checking the more /184 responsible results under conditions of space flight. The main parameters in simulating the effects of short-wave solar radiation on TCC are:

1. the spectral composition and intensity of the radiation source (spectral irradiation of specimens);
2. environment pressure;
3. exposure time;
4. temperature of the specimen.

During simulation it is very important to establish the necessary limiting values of the parameters — maximum evacuation of the vacuum chamber and the spectral composition of the radiation source — and to demonstrate that placing more rigid requirements on these parameters (for example, a decrease of maximum pressure) is unjustified, since this will make the test equipment more complicated and expensive, without having any appreciable effect on test results.

We shall present some concepts on selecting the indicated simulated parameters. Data on sources suitable for simulation of short-wave solar radiation and recommendations on selection of them are presented in Section 6, Chapter 4. Since the main part of the energy of short-wave solar radiation (about 75%) is contained in the near ultraviolet region of the spectrum (3800 - 2000 Å), high-pressure xenon or mercury quartz lamps are usually employed for comparative testing of TCC. It is desirable during the second phase of testing, when checking the characteristics of the selected covering, to verify the stability of this covering to radiation at $\lambda < 2000$ Å.

Control of variation of the optical properties of TCC during tests should be accomplished without removing the specimens from the vacuum chamber, because some types of damage which occur in a vacuum under the effects of UV radiation may disappear in the atmosphere. Thus, for example, TCC on a base of ZnO, which have been darkened in a vacuum chamber due to UV radiation, again become light (the "bleaching" effect) when removed into the atmosphere, and the error in measurement of the absorption coefficients of the coverings in the atmosphere may exceed 50%.

The temperature range of testing TCC specimens should reproduce with some reserve the real temperature conditions on the spacecraft surface. In individual cases, simulation of cyclic temperature variations during the process of UV irradiation (which occur when an artificial Earth satellite enters the Earth's shadow during its motion in orbit) may be employed, because certain polymer materials may become brittle as a result of such effects.

One of the main problems of simulation is the selection of the exposure time of TCC specimens. The problem is complicated by the fact that most spacecraft are in flight for a prolonged period, but it is very inconvenient and complicated to /185 reproduce continuous tests of many months' duration under laboratory conditions. It becomes necessary to develop accelerated methods of testing and procedures for predicting the behavior of materials in time. Two main methods of accelerated tests may be distinguished.

1. The method of testing under normal conditions, in which the effect of various factors (for example, radiation and temperature) on the material is equal or similar to the effect of factors present in space. In this case, the test time selected is less than that necessary, and prediction is made after the nature of changes in the parameters of the material in time has been established.

2. The method of reducing test time K times due to increasing the intensity of factors acting on the materials. Here K is the coefficient of test acceleration whose values range from several units to several hundreds.

The second method, although it permits a considerable reduction in test time, creates additional difficulties with selection of the required relationship between the time and intensity of UV irradiation, because an increase of intensity to reduce test time may only be carried out while the linear dependence between the increase of the factor and variation of the material parameter is maintained.

The first method is simpler and, apparently, use of it will be more convenient in a number of cases, while the test data will be more reliable. In this case, partial use of the second method simultaneously is possible at high values of K, so long as it does not cause disturbances of the linear dependence and so long as it permits test time to be reduced somewhat.

Two versions of test facilities are usually employed to test TCC. In the first version the facility consists of several separate chambers for each specimen, which are arranged in a circle and which have windows transparent to UV radiation. The specimen holder may be heated by an electric coil or cooled by liquid nitrogen vapors, by which the required test temperature conditions are provided. The radiation source is placed in the center of the circle outside the chambers. Relative variation of the absorption coefficient during testing is checked by a contact photometer, if the specimens are located in direct proximity to the windows.

A structure with separate chambers permits variation of test conditions for each specimen, and the possibility of mutual contamination of specimens is practically excluded. The disadvantages of such a design are related to the fact that only a small number of specimens may be tested in it simultaneously, and during testing the windows of the chambers may become contaminated by decomposition products, evaporated from the surface of the specimen being heated. /186

In the second version, the facility consists of a single vacuum chamber, inside which is located a large number of TCC specimens. The radiation source may be placed either inside or outside the vacuum chamber, with sources of both electromagnetic and corpuscular radiation employed simultaneously. This is done

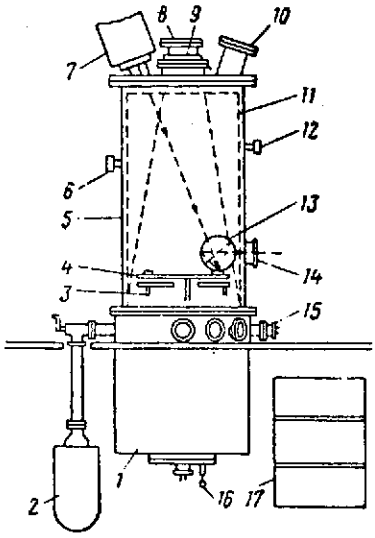

Figure 3.31. Facility for testing stability of temperature controlling coverings: 1 - sputter-ion pump (500 l/sec); 2 - sorption pump; 3 - immobile part of table for specimens; 4 - mobile part of table for specimens; 5 - vacuum chamber; 6 - high-voltage lead-in; 7 - projector; 8 - proton gun flange; 9 - flange with 150-mm quartz window for input of UV radiation; 10 - electron gun flange; 11 - "black" nitrogen shield; 12 - mass spectrometer flange; 13 - integrating sphere; 14 - 100-mm quartz window for photospectrometer; 15 - electric lead-ins; 16 - titanium sublimation pump (5000 l/sec); 17 - rack with control and monitoring equipment.

to bring the test conditions closer to those of space and to determine so-called synenergistic effects, which lead to the fact that variation of TCC characteristics caused by the total of individual effects of each component in space, differs from those which take place during the simultaneous action of all components. The possibility of measuring TCC parameters during testing without removing the specimens from the vacuum chamber is provided in such facilities. Let us present the layout and brief description of one of such facilities used for testing TCC in the United States as an example [152].

The facility (Figure 3.31) consists of a vacuum chamber 5, in the upper portion of which are located the radiation sources — an electron gun with an accelerating voltage up to 20 kV and an electron beam scanning system (beam current of 0 - 300 mA), a proton source with a regulated particle energy of 1 - 5 keV, and a 5-kilowatt high-pressure mercury-xenon arc lamp. The emission of the lamp is projected onto the specimens by an aluminum-coated parabolic reflector through a quartz window 150 mm /187 in diameter. Irradiation of specimens may be varied from 1 to 6 EUVS.*

A hydrogen lamp made in the form of a pyrex tube, mounted on a flange of stainless steel with a window of lithium fluoride, is used to simulate far UV radiation. A discharge in the hydrogen is generated by a high-frequency generator, and the irradiation in the plane of the specimen in the range of 1100 - 2000 Å

*EUVS — equivalent ultraviolet solar radiation — is total energy at 4000 Å in a vacuum, corresponding to irradiation at a distance of 1 AU from the Sun.

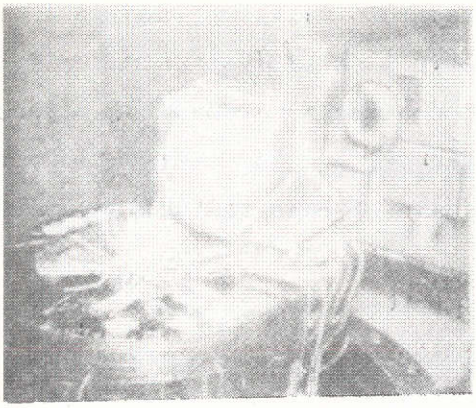

Figure 3.32. Overall view of table with specimens, the integrating sphere and monochromator of the photospectrometer.

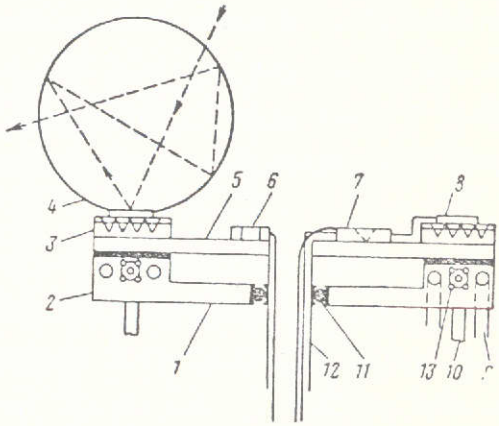

Figure 3.33. Rotating table for moving the specimens: 1 - immobile part of table; 2 - temperature control unit; 3 - specimen heater; 4 - integrating sphere; 5 - rotating part of table; 6 - Faraday cylinder for monitoring corpuscular radiant fluxes; 7 - thermopile; 8 - TCC specimen; 9 - cooling tubes; 10 - holder racks; 11 - bearing; 12 - rotation axis; 13 - wire heater.

comprises approximately 4 - 5 EUVS. A hydrogen lamp is installed in place of a proton or electron injector. The total intensity of UV radiation during testing is monitored by a radiometer, which is a silver-bismuth thermopile, installed in the water-cooled housing.

A rotating table 4 (see also Figures 3.32 and 3.33), on which are located 30 specimens 22 mm in diameter, is positioned inside the chamber. The table consists of two halves. The lower immobile section, inside which are located segmented wire heating elements and a cooling system, serves to provide the specimens with a given temperature. Individual sections of the segmented heater make it possible to obtain five different temperatures during irradiation which act simultaneously on each of six specimens. The upper mobile part serves to rotate the specimens from the irradiation zone to zones for measuring optical characteristics.

Spectral reflection (absorption) coefficients are varied with the aid of an integrating sphere 13 (see Figure 3.31) 135 mm in diameter. The specimen being measured is brought under the opening of the integrating sphere and is illuminated through projector 7 by a lamp having a tungsten filament temperature of 3200° K. The reflected energy, collected by the integrating sphere, impinges through quartz /188
window 14 on the optical system of the photospectrometer monochromator, which provides automatic recording of the spectral reflection curve of the covering in the range of 0.35 - 2.1 microns.

The total normal radiation of the specimens is measured with the aid of a radiometer, located under the rotating table (its arrangement is seen in the left lower corner of Figure 3.32). The radiometer consists of two thin-film gold-telluride infrared radiation receivers, having identical sensitivity. One receiver is turned toward the specimen being measured, and the second — toward the control specimen ("black body"), maintained at the same temperature. The emissivity of the specimen was determined as the ratio of the output data of both radiation receivers.

The vacuum pumping system of the facility is a three-stage "oilless" type, the sorption pumps are a sputter-ion and titanium pump with an auxiliary cryosorption pumping system (a cylindrical sleeve filled with nitrogen). After heating and evacuation at 300° C, the system provided a vacuum in the chamber of 10^{-11} torr.

A facility of this type is universal to an adequate degree, permits comparative testing of different TCC, and determination of the stability characteristics of the selected covering. Other single-chamber facilities of a similar designation are constructed approximately according to the same principle.

12. Simulation of the Interaction of Atmospheric Molecules with the Spacecraft Surface

The main difficulty in determining the energy given off during interaction of the spacecraft surface with the molecules and atoms of the upper atmosphere consists /189 in calculating the thermal accommodation coefficient a. This coefficient is a complex function of particle speed, wall temperature, ratio of the molecular weights of the wall material and gas, roughness, and presence on the surface of the body of adsorbed layers of gas molecules and atoms.

When a spacecraft is launched from the Earth, its surface is covered with several monomolecular layers of gases, chemisorbed in the form of oxides or hydrides or physically sorbed by Van der Waals forces. Each monomolecular film contains $5 \cdot 10^{14}$ gas molecules per 1 cm^2 and creates a dividing barrier for incident molecules, atoms and ions. This barrier layer does not remain constant, but is broken down under the effects of external conditions, in particular, due to aerodynamic heating of the spacecraft surface during launch or due to the effects of the impacts of incident molecules.

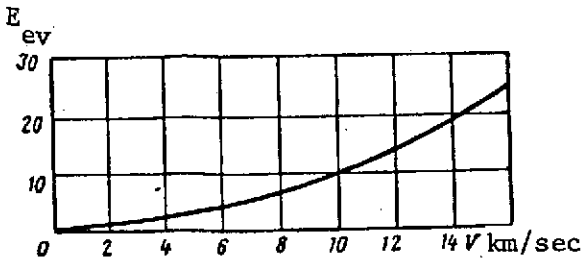

Figure 3.34. Dependence of energy of impacting molecules of air on velocity of spacecraft at an altitude of 300 km.

The binding energy of adsorbed atoms and molecules (2 - 3 eV) is less than that of impacting molecules (Figure 3.34). Therefore, during orbital injection of the spacecraft, its surface is gradually cleaned of the layer of chemisorbed or physically sorbed molecules. The rate of cleaning depends on flight altitude, wall material and the temperature of the solid. Theoretical prediction of the variation of the accommodation coefficient under the effects of the enumerated factors is extremely difficult. Therefore, the value of a is derived experimentally in vacuum facilities, where a molecular gas beam, having a velocity of approximately 8 km/sec is directed toward the target being investigated.

The interaction of molecules and the spacecraft surface is manifested not only in the form of direct heat dissipation, which is calculated by the formula $Q \approx a\rho V^3$, but also in the form of breakdown of the solid surface, which may lead to a variation of the optical characteristics $R(\lambda)$ and $\varepsilon(\lambda)$. This is related mainly to organic /190 coverings. Atomization threshold energy for pure metals is higher than the energy of molecules even escape velocity.

In experiments in facilities using molecular beams, special attention is devoted to the effects of residual gas inside the evacuated space, because low-energy particles of residual gas are more easily adsorbed by the surface and create molecular layers on it, which are essentially absent under real conditions. Conformity to conditions insuring cleanliness of the surface during experiments when investigating the accommodation coefficient is an important procedural condition.

Removal of the adsorbate by heating the specimen (filament) under high-vacuum conditions is not always permissible, because high temperatures (1500 - 2000° K) are required to remove chemisorbed molecules. Heating of a specimen to such temperatures may induce irreversible changes in the properties of the body surface. The background of low-energy molecules may be reduced, by decreasing pressure in the vacuum chamber to approximately 10^{-11} torr and simultaneously increasing the density of the main molecular beam by more than 10^{14} 1/cm^3. These contradictory requirements may be accomplished if the absorption capacity of the chamber walls (cryogenic panels) is sufficiently high.

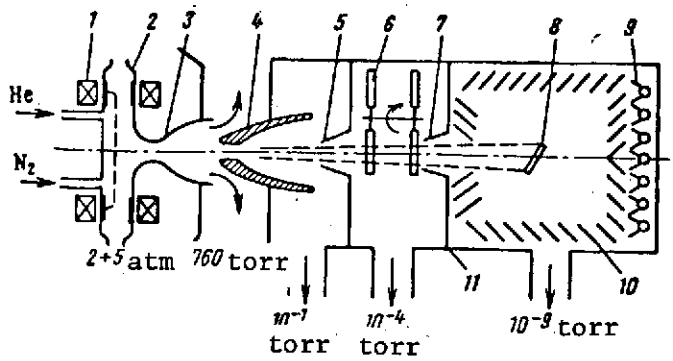

Figure 3.35. Diagram of facility for obtaining molecular beams with a velocity of ~8 km/sec: 1 - plasmatron magnet; 2 - plasmatron; 3 - accelerating nozzle; 4 - nozzle for selection of gas; 5 - cone; 6 - shutter; 7 - cone; 8 - target; 9 - cryogenic pump; 10 - panels with liquid nitrogen; 11 - vacuum chamber.

There are several methods for obtaining neutral and partially ionized particle fluxes with a density of more than 10^{14} 1/cm^3 and velocity higher than 7 km/sec. Some of them are accomplished in laboratory experimental facilities (facilities with a non-isothermal plasma source with subsequent recharging of the facilities with an effusive source of strongly heated mixtures of light and heavy gases, for example, H_2 and Ar, He and N_2, etc., are regarded as promising). The lighter gas in such sources serves as the accelerating gas. Helium is a suitable accelerating gas, because it is monatomic and does not react chemically. A diagram of one of these facilities is presented in Figure 3.35. The heater of the working gases is a plasmatron 2 with an arc rotating in a magnetic field. The gas, heated to 6000 - 10,000° K, is accelerated in nozzle 3, and then its greater portion is ejected into the atmosphere. Nozzle 4 serves to separate the required fraction of the heated gaseous mixture from the total flow. A pressure of 10^{-1} torr is maintained at the nozzle cutoff. Since the mass flow of the gas passing through the nozzle is small, ordinary supersonic gas ejectors or previously evacuated vacuums or high-capacity pre-evacuation pumps are used to evacuate the chamber 11. One or several truncated cones 5 and 7, the space between which is evacuated by diffusion pumps, are installed behind nozzle 4. According to the movement of gases from the heater toward the chamber 11, the light component, initially having a greater velocity than the heavy component, gradually decelerates, and its /191 relative concentration at the flow axis decreases. One or another flow velocity may be obtained, depending on the initial ratio of light and heavy gases in the chamber. In order to pass a beam with a very narrow velocity range into the chamber, two shutters with offset apertures, rotating on a single axis, are installed in the path of the beam. The rotational speed of the shutters and the angular displacement of the apertures are selected such that only those particles having the velocity required by the experimental conditions are passed. A low molecular collision coefficient is provided by a system of cryogenic shields 9 and 10, cooled by liquid nitrogen and gaseous or liquid helium.

Experiments carried out in such facilities showed that high-speed flow of molecules actually leads to increased sublimation of materials in a vacuum and to variation of coefficients of surface darkness, but not so great as was predicted by some theories.

13. Requirements for Simulation of a Space Vacuum

The spacecraft in space. The gaseous composition and gas concentration in space were considered in the first section of Chapter 1. In view of the fact that these data are used to simulate the space vacuum in laboratory vacuum facilities, it is expedient, as is accepted in vacuum technology, to also characterize the space vacuum with the aid of pressure. In this case, static and dynamic pressures are distinguished.

The pressure in the Earth's atmosphere varies from ~760 torr at sea level to ~10^{-14} torr at distances of the order of 20,000 km (Table 17). The pressure in the /192 lunar atmosphere varies from ~10^{-10} torr at the surface (day)* to ~10^{-12} torr at a distance of 200 km.

TABLE 17

GAS PRESSURE AT VARIOUS DISTANCES FROM THE EARTH'S SURFACE

Distance from Earth's surface km	Pressure torr
0	$760 \simeq 10^3$
100	$2{,}2 \cdot 10^{-4}$
500	$7 \cdot 10^{-9}$
1000	$\sim 10^{-10}$
5000	$\sim 10^{-12}$
10 000	$\sim 10^{-13}$
20 000	$\sim 10^{-14}$
60 000	$\sim 10^{-15}$
100 000	$\sim 10^{-11} \div 10^{-13}$

The pressure in the atmosphere of Mars varies from 4 - 7.5 torr at the surface to ~10^{-12} torr at a distance of 10,000 km (Table 18).

*According to data obtained from Apollo-14, pressure in the lunar atmosphere varies from $5 \cdot 10^{-9}$ torr during the day to $2 \cdot 10^{-12}$ torr at night (F. S. Johnson et al., Observation of Lunar Atmosphere. Preprint No. 77058, 1971, NASA, Manned Space Center, Houston, Texas).

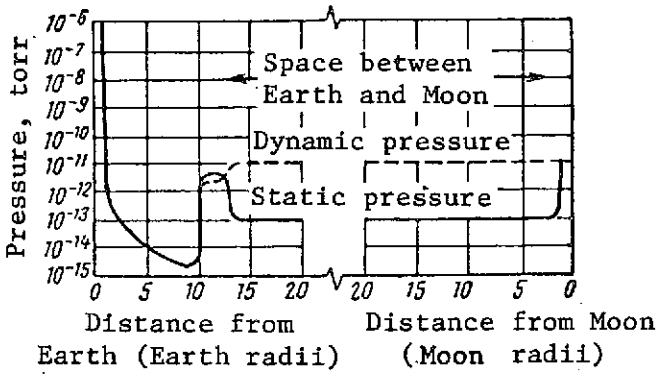

Figure 3.36. Pressure distribution in interplanetary space between the Earth and Moon.

TABLE 18*

GAS PRESSURE IN ATMOSPHERE OF MARS [271]

Distance from Surface of Mars, km	Pressure torr
0	6,0
100	$1,4 \cdot 10^{-6}$
500	$1,0 \cdot 10^{-11}$
1000	$5,7 \cdot 10^{-12}$
5000	$3,7 \cdot 10^{-12}$
10000	$3,49 \cdot 10^{-12}$

*Commas represent decimal points.

The average static pressure in the interplanetary medium is equal to $\sim 10^{-13}$ torr, and the average dynamic pressure comprises $\sim 10^{-11}$ torr (Figure 3.36).

The pressure on a moving spacecraft is distinguished from that in space on an immobile area (with respect to Earth) and is a function of the ratio v/V. This is the result of the fact that spacecraft speed and the average velocity of particles /193 in space may differ considerably. In this case, pressure on the different parts of the spacecraft is non-uniform. Thus, the pressure on the front portions of the spacecraft (according to the speed vector) may exceed that at a given point of the spacecraft on an immobile area by several tens of times, and pressure immediately behind the spacecraft may be several orders lower [250]. Consequently, available data in the literature on the pressures of the cosmic gas are only base values, on the basis of which the actual pressure on the various parts of the spacecraft moving in space may be estimated.

It is noted in [250] that:

1. molecular flows impinging on a spacecraft in high- and ultrahigh-vacuum simulators may be comparable in value to those in space ($\sim 10^{12}$ - 10^{9} molecules/cm^2 • sec);

2. the kinetic energy of molecules in space is several orders higher than that in ordinary simulators — without molecular beams ($\sim 10^{5\circ}$ K and $\sim 10^{2\circ}$ K, respectively);

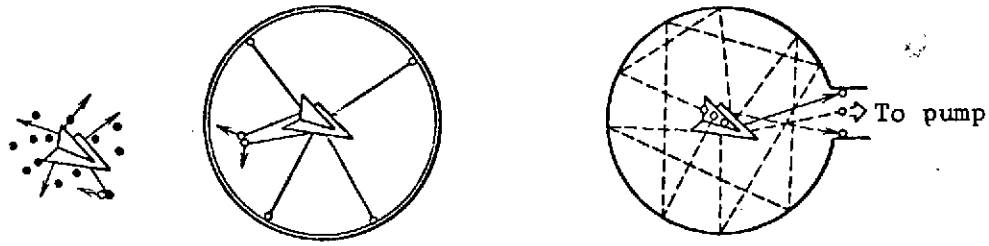

Spacecraft in space | Spacecraft in a facility Internal pumping | Spacecraft in a facility External pumping

Figure 3.37. Schematic diagram of vacuum conditions of a spacecraft in space and in a facility.

3. residual gas particles in simulators differ from cosmic gas particles (H_2, CO, He and H^+, He^+ and e, respectively).

When a spacecraft is flying in space, only a small fraction of the molecules evaporated from it will be returned (Figure 3.37). This circumstance is taken into account by the collision coefficient. The collision coefficient Z_0 is calculated by the ratio of the number of particles, returning to the spacecraft per unit time, to the number of particles evaporated from it.

In space, $Z_0 \neq 0$ due to mutual collisions of the molecules sublimated from the /194 spacecraft. This coefficient may be calculated by the refined formula of Borovik and Mikhaylov

$$Z_0 \simeq 0.05 \cdot \frac{L_0}{l}, \tag{3.110}$$

where L_0 is the distance from the object;

l is the mean free path of molecules at the saturated vapor pressure of the material evaporated or sublimated from the spacecraft surface. For example, at a pressure above the surface of $\bar{p}_{0_s} \approx 10^{-6}$ torr for particles with a mass of ~30 and L_0 = 1 m, the collision coefficient is $Z_0 \approx 10^{-3}$.

The spacecraft in a facility. A low collision coefficient under laboratory conditions may be obtained in a facility having walls similar to a molecular trap. If the walls of the facility are not like this, many of the molecules leaving the object will be reflected from them and will return to the object several times until they are captured by the walls.

As indicated in [10, 11, 165, and 250], the collision coefficient for these conditions is calculated in the following manner:

$$Z=\frac{b(1-a)}{a}, \tag{3.111}$$

where Z is the collision coefficient which determines the number of collisions of a molecule from the surface of an object until it is pumped out ($Z \geq 1$) or the probability that the molecule will return a second time to the evaporation surface ($0 < Z < 1$);

b is the probability of return of a molecule, reflected from the facility wall, to the object;

a is the probability of capture of the molecule by the wall.

Formula (3.111) is derived on the assumption that the surface evacuation coefficient of the object $C_m = 0$. In the case when $C_m \neq 0$, the collision coefficient is

$$Z=\frac{Z_0}{1+C_m Z_0}. \tag{3.112}$$

The value of a is calculated as $a = KC_e$, where K is a fraction of the evacuating surface and C_e is the effective pumping coefficient of the facility walls.

Since coefficient C_e is different for different gases, coefficient C will also be different for different gases. Therefore, the collision coefficient is usually referred to according to a specific gas (for example, the collision coefficient Z of nitrogen).

Formulas are presented below for calculating b — the probability of molecules, reflected from the facility surface, impinging on an object.

Formulas (3.113) - (3.118) are derived [10] on the basis of the diffusion law of reflection of molecules from the facility walls:

1. The facility and object are spherical (the diameters of the object and chamber are d_m and d_c): /195

$$b=b_0=\frac{d_m^2}{d_c^2}. \tag{3.113}$$

2. The facility is spherical (diameter d_c) and the object is cylindrical (diameter d_m, length L_m):

$$b=b_1=\frac{d_m^2+2d_mL_m}{2d_c^2}. \tag{3.114}$$

3. The facility is cylindrical (diameter d_c and length L_c) and the object is spherical (diameter d_m):

$$b=b_0\xi. \tag{3.115}$$

4. The facility is cylindrical (diameter d_c and length L_c) and the object is cylindrical (diameter d_m and length L_m):

$$b=b_1\xi. \tag{3.116}$$

If the lateral surface of the cylinder is the pumping surface, then

$$\xi=\xi_1=2\left(1-\frac{L_c}{\sqrt{d_c^2+L_c^2}}\right). \tag{3.117}$$

If the ends of the cylinder are the pumping surface, then

$$\xi=\xi_2=\frac{d_c}{\sqrt{d_c^2+L_c^2}}. \tag{3.118}$$

The collision coefficient will be least when the ratio of effective pumping surface to total surface is close to unity.

Let us carry out a numerical calculation of collision coefficients for cases of external and internal pumping (see Section 1, Chapter 4). For the calculation, let us assume the pumping coefficient of the object $C_m = 0$, so that $Z = Z_0$.

It is known from practice that in the case of external pumping (diffusion pumps, etc.) for small facilities $a \approx 0.1$; and for large facilities, $a \approx 0.01$.

If we assume $b \approx 0.1$, for the case of external pumping, we will obtain a collision coefficient equal to $Z = Z_0 \approx 10$, and, consequently, each molecule will return to the object being investigated 10 times, before it is captured by the wall. In this case, simulation of the vacuum conditions of space will be incomplete.

In order to obtain a more perfect vacuum simulation, it is necessary to adopt a system of internal pumping, where the pumping devices are part of the internal surface of the facility and pumping is accomplished by surface effect pumps — cryogenic pumps, etc. (see Section 2, Chapter 4). /196

In the latter case, a ≈ 0.8 and the collision coefficient (at b = 0.1) is equal to:

$$Z=\frac{b(1-a)}{a}=\frac{0.1\cdot 0.2}{0.8}=2.5\cdot 10^{-2},$$

i.e., vacuum conditions in the facility approximate those in space.

It is proposed in [165] that the degree of perfection of simulating the space vacuum be estimated by the coefficient of "self-contamination" C_s, which is calculated as the ratio of the speed of return of molecules to an object after their reflection from the pumping walls to the speed at which they are evaporated from the object:

$$C_s=\left[1+\frac{a}{C_m(1-a)\,b}\right]^{-1} \tag{3.119}$$

(here and in the following discussion K ≈ 1).

Equation (3.112) is related to equation (3.119) in the following manner:

$$C_s=ZC_m. \tag{3.120}$$

The length of formation of the panel layer on the surface of the object being tested (τ_m^*) is introduced [261] as yet another characteristic of simulating space vacuum conditions:

$$\tau_m^*=\frac{\tau_i^*}{ZC_m}, \tag{3.121}$$

where τ_i^* is the duration of sublimation (evaporation) of the monolayer from the single surface of the spacecraft, calculated by the Knudsen-Langmuir formulas [43].

The rate of non-equilibrium evaporation (sublimation) of a pure material from a surface is written in the following manner [191]:

$$G_i=C_i(p_s-p_v)\sqrt{2\pi RT_s}, \tag{3.122}$$

where G_i is the mass of the material, sublimated per unit time from unit area;

C_i is the evaporation coefficient ($0 < C_i \leq 1$);

p_s is the equilibrium saturated vapor pressure of the material at its surface temperature T_s;

T_s is the surface temperature of the material;

p_v is pressure in the vapor cloud;

$$R = \frac{R_0}{M},$$

R_0 is the universal gas constant;

M is the molecular weight of the vapor.

The rate of non-equilibrium condensation is equal to /197

$$G_c = C_c(p - p_s)\sqrt{2\pi R T_s}, \tag{3.122a}$$

where G_c is the mass of the material being condensed per unit time per unit area;

C_c is the condensation coefficient ($0 < C_c \leq 1$);

p is the equivalent vapor pressure at the surface temperature T_s, which ensures the condensation rate, determined under experimental conditions.

If

$$T' > T_s, \text{ then } p = p'\sqrt{\frac{T_s}{T'}}. \tag{3.122b}$$

During sublimation in a high and ultrahigh vacuum $p_v \approx 0$; Equation (3.122) is simplified and assumes the form

$$G \approx C_i P_s / \sqrt{2\pi R T_s} = C_i G_m, \tag{3.123}$$

where G_m is the total mass of particles which collide per unit time from a unit area of the sublimation surface under comditions of thermodynamic equilibrium, calculated after transformation as

$$G_m = 0.058 P_s \sqrt{\frac{M}{T_s}} = (P_s/17.14)\left(\frac{M}{T_s}\right)^{1/2} \text{G} \cdot \text{cm}^2 \cdot \text{sec}^{-1} \tag{3.124}$$

Equation (3.124) may also be transformed to another form [207], suitable for use, where

$$G_m = 1.85 \cdot 10^6 \cdot P_s/\rho (M/T_s)^{1/2} \text{ cm} \cdot \text{year}^{-1} \tag{3.125}$$

and ρ is the density of a solid material in $g \cdot cm^{-3}$.

The dependence of C_i on T_s is unclear; contamination of the surface leads to a considerable decrease of C_i.

It was established [95] that if $C_i \ll 1$, vapor molecules are distinguished from condensate molecules due to association, dissociation or polymerization. In this case, the pattern of kinetic equilibrium, on the basis of which Equation (3.122) is derived, is disrupted. In connection with this, materials may be arbitrarily subdivided into a class of materials with $0.1 \leq C_i \leq 1$ and a class of materials with $C_i < 0.1$.

Equations (3.122) - (3.125) are well satisfied only on the condition that the pressure of the surrounding medium is at least an order of magnitude lower than the equilibrium vapor pressure ($p_v \ll p_s$) and that only a negligibly small amount of evaporating atoms or molecules return to the evaporation surface. If the vacuum is insufficient ($p_v \sim p_s$), the evaporated molecules will collide with those of the residual gas and will return to the evaporation surface. In this case, the actual evaporation rate will be lower than calculated.

Similar to the introduction of the "self-contamination" coefficient C_s, the "contamination" coefficient C_c, which takes into account the total contamination of the investigated surface by particles, being evaporated from it upon their repeated return, as well as by "foreign" particles from the walls and other elements of the facility, may also be introduced: /198

$$C_c = \frac{C_s}{1 + C'_m b}, \tag{3.126}$$

where C'_m is the coefficient of pumping by the surface of the object of other gases.

Hence, the new duration of formation of the monolayer under conditions of total contamination of the surface being investigated under the condition $\tau_i^* < \tau'^*_i$ is:

$$\tau^*_{m\Sigma} = \frac{\tau_i^*}{C_c}. \tag{3.127}$$

The calculated characteristics of vacuum simulation for an arbitrary chamber with a diameter equal to $d_c \approx 2.5$ m, and a spherical object having a diameter equal to $d_m \approx 0.25$ m at K = 1 for cases $C_e = 0.7$ and 0.3 are presented in Table 19.

TABLE 19**

COMPARISON OF VACUUM CHARACTERISTICS OF ARBITRARY FACILITIES

d	d_m	C_e	C_m	Z_0	Z	C_s	τ^*
2,5	0,25	0,7	0,1	$4\cdot10^{-3}$	$4\cdot10^{-3}$	$4\cdot10^{-4}$	$2{,}5\cdot10^{3}$
2,5	0,25	0,3	0,1	$2\cdot10^{-2}$	$2\cdot10^{-2}$	$2\cdot10^{-3}$	$5\cdot10^{2}$

**Commas represent decimal points.

The data of Table 19 indicate that satisfactory simulation of certain vacuum conditions of space is possible under laboratory conditions.

It follows from Equations (3.111), (3.112), (3.119) and (3.126) that the coefficients introduced by various authors as criteria for the degree of perfection of simulating vacuum conditions of space in laboratory facilities, are interrelated.

We note that while coefficients Z and Z_0 have a more general value in assessing the degree of perfection of simulating vacuum space conditions and may be used in the design of facilities, coefficients C_s, C_c, τ^*_m, and $\tau^*_{\Sigma m}$ are more applicable for calculations in an investigation of surface phenomena when consideration of coefficients Z alone is inadequate.

However, experimental methods of measuring the indicated coefficients C_s, C_c, τ^*_m, and $\tau^*_{\Sigma m}$ have not been developed at present. /199

Pressure in the facility. As was indicated earlier, the main method of evacuation in space simulation is internal pumping, accomplished by surface effect pumps. Therefore, if the vacuum conditions in facilities using external pumping are essentially similar to isotropic, vacuum conditions under conditions of internal pumping are distinguished by considerable anisotropy. The velocity distribution of residual gas molecules in this case inside facilities is no longer subject to Maxwell's law, and pressure is not a scalar value. In this case, there are non-equilibrium molecular flows from the object being investigated to the walls of the facility and from the walls of the facility toward the object.

The flow rate of molecules in facilities from the object toward the pumping wall is several orders higher than that of molecules moving in the direction of the object. Accordingly, wall pressure may considerably exceed that on the objects being tested [102, 250].

In the general case, pressures on the walls and on the object are not equal and are calculated in the following manner [10]:

$$p_c = \frac{q_c + q_m}{S}, \tag{3.128}$$

$$p_m = b\frac{F_m}{F_c}\left[(1-a)\frac{q_m}{S} + \frac{q_c}{S}\right], \tag{3.129}$$

where S is the rate of pumping gas from the facility;

p_c is pressure on the wall;

p_m is pressure on the object being investigated;

q_c is the total gas load created by the facility;

a_m is outgassing of the object;

F_m and F_c are the surfaces of the object and facility, respectively;

a and b were defined previously.

It follows from Formula (3.129) that only pressure on the walls is expressed by the general formula of the type $p_c = q/S$. If $q_m \gg q_c$, pressure on the object will be equal to

$$p_m \approx Z p_s, \tag{3.130}$$

where p_s is the saturated vapor pressure of the material of the object surface at a surface temperature of T_s.

According to data of [102], in the case of a gas load in the form of water vapor, a vacuum manometer, oriented toward a wall cooled by liquid nitrogen, will indicate a pressure two orders or more lower than one oriented toward the spacecraft being tested.

The formulas presented above for calculation of facility wall pressures of the object being tested were derived on the assumption of spherical symmetry of the chamber and the object, of an equitemperature wall field and uniform distribution of pumping surfaces throughout the facility. /200

In real facilities, simulating vacuum conditions in space, gas pressures on various sections of the internal surface of the facility or object (as indicated in [163], in which the molecular kinetics in a space vacuum simulation facility was investigated) may differ considerably. The given difference, caused by the presence of elements in a facility having a different degree of outgassing (for example, solar simulators), leads to the fact that flows toward the object vary from position to position by one or two orders of magnitude. Moreover, temperatures of sections of the inner surface of facilities differ considerably in real facilities.

Consequently, it is insufficient to differentiate average pressures on the object and facility wall to measure pressure. The pressure and temperature fields of the walls throughout the entire space of the facility must be measured.

The range of pressures in facilities is very wide: from atmospheric to $\sim 10^{-14}$ torr.

In the range of pressures of 760 - 10^{-6} torr, use of mechanical, thermopile and ionization manometers is expedient for measurements.

In the range of ultra high vacuum (10^{-7} - 10^{-12} torr), the main instruments for measuring pressures are Bayard-Alpert type ionization manometers (up to 10^{-10} torr) and Redhead type inversion magnetron manometers with a cold cathode (10^{-12} torr) (Table 20).

Magnetron manometers with a hot cathode (of the Lafferty type) are best for measuring pressures in an ultrahigh vacuum and lower ranges (to 10^{-14} torr) [74, 91].

Measurement of ultralow pressures is related to the necessity of measuring currents to $\sim 10^{-17}$ a; therefore, it is desirable to use an ion detector with an electronic multiplier in ionization manometers. The most reliable measurement of

TABLE 20

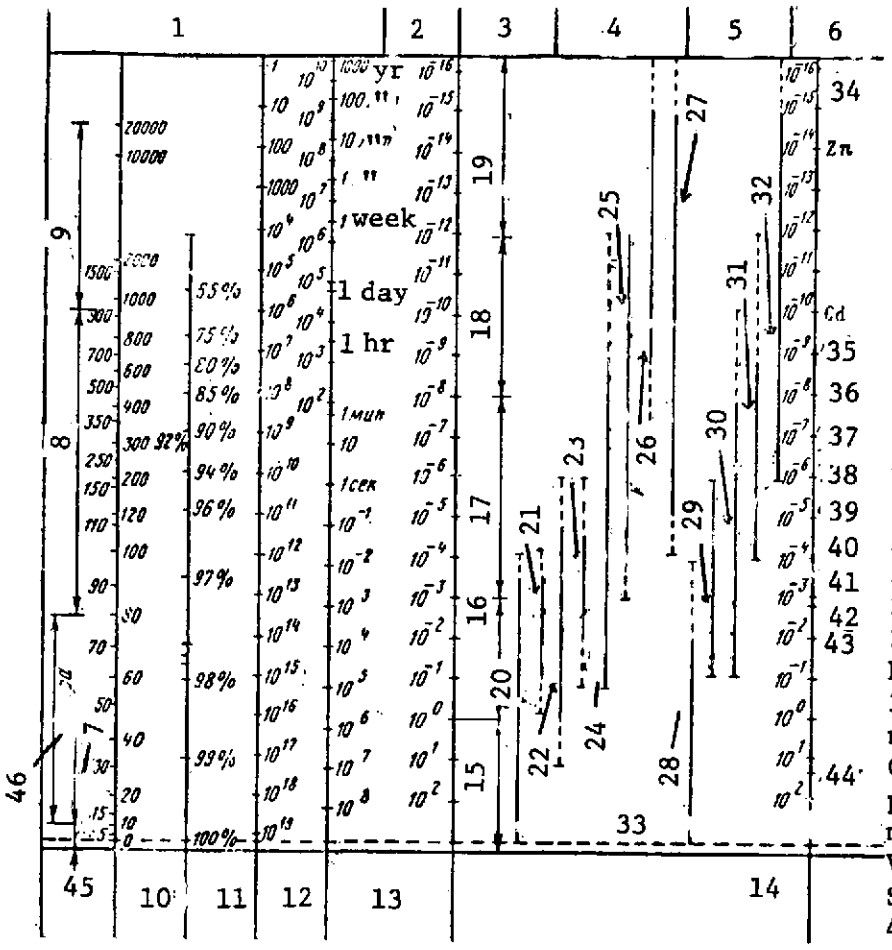

Key to Table 20.

1 - Characteristics of space vacuum; 2 - Pressure; 3 - Characteristics of vacuum; 4 - Vacuum manometers; 5 - Vacuum pumps; 6 - Vapor pressure at room temperature; 7 - Troposphere; 8 - Ionosphere; 9 - Exosphere; 10 - Variation of molecular weight with altitude in %; 11 - Number of particles per 1 cm^3; 12 - Time of formation of gaseous monolayer in sec; 13 - Pressure in torr; 14 - Saturated vapor pressure in torr; 15 - Low; 16 - Average; 17 - High; 18 - Ultrahigh; 19 - Extremely High; 20 - Alphatron; 21 - Thermopile; 22 - MacLeod; 23 - Pirani; 24 - Bayard-Alpert; 25 - Ionization (cold cathode); 26 - Ionization (hot cathode); 27 - Mass spectrometer; 28 - Mechanical; 29 - Diffusion; 30 - Diffusion (trap with liquid nitrogen); 31 - Ion getter; 32 - Cryogenic; 33 - (Atmospheric pressure 760 torr); 34 - Other metals; 35 - Nylon fiber; 36 - Vinyl; 37 - Polyethylene; 38 - Saran; 39 - Teflon; 40 - Mylar; 41 - Butyl rubber; 42 - Natural rubber; 43 - Mercury; 44 - Water 45 - Altitude in km; 46 - Stratoshpere

ultralow pressures (below 10^{-14} torr) at present may be accomplished with the aid of mass spectrometer devices. For this purpose, sectional mass spectrometers with an electron multiplier, mass spectrometers of the "omegatron" and "chronotron" types, mass filters, etc., may be used (see Table 20) [91].

It follows from the foregoing that measurement of pressures in facilities for simulating a space vacuum is a complex technical problem.

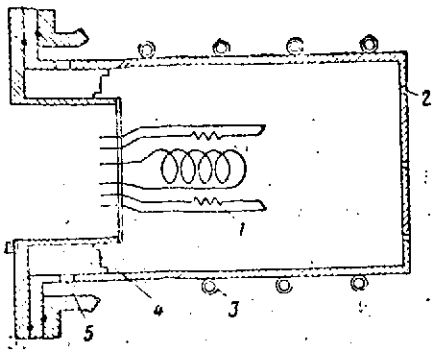

Figure 3.38. Manometer with large angle of vision, located inside a space vacuum simulation facility: 1 - tube; 2 - aperture; 3 - coil; 4 - barrier to reduce reverse leakage into tube; 5 - evacuation opening.

It is important to know the true pressure on an object, achieved in a system, for purposes of simulation. A manometric tube, oriented by an /201 input aperture toward the test object, will measure pressure corresponding to flow from the object toward the facility wall. A tube located on the test object, having an input aperture oriented /202 toward the facility wall, will measure the pressure on the object. However, it is complicated and not always possible to locate a measuring tube on an object.*

It is technologically simple to position a tube on the facility wall. However, in this case there will be a pressure drop between the tube and the facility, mainly due to outgassing of the exhaust fitting connecting the tube and the facility. The exhaust tube should be carefully heated for a long period to remove gas. The use of cryogenic systems for space simulation makes it possible to dispense with heating.

Santeller et al. [102, 250], proposed principles for measuring pressure in unheated facilities, simulating a space vacuum. Two types of manometric tubes are suggested for simulation.

The first type may be used in small facilities with test objects which may be placed in the field of vision of the lamp, or in those cases for large facilities, when the tube must be removed a considerable distance from the internal wall of the facility. The tube is surrounded by a shield, cooled to a temperature corresponding to the cooling agent of the cryopump. The length and diameter of the fitting are selected such that the fraction of molecules entering the tube without collisions is equal to the fraction of molecules which are not pumped out by the facility walls. In this case, the partial pressure of non-condensible gases inside the tube will be identical to their partial pressure outside the facility. The manometer in this case measures the pressure of non-condensed gases on the object.

Another type of tube, presented in Figure 3.38, was developed to increase the angle of vision of the tube and in order to render the lamp insensitive to the dimensions of the object.

*This may be done only in the case of an extended object.

A manometric tube, located in the walls of the facility, is covered by a shield cooled by liquid nitrogen or other cryogenic coolent.

In this case, the manometer measures the pressure of "background" gases of the facility on the object. /203

The second type of manometer may also be located directly on the test spacecraft and oriented toward the facility walls. In this case, there should be openings in the cooled shield, the total conductivity of which should correspond to the rate of evacuation of the manometric tube itself, which acts as an ion pump, in order to obtain the required decrease in the pressure of the condensed gases without affecting the partial pressures of non-condensed gases.

The first type of manometer may be utilized only when the test spacecraft is the main source of outgassing. The second type may be used successfully if there is also considerable outgassing from the facility walls.

Measurement of partial pressures in facilities is accomplished in a similar manner. In this case, instead of manometers, mass spectrometric partial pressure analyzers are installed.

If the pressure of molecular flow on the test object and on the facility walls has been measured, then, disregarding external leakage and outgassing of the facility walls, the collision coefficient Z may be calculated approximately in the following manner:

$$Z \approx \frac{p_1}{p_2}, \tag{3.131}$$

where p_1 is the pressure created by the flow of molecules travelling toward the object;

p_2 is the pressure created by the flow of molecules travelling away from the object toward the wall.

The collision coefficient calculated in this manner will depend on direction for the reasons given above.

A quartz microbalance, cooled to temperatures of ~4.2, 21 and 77° K and having a maximum sensitivity of $1 \cdot 10^{-10}$ G/cm^2 (the monolayer of the gas is ~10^{-8} G/cm^2), were used for the indicated purpose in investigations [261]. Forward and reverse flows of molecules were measured with the aid of the indicated microbalance. The value of Z and other characteristics may be calculated from the values of these flows.

Selection of pressures. The main problem in simulating a space vacuum is reproduction of the individual effects of a vacuum on the test spacecraft. It is necessary to take a differential approach as a function of the type of phenomenon being investigated in selecting the pressures required to carry out laboratory investigations. For this, the type of phenomenon may be arbitrarily divided into three groups:

1. phenomena related to the effects of pressure drop (stability, sealing, etc.);

2. volumetric phenomena, caused by particle concentration in space (thermal and electrophysical processes);

3. surface phenomena, caused by the particle flow rate on the surfaces being /204 investigated (evaporation, sublimation, friction, adhesion, etc.).

The determining parameter for phenomena of the first group is the pressure drop, that for the second group is volumetric particle concentration, and that for the third group is particle flow toward the surfaces being investigated.

Recommendations on selection of the pressures required to reproduce space vacuum conditions in investigations of various physical phenomena under model conditions are presented in Table 21. The indicated pressures may be regarded as approximate. More precisely, pressures are calculated in each specific case of simulation, based on specific (kinetic and other) relationships inherent to the phenomena being investigated.

Several conditions, on the basis of which selection of the pressure required to simulate the effects of a vacuum may be approached, usually exist in the consideration of each specific phenomenon. One of them may be regarded as general, and the remaining ones are auxiliary. For phenomena of the second and third groups,

TABLE 21

PRESSURES REQUIRED TO REPRODUCE UNDER LABORATORY CONDITIONS THE VARIOUS PHYSICAL PHENOMENA WHICH OCCUR IN SPACE

No. of Item	Investigated phenomenon	Required pressure
1	Mechanical strength of pressurized spacecraft hull under effects of pressure drop	~10 torr
2	Spacecraft vibration (absence of damping of surrounding atmosphere)	$\leq 10^{-3}$ torr
3	Radiant heat transfer	Below $\leq 10^{-4}$ torr
4	Electric discharges and breakdowns	Below $\leq 10^{-7}$ torr and complete simulation of space conditions
5	Physical properties of materials, design strength, creep, internal damping, etc.	$\leq 10^{-6}$ torr as a function of saturated vapor pressure of materials being investigated.
6	Operation of ion and plasma engines	$\leq 10^{-7}$ torr
7	"Cold" welding*	$\leq 10^{-7}$ torr
8	Evaporation*	Length of average free path of molecules should be greater than the characteristic dimensions of the chambers Low collision coefficient
9	Sublimation*	The same
10	Destruction of molecules	$<10^{-3}$ torr and high pumping rate
11	Occlusion of gases*	$<10^{-3}$ torr and high pumping rate
12	Absorption*	$<10^{-3}$ torr and high pumping rate
13	Adsorption*	$<10^{-7} - 10^{-14}$ torr
14	Chemical interaction of residual gas and surface material*	$<10^{-7} - 10^{-14}$ torr
15	"Dry" friction*	$<10^{-7} - 10^{-14}$ torr

*Note. In the cases marked by an asterisk, besides the value of pressure, it is necessary in each specific case of simulation to maintain the relationship between the rate of oxidation and reduction processes. Moreover, the input of residual gases in an atomic state must be simulated (or assessed) to investigate a number of surface phenomena with respect to a space vacuum, due to the difference in rates of surface reactions for a gas in molecular and atomic states. The effect of the different rates of these reactions on the physicochemical and chemical processes taking place during friction and other surface phenomena has been inadequately studied at present [48].

the following are adopted as a general condition: the absence of collisions between particles in space, determined by the ratio $l \gg L_0$, i.e., when the value of the mean free path of residual gas particles considerably exceeds the linear characteristics of the system dimensions.

Auxiliary conditions are selected separately for each phenomenon or process, on the basis of specific relationships characteristic for each given phenomenon separately.

There may sometimes be several rather than single auxiliary conditions. Each of the conditions leads to a specific pressure. The required pressure is selected as the lowest from the number of pressures calculated for different simulation conditions.

Let us consider briefly an example of selecting the pressure required to simulate a vacuum in the case of thermal sputtering of SiO_2 films. The vacuum facility is spherical ($d \approx 23$ cm), and the internal surface is surrounded on all sides by shields cooled to liquid nitrogen temperature ($T_s \sim 100°$ K).

Based on the condition that $l \gg L_0$, and also assuming that the background gas is cooled to $T_s \sim 100°$ K, we obtain a required pressure of $p \sim 10^{-6}$ torr from Formula (3.124). As an additional condition, we assume the following: the length of formation of a monomolecular layer of the SiO_2 condensate should exceed by $\sim 10^3$ times the rate of formation of the contaimination monolayer ("background" gases), including the oil mist of the auxiliary oil-diffusion pump. This condition is similar to the requirement for maintaining the surface of each condensate layer in an atomically pure state (i.e., in order to fulfill this condition, there must be approximately one contamination atom per 1000 atoms of base material). When Equation (3.124) is used, the latter condition yields a pressure of $p \approx 10^{-2}$-1 torr. Hence, we shall select the required pressure for simulation as equal to $p \approx 10^{-6}$ torr. /206

Pressures of the order of $10 - 10^{-3}$ torr are required to simulate the effects of vibrations of pressure drop on the strength of the spacecraft structure.

For rough estimates of leakage, the tests may be carried out initially under conditions of excess pressure such that the pressure drop between the pressurized cavity or compartment and surrounding space will equal 1 atmosphere, rather than in a vacuum. However, it is then necessary to carry out controlled (verification) tests under high vacuum conditions as well ($\sim 10^{-6}$ - 10^{-7} torr) to take into account the possibility of microleaks in sublimation of the material.

Pressures on the order of $\sim 10^{-3}$ - 10^{-5} torr, provision of a high degree of darkness of the internal surface of the facility and cooling it by rarefied gases ($\leq 100°$ K) are required to investigate the thermal conditions of spacecraft [119]. This is determined by the fact that heat exchange with the surrounding medium at such pressures is accomplished essentially by radiant transfer alone. The thermal conductivity of the residual gas at such temperatures will be insignificant ($\leq 1\%$) compared to the value of radiant heat transfer.

In this case, it is assumed that the effects of lower pressures on the surface elements of temperature control systems (temperature controlling coverings, etc.) should be investigated separately (pressure is selected in accordance with the requirements for investigation of surface phenomena). Experimental investigations [151, 266] indicate the effect of dimensions and the degree of outgassing of the objects being investigated on the relative role of radiant heat transfer compared to thermal conductivity and convection.

Thus, pressures of $\sim 10^{-4}$ - 10^{-5} torr (Figure 3.39) are required to test objects of small dimensions and having a low degree of outgassing (for example, exposed multilayer insulation), while large objects having high outgassing may be tested to determine thermal conditions at pressures not greater than $\sim 10^{-3}$ torr [151]. Investigations of electric discharges in a vacuum require pressures of $\sim 10^{-7}$ - 10^{-9} torr, "oilless" pumping and other conditions of space (charged particles).

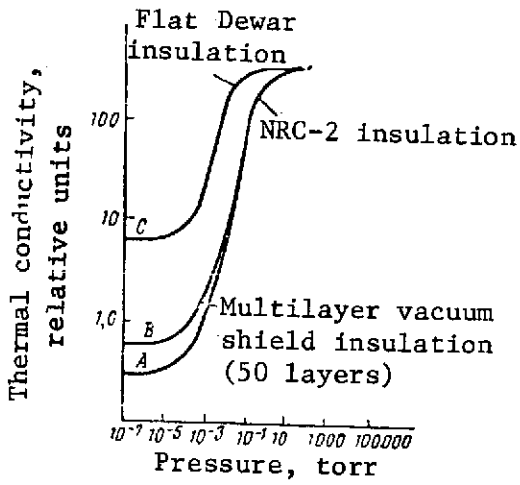

Figure 3.39. Dependence of thermal conductivity of some insulation materials on pressure.

Low pressures ($\leq 10^{-7}$ torr) are required to investigate surface phenomena such as sublimation, energy transfer, adsorption, etc. To investigate such processes, the vacuum system of space vacuum simulation facilities should provide low pressure and, moreover, a low collision coefficient Z. The latter leads to the relation $\tau_{\phi}^{*} \gg \tau_{i}^{*}$.

In an investigation of sublimation, when there are protective oxide films on the evaporation surfaces (for example, of metals), it is necessary that the rate of formation of protective films, i.e., the rate of oxidation processes on the surfaces, be less than the rate of their breakdown, because the presence or absence of oxide films may distort the kinetics of the evaporation rate (sublimation) being investigated. /207

When investigating the optical radiation coefficients of the surface, besides the condition $l \gg L_0$, it is very important that the thickness of the applied contamination layer during the experiment not exceed the limit of the light wave length at which the investigation is being conducted.

Chemical interation of gases and the surface, besides condition $l \gg L_0$, requires additional conditions $\tau_c^{*} \gg t_{exper}$ and $P_{O_2} < p'$; sputtering (recondensation) requires that τ_s^{*} of the sputtered material be much less than τ_{ϕ}^{*}, etc.

We know [54] that a monomolecular adsorbed air layer may be formed (at $C_c \approx 1$) (see Table 20) on a once cleaned surface at a pressure of $p \sim 10^{-6}$ torr within ~1 sec; at a pressure $\sim 10^{-9}$ torr — within several tens of minutes (which may be adequate to carry out an experiment of limited duration); at a pressure of $\sim 10^{-10}$ torr — within several hours, and at the lowest maximum pressures of space — within several thousand years.

Consequently, the pressure required to simulate space vacuum in an investigation of surface processes, if a rate of formation of a monolayer of oxide equal to the rate of formation of a monolayer of gas is assumed, may be calculated from the following kinetic relation: the rate of breakdown of protective oxide layers should be equal to or greater than the rate of their restoration on the evaporation surface, calculated in the first approximation by Knudsen-Langmuir Equations (3.122) - (3.125).

In reality, the oxide monolayer, as a result of the chemosorption process, is formed within a time considerably greater than that required for the formation of a physically adsorbed gas layer. This occurs due to the fact that the chemosorption process takes place in stages: physical adsorption — chemosorption.

The probability of each of these processes is determined by their own indices. /208 Thus, the probability of the process of physical adsorption is determined by the condition $0 \leq C_c \leq 1$; the probability of the chemosorption process, in accordance with Arrhenius' equation, is equal to:

$$W = b' e^{-\frac{E_a}{R_0 T}}, \tag{3.132}$$

where $0 \leq W \leq 1$; b' is a constant $(1 - 10^{-2})$; and E_a is the activation energy (it has a value of the order of tens of kcal/mole). Consequently, at $C_c < 1$ and $W < 1$, the total probability of the formation of an oxide will be equal to the product of the above-mentioned probabilities and will be much less than unity. Moreover, reduction of protective oxide films is possible only in the presence of oxygen or sources of its liberation (diffusion and dissociation) in the composition of residual gases.

Oxygen (molecules, atoms and ions) is encountered in space only at distances not exceeding several thousand kilometers from the Earth's surface (near space). Therefore, at greater distances from the Earth's surface, the medium will no longer be oxidizing but rather reducing (hydrogen atoms).

Consequently, values of partial oxygen pressures in the medium of the residual space gas, rather than total pressures, must be used to calculate the length of formation of a protective oxide film.

In connection with the fact that the contribution of oxygen to the total concentration is small and decreases as the distance from the Earth's surface increases, the times for formation of an oxide monolayer will be considerably greater than those which are presented in Table 20. Moreover, the state of the particles (molecules, atoms and ions) is important, due to the difference in rates of physicochemical processes for such states.

When investigating the coefficient of gaseous particle accommodation with solid surfaces, one should take the fact into account that particles may have an energy up to 10 - 15 eV in space. The interaction of particles with such energies with a surface differs considerably from that of particles having thermal energies which are usually present in laboratory vacuum facilities.

The foregoing confirms the importance of simulation in a number of cases, related to the investigation of thin surface effects, not only of total reduced pressures, but also of the specific chemical composition, state (atoms and ions), as well as the corresponding energy characteristics of the residual gas (molecular beams).

The presence of vapors of organic products, migrating from diffusion pumps, as well as outgassing from sealing materials in the composition of residual gas in vacuum facilities may considerably distort the evaporation pattern and other surface processes being investigated. For example, upon condensation on friction surfaces even in the form of thin layers, such organic products act as lubricating materials and may distort the friction pattern. This confirms the necessity of using "oilless" pumping in surface investigations. /209

The pressures required to investigate friction, wear and the behavior of lubricants during friction in a vacuum are within the range of 10^{-7} - 10^{-14} torr. In this case, the general requirements are similar to those in an investigation of sublimation and other phenomena, and all the foregoing remain valid for this case as well.

The criterion, calculated by the relationship between the rate of monolayer formation on the friction surface and the "lifetime" of unit roughness, may be employed as the main kinetic relationship which determines pressure in a vacuum system in an investigation of friction.

In the case of simulating vacuum conditions to investigate the behavior of charged particles, it is necessary that the time of particle flight be less than the time of particle charge exchange (pressure is usually 10^{-5} - 10^{-7} torr). Moreover, in the this case, it is important to employ "oilless" pumping due to possible cracking of the hydrocarbon layers on the target upon collision with the beam.

Pressures of 10^{-8} - 10^{-9} torr, at which most individual effects of space vacuum may be reproduced simultaneously, are usually selected to carry out complex vacuum tests of spacecraft.

Only certain partial concepts may be expressed at present with respect to accelerated time simulation of the effects of a space vacuum to reduce the length of laboratory vacuum tests. The indicated time simulation should also be regarded separately for each process or phenomenon being investigated. Thus, for example, when investigating sublimation, conducting the process at higher temperatures (retaining the thermal stability of the materials being investigated) should lead to reduction of the periods required to obtain the total effect.

A method of accelerating the process by increasing partial oxygen pressure in the residual gas (pressure acceleration) was also suggested to investigate oxidation processes. As a whole, the general problems of time simulation in vacuum tests require their own treatment.

It may be concluded on the basis of the foregoing that simulation of the effects of space vacuum conditions requires:

— knowledge and consideration of space vacuum conditions in which the spacecraft will be in space (in orbit, trajectory, etc.); /210

— provision in the laboratory of a pressure corresponding to the specific pressure of the phenomenon or process being investigated and the required speed;

— provision in the laboratory facility, if necessary, of a low collision coefficient and other characteristics of vacuum simulation;

— provision in a number of cases in the laboratory facility of the required composition and energy characteristics of the residual gas, by preventing its contamination by oil and other products which are absent in a space vacuum.

Fulfillment of each of these requirements is dictated by the specific simulation problem.

14. Thermal Testing of the Cosmonaut's Spacesuit

The spacesuit in which the cosmonaut emerges into space or onto the lunar surface should provide a microclimate approximating as closely as possible the usual Earth microclimate.

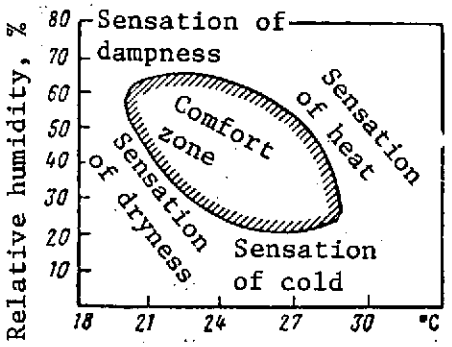

Figure 3.40. Comfort zone in quiet atmosphere.

The required temperature conditions inside the spacesuit are maintained with the aid of an active temperature control system, which is an integral part of a cosmonaut's autonomous life-support system.

The more favorable (comfortable) conditions for a cosmonaut depend not only on absolute values of temperature and humidity inside the spacesuit, but on their relative distribution throughout the spacesuit as well, on the intensity of ventilation, temperature drop between various portions of the cosmonaut's body, and on his heat dissipation and perspiration. The arbitrary limits of the zone of temperature comfort are shown in Figure 3.40 [106]. It is assumed that the maximum temperature difference between two sections of the cosmonaut's body should not exceed 5 degrees at a humidity from 30 to 80% [49]. The cosmonaut's energy expenditure may vary from 100 kcal/hour at rest to 800 kcal/hour during very intensive work. The calculated level of the cosmonaut's prolonged heat dissipation on the Moon is assumed to be equal to 400 - 500 kcal/hour. Perspiration, which determines to a considerable /211 extent the subjective sensation of heat or cold, is different in different people. It depends not only on the temperature and humidity of the atmosphere, but on the mental state of the cosmonaut as well. Perspiration varies over a very wide range for different parts of the human body.

When working in open space, the cosmonaut may naturally vary his position continuously; he sometimes enters shadow and sometimes is illuminated by the Sun. As a result of this, the external heat fluxes on the spacesuit surface may vary tenfold. Changes in the position of the body, arms, legs and head may lead to a variation of internal thermal resistance between the sections of the body and external radiation surfaces. Therefore, when testing the thermal conditions of the

spacesuit, human body simulators are employed only during the first stage of checking and debugging the temperature control system. A series of tests of all systems of the spacesuit and cosmonaut then follows. The first experiments are carried out in the atmosphere with an excess pressure in the spacesuit. However, such experiments cannot reproduce the real heat fluxes through the multilayer covering of the spacesuit, because the external vacuum shielding thermal insulation (VSTI) of the spacesuit has low thermal conductivity coefficients only in a high vacuum ($p = 10^{-5} - 10^{-8}$ torr). The cosmonaut's efficiency in the spacesuit at an ambient pressure of $10^{-5} - 10^{-8}$ torr is checked at various external thermal loads. High external thermal inputs may take place if the cosmonaut, for example, is located near the illuminated surface of a spacecraft of large dimensions, having high values for the reflection coefficient of solar rays in the visible region, or on the lunar surface at lunar mid-day. In the latter case, infrared radiation from the lunar surface at a density of approximately 1200 W/m^2, which impinges on the spacesuit from practically all directions of half-space (the solid angle of the planet is equal to 2π steradians), is added to the direct solar flux (1400 W/m^2). Maximum external radiant fluxes will occur in the case when solar rays impinge on the cosmonaut at some angle to the vertical (15 - 25°), rather than from directly overhead. The temperature of the lunar surface for such angles of inclination of the Sun differs very little from the maximum temperature, and projection of the spacesuit surface illuminated by solar rays to a plane, perpendicular to the direction toward the Sun, is much greater than in the case when the Sun is at its zenith.

External thermal inputs are reduced to a minimum when the cosmonaut is on the lunar surface during the lunar night or near the shaded side of the spacecraft, if this surface of the spacecraft has a low temperature.

It is very important in multiple tests of spacesuits that the "solar" radiant flux in the chamber has a spectrum close to the real spectrum. Strong deviations /212 in spectral composition may lead to disruption of the thermal conditions of the protective light filter of the spacesuit visor and cause subjective sensations of heat or cold.

The quality of the pressure helmet light filters, which should absorb the ultraviolet component of the solar spectrum, is also checked in such experiments; the fatigueability of the cosmonaut's eyes from rays, the spectral composition of which differs from that on Earth, is investigated.

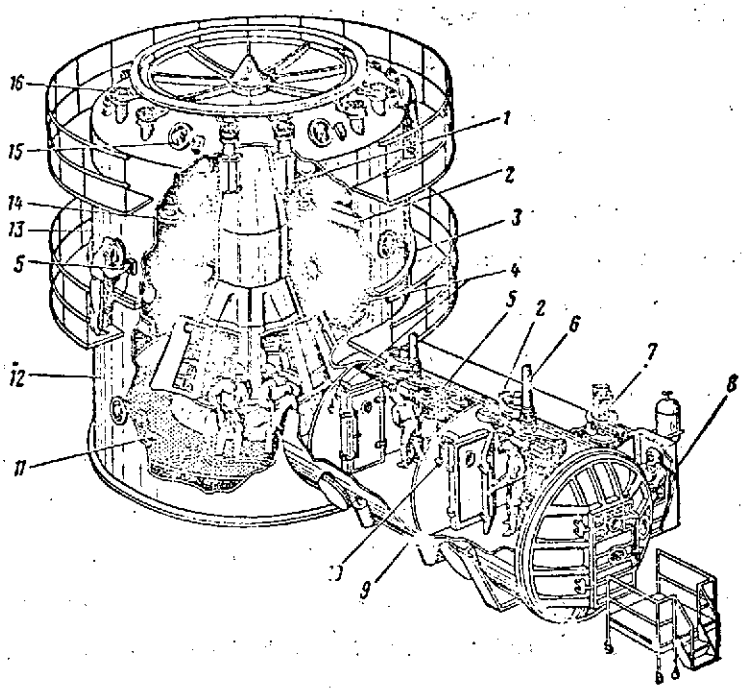

Figure 3.41. Structural layout of facility for multiple tests of spacesuits: 1,16 - radiation system; 2 - dark shields; 3 - power element; 4 - television cameras; 5 - telephone communication system; 6, 7, 8 - life-support system; 9 - airlock chamber; 10 - signalling system; 11 - spacesuit power supply; 12, 13 - upper and lower halves of chamber; 14 - illuminator; 15 - observation port.

The objects surrounding the cosmonaut should have angular and optical coefficients close to actual values. This is necessary not only for maximum precise reproduction of actual thermal conditions, but for training the cosmonaut, for him /213 to learn how to orient himself and to work under conditions of increased light contrasts.

Along with debugging the autonomous life-support system, the ability of the cosmonaut to analyze the situation, to make repairs of spacecraft systems which break down, and to carry out different types of operations not envisioned by the main program (for example, in the case of emergency situations), is also checked in these experiments.

The structural layout of one of the facilities for multiple tests of spacesuits is shown in Figure 3.41.

CHAPTER 4 /214

FACILITIES WHICH SIMULATE CONDITIONS OF SPACE

1. Vacuum Systems

Vacuum systems, designed for pumping vapors and gases, given off by test objects and facility elements, and maintaining operating pressures in them, in a number of cases low pressures (up to $p \leq 10^{-14}$ torr), are required to create conditions which simulate the space vacuum. In the case of high outgassing of test objects, high pumping rates (to $\sim 10^{8}$ l/sec) and low collision coefficients ($\sim 10^{-2} - 10^{-3}$) must be provided in the facilities. Moreover, in some cases (for example, investigation of surface chemical reactions), specific composition and energy characteristics of the residual gas must be provided.

Let us consider the main sources of outgassing in simulators and the approximate composition of vapors and gases subject to evacuation in order to select the structure of vacuum pumping systems.

This is primarily atmospheric air or another ballast gas, with which the facilities are filled prior to beginning evacuation. Secondly, these are vapors and gases given off by the test objects and various elements of the facilities, which consist of volatile components of seals, cables, insulation and sublimating metals (for example, zinc, cadmium, etc.); volatile materials from the surface coverings for passive temperature control and the thermal protective coating of the nose section of the spacecraft, by-products of engine exhaust, gas leaks from the pressurized compartments of the test objects, etc. Moreover, there are usually vapors of various substances in the facilities, introduced by the pumping systems

(for example, the oil mists of diffusion pumps; methane from titanium sorption pumps, vapors of low-boiling cooling liquids, which percolate into the vacuum through leaks in the cryopump panels, etc.).

The presence of the above vapors and gases alters the gaseous composition of the environment being simulated, and may cause a number of undesirable phenomena in the systems and devices of test objects (in the optical systems, thermal coatings, /215 bearings, electromechanical devices, etc.).

The presence of organic vapors (oils), which enter from the pumping systems, is especially undesirable, and in a number of cases impermissible in the facilities. The presence of traps, cooled by liquid nitrogen, only reduces (but does not eliminate) the presence of such vapors. These vapors are absent in a space vacuum.

In this regard, it becomes necessary to use so-called "oilless" evacuation, i.e., evacuation by pumping systems which do not use oil and other organic products as working fluids.

Several pumps of different types must be utilized simultaneously in the vacuum systems of simulators. This is a result of the selective evacuation capacity of each type of pump, and the large variety of vapors and gases subject to evacuation.

Pumps for main, auxiliary, and preliminary evacuation are used.

Pumps for preliminary evacuation are intended for initial evacuation of the facilities (from $\sim 10^3$ to 10^{-3} - 10^{-4} torr), after which the pumps for main and auxiliary evacuation usually begin to operate.

Pumps for main and auxiliary evacuation are intended for evacuating vapors and gases in the operating pressure range (10^{-5} - 10^{-14} torr). The main quantity of vapors and gases is evacuated with the aid of main evacuation pumps, and, therefore, these pumps have the highest volumetric output of all types used.

Auxiliary evacuation is necessary due to the selective pumping action of the main evacuation pumps.

So-called surface effect pumps, which use to the maximum extent possible the internal surface of the facility (internal evacuation), are the most suitable as main evacuation pumps (see Figure 3.37).

External evacuation, i.e., evacuation by pumps connected from the outside with the aid of connecting pipes, is unsuitable as main evacuation, since the effective evacuation rate in this case is limited by the vacuum conduction of these pipes.

In order to provide the appropriate values of vacuum simulation characteristics in this case, it becomes necessary to use a large number of pumps (for example, for large facilities) — from 50 to 100 oil-diffusion main evacuation pumps — outside the facility. Such pumps create great design and operational difficulties and lead to intensified oil migration. Therefore, the main evacuation in simulators is usually accomplished by cryogenic pumps (condensation and sorption types) (see /21
Section 3, "Cryogenic Pumping"), which utilize to the maximum extent possible the internal surface of the facility.

The use of cryogenic pumps makes it possible to obtain any required pressures, even to very low pressures ($\sim 10^{-14}$ torr), high evacuation rates ($\sim 10^{8}$ l/sec), low collision coefficients ($\sim 10^{-2} - 10^{-3}$), as well as a gas composition approximating that in space, but far from duplicating it.

In view of the fact that cryogenic pumps have a selective evacuation action with respect to different gases, they are employed simultaneously with auxiliary evacuation pumps. Since the latter are designed for evacuation of large quantities of gases, which are not evacuated by the main pumps, externally connected pumps (external evacuation) may be employed as such pumps.

Oil-mist diffusion pumps, which are universal pumps, i.e., suitable for evacuation of any vapors and gases, were previously employed exclusively as auxiliary evacuation pumps. The great disadvantage of these pumps is the presence of return flow of oil mists inside the simulator, the inadmissibility of which, at least for investigating a number of surface phenomena (investigation of friction in a vacuum, etc.), was discussed above.

Therefore, when using oil-diffusion pumps, special types of valves, as well as traps, cooled by liquid nitrogen, must be designed to reduce (but not exclude) migration of oil mists into the vacuum facility.

Cryosorption and ion pumps have recently been used as auxiliary evacuation pumps. Because of the high specific surfaces of sorbents, cryosorption pumps may also considerably increase the length of continuous operation of condensation pumps.

Cryosorption pumps are employed in large facilities as the main evacuation pumps. Ion and titanium pumps (so-called azotites), made in the form of standard industrial units, are used jointly with cryogenic pumps as auxiliary evacuation pumps in medium and large simulators [240]. Mechanical pumps (rotary, Roots double-rotor blower, etc.) are usually employed as preliminary evacuation pumps.

In view of the fact that such pumps permit migration of oil into the facilities, there is also a tendency to use cryogenic "oilless" evacuation pumps (for example, cryosorption zeolite types of molecular "sieves") (see the section "Cryogenic Pumping") as preliminary evacuation pumps, and vapor-discharge pumps for large facilities. Thus, it is more expedient in the creation of vacuum systems for simulators to employ /217 multistage evacuation in which each type of pump is employed in the optimum manner. For example, in such a system water vapor may be evacuated by condensation on surfaces cooled to liquid nitrogen temperatures (100 - 77° K), O_2 and N_2 — by condensation on surfaces cooled to gaseous helium temperatures (~20° K), Ar — by condensation on surfaces cooled to liquid (~4.2° K) or "cold" (~10° K) gaseous helium, and H_2 — by a titanium sorption pump (azotite type).

A very effective technological method, which facilitates obtaining ultralow pressures, is heating of the facilities for intensive outgassing from the individual sections of the facility. In this respect, facilities are heated and unheated.

Heating of facilities is very effective at temperatures of ~450° C. Small and sometimes medium-size facilities are usually heated.

The dependence of outgassing rates of stainless steel, heated and unheated, from which facility walls are made, on the length of time in a vacuum is presented in Figure 4.1. As can be seen from the figure, this rate is lower for a heated than for an unheated material.

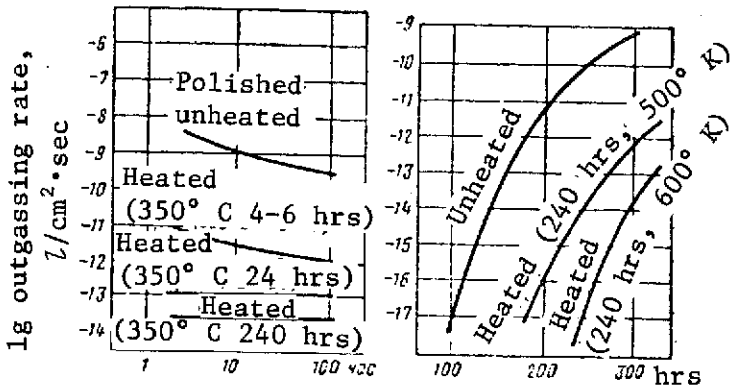

Figure 4.1. Dependence of outgassing rates on length of time in a vacuum for heated and unheated stainless steel.

Large facilities, which are essentially unheated, are sometimes heated during the test cycles to facilitate outgassing. In this case, the internal parts of the facilities are heated to ~100° C by passing heated nitrogen through the pipes of the cryogenic panels. Rapid cooling of the facilities when they are shut down is also accomplished in a similar manner.

2. Cryogenic Systems /21

Cryogenic systems are employed in facilities to solve two problems: simulation of spacecraft radiation absorption by space and to accomplish cryogenic vacuum pumping in the facilities [197].

The heat fluxes emitted from spacecraft surfaces, having a temperature $T_s \approx 300°$ K, are almost completely absorbed by space ($T_0 \approx 3°$ K).

The amount of heat absorbed per unit time from a unit surface is calculated by the Stefan-Boltzmann equation.

This phenomenon is usually simulated in facilities with the aid of surfaces having a high degree of darkness and cooled to liquid nitrogen temperature (~100° K). In this case, the error caused by the temperature difference of the surrounding medium in space and in the facility does not exceed ~1%.

We note that the indicated device is, at the same time, a nitrogen cryocondensation pump, which evacuates H_2O, CO_2 and other vapors and gases.

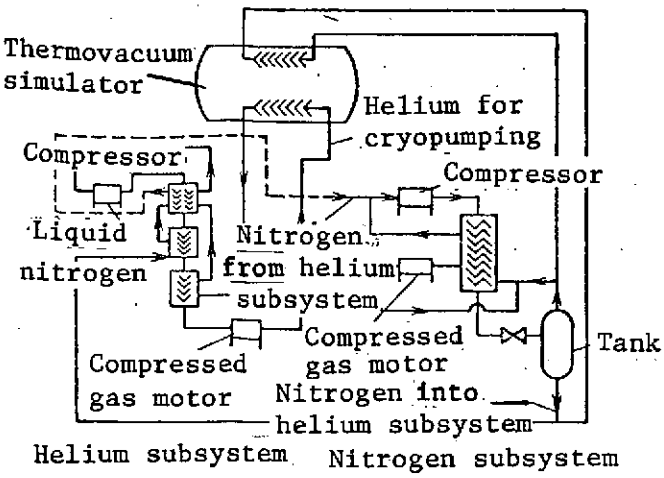

Figure 4.2. Typical cryogenic system of simulator for thermovacuum tests.

The heat loads on individual sections of such surfaces may reach ~1400 W/m^2 (the Earth's "orbit") and higher values.

Cryogenic pumping in facilities is accomplished with the aid of cryopumps, which use liquid nitrogen (77 - 100° K), and gaseous (~10 - 20° K) and liquid (4.2° K) helium. These pumps are made in the form of cryolattices of different configuration, cooled by special coolants (see the section, "Cryogenic Pumping").

The more common types of cryolattices, as well as their main characteristics, are presented in Table 26.

In order to supply the cooling systems of facilities with liquid nitrogen and gaseous or liquid helium, facilities are used which operate under refrigerator or liquifier conditions, cryostats, pumps for transfer of liquid nitrogen, tanks for storage of large quantities of liquid nitrogen, and special vacuum pipelines for the transfer of liquid nitrogen.

The consumption of low-boiling cooling liquids for these purposes is high. Thus, whereas in 1964 the daily consumption of liquid nitrogen in the United States to supply the cryogenic systems of large facilities reached 500 tons, in 1970 it increased to 2000 tons [225].

A diagram of the arrangement of a typical cryogenic system of a space vacuum simulator, cooled by liquid nitrogen and "cold" (20° K) gaseous helium, is presented in Figure 4.2.

The facilities are usually supplied with liquid nitrogen by two methods:

a. by pumping of liquid nitrogen through a system of cryolattices or pouring /219 the liquid nitrogen into a cooling sleeve under atmospheric pressure (an open system);

b. by pumping liquid nitrogen through a cryolattice under increased (up to ~10 atm) pressure (a closed system).

The second method is more complicated from a design point of view, compared to the first method, but is more economical from the standpoint of liquid nitrogen consumption, and more importantly, makes it possible to prevent the nitrogen from boiling in the system and vapor locks from forming. The nitrogen temperature under excess pressure is higher than that evaporated under atmospheric pressure. This circumstance may be essential for certain types of pumps (for example, titanium).

Liquid nitrogen is pumped into the cryogenic system from special transport vessels (tanks), equipped for pumping under pressure by special liquid pumps of the immersion type. The tanks may be filled with liquid nitrogen either brought in externally from industrial enterprises or produced locally in liquifiers.

Supply of cryogenic systems with liquid and "cold" (20° K) gaseous helium may be accomplished in the following manner:

a. liquid helium is produced at industrial enterprises and is delivered in Dewar vessels;

b. liquid helium is produced locally in liquifiers and is supplied to the /220
facilities in Dewar vessels;*

c. "cold" (10 - 20° K) gaseous helium is produced locally in closed-type facilities, operating on a refrigerator cycle.

The latter scheme is usually employed to supply large facilities.

The requirements for the cooling capacity of helium cryopumps is ~10 W per 1 m^2 of cryosurface [209, 210].

---

*Schemes "a" and "b" are usually employed to supply small facilities.

3. Cryogenic Pumping

Methods of achieving a vacuum (up to ultrahigh and extremely high, inclusively) as a result of processes of gas condensation or adsorption on solid surfaces, cooled to cryogenic ($\leq 100°$ K) temperatures (henceforth, these surfaces will be called cryosurfaces), are called cryogenic pumping (cryopumping). Enormous pumping rates ($\leq 10^8$ l/sec) and extremely low pressures ($\leq 10^{-12}$ torr) are achieved at present with the aid of cryopumping.

Cryopumping combines three related methods: cryocondensation, cryosorption and cryocapture [198]. These methods are usually employed in combination with each other rather than separately. Their common feature is that evacuation takes place due to collision of the molecules of the gas being evacuated from cryosurfaces, cooled to temperatures corresponding to the boiling points of liquid nitrogen (T_s = 77° - 100° K), liquid hydrogen (T_s = 20° K) and liquid ($T_s \approx$ 4.2 - 2.5° K) or "cold" gaseous ($T_s \approx$ 10 - 20° K) helium* and to the processes of condensation, physical adsorption, chemosorption and diffusion.

Cryocondensation. The essence of this method includes formation of a solid or liquid phase of the material on the cryosurfaces being evacuated and, as a result, a decrease of partial (as well as total) gas pressures in the space being evacuated. The partial pressures of the residual gas components are determined (under equilibrium conditions) by the saturated vapor pressures of the materials being evacuated at cryosurface temperatures T_s (Table 22). Under non-equilibrium conditions, these pressures may be considerably lower than saturated vapor pressures.

The value of equilibrium saturated vapor pressure p_s is calculated by the Clapeyron-Clasius equation:

$$\ln p_s = \alpha - \beta / T_s, \tag{4.1}$$

where α and β are constants;

T_s is the cryosurface temperature.

---

*In some cases the cryosurfaces are cooled with liquid neon ($T_s \approx$ 30° K) to accomplish cryopumping.

TABLE 22 **

SATURATED VAPOR PRESSURE (°K) OF CERTAIN GASES AT LOW PRESSURES [77, 193]

Name of Gas	Symbol	Saturated Vapor Pressure, torr																
		10^{-13}	10^{-12}	10^{-11}	10^{-10}	10^{-9}	10^{-8}	10^{-7}	10^{-6}	10^{-5}	10^{-4}	10^{-3}	10^{-2}	10^{-1}	1	10^{1}	10^{2}	10^{3}
Nitrogen	N_2	18,1	19	20	21,1	22,3	23,7	25,2	27	29	31,4	34,1	37,5	41,7	47	54,0	*63,4	80,0
Ammonia	NH_3	70,9	74,1	77,6	81,5	85,8	90,6	95,9	102,0	108,5	116,5	125,5	136,0	148,0	163,0	181,0	*206	245
Argon	Ar	20,3	21,3	22,5	23,7	25,2	26,8	28,6	30,6	33,1	35,9	39,2	43,2	48,2	54,4	62,5	73,4	89,9
Water	H_2O	113,0	118,5	124,0	130,0	137,0	144,5	153,0	162,0	173,0	185,0	198,5	215	233	256	*284	325	381
Hydrogen	H_2	2,67	2,83	3,01	3,21	3,45	3,71	4,03	4,40	4,84	5,38	6,05	6,90	8,03	9,55	11,7	*15,1	21,4
Carbon dioxide	CO_2	59,5	62,2	65,2	68,4	72,1	76,1	80,6	85,7	91,5	98,1	106,0	114,5	125,0	137,5	153,5	173,0	198,0
Nitrous oxide	N_2O	55,8	58,3	61,1	64,2	67,6	71,3	75,5	80,3	85,7	91,9	99,0	107,5	117,5	129,5	144,0	162,5	*189,3
Oxygen	O_2	21,8	22,8	/24,0	25,2	26,6	28,2	29,9	31,9	34,1	36,7	39,8	43,3	/48,1	54,1	*62,7	74,5	92,8
Krypton	Kr	27,9	29,4	30,9	32,7	34,6	36,8	39,3	42,2	45,5	49,4	53,9	59,4	66,3	74,8	85,9	101,0	*123,5
Xenon	Xe	38,5	40,5	42,7	45,1	47,7	50,8	54,2	58,2	62,7	68,1	74,4	82,1	91,5	103,5	118,5	139,5	*170,0
Methane	CH_4	24,0	25,3	26,7	28,2	30,0	32,0	34,2	36,9	39,9	43,5	47,7	52,9	59,2	67,3	77,7	*91,7	115,0
Neon	Ne	5,50	5,79	6,11	6,47	6,88	7,34	7,87	8,48	9,19	10,05	11,05	12,30	13,85	15,80	18,45	22,1	*27,5
Nitric oxide	NO	37,7	39,4	41,3	43,4	45,6	48,1	50,9	54,0	57,6	61,6	66,3	71,7	78,1	85,7	95,0	106,5	*123,5
Carbon monoxide	CO	20,5	21,5	22,6	23,8	25,2	26,7	28,4	30,3	32,5	35,0	38,0	41,5	45,8	51,1	57,9	67,3	*84,1
Hydrogen sulfide	H_2S	57,1	59,8	62,7	65,9	69,5	73,5	78,0	83,1	89,0	95,7	103,5	/113,5	124,5	/138,5	156,5	180,5	*218
Sulfur dioxide	SO_2	78,9	82,4	86,3	90,4	95,1	100,0	105,0	112,5	119,6	128,0	137,5	148,5	161,5	177,0	195,5	*225	269
Chlorine	Cl_2	66,1	69,1	72,4	76,0	80,0	84,4	89,4	95,1	101,5	109,0	117,5	127,5	140,0	155,0	*173,0	201	245

Note: The asterisk (*) denotes the location of a tertiary point between corresponding temperatures and the slash (/) — the existence of a crystalline phase transition.

**Commas represent decimal points.

/221

Cryocondensation may be used effectively for evacuation of gases whose equilibrium saturated vapor pressure at cryosurface temperature is lower than the required vacuum (or $T_s \ll T_b$, where T_b is the boiling point). For example, N_2 and O_2 may be effectively evacuated by condensation on cryosurfaces at $T_s \approx 20°$ K at pressures greater than $\sim 10^{-11}$ torr. /222

It follows from Table 22 that for every cryosurface temperature there are specific (so-called "non-condensible") gases, whose equilibrium saturated vapor pressure is higher than the given pressure. For example, inert gases (equilibrium saturated vapor pressure is $\sim 10^3$ torr) do not condense at liquid nitrogen temperature; hydrogen and helium — at liquid hydrogen temperature; and helium and partially hydrogen — at liquid helium temperature (equilibrium pressure $p_{s\ He} \approx 10^3$ torr; $p_{s\ H_2} \approx 10^{-7}$ torr).

Therefore, cryopumping to superhigh pressures with the aid of cryocondensation usually assumes the simultaneous use of auxiliary evacuation of "non-condensible" gases by other means (oil-diffusion pumps, cryosorption pumps, etc.). Cryosurface cooling to $T_s \leq 2.5°$ K and lower by reducing the pressure over boiling helium is employed in some cryopumping systems. At this temperature, equilibrium saturated vapor pressure of hydrogen becomes very low ($<10^{-13}$ torr).

The primary act in the process of cryocondensation is collision of the gas particles being evacuated with the cryosurface. In this case, according to Frenkel' [128], the particle either adheres (physical adsorption) to the cryosurface (the phenomenon of "condensation") or rebounds from it (the phenomenon of "accommodation"). These phenomena are related to some average existence τ ("lifetime") of particles on the cryosurface.

This time is very short ($\tau_0^* \approx 10^{-13}$ sec) for reflected particles, and is comparable to the length of collision of two gas molecules or to the period of oscillation of atoms of a solid near an equilibrium position in the lattice. For adsorbed particles at a low degree of coverage 0, this period is equal to an average of

$$\tau^* = \tau_0^* e^{\frac{E_d}{R^\circ T_s}}, \tag{4.2}$$

where E_d is the desorption energy which varies from unity to tens of kcal/mole, and R is the universal gas constant ~ 2 cal/deg•mole. For example, for adsorption of argon in argon $E_d \approx 1.9$ kcal/mole, and for krypton in krypton $E_d \approx 2.59$ kcal/mole [33].

In the quantitative sense, both these phenomena may be characterized by accommodation α_t and condensation C_c coefficients, respectively. The first of them /22 determines the degree of energy exchange between the gas and the cryosurface, and the second — the ratio of the number of particles condensed during the first collision to the number colliding with the cryosurface.

Evacuation with the aid of cryocondensation, taking into account the phenomena of accommodation, condensation and desorption, is characterized by the evacuation coefficient [192]

$$C = \frac{S}{S_{max}}, \tag{4.3}$$

where S and S_{max} are the specific effective and theoretical evacuation rates, respectively ($l \cdot cm^{-2} \cdot sec^{-1}$). It is usually assumed that the accommodation coefficient for the desorbed gas particles approaches unity (i.e., during the time period τ^* these particles acquire a temperature of $\sim T_s$).

The theoretical evacuation rate S_{max} in the molecular mode is determined by the molecular flux toward the surface. It denotes the maximum possible number of molecules which may be evacuated by a unit area of the cryosurface per unit time on the condition that each molecule is captured upon collision, and is calculated by the formula

$$S_{max} \approx 3.64 \sqrt{\frac{T_g}{M}}\ l \cdot cm^{-2} \cdot sec^{-1} \tag{4.4}$$

where T_g is the gas temperature in °K;

M is the molecular weight of the evacuated gas.

The values of S_{max} for a number of gases are presented in Table 23.

The effective specific evacuation rate S on the condition that $T_g > T_s$ and the cryosurface comprises a small portion of the facility walls, and desorption corres- /224 ponds to equilibrium conditions, is equal to [192]:

TABLE 23*

THEORETICAL SPECIFIC EVACUATION RATES S_{max} FOR A NUMBER OF GASES AT DIFFERENT TEMPERATURES [173]

Gas	S_{max} [$l \cdot cm^{-2} \cdot sec^{-1}$] at gas temperatures in °K			
	77	195	300	400
N_2, CO	6,04	—	11,96	13,8
CO_2, N_2O	—	7,68	9,53	11,02
Ar	5,06	—	10,00	11,55
O_2	5,36	—	10,58	12,2
90% N_2/10% O_2	5,97	—	11,81	13,72
80% N_2/20% O_2 (~air)	5,90	—	11,15	13,49

*Commas represent decimal points.

$$S = C_c S_{max} \left[1 - \frac{p_s}{p_g} \left(\frac{T_g}{T_s} \right)^{1/2} \right]. \tag{4.5}$$

According to Frenkel' [128], if the energy of the incident particles is distributed according to the Maxwell law for a temperature T_g, and $T_s \approx 0$, then

$$C \approx C_c \approx 1 - e^{-\frac{E_0'}{kT_g}}, \tag{4.6}$$

where E_0' is the least energy at which condensation becomes possible; E_0' is related to the energy on the condensation surface, and varies from tens to hundreds of cal/mole.

At $T_s \neq 0$, the evacuation coefficient is equal to

$$C \approx C_c \left(1 - e^{-\frac{E}{kT_s}} \right) \tag{4.7}$$

or, by setting

$$d = \left(1 - e^{-\frac{E}{kT_s}} \right), \tag{4.8}$$

we obtain

$$C \approx C_c d. \tag{4.9}$$

Values of E_0'/R_0 for certain gases [173]

Gas	E_0'/R_0
N_2	290° K
Ar	293 »
CO_2	289 »
CO	532 »
N_2O	288 »
O_2	532 »
90% N_2/10% O_2	361 »
80% N_2/20% O_2	416 »

Equations (4.5) - (4.9) are approximate and suitable only for a qualitative consideration of the cryocondensation process.

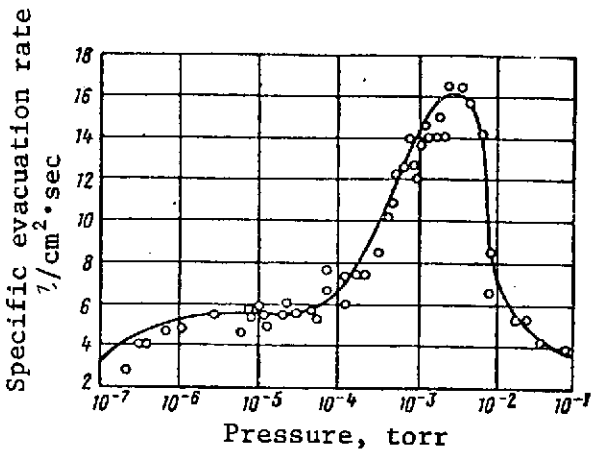

Figure 4.3. Dependence of specific evacuation rate of CO_2 on pressure during cryocondensation.

Within the limits of the molecular mode, as the pressure increases, the specific evacuation rate in accordance with (4.5) increases from zero (for a pressure equal to saturated vapor pressure of the condensate) to S_{max} (Figure 4.3).

The evacuation rate at pressures corresponding to the molecular-viscous mode again increases to a maximum value, and then drops sharply in the region of the viscous mode.

The secondary increase in the specific evacuation rate in the region of the molecular-viscous mode may be explained on the basis of simulation concepts of the cryosurface operation, as an ideally evacuating opening, and the subsequent drop in the region of the viscous regime — by diffusion and convection processes [174].

Experimental dependences of the specific evacuation rate of carbon dioxide on the cryosurface (77° K) on pressure (T_g = 300° K) are presented in Figure 4.3.

Composite data of experimental calculation of the evacuation coefficient for a number of gases at different values of T_g and T_s, obtained by Dawson and Haygood /225
[173, 174], Brown and Wang [158], Chubb [166] and others, are presented in Table 24.

Comparison of calculated [by formula (4.5)] and experimental condensation coefficients of certain gases at T_g = 300° K and T_s = 77° K is presented in Table 25. The depth of the potential "hole" of the Lennard-Johnson potential [39] for

TABLE 24 *

COMPOSITE DATA FOR VARIOUS GASES ACCORDING TO THE EVACUATION COEFFICIENT

Gas	Gas temperature T_g, °K	Surface temperature T_s, °K	Evacuation coefficient C
H_2	100	3,5—3,9	1,00
	300		0,9
	500		0,81
	700		0,7
N_2	77	10	1,00
	300		0,67
	400		0,47
	77	15	0,97
	300		0,64
	400		0,47
	77	20	0,87
	300		0,61
	400		0,47
	77	25	0,8
	300		0,61
	400		0,47
Ar	250	3,8	0,998
	350		0,997
	500		0,996
	77	10	1,00
	300		0,68
	400		0,5
	77	15	0,92
	300		0,66
	400		0,47
	77	20	0,78
	300		0,65
	400		0,47
	77	25	0,77
	300		0,65
	400		0,47
CO	77	10—25	1,00
	300		0,88
	400		0,73

Gas	Gas temperature T_g, °K	Surface temperature T_s, °K	Evacuation coefficient C
N_2O	300	10—25	0,62
	400	10—25	0,43
	300	77	0,61
CO_2	195	10	1,00
	300	10	0,73
	195	15	0,95
	300	15	0,63
	400	15	0,51
	195	20	0,9
	300	20	0,66
	400	20	0,44
	195	25	0,83
	300	25	0,62
	400	25	0,46
	300	77	0,62
H_2O	300	77	0,92
NH_3	300	77	0,45
CH_3OH	300	77	1,00
C_2H_5OH	300	77	1,00
CCl_4	300	77	1,00
CCl_3	300	77	0,93
CH_2Cl_2	300	77	0,82
CF_2Cl_2	300	77	0,76
SO_2	300	77	0,74
CH_3Cl	300	77	0,56
CH_3COCH_3	300	77	0,55
O_2	77	20	1,00
	300	20	0,86
	400	20	0,73

*Commas represent decimal points.

Table 25*

CALCULATED AND EXPERIMENTAL VALUES OF CONDENSATION COEFFICIENT

(T_g = 300° K; T_s = 77° K)

Gas	E_0'/R, °K	(Experimental)	(Calculated)	$\frac{C_c'-C_c}{C_c}$
CO_2	213	0,62	0,51	—18%
CH_3OH	507	1,0	0,82	—18%
N_2O	220	0,61	0,52	—15%
H_2O	380	0,92	0,73	—20%
C_2H_5OH	391	1,0	0,73	—27%
CH_3Cl	855	0,56	0,94	+68%
CH_2Cl_4	406	0,82	0,75	—9%
CCl_3	327	0,93	0,63	—32%
CCl_4	327	1,0	0,63	—40%
CF_2Cl_2	345	0,76	0,7	—0,9%

*Commas represent decimal points.

the corresponding gases is taken as E_0'. The differences between them, with the exception of a single case, range between 0.9 - 40%.

As follows from Table 24, the function $C = f(T_g)$ may be arbitrarily divided into three zones. The dependence of C on T_s is slight for two of them (at low and high values of T_g). It is manifested more strongly only for the average temperature range. The determining factor in the region of low values of T_g is the process of particle condensation during primary collision. On the other hand, the determining factor in the range of high values of T_g is the process of particle reflection during primary collisions. Thus, in these temperature ranges, the particles seemingly do not "sense" the cryosurface temperature. A marked dependence of C on T_s is observed only in the moderate temperature range.

Cryosorption. Cryosorption evacuation takes place due to physical and chemical adsorption of gases on special solids (sorbents), cooled to $T_s \leq 100°$ K. Cryosorption may be employed for evacuation of gases whose equilibrium saturation vapor pressre at cryosurface temperatures exceeds the required pressure (or $T_s \geq T_b$).

In the quantitative sense, cryosorption is characterized by the adhesion coefficient C, similar to the condensation coefficient [192].

We shall consider cryosorption mainly from the viewpoint of the possibility /227
of pumping hydrogen, helium and other gases, which are not evacuated with the aid of cryocondensation in practice.

Two methods of cryosorption evacuation are mainly used in vacuum facilities: a) adsorption of gases on metallic films which are cooled and deposited continuously on substrates during the evacuation process; and b) adsorption of gases by cooled porous solids. We also know that in a number of cases, condensed layers of another gas (CO_2, H_2O, etc.) may be used as the sorbent, as well as the pure metal films of vacuum facilities (for example, Cu) [42].

The effective sorption of hydrogen on cryodeposits of nitrogen, oxygen and argon (at $T_s < 10°$ K) is noted in [195]. Yuferov et al. [142, 143] investigated cryosorption of H_2 and N_2 on cryodeposits of CO_2 and other gases in the pressure range of 760 - 10^{-3} torr and 10^{-3} - 10^{-9} torr. Brackman and Fite [154], Hunt [195] and others investigated sorption on presolidified ($T_s \approx 11°K$) gas coatings. Evacuation of gases by deposited metal films at normal and elevated temperatures is /228
accomplished mainly due to chemosorption. An additional mechanism of such a process, as demonstrated by Clausing [167], may be diffusion of the gas being evacuated into a solid cryodeposit and, with sufficient thickness of the latter, solution in it.

The characteristic feature of the process of cryosorption on cooled, deposited films is the continuous renewal of the sorbing surface, due to which such devices do not require regeneration by heating.

When the film is cooled to low temperatures, chemosorption increases due to an increase in the gas-absorption capacity of the film.

The gas evacuated by the cooled films, upon heating of the latter, is partially dissipated, which may indicate the presence of the physical adsorption process along with the chemosorption process during evacuation by the cooled films [192].

Titanium, molybdenum, tungsten, palladium, nickel and other metal films, deposited on metallic substrates cooled to low temperatures, are used as gas absorbers. Titanium films are most widely used. It was established as a result of experimental investigations [103, 37] of hydrogen and nitrogen sorption on

titanium films over a wide temperature range (-195 to -100° C) that hydrogen sorption on a titanium film at room temperature is accompanied by synthesis of methane (CH_4) and other volatile hydrocarbons, whose partial pressures also determine the maximum vacuum of the sorption pump.

When the film temperature is reduced to -195° C, the adhesion coefficient of hydrogen increases four- to fivefold compared to the adhesion coefficient of hydrogen at room temperature; in this case, the chemical reactions which take place to form methane are suppressed, and physical adsorption comprises the basis of the process. The adhesion coefficients of hydrogen on Ti, Mo, Pd, Ni and Ta films, deposited onto a substrate cooled to -195° C, are presented below [192].

Film	Adhesion coefficient of H_2 on Cooled Substrates
Ti	0.21
Mo	0.35
Pd	0.4
Ni	0.17
Ta	0.21

Sorption of N_2, O_2, CO, CH_4 and other gases on renewed sorption surfaces of titanium is quite effective [103]. The adhesion coefficient during sorption on deposited, cooled films decreases in time. This may apparently be explained by the difference in the values of adhesion coefficients measured by different authors (see C_{H_2} = 0.21, above, and C_{H_2} = 0.95, below). The initial values of the adhesion coefficients of certain gases on cooled titanium films are presented below. /229

Gas	Adhesion coefficient (at t = -196° C)
N_2	0.96
O_2	0.98
CO	0.96
CH_4	0.9
H_2	0.95

Sorption of inert gases on freshly deposited titanium at liquid nitrogen temperature is accomplished with very low adhesion coefficients. Therefore, the most effective method for evacuation of inert gases may be cryocondensation at corresponding values of T_s.

The rate of evacuation of titanium pumps decreases as pressure increases (Figure 4.4) [209].

Another widely used method of cryosorption pumping is evacuation of gases on cooled ($T_s \leq 100°$ K) porous solids (of the molecular sieve type) [191, 192] and other sorbents (silica gels, alumogens, etc.).

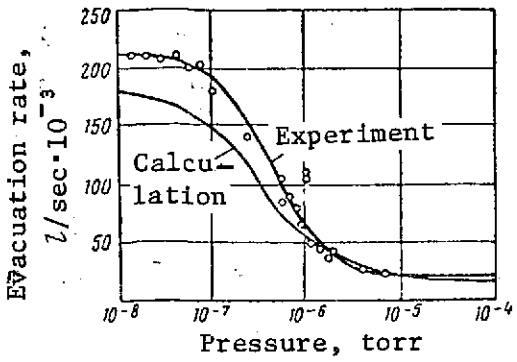

Figure 4.4. Dependence of rate of nitrogen evacuation by titanium sublimation pump on pressure.

Molecular sieves are porous crystals of natural or synthetic minerals (zeolites). The pore dimensions of these crystals are comparable to the dimensions of the gas molecules being evacuated. In this regard, the indicated materials have a well developed specific surface (up to 10^3 m^2/G).

The absorptivity of the sorbent in relation to a specific gas is especially important for the process.

The sorption capacity of molecular sieves for different gases depends mainly on the specific surface of the sorbent. The most widely used sorbents are activitated carbon and zeolite, which have the greatest specific surfaces (close to 10^3 m^2/G).

As indicated by Fedorov [121], the sorption of different gases (H_2, He, Ne, Kr, Ar, etc.) by molecular sieves and other sorbents is possible at temperatures < 100° K. However, the apparent binding energy, due to reasons related to the configuration of the sorbent cell (for example, cylindrical cells, etc.), may in a /230 number of cases exceed the apparent energy of the chemical bond [192]. Therefore, in the given case, comparison of the binding energies may not be a criterion for determining the nature of the adsorption process (physical adsorption or chemosorption).

The effectiveness of cryosorption pumping on sorbents increases as pressure increases. Specific evacuation rates close to theoretical may be achieved at pressures of ~10^{-6} torr and higher.

The maximum vacuum of cryosorption pumps, using cooled porous solids, does not depend on the type of sorbent, but is determined mainly by the type of cryogenic coolant (nitrogen, hydrogen or helium); however, the length of evacuation to the maximum vacuum is considerably dependent on the nature and type of sorbent.

Placement of molecular sieves on cryosurfaces permits evacuation of all residual gases without exception. In this case, it is no longer necessary to use auxiliary pumps.

The adhesion coefficient of hydrogen at $T_s \approx 20°$ K and pressures of $p \approx 10^{-8}$ torr on a surface unprotected by a heat shield is equal to 0.16, and on a shielded surface it is ~1. Consequently, H_2 may be effectively evacuated by cryosorption at a temperature close to its boiling point ($T_b \approx 20°$ K) [210].

Cryosorption may also be used for evacuation of helium. Molecular sieves, cooled to $T_s \approx 4°$ K (i.e., somewhat lower than the boiling point of helium), are used for this purpose. Data are presented in [191] on cryosorption of helium in molecular sieves, cooled to $T_s = 4.2°$ K, with values of the adhesion coefficient of $C_{He} = 0.91 - 0.67$ at pressures of $10^{-7} - 10^{-8}$ torr. However, even at a temperature equal to $T_s^0 \approx 11°$ K, the helium evacuation rate is close to zero [210].

The use of cryosorption pumps as preliminary evacuation pumps is of interest.

Cryosorption surfaces of the second type may be operated in a facility without regeneration for several months.

Cryocapture (cryopumping of gas mixtures). This is incidental evacuation of non-condensible gases during evacuation of condensible gases, making up gaseous mixtures. This process is similar to "embedding" of inert gases in sorption and sputter-ion pumps.

Despite the considerable number of investigations in this field, there are not yet any final conceptions on the mechanism of the cryocapture process.

One of the possible mechanisms of "capture" of a non-condensible gas may be sorption of the molecules of the non-condensible gas in the vessel on the molecules /23 of the condensible gas with subsequent condensation of similar associates. Another possible mechanism may be sorption of the condensible gas on cryodeposits and their subsequent covering by a layer of molecules of the condensible gas, which may lead to embedding of the captured molecules in the mass of the cryodeposit. It is possible that both mechanisms act simultaneously in cryocapture.

The process of cryocapture is quantitatively characterized by the coefficient of cryocapture $C_{i/j}$, which determines the number of captured molecules of the "non-condensible" gas, present per molecule of condensible gas.

The phenomenon of cryocapture has been extensively investigated experimentally. Wang et al. [296], Shumskiy* [138, 139], Bender and Blinov** and others have investigated nitrogen capture upon condensation of water vapor on surfaces cooled to liquid nitrogen temperature. Although it was also discovered experimentally that nitrogen (as well as air) may be evacuated by cryocapture upon condensation of water vapor on surfaces cooled to liquid nitrogen temperature, the efficiency of such evacuation is low ($C_{N_2}/H_2O \approx 10^{-4} - 3 \cdot 10^{-5}$), i.e., the number of water molecules present per captured nitrogen molecule is equal to $\sim 10^4 - 3 \cdot 10^5$, which makes it difficult to accomplish cryocapture of nitrogen by water vapor. Investigations are continuing at present on the cryocapture of nitrogen by water vapor at lower temperatures.

Hydrogen and helium may also be captured on cryosurfaces ($T_s \leq 10°$ K) upon condensation of CO_2.

Hengevoss and Trendelenburg [187] investigated the cryocapture of hydrogen ($T_s = 4.2°$ K). The characteristic feature of this type of capture is the similarity of partial argon hydrogen partial pressures. In this case, it was determined that there is one captured hydrogen molecule per two condensed argon molecules ($C_{H_2/Ar} = 0.5$), while there is one helium molecule per 30 argon ($C_{He/Ar} \approx 0.03$).

Moreover, Hengevoss and Trendelenberg [186] also investigated the condensation of an argon and hydrogen mixture in the range of $T_s = 4.2 - 15°$ K. The results of these experiments indicate that the ratio of the number of captured to the number of condensed molecules decreases exponentially as the cryosurface temperature increases.

The dependence of the adhesion coefficient of carbon upon condensation of argon on a cryosurface at $T_s \approx 4.8°$ K on the ratio of partial pressures p_{H_2}/p_{Ar} is presented in Figure 4.5 [192].

---

*Shumskiy, Bender and Blinov, while investigating the capture of nitrogen molecules, also studied capture of oxygen, argon, hydrogen and helium molecules during condensation of water on surfaces cooled by liquid nitrogen.

**See the collection: Fizika i tekhnika sverkhvysokogo vakuuma (The Physics and Technology of Ultrahigh Vacuum), "Mashinostroyeniye" Press, Moscow, 1968.

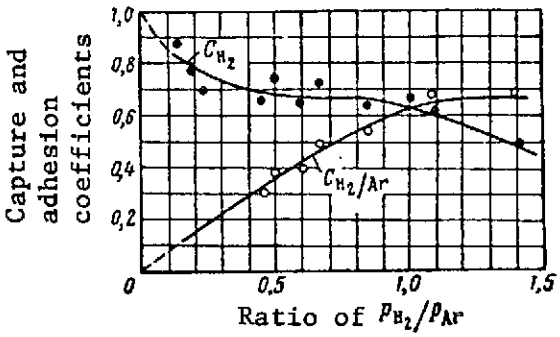

Figure 4.5. The dependence of the adhesion and cryocapture coefficients of hydrogen upon condensation of argon on the ratio of partial pressures of hydrogen and argon.

According to data of Bender and Blinov, the rate of evacuation during cryocapture is linearly dependent on the rate of condensation, and in the pressure range of $2 \cdot 10^{-8}$–$1 \cdot 10^{-4}$ torr, does not depend on pressure. /232 According to these same data, argon is evacuated best of all by cryocapture with the aid of water vapor, then nitrogen and air, and worst of all — oxygen. The rate of cryocapture of helium and hydrogen is very low.

The combination of cryocapture and cryocondensation is apparently a promising method for use in the evacuation systems of vacuum facilities, using internal cryogenic pumping; in this case, the use of auxiliary pumping is no longer necessary.

By creating a system of openings through which the vapor being condensed on the cryosurfaces is introduced into the facility, cryocapture of non-condensible gases may be accomplished. Such a facility permits "oilless" pumping and elimination of excessive condensation of gases on cryosurfaces cooled by helium.

Thus, Haygood et al. [184], and also Tseytlin and Falalayev [131], on the basis of the cryocapture phenomenon, developed so-called "cold" diffusion pumps.

The cryopump. Cryopumping is accomplished by devices which contain surfaces, cooled to temperatures ≤ 100° K. These devices are called cryopumps. Cryopumps may be condensation, sorption, and mixed types.

Schematically, a cryogenic pump is two parallel surfaces, one of which — the "hot" one — gives off gas, and the other, cooled to a low temperature, is the condenser. However, it is irrational to design such a simple layout due to the high consumption of coolant with a high heat input to the surface being cooled as a result of thermal radiation from the "hot" surface.

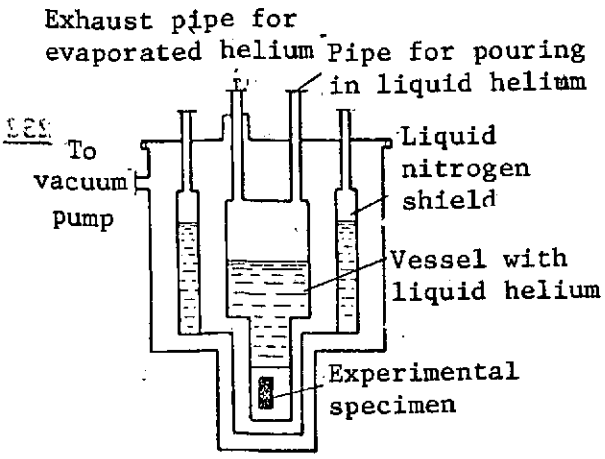

Figure 4.6. Diagram of cryocondensation pump.

There is a critical specific heat flux for every low-boiling liquid, at which the bubbling of the liquid changes to film boiling, which considerably deteriorates the heat transfer process. A gas bubble forms between the solid wall and the liquid, and wall temperature increases sharply. The value of critical heat flux is approximately equal to: /233

$Q_{\Sigma N_2} \approx 1 - 2$ W/cm^2 for liquid nitrogen

$Q_{\Sigma H_2} \approx 4 \cdot 10^{-2}$ W/cm^2 for liquid hydrogen;

$Q_{\Sigma He} \approx 4 \cdot 10^{-4}$ W/cm^2 for liquid helium.

Therefore, in order to reduce the heat fluxes from the object to the cryosurface to critical values, the cryosurface is shielded by surfaces cooled to liquid nitrogen. Because of this, the consumption of low-boiling liquid is decreased, which determines the demands made on the cooling system.

The working principle of a cryopump, having a cooled condensation surface and heat shields, is depicted schematically in Figure 4.6. An additional effect of the shield is that the gas molecules, which are not evacuated by the shield, acquire a temperature of ~100° K after repeated collisions with the shield, which facilitates their subsequent evacuation by the cryosurfaces. The molecules of the gas being evacuated may penetrate to these cryosurfaces along the channels in the cryolattices.

The screening factor of thermal radiation β is also introduced [11] for the characteristics of the cryolattices, besides the evacuation coefficient C.

The cryosorption panels are stainless steel or aluminum plates, on the surface of which a thin layer (from 1.5 to 3 mm) of zeolite is applied by sputtering. A coil, through which is pumped "cold" (~20° K) gaseous or liquid (4.2° K) helium, is soldered to the opposite side of the panel. The panels are made in a single piece for large facilities (Figures 4.7 and 4.15).

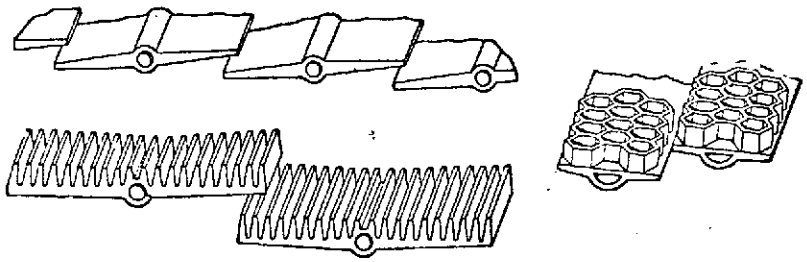

Figure 4.7. Various types of cryolattices.

In order to protect the cryosurfaces against condensation of undesirable gases (nitrogen, oxygen, etc.) on them, the panels should be shielded by surfaces cooled /234 to 20° K, and the latter, in turn, by surfaces cooled to 100° K, with the double shields forming cryolattices. As a result, the molecules of the gas being evacuated (for example, nitrogen) are cooled upon collision with the cryolattice shields, as a result of which the adhesion coefficient of hydrogen increases to a value close to unity [210].

Consequently, the principal characteristics of cryopumps are the effective evacuation coefficient C_e and the thermal radiation screening factor β.

The evacuation coefficient, which determines the nature and state of the gas being evacuated and the cryosurface (T_g, T_s, etc.), is related to a plane surface, and the effective evacuation coefficient, which determines the geometry of the cryolattice, is related to the complex three-dimensional structure of the cryolattice. For example, according to Moore et al. [233], the effective evacuation coefficient (sometimes called the capture probability) for a herringbone type cryolattice is equal to:

$$C_e = w_s \left\{ \frac{1 - 2(1 - w_c)(1 - C) + (1 - w_c)^2 (1 - C)^2 - w_c^2}{1 - (1 - w_c)(1 - C)(2 - w_s) + (1 - w_s)^2 (1 - C)^2 - w_c^2} \right\}, \tag{4.10}$$

where C_e is the effective evacuation coefficient of the cryolattice;

C is the evacuation coefficient for a plane cryosurface;

ω_s is the probability of penetration of the molecules being pumped through the herringbone radiation shields into the cavity being evacuated;

ω_c is the probability of penetration of molecules through the cryosurface.

It follows from Formula (4.10) that C_e is a function of the cryosurface evacuation coefficient, as well as of the configuration of the cryolattice elements.

Some similar designs of cryolattices, suggested by Santeller et al. [250], for condensation pumps, as well as the principal characteristics of the indicated cryolattices, calculated on a digital electronic computer using the Monte Carlo method, /236 are presented schematically in Table 26 and in Figure 4.7. The schematic working principle of the cryolattice of a sorption pump is presented in Figure 4.12.

The cryodeposit. The condensation of gases on cryopanels and shields causes formation of a cryodeposit on them. The presence of the cryodeposit changes (usually by reducing) the absorption capacity of the cryolattice surfaces.

Variation of the absorption capacity of the cryolattice surfaces, facing the test spacecraft, acts on the thermal balance of the latter, which is being investigated in the facility. This pertains to the shields cooled with liquid nitrogen, since those cooled with liquid or gaseous "cold" helium do not "see" the test object.

The cryodeposit on shields cooled with liquid nitrogen consists mainly of water, carbon dioxide and organic materials, as well as sublimating materials, which impinge on these panels due to recondensation from the surfaces of the test object and from the components of the facility.

The radiation characteristics of the "deposit — wall" system depend on the nature, thickness and structure (crystalline, amorphous, porous, solid, etc.) of the cryodeposit, as well as on the initial radiation characteristics of the substrate-wall.

As the thickness of the cryodeposit increases, the absorption capacity of the "deposit — wall" system decreases from 0.98 - 0.95 to 0.8 - 0.7 due to partial absorption and reflection of the incident radiation. However, this variation is typical only for relatively thin (thickness to 0.8 - 1 mm) deposits; as the thickness of the deposit further increases, the absorption capacity of the system hardly changes. In view of the fact that the cryodeposit has a selective absorption capacity, typical for dielectrics, the spectral characteristics of the reflected radiation also change.

TABLE 26*

TYPES OF CRYOLATTICES AND THEIR PRINCIPAL CHARACTERISTICS

/235

Plane closed Lattice 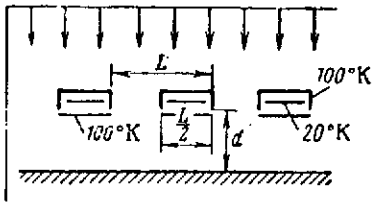 Chamber walls	$\frac{d}{L}$	16	25	50
	C_e	0,16	0,21	0,23
	$\beta = \frac{Q_t}{Q_i A_s}$	0,009	0,014	0,015
Plane open Lattice 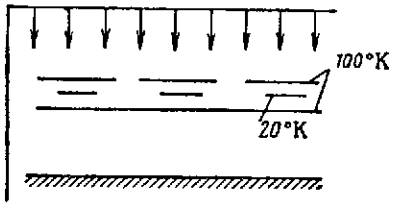 Chamber walls	$\frac{R_1}{R_2}$	63	52	31
	C_e	0,30	0,34	0,44
	$\beta = \frac{Q_t}{Q_i A_s}$	0,017	0,017	0,016
Herringbone lattice 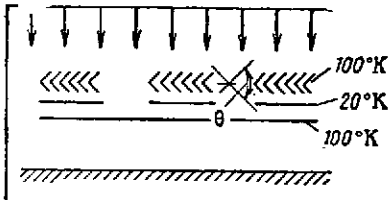 Chamber walls	$<\theta$	60	90	120
	C_e	0,44	0,48	0,52
	$\beta = \frac{Q_t}{Q_i A_s}$	0,020	0,022	0,022
Santeller lattice 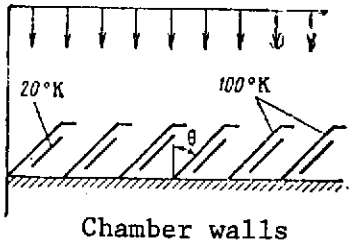 Chamber walls	C_e	0,51	—	—
	$\beta = \frac{Q_t}{Q_i A_s}$	0,031	—	—
	$<\theta$	45°	—	—

*Commas represent decimal points.

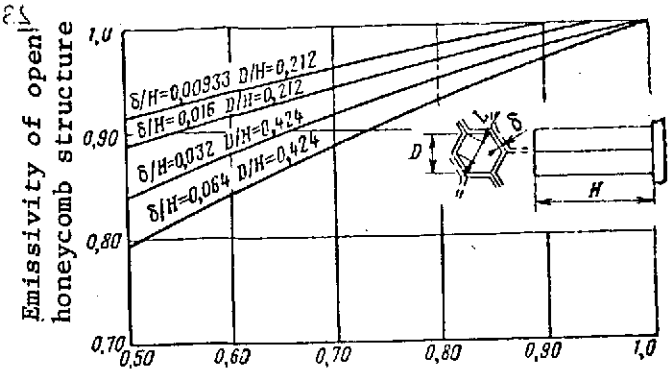

Figure 4.8. Dependence of the emissivity of honeycomb surfaces on the emissivity of a local plane surface.

The effect of the nature and structure of the cryodeposit is manifested mainly due to the fact that the microroughnesses of the deposit act as centers for diffusion of the incident radiation. In order to reduce the effect of the cryodeposit on the absorption capacity of the facility walls, the surfaces of the cryopanels are sometimes structurally executed in the form of open honeycomb structures, which permits high integral values of the absorption capacity of the entire surface to be obtained at relatively lower values of the absorption capacity of the local surfaces (Figure 4.8).

The cryodeposit on helium-cooled surfaces consists mainly of solid nitrogen, oxygen and hydrogen. The main problem here is to keep the given temperature of the cryosurface constant.

In order to determine whether the growth of the cryodeposit acts as one of the possible causes of the indicated phenomenon, let us estimate the thickness of a cryodeposit of solid nitrogen, required to raise the temperature of the cryopanel by 1° K. /237

Considering the idealized process of cryodeposit growth with a structure uniform in thickness [218], we may assume that the temperature decreases linearly through the mass of the cryodeposit:

$$T_s = T_0 + \delta \frac{Q_t}{\lambda'}, \tag{4.11}$$

where T_s is the surface temperature of the cryodeposit in °K;

T_0 is the cryosurface temperature in °K;

δ is the thickness of the cryodeposit in cm;

λ' is the coefficient of thermal conductivity of the cryodeposit in joules/cm·sec·°K;

Q_t is the specific heat flux on the cryosurface $T_s \simeq 20°$ K.

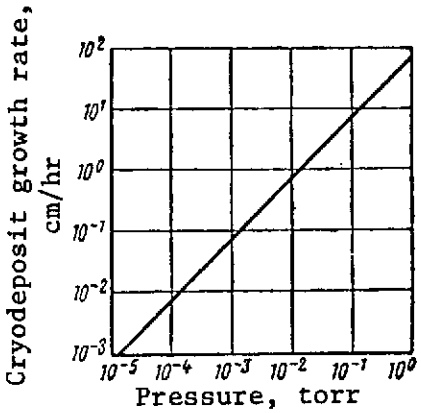

Figure 4.9. Dependence of cryodeposit growth rate on pressure.

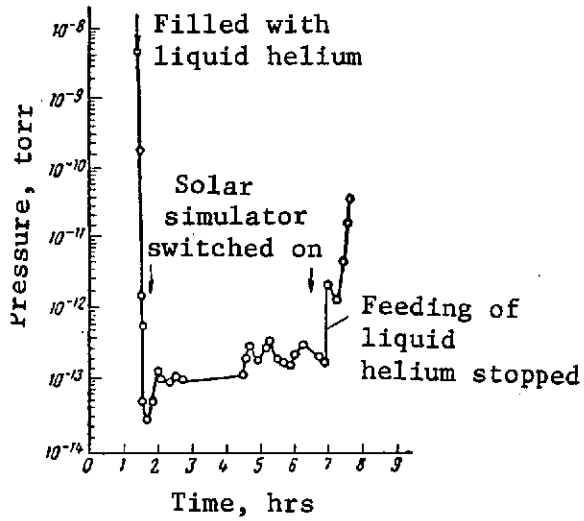

Figure 4.10. Variation of pressure in a vacuum facility under different operating conditions (Lewis Center,NASA).

To calculate the thickness of the layer, let us assume the following data: $Q_i \approx 0.14$ W/cm ; $A_s = 0.2$; $\beta = 0.031$ [a cryolattice of the Santeller type (see page 238)]; $\Delta T = T_s - T_0 = 1°$ K and $\lambda_{N_2} = 1.67 \cdot 10^{-3}$ joules/sec·cm·°K [90].

Hence, the thickness of the deposit, which causes the temperature to be raised by 1° K, is equal to:

$$\delta \approx \frac{\lambda' \Delta T}{Q_i A_s \beta} \approx \frac{1.67 \cdot 10^{-3}}{0.14 \cdot 0.2 \cdot 0.031} \approx 2 \text{ cm},$$
$$\beta = \frac{Q_i}{Q_i A_s}, \qquad (4.12)$$

where β is the screening factor of thermal radiation;

Q_i is the specific heat flux on the cryosurface (77° K);

A_s is the absorbance of the cryosurface (20° K).

Let us assume that the pressure in the facility is equal to $\sim 10^{-5}$ torr and, in accordance with the dependence of the deposit growth rate on pressure [218] (Figure 4.9), the growth rate is equal to $2 \cdot 10^{-3}$ cm/hr.

Consequently, to obtain such a layer, even with evacuation at $C \approx 1$, $\sim 10^3$ hours are required, which exceeds the possible duration of continuous operation of the facility.

It may be concluded from the foregoing that deposition of a cryodeposit on helium-cooled panels is not an appreciable limitation for operation of facilities.

4. Design Characteristics of Vacuum Facilities

Let us consider the schematic arrangement and certain design characteristics of simulators.

The vacuum system. The arrangement of a small unheated facility (a cryopump), designed on the basis of a cryostat for liquid helium [12] and intended for obtaining pressures of $< 10^{-12}$ torr, is presented schematically in Figure 4.6.

A small facility of a similar type (available capacity of ~0.2 m^3), equipped with a solar simulator, in which a maximum vacuum of $2 \cdot 10^{-14}$ torr is achieved, measured with the aid of a Lafferty and Redhead type manometer (Figure 4.10), is described in [226].

The National Research Corporation (USA) has created a small facility for space environment simulation in which pressures of $\sim 10^{-12} - 10^{-14}$ torr have been obtained [230].

The facility is constructed by placing one chamber inside another and evacuating each chamber with an independent high-vacuum pump, which ensures that an ultrahigh vacuum will be achieved in the inner chamber with the gas-tightness of each of the chambers which can be achieved in practice. /239

The cross section of this facility is depicted schematically in Figure 4.11. The main inner chamber is evacuated to pressures of $\ll 10^{-10}$ torr ($\sim 10^{-12} - 10^{-14}$ torr).

The facility contains so-called intermediate walls which partially shield the main inner chamber.

There is only a single opening for evacuation of residual gases in the inner chamber, in which the greatest rarefaction is achieved. The cooled intermediate walls, surrounding the inner chamber, form an intermediate space by which the path of gas evacuation from the inner chamber is extended, and the probability of gas condensation on the inner surfaces of the intermediate walls is increased.

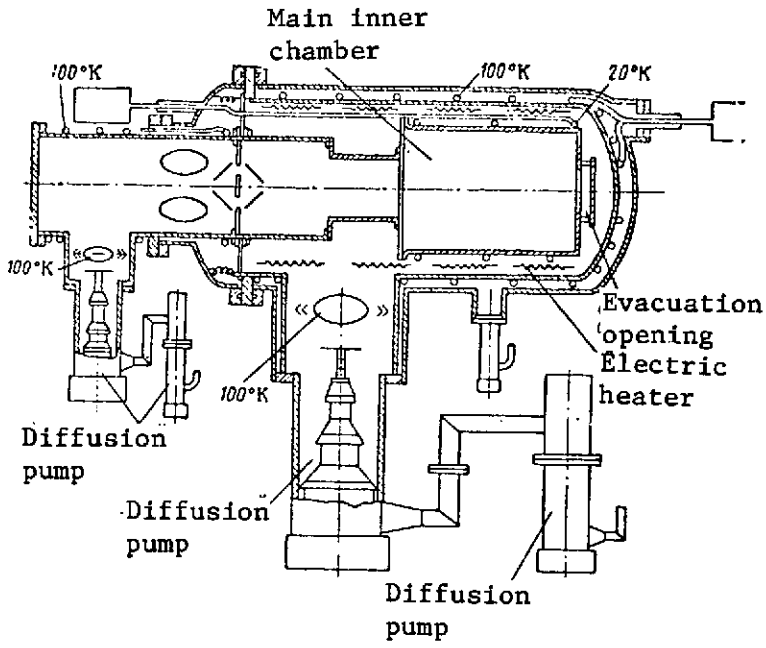

Figure 4.11. Schematic diagram of ultrahigh vacuum facility of the National Research Corporation.

A high-vacuum oil-diffusion pump, intended for evacuation of non-condensible gases, is located on the opposite side of the evacuation opening. Because of the long evacuation path, it is difficult for volatile by-products to reach the inner chamber by counterflow from the diffusion pump.

The surface of the inner chamber may also condense volatile gaseous by-products. /240 Consequently, in this case a dual condensation effect is accomplished which contributes to lower pressures in the inner chamber.

The intermediate walls should also be cooled with liquid nitrogen. They not only condense some gases, but also shield the main portion of the walls of the inner chamber.

Heaters are provided for preheating the inner walls.

The intermediate chamber is made of metal or other heat-resistant materials having low outgassing. Elastomers are used only as packing for the two parts of the outer chamber. The gases given off from them are evacuated by the pump of the outer chamber and do not reach the inner chamber.

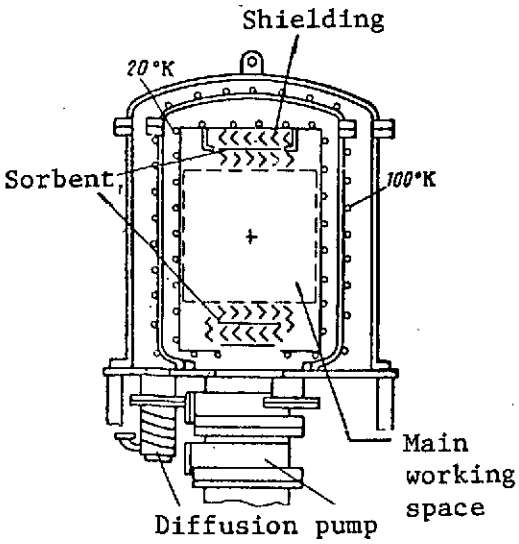

Figure 4.12. Schematic diagram of cryosorption pump.

The characteristic feature of the facility is the presence of outer walls as well, which are arranged such that the chambers formed by these walls are separated, and direct access to the inner chamber is possible only through the evacuation opening.

The inner chamber is rigidly connected and supported by a cantilever with the aid of an empty vacuumized pipe, which is hermetically sealed with respect to the inner chamber. The pipe is cooled to liquid nitrogen temperature and has a section connected to the inner chamber by the walls. The intermediate walls, forming the intermediate chamber, have two sections: one connected to the outer chamber and the other — to the inner chamber.

A facility has been prepared at NASA's Goddard Space Center in which pressures $< 10^{-12}$ torr have been achieved with the aid of cryosorption pumps. The cryosorption pump consists of aluminum panels with a sorbent of the molecular sieve type applied, cooled by gaseous helium, and also consists of double herringbone shields, also cooled by gaseous helium. Moreover, the facility contains shields cooled by liquid nitrogen (Figure 4.12).

A facility with a working space of ~10 m^3 is described in [261]. The facility differs from other similar facilities by the high degree of particle capture on the walls, equal to 99.97% (which corresponds to a collision coefficient equal to $3 \cdot 10^{-4}$).

Structurally, it consists of two spheres divided by a vacuum: the outer sphere is the power shell of the facility (Ø 3 m, carbon steel) and the inner sphere is pressurized (Ø 2.5 m, stainless steel). The inner sphere forms the working cavity of the facility. These cavities are connected to each other with the aid of a special valve.

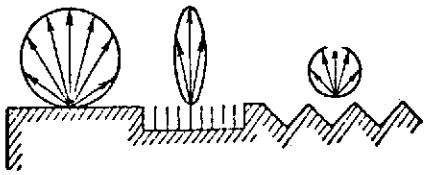

Figure 4.13. Projection diagrams of desorbed molecules for different surface configurations.

The inner sphere is made of sheet aluminum in the form of corrugated wedge-like ribs (Figure 4.13), to which are welded pipes in which "cold" (20° K) gaseous helium circulates. Titanium is continuously sputtered onto the /24 cooling surface of the ribs with the aid of an electron gun. This configuration ensures a high evacuation coefficient.

Main evacuation of the facility is accomplished by cryogenic (condensation and sorption), as well as by oil-diffusion pumps; and preliminary evacuation — by turbomolecular and cryosorption pumps.

The combination of corresponding vacuum pumping and rational geometry of the traps permits a low collision coefficient to be obtained in this facility. The calculated hydrogen evacuation rate by the main evacuation pumps in the facility is equal to $7 \cdot 10^6$ ℓ/sec. The facility is designed so that it may be easily dismantled with the aid of a hydraulic screw jack for cleaning, which is accomplished by blowing out the inner surface with glass sand.

The General Electric Company (the Missile and Spacecraft Division) has constructed three large simulators at Valley Forge, California. The "Mariner," "Telstar," "Nimbus," and other spacecraft were tested in these facilities [213].

The main characteristics of the vacuum and cryogenic systems of these facilities are presented below:

Volume:

- Total . . . . . ~1250 m^3
- Net . . . . . ~850 m^3

Dimensions of vacuum chamber:

- Diameter . . . . . 9.75 m
- Height . . . . . 16.46 m

Maximum vacuum . . . . . $5 \cdot 10^{-10}$ torr

Evacuation rate (at $1 \cdot 10^{-6}$ torr):

Nitrogen . . . . . $3.4 \cdot 10^{6}$ l/sec

Water vapor . . . . . $4.2 \cdot 10^{7}$ l/sec

Non-condensible gases . . . . $1.5 \cdot 10^{4}$ l/sec

Maximum thermal load in chamber

from object . . . . . 150 kW

Rate of cryogenic coolant circulation in cooling systems of facility:

Liquid nitrogen . . . . . ~5 m^3/min

Gaseous helium . . . . . ~320 kg/hr

Refrigerating capacity of auxiliary cyogenic facilities:

Nitrogen facility . . . . . ~300 kW

Helium facility . . . . . ~2.4 kW

Main evacuation of the facility is accomplished by cryogenic pumps; auxiliary evacuation — by high-vacuum oil-diffusion pumps, and preliminary evacuation — by mechanical prevacuum pumps.

The walls of the facility in the upper section are lined on the inside with blackened aluminum panels, through which liquid nitrogen is pumped.

Another group of plates in the lower section of the facility, which are cooled by "cold" (20° K) gaseous helium, serves for evacuation of residual gas molecules.

Besides the vacuum conditions of space, solar radiation is also simulated in the facility.

The Boeing Company has constructed a more modern large facility for space vacuum simulation, designed for testing the "Lunar Orbiter" and "Surveyor" spacecraft [209]. Unlike the facilities of the General Electric Company, evacuation in the Boeing facility is accomplished by "oilless" means. The facility is shaped like a vessel of almost spherical shape (Ø 12 x 15 m). Main evacuation is accomplished by a helium cryopump. The inner cavity is a sleeve cooled by liquid nitrogen, in which are installed cryopanels, cooled by "cold" (15° K) gaseous helium (Figure 4.14).

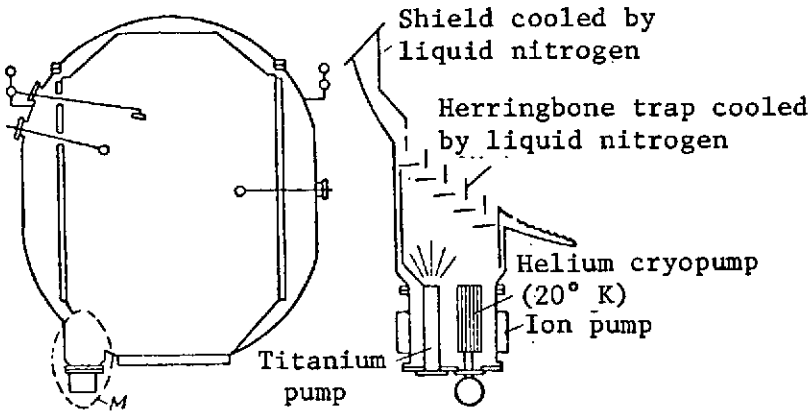

Figure 4.14. Schematic diagram of Boeing facility.

External evacuation was previously accomplished by three oil-diffusion pumps with a total (air) evacuation rate of ~200,000 l/sec. This permitted testing small spacecraft without use of the helium cryopump for main evacuation.

These auxiliary pumps for external evacuation were recently replaced with two compartments containing titanium sorption, cryogenic and magnetic-discharge pumps. The (air) evacuation rate of these pumps was equal to ~200,000 l/sec. Argon evacuation at a rate of $1.5 \cdot 10^4$ l/sec is accomplished by two cryopumps (20° K). Helium /243 is evacuated by a diode magnetic-discharge pump (evacuation rate of ~2000 l/sec), which may also evacuate traces of any gases not evacuated by the other pumps. The arrangement of one of the compartments is depicted schematically in Figure 4.14.

The facility is preliminarily evacuated in sequence by connected mechanical pumps through a trap cooled by liquid nitrogen. The cooled trap is also a surface onto which titanium is sputtered.

The principal characteristics of the vacuum and cryogenic systems of the facility are presented below:

Volume:

Total . . . . . ~1500 m^3

Net . . . . . ~1000 m^3

Dimensions of vacuum chamber:

Diameter . . . . . ~12 m

Height . . . . . ~15 m

Maximum vacuum . . . . . $\sim 10^{-9}$ torr

Evacuation rate (at $1 \cdot 10^{-6}$ torr):

Nitrogen (main) . . . . . $2 \cdot 10^{6}$ l/sec

Nitrogen (auxiliary) . . . . $2 \cdot 10^{5}$ l/sec

Argon (auxiliary) . . . . . $1.5 \cdot 10^{4}$ l/sec

Refrigerating capacity of helium facility for main evacuation (20° K) . . . . . 1.2 kW x 2 = 2.4 kW

The advantages of this facility, besides the presence of an "oilless" evacuation system, is reduction of evacuation time by 6 - 8 hours in each test cycle, high operational reliability, and a considerable reduction of operating costs.

Let us estimate (approximate calculation) the evacuation rates of this facility /244 [209]. Let us take the following as initial data for the calculation:

Working pressure in the facility is $p = 5 \cdot 10^{-7}$ torr;

Gas load $q = 10^{-1}$–1 $l \cdot$torr/sec, depending on the dimensions of the test spacecraft (according to data of [261], the specific gas load of the object is $\sim 10^{-5}$ $l \cdot$torr/cm$^2 \cdot$sec);

The minimum rate required for evacuation is:

$$S_1 = \frac{10^{-1}}{5 \cdot 10^{-7}} = 2 \cdot 10^5 \ \ l/\text{sec};$$

The maximum rate required for evacuation is:

$$S_2 = \frac{1}{5 \cdot 10^{-7}} = 2 \cdot 10^6 \ \ l/\text{sec}.$$

The evacuation system of the facility is assumed to be "oilless." At low gas loads (up to $q \leq 10^{-1}$ $l \cdot$torr/sec) the facility is evacuated by a system of auxiliary evacuation pumps, which include a titanium sorption pump (azotite), a magnetic discharge pump, and a small helium (20° K) cryopump. At high gas loads ($q \leq 1$ $l \cdot$torr/sec) main evacuation of the chamber is accomplished by a helium cryopump (20° K)

system and a system of auxiliary evacuation pumps, which are employed in this case for evacuation of "non-condensible" gases (helium, neon, hydrogen, etc.).

Let us calculate the area of the cryosurface (20°), taking the Santeller cryolattice as a basis (see page 238). The effective evacuation coefficient for the selected type of cryopanel (at $\angle\ \theta = 45°$) $C_e = 0.51$. For air we may assume that the condensation coefficient at 20° K is $C_c \approx 0.9$ (see page 227).

The area of the helium cryopanels is equal to:

$$F = \frac{S_2}{S_{max} C_e} = \frac{2 \cdot 10^6}{5.9 \cdot 0.51} \approx 6.7 \cdot 10^5 \text{ cm}^2 \approx 67 \text{ m}^2.$$

The surface of the helium cryopanels is assumed to have a reserve equal to 85 m^2.

Let us calculate the required helium evacuation rate. We assume that the main source of helium is the leakage in the cryopanels. The extent of leakage is determined by the greatest sensitivity of the leak detector ($q \approx 10^{-9}$ l•torr/sec). For reliability, this value is multiplied by 100.

The required helium evacuation rate at a maximum vacuum of the facility ($\sim 10^{-9}$ torr) is equal to:

$$S_{He} = \frac{10^{-7}}{10^{-9}} \approx 100 \ l/\text{sec}.$$

For helium evacuation, let us use a sputter-ion pump with an evacuation rate of S = 200 l/sec for helium, taking the fact into account that neon must also be evacuated.

For evacuation of hydrogen during operation of the main cryopumping system, /245
and also for evacuation of air only during operation of the auxiliary system, we shall use a titanium sorption pump (azotite). The titanium pump should provide an evacuation rate of $S_{Ti} = 2 \cdot 10^5$ l/sec.

The titanium is sputtered onto a surface cooled by liquid nitrogen. Let us calculate the required area of this surface:

$$F = \frac{S_{Ti}}{S_{max} C},$$

where S_{max} is the theoretical surface evacuation rate for air (in accordance with Table 24), equal to ~ 11.15 l/sec.

We shall assume the adhesion coefficient to be equal to C ≈ 0.2.

Then

$$F_{Ti} = \frac{2 \cdot 10^5}{11.16 \cdot 0.2} \approx 10^5 \text{ cm}^2 \approx 10 \text{ m}^2.$$

Let us calculate the required evaporation rate of titanium on the basis that there must be 10 titanium atoms per one sorption atom or molecule of the gas being evacuated.

The sputtering rate of metal at a gas load of q = 0.1 l•torr/sec is equal to:

$$q_{Ti} = \frac{0.1 \cdot 3 \cdot 10^{19}}{3.5 \cdot 10^{18}} \cdot 10 \approx 10 \text{ G/sec}$$

$$\left(1 \frac{\text{G}}{\text{hr}} = 3.5 \cdot 10^{18} \frac{\text{atoms Ti}}{\text{sec}}\right)$$

Since the titanium pump barely evacuates Ar, the helium cryopump for auxiliary evacuation is used for evacuation of this gas.

Let us calculate the required evacuation rate for argon. The evacuation rate (for air) for the titanium pump is equal to ~$2 \cdot 10^5$ l/sec. Since the atmosphere contains ~1% argon, the argon evacuation rate should be equal to S_{Ar} ~ $2 \cdot 10^3$ l/sec.

Let us calculate the cryosurface required for this evacuation, assuming that at T_s = 20° K, C_{cAr} ≈ 0.5 (see Table 24).

Let us assume a reserve of F ≈ 1000 cm^2 ≈ 0.1 m^2. A refrigerating capacity of the refrigerator of ~1 W is sufficient for cooling such a cryopanel surface to 20° K.

The small refrigerator is switched on only when the helium cryopump for main evacuation is not operating.

Thus, in the case of small loads of q = 0.1 l•torr/sec, evacuation is accomplished at a rate of $2 \cdot 10^5$ l/sec by the titanium, magnetic discharge and cryogenic pumps for auxiliary evacuation. In the case of high gas loads, main evacuation ($S \approx 2 \cdot 10^6$ l/sec) is accomplished by the main helium cryopump ($F_{He} \approx 200$ m^2), and /246
auxiliary evacuation of the non-condensible gases, helium and hydrogen ($S_{He} \approx 2 \cdot 10^2$ l/sec and $S_{H_2} \approx 2 \cdot 10^5$ l/sec) — by the titanium magnetic discharge pumps.

All the facilities described previously were designed for testing so-called "cold" objects ($T_s \approx 300°$ K). Facilities are also being operated at present which are designed for testing so-called "hot" objects, whose surface temperature considerably exceeds 300° K.

A vacuum facility is described in [237], which is designed for testing a closed high-temperature liquid-metal profile ($T_s \approx 1315°$ C). The facility produces a working pressure of $1 \cdot 10^{-7}$ torr and performs continuous testing for ~10,000 hours.

The body of the facility has a cylindrical shape (Ø 1.80 m and H ≈ 3.65 m). The cylindrical portion is constructed of sheets of carefully polished stainless steel, welded in sections. The vacuum system includes four diffusion and mechanical pumps, used to create a prevacuum up to $\sim 10^{-4}$ torr. The facility is equipped with a water cooling system, calculated to draw off approximately 7500 kcal/hr, which permits the external surface temperature of the facility wall to be maintained at ~65° C during tests of high-temperature profiles. The external surface of the facility is heat-insulated with the aid of a layer of fiberglass and asbestos 63.5 mm thick. These characteristics are the main differences between facilities for testing "hot" objects from those for testing "cold" objects.

When the facility is started up, primary heating of the test profile up to 1400° C is accomplished with the aid of electric heaters within 6 hours at a rated input of 30 kW. The maximum vacuum of $\sim 1 \cdot 10^{-8}$ torr is achieved within 24 hours. Pressures are recorded with the aid of a mass spectrometer.

Thus, the experiments confirmed the possibility of creating facilities for testing "hot" objects, which create a pressure of $1 \cdot 10^{-7}$ torr without resorting to cryogenic pumps and cooling of walls to cryogenic temperatures for such cases.

The structure of the facility [199] and its dimensions are usually determined by the dimensions of one or several types of spacecraft, intended for investigation, as well as by the dimensions of the simulators and auxiliary devices.

The material for manufacturing the facility is selected on the basis of the characteristics of strength, interaction with cryogenic liquids, and outgassing. The shape of the body is usually either spherical (which is preferable) or cylindrical with hemispherical covers. The body of the facility is made of low-carbon stainless steel 15 - 25 mm thick.

The body should conform to the standards provided for the manufacture of vacuum /247 vessels, which require strength tests after welding under a pressure of ~1.5 atm. The body is usually made of separate shaped sections by subsequent straightening and welding. All welded seams should be subjected to 100% control, including X-ray inspection.

All internal surfaces of the facility body should be carefully polished to reduce heat exchange with the cryosurfaces. The detachable sections are usually sealed to reduce leakage with the aid of double circular rings with the space between them evacuated.

The vacuum systems provide the given evacuation rates and low pressures with the aid of pumps for main, auxiliary (diffusion, electrophysical and cryogenic pumps) and preliminary evacuation.

The pumps should be selected on the basis of the requirements for reducing the pressure in the facility from $\sim 10^{3}$ to $\sim 10^{-6}$ torr within several hours. In this case, the pressure in the facility without the object is usually reduced with the aid of the pumps only for auxiliary evacuation to $5 \cdot 10^{-6}$ torr within 5 - 6 hours, including pressure up to $\sim 10^{-2}$ torr within 0.5 - 1 hour.

Total (air) leakage of a facility with a volume of $\sim 10^3$ m^3 should be on the order of 10^{-4} $l \cdot$torr/sec [199].

The specific gas load of the object should usually be on the order of $\sim 10^{-5}$ $l \cdot$torr/$cm^2 \cdot$sec [261], which includes both leakage from the cavities of the object, under excess pressure, and outgassing of the surface sections of the test spacecraft.

The composition of outgassing from the test object will be different for each object and should be preliminarily estimated prior to testing a spacecraft in the facility.

The cryogenic system. It consists of the nitrogen and helium subsystems. The nitrogen subsystem provides for simulation of the spacecraft radiant energy absorption by space, and also accomplishes cryopumping of water vapor, carbon dioxide, and other gases. The helium subsystem accomplishes cryopumping of nitrogen, oxygen, and other gases.

Structurally, the subsystems inside the facility are made in the form of cryopanels which should essentially enclose the test object completely. The cryopanels, cooled by liquid nitrogen, should be designed to receive a maximum thermal load in that section of the facility in which they are located [189].

For example, the panels located directly opposite the solar simulator are usually designed to maintain a temperature of ~100° K and should handle up to $2 \cdot 10^3$ W/m^2 of direct "solar" radiation, as well as an additional thermal load equal to ~330 W/m^2.

This additional load consists of the "solar" radiation reflected from the spacecraft, the albedo and the "Earth's" natural radiation, as well as the thermal /248 load of the elements of the facility, equal to ~40 W/m^2. The cooling pipes should be arranged so that the consumption of coolant in each section of the facility is proportional to the incident heat flux. This is solved by a denser arrangement of the cooling pipes at the points of highest load or by increasing the diameter of the pipes for increased flow rate of the coolant.

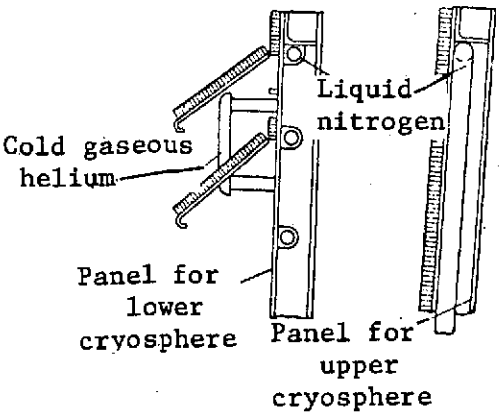

Figure 4.15. Structural diagrams of cryolattices.

There are two types of cryopanel designs. The first (Figure 4.15, on the right) — arbitrarily flat — is operated at temperatures of ~100° K, cooled by liquid nitrogen and has a high absorption capacity (~0.95 in the range of wavelengths from 0.3 to 2.7 microns).

The second (Figure 4.15, on the left), unlike the first, contains ribs arranged at an angle of 45° to the panel surface for shielding the surfaces cooled by "cold" (20° K) gaseous helium.

The diameters of the pipes for pumping liquid nitrogen are usually taken as equal to 25.4 mm, and those for pumping gaseous helium are ~19 mm. The panels are made in the form of sections (1.2 x 3.3 m) of aluminum alloy up to 3 mm thick, with a high Al concentration (99.5%). These panels are either irregularly shaped, containing different profiles on the front section and channels for pumping the coolant in the mass, or in the form of flat plates, to the reverse side of which are welded pipes for pumping coolants (Figure 4.7). Honeycomb surfaces are welded along the entire nominal surface of the front section of the flat panels to ensure the best simulation of "black" space. The reverse sides of the panels facing the walls of the facility should have a relatively high reflectivity.

The liquid nitrogen supply. The circulation of liquid nitrogen under pressure, which is preferred in view of the fact that this scheme prevents effervescence of nitrogen into the main lines, is depicted schematically in Figure 4.16. The feed line is connected to the vessel containing liquid nitrogen (the tank), located near (~0.9 - 1 m) the facility, with the aid of three-inch pipes and a collector. Further, the feed line is divided into a number of pipes of lesser diameter, passing inside the facility through the panels and then directed to the drain line, which is also connected to the tank by three-inch pipes.

The rate of liquid nitrogen circulation in the pipes usually varies from 0.5 to 5 m/sec at pressures up to 10 - 12 kgf/cm^2 and an average temperature of ~80° K in the feed line (an increase of temperature in the cryopanel system of ~1° K). The

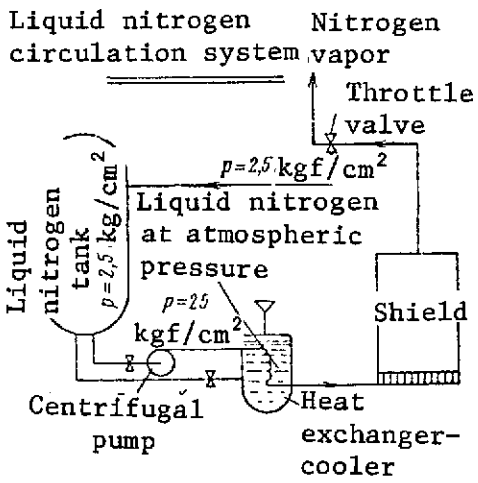

Figure 4.16. Schematic design of liquid nitrogen circulation under pressure.

pressure in the drain line is ~6 - 7 kgf/cm^2, and the temperature ranges up to 93° K. The pressure in the tank is maintained at ~2 kgf/cm^2.

The pipes are made of stainless steel /249 or, in the case of irregularly shaped panels, of aluminum alloys (Al ≈ 99.5%). The diameter of the major pipes is ~76 mm, and the wall thickness is ~2.1 mm. The diameter of the distribution pipes of the panel is ~25.4 mm, and the wall thickness is ~1.6 mm.

The pressure drop in the liquid nitrogen line reaches ~3 kgf/cm^2 and the temperature increase reaches 13° K. Since the temperature of liquid nitrogen at ~7 kgf/cm^2 is equal to ~98° K, the difference between the highest liquid nitrogen temperature and its boiling point at a given pressure reaches $\Delta T = 5°$ K. This temperature difference prevents local effervescence of the nitrogen in the main line. Consequently, the nitrogen circulates in the evaporator only in liquid form, which improves the conditions for heat exchange.

The pressure drop in the feed pipes, valves, and other assemblies reduces this reserve.

The hydraulic resistance (in the case of the circulation of liquid nitrogen alone) consists of friction (Δp_f) and local drag (Δp_l) [120].

Pressure losses to friction are:

$$\Delta p_f = \varkappa \frac{\varrho u^2}{2} \frac{L_0}{d}, \tag{4.13}$$

where Δp_f is the pressure drop in newtons/m^2;

ϱ is density in kgf/m^3;

u is average velocity in m/sec;

L_0 is the length of the pipe in m;

d is the inner diameter of the pipe in m;

$\varkappa$ is the coefficient of friction losses.

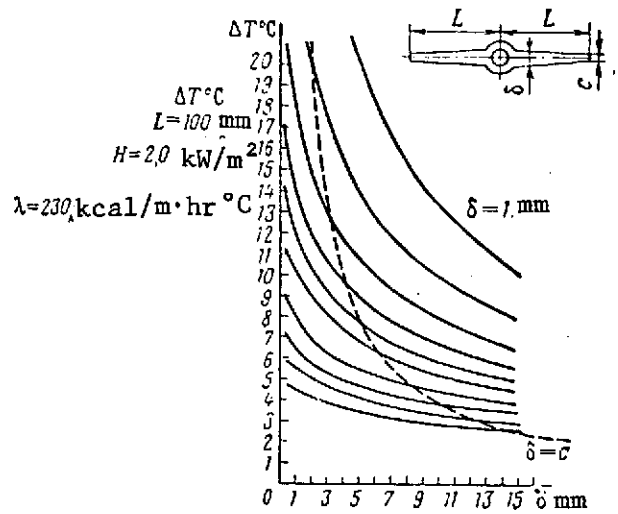

Figure 4.17. Dependence of temperature drop ΔT_1 on rib thickness for panel ribs of different cross section.

For isothermal laminar conditions (Re < 2300), the coefficient $\kappa = 64/\mathrm{Re}$ for circular pipes. For rarefied gases, we usually assume that u = 0.05 - 5 m/sec [77, 120]. /250

Pressure losses to local drag are equal to:

$$\Delta p_l = \sum \xi \frac{\varrho u^2}{2}, \qquad (4.14)$$

where ξ is the coefficient of local resistance which is determined by the type of resistance.

Let us estimate the value of pressure losses (without taking into account losses to local resistance) for a nitrogen feed line by Formula (4.13) with the following initial data [199]: ∅ 75 mm; L ≈ 1 m; q ≈ 600 l/min; ϱ_{N_2} ≈ kgf/m³; μ_{N_2} ≈ 100 kgf/m·sec; and Re ≈ $6.3 \cdot 10^{-2}$. We obtain:

$$\Delta p_f = \frac{64}{6{,}3 \cdot 10^{-2}} \cdot \frac{600 \cdot 2 \cdot 10^{-2}}{2} \cdot \frac{1}{75 \cdot 10^{-3}} \cdot \frac{1}{10^{-5}} \approx 0{,}8 \text{ kgf/cm}^2 \cdot \text{m}$$

In the case of a long pipe, losses increase in proportion to length.

A temperature gradient develops along the rib surface, independently of the type of cooling surface — ribbed or solid (Figure 4.17). The temperature difference may reach ΔT ≈ 20° K. The difference between the liquid nitrogen temperature in the pipe and the temperature of the metal at the apex of the rib, i.e., at the point corresponding to half the distance between the two cooling pipes, may be calculated for panels of the simplest configuration by Formula (4.15) [251]: /251

$$\Delta T_1 = a \frac{H b^2}{2\lambda\delta} \,^\circ\mathrm{K}, \qquad (4.15)$$

where b is the width of the rib in m, i.e., half the distance between two adjacent cooling pipes;

H is the heat flux density of radiant energy in kW/m²;

λ is the thermal conductivity of the pipe wall in kcal/m·hr °K;

δ is wall thickness in m;

a is the conversion factor equal to 860 kcal/kW·hr.

It follows from Formula (4.15) that the greater the value of δ, the less will be ΔT_1. However, in this case, the heavier the structure, consequently, the less will be the cooling intensity. Moreover, when the wall thickness is large, considerable difficulties arise in designing supports for the entire structure. It is calculated that the optimum thickness is $\delta \approx 3$ mm. The pipes are usually made of copper or aluminum.

The results of calculations for ribs of different dimensions are presented in Figure 4.17.

The temperature of the ends of the panel ribs, cooled by liquid nitrogen, is equal to the temperature of the exhaust liquid nitrogen plus the temperature difference in the ribs themselves [254]:

$$T_R \approx 93^\circ \mathrm{K} + \Delta T_1. \tag{4.16}$$

The maximum permissible temperature of the material of the rib ends may be equal to ~113° K, and this temperature will only be reached in the sections of the panels, exposed to the maximum flux of "solar" radiation. Moreover, a temperature difference ΔT_2, caused by the cryodeposit on the panels, occurs (4.11), and also the temperature difference

$$\Delta T_3 = \frac{Q}{4 \cdot 186 m c_v},$$

where Q is the heat flux which must be drawn off by the coolant;

m is the mass flow rate of the coolant in g/sec;

c_v is the specific heat of the coolant;

ΔT_3 is the temperature difference between the liquid and the pipe walls, calculated by standard methods.

Heat leaks, supports and compensators. Heat leaks due to the thermal conductivity through the supports to the surfaces of a facility, having a low temperature, as well as the heat flux, transmitted by radiation to the external surface of the facility, should be reduced to a minimum. /252

The heat delivered to the facility due to thermal conductivity may be reduced by the use of special structural materials (Invar and stainless steel) with a low coefficient of thermal conductivity, as well as by using a facility with supporting rods of small cross section. In order to reduce the amount of heat transferred by radiation, the chamber surface should be covered with a layer of sputtered aluminum, having a low degree of darkness.

When sections of the facility are cooled to liquid nitrogen temperature, the linear dimensions of the facility are reduced. Thus, a copper shield ~6 m long is reduced by ~19 mm upon cooling. If the facility is arranged horizontally, it may be suspended on flexible supports. The coolant may be supplied to it with the aid of metal undulated pipes. The supports and delivery of the coolant for a vertically arranged facility may be placed in its lower section.

The coolant should be supplied through heat-insulated pipes (high-vacuum or powder insulation). Copper pipes will shrink by 9.5 mm for every 3 m of length and, therefore, either undulated pipes or special loop compensators should be installed to compensate for thermal deformations. Invar, which has a very low thermal expansion coefficient, may be employed as the material for internal pipes, designed for delivery of the coolant, in order to prevent thermal shrinkage upon cooling; stainless steel may be used for the external pipes. In this case, installation of undulated pipes or compensators on the pipes is not required.

Heavy-current electric leads for high-vacuum test facilities. They are distinguished by simplicity of construction and simplicity of manufacture. An electric lead, designed for supplying a current of 1000 amperes, is shown in Figure 4.18. The electrodes are copper, and the assembly plate 25 mm thick is made of aluminum. The dielectric is an epoxy compound with a dielectric strength of ~10 kV/mm.

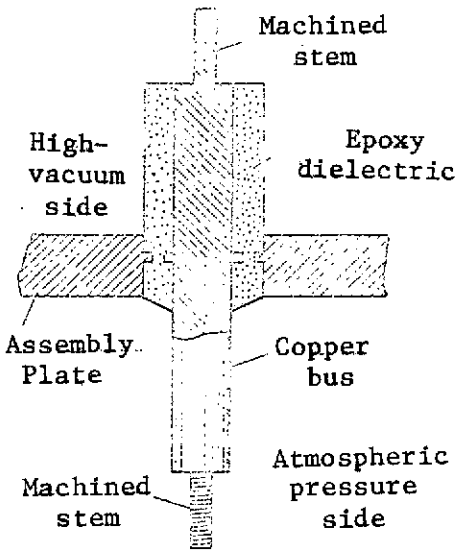

Figure 4.18. Schematic diagram of heavy-current vacuum electric lead.

The design of the electrodes is shown schematically in Figure 4.18. The electrodes may be made of any good conductor. The assembly plate should be made of a non-magnetic material to prevent heating of the plate by Foucault currents. The annular grooves in the assembly plate and the ring near the center of the conductor should prevent displacement of the dielectric under pressure loading. The ring of epoxy resin around the electrode on the vacuum side creates a reliable insulation of the metal against electrical discharges in a vacuum.

Two leads, the schematic diagram of which is shown in Figure 4.18, have operated normally for more than two years at a voltage of 480 V in a facility with a pressure up to $1 \cdot 10^{-7}$ torr. /253

Transmission of electrical energy to a spacecraft, rotating in a high vacuum. Facilities are usually equipped with solar simulators and other sources of radiation in order to simulate the thermal vacuum conditions of space flight. In this case, the test spacecraft should have at least two degrees of rotational freedom with respect to the radiation simulators in order to simulate spacecraft flight in orbit.

Two versions of devices for providing electric power to a rotating spacecraft, suspended in a facility on a gimbal suspension, are considered in [217]. The first variant is supply of electric power with the aid of cables, winding and unwinding on drums, and the second uses a collector having sliding rings (a rotating transformer). The disadvantages of devices of the first variant are the limited spacecraft rotational velocity, and those of the second are additional thermal radiation of the energy conversion device to the cryopanels, cooled to liquid nitrogen temperature, and contamination of the inside of the vacuum facility by outgassing from the transformer surface.

It is more expedient to cool the energy conversion device with the aid of liquid nitrogen to reduce heat emission and outgassing.

5. Solar Radiation Simulators* [147, 149, 151, 152, 161, 171, 189, 199, 213, 222, 235, 245, 255, 257]

The quality of solar radiation simulators is characterized by the value of the beam divergence angle in the working zone, homogeneity of irradiation, the value of beam polarization and the degree of conformity of the radiant flux spectrum to that /254 of the natural Sun. It is impossible to achieve absolutely precise reproduction of solar radiation in any simulator due to a number of technical difficulties.

A simulator is regarded as very perfect if the inhomogeneity of the radiant flux field throughout the working zone does not exceed ±5%, beam divergence — not more than ±2°, mean square deviation of the spectrum from the solar radiation intensity distribution curve — not more than ±5%, according to Johnson, at wavelengths from 0.2 to 3 microns, and the degree of polarization does not exceed 3 - 5%. A simulator with these parameters permits sufficiently accurate thermal experiments for the most unfavorable combination of spectral characteristics of a spacecraft having a complex spatial configuration and low thermal conductivity.

For some special cases, the requirements on the solar simulator may be decreased considerably without sacrificing the accuracy of reproducing spacecraft thermal conditions. This factor is often employed when a solar simulator is created for testing spacecraft of some specific type.

Types of Collimating Systems for Solar Simulators

Based on the method of producing the radiant flux, the optical arrangements of solar simulators may be divided into axial and non-axial. The working zone in non-axial arrangements is located on the side of the main optical axis, due to which the return of beams, reflected from the spacecraft back into the working zone, is excluded. The simulators may contain refracting and reflecting optics or both simultaneously; the shape of the surface of the reflecting elements may be spherical or aspherical. Different types may include simulators consisting of one or many identical modules. According to spectral composition, simulators are divided into optical and infrared.

---

*Range of wavelengths from 0.2 to 3 microns.

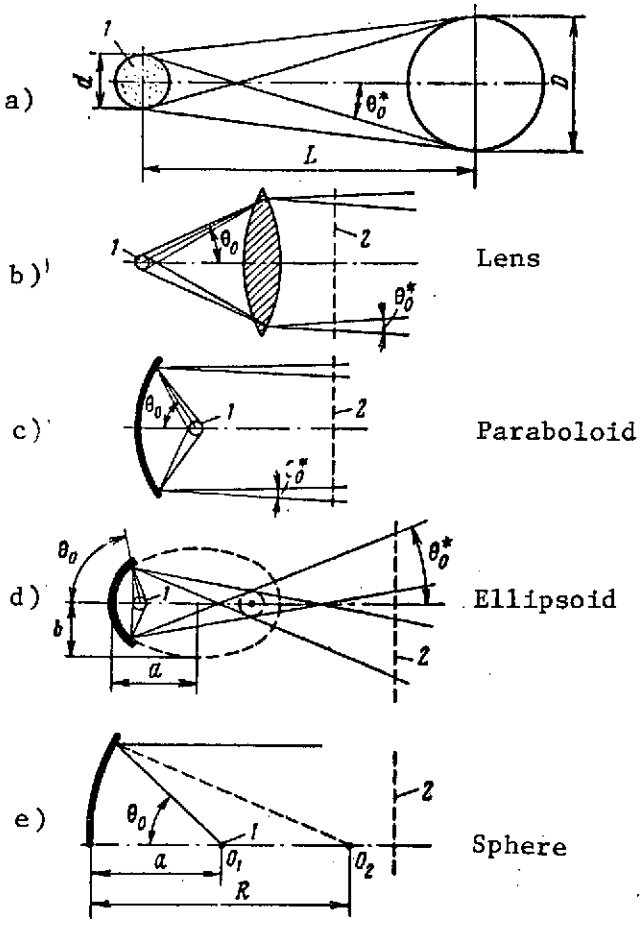

Figure 4.19. Simplest collimating systems for solar simulators: 1 — radiation source; 2 — correcting filter.

These features do not exhaust the entire diversity of solar simulator characteristics. These features are combined in the most varied manner in simulator designs, which makes it difficult to classify them precisely. Some of the more typical arrangements most often employed in simulators will be considered below.

The Simplest Simulator Arrangements

The simplest arrangement of a solar simulator, satisfying the above requirements, would be a diffusely radiating sphere of diameter d at a distance of $L \approx 30(d + D)$, where D is the working zone dimensions (Figure 4.19a). The sphere should radiate as a black body at T = 5785° K. The energy consumption factor η_e of such an arrangement /255 would be equal to 0.008%. Due to low efficiency, such systems are not employed in practice. An optical system, which would permit an increase of the solid angle, within the limits of which all beams emitted from the source impinge within the working zone, must be employed to increase the efficiency of the simulator. In particular, a sorption lens, within whose focus is placed a radiant energy source, may act as such a system (Figure 4.19b). The energy /256 efficiency of such a system* will be equal to the ratio of solid angle Ω, at which the lens is visible from point 0, to the solid round angle Ω_0, equal to 4π:

$$\eta_g = \frac{\Omega}{\Omega_0} = \sin^2\left(\frac{\vartheta_0}{2}\right). \tag{4.17}$$

*For the time being, let us digress from absorption losses in the lens.

If the source radiates diffusely (like the Sun or the crater of an arc [sic]), i.e., the brightness of the source B is constant along its surface s, and the radiation intensity in a given direction varies according to the law $J = Bs \cos \theta_0$, the total radiant flux energy of such a simulator will be equal to

$$\Phi_1 = \pi B s \sin^2 \theta_0. \tag{4.18}$$

If the source radiates such that the radiation intensity J (as in tungsten arc lamps) remains constant in all directions, then

$$\Phi_2 = 4\pi J_0 s \sin^2 \frac{\theta_0}{2}. \tag{4.19}$$

For optical systems with low aperture angles θ_0, Formulas (4.18) and (4.19) yield the same result:

$$\Phi = \pi J_0 \theta_0^2. \tag{4.20}$$

For optical systems with high values of θ_0, sources of the second type (J = const) yield greater fluxes than those of the first type (B = const). Thus, at $\theta_0 = 90°$, $\Phi_2/\Phi_1 = 2$. Despite this, it is more expedient to use sources of the first type, because they are tens of times brighter than those of the second type.

Let us find the average radiant flux density in the working zone (or irradiation), dividing the flux Φ by the cross-sectional area of the working zone:

$$E = \frac{\Phi}{\pi R^2}. \tag{4.21}$$

According to Langrange-Helmholtz law,

$$r \sin \theta_0 = R \sin \theta_0^*, \tag{4.22}$$

where r is the source radius, and θ_0 and θ_0^* are the angles at which the optical system (in our case the lens) is visible from the source and from the center of the image. Substituting R from (4.22) into (4.21), we find that

$$E = \frac{\Phi}{\pi r^2} \left(\frac{\sin \theta_0^*}{\sin \theta_0} \right)^2.$$

For a source of the first type, according to (4.18), we obtain

$$E = \pi B \sin^2 \theta_0^*. \tag{4.23}$$

For a source of the second type /257

$$E = \pi B \frac{\sin^2 \theta_0^*}{\cos^2\left(\frac{\theta_0}{2}\right)}. \tag{4.24}$$

It is obvious from Formulas (4.23) and (4.24) that, when the given irradiation in the working zone remains constant, the decrease in the beam divergence angle is related to an increase in source brightness or to a decrease of θ_0, i.e., to an increase of the focal distance of the optical system and to a decrease of its efficiency.

Another limitation on an increase of angle θ_0 is the deterioration of irradiation uniformity in the working zone. The dependence of the relative radiant flux density on angle θ_0 for a double-convex lens and an axial parabolic mirror (Figure 4.19c) is shown in Figure 4.20 [178, 257].

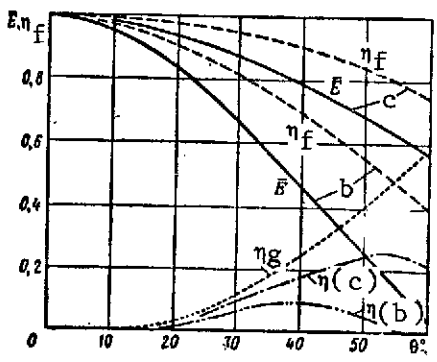

Figure 4.20. Relative irradiation intensity $\bar{E}$, total transmission coefficient of the correcting filter η_f and total energy consumption factor as a function of angle θ_0 for a lens (o) and for a paraboloid (c).

The uniformity of the radiant flux field may be increased with the aid of a gray absorbing filter having maximum absorption in the center and minimum (zero) absorption along the edges (Figure 4.20). The total transmission coefficient of the filter η_f, completely equalizing the field, is a function of angle θ_0. The greater θ_0, the greater is the inhomogeneity and the smaller is the transmission coefficient η_f. But, on the other hand, according to (4.17) the geometric efficiency of the system (η_g) should increase as θ_0 increases. Therefore, the total efficiency of the entire system, taking into account the correcting filter $\eta = \eta_g \eta_f$, will have an extremum. The curves showing the dependence of η on θ_0, from which it is obvious that the efficiency of the system may be approximately 2.5 times higher with the aid of reflective

optical elements than that of a system having a double-convex lens, are presented in Figure 4.20. Comparison of these curves with the curve η_g shows that near the maximum value of η about 50% of the total output of the source will be absorbed and scattered in the filter. This means that the filter itself is a powerful source of diffuse infrared radiation, which inevitably leads to appreciable methodical errors. For this reason, arrangements of solar flux simulators with correcting filters have not found widespread application.

Refracting optical systems are employed only for small simulators in which the /258 cross-sectional area of the working zone does not exceed 1 m^2. The optical elements of the refractor system should admit radiation at wavelengths from 0.2 to 3 microns; therefore, the material for them should be fused quartz or leukosapphire. Lenses of these materials are very expensive and very difficult to make in large sizes.

In large reflector schemes, quartz and leukosapphire are used as the material for the windows, which serve to admit a concentrated beam into the chamber, and for small lenses.

Axial Reflector-Refractor Schemes [232]

A solar simulator, based on the axial scheme (the Cassegrain system) has found practical implementation in one of the simulators of NASA's Jet Propulsion Laboratory (JPL). It is a vertical cylinder 8.2 m in diameter and 14.3 m high (Figure 4.21). The solar simulator is located in a ten-meter superstructure above the chamber and provides a vertical axial radiant flux with a maximum intensity of 2700 W/m^2.

The radiant energy source in this scheme is mercury-xenon lamps with an output of 2.5 kW each, located outside the chamber in a flat of concave shield 1. The beams from 131 lamps are collected by the parabolic mirror 2 and concentrated on the pseudohyperbolic curvature of mirror 3, which consists of 19 hexahedrons 0.165 m in diameter, made of stainless steel. The beam then passes through lens 4, which simultaneously fulfills the role of an aperture, and strikes the dispersion mirror 5, which transmits the beams to the main parabolic mirror 6, which also forms the /259 collimating flux in the working zone 7.

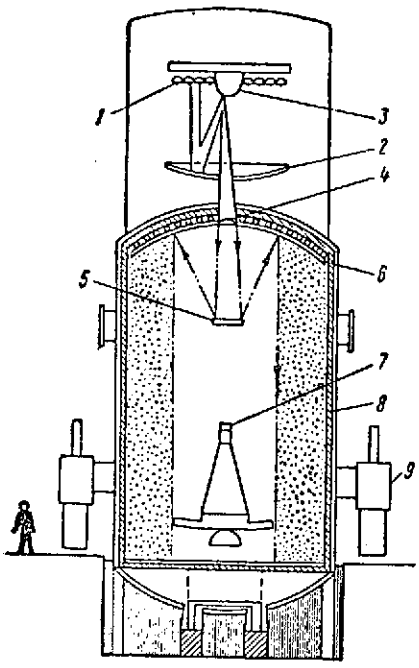

Figure 4.21. Schematic diagram of JPL facility with axial solar simulator: 1 — mercury-xenon lamps; 2 — parabolic mirror; 3 — hyperbolic mirror; 4 — lens 0.9 m in diameter; 5 — polyhedral reflector; 6 — main collimating parabolic mirror; 7 — working zone with spacecraft; 8 — cryogenic shields; 9 — diffusion pumps.

The irradiated area is a hexahedron with a side of 3.35 m (the maximum diameter of the circle is ~ 6 m). Field inhomogeneity varies from ±10 to ±15%. The divergence angle on 50% of the area does not exceed 3°; it reaches 5° on the remaining surface. Each lamp illuminates its own section in the working zone; therefore, individual regulation of each lamp from a main control desk has been provided to ensure field uniformity. The quartz lens 4, 0.91 m in diameter, convex on the top and flat on the bottom, is unique and is apparently the largest one in existence. Teflon was used as the sealing material in fixing the lens in the holder.

The dispersion mirror 5, 0.765 m in diameter, consists of 1150 separate water-cooled parabolic mirrors of stainless steel. Each facet reflects light to a separate section of a large internal parabolic reflector 7.65 m in diameter. A secondary reflector 10, 0.765 m in diameter and a small reflector 0.127 m in diameter, located above the polyhedral reflector 5, serve to eliminate shadows from mirror 5. The beams impinge on the secondary reflector (0.127 m in diameter), pass through the lens, 0.18 m in diameter, located in the center of the polyhedral mirror 5, are then reflected onto the parabolic reflector located above the polyhedral mirror, and then proceed downward in the form of an almost parallel beam, filling the shadow created by mirror 5. The main parabolic reflector 6 consists of 324 separate sections, each of which is mounted with the aid of three regulating screws. Each section has from 6 to 10 flexible metal strips, having high thermal conductivity and connected to a pipe filled with nitrogen cooled to 80° K, for cooling the mirror to 200° K. Because of the extreme complexity of design, the field uniformity in the working zone is achieved by meticulous and painstaking alignment of all elements of the scheme.

The described simulator was unsatisfactory for a number of reasons. Its main disadvantages include the following.

The last and largest parabolic mirror is located so that it re-emits beams from one section of the test spacecraft to another. The spacecraft seemingly "sees" itself in the mirror, which causes uncontrolled secondary radiant fluxes which lead to thermal errors.

The simulator has a very low conversion factor of the electrical power into effective radiant flux. It requires 322.5 kW supplied to the sources to obtain 10 kW of effective radiant flux in the working zone. (The energy balance of the system is shown in Figure 4.22.)

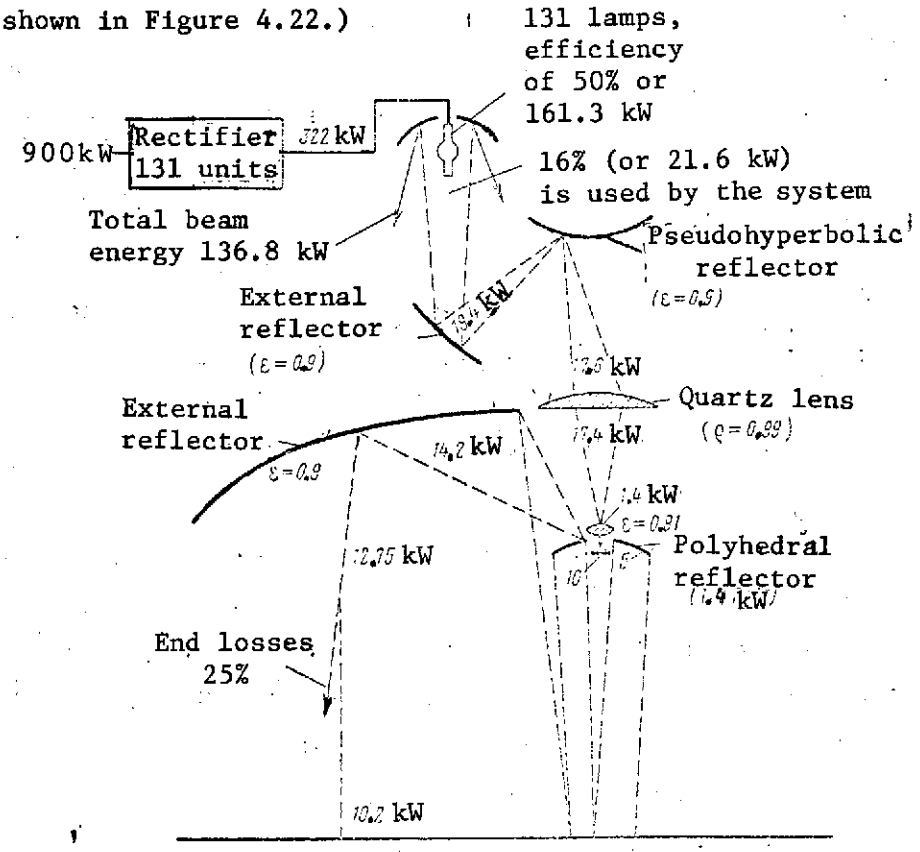

Figure 4.22. Energy balance of NASA JPL solar simulator.

The system contains small mirrors on which are concentrated powerful radiant fluxes, causing them to heat up. Cooling of these mirrors, in particular those inside the chamber, complicates the problem of hermetic sealing of the facility as a whole. /260

The presence of a large number of optical elements makes the system very expensive, leads to large optical losses and creates great difficulties in initial alignment and subsequent regulation during operation.

Aspherical optics, complex in manufacture, are employed in the system.

Losses in the Optical System

The energy consumption factor in a simulator of the radiant flux of the Sun or planet is calculated as the ratio of the energy of radiant flux, passing through /261 the cross section of the working zone, to the energy supplied to the radiation source.* This coefficient amounts to one percent or a fraction of a percent and only in the best simulators reaches 15 - 20%.

The distribution of power losses in the units of the optical system may be considered on the example of the solar simulator of the NASA JPL chamber (Table 27).

The total energy consumption factor of the JPL solar simulator is:

$$\eta = 0.358 \cdot 0.5 \cdot 0.97 \cdot 0.913 \cdot 0.15 \cdot 0.9 \cdot 0.99 \cdot 0.99 \times$$
$$\times 0.816 \cdot 0.9 \cdot 0.8 \approx 0.0114 (\approx 1.14\%).$$

Without taking into account losses in the rectifier η = 3.16%. /262

As can be seen from Table 27, the overall low efficiency of the simulator is determined mainly by the large energy losses (~85%) due to incomplete use of the radiant flux of the source, which is typical for optical systems constructed according to the Cassegrain system. Considerable losses are also caused by absorption of beams in the numerous lenses and mirrors.

A more perfect facility is the solar simulator used in the large chamber of the General Electric Company and in the TRW facility [161] (USA) (Figures 4.23, 4.24 and 4.25). Because of the smaller number of reflecting and refracting optical elements and the more perfect design, the total coefficient of the solar simulator in the TRW chamber was 7.3% and that in the General Electric chamber was 12%.

*We will also include the power supply system, for example, the rectifier or high-frequency generator, in the radiation source.

TABLE 27

No. of item	Power distribution in assemblies of optical system	Output kW	Power losses in %
1	Electric power supplied to simulator	900	—
2	Electric power after rectifiers and smoothing filters	322.5	64.2
3	Total radiant flux output in range from 0.2 to 4 microns, given off in arc lamps	161.3	50
4	Radiant flux output after absorption in the quartz bulb of the xenon lamp	150	7
5	Radiant flux output after reflection from mirror with consideration of shading by lamp and by the counter-reflector	137	8.7
6	Radiant flux output trapped by the optical system	21.6	85
7	Radiant flux which is reflected from the upper flat mirror	19.4	10
8	Radiant flux which is reflected from the pseudohyperbolic mirror	17.6	10
9	Radiant flux output after large quartz lens	17.4	1
10	Radiant flux reflected from polyhedral reflector	14.2	18.4
11	Radiant flux reflected from large internal paraboloid	12.75	10
12	Radiant flux in working zone, taking into account boundary scattering losses	10.2	20

More economical is a simulator in which an arc lamp with an ellipsoidal reflector and a single non-axial parabolic or spherical mirror is employed (see Figure 4.28). Total energy losses in a simulator of this type do not exceed 84% (Table 28). /263

The total energy consumption factor of the solar simulator is

$$\eta = 0.50 \cdot 0.8 \cdot 0.8 \cdot 0.7 \cdot 0.9 \cdot 0.8 = 0.162$$
$$(16.2\%).$$

Using a DKSR-40,000 lamp as a radiation source (see page 294), a single solar constant (1.4 kW/m^2) on an area of more than 4 m^2 may be obtained.

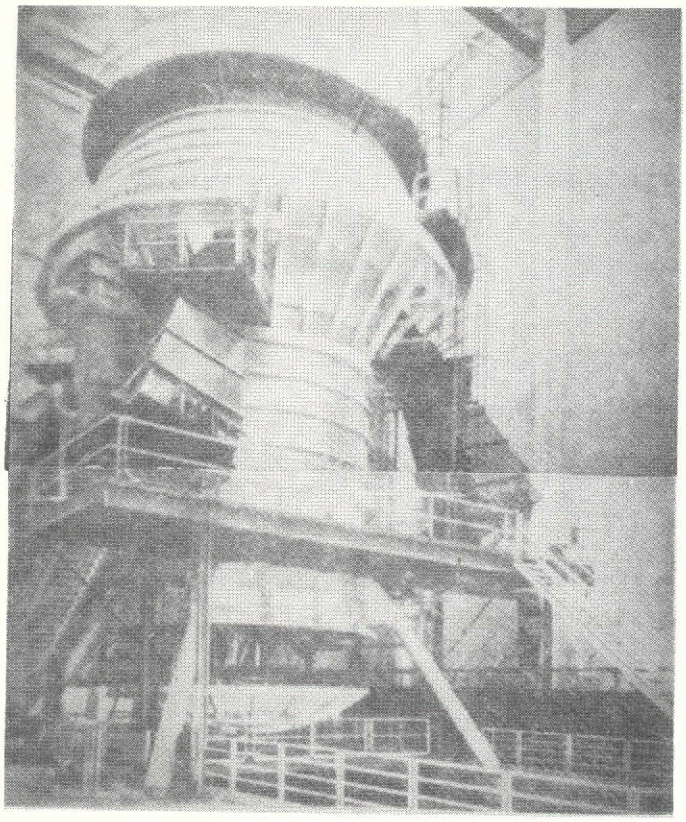

Figure 4.23. TRW Simulator.

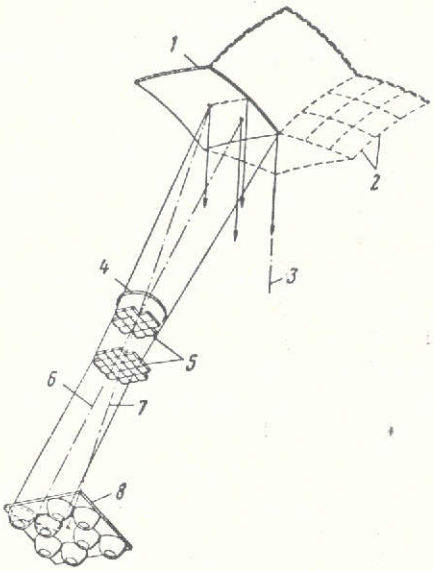

Figure 4.24. Optical diagram of solar simulator in TRW chamber: 1 — collimating mirror; 2 — facets; 3 — chamber axis; 4 — window; 5 — mosaic lenses; 6 — module axis; 7 — section axis; 8 — lamp modules.

TABLE 28

Power distribution	Output kW	Energy losses in %
Electric power supplied to source	40	—
Power emitted in electric arc in range from 0.2 to 4 microns	20	50
Radiant energy trapped by ellipsoidal reflector((taking into account shading by electrodes)	16	20
Reflected from ellipsoidal mirror	12.8	20
Passing through two quartz windows and a layer of water	9	30
Radiant flux after reflection from spherical mirror	8.1	10
Radiant energy flux in working zone, taking into account boundary losses	6.5	20

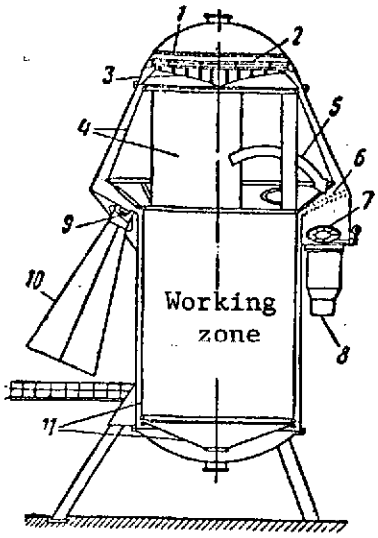

Figure 4.25. Diagram of simulator (right-hand portion of chamber arbitrarily rotated by 45°, so that the diffusion pump is visible): 1 — service area; 2 — adjusting device for main mirror; 3 — collimator; 4 — cryopanels at liquid nitrogen temperature; 5 — direction of evacuation; 6 — herringbone traps; 7 — seal; 8 — diffusion pump; 9 — mosaic lenses; 10 — sleeve covering solar simulator lamps.

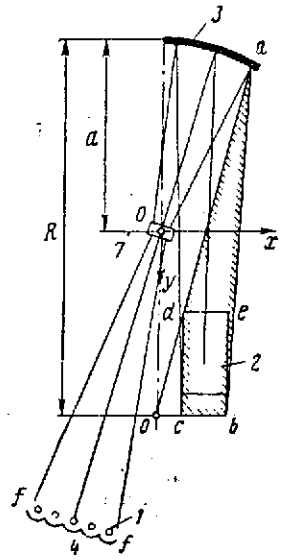

Figure 4.26. Diagram of mutual arrangement of radiation sources (1) of an inclined spherical mirror (2) with the center at point 0.

A Non-Axial Simulator with a Spherical Mirror [232] /264

Arrangement of the working zone toward the axis of symmetry of the main mirror (see Figure 4.19e), forming an almost parallel flux, avoids mutual re-radiation between the mirror and the test spacecraft. Zone 2, in which any light beam directed toward the mirror does not return to the zone being considered, is depicted in Figure 4.26 by the cross-hatching. The working zone may be regarded as any space inscribed in zones a, b, c and d. In particular, it may be a cylinder, as in the JPL SS-A simulator. A combination of 19 mercury-xenon and xenon lamps with an output of 5 kW each, located at a distance of 10.7 m from the input window 7 in plane f - f, is used as the radiant energy sources in this simulator. Each lamp is equipped with an individual reflector 4 to increase the angle of contact. A multicomponent honeycomb lens system with the number of elements equal to the number of lamps is employed to increase the field uniformity in the working zone, as well as for possible subsequent increase of beam intensity by increasing the number of lamps. /265 The lenses are designed so that the beams from each source impinge on the entire working zone 2. A total of 19 beams from 19 lamps, superimposed on each other, jointly compensate for possible field inhomogeneities which may be the result of individual

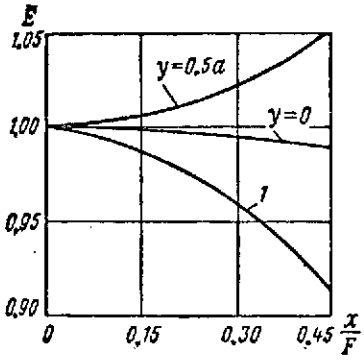

Figure 4.27. Distribution of relative flux intensity formed by spherical collimating mirror: 1 — curve for paraboloid.

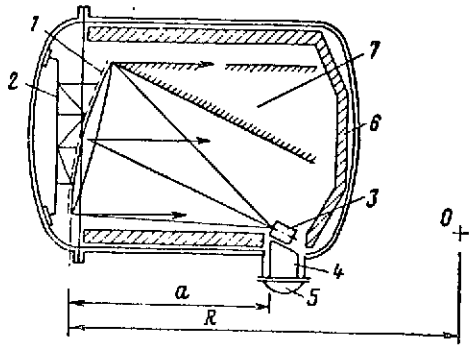

Figure 4.28. Diagram of the facility for a solar simulator module in a horizontal chamber: 1 — spherical mirror; 2 — bracket for attaching and adjusting mirror facets; 3 — radiant energy source; 4 — bracket for attaching source; 5 — hatch cover; 6 — cryogenic shields; 7 — zone of non-return of beams.

errors in preparation of the lenses, small reflectors, and the sources themselves. Because of this design, high field uniformity in the space is achieved. Deviations of the local value of radiation intensity from the average are within the range of ±5%. The average beam divergence angle is 2°.

In order to obtain a radiant flux intensity, equal to a single solar constant, i.e., E = 1396 W/m^2 on an area of 2.6 m^2, a total of 12 lamps of 5 kW each (efficiency = 6%) was required; 19 lamps are required to obtain E = 2850 W/m^2 (efficiency = 7.3%); and 54 lamps (efficiency = 8.85%) — for E = 9200 W/m^2.

The main collimating mirror in this scheme is spherical. Such a mirror is considerably simpler to manufacture than a parabolic mirror, but it yields a spherical aberration, which distorts field uniformity and increases the non-parallelism of the beams. By varying the ratio a/R, a satisfactory field uniformity may by achieved in any selected cross section — for example, in section d — e (see Figure 4.26). Uniformity will be worse in the other sections of the working zone (c — b).

The results of calculating the intensity distribution of a flux, formed by a spherical collimating mirror for different cross sections of the working zone (for a/R = 0.5), are presented in Figure 4.27.

The disadvantage of a facility with a solar simulator, executed by the scheme described above and including the complexity of manufacture of the integral lens 7 and multipoint source 1, may be avoided if the solar simulator is executed according to a scheme with a single powerful source, located at the focus of the spherical mirror inside the chamber (Figure 4.28). A DKSR-40,000 high-pressure metal arc lamp of VNISI, which operates on pure xenon (see Section 5, Chapter 4 for a description of the lamp [98]), may be used as such a source. /266

The scheme shown in Figure 4.28 is designed to achieve horizontal fluxes, because the DKSR-40,000 lamp with a freely burning arc may normally operate only in a horizontal position.

A Non-Axial Simulator with a Parabolic Mirror [144]

A solar radiant flux simulator, executed according to a scheme using a non-axial parabolic mirror, is employed for both small chambers with working dimensions < 1 m and for very large chambers, for example, in the General Electric simulator, which began operation in 1963 (Figure 4.29). The diameter of the chamber is 9.6 m, and its height is 16.5 m. The main collimating mirror 6.7 m in diameter, with the shape of four paraboloid sections, is made of 1560 small mirrors. The entire system is aligned by a computer, which finds the optical position of each element of the mirror to achieve the best uniformity in the cross sections of the working zone. During operation of the facility, a given or time-constant radiation intensity of the test spacecraft is maintained with the aid of special radiant flux sensors and a feedback control system. The efficiency of this simulator is rather high: as indicated above, about 12% of the electric power supplied to the lamps impinges in the form of radiant energy in a working zone 5 m in diameter. Maximum radiation density corresponds to a single solar constant

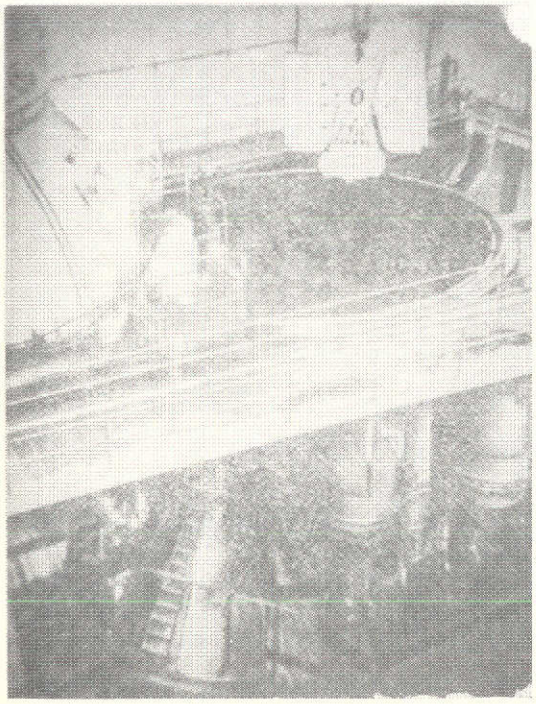

Figure 4.29. "Nimbus" satellite in the test chamber of the General Electric Company.

(S_Θ = 1496 W/m^2). Measurements of intensity distribution in the cross sections of the working zone by a 2.5 mm pickup showed that 70% of the irradiated surface had an inhomogeneity of ±5%, 25% of the area — ±10%, and only 5% of the area had an inhomogeneity > ±10%. The non-parallelism of the beams was within the range from 2.5 to 3.5°. Because of cooling, the main mirror emitted infrared radiation only 1.36 times greater than cryogenic panels at T = 100° K. A total of 148 xenon lamps of 5 kW each was used as radiant energy sources. The lamps were arranged in groups (37 units in each group) on four sides of the chamber. The /267 conformity of the spectrum obtained to the solar spectrum (the Johnson curve) is illustrated by Table 29.

TABLE 29 *

Wavelength range, microns	Solar spectrum in space		Measured spectrum of solar radiation simulator		Deviation of solar Spectrum in % of total energy
	W/m^2	% of total energy	W/m^2	% of total energy	
0,18—0,25	3,3	0,13	—	—	—
0,25—0,33	42,4	2,9	18,9	1,3	—1,6
0,33—0,40	86,5	6,0	58,5	4,0	—2
0,40—0,50	210	14,5	149	10,3	—4,2
0,50—0,70	365	25,3	295	20,5	—4,8
0,70—0,80	131	9,1	123	8,6	—0,5
0,80—0,90	105	7,2	182	12,5	5,3
0,90—1,10	153	10,6	299	20,6	10,0
1,10—1,50	172	11,9	166	11,5	—0,4
1,50—2,00	91	6,3	99	6,8	0,5
2,00—3,00	58	4,0	49	3,4	—0,6

*Commas represent decimal points.

A Solar Simulator with Infrared Emitters

The spectrum and angular beam distribution must coincide when testing spacecraft of very simple geometrical shape, for example, in the form of a cylinder having a covering in which the degree of darkness depends on the angle of incidence of beams and is constant over the surface (see Section 4, Chapter 3, classes of spacecraft I, III, IV, XI, and XII). Therefore, infrared emitters, which create a radiant flux equivalent to solar, may be used instead of optical solar simulators with arc sources. Metal ribbons, rods, pipes and disks, heated by electric current, as well as tungsten iodide lamps in the form of spherical bulbs or elongated cylinders may

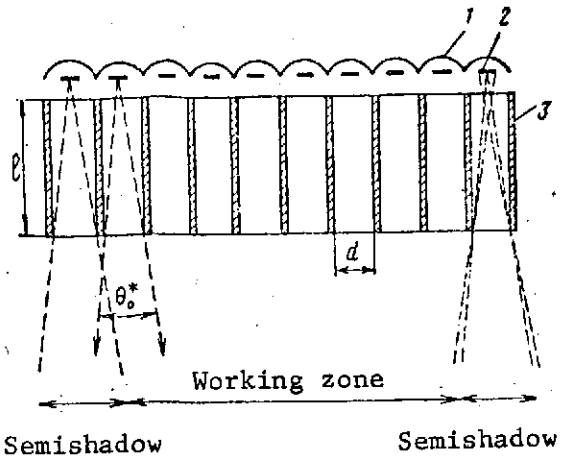

Figure 4.30. Diagram of a solar simulator with infrared heaters: 1 — reflectors; 2 — heaters; 3 — absorption lattice cooled by water or liquid nitrogen.

be used as the emitters of such simulators. The low radiation density of such sources, caused by the comparatively low temperature (usually T = 700 - 1200° K), is compensated for by the large radiation surface. Reflectors in the form of cups or grooves, depending on the shape of the sources, are installed on the rear side of the emitter to increase the efficiency of infrared simulators. /268

Ordinary optical schemes with refracting or reflecting elements may not be utilized effectively in this case to obtain uniform parallel fluxes, because the dimensions of the emitters become comparable to those with dimensions of the optical elements. In this case, various collimators in the form of lattices with black cooled walls, which form an aggregate of narrow parallel channels through which the radiant flux passes, are employed to form a uniform infrared radiant flux with small beam divergence angles. The geometry of the channel of a diffuser grid, namely the ratio d/l (Figure 4.30), determines the maximum angle of beam divergence θ_0^*. The less is the required angle θ_0^*, the more beams are absorbed by the diffuser grid and the lower will be the efficiency of the entire simulator.

At identical angles of θ_0^*, the efficiency of the infrared simulator is much lower than that of a simulator in which highly intense "point" sources of radiation are employed.

The beam divergence angles θ_0^* are increased considerably, and the diffuser grids are not installed at all in order to increase the efficiency of an infrared simulator. This permits operating expenses to be reduced to the level of optical simulators (Table 30). /269

The radiant flux simulator of the Lockheed HIVOS (High Vacuum Orbital Simulator) facility [257], which simultaneously reproduces the total heat flux of the Sun and planet, is constructed on this principle. The radiators of the heat flux simulator

TABLE 30

Name of chamber	Type of solar simulator	Dimensions of working zone	Cost of facility in millions of dollars
HIVOS	Infrared	H = 5.1 m D = 2.9 m V = 34 m^3	3
TRW	Optical	H = 10.7 m D = 4.6 m V = 176 m^3	2.4

consist of quartz lamps with a tungsten filament, installed in two rows on polished aluminum reflectors, cooled by methylene chloride (T = 197 - 277° K) (Figure 4.31). The reflectors are attached to the upper and lower rings of horizontal supports, forming a cylindrical frame with an inner diameter of 2.9 m and a height of 5.1 m. The radiators of the simulator are divided into 26 zones, each of which is controlled separately. Twelve zones are located in the upper section of the cylindrical frame 2.1 m /270 high. The lower section 3.05 m high also contains 12 zones and one zone each above and below, perpendicular to the axis of the cylindrical frame. Regulation of the radiation intensity of each zone is accomplished in accordance with the magnitude of the total radiation from the Sun and planet, which is calculated for a given configuration of the outer hull of the test spacecraft. The maximum radiation density of such a simulator is calculated at 2240 kcal/m^2•hr, which corresponds approximately to the total assumed solar radiation intensity near the planet Venus.

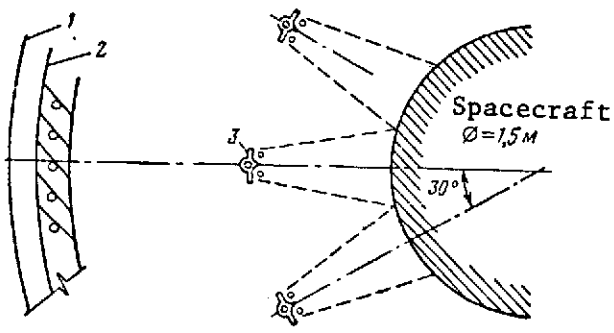

Figure 4.31. Diagram of cross section of heat flux simulator in HIVOS facility: 1 — chamber wall (5.5 m in diameter); 2 — heat absorber with cryogenic shields (outer diameter ~5.2 m and inner diameter ~4.9 m); 3 — lamps with reflectors (inner diameter ~2.9 m).

Extensive checking and debugging of the "Agena" rocket were carried out in the HIVOS facility.

The radiant flux simulators of the three spherical chambers, having a diameter of 11.7 m, of the General Electric Company, which were manufactured for it by the Stokes Company, are similar in arrangement and design. The infrared radiation source in them is comprised of quartz tungsten iodide lamps with an output of 0.5 kW, in which the length of the glowing filament is about 76 mm. Each of the 600 lamps of the simulator is equipped with a reflector 127 x 10 mm, made of molded copper and covered with pure sputtered aluminum and a thin quartz film. All radiators are assembled on a light openwork drum, which barely shades the cold cryogenic shields. Total shading does not exceed 7%.

The main disadvantages of infrared solar simulators include the following:

1. Large beam divergence angles and nonconformity of the spectrum restrict the class of spacecraft which may be tested in the chamber of an infrared solar simulator, due to considerable temperature errors (see Section 12, Chapter 4).

2. Servicing of the radiation sources, which occupy large areas inside the chamber, is possible only when the chamber is depressurized and produces considerable idle time of the facility.

3. The heating elements and cooled diffuser grids, exposed to partial thermal /271 shocks, are a source of increased gas load for the pumping system of the chamber. Leak detection and elimination of leaks in the developed hydraulic system of the diffuser grids is difficult.

4. The square dimensions of the infrared solar simulator are structurally much more complex and more expensive than a mirror of the same dimensions.

5. The electrical insulation of the power supply conductors, which are located in the vacuum of the radiators, is a technically complex problem due to the corona discharge occurring at a pressure of 10^{-1} - 10^{-4} torr.

These disadvantages are negligible in small simulators. However, for simulators which irradiate tens and hundreds of square meters, the efficiency and increased outgassing in the chamber are decisive factors, because they determine in the final analysis the consumption of electric power, water, and liquid nitrogen. It is

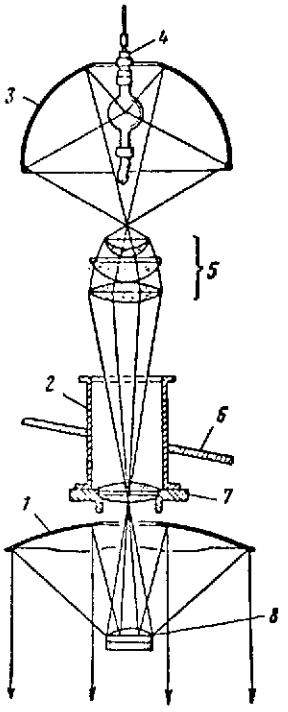

Figure 4.32. Diagram of lamp module of solar radiation simulator: 1 — paraboloid reflector; 2 — pressure seal in dome of chamber; 3 — ellipsoidal reflector; 4 — mercury-xenon lamp; 5 — condenser lenses; 6 — chamber wall; 7 — input lenses; 8 — hyperboloid reflector.

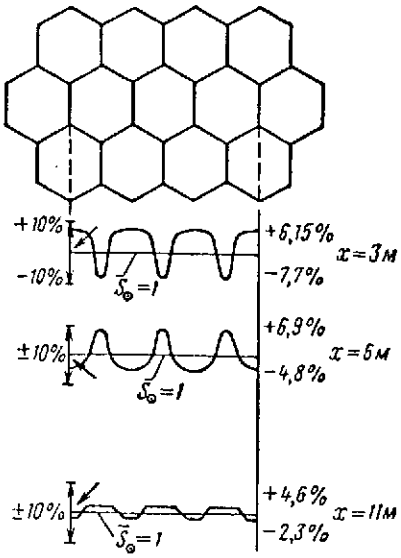

Figure 4.33. Radiant flux intensity distribution in the cross section of the working zone at distances of 3, 6, and 11 m from the solar simulator modules. The surface area of the calorimeter probe is 26 cm^2.

obvious that for these reasons solar simulators using infrared radiators have not found broad application. About 6% of American chambers are equipped with them, and then only those of small and medium dimensions (see Table 8 of the Appendix).

Multimodule Schemes [178]

Solar simulators, constructed on the module scheme, consist of a set of identical lamps with individual reflectors (modules), installed adjacent to each other. Each module provides a uniform weakly divergent beam with an intensity equal to the average nominal radiation intensity for the entire working zone.

A diagram of the module of the Honeywell Company is presented in Figure 4.32. A xenon or mercury-xenon lamp 4 with an output of 2.5 kW (or 5 kW) is surrounded by a deep ellipsoid, which collects about 85% of the total radiation. The beam is then transmitted onto the hyperbolic reflector 8 with the aid of condenser lenses

5 and the lens window 7. The hexahedral parabolic reflector 1 then converts the diverging beam into an almost parallel uniform flux. The hexahedral configuration of the reflector 1 permits the modules to be arranged adjacent to each other.

The radiant flux field of the solar simulator based on modules has a characteristic periodic irregularity, which decreases as the distance from the module increases (Figure 4.33). Despite the fact that the flux formed by the module is not strictly parallel, but divergent at an angle of ~2°, the average irradiation does not decrease as distance increases, because there is mutual compensation for the decrease of irradiation from adjacent fluxes.

Fused quartz is the material of all lenses of the module. The first lens in the modules, made by the Honeywell Company for the solar simulator of the large test /272 facility of the Goddard Space Flight Center (NASA), has a diameter of 89 mm and center thickness of 32 mm. The second double-convex lens has a diameter of 152 mm and thickness of 41 mm, and the third double-convex lens has a diameter of 171 mm and thickness of 38 mm. The lower surface of the third lens has an aspherical shape, while all the others are spherical. The first ellipsoid reflector 0.43 m diameter and the hyperboloid and paraboloid reflectors are manufactured by electrodeposition of copper and nickel with subsequent covering by pure aluminum. During operation, reflectors 1 and 8, located inside the chamber, are cooled by liquid nitrogen. Nevertheless, their temperature is maintained at a level of 0 and 23° C, respectively. The conversion factor for electrical into radiant flux energy in the Honeywell module comprises about 12%, but the cost of the modules is comparatively high.

An area of any configuration may be irradiated with the aid of such modules. /273 If the modules are mounted on the upper cover of the chamber, the cross section of the light spot in the working zone usually has the shape of a hexagon. The method of installing modules in the large simulation chamber of the Goddard Space Center is shown in Figure 4.34. The chamber diameter is 10 m, height is 17.7 m, volume is 1416 m^3, the diameter of the working zone is 8.5 m and height is 12.2 m. The lower section of the chamber contains a U-shaped gimbal suspension, designed for holding a spacecraft weighing up to 7000 kg. The rotating device of the gimbal suspension rotates the test spacecraft at a speed of up to 80 rpm. The internal surface of the chamber has nitrogen shields, cooled by liquid nitrogen to T = 100° K. A total of 127 modules are installed in the cover of the chamber, which produces an irradiation intensity equal to a single solar constant on an area of about 30 m^2. The cost of the entire facility is about 15 million dollars.

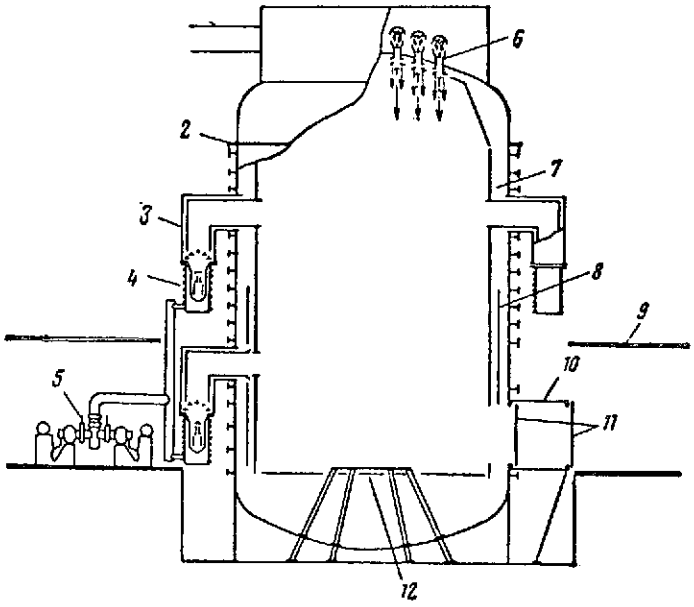

Figure 4.34. Method of installing modules in large simulation chamber of the Goddard Space Center: 1 — cooling system for solar simulator; 2 — flange for chamber cover; 3 — cooled pipe for connection to vacuum pump; 4 — diffusion vacuum pump; 5 — mechanical pumps; 6 — solar simulation modules; 7 — shields cooled by liquid nitrogen; 8 — helium cryogenic pump (T = 20° K); 9 — floor level; 10 — lock; 11 — doors; 12 — table for installation of spacecraft.

A similar modular scheme for a solar simulator is employed in Chamber A, designed for testing "Apollo" spacecraft and /27/ in Chamber B for training astronauts under conditions which simulate the lunar environment. Both chambers belong to the Manned Space Center in Houston (NASA). The height of Chamber A is 36.5 m, and diameter is 20 m. The dimensions of the internal free space are: D = 16.7 m and H = 27.4 m; the dimensions of the working zone are D = 10.7 m and H = 22 m; the maximum weight of the test spacecraft is 68,000 kg. The lunar surface simulator may rotate 180°. The pressure in the chamber during experiments is ~10^{-5} torr.

The main parameters of Chamber B are the same as those of Chamber A.

Chamber A is equipped with a lateral solar simulator, consisting of 104 modules,* and an upper simulator consisting of 12 modules.

Chamber B is equipped only with an upper solar simulator (consisting of three modules), which has an area 1.7 m in diameter, although the light spot may be increased to 6 m.

Each module irradiates an area of ~0.9 m^2. The largest reflector of the module has a hexahedral shape with an inscribed circumferential diameter of 1.2 m. The radiant energy source of the module is a carbon arc with an output of 32 kW (at a

*The simulator was developed by the Radio Corporation of America (RCA).

current intensity of 400 A). The anode rod (positive) is carbon, and the cathode (negative) is made of tungsten. The diameter of the rods is 16 mm.

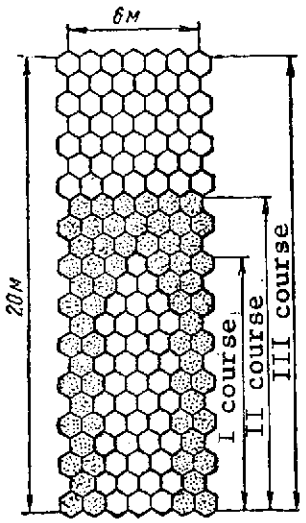

Figure 4.35. Dimensions of surface irradiated by lateral solar simulator in Chamber A.

The inhomogeneity of the radiant flux field in the working zone reaches ±10% and the beam divergence angle is ~2°.

The configuration of the area irradiated by the modules in Chamber A is presented in Figure 4.35. The solar radiation simulator is the American "Mark-1" facility (Figure 4.36), whose diameter is 12.8 m and height is 25 m, consists of 77 modules with carbon lamps. The combination of such modules permits irradiation of an area 9.75 m high and 1.5 m wide. Each arc source has a length of about 3 m and weighs 272 kg. The optical arrangement of the module (according to the Cassegrain system) includes both refracting and reflecting elements (Figure 4.37). A quartz lamp is installed in the focal plane of the optical system to compensate for the inadequate radiation of the carbon arc in the ultraviolet region. /276

6. Radiation Sources for Solar Spectrum Simulation

The Short-Wave Region

The suitability of a given radiation source for simulation of solar radiation is determined primarily by its spectral and energy characteristics.

We know that certain gases or vapors of metals emit intensive radiation in the near and vacuum regions of the ultraviolet portion of the spectrum during electrical gaseous discharge. Therefore, the radiation of a gaseous discharge and, in particular, certain gas-discharge lamps may be employed to simulate solar ultraviolet radiation. However, sources which could accurately reproduce the entire spectrum of solar radiation in the ultraviolet and X-ray regions are as yet unavailable. Radiation sources of various types must be employed to simulate the different sections of these solar spectrum regions. An approximate list of such sources is indicated in Table 31.

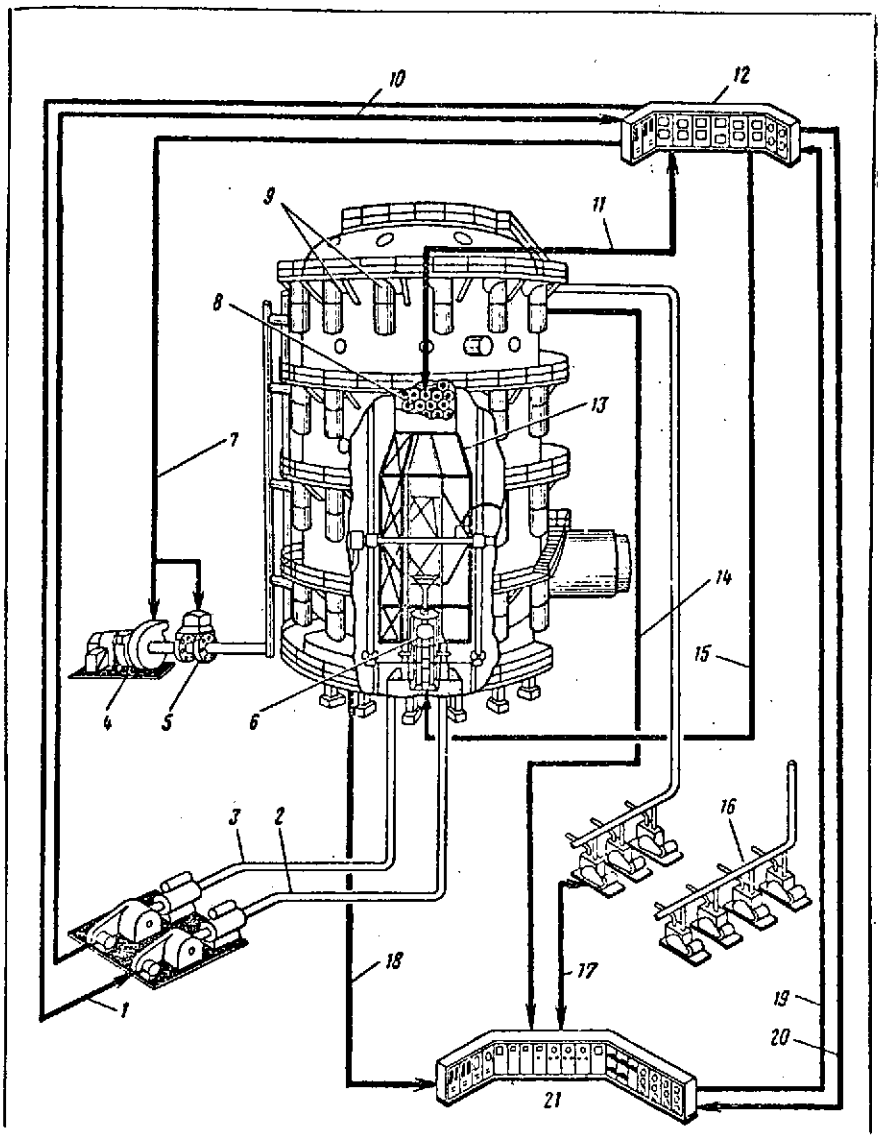

Figure 4.36. Schematic diagram of the Mark-1 facility: 1 — cryogenic system; 2 — liquid nitrogen; 3 — liquid helium; 4 — compressor; 5 — throttle valve; 6 — system simulating vibrational loads; 7 — line for regulating initial vacuum pumping; 8 — solar and planetary radiation simulator modules; 9 — diffusion pumps; 10 — control line of cryogenic system; 11 — solar and planetary radiation control line; 12 — central control console; 13 — system for securing spacecraft in the chamber; 14 — vacuum regulating line; 15 — line for controlling vibration bench and spacecraft; 16 — pumps; 17 — pump control line; 18 — gas analyzer; 19 — vacuum measuring line; 20 — pressure monitoring; 21 — main control console for vacuum system.

C4

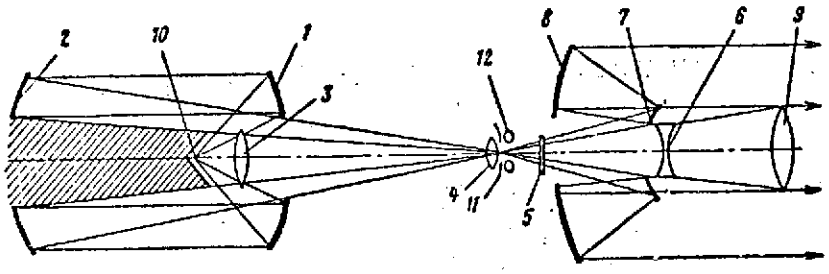

Figure 4.37. Diagram of optical system of carbon-arc module: 1, 2, 7, 8 — curvilinear mirrors; 3, 4, 6, 9 — lenses; 5 — sapphire window of vacuum chamber; 10 — crater for positive electrode 10 mm in diameter; 11 — diaphragm; 12 — lamp with reflector for ultraviolet radiation.

TABLE 31

SHORT-WAVE SOLAR RADIATION AND SOURCES FOR SIMULATION OF IT

Solar radiation			Possible sources for simulation
Region of spectrum	Wavelength, Å	Irradiation created at distance of 1 AU, mW/cm^2	
Near ultraviolet region			High-pressure gas-discharge lamps (mainly mercury and xenon)
Region A	3200 - 3800	7.04	
Region B	2800 - 3200	2.45	
Region C	2200 - 2800	0.81	
Vacuum ultraviolet region	1600 - 2200	0.1	Hydrogen arc lamps and plasmatrons;
	1000 - 1600	$1.3 \cdot 10^{-3}$	
	100 - 1000	$0.3 \cdot 10^{-3}$	Flow-type windowless gas-discharge sources (hydrogen, helium, argon, xenon, etc.)
Region of soft X-radiation (variation of radiation during quiet Sun, according to data of [67])	100 - 20	$10^{-5} - 10^{-4}$	Special tubes for soft X-radiation
	8 - 20	$10^{-8} - 10^{-6}$	
	2 - 10	$10^{-9} - 10^{-7}$	

High-pressure mercury-quartz lamps of the PRK type are widely employed in photochemical investigations. These lamps are made in the form of quartz tubes filled with argon and a small amount of mercury. The working pressure of the mercury vapor is up to 1.5 atm. The bright-line radiation spectrum in the ultraviolet region is emitted by the lamp under the effect of an electric discharge

between the electrodes in the mercury vapor. The lower boundary of the spectrum is near 2400 Å. The relative radiant energy distribution of the lamp over the spectrum is presented in Table 32.

TABLE 32

RELATIVE RADIANT ENERGY DISTRIBUTION ACCORDING TO SPECTRUM OF PRK MERCURY-QUARTZ LAMPS

Wavelength Å	Relative value of radiant energy* in %	Wavelength Å	Relative value of radiant energy* in %
2400	3.6	2970	14.3
2480	12	3020	31.5
2540	26	3130	68.2
2650	26.9	3650	100
2700	5.7	4040	32.9
2750	3.9	4360	57.3
2800	12.1	5460	65.3
2890	5.4	5780	73.6

*The energy at a wavelength of 3650 Å is assumed to be 100%.

Soviet industry manufactures mercury-quartz lamps of type PRK4, PRK8, PRK5, PRK2 and PRK7 with outputs of 220, 230, 240, 375 and 1000 W, respectively. The PRK2 lamp, whose radiation, according to [135], is very stable, is most often used; first annealed for 100 hours, the lamp may be used as a standard for spectral energy distribution and employed for different measuring purposes. The values of the radiation intensity of the PRK2 lamp, according to data of [135], are presented in Table 33. /278

In order to increase the accuracy of measurements with standard PRK2 lamps, one should take into account, besides the spectral emission lines, continuous background radiation, which comprises about 12% of the total radiation in the range of wavelengths of 2200 - 3800 Å.

The radiation spectrum of mercury-quartz lamps is the bright-line spectrum and differs considerably from solar radiation in this region. Therefore, PRK type lamps are hardly suitable for simulation of short-wave solar radiation. However, in view of the high radiation intensity in the ultraviolet region, the low cost and simplicity of operation, these lamps may be used in individual cases to check the effect of intensive ultraviolet radiation on materials.

TABLE 33

RADIATION OF PRK2 LAMP

Region of spectrum	Relative radiation distribution in %	Irradiation at distance of 1 m in mW/cm^2
Visible region (4000 - 6000 Å)	43.6	0.38
Ultraviolet region A (3200 - 3800 Å)	20.1	0.17
Ultraviolet region B (2800 - 3200 Å)	22.4	0.2
Ultraviolet region C (2200 - 2800 Å)	13.9	0.13
Total radiation	100	0.88

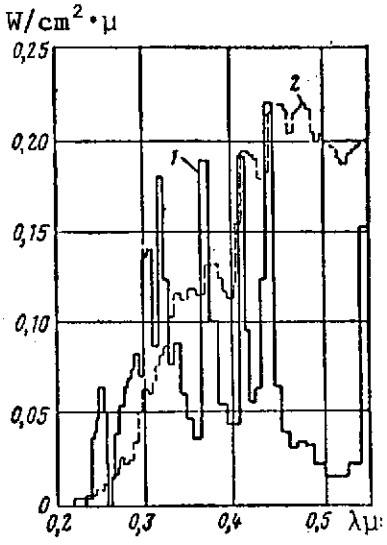

Figure 4.38. Radiation spectrum of B-H6 ultrahigh pressure mercury-quartz lamp with a power of 900 W (1); solar radiation spectrum (2).

Ultrahigh-pressure mercury lamps are widely employed in the United States to investigate the effects of ultraviolet radiation on materials [157, 229]. Type H6 (modification of A-H6 with water cooling and B-H6 with air cooling) lamps are usually employed for these purposes. Soviet industry produces ultrahigh pressure mercury-quartz lamps under the trademark DRSh, with powers of 250, 500 and 1000 W. Such lamps have a spherical container of quartz glass. Three electrodes are soldered in the /279 container: two main and one auxiliary lateral electrode, which provides a discharge between the main electrodes. The container is filled with mercury vapor whose pressure in the working state reaches 30 - 50 atm. Under these conditions, the arc discharge is concentrated between the ends of the electrodes, and a continuous bright background stretching from the ultraviolet to infrared regions, is superimposed on the bright-line structure of the mercury vapor spectrum; the color of the discharge approximates that of day light in this case. The spectral characteristics of an ultrahigh pressure mercury-quartz lamp are presented in Figure 4.38 [229].

An ultrahigh pressure mercury-quartz lamp with water cooling consists of a quartz tube placed in a metal or glass jacket with circulating water. The ends of the jacket should be made of quartz to admit ultraviolet radiation. A lamp in such a jacket may be located inside a vacuum chamber, which has certain advantages in testing materials.

According to data of [47], the spectral distribution of the radiation from water-cooled ultrahigh pressure mercury lamps is approximately as follows: about 46% is emitted in the ultraviolet region, about 27% — in the visible region, and about 27% in the infrared region.

The comparatively small fraction of the infrared portion in the total composition of radiation reduces the heating of the surfaces being irradiated. Operation of water-cooled mercury-quartz lamps is somewhat complicated by the necessity of selecting the appropriate water flow rate, by the pressurization conditions, and by selection of the insulation system for the leads. The principal characteristics of DRSh lamps are presented in Table 34.

TABLE 34

TECHNICAL CHARACTERISTICS OF DRSh LAMPS

Characteristics	Types of lamps		
	DRSh-250	DRSh-500	DRSh-1000
Output of lamp, W	250	500	1000
Circuit voltage, V	127	220	220
Lamp voltage, V	72	75	90
Luminance in center of discharge (minimum), Mnt	100	130	120
Light flux, lumens	$12.5 \cdot 10^3$	$22.5 \cdot 10^3$	$53 \cdot 10^3$
Dimensions			
greatest diameter, mm	22.5	33	40
greatest length, mm	145	190	232
distance between electrodes, mm	3.9	4.5	8

The steady combustion mode of the lamps begins within 10 - 15 minutes after ignition.

Ultrahigh pressure arc lamps filled with xenon are of great interest for simulation of solar radiation in the near ultraviolet region of the spectrum. An electrical discharge in xenon at high pressure yields radiation at a luminous temperature of 5200 - 5700° K, similar to the composition of solar radiation. Soviet industry produces tubular xenon lamps with air (DKsT) and water (DKsTV) cooling, as well as in spherical tubes of quartz glass (DKsSh and DKsR). Gas pressure in the /280

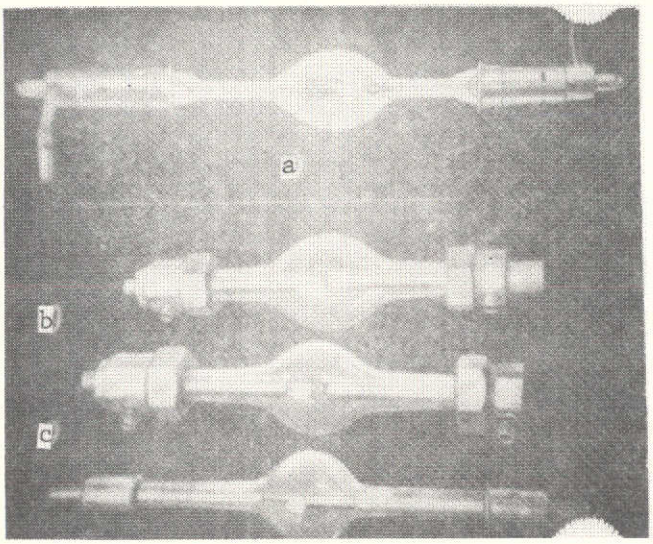

Figure 4.39. Overall view of ultrahigh pressure xenon arc lamps (not shown to the same scale).
a — 10 kW; b — 3 kW; c — 5 kW; d — 1 kW.

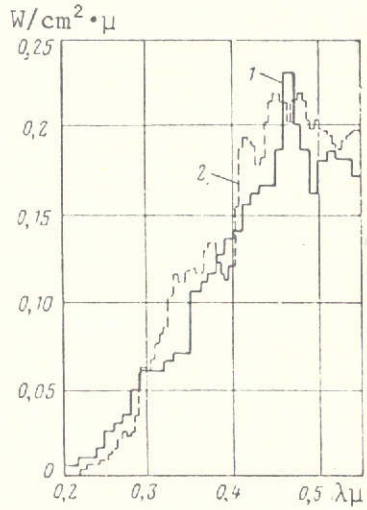

Figure 4.40. Radiation spectrum of ultrahigh pressure xenon arc lamp with power of 2.2 kW in the short-wave portion of the spectrum (1); solar radiation spectrum (2).

working state of spherical lamps reaches 10 - 20 atm. Under these conditions, the discharge is concentrated between the ends of the electrodes, and the brightness of the discharge space reaches large values.

An overall view of ultrahigh pressure xenon arc lamps is shown in Figure 4.39, and their radiation spectrum — in Figure 4.47. The radiation of xenon lamps has intensive maxima in the region of 8400, 9000, and 10,000 Å, and the radiant energy in the infrared region of the spectrum comprises more than 50% of the total radiation. If thermal radiation leads to inadmissible overheating of specimens during testing, this radiation may be reduced by a water filter. Chemicals which absorb infrared rays (for example, copper sulfate [122]) are sometimes added to the water. Ultraviolet radiation in this case is reduced slightly. The spectral distribution of radiation from an ultrahigh pressure xenon lamp in the ultraviolet portion of the spectrum is presented in Figure 4.40 [229]. The radiation of a xenon arc lamp in the region of wavelengths shorter than 4000 Å comprises approximately 10% of the total radiation. The characteristics of some xenon lamps are presented in Table 35.

TABLE 35

/282

CHARACTERISTICS OF XENON ARC LAMPS

Characteristics	DKsSh-200	DKsSh-1000	DKsR-3000	DKsT-5000	DKsT-2000	DKsT-5000	DKsTV-6000
Output, W	200	1000	3000	5000	2000	5000	6000
Supply voltage, V	70	50	60	80	60	110	220
Lamp voltage, V	22	23	32	40	50	100	200
Brightness in center of discharge, Mnt	90	180	500	—	—	—	—
Luminous flux, lm	—	—	—	—	$33 \cdot 10^3$	$88 \cdot 10^3$	$2 \cdot 10^5$
Dimensions diameter, mm	26	44	45	55	24	22	
length, mm	—	258	—	—	280	25	—
distance between electrodes, mm	—	4.3	—	—	140	430	250

It is obvious from Figure 4.40 that the radiation of an ultrahigh pressure xenon lamp in the ultraviolet region of the spectrum more closely approximates solar radiation when compared to other lamps. Therefore, from the viewpoint of solar radiation simulation accuracy, these lamps are more suitable. However, in some cases, especially in accelerated tests of materials, a source may be required with greater radiation intensity in the ultraviolet region of the spectrum. In this regard, an ultrahigh pressure mercury lamp has advantages over a xenon lamp, because its ultraviolet radiation comprises about 35% of the total energy, and in absolute value, for example, the ultraviolet radiation of a 900-watt B-H6 mercury lamp is three times greater than that of a xenon arc lamp of 2.2 kW [229]. Moreover, mercury lamps are much cheaper than xenon and do not require special heavy-current rectifiers for the power supply. Obviously, all these concepts may explain the fact that in most articles, devoted to investigation of the resistance of space technology materials to UV radiation and published in the American periodical literature, ultrahigh pressure mercury lamps of type H6 are mentioned as a radiation source, although the radiation of these lamps in the UV region of the spectrum differs somewhat from solar radiation. The latter fact should be kept in mind when conducting tests.

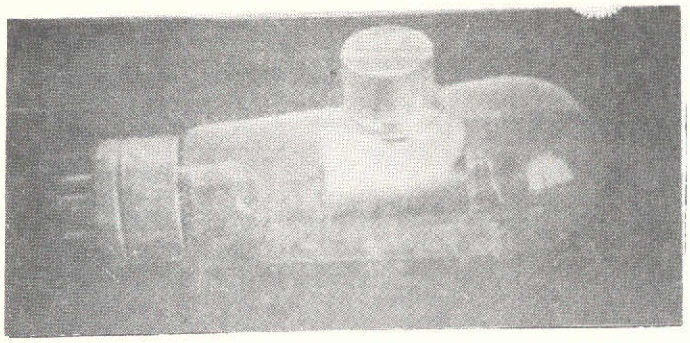

Figure 4.41. Overall view of DVS-200 hydrogen arc lamp.

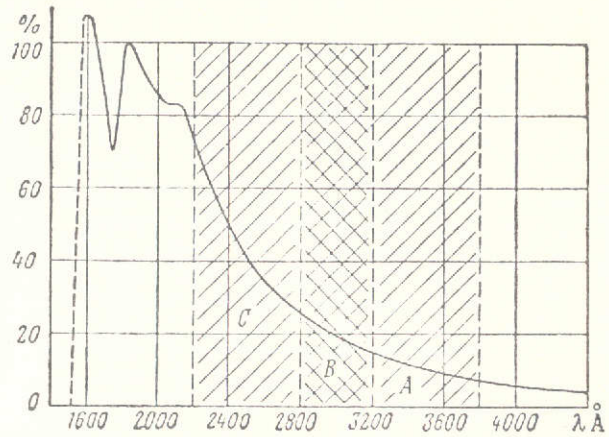

Figure 4.42. Radiation spectrum of DVS-200 hydrogen arc lamp.

Ultraviolet radiation at wavelengths up to 1200 - 1500 Å may be obtained from hydrogen spectral arc lamps. Such lamps with powers of 25, 40 and 200 W (DVS-25 [VLF25], DVS-40 and DVS-200) are produced in the Soviet Union. The lamps emit a continuous hydrogen spectrum from 3600 Å to the transmission cutoff threshold of the output window. Lamps of 25 and 40 W are produced with windows of uviol glass, lithium fluoride or fluorite. The DVS-200 lamp has an output window of a flat plat of fused quartz, and this lamp is presently the most suitable source for simulation of the effects of solar UV radiation in the range of 1550 - 2200 Å.

The DVS-200 hydrogen lamp is a low-pressure arc lamp (2 mm Hg) with a heated cathode (Figure 4.41). The anode voltage of the lamp is 200 - 400 V, and nominal anode current is 3 A. The radiation pattern of the lamp has the shape of a cone at an angle of 35°, the apex of which lies within the center of the luminous aperture of the anode. The spectral distribution of radiation of the DVS-200 is presented in Figure 4.42. Because of heating of the electrodes during operation, the portion of infrared radiation comprises more than 80% of the total radiation of the /284 lamp. Ultraviolet radiation comprises 10 - 12% of total radiation.

The short-wave radiation threshold of the DVS-200 hydrogen lamp (~1500 Å) is determined by the transmission of the quartz window. Another material, for example, lithium fluoride, should be used instead of quartz to obtain radiation of shorter wavelengths. This permits the region of UV radiation to be expanded to 1100 Å. Because the transmission of lithium fluoride deteriorates in time under intensive UV radiation, the possibility of replacing the windows should be considered. This may be accomplished by making the lamp detachable from the power supply during operation with hydrogen from a separate gas source.

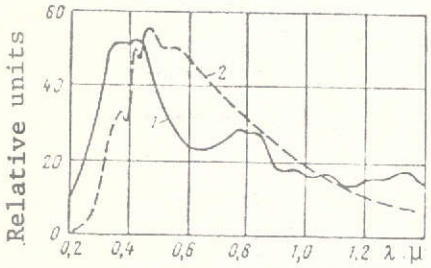

Figure 4.43. Radiation spectrum of argon plasma arc (1); solar radiation spectrum (2).

The use of a plasma arc as a source, simulating the effects of short-wave solar radiation on materials, is reported in [171]. The plasma formed due to the effect of an electric arc discharge may actually act as an intensive radiation source in the UV region of the spectrum. The spectral composition of radiation depends on the selection of the plasma-forming gas. For example, pure argon permits intensive radiation in the UV region (Figure 4.43) to be obtained, and a mixture of xenon and argon emits radiation even more closely approximating the composition of solar radiation. /285

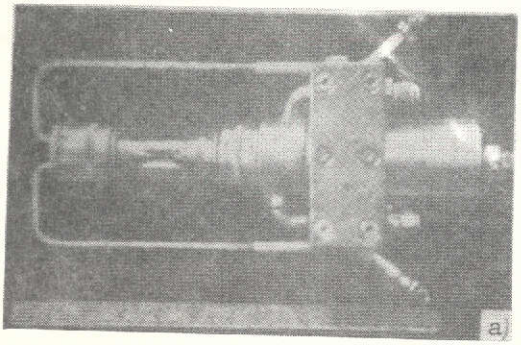

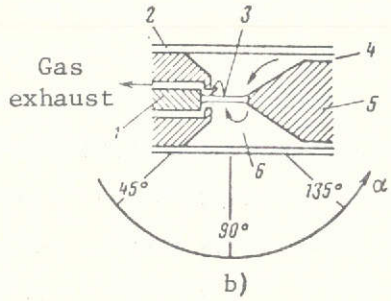

Figure 4.44. Electric arc plasmatron: a — overall view; b — schematic diagram; 1 — anode; 2 — quartz cylinder; 3 — arc; 4 — gas injector forming flux; 5 — cathode; 6 — vortex flow.

One of the variants of an electric arc plasmatron, which may be used to simulate solar radiation [238], is shown in Figure 4.44. The plasmatron is mounted in a quartz discharge chamber, the walls of which are transparent to UV radiation. The argon passing through the mixing nozzle forms a spiral-like "twist" in the working space and emerges through the axial nozzle in the body of the anode. The discharge electrodes and the ends of the quartz tube are cooled by circulating water. A brightly luminescent plasma arc is formed upon an electric arc discharge between the anode and cathode. In the simulator described in [171], the arc had a diameter of 4 mm and a length of 12 mm. The required output varied from 10 to 20 kW and radiation at 17 kW had an effective temperature of ~7000° K. The radiation spectrum was continuous — from 1500 to 7000 Å, with a maximum in the region of 4500 Å. Radiation intensity exceeded solar radiation by more than a hundredfold at a distance of 1 AU at 1500 Å, more than 2.5 times at 3000 Å and was less than

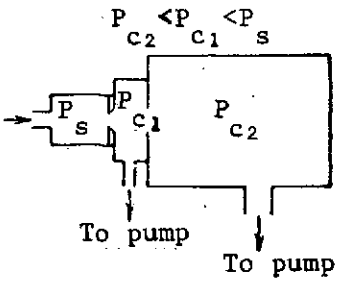

Figure 4.45. Diagram of differential vacuum pumping of test chamber with radiation source.

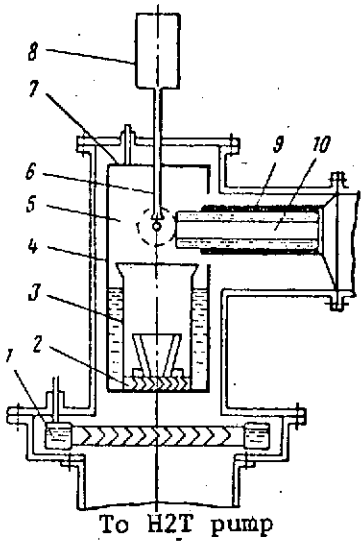

Figure 4.46. Source of vacuum ultraviolet radiation with electron excitation of supersonic gas jet: 1 — pump trap; 2 — copper louvers and cones; 3 — condensation pump; 4 — nitrogen shield; 5 — electron gun; 6 — Laval nozzle; 7 — source chamber; 8 — discharge chamber; 9 — nitrogen shield; 10 — channel for radiation input.

solar radiation at 4500 Å. Variants of the design and some operating characteristics of plasmatrons for simulating solar radiation are presented in [238].

Gas-discharge tubes, in which the discharge is induced either by a constant high voltage or by a high-frequency generator, may be used to simulate solar radiation in the far UV region of the spectrum. Depending on the selection of gas, its pressure and the method of obtaining the electric discharge, various bright-line radiation spectra or continuous spectra (continuums) may be obtained in the region of the vacuum ultraviolet. Discharge tubes with various radiation characteristics are described in [45] and in a number of other papers. Such radiation sources are usually windowless, and the radiation is introduced into the vacuum chamber through a capillary opening. The gas leaks into the test vacuum chamber through this opening, which leads to a sharp deterioration of the vacuum in the chamber during operation of the radiation source. In order to reduce the effect of inleakage, systems of differential vacuum pumping are used which permit a pressure p_{c2} to be maintained much lower in the test chamber than in the radiation source chamber p_s (Figure 4.45).

With electron excitation of the supersonic gas jet, a powerful windowless source of vacuum ultraviolet radiation may be obtained which permits the radiation to be introduced into the vacuum chamber without differential pumping. The design of such a radiation source has been worked out [30a]. The supersonic gas jet is created when it is discharged into the vacuum through a Laval nozzle (Figure 4.46).

The jet is stimulated by an electron beam with an energy up to 2 keV, located /286
in the plane perpendicular to the axis of the jet (in Figure 4.46 the excitation source is not shown). Upon electron stimulation of the argon jet, the source emits a bright-line spectrum in the region below 1066 Å, created by radiation of highly ionized argon atoms; beginning from 1066 to 1500 Å, an intensive continuous spectrum is observed with a maximum in the region of 1270 Å. The integral radiation intensity in the region below 1100 Å at a particle density of about $7 \cdot 10^{17}$ cm^{-3} in the output section of the nozzle, electron current density of 0.07 A/cm^2 and electron energy of 1.1 keV comprises 0.28 mW/cm^2 at a distance of 80 mm from the jet.

The source chamber is evacuated by an H-2T oil-diffusion pump. To increase the evacuation rate of large quantities of gas entering the chamber with the supersonic jet (average flow of ~23 cm^3/sec), a cryogenic condensation pump is installed inside the chamber (see Figure 4.46). The radiation is fed into the high vacuum chamber through a channel about 300 mm long and 40 mm in diameter, cooled by liquid hydrogen and protected by a nitrogen shield against the thermal radiation of the chamber walls. The gas pressure in the region of the jet may have a value from one to tenths of a torr, while at the same time, due to condensation of the jet material on the cold walls, the pressure in the source chamber is several orders lower (up to 10^{-5} torr). Because of this, the radiation may be introduced /287
into the chamber at an ultrahigh vacuum of 10^{-8} - 10^{-9} torr without discernible deterioration of the latter.

The composition of the solar spectrum may be approximated by selection of the gas composition and the operating conditions of the source. Such a radiation source is of specific interest for investigations related to simulation of short-wave cosmic solar radiation, since it permits direct introduction of radiation at a large solid angle into an ultrahigh vacuum chamber.

Simulation of the X-ray region of the solar radiation spectrum presents specific difficulties. The use of ordinary X-ray tubes permits radiation at wavelengths from tenths of angstroms to a few angstroms to be obtained. The concentration of this type of radiation in the solar spectrum is negligible (see Table 31). It is of greater interest to obtain "soft" radiation at wavelengths up to 100 - 200 Å. Special X-ray tubes with "soft" X-radiation have now been created to simulate the "soft" X-radiation of the solar spectrum.

Thus, in principle, simulation of the radiation of any portion of the solar spectrum is possible. Simulation of the entire shortwave region of the spectrum simultaneously requires introduction of radiation from several different sources into the vacuum chamber, which may sometimes cause specific difficulties. Apparently, in a number of cases, depending on the effect expected, one may limit oneself to a single specific radiation source. Practical use of sources for simulation of the far (vacuum) ultraviolet and "soft" X-radiation is very limited in view of the negligible value of the energy of this radiation. Actually, the energy of such radiation in the composition of the solar spectrum is negligible — millionths and ten millionths of a watt per square centimeter (see Table 31).

The Long-Wave Region of the Spectrum

The above-described xenon lamps are employed not only to simulate the shortwave portion of the solar spectrum, but also to reproduce the visible and infrared portions. Type DKsT lamps are often used in small simulators. More powerful quartz arc lamps with an output of 10, 15, and 20 kW, filled with xenon and mercury-xenon (see Figure 4.42), as well as carbon arcs and plasmatrons, are employed in solar simulators with a light spot greater than 1 m^2.

Xenon lamps have considerable light output. Thus, a luminous flux of 235 klm may be obtained from a lamp with an output of 6000 W.

The approximate thermal balance of a quartz xenon lamp is: /288

Energy carried away by water	1.7 kW
Radiation in visible region	1.25 kW
Radiation in ultraviolet region	0.35 kW
Radiation in infrared region	2.1 kW
Miscellaneous losses	0.6 kW
Total	6.0 kW

Thus, of 6 kW of the output required by the lamp, almost 3.7 kW (62%) is dissipated in the form of radiant energy, which may be used in a solar or planetary simulator.

TABLE 36

DATA ON SOME HIGH-OUTPUT QUARTZ LAMPS

Type of lamp	Output kW	Filler	Outer diameter of bulb, mm	Total length mm	Arc length mm	Internal pressure atm	Working voltage V	Current intensity a	Luminance		Luminous flux lm	Service life in hours
									Max Mnt	Avg Mnt		
932B "Hanovia" USA	5	Hg-Xe	86	343	5	15	50-60	100	2250	780	230,000	—
XE-10000 "Duro-test" USA	10	Xe	92	699	8	10	40	250	9500	1250	480,000	500
XE-20000 "Duro-test" USA	20	Xe	120	851	13.5	6	50	400	7500	1700	1,000,000	—

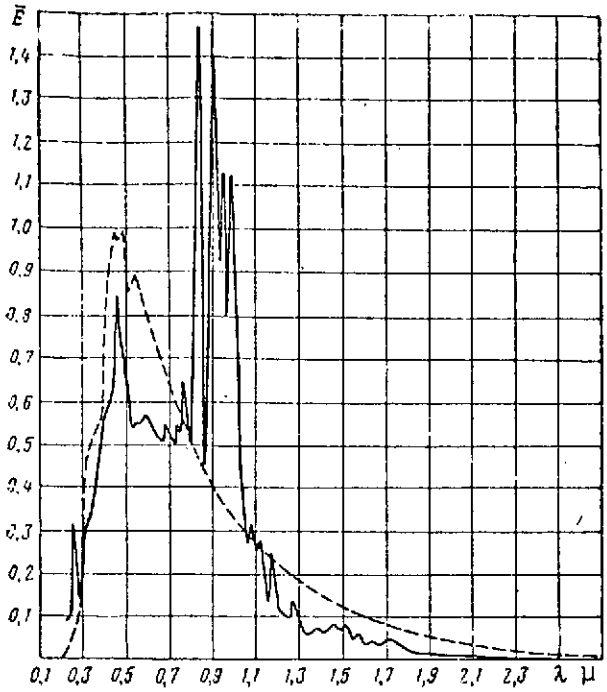

Figure 4.47. Radiation spectrum of xenon arc lamp (solid line) and solar spectrum (dashed line) in relative units.

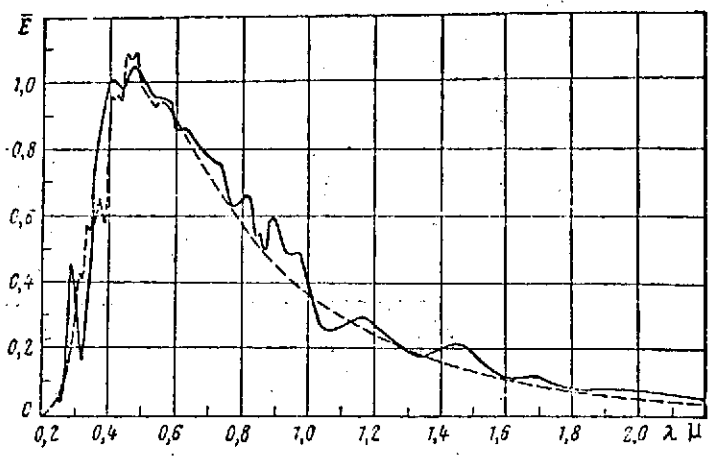

Figure 4.48. Spectrum of A-1200 type solar radiation simulator (xenon lamp with filter) and solar spectrum (dashed line) in relative units.

The data of some high-pressure quartz lamps are presented in Table 36.

Quartz lamps may be used with spherical counterreflectors, which are installed on the side opposite the main reflector. A counterreflector collects radiant energy within the limits of a solid angle of 2π steradians (angle of contact 180°) and returns it into the discharge zone. The counterreflector projects its inverted image onto the discharge zone and at the same time makes the projection diagram of /289 lamp radiation more uniform.

Beginning from the ultraviolet end of the spectrum to the infrared portion, the spectral curve of a xenon lamp approximates the solar curve (Figure 4.47). The spectrum of a lamp may more closely approximate that of the sun (Figure 4.48) [178] with the aid of special light filters (see below p. 301).

High-pressure xenon lamps with spherical quartz bulbs are subject to explode. The probability of the lamp exploding varies over a wide range, depending on the technique of manufacture. The explosion hazard for a 6-kilowatt lamp is approximately equal to 0.01 and that for a 10-kilowatt lamp — about 0.04. These values vary with time when lamps are stored. For this reason, xenon lamps are more often used in arrangements where the radiation sources are located outside the vacuum chamber.

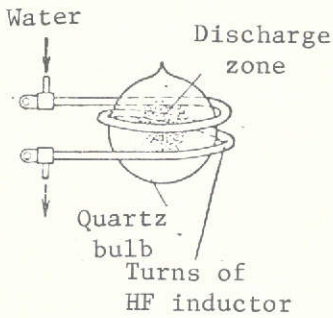

Figure 4.49. Diagram of lamp with high-frequency discharge.

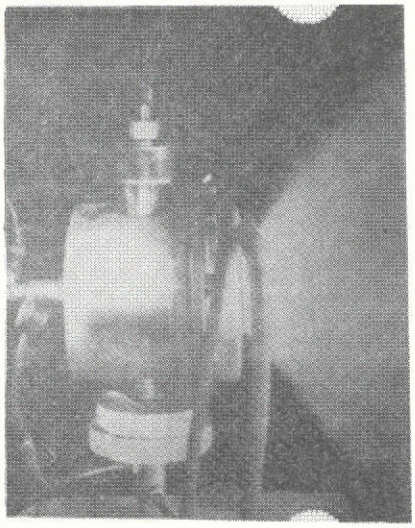

Figure 4.50. Overall view of switched-on VNISI metal lamp (40 kW).

A certain operational instability, which is manifested in a decrease of radiation in time with a constant power supply, is inherent to high pressure gas-filled quartz arc lamps. The radiation intensity decreases by an average of 30% with 300 - 500 hours of operation. Aging of lamps proceeds non-uniformly for /291 different specimens. The difference in the radiation intensity of lamps at the end of their service life comprises 10 - 15%. A system for regulating the input power of the lamps is introduced into the optical circuit of the simulator to compensate for the effect of aging. The system is controlled automatically by radiant flux sensors which are installed individually for each lamp.

An explosively dangerous xenon lamp is one with high-frequency excitation of discharge (Figure 4.49). The working pressure in the lamp is about 1 - 2 atm. Plasma temperature is 6000 - 9000° K. The lamp is supplied from a high-frequency generator. The frequency depends on the dimensions of the lamp and is usually with the range of 10 - 20 MHz.

The DKSR-40,000 high-pressure metal xenon lamp, developed by VNISI (Figures 4.50 and 4.51) [98], is suitable for practical application in solar simulators. The internal portion of the lamp body is made in the form of a reflecting ellipsoid, in one of whose foci an arc burns (see Figure 4.19d). Therefore, the lamp simultaneously fulfills the role of a light source. The increased image of the bright spot of the arc is located in the other focus beyond the confines of the lamp. An increase of the image (D/d) is determined by the parameters of the ellipsoid. The dimensions of the semi-minor axis of the ellipsoid reflector for an arc 4 - 5 cm

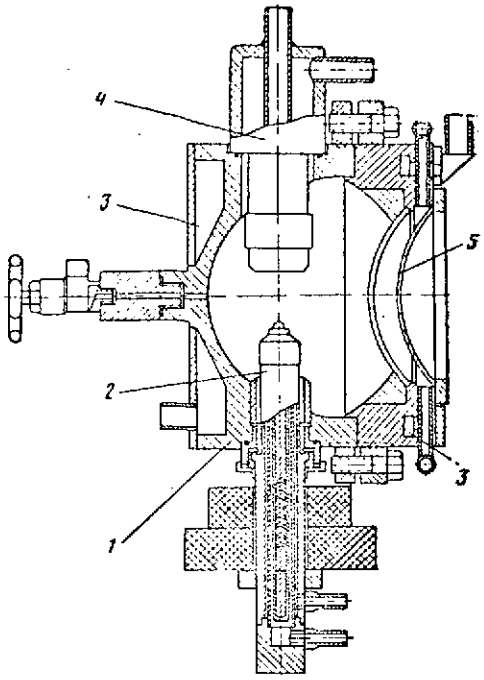

Figure 4.51. Diagram of DKSR-40,000 metal xenon lamp (40 kW) (VNISI) with freely-burning arc: 1 — metal body; 2 — cathode; 3 — channels for water cooling; 4 — anode; 5 — double water-cooled quartz window.

long are selected from 100 to 120 mm; eccentricity e ≈ 0.5. (Screening of reflected radiation by the electrodes increases at high eccentricity and, moreover, a large output window is required in the second focus due to the large increase in the image of the arc. At low values of e, a considerable portion of the radiation of the arc is not utilized.)

A variant of a 40-kilowatt lamp, in which the size of the image of the luminous spot is approximately equal to 90 mm, is presented in Figure 4.51. The body of the lamp, made of bronze or aluminum alloy, is cooled by circulating water and has a low operating temperature (~40° C). The front part of the body is made in the form of a sphere from the inside and also has a reflecting surface, which permits the efficiency to be increased somewhat due to reflection of the beams, which do not impinge at an angle of contact of 2β, back into the discharge zone. /292

The radiation indicatrix of the lamp is somewhat asymmetrical with respect to its longitudinal axis. This leads to non-uniform irradiation of the mirror of the solar simulator. Typical radiation distribution on the portion of a spherical surface with a radius of 2000 mm with the center in the middle of the window of the lamp is presented in Figure 4.52. The lines of equal radiation, which indicate that 80% of the total radiant flux is concentrated in the cone of beams with an angle at the apex of ~60°, are depicted in this case. The inhomogeneity of irradiation within the limits of this angle does not exceed ±15% over an area of 80%. Deviations of more than ±20% occupy an area less than 8%. The total light output of the lamp is directly proportional to the required electrical input. The radiant flux input at a lamp output of 42 W comprises about 10 kW.

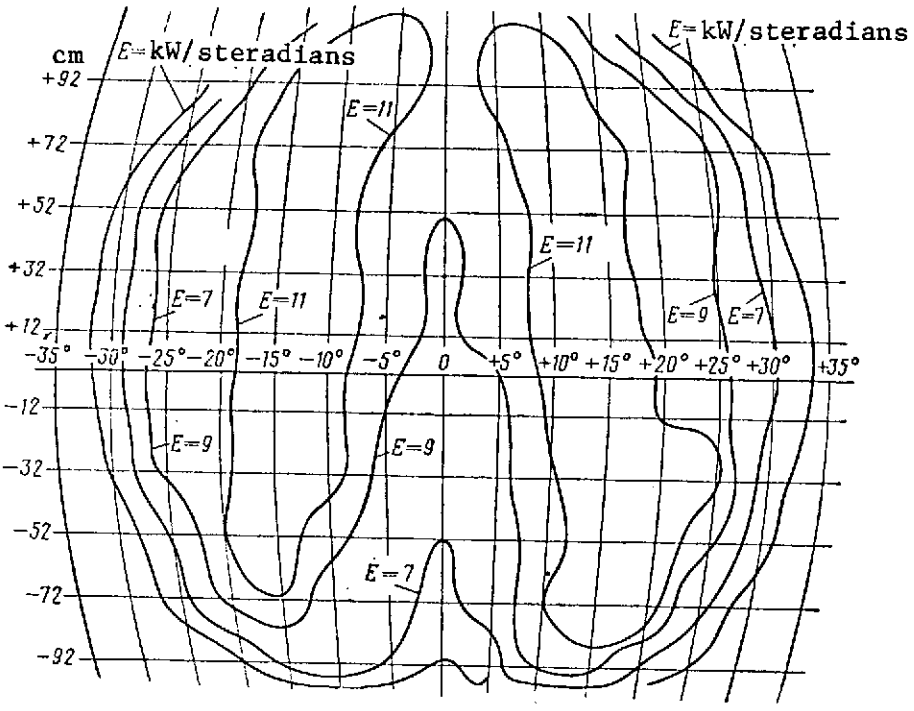

Figure 4.52. Radiation pattern of DKSR-40,000 lamp. When measuring irradiation, the radiometer was moved along the sphere of a radius of 2 m with the center in the middle of the window of the lamp.

The radiation pattern of the lamp hardly varies in time. It is assumed /293
that the lamp has exhausted its resources if its light output drops by 20% compared to the initial value. The dismountable design of the body permits repeated use of the lamp after the reflecting properties of the internal reflecting surfaces have been restored.

The explosive safety of the VNISI lamp-luminaire is ensured by using concave quartz glass operating under compression. The lamp anode is copper and cooled by water. The cathode of thoriated tungsten (VT-15 or VT-50) is fused into a solid copper base, which has good thermal contact with the water-cooled copper seat. The arc is ignited by touching the electrode. For this, the cathode, the lower part of which is equipped with a magnetic core, is raised with the aid of an electromagnetic coil until it touches the anode, after which it is again lowered into the copper seat. In order to prevent interruption of electric contact between the seat and the cathode at the moment of contact between the anode and cathode, the latter has annular grooves filled with copper balls. The balls ensure numerous points of contact of mutually moveable parts in any position of the cathode. The arc is ignited at a current of

10 - 15 A to avoid destruction of the electrodes. The lamp is supplied by direct current. Ignition voltage is ~220 V. At maximum current (500 A) the voltage on the electrodes is about 100 V.

The current-voltage characteristic of the lamp depends on the current rate of variation, since the gas in the lamp is heated and its pressure increases as current increases, inducing in turn an increase of voltage in the arc. Therefore, the quasistatic current-voltage characteristic, obtained with slow current variation, is considerably steeper than the dynamic characteristic, when current varies rapidly and the gas in the lamp does not manage to heat up to an equilibrium state. The lamp may operate both inside (in a vacuum) and outside the chamber.

For normal operation of the described lamp-luminaire, it is necessary that the longitudinal axis of the lamp be horizontal or not deviate from this position more than 10 - 15°. This condition somewhat limits the use of the lamp.

A good approximation of the solar spectrum was obtained with the aid of a quartz arc lamp, filled with mercury vapor containing additives of aluminum chloride ($AlCl_3$), indium iodide (InI_3) and tin bromide ($SnBr_2$) (Figure 4.53). Some characteristics of these lamps are presented in Table 37.

TABLE 37

CHARACTERISTICS OF EXPERIMENTAL QUARTZ ARC LAMPS

Filler	Electric capacity W	Working pressure atm	Distance between electrodes mm	Light output lm/W	Color temperature °K	Power concentration at discharge W/cm^2	Service life
Mercury vapor +$AlCl_3$	650	3-4	8	100	—	3000	Several hours
Mercury vapor +InI_3	1600	22	18	75	7500	—	200 hrs
Mercury vapor +$SnBr_2$	400	—	60 (tubular)	50	5500	—	6000* hrs

*Light output decreases by 20% after 6000 hours.

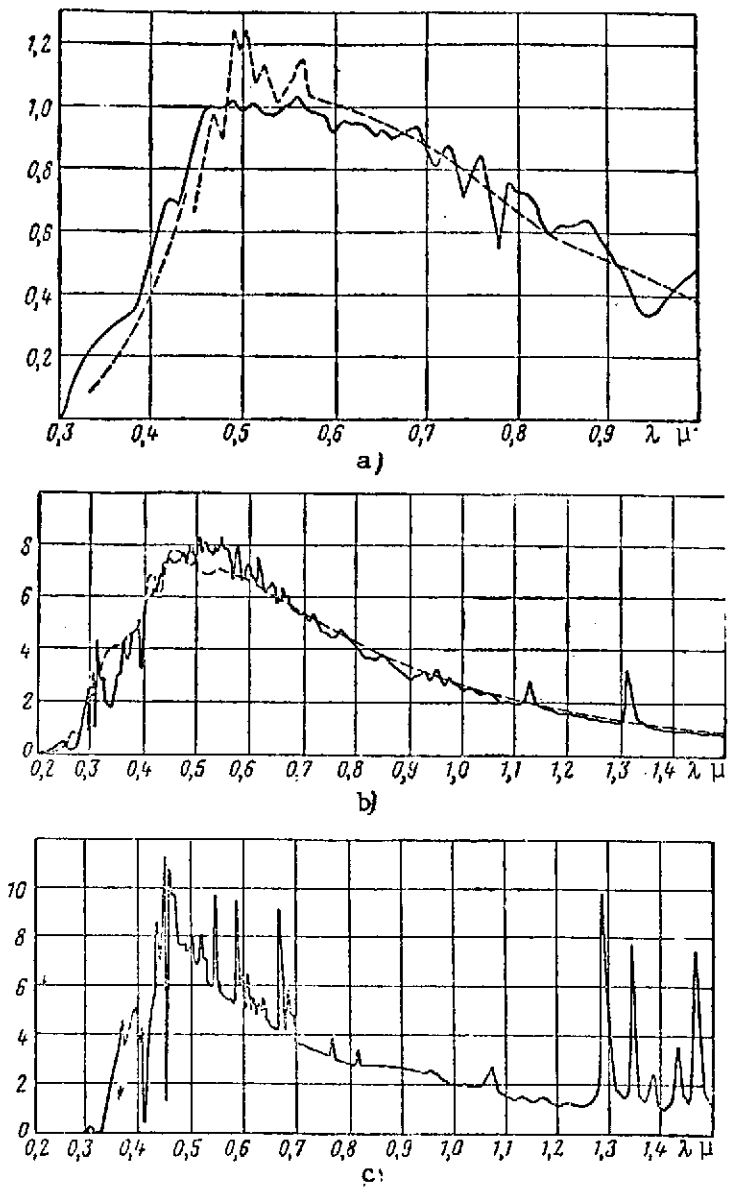

Figure 4.53. Spectra of quartz arc lamps in relative units, filled with tin bromide (a), aluminum floride (b) and indium iodide (c). (The dahsed line is the solar spectrum).

Structurally, these lamps hardly differ from ordinary xenon lamps. The important advantage of lamps of this type over ordinary xenon or mercury-xenon lamps is that they emit a spectrum approximating the solar spectrum, without using additional light filters. However, at present, these lamps may not be used for large solar /295 simulators due to the fact that the resources of the first two (see Table 37) are too small and the output of the third one is inadequate.

Carbon Arc Sources

The great brightness of a carbon arc and spectral distribution approximating the solar spectrum (Figure 4.54) makes carbon arc sources suitable for use in solar radiation simulators. /296 However, the practical application of these sources encounters a number of difficulties related mainly to the high rate of consumption of the positive electrode. This rate of consumption increases sharply as the output of the arc increases (Table 38).

Thus, a carbon rod 16 mm in diameter and 580 mm long in a 28-kilowatt arc burns up within 30 minutes. Therefore, to ensure prolonged operation of arc sources, their output does not usually exceed 30 - 40 kW.

TABLE 38

Current intensity A	Working voltage V	Rate of consumption of anode mm/hr	Power of kW	Total Brightness of Crater cp	Electrode Diameter mm
145	77	457	—	—	13.6
187	83.1	1500	15.6	74,300	10
384	85.1	4900	32.4	119,400	10

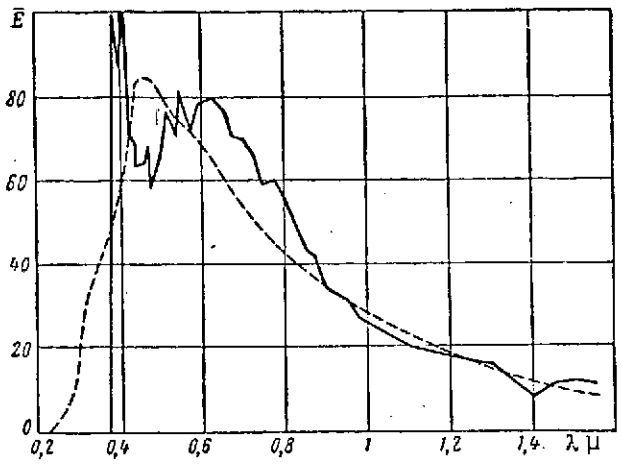

Figure 4.54. Spectrum of carbon arc and solar spectrum (dashed line), Ē — relative values.

For stable combustion of the arc and uniform consumption of the carbon rod, during operation it is rotated at a rate of 10 - 15 rpm. The negative carbon electrode (cathode) is consumed at a rate 10 times less than the positive electrode, and if it is made of water-cooled tungsten, it will hardly be consumed. The problem of replacing the positive carbon electrode in the "Mark-1" facility was solved with the aid of an automatic feed system with the magazine in the form of a rotating drum, containing 20 rods each 666 mm long (Figure 4.55). A single loading of the drum is sufficient for continuous operation of the carbon-arc source for 24 hours.

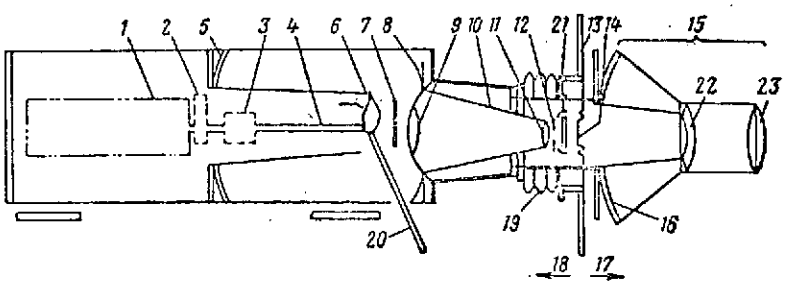

Figure 4.55. Schematic diagram of arc module: 1 — magazine with positive electrodes; 2 — screw-cutting machine for electrodes; 3 — mechanism for feeding and rotating electrodes; 4 — positive electrode; 5 — mirror; 6 — arc in shielding housing; 7 — quartz protective glass; 8 — mirror; 9, 11, 22, 23 — lenses; 10 — cone; 12 — diaphragm; 13 — vacuum chamber wall; 14 — vacuum chamber window; 15 — collimator; 16 — reflector; 17 — low pressure; 18 — atmospheric pressure; 19 — bellows; 20 — negative electrode; 21 — lamp with reflector for UV radiation.

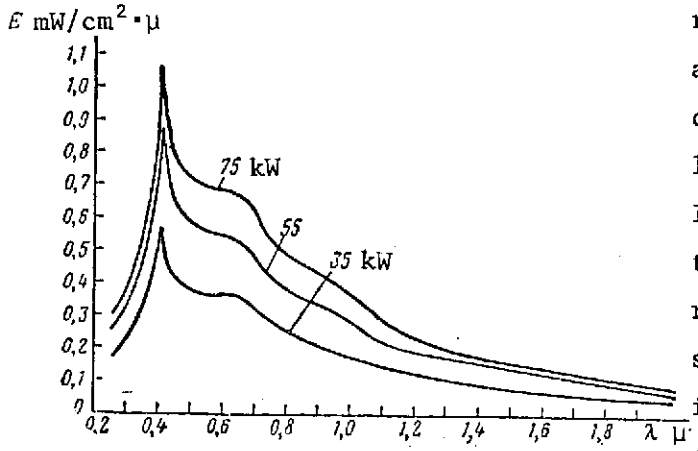

Figure 4.56. Spectral distribution curves of open arcs with an output of 35, 55, and 75 kW, measured with the aid of interference filters.

There are presently no great difficulties related to obtaining more powerful carbon arc sources. The spectral characteristics of arcs with outputs of 25, 50, 75, and 100 kW have been obtained and investigated. It is typical that, as output increases, the curves of spectral energy distribution remain similar to and approximate the solar spectrum curve, according to Johnson. This is easily seen in Figure 4.56, where the spectral curves are shown for the crater of an arc, the anode of which is made of graphite with a core of molded powder of rare-earth oxides. The brightness distribution in carbon arcs is considerably more uniform than in the arcs of xenon lamps (Figure 4.57).

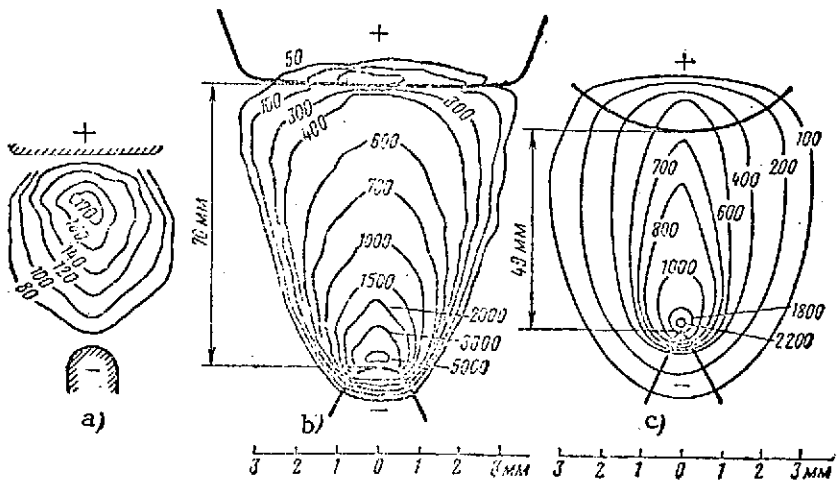

Figure 4.57. Typical brightness distribution through arc in relative units: a — carbon arc of 55 kW; b — xenon lamp of 5 kW; c — mercury-xenon lamp of 5 kW.

A Plasma Arc

Very high radiant flux densities may be obtained with the aid of plasmatrons, in which a plasma temperature is achieved much higher than that on the surface of the Sun. The lifetime of plasmatrons, like carbon-arc sources, is short. This obviously explains the fact that only approximately 0.5% of all facilities for testing spacecraft in the United States are equipped with simulators having plasma radiation sources.

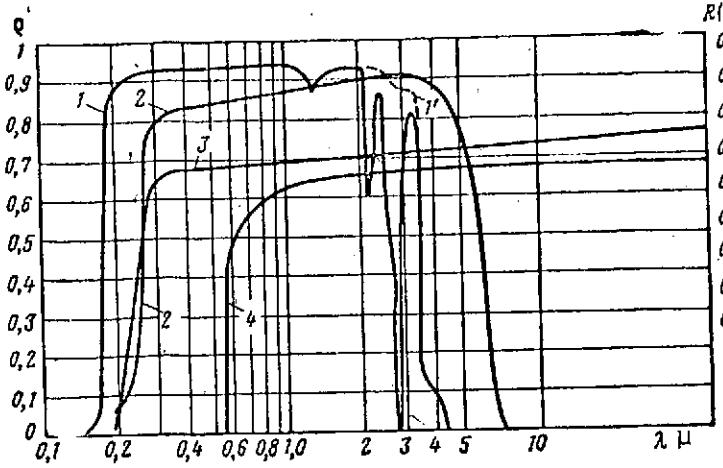

Figure 4.58. Transmission spectrum of different materials: 1 — fused quartz; 2 — leukosapphire; 3 — KRS-5; 4 — KRS-6.

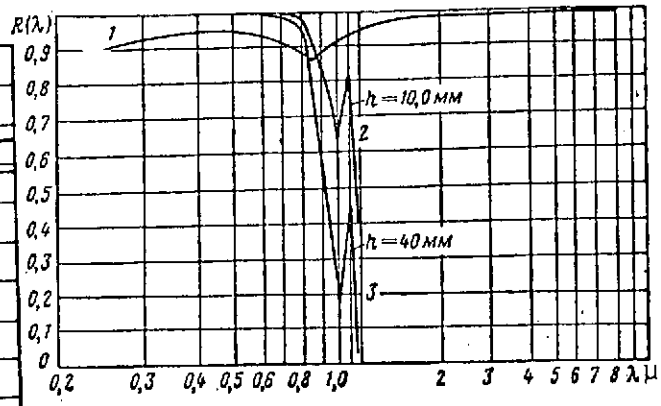

Figure 4.59. Reflectivity of an aluminum mirror (1) — sputtering at 10^{-5} torr — and transmission coefficient of water layer 10 mm (2) and 40 mm (3) thick.

Glass, Lenses and Light Filters

The refracting optics, used in solar and planetary radiation simulators, should be transparent in the wavelength range from 0.2 to 3 microns, since 99% of solar energy lies within this range.

The best materials for windows, lenses and bulbs may be fused quartz and leukosapphire. The transmission curves of these materials for different portions of the spectrum are presented in Figures 4.58 and 4.59. It is obvious, by comparing the solar spectrum to the transmission curves of quartz and leukosapphire, that these materials transmit almost the entire energy of the Sun, with the exception of the far ultraviolet and far infrared regions.

There are also other materials with suitable spectral transmission curves, for example, NaCl, KBr, CsI, KRS-5, "Irtran-I," "Irtran-II" glass, etc. However, these materials are hardly suitable for use as the optical elements in simulation chambers, because they either do not have the necessary mechanical properties or are hygroscopic or alter their characteristics under the effects of short-wave radiation.

Various light filters (for example, glass KG-2, UV-6, WG-5, etc.) are employed to approximate the spectra of radiant energy sources in solar simulators to that of the Sun. Light filters are usually installed at the point of radiant flux where the flux is not too wide, in order not to increase the dimensions of the light filter excessively. An increase in the dimensions of light filters is undesirable for a number of reasons, including the high cost. However, placing a light filter in the zone of increased radiant flux density leads to considerable heating. A strongly heated light filter may impart its own uncontrollable contribution to the infrared component of the spectrum and, moreover, increases the probability of variation of its optical property. Cooling of the light filter complicates its design, especially if the filter is located inside the chamber. /30

Variation of the optical properties of the filter may also occur in time due to the effects of the ultraviolet component. Thus, after several tens of hours of operation in a solar simulation system, consisting of a radiant flux source, light filter and optical element, very appreciable deviations from the initial carefully calibrated spectrum may appear. The time required for testing some types of spacecraft reaches 2000 hours. By the end of the test period, the spectrum may vary by an inadmissable value, if it is not additionally corrected by replacing the light filter and by appropriate regulation of the source output.

7. Measuring the Radiant Flux Characteristics of a Solar Simulator

When assessing the accuracy of simulating solar radiation, the following factors should be taken into account:

1. conformity of the spectral composition of the source radiation to the spectral curve of solar radiation;
2. conformity of source radiation intensity to solar radiation intensity in a given portion of the spectrum;
3. uniformity of radiation;
4. angular distribution.

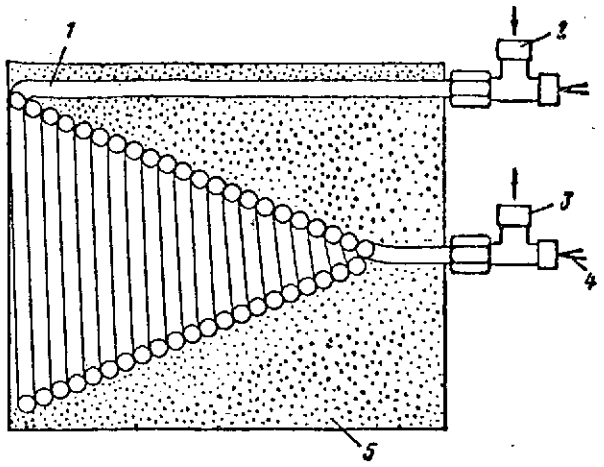

Figure 4.60. Diagram of conical tubular calorimeter: 1 — copper tube, d = 5.6 mm; maximum diameter of winding is 100 mm; 2 — water input; 3 — water removal; 4 — thermocouples; 5 — heat insulation.

The conformity of the spectral composition of the source radiation to the spectral curve of solar radiation is checked with the aid of vacuum monochromators, designed for measurements in the ultraviolet region of the spectrum. The method of working with such spectral devices is outlined in the appropriate special literature [45, etc.].

Radiation intensity may be determined by using various electromagnetic radiation detectors.

The following methods of measuring radiation intensity find application in experimental practice.

The calorimetric method is based on measuring the amount of heat received by a sufficiently black surface (ε = 0.95 - 0.98). The degree of darkness of the radiation detector, which is close to unity, may be achieved with the aid of special black enamels in combination with a geometry which leads to multiple re-radiation and absorption within the detector of all beams impinging on it. /301

The diagram of a radiation detector, made in the form of a cone of thin-walled pipes, inside which circulates water, is presented in Figure 4.60. The temperature difference of the liquid at the input and output permits the amount of radiant energy absorbed by the sensor to be determined. The sensor is covered on the top by a layer of heat insulation to reduce spurious heat leaks [253].

Such sensors usually have dimensions from 3 to 60 cm. Since the degree of blackness of such sensors does not depend on wavelength, they may be used not only to measure the intensity of solar radiation simulators, but also to check simulators of the infrared and reflected radiation of a planet.

The disadvantage of a radiation detector of the type described is its high inertia and necessity of introducing flexible pipes into the vacuum chamber for delivery of water.

Sensors which use thermocouples are more suitable.

The thermoelectric method is based on the use of thermoelectric radiation detectors — thermocouples, thermopiles, or bolometers. These detectors are suitable since they are non-selective, i.e., their sensitivity does not depend on wavelength. The disadvantages of thermodetectors (especially thermocouples) is their low sensitivity; therefore, when working with spectral devices it is necessary to install wide slits, which impairs the monochromaticity of the radiation flux. /302

The photoelectric method employs photoelectric radiation detectors — photocells and photomultimpliers. The sensitivity of these detectors is much greater than that of thermodetectors, but in measurements the spectral characteristics of photodetector sensitivity must be taken into account, which depends on the wavelength of the radiation being recorded.

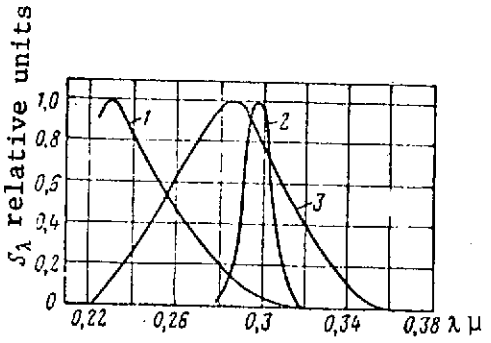

Figure 4.61. Averaged curves of the spectral sensitivity of photo-cells: 1 — F-7 magnesium photo-cell; 2 — magnesium photo-cell with BF-4 light filter; 3 — antimony-sodium photo-cell.

Magnesium and antimony-sodium photo-cells (the curves of the spectral sensitivity of these photo-cells are shown in Figure 4.61) were developed at the Moscow Electric Lamp Plant for measuring radiation in the near UV region of the spectrum. Since the photo-cells are sensitive only in the UV region of the spectrum, light filters and correcting devices, which cut off longer-wave radiation, are no longer necessary. These photo-cells are used in UFM-11 and UFM-13 uvimeters and UFD-4 uvidosimeters, produced by industry — instruments for measuring ultraviolet radiation and the amount (dose) of ultraviolet radiation [25]. Windowless photoreceivers (various types of such receivers are described in [45]) are employed to measure radiation in the vacuum ultraviolet region of the spectrum.

The luminescent-photoelectric method is based on measurement of the luminescence of phosphors, which begin to radiate when ultraviolet radiation impinges on them. The spectral composition of the luminescence of a number of phosphors does not depend on the wavelength of the exciting radiation. Most widely used for measurements in the vacuum ultraviolet region of the spectrum are phosphors obtained by sputtering of a saturated alcohol solution of sodium salicylate. Sodium salicylate has a constant quantum output at wavelengths of exciting radiation from 400 to 3400 Å. The maximum luminescence lies within the range of 4300 Å. A phosphor of $Sr_3(PO_4)_2$, activated by Eu, has been recently suggested to record vacuum UV radiation. The output of this phosphor is four times greater than that of sodium salicylate in the region of 580 Å and 30 times greater than that in the region of 98 Å [86].

Comparison of radiation of different spectral composition with the aid of a phosphor with a constant quantum output is very simple, because radiation of the same spectral composition is compared after the phosphor, and the spectral sensitivity of the photodetector does not have to be taken into account. /303

It is recommended that a photodetector be used which has maximum sensitivity in the region of phosphor luminescence.

The photochemical method is based on measurement of radiation intensity with the aid of photochemical reactions. A number of primary photochemical reactions which may be employed to record the vacuum ultraviolet are: transformation of oxygen to ozone, dissociation of carbon dioxide, dissocation of ammonia, dissociation of uranyl-oxylate with formation of CO and CO_2, dissociation of nitrous oxide with formation of N_2O_2 and NO and other reactions. They are indicated in [45]. The quantum efficiency of all these reactions is known and is constant within a specific spectral range. However, the use of photochemical methods for recording UV radiation is quite cumbersome, because it involves chemical anlyses.

The photographic method makes use of the phenomenon of darkening of special photographic emulsions, sensitive to a specific region of the spectrum. The degree of darkening of the photoemulsion is proportional to the amount of radiant energy impinging on it and is determined with the aid of a microdensitometer.

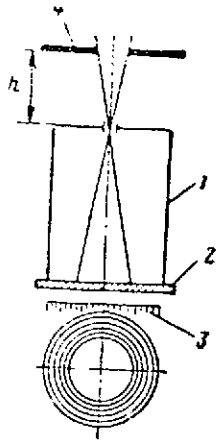

Figure 4.62. Diagram of device for determining angle of radiation (nonparallelism): 1 — cylinder with opening; 2 — frosted glass; 3 — scale with divisions; 4 — interchangeable diaphragm.

The photoionization method is based on measurement of the gas degree of ionization in an ionization chamber due to the effects of radiation. Radiation at wavelengths shorter than 1022 Å may be recorded with the aid of an ionization chamber filled with inert gases (for example, with xenon). The cameras are filled with nitric oxide to record longer-wave radiation ($\lambda < 1350$ Å), and with xylene vapor — for even longer-wave radiation. Many other gases may also be used to fill the chamber.

The working principle and application of ionization chambers are discussed in [29] and [45] and in a number of special investigations.

Thermoelectric detectors are more suitable for measuring radiation, but their sensitivity may often be insufficient. In this case, photodetectors are employed, more often in combination with the luminescent-photoelectric method of measurement. Chemical actinometers are used comparatively rarely to measure radiation due to the complexity of measurements; the photographic method also finds limited application due to the complexity of calibration.

The uniformity of radiant flux density is checked by moving the radiation detector through the entire space of the working zone of the simulator and varying its angle of orientation.

The angular distribution of beams from the solar simulator may be measured /304
with the aid of the simplest device, which is a lightproof chamber with a large opening on one of its walls (Figure 4.62) and frosted glass with a grid or divisions on the opposite wall. If the opening is directed toward the incident radiant flux, the image of the radiation source appears on the frosted glass. By investigating radiation intensity distribution on the frosted glass, it is possible to judge not only the complete angle of non-parallelism of beams, but also to determine the energy distribution by the angle of view. For convenience in obtaining quantitative data, sensitive radiation detectors, for example, silicon photo-cells, the dimensions of which should be comparable to those of the opening and much less than the distance between the sensor and the opening, may be installed instead of frosted glass.

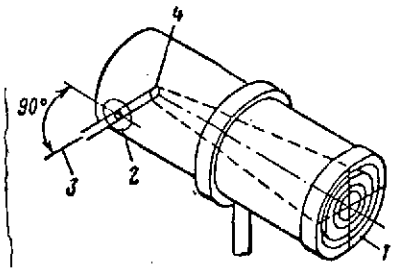

Figure 4.63. Optical device for determining angle of radiation: 1 — grid for readout; 2 — aperture opening; 3 — beam axis; 4 — mirror.

There is a similar device in which two photocells measuring 2.5 x 2.5 mm are used. The photo-cells may be moved in two mutually perpendicular directions. The angular distribution of energy in any two mutually perpendicular directions may be measured by rotating the device around the longitudinal optical axis.

In more perfected devices, a high-power objective is used which permits brighter source images to be obtained (Figure 4.63).

In order to determine the angular distribution of the beams of a planetary radiation simulator, the aperture angle of the device must be limited, because the beams from a planetary simulator may impinge in the device opening within the range of a large solid angle up to 2π. For this, an additional diaphragm 4 is installed in front of the above-described device (see Figure 4.62). By varying /305 distance h, the aperture angle of the detector may be regulated over a wide range. When using such a device to investigate the radiant flux field of an infrared planetary radiation simulator, the body of the device and its diaphragms must be cooled with liquid nitrogen. Such cooling results in minimum errors due to the natural thermal background of the radiation detector.

8. Planetary Radiation Simulator for Orbital Spacecraft

As was indicated above in Section 3, Chapter 1, the radiant flux of a planet makes a considerable contribution to the thermal balance of the spacecraft, and it must be reproduced along with the solar radiant flux.

Creation of a perfect planetary radiation simulator is a considerably more difficult task than creation of a solar simulator. In connection with this, wherever possible, an attempt is made to use simpler means of simulation, in this case leading to inaccurate reproduction of natural heat fluxes. Considerable design simplifications of a planetary radiation simulator may be obtained primarily by deviations from angular distribution and spectrum by using a small number of infrared heaters, incandescent lamps, and other sources. Such

simplified simulators are convenient in operation and are effective in testing orbital spacecraft related to classes I, III, IV and XI (see Section 4, Chapter 3), i.e., to spacecraft with a very simple geometrical shape of the hull and an active temperature control system. Simplified planetary radiation simulators are suitable to a considerably less degree for spacecraft of classes V, VI and IX. When testing spacecraft in classes II, VII, VIII, IX and X, only minimum deviations of external radiant fluxes from natural ones are permitted, and therefore use of rough simulators in this case may lead to very large temperature errors.

The requirements outlined below are placed on planetary radiation simulators suitable for testing orbital spacecraft of any class.

The direction of the course of the beams (angular distribution characterized by the so-called angle of contact) should correspond to the distance of the spacecraft from the planet and should vary in time according to variation of the orbital parameters.

Space-time variation of the main radiation vectors of a planet ($\vec{\Phi}_e$, $\vec{\Phi}_s$) should be related to variation of the vector $\vec{S}_\Theta$ and spacecraft orientation throughout the entire period of the experiment when investigating the thermal conditions of a spacecraft in a thermal vacuum chamber. /306

The radiation intensity of a spacecraft from different directions should correspond to the local distribution of the planetary albedo and to the mutual position of the Sun, planet and spacecraft (this condition is obligatory for spacecraft having axial symmetry and oriented so that their axis is always directed toward the center of the planet, see Chapter 2, Section 2).

The spectral composition of the radiant flux of a simulator should correspond to the spectra of natural and reflected radiation, which are dependent on the geographic (selenographic) coordinate and the state of the cloud cover. In view of the inadequate knowledge about the spectral and space-time distribution of the albedo, as well as about the infrared spectrum of the planet, this condition is replaced by the condition of adhering to the average infrared spectrum for the entire planet and the average spectrum of reflected radiation for the planet, identical to the solar spectrum (see page 49).

Design of the Planetary Radiation Simulator of the Philco Company [144]

One of the possible designs of a planetary radiation simulator, meeting most of the above-enumerated requirements, is one whose schematic diagram is presented in Figure 4.64.

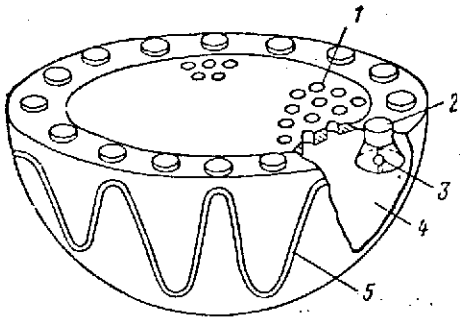

Figure 4.64. Diagram of planetary radiation simulator of Philco Company: 1 — directionally radiating surface (openings over the entire surface of the plate); 2 — attachment of reflected solar radiation source; 3 — high-pressure arc lamp; 4 — semi-spherical body of simulator, white on the inside; 5 — system for regulating the temperature of the body.

The radiant flux field in the working zone is formed with the aid of a directionally radiating surface. It is a plate with many conical openings. The openings are located adjacent to each other; their internal walls are made of mirrors. Because of these characteristics, diffuse radiation passing through the reflecting cone acquires a specific directionality of the beams (Figure 4.65). To reduce the background of diffuse infrared radiation of the plate itself, its surface is cooled by liquid nitrogen.

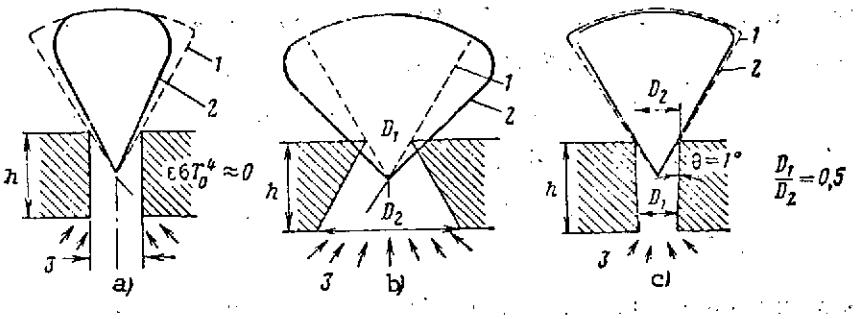

Figure 4.65. Shapes of openings in plate forming directed radiation: a — cylinder with black walls; b — right cone with black walls; c — reverse cone with reflecting walls; 1 — ideal radiation; 2 — actual radiation; 3 — diffuse radiation.

The semi-spherical body 4 (see Figure 4.64), the wall temperature of which is regulated within the required range with the aid of heater 5, acts as the source of simulated infrared radiation of the planet. The internal surface of the body, /307 covered with a white paint, acts simultaneously as a diffuse reflector for the

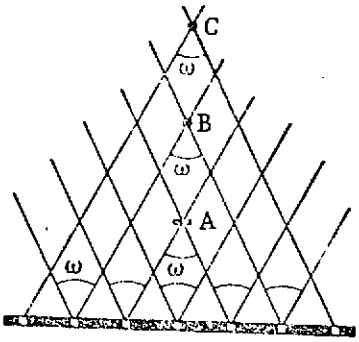

Figure 4.66. Diagram of plate radiation with conical beam sources.

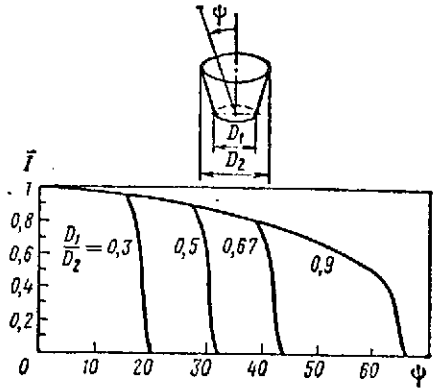

Figure 4.67. Relative radiant flux intensity $\bar{I}$ as a function of direction ψ for openings with different D_1/D_2.

visible radiant flux, emitted by the sources 3. High-pressure xenon or mercury-xenon lamps with correcting light filters are employed as the sources. The intensity of luminous flux emitted by them is varied within the required range with the aid of regulated diaphragms. As a result of repeated reflections, the diametral plane of the semi-sphere radiates like a flat disk with a brightness almost equal to that of the internal surface of the semi-sphere. The intensity of the arc lamps is selected such that the intensity of radiation "reflected from the planet" comprises 570 W/m^2.

The working principle of the described simulator may be explained with the aid of Figure 4.66. A radiant flux within the range of solid angle ω is emitted from each opening of the plate. Beams within the range of the same cone at an apex angle of ω will impinge on the elementary horizontal surface located at points A, B, C, ... Since the intensity I of all sources is identical, regardless of its location, the elementary surface will receive the same amount of energy Q, hence, $Q = I\omega$. It is easy to establish that the intensity of incident radiation remains constant for an inclined surface as well, if it is moved forward within the limits of the entire working zone. Because of the finiteness of the number of sources, the intensity distribution in the space of the working zone will not be uniform, but saw-toothed. However, the amplitude of intensity deviation from an average value decreases rapidly (according to the square of the distance) as the distance from the plate and the number of sources increase.

Variation of simulated orbital altitude H is achieved by varying the angle ω by changing the angles of the conicity of the openings ω_1 or the ratio D_1/D_2 (see Figures 4.65 and 4.66).

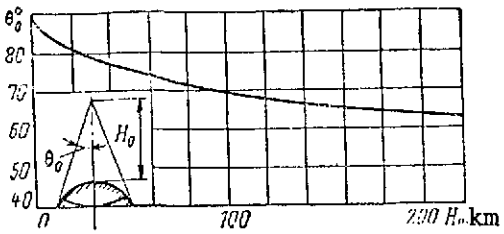

Figure 4.68. Angle of scanning the Moon as a function of orbital altitude.

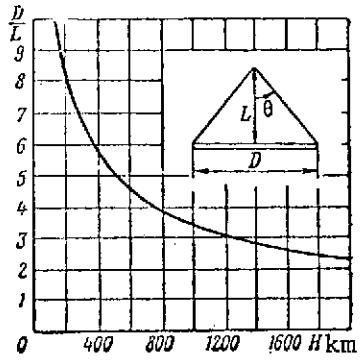

Figure 4.69. Dependence of relative dimensions of simulator on reproduced orbital altitude. /308

Variation of the radiant flux density of the opening according to direction for different ratios of D_1/D_2 is shown in Figure 4.67. It follows from the curves in the figure that the greatest field uniformity may be obtained for small angles of ω, i.e., for high altitudes. When simulating low flight altitudes, yet another difficulty arises, related to an increase in the dimensions of the simulator. As altitude decreases, the angle $\omega = \theta_0$ increases rapidly (Figure 4.68), which inevitably leads to an increase in the diameter of the radiating plate when the vertical dimensions of the test spacecraft remain constant. The dependence of the ratio of dimensions of the planetary simulator D to the vertical dimensions of the working portion L, where the test spacecraft is located, on orbital altitude H /309 is presented in Figure 4.69.

For some tests, the diameter of the radiating plate of the simulator may be decreased, without introducing any appreciable errors. For example, for testing ground sensors, a cylinder may be used, the opening in the walls of which emits radiation at a small solid angle, so that the horizon will be visible at a constant angle when the sensors are moved.

9. Radiation Simulators for a Spacecraft Located on the Surface of the Moon

The Main Requirements on the Simulator

Solar Radiant Flux

The extremely rarified atmosphere of the Moon (see Section 1, Chapter 1) does not distort the solar radiation spectrum and does not reduce its intensity, regardless of whether the Sun is located at its zenith or near the line of the horizon.

Therefore, the requirements on the accuracy of observing the spectral composition of the solar flux are the same as those for spacecraft located in space in lunar or Earth orbit. Slight deviations in the value of $S_{\oplus}$ occur due to the fact that, moving around the Earth, the Moon now approaches, now moves away from the Sun. These variations are negligible and on the average comprise less than 1% (less than 0.01). At the same time, for the visible side of the Moon, deviations from the average value of $S_{\oplus}$ lie within the range from 0% at the morning and evening terminator to -0.5% at lunar midday. On the opposite side of the Moon, the corresponding deviations lie within the range from 0% to +0.5%. The lunar day lasts for 14 days 18 hours 22 minutes 1.39 seconds (half a synodic month — the interval of time between two sequential new Moons).

The maximum rate of angular displacement of the Sun through the celestial sphere [on the lunar surface] comprises a little more than 0.5° per hour. In connection with this, the continuous variation of the Sun's position is not simulated in most thermal vacuum chambers for testing lunar spacecraft, but is replaced by intermittent variation of the vector $\vec{S}_0$.

The Reflected Solar Radiant Flux

As was shown in Section 3, Chapter 1, different sections of the Moon may have an albedo within the range of 0.054 to 0.18. Despite the fact that the intensity of reflected solar radiant flux is much less than the direct radiation of the Sun, the reflected radiation cannot be ignored, because, when comparing the heat fluxes of direct and reflected solar radiation, received by the spacecraft, the angular distribution of the beams must be kept in mind in addition to absolute radiation intensity. A spacecraft located on the Moon receives reflected radiation on its entire surface (the angle of radiation capture for a sphere is equal to 360°), while at the same time the direct solar flux is received only by the middle of the spacecraft (the angle of capture for a sphere is 180°).

It follows from analysis of data on the thermal radiation of the Moon /310
(section 3, Chapter 1) that a simulator of reflected solar flux should have an asymmetrical projection diagram of radiation with a maximum located on the extension of the projection of vector $\vec{S}_{\oplus}$ onto the lunar surface at the point where the spacecraft is located, and with a minimum on the opposite side. The magnitude of asymmetry should be a function of the angle γ_s. Despite the fact that slight

coloring of lunar formations is distinguished in the visible portion of the spectrum, on the whole the spectral distribution of the lunar albedo does not differ significantly from a gray body. There are data that the reflection coefficient of the lunar surface increases in the infrared region. However, since the spectral distribution of the lunar albedo has not yet been adequately studied, it is assumed in the first approximation that the spectrum of reflected solar light is similar to that of the initial incident radiation.

Unlike direct solar radiation, the beams reflected from the lunar surface are polarized. It was shown in Section 10, Chapter 4 that in a number of cases polarization should be taken into account; otherwise this may result in appreciable errors in calculating the thermal balance of the spacecraft or its components. Therefore, it is desirable that a simulator of reflected radiation provide a radiant flux with natural polarization. However, this requirement is difficult to fulfill and, therefore, in practice the phenomenon of polarization must be disregarded, particularly since maximum polarization (~17%) is achieved for portions with minimum albedo (~0.05).

Nothing can yet be confirmed about the effect of the luminescence of the lunar surface on spacecraft thermal conditions, because published quantitative data on this problem are still too sparse.

The Infrared Radiation of the Moon

This type of radiation is very important in the simulation of spacecraft thermal conditions. Since the average albedo of the Moon is negligible (A = 0.07), the greater part of the solar flux is absorbed and reemitted in the infrared region. The absorbed solar energy depends on the micro- and macrorelief of the terrain. Therefore, the infrared radiation of the lunar surface, like reflected radiation, is asymmetrical with respect to the line perpendicular to the projection of solar rays onto the horizontal plane (see Figure 1.26).

This asymmetry is discernible most of all when the Sun is located near the lunar horizon, and disappears completely when the Sun is at its zenith. The graphs presented in Figure 1.26 are approximate, because local relief is not taken into account: whether the point being considered is located on the surface of a "sea," in a crater, or on a "continent."

Maximum differences from true temperatures when using the graphs of Figure 1.26 should be expected near the morning and evening terminators. In these regions the error in calculating absolute temperatures may reach 80 - 100° K. /31

Field Homogeneity

The radiant energy flux on the control surface should not depend on the location of the surface within the working zone of a lunar radiation simulator, but depends only on its orientation. The visual angle of the "Moon" in the simulator should also be constant and equal to 2π* for any point of the working zone.

The dependence of incident radiant flux per unit area on the angle between its normal and the direction toward the local vertical (in the case when $\gamma_s = 0$) is described by the formulas of Tables 10 and 11.

Lunar simulators essentially consist of individual radiators which emit an intermittent projection diagram of radiation. The non-uniformity of radiant flux density which occurs as a result of this and violation of the full-scale angular distribution of beams may cause errors in the reproduction of radiant fluxes absorbed by the spacecraft surface and may lead to distortion of the thermal conditions of the test spacecraft.

The non-uniformity of the radiation field is ±15 - 20% for most lunar spacecraft in a region not exceeding 0.1 of the spacecraft dimensions, and beam deviations by 10 - 15° from their natural distribution do not lead to temperature errors of the spacecraft by more than 5 - 10° C. However, for some special cases the indicated deviations of radiation density and angular distribution may be too large.

Design of the Simulator

The simplest simulator of lunar radiation is a horizontal disk of finite dimensions, in the center of which the test spacecraft is installed. The thermophysical and optical characteristics of the disk material should approximate as closely as possible the characteristics of the lunar surface. This means that the

*Special cases are not considered here when the spacecraft is located near a steep slope or on top of a mountain, and visual angle of the lunar surface differs from 2π.

degree of blackness of the surface of the simulator disk should be selected from 0.05 to 0.17, and the parameter of thermal inertia $\gamma = (\lambda\rho c)^{-1/2}$ — from 100 to 1000. The values of γ are different for different formations on the Moon. Thus, $\gamma = 590$ for Kepler Crater, $\gamma = 310$ for Aristarchus Crater, $\gamma = 300$ for Copernicus Crater, and $\gamma = 182$ for Tycho Crater. For comparison, we point out that the thermal inertia /312 of terrestrial rocks, characterized by the value of γ, comprises 20 for pumice, 100 for sand and gravel and 1000 for powder in a vacuum. The surface of the disk D acquires an equilibrium temperature T_1, approximating that of the lunar surface, under the effects of the radiant flux from the solar simulator. The heat flux from a disk of radius r_0, impinging on the vertical element of a surface dA, located in the center of the disk at a distance H, may be calculated by the formula

$$q(H, r_0)\,dA = \frac{\varepsilon_1 \sigma T_1^4}{\pi}\left[\operatorname{arctg}\left(\frac{r_0}{H}\right) - \frac{r_0/H}{\left(\frac{r_0}{H}\right)^2+1}\right]. \tag{4.25}$$

At $r_0 \to \infty$, this expression is transformed to the form

$$q(H, \infty)\,dA = \frac{\varepsilon_1 \sigma T_1^4}{2}\,dA. \tag{4.26}$$

The relative error in the incident heat flux, which occurs when the infinite plane is replaced by a disk of finite dimensions, is equal to

$$\frac{dq}{q} = q\,\frac{(H, \infty) - q(H, r_0)}{q(H, \infty)} = 1 - \frac{2}{\pi}\left[\operatorname{arctg}\left(\frac{r_0}{H}\right) - \frac{r_0/H}{\left(\frac{r_0}{H}\right)^2+1}\right] \tag{4.27}$$

It is obvious from the graph of the dependence $(dq/q)\cdot[(r_0)/H]$ from Formula (4.27), which is plotted in Figure 4.70, that small errors (~10%) may be achieved only at $r_0/H > 10$, which is difficult to accomplish due to the limited dimensions of the vacuum chamber, which, as a rule, only exceeds the spacecraft dimensions by several times.

Radiation of the lunar surface beyond the range of the external contour of the /313 simulator disk may be compensated for by various methods. Some of these methods are depicted in Figure 4.71. In one of them the simulator disk as a whole is maintained at a higher temperature than that which the lunar surface has for a given

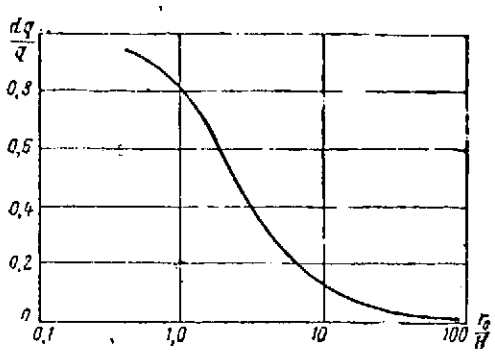

Figure 4.70. Relative error in incident heat flux from lunar radiation simulator of finite dimensions.

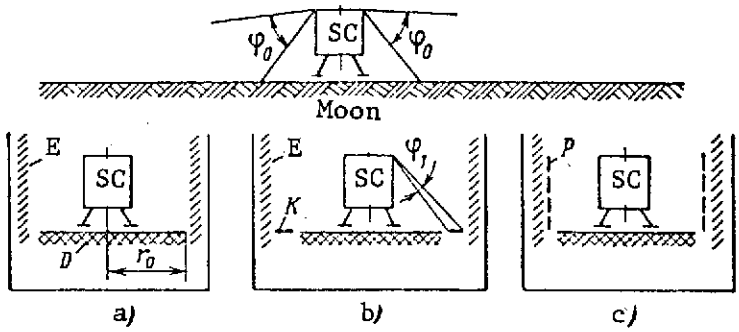

Figure 4.71. Some of the possible schemes for simulators of lunar surface radiation: D — disk of lunar surface simulator; K — radiating ring; P — grid of annular radiators; E — cryogenic shields.

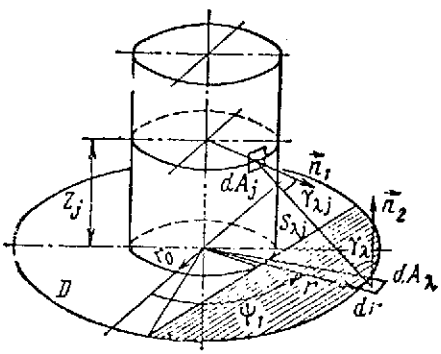

Figure 4.72. Explanatory diagram for calculation of heat transfer between the element of control surface and segmented portion of the disk of lunar surface simulator.

position of the Sun under the local horizon (Figure 4.71a). This is a very rough simulation. More accurate results may be obtained if additional radiators are used which compensate for the radiant fluxes from the portion of the lunar surface beyond the limits of the area bounded by a disk of radius r_0.

Such compensating radiators may be horizontal or vertical rings p (Figure 4.71b and c), the angular coefficient of which is selected small enough not to induce effects of mutual re-radiation and not to shade the radiant flux from the solar simulator.

The temperature of the annular heaters of a lunar radiation simulator may be calculated with the aid of an arbitrarily selected control surface, which limits the working zone of the facility, inside which the test spacecraft will be placed. Such a surface, in particular, may be a vertical circular cylinder, whose axis passes through the center of disk D, simulating the lunar surface in direct proximity to the spacecraft (Figure 4.72).

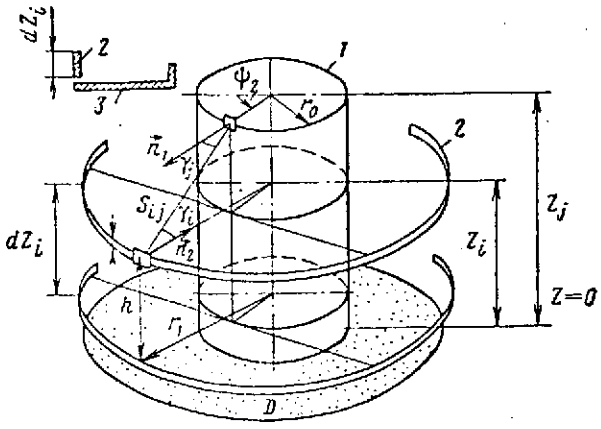

Figure 4.73. Calculation of radiant flux impinging on control surface 1 from coaxial annular radiators 2; 3 — cooled black shield.

Let us consider an elementary area dA_j, located on the external surface of a control cylinder at a height z_j from disk D. Beams proceeding only underneath may impinge on this area dA_j in full scale. In order to prevent radiation of the surface from above and thus to observe the natural angular distribution of beams, each annular radiator should have a black absorption shield 3, /314 cooled to liquid nitrogen temperature (Figure 4.73).

The amount of heat Q_D, which impinges on the area from disk D, added to the heat ΣQ_j which impinges on the element dA_j from all rings located below area dA_j (i.e., $z_i \leq z_j$), should be equal to the radiant energy flux Q_r, impinging on the same area, if it were located on the Moon, i.e.,

$$Q_D + \sum Q_j = Q_r. \tag{4.28}$$

This equation is written in sequence for each ring, beginning with the first one; the temperature of all rings is calculated by the numerical method (with the aid of an electronic computer). In calculations it is assumed that $\varepsilon_j = 1$, and $\varepsilon_i(\lambda)$ corresponds to the material of the radiator. The results of calculations for identical rings of stainless steel, covered with spray-coated zirconium oxide (Figure 4.74), show that the temperature of all rings is approximately the same, with the exception of the first two or three (Table 39).

As the relative distance between the rings increases, the non-uniformity of the radiation field of the control cylinder and radiator temperature increase. /315 The increase of radiator temperature leads to an increase in the error due to non-conformity of the radiator spectrum to the infrared spectrum of the Moon (Figure 4.75).

The spectral errors may be determined from comparative analysis of the distribution curves of the heat fluxes, absorbed by the control cylinder, whose material is selected as that found in a spacecraft structure (for example, oxidized aluminum, titanium alloy, white ceramic paint and stainless steel, see Figure 3.13).

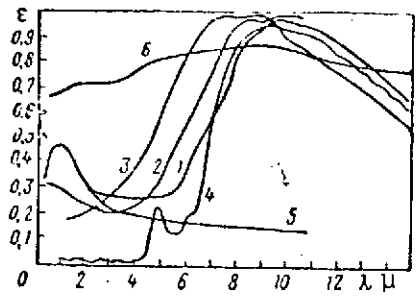

Figure 4.74. Spectral degree of blackness of various radiators at high temperature: 1 — magnesium oxide, 1900° K; 2 — zirconium oxide, 1800° K; 3 — beryllium oxide, 2000° K; 4 — aluminum oxide, 1725° K; 5 — tungsten, 2900° K; 6 — globar (a layer of thorium dioxide on rough silicon carbide).

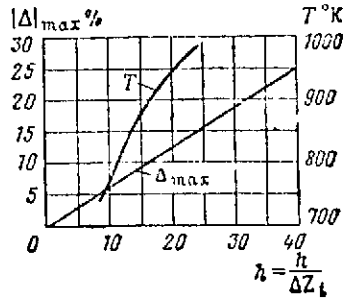

Figure 4.75. Maximum relative error in reproduction of radiant flux impinging on control cylinder ($\varepsilon = 1$), and average temperature of radiators as a function of the distance between rings $r_1/r_0 = 1.82$, $\gamma_s = 0$ (the Sun is at its zenith; the radiator is zirconium oxide).

TABLE 39 *

DEPENDENCE OF THE RING TEMPERATURE OF LUNAR RADIATION SIMULATOR ON THE DISTANCE OF THE RING TO DISK D FOR DIFFERENT ΔZ_i; r_1 = 200 cm, r_0 = 110 cm (THE TEMPERATURE OF THE LUNAR SURFACE IS EQUAL TO 410° K; THE STAINLESS STEEL RINGS ARE COVERED WITH ZIRCONIUM OXIDE)

$\bar{h}=h/\Delta Z_i=10$		$\bar{h}=15$		$\bar{h}=20$	
$\bar{Z}_i=\frac{Z_i}{r_1}$	T_i °K	$\bar{Z}_i$	T_i °K	$\bar{Z}_i$	T_i °K
0,05	876,0	0,050	918,0	0,05	957,5
0,10	774,5	0,125	877,1	0,15	958,8
0,15	775,6	0,200	878,0	0,25	959,0
0,20	775,6	0,275	878,3	0,35	959,5
0,25	776,7	0,350	879,2	0,45	959,5
0,30	777,0	0,425	879,0	0,55	959,5
0,35	777,5	0,500	879,0	0,65	959,5
0,40	777,5	0,575	879,1	0,75	959,8
0,45	777,8	0,650	879,0	0,85	959,5
0,50	777,8	0,725	879,0	0,95	959,8
0,55	777,6	0,800	879,2	. . .	. . .
0,60	777,6	0,875	879,3	2,50	959,8
0,65	777,8	0,950	880,0	—	—
0,70	777,5	. . .	. . .	—	—
0,75	778,0	—	—	—	—
0,80	777,5	2,50	880,0	—	—
0,85	778,0	—	—	—	—
. . .	. . .	—	—	—	—
2,50	778,0	—	—	—	—

*Commas represent decimal points.

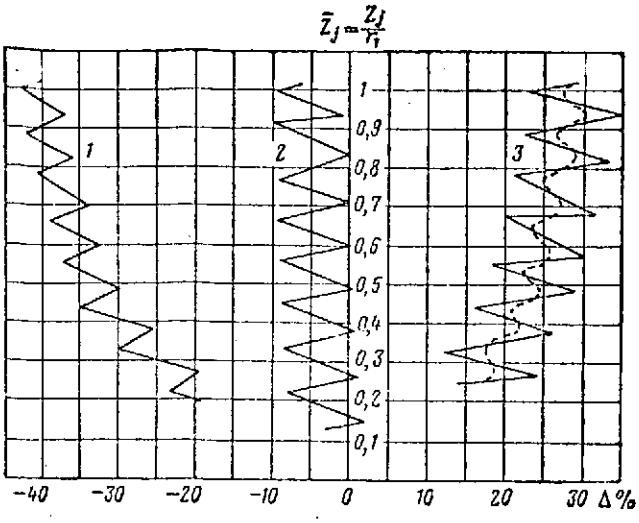

Figure 4.76. Relative error in simulation of real indicatrix of irradiation on a surface of different materials: 1 — anodized aluminum; 2 — white enamel; 3 — titanium alloy.

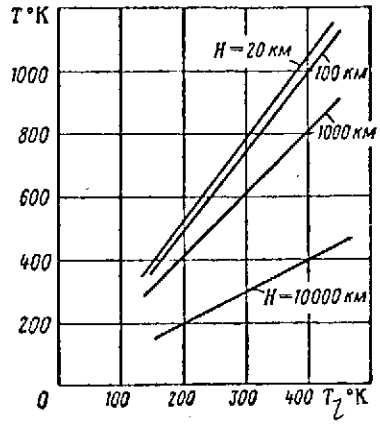

Figure 4.77. Radiator temperature as a function of lunar surface temperature and flight altitude.

One can see in Figure 4.76 how the intensity distribution of the radiant flux of the annular radiators, absorbed by the lateral surface of the control cylinders of various materials, varies.

When the simulator is adjusted for a gray or black control surface, the sections /317 of the spacecraft of titanium alloy receive approximately 15 - 20% more heat, and the sections of anodized aluminum receive 20 - 25% less heat than the same sections under real conditions. The spectral errors for white enamel and stainless steel are quite small. However, there are coverings for which the error, caused by the selectivity of the degree of blackness reaches more than 50%.

The results of calculating the irradiation curve for radiators in the form of thin rings, the height of which may be disregarded in comparison with their diameter, are presented in Figures 4.75 and 4.76. Whereas the height of the annular radiators is taken into account in these calculations, the amplitudes of the saw-toothed curves for the heat flux become considerably less. These curves are depicted by the dashed line in Figure 4.76.

The temperature of the annular rings is linearly related to the temperature of the lunar surface (Figure 4.77). After the radiator temperature has been selected, which provides an average heat flux on the control surface equal to the flux of the Moon, the resulting errors of simulating the heat flux not only on the control

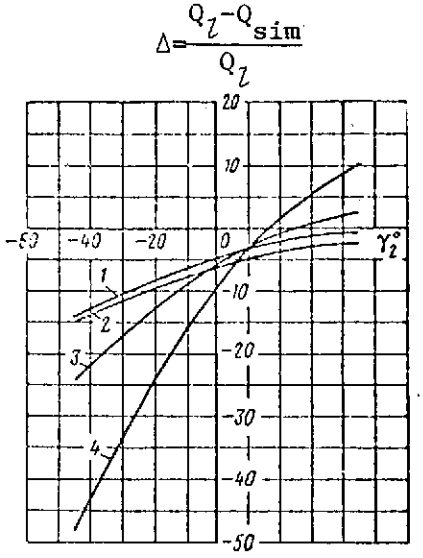

Figure 4.78. Relative error in reproduction of lunar radiation impinging on control surface ($\varepsilon = 1$) as a function of the angle of inclination γ_2 at $\gamma_1 = 0$:
curve 1 — $\bar{r}_0 = 0.022$, $\bar{z}_j = 0.9$;
curve 2 — $\bar{r}_0 = 0.49$, $\bar{z}_j = 0.22$;
curve 3 — $\bar{r}_0 = 0.49$, $\bar{z}_j = 0.9$;
curve 4 — $\bar{r}_0 = 0.8$, $\bar{z}_j = 0.9$.

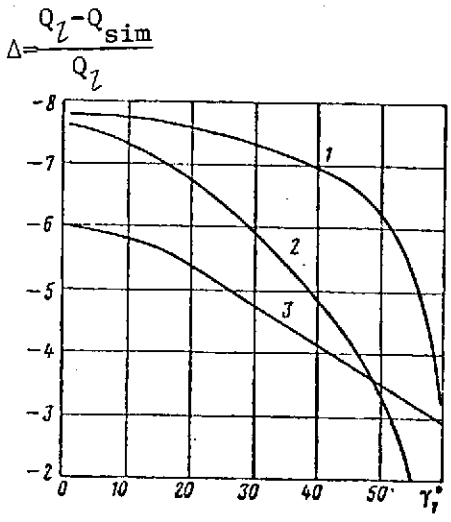

Figure 4.79. Relative error in reproduction of lunar radiation impinging on a control surface ($\varepsilon = 1$) as a function of angle γ_1:
curve 1 — $\bar{r}_0 = 0.8$, $\bar{z}_j = 0.22$;
curve 2 — $\bar{r}_0 = 0.8$, $\bar{z}_j = 1.0$;
curve 3 — $\bar{r}_0 = 0.5$, $\bar{z}_j = 1.0$.

surface, but on the other elementary areas inside the space delineated by the control surface, are calculated. By placing the control surfaces at arbitrary distances from the cylinder axis (see Figure 4.73) and rotating them around the vertical or horizontal axes, the deviations of the heat flux, impinging on these surfaces, from true values may be found. Figures 4.78 and 4.79 show that the effect of the angle of rotation around the vertical axis γ_1 on the error $(Q_l - Q_{sim})/Q_l$ is insignificant, and rotation around the horizontal axis γ_2 may in some cases yield an error exceeding 40%, if the ratio $r_0/r_1 = \bar{r}_0$ is assumed to be more than 0.8.

These examples show that a decrease of the solid angle of the radiators and an increase of their temperature may be a cause of the considerable field inhomogeneity of the radiant flux and may lead to errors caused by the inadequacy of the radiator and lunar surface spectra.

10. Methodical Errors in Simulation of Radiant Fluxes Impinging on a Spacecraft [144, 146, 151, 286] /319

Simulation of the space environment in facilities for simulation of spacecraft thermal conditions is never absolutely accurate even in the most perfect designs. Because of this, the temperature field of the test spacecraft always differs somewhat from the true temperature field of the spacecraft when operating in space. Temperature deviations may be caused, on the one hand, by inaccuracy of measuring the space parameters being simulated — for example, the solar spectrum, the albedo of a planet, the angular distribution of beams, radiation density, etc.

An attempt is made in this section to show in individual examples the effect of inaccurate reproduction of a certain factor, taken separately, on the temperature error in testing a spacecraft in a simulator. The methodical errors considered below, of course, do not exhaust all possible sources of thermal perturbations which distort the pattern of the test spacecraft temperature field. An exhaustive and complete analysis of methodical errors is possible only with consideration of the specific design of a spacecraft, complex consideration of the characteristics of its temperature control system and space factors.

The Non-Parallelism of the Beams of the Simulated Solar Flux

The limited brightness of the sources used in solar flux simulators and the imperfection of optical systems do not provide beam divergence angles less than 1 - 2° in the working zone. In cruder (infrared) solar simulators, this value reaches 15 - 20°, which exceeds by many times the natural angle (32', or ~0.01 radian), at which the solar disk is visible in Earth orbit. Located in the working zone of a thermal simulator, the observer would see the image of the "artificial Sun" at a much greater solid angle than under natural conditions, the beam divergence angle possibly being different for different points of the working zone. The effect of an increase in the solid angle of the "artificial Sun" on spacecraft thermal conditions may be manifested primarily for those sections of the spacecraft surface which are parallel or inclined toward the solar rays at a small angle. Let us consider some cases.

1. Let coefficients A_s and ε of the section of the surface being considered not be dependent on the angle of incidence of the beams and on the wavelength of the radiation. In this case, the relative variation of the radiation of such surfaces may be very large, although the absolute error in the solar flux being reproduced is small.

To calculate the resulting temperature error, let us write the equation of thermal balance for a surface element located in space, assuming that the Sun and space are natural external heat sources: /320

$$A_s E_s \varphi_{1-s} F + Q_i + \sigma \varepsilon_c \left(\frac{T_c}{100}\right)^4 F = \sigma \varepsilon F \left(\frac{T_w}{100}\right)^4. \tag{4.29}$$

Here the subscript "c" indicates that ε and T refer to space; T_c is the equivalent temperature of space; E_s is the radiant flux density of the solar surface equal to 62,000 kW/m^2. Let us consider the elementary surface F, which is part of the lateral surface of a cylinder whose axis is directed toward the Sun. For such a surface

$$\varphi_{1-s} = \frac{1}{\pi}(\theta_s - \sin\theta_s \cos\theta_s),$$

where θ_s is half the angle at which the solar disk is visible from the point being considered (in radians).

For small angles, expanding $\sin\theta_s$ and $\cos\theta_s$ into series and disregarding the terms of higher order of smallness, we obtain

$$\varphi_{1-s} \approx \frac{2}{3\pi}\theta_s^3.$$

The solar energy flux impinging on a flat surface, the normal to which is directed toward the Sun, is equal to

$$E_s \sin^2\theta_s \approx E_s \theta_s^2 = S_{\odot}.$$

Consequently, Equation (4.29) may now be rewritten in the form

$$\frac{2}{3\pi} A_s S_{\odot} \theta_s F + Q_i + \sigma \varepsilon_c \left(\frac{T_c}{100}\right)^4 = \sigma \varepsilon F \left(\frac{T_w}{100}\right)^4. \tag{4.29'}$$

A similar equation for a surface located inside the chamber will be:

$$\frac{2}{3\pi} A_s^* S_\odot^* \theta_s^* F + Q_i + \sigma\varepsilon^* \left(\frac{T^*}{100}\right)^4 = \sigma\varepsilon F \left(\frac{T_w^*}{100}\right)^4. \tag{4.30}$$

Here θ_s^* is half the beam divergence angle in the working zone of the TS;

T_w^* is the temperature of the element being considered;

ε^* and T^* are the degree of blackness and the temperature of the inner walls of the chamber being cooled;

A_s^* is the absorption coefficient of the solar simulator beams for element F;

$S_\odot^*$ is the "solar" constant of the given simulator.

Since we are interested in the order of magnitude, for simplicity let us assume that $\varepsilon^*\varphi_{1-s} = 1$. Solving Equations (4.29') and (4.30) simultaneously, we find the temperature which the wall of the spacecraft acquires when it is irradiated in the chamber: /321

$$T_w^* = T_w \sqrt[4]{1 + \left(\frac{T^*}{T_w}\right)^4 + \left(\frac{T_c}{T_w}\right)^4 + \frac{\frac{2}{3\pi}\left(A_s^* S_\odot^* \theta_s^* - A_s S_\odot \theta_s\right)}{\varepsilon\sigma \left(\frac{T_c}{100}\right)^4 + A_s S_\odot \frac{2}{3\pi}\theta_s + q_i}}. \tag{4.31}$$

Here $q_i = Q_i/F$.

Let us assume that the radiation spectrum of the simulator is similar to full-scale, $S_\odot = S_\odot^*$, $A_s = A_s^*$ and the chamber walls are maintained at a temperature much less than that of the outer hull of the test spacecraft ($T^* \ll T_w$). Then, taking the fact into account that $T_c \ll T_w$, we have

$$T_w^* = T_w \sqrt[4]{1 + \frac{\theta_s^* - \theta_s}{\theta_s + \bar{q}}}, \tag{4.32}$$

where $\bar{q} = (Q_i 3\pi)/(2FA_s S_\odot)$ is the dimensionless specific heat input to the cylinder wall from the internal energy sources.

We obtain a relative error in the temperature of the element (Figure 4.80) in the form

$$\frac{\Delta T}{T_w}=\sqrt[4]{1+\frac{\theta_s^*-\theta_s}{\theta_s+\bar{q}}}-1. \tag{4.33}$$

The absolute temperature error (Figures 4.81 and 4.82) may be calculated by the formula

$$\Delta T=T_w^*-T_w=100\sqrt[4]{\frac{\theta_s+\bar{q}}{3\pi\sigma\varepsilon/A_sS_{\odot}2}}\left(\sqrt[4]{1+\frac{\theta_s-\theta_s}{\theta_s+\bar{q}}}-1\right). \tag{4.34}$$

For $\bar{q} \gg 1$ and values of θ_s^* from 5 to 20° (from 0.087 to 0.35 rad), instead of (4.39) it is convenient to use the approximate formula

$$\frac{\Delta T}{T}\approx\frac{A_sS_{\odot}F\theta_s^*}{6\pi Q_l}. \tag{4.35}$$

2. In the general case, the absorption coefficient of solar rays may depend both on wavelength and on the angle of incidence of the beams:

$$A_{s\lambda}=A(\lambda,\ \gamma_s,\ \delta)\ \text{ or }\ A_{s\lambda}=A(\vec{s},\ \lambda),$$

where γ_s is the angle between the normal to the surface n and the direction toward the radiation source and δ is the azimuthal angle.

The curves of the dependence of the relative reflectivity $\vec{R}$ of different materials on the angle of incidence of beams for wavelengths from 0.46 to 2.25 microns, i.e., in that portion of the spectrum where the Sun emits the greater part of its energy, are presented in Figures 4.83 - 4.85. The absolute absorptivity in terms of direction is related to the relative reflectivity by the relation /323

$$A_s(\lambda,\ \gamma_s,\ \delta)=1-R_N(\lambda)\vec{R}(\lambda,\ \gamma_s,\ \delta),$$

where $R_N(\lambda)$ is the spectral reflection coefficient in a direction close to the normal to the surface.

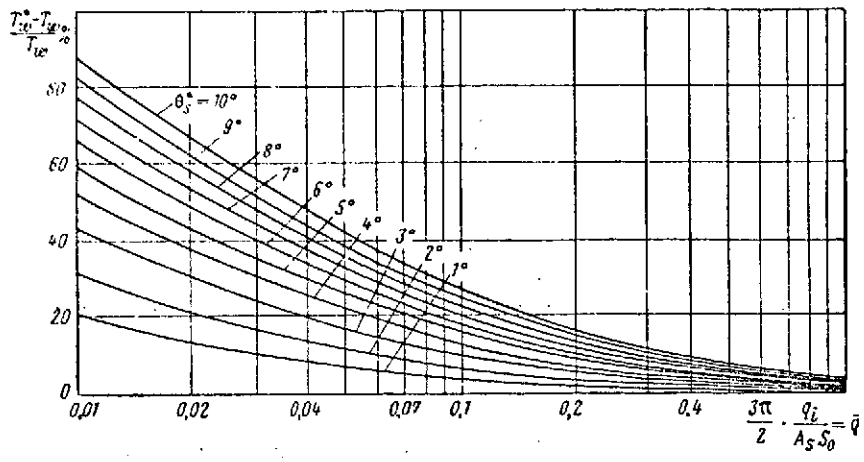

Figure 4.80. Effect of non-parallelism of solar simulator beams on relative error in the temperature of the spacecraft hull.

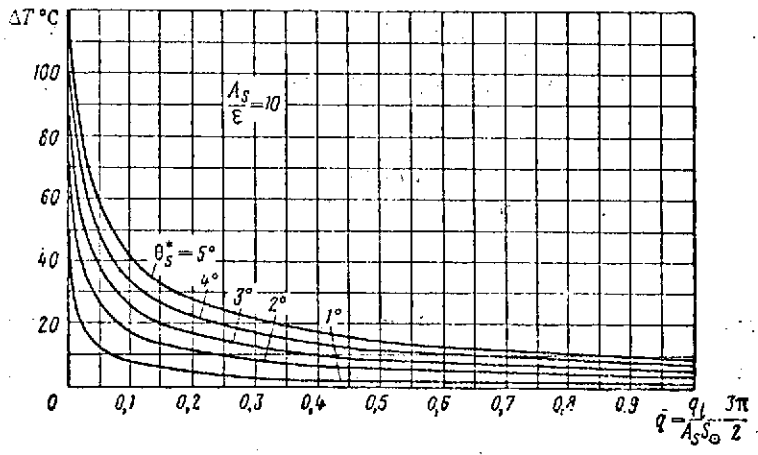

Figure 4.81. The effect of the non-parallelism of solar simulator beams on the temperature error.

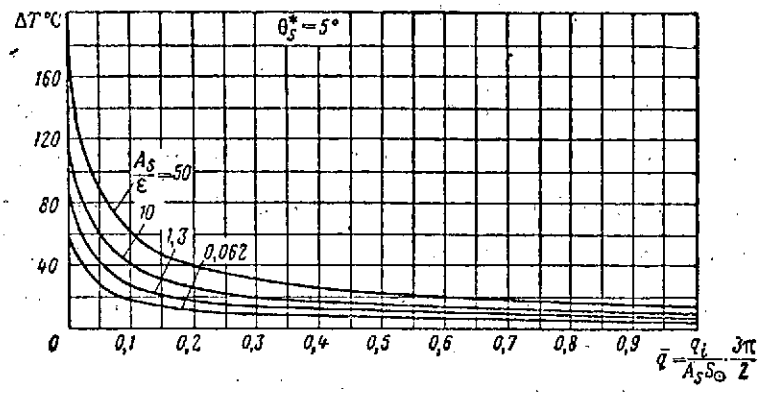

Figure 4.82. The effect of the ratio A_s/ε on the temperature error at $\theta^*_s = 5°$.

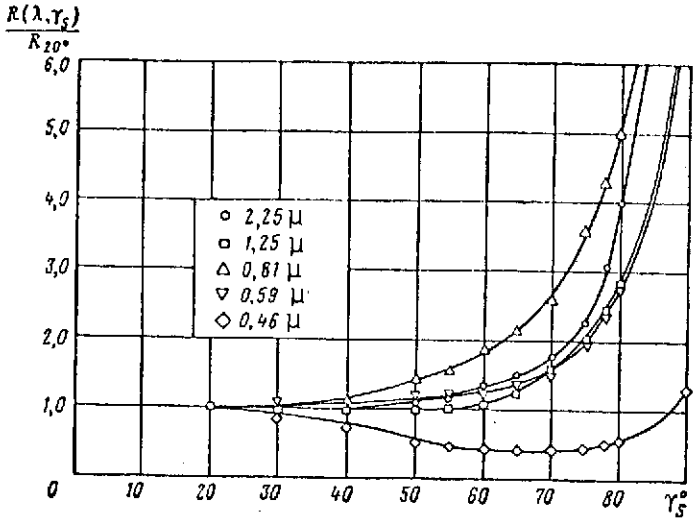

Figure 4.83. Relative directional reflectivity of a silicon battery with a glass covering.

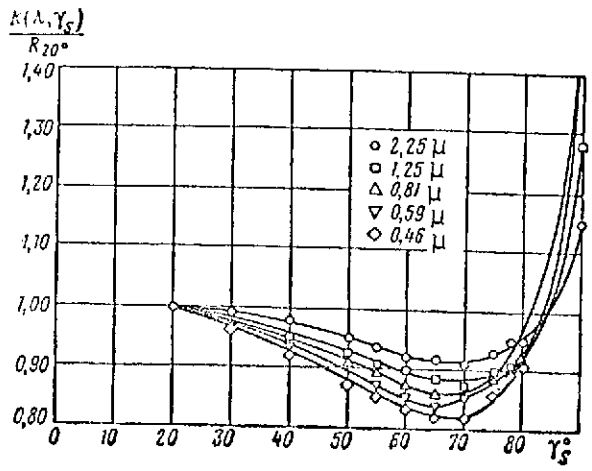

Figure 4.84. Relative directional reflectivity of anodized aluminum.

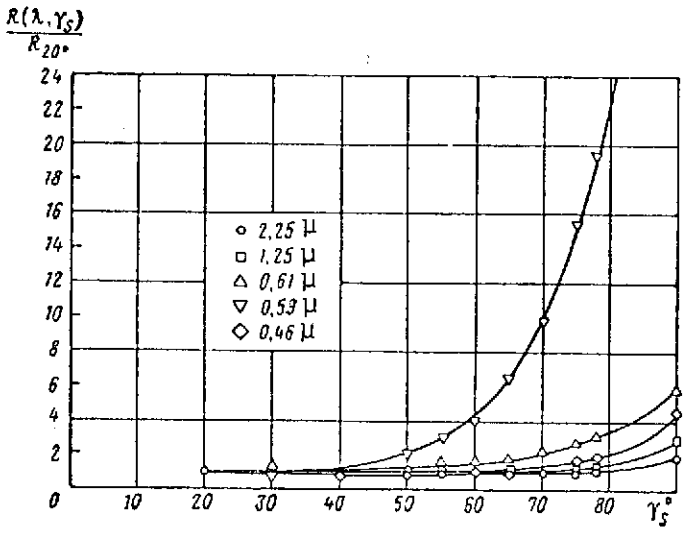

Figure 4.85. Relative directional reflectivity of aluminum foil covered with oxidized titanium.

As can be seen from Figures 4.83 - 4.85, the law governing reflective diffusion (Lambert) of the materials is violated for angles of γ_s, greater than 20 - 30°; deviation from the Lambert law is different for different wavelengths of incident radiation.

For a surface F, the normal to which $\vec{n}$ in the general case does not coincide with the direction toward the Sun $\vec{S}_\Theta$, the absorption coefficient of solar rays A_s may be calculated by the formula

$$A_s = \frac{\int_0^\infty \int_\Omega I(\vec{s}, \lambda) F_{\vec{n}(\vec{s})} A(\vec{s}, \lambda)\, d\omega d\lambda}{\int_0^\infty \int_\Omega I(\vec{s}, \lambda) F_{\vec{n}(\vec{s})}\, d\omega d\lambda}, \qquad (4.36)$$

where Ω is the solid angle of the Sun, $I(\vec{s}, \lambda)$ is the spectral intensity of solar radiation in the direction $\vec{s}$, and $F_{\vec{n}(\vec{s})}$ is the projection of the surface F in the direction $\vec{s}$. The same surface, irradiated by the rays of the solar simulator in the chamber, will have an average absorption coefficient /325

$$A_s^* = \frac{\int_0^\infty \int_{\Omega^*} I^*(\vec{s}, \lambda) F_{\vec{n}(\vec{s})} A(\vec{s}, \lambda)\, d\omega d\lambda}{\int_0^\infty \int_{\Omega^*} I^*(\vec{s}, \lambda) F_{\vec{n}(\vec{s})}\, d\omega d\lambda}, \tag{4.37}$$

where Ω^* amd $I^*(\vec{s}, \gamma)$ are the solid angle and spectral intensity of "artificial solar" radiation, respectively. The radiation intensity of the solar simulator is selected such that a flat black surface, the normal to which coincides with the direction toward the center of the visible "artificial Sun," would be exposed to as much energy as would emanate from a natural Sun under similar conditions, i.e., the denominators in Formulas (4.36) and (4.37) should be equal to the solar constant $S_\odot$. Turning to the graphs in Figures 4.83 - 4.85, we conclude that even for an imperfect simulator with a large value of Ω^*, the deviation of A_s^* from A_s will be very small. (For now, let us assume that the spectrum of the "solar" simulator approximates that of the natural solar radiation.)

For inclined surfaces ($\gamma_s > 30°$), the value of A_s^* will not be equal to A_s. This will lead to a temperature error whose value may be calculated by Formula /326
(4.31) or by the approximate formula

$$\frac{T_w^* - T_w}{T_w} \approx \frac{1}{4}\left(\frac{A_s^* - A_s}{A_s}\right). \tag{4.38}$$

3. When investigating the operating efficiency of electric generators using solar energy concentrators, the solid angle of the "artificial Sun" will lead to an increase of its image at the focus of the optical system of the concentrator.

For some types of solar concentrators, diffusion of the solar image at the location of the radiant energy detector may lead to distortion of its thermal conditions and electrical characteristics.

Inadequacy of the Spectra of the Infrared Radiation Source and the Planet

Let us assume that a spacecraft is being tested in a simulator, the surface of which is convex and consists of sections A, B, ..., G of area F_a, F_b, ..., F_g with known spectral degrees of blackness $\varepsilon_a(\lambda)$, $\varepsilon_b(\lambda)$, ..., $\varepsilon_g(\lambda)$. The amount of

radiant energy in the infrared region which section A received from the Earth may be written in the form

$$Q_A = \varphi_{a-1} F_a \int_0^\infty \Phi_{\lambda e} \varepsilon_a(\lambda)\, d\lambda, \tag{4.39}$$

where φ_{a-1} is the angular coefficient of surface A with respect to the Earth. For a plate parallel to the local horizon, $\varphi_{a-1} = [R_{eff}/(R_{eff} + H_0)]^2$, where H_0 is flight altitude, R_{eff} is the effective radius of the Earth and Φ_{λ_e} is the Earth's radiation (see Figure 1.14).

In the facility the same specimen will receive a radiant energy of

$$Q_A^* = \varphi \frac{F_a}{\sum F} S' \int_0^\infty \varepsilon_a(\lambda)\, \alpha(\lambda) \beta(\lambda) \varepsilon'(\lambda) I(\lambda, T)\, d\lambda, \tag{4.40}$$

where φ is the fraction of radiant energy, which is trapped by the optical system of the infrared radiator (if the dimensions of the source are small and it radiates uniformly in all directions, then $\varphi = \Omega/\Omega_0$, $\Omega = 4\pi \sin^2 \gamma/2$); γ is the semi-angle of the aperture angle; S' is the area of the source; $\Sigma F = F_a = F_b + \ldots + F_g$; $\alpha(\lambda)$ and $\beta(\lambda)$ are the total transmission coefficients of the optical system and of the correcting filters; $\varepsilon'(\lambda)$ is the monochromatic degree of blackness of the source; and $I(\lambda, T)$ is the emissivity of an absolutely black body at temperature T, /327

$$I(\lambda, T) = \int_0^\infty \frac{C_1 d\lambda}{\lambda^5 \left(e^{\frac{C_2}{\lambda T}} - 1\right)} = \pi \Phi_\lambda \text{ — is the Planck formula,}$$

where Φ_λ is the monochromatic brightness for unpolarized light;

$C_1 = 2\pi hc^2 = 3.74 \cdot 10^{-12}$ W·cm^2;

$C_2 = ch/k = 1.4387$ cm·deg;

$h = 6.6252 \cdot 10^{-34}$ J·sec is the Planck constant;

$k = 1.38 \cdot 10^{-24}$ J·deg is the Boltzmann constant;

$c = 3 \cdot 10^8$ m/sec;

λ = wavelength in cm

or

$$I(\lambda, T) = \int_0^\infty \frac{3.74 \cdot 10^{-12}}{\lambda^5 \left(e^{\frac{1.44}{\lambda T}} - 1\right)} d\lambda \text{ W/cm}^3.$$

For any covering (let us call it covering A), it is always possible to select the intensity of irradiation by an infrared source (or $\Phi_\lambda[T]$) such that the error of reproducing the absorbed heat flux is equal to zero for this section, i.e.,

$$Q_A = Q_A^*. \tag{4.41}$$

However, if this same infrared radiant flux impinges on another section of a spacecraft with a covering B, in the general case Q_B^* (in the chamber) does not have to equal Q_B in full scale. The relative error for section B

$$\Delta\overline{Q}_B = \frac{\Delta Q_B}{Q_B} = \frac{Q_B - Q_B^*}{Q_B} \tag{4.42}$$

will be greater, the more the investigated covering differs from a gray body in the wavelength range where the maximum radiation of the planet (Earth) is located (i.e., in the range of 6 - 12 microns).

The errors of $\Delta\overline{Q}_C$, $\Delta\overline{Q}_D$, etc., may be calculated similarly. Depending on the /327 type of curve of $\varepsilon(\lambda)$, the error for different sections of the spacecraft may be negative or positive.

If it is not known beforehand what coverings will be on the test spacecraft, and no single covering may be given preference, for convenience, calculation of the quality of the infrared radiation simulator are adjusted for a black body $\varepsilon(\lambda) = 1$. /328 In this case Equation (4.40) is written as

$$\varphi_{a-1} F_a \int_0^\infty \Phi_{\lambda e} d\lambda = \varphi \frac{F_a}{\sum F_a} S' \int_0^\infty \alpha(\lambda)\beta(\lambda)\varepsilon'(\lambda) I(\lambda, T) d\lambda; \tag{4.43}$$

Substituting (4.40) and (4.43) in (4.42), we find that

$$\Delta\overline{Q}_A = 1 - \frac{\int_0^\infty \Phi_{\lambda e} d\lambda \int_0^\infty \alpha(\lambda)\beta(\lambda)\varepsilon'(\lambda) I(\lambda, T) d\lambda}{\int_0^\infty \varepsilon_a(\lambda)\Phi_{\lambda e} d\lambda \int_0^\infty \alpha(\lambda)\beta(\lambda)\varepsilon'(\lambda) I(\lambda, T) d\lambda}. \tag{4.44}$$

Similarly, we write $\Delta\overline{Q}_B$, ..., $\Delta\overline{Q}_G$.

The results of calculating the relative errors for some of the more commonly used materials and coverings are presented in Table 40.

TABLE 40

DEPENDENCE OF RELATIVE TEMPERATURE ERROR DUE TO POOR SIMILARITY BETWEEN SIMULATOR SPECTRUM AND THE INFRARED RADIATION SPECTRUM OF THE EARTH

Radiator	Spacecraft covering material	Relative error, $\Delta E/E$ in %
Auer mantle	Platinum black	0
	Aluminum oxide	+23
	White paint	-42
Nernst pin	Platinum black	0
	Aluminum oxide	+200
	Beryllium oxide	+300
Thorium oxide	Carbon black	0
	Silver	-20
	Steel	-23
	Nickel	-10
	Aluminum oxide	-10
Thorium oxide with light filter of indium antimonide	Carbon black	0
	Silver	-4
	Steel	-18
	Nickel	0
	Aluminum oxide	-1

All values are calculated for specimens whose area is equal to 1 m^2.

Indium antimonide (InSb) was used as the light filter for correcting the infrared source spectrum. It was also assumed that $\alpha(\lambda) = 1$ and $\beta(\lambda) = 1$. In order to establish which of the filters yields the minimum total error, it is necessary to /329 know the contribution of each section, i.e., the absolute thermal errors must be compared, taking into account the areas of the sections. The best simulator is an optical system in which the minimum algebraic sum will be

$$\Delta\overline{Q}_A Q_A F_A + \Delta\overline{Q}_B Q_B F_B + \ldots + \Delta\overline{Q}_O Q_O F_O.$$

In a number of cases, a more proper criterion of the quality of the infrared simulator may be the sum of the temperature deviations of the sections rather than the sum of the temperature deviations of the fluxes.

Temperature conversion requires a knowledge of the internal heat inputs to the surface. Such an analysis may be accomplished for each specific spacecraft design.

Thermal Radiation of the Cryogenic Panels of the Chamber

When calculating the accuracy of simulating spacecraft thermal conditions, it is necessary to take into account the energy emitted by the cryogenic shields. Without carrying out calculations, we may a priori assert that, having cooled the wall to liquid helium temperature (4.2° K) and having made it black ($\varepsilon = 0.95$), we at the same time reduce the thermal background in the chamber to the level of the background in space. However, such a solution would lead to excessive losses. Calculations indicate that the temperature of the cryogenic panels may be raised to a level of 80 - 100° K without significant errors in the thermal balance of the test spacecraft.

Let us consider a spacecraft located in a thermal simulator whose temperature as a whole is determined by the output of the radiation from the solar and planetary simulators, impinging on the spacecraft. The internal heat dissipation of the spacecraft is equal to zero. This is a more difficult case from the viewpoint of the effect of the infrared radiation of the chamber shields.

The magnitude of the error of reproducing the spacecraft covering temperature depends on A_s and ε of the spacecraft, its temperature T_w, the temperature of the cold shields T_c and also on ε_c of the cryogenic panels. The curves showing the dependence of the absolute error of the spacecraft wall temperature on T_c, T_w and the ratio A_s/ε [245] are presented in Figure 4.86.

The Effect of Uncooled Surfaces

The presence of uncooled surfaces, which have a higher temperature or lower degree of blackness, also affects the temperature of the test spacecraft. Such surfaces include inspection holes, uncooled units for attaching the spacecraft in the chamber, parts of the chamber hull not covered by cryogenic shields, etc. In order that these surfaces do not affect the thermal balance of the test spacecraft, it is necessary that the energy emitted by them be equal to or less than the energy emitted by the cooled shields. For this purpose, the area of the unshielded surfaces should not comprise more than 3% of the total area of the cooled shields on the condition that $T_w = 280°$ K and $\varepsilon = 0.5$.

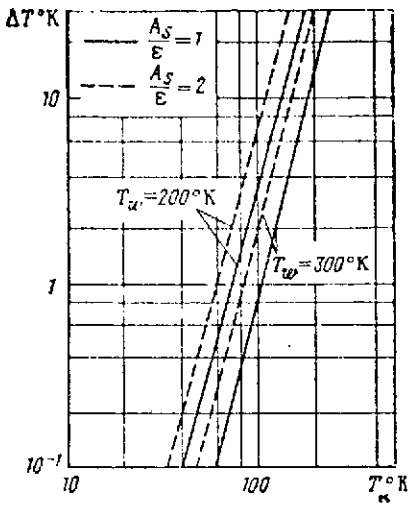

Figure 4.86. Dependence of absolute temperature error of heat-insulated spacecraft covering on its temperature T_w, the temperature of heat-absorbing shields T_c and the ratio A_s/ε of the hull covering ($\varepsilon_c = 1$).

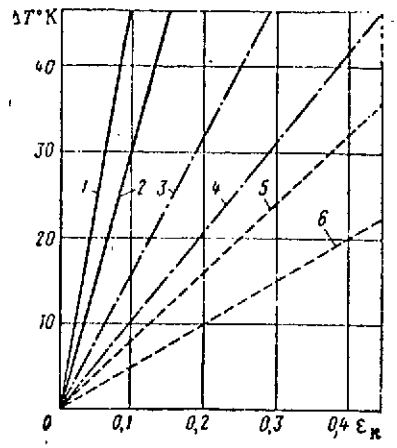

Figure 4.87. Dependence of absolute temperature error of a heat-insulated spacecraft hull on its temperature T_w, the optical characteristics A_s/ε and the degree of blackness of the heat-absorbing shields ε_c: curve 1 — T_w = 300° K, A_s/ε = 3; curve 2 — T_w = 350° K, A_s/ε = 3; curve 3 — T_w = 300° K, A_s/ε = 1; curve 4 — T_w = 350° K, A_s/ε = 1; curve 5 — T_w = 300° K, A_s/ε = 0.5; curve 6 — T_w = 350° K, A_s/ε = 0.5.

The Inhomogeneity of Radiant Flux Density

The inhomogeniety of the radiant flux density in the working zone of a thermal simulator is determined by the formation of the radiant flux and by the quality of the optical system. Systems with diverging beams yield the greatest inhomogeneity. For such systems the field inhomogeneity is inversely proportional to the square of the distance of the source or its image in the optical system: /331

$$\frac{I}{I_0}=\left(\frac{R}{R+H}\right)^2.$$

The further the source and the less the relative dimensions of the working portion, the more uniform is the field.

In diverging beams, the longitudinal non-uniformity of the radiant flux intensity is much greater than the lateral non-uniformity. Therefore, if a plate of finite dimensions is placed in the working zone and if its angle of inclination θ is varied with respect to the flux axis, the irradiation inhomogeneity occurring on its surface will lead to a temperature error. The curves for the dependence of

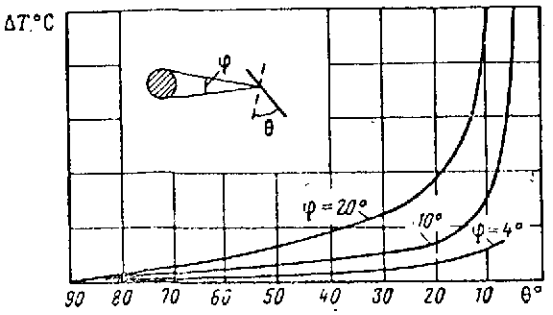

Figure 4.88. Dependence of absolute temperature error of the spacecraft wall on its inclination with respect to the incident beams at different angles of beam divergence.

the temperature error on the angle of inclination of a plate [266] are presented in Figure 4.88 as an example. At high angles of inclination of the plates, very large errors may occur. The curves presented in Figure 4.88 indicate that a system with diverging beams yields very large errors.

However, there is a method which permits a very high field homogeneity in the working zone to be achieved with the aid of diverging beams. The essence of this method is that a very large number of sources with diverging beams are taken and are arranged next to each other in the plane. The axes of all beams should be parallel and directed in a single direction. Taking the working zone at distance L, much greater than that between the sources d, as much field homogeneity of the radiant flux may be obtained as is desired. This method is described in more detail in Section 7, Chapter 4.

Deviation from the Solar Spectrum

When creating solar radiant flux simulators, the question arises of how important it is to maintain the conformity of the spectrum of the radiation sources to the spectral composition of natural solar radiation. If the spacecraft had a uniform covering with a known coefficient ε_0, a radiator output could always be selected for it such that the material would absorb as much energy as it is exposed /332 to under a natural solar flux, i.e.,

$$\int_0^\infty \Phi_{\lambda_\odot}\varepsilon_0(\lambda)\,d\lambda = k\int_0^\infty \Phi^*_{\lambda_\odot}\varepsilon_0(\lambda)R(\lambda)\,d\lambda, \qquad (4.45)$$

where $R(\lambda)$ is the spectral absorption coefficient of the optical system of the solar simulator (i.e., the glass of the entrance hatch, mirrors and lenses);

$\Phi^*_{\lambda_\odot}$ is the spectral intensity of the source radiation which may generally differ considerably from the solar spectrum $\Phi_{\lambda_\odot}$. If we now substitute another value $\varepsilon_i(\lambda)$ into the same "solar" radiant flux, the amount of heat absorbed by it

$$Q_i^* = \int_0^\infty k\Phi_{\lambda\odot}^* \varepsilon_i(\lambda)\, d\lambda \tag{4.46}$$

may differ from the amount of heat which this body would receive from the natural Sun:

$$Q_i = \int_0^\infty \Phi_{\lambda\odot} \varepsilon_i(\lambda)\, d\lambda. \tag{4.47}$$

The results of calculating the relative error

$$\Delta_i = \frac{Q_i^* - Q_i}{Q_i} \tag{4.48}$$

for four radiators (a xenon lamp, a xenon lamp with filter, tungsten at 1000° K and zirconium oxide at 900° K) and seven types of surface material are presented in Table 41.

TABLE 41

EFFECT OF DEVIATION OF SPECTRUM OF SOLAR RADIATION SIMULATOR FROM SOLAR SPECTRUM ON RELATIVE ERROR OF ABSORBED HEAT IN PERCENT

Surface material	Radiator			
	Xenon lamp	Xenon lamp with filter	Tungsten 1000°K	Zirconium oxide 900°K
Aluminum oxide	+14	+7	-42	-30
Aluminum	+25	+22	-74	-79
Stainless steel	+24	+19	-68	-75
Beryllium	+34	+26	-93	-96
Titanium alloy	+30	+13	-48	-55
Silicon solar batteries	+22	+12	-46	-50
White ceramic paint	0	0	0	0

When making calculations, the intensity of the solar simulator radiator is selected so that the relative error for a white ceramic paint is equal to zero. It is obvious from Table 41 that use of a xenon lamp with a filter as the radiator gives the best result. Somewhat worse results (although not much) are obtained

for a xenon lamp without a filter. Considerable errors, reaching 95%, were obtained when using infrared heaters of tungsten or zirconium oxide as the source for the solar simulator.

Poor Similarity between the Spectrum of an Earth Albedo Simulator and the Terrestrial Spectrum of Reflected Radiation /333

After reflection from the Earth, the initial solar spectrum may be varied (see Figure 1.14). This variation of the spectrum may be transformed with the aid of the Johnson curve into the spectral distribution of the albedo $A(\lambda)$. The spectra of reflected and incident radiation differ from each other in approximately the same manner as the solar spectrum differs from the adjusted spectrum of a xenon lamp. Therefore, the error, caused by the difference of the adjusted spectrum of the xenon lamp from the spectrum of reflected radiation, is of the same order of magnitude as the error caused by the difference of the solar spectrum from that of the xenon lamp. The results of calculating the error which is made, if the spectral distribution of the albedo is not taken into account, are presented in Table 42.

The following notations are introduced in this table:

$\Delta Q_1/Q_1$, ΔQ_1 are the relative and absolute ($kcal/m^2 \cdot hr$) errors made when the spectral albedo is replaced by its average value;

$\Delta Q_2/Q_2$ is the relative error due to poor similarity between the spectrum of a xenon lamp with a filter and the solar spectrum;

$\Delta Q_3/Q_3$ is the relative error due to the poor similarity between the spectrum of a xenon lamp without a filter and the solar spectrum.

It is obvious from these data that the relative error exceeds 10% only for some materials.

Polarization /334

Natural sunlight beyond the limits of the Earth's atmosphere is almost completely unpolarized. The radiant flux may be polarized in solar simulators after repeated reflection from the reflecting surfaces. The coefficients of absorption and reflection for polarized beams differ considerably from the optical coefficients for an

TABLE 42 *

RELATIVE AND ABSOLUTE ERRORS DUE TO POOR SIMILARITY BETWEEN SPECTRA OF THE SIMULATOR OF THE EARTH'S ALBEDO AND THE TERRESTRIAL SPECTRUM OF REFLECTED RADIATION

Material	$\frac{\Delta Q_1}{Q_1}$	ΔQ_1	$\frac{\Delta Q_2}{Q_2}$	$\frac{\Delta Q_3}{Q_3}$
Aluminum oxide	—2,60	—5,80	+0,42	—1,35
Machined aluminum	—0,43	—0,83	—2,41	+0,36
Polished constantan	+1,2	+3,64	—1,94	—0,49
Polished silver	—4,98	—1,97	—2,10	—3,20
Smooth unoxidized tungsten	+2,09	+9,53	—3,67	—1,15
Reflecting metal	+3,26	+11,3	—2,35	+2,69
Stainless steel	+1,40	+8,95	—0,90	+1,09
Molybdenum	+1,34	+5,94	—3,83	—3,14
Tantalum	+7,30	+33,3	—4,21	+7,59
Beryllium	+2,22	+8,94	—4,15	—2,51
Platinum black	+0,105	+1,05	—0,01	+0,158
Titanium alloy	—1,27	—7,99	—0,01	+0,158
Copper oxide	—2,79	—18,2	+1,34	—2,74
Magnesium oxide	+1,06	+1,88	—2,88	+6,30
Beryllium oxide	+1,93	+8,62	—2,27	+1,90
Nickel oxide	—9,61	—41,81	+4,68	—8,07
Molybdenum oxide	—16,77	—47,9	+8,79	—11,07
Siberian graphite	+0,635	+4,86	—0,78	—0,088
Brand E Siemens graphite	+0,613	5,68	—0,84	—0,043
Haines nickel alloy	+4,52	+23,34	—3,14	+5,12
White enamel	—1,72	—7,45	+2,30	+2,93

*Commas represent decimal points.

unpolarized radiant flux. Therefore, when calculating the energy, absorbed by a certain section of the spacecraft, it is necessary to take into account not only the dependence of spectral characteristics on direction, but also polarization, i.e., each of the components of the reflectivity of a body surface for two mutually perpendicular directions. /335

This effect is even more intensified if multiple reflections for the elements of a spacecraft of complex configuration are considered. We can cite the results of calculation by Edwards and Bivens [141] as an example indicating the importance

of taking into account polarization for some cases. They considered the case when solar rays, reflected from the battery of the solar elements, impinge on the surface of an instrument container of pure aluminum (or covered with various paints). The calculations showed that disregard of polarization leads to the fact that the calculated heat flux toward the container housing differs by more than twofold from the true value.

The Thermal Conductivity of the Residual Gas in the Chamber

The pressure in the vacuum chamber during thermal tests of spacecraft decreases to a value at which the molecular thermal conductivity of the residual gas may be disregarded in comparison with radiant heat transfer. The value of this maximum pressure may be calculated by the formula

$$p \leqslant \frac{0.782kT \cdot 10^{16}}{\delta \pi A_1^2 \left(1 + \frac{C}{T}\right)} \text{ kgf/m}^2, \tag{4.49}$$

where δ is the distance between the test spacecraft and the heat-absorbing shields in cm; T is wall temperature in °K; k is the Boltzmann constant ($k = 1.38 \cdot 10^{-23}$ J/deg); and A and C are constants. For nitrogen A = 3.22 and C = 105. The value of the heat flux through the gas, due to thermal conductivity for the conditions when $l > \delta$, is calculated by the formula

$$q = \frac{\varkappa + 1}{8(\varkappa - 1)} p \sqrt{\frac{R}{2\pi T}} (T_{w_2} - T_{w_1}) \frac{a_1 a_2}{a_1 + a_2 - a_1 a_2}, \tag{4.50}$$

where $\kappa = c_p/c_v$, R = 29.27 deg and a_1 and a_2 are the accommodation coefficients, respectively, for wall "1" and wall "2."

In most cases, for thermal tests of spacecraft in vacuum chambers, a rarefaction of 10^{-5} - 10^{-6} torr is sufficient.

Other Sources of Methodical Errors

Many other sources of errors, besides those enumerated, which affect the accuracy of simulating spacecraft thermal conditions during experiments in vacuum facilities using radiant simulators, may be cited. They include errors due to:

— reflection of "solar" rays from the heat-absorbing shields and internal assemblies of the chamber; /33

— secondary re-reflection by the mirrors of the solar simulator and return of beams scattered by the test spacecraft into the working zone;

— violation of the angular distribution of planetary radiation;

— inaccuracy of measuring the intensity fields of radiation from simulators;

— thermal conductivity through the systems for attaching the spacecraft;

— shading by the systems for attaching the spacecraft of radiant fluxes from the solar and planetary simulators;

— the effect of natural convection inside the spacecraft, as a result of the Earth's gravitation;

— dissimilarities between the spectrum of lunar infrared radiation and the radiation spectrum of the simulator.

11. Equipment for Simulating Corpuscular Streams and Micrometeor Showers

Investigations of the resistance of temperature controlling coverings to the effects of various types of corpuscular streams have been conducted in various facilities. For systematization, such facilities may be arbitrarily divided into five groups, each of which is designed to simulate completely specific types of corpuscular streams which damage coverings.

The first group of equipment provides for simulation of the effects of the ions in the upper atmosphere of the Earth and other planets on temperature controlling coverings. Study of the effects of ion streams, and especially of neutral particles, in the energy range of 1 - 20 eV on the surface of coverings entails considerable experimental difficulties [2].

The main parameters of ion beams for simulating the interaction of particles of the ionosphere of the Earth, Mars and Venus with various types of temperature controlling coverings are the following [2]:

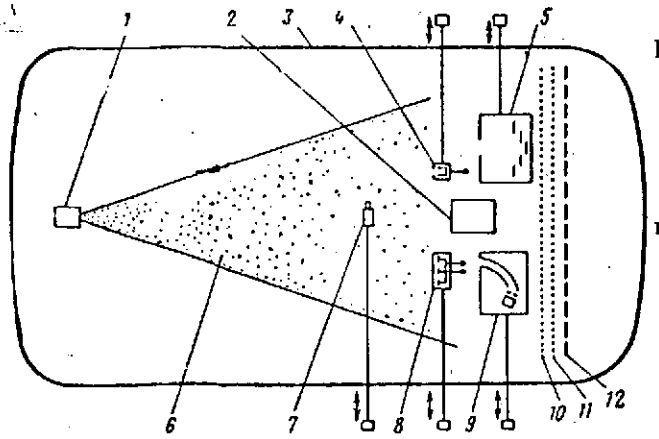

Figure 4.89. Diagram of a plasma wind tunnel: 1 — plasma source; 2 — test object; 3 — vacuum chamber; 4 — thermoproble; 5 — beam divergence analyzer; 6 — plasma beam; 7 — emission probe; 8 — network analyzer; 9 — electrostatic analyzer of ion energy; 10 — limiting grid; 11 — suppression grid; 12 — ring collector.

1. type of ions: O^+; N^+; NO^+; He^+; H^+; CO_2^+;

2. energy of ions $E_i \approx 1 - 20$ eV;

3. intensity of ion beams 100 - 1000 microamperes/cm^2;

4. integral fluxes $10^{19} - 10^{20}$ ions/cm^2;

5. irradiated surfaces ~100 cm^2;

6. total ion beam — up to 100 ma;

7. minimum of ions of impurities from electrodes and other parts of the facility;

8. temperature of irradiated specimens of coverings is -150 to +150° C;

9. measurement of A_s of coverings is accomplished in a vacuum without bringing radiated coverings into the atmosphere.

It is difficult to obtain ion beams with these parameters by classical methods, used in ion-beam devices and in the equipment of ion technology, due to the defocusing effect of the large electric space charge and the uncontrollable electrostatic /337 fields from charges which build up on the oxide films of the walls of the ion conductor.

The use of plasma accelerators is apparently more promising for these purposes. However, the cumbersomeness of the equipment, the pulsed mode of operation and the contamination of plasma beams by the impurities of metallic electrodes presently complicate materials testing of the above-indicated class. A diagram of the arrangement of measuring instruments in a plasma wind tunnel, where it is possible to carry out investigation of temperature controlling coverings on the condition that the beam density be increased [129], is presented in Figure 4.89.

The method of using a high-frequency electrodeless discharge [2, 172] may have a number of advantages in obtaining qualitative results on the interaction of low-energy ions with the materials of coverings due to its simplicity.

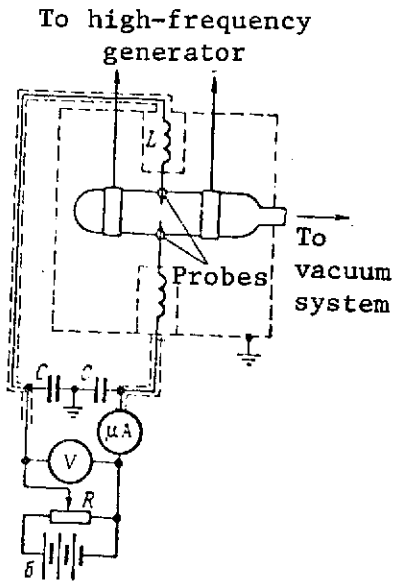

Figure 4.90. Circuit for measuring the parameters of a high-frequency discharge, stimulated by the volumetric method, with the aid of a double probe.

The use of a high-frequency electrodeless discharge to obtain ion fluxes with an energy of 5 - 20 eV has its positive aspects, but also a number of disadvantages. The main advantage of the method is simplicity and the absence of contamination from the atomized electrodes. The main disadvantages are high gas pressure in the working space (10^{-2} - 10^{-3} torr) and the presence of impure atomic flows with thermal energy.

It is more convenient to stimulate a high-frequency discharge in a glass cylinder by the volumetric method with the aid of external electrodes (Figure 4.90) or by the inductive method from an external inductor. The internal wall surface of a /338 glass cylinder or a test specimen of material placed in a plasma in a steady mode of high-frequency discharge acquires a negative potential with respect to the plasma. The particle flow impinging on the wall and, consequently, on the specimen, is determined by bipolar diffusion. The negative electric potential on the specimen surface ΔV corresponds to average electron energy in the plasma of the high-frequency discharge and penetrates the plasma for a distance exceeding the Debye radius r. In the bipolar diffusion mode $r > \lambda$, where λ is the length of the particle mean free path in the discharge tube. The ions in the space between the test specimen and the plasma zone acquire an average energy E_i without collision. The discharge is excited at a frequency of f = 55 MHz at a discharge output of 100 - 200 W. Oxygen, nitrogen, helium, and hydrogen are used as the working gases. Residual pressure in the facility is ~10^{-5} torr. Carbon sorption pumps are used in the vacuum pumping system.

The main parameters of a high-frequency discharge plasma (E_i is the energy of ions impinging on the specimen; i is the density of ion flow, n_e and n_i are electron and ion concentration in the plasma; and T_e is the temperature of the electron gas) were determined with the aid of the double and triple probe method. The wall potential ΔV with respect to the plasma is found from the expression

$$e \cdot \Delta V = \frac{kT_e}{2}(\ln A + 2{,}5) = E_e(\ln A + 2{,}5) = E_i,$$

where E_e is electron gas temperature in eV;

A is the atomic number of the ion;

e is the electron charge;

k is the Boltzmann constant.

It is possible to obtain ΔV, n_e, n_i, j and T_e from an analysis of the current-voltage characteristic, obtained with the aid of a triple probe. At f = 55 MHz, $p \approx 10^{-2}$ torr and a discharge tube length equal to 20 - 30 cm, for O_2, N_2 and He gases, $j \approx 10^{15}$ ions/cm^2·sec, $E_e \approx 2$ eV and $E_i \approx 5 - 8$ eV.

Application of a magnetic field H ≈ 100 - 200 oersteds along the axis of the discharge tube reduces the coefficient of bipolar diffusion and decreases E_i by several times compared to a high-frequency discharge without a magnetic field. A high degree (1 - 10%) of gas dissociation is observed in the above-indicated modes of high-frequency discharge. The atoms formed have a high chemical activity and, impinging on the surfaces of temperature controlling coverings, may cause phenomena similar to those of ion bombardment. /339

The recombination of atoms and ions on the surface of the test specimen, as well as the light emission of the high-frequency discharge, may heat the surface of the irradiated coverings to 50 - 100° C. The effect of the ultraviolet component of the discharge radiation on the variation of the optical parameters of the coverings was not noted.

The second group of equipment is related to simulation of the effects of low-energy corpuscular solar radiation (the "solar wind" and transient solar plasma fluxes), protons and electrons, which comprise the Earth's electronosphere and protonosphere, on temperature controlling coverings. The main parameters of corpuscular streams, with the aid of which the effects of the above-indicated radiant fluxes on temperature controlling coverings may be simulated, taking into account an artificial Earth satellite flying for one year, are presented below:

1) $E_p \approx 0.5 - 100$ keV; $\Phi_p \approx 10^{16} - 10^{17}$ protons/cm^2; $j_p \approx 10^{13}$ protons/cm^2·sec;

2) $E_\alpha \approx 2 - 20$ keV; $\Phi_\alpha \approx 10^{15} - 10^{16}$ α/cm^2; $j_\alpha \approx 10^{13}$ α/cm^2·sec;

3) $E_e \approx 1 - 200$ keV; $\Phi_e \approx 10^{16} - 10^{17}$ electrons/cm^2; $j_e \approx 10^{11} - 10^{13}$ electrons/cm^2·sec.

It is more convenient to use standard electron and ion-beam devices: electron and ion guns, mass separators, mass spectrometers and electronographs [4, 6, 7, 31], to obtain electron, proton and helium ion beams with the indicated characteristics. When using standard devices as charged particle sources, it is necessary to take steps to improve the vacuum pumping system. The method of irradiation in a high-frequency discharge [51] is sometimes employed to simulate the effects of the solar wind on temperature coverings.

The third group of equipment provides for simulation of the interaction of proton and electron beams in the Earth's radiation belts with temperature controlling coverings. The main parameters of such fluxes are the following:

$E_p \approx 0.1 - 4$ MeV; $\Phi_p \approx 10^{14} - 10^{15}$ protons/cm^2;

$j_p \approx 10^{10} - 10^{12}$ protons/cm^2·sec;

$E_e \approx 0.1 - 1$ MeV; $\Phi_e \approx 10^{15} - 10^{16}$ electrons/cm^2;

$j_e \approx 10^{12} - 10^{13}$ electrons/cm^2·sec.

Electrostatic accelerators, cyclotrons and high-voltage accelerators are more /340
suitable for simulation. A list of charged particle accelerators used in [3] and their operating conditions are presented in Table 43 as an illustration. These accelerators were used to simulate the effects of the ion component of solar corpuscular radiation and of the Earth's radiation belts on temperature controlling coverings and other surface elements.

The characteristics of different types of ionizing radiation sources, which may be used to investigate the radiation resistance of spacecraft materials and elements, are presented in Figure 4.91.

TABLE 43

Type of radiation	Energy MeV	Flux density particles/cm^2·sec	Integral flux particles/cm^2	Type of facility
Protons p	1 - 6.5	10^9 - 10^{10}	10^{14}	R-7 cyclotron
Protons p	0.1 - 0.5	10^{11} - 10^{12}	10^{16}	KG-500 high-voltage accelerator
Protons p	0.01 - 0.04	10^{11} - 10^{13}	10^{17}	SP-26 electro-magnetic separator
Helium ions α	4 - 25	10^{10} - 10^{11}	10^{14}	R-7 cyclotron
Helium ions α	0.1 - 0.5	10^{10} - 10^{13}	10^{15}	KG-500 high-voltage accelerator
Helium ions α	0.01 - 0.04	10^{11} - 10^{13}	10^{16}	SP-26 electro-magnetic separator

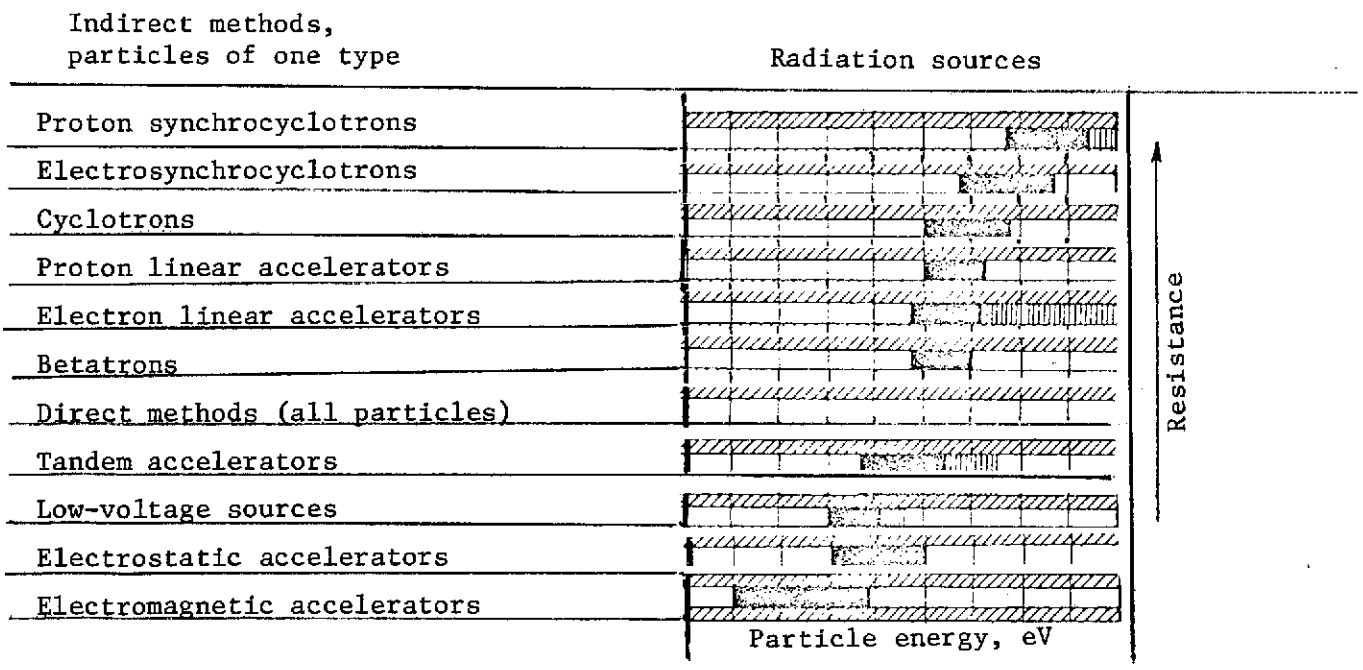

Figure 4.91. Comparative characteristics of various types of charged particle accelerators and ionizing radiation sources.

Specific requirements are placed on equipment for simulating space corpuscular radiation. For example, in nuclear facilities an attempt is made to use monoenergetic focused high-density accelerated particle beams. When investigating the radiation resistance of space materials and elements installed on the external surface of spacecraft, the requirements for charged particle beams are quite different.

Charged particle accelerators should ensure simultaneous electron and positive ion irradiation (by protons, helium ions, etc.) of the materials being investigated. Electron and proton beams should have a uniform density and should permit irradiation of the surface of materials being investigated in a vacuum, equal to hundreds of square centimeters, at a beam density of several microamperes/cm^2 and below. Proton energy may not be greater than 3 - 4 MeV and electron energy — no greater than 0.2 - 0.5 MeV. It is feasible to vary proton and electron energy over a wide /341 energy range and to employ facilities with continuous charged particle acceleration (high-voltage accelerators, electrostatic accelerators, etc.).

It is desirable to convert monoenergetic charged particle beams to those with a dense energetic spectrum, approximating that of the cosmic spectrum.

The main requirements on the experimental chamber in which temperature coverings are being irradiated may be formulated in the following manner: The vacuum in the chamber should not be lower than 10^{-5} - 10^{-6} torr. It is expedient to use oilless means of vacuum pumping to reduce the partial pressure of hydrocarbons. In those cases when it is not possible to fulfill these requirements, modern cryogenic methods of evacuation should be used. The temperature of the irradiated coverings should be varied and measured from -150 to +150° C.

A sufficiently large number of test coverings may be placed in the experimental chamber simultaneously to increase the efficiency of investigation. In some cases it is feasible, without disrupting the vacuum in the chamber, to provide the possibility of blocking the coverings. Sequential irradiation of coverings may be accomplished either by moving them under the charged particle beams or by scanning a large area with the beams.

A Faraday cylinder and a device for calculating the uniformity of particle flux /342 density through the beam cross-section are required for accurate dosimetry of charged particle beams. A mass spectrometer or omegatron for mass analysis of outgassing of the irradiated coverings may be attached to the experimental chamber. The arrangement of the experimental chamber should provide the possibility of measuring the coefficient A_s of the coverings during their irradiation with charged particles or ultraviolet radiation immediately after exposure, without removing the coverings from the vacuum chamber [164, 223, 273]. Measurements of A_s of the coverings may be accomplished by the calorimetric method or with the aid of a spectrophotometer by measuring the spectral dependence of the reflection coefficient R_λ. To measure the coefficient R_λ of the covering, the integrating sphere of the spectrophotometer is placed in the vacuum experimental chamber, and the source and light radiation detector are located outside the chamber. Preparation and adjusting of the vacuum spectrophotometer under laboratory conditions involve technical difficulties.

Calorimetric methods of measuring A_s of coverings in a vacuum are simpler, but, naturally, have a higher error in measurement of A_s. The main advantages of calorimetric methods are:

— continuous control of temperature and the coefficient A_s of the coverings during irradiation;

— small detector dimensions and absence of moving parts, which facilitates the creation of small vacuum facilities;

— the possibility of measuring not only the coefficient A_s, but the ratio A_s/ε as well;

— the use of calorimetric devices in laboratory investigations permits their more reliable calibration, by comparing their readings with those of flight tests. The diagrams of experimental facilities for irradiating coverings with protons, electrons and ultraviolet radiation are shown in Figures 4.92 and 4.93 [240, 244].

The fourth group of simulation equipment should provide acceleration of microparticles measuring on the order of a micron to $v \approx 10 - 20$ km/sec and higher to investigate the effect of micrometeoric erosion on variation of the optical characteristics of coverings. There are various methods of obtaining microparticles at cosmic velocities [182]. Let us dwell only on the method of acceleration using electric fields, because this method, we feel, is the more suitable when investigating

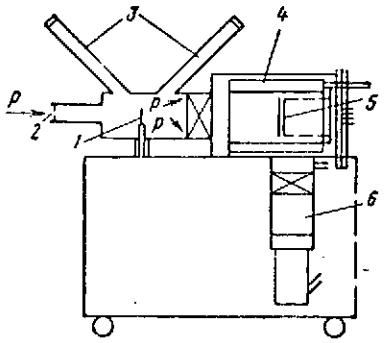

Figure 4.92. Diagram of experimental facility for proton irradiation of coverings: 1 — gold foil for proton scattering; 2 — collimator; 3 — semiconductor counters; 4 — shield, cooled by liquid nitrogen; 5 — specimen holder; 6 — diffusion pump; p — protons.

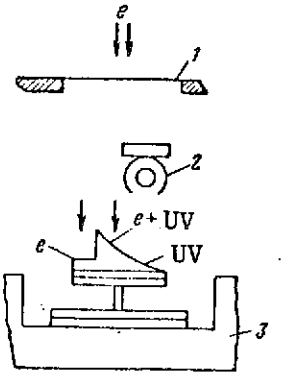

Figure 4.93. Diagram of experimental facility for simultaneous irradiation of coverings by electrons and ultraviolet radiation source; 3 — nitrogen trap.

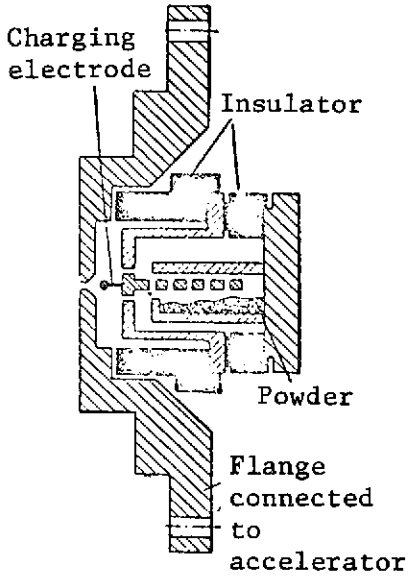

Figure 4.94. Diagram of charged microparticle injector.

the effect of micrometeoric erosion on the optical parameters of temperature controlling coverings [17, 28, 83, 176]. This method has become most popular due to the possibility of using standard industrial accelerators, the possibility of smooth regulation of microparticle velocity, and the purity of the experiment. Electrostatic accelerators /343 are most often used to obtain accelerated microparticles [17, 28]. An electric charge must be imparted to microparticles to accelerate them.

Microparticles are usually charged by the contact method in a special injector (Figure 4.94). Metal particles measuring on the order of a micron, upon approaching the charged electrode, acquire a charge proportional to the electric field intensity for sharp charging electrodes. The charged particle is repelled from the electrode injected into the accelerator tube. The acquired velocity v for a spherical particle at the accelerating potential difference in an electrostatic accelerator U will be calculated by the expression

$$v=(2UQ/m)^{1/2},$$

where Q is particle charge in coulomb;

U is potential difference in MV;

m is particle mass in kg.

The main requirement on the injector is the possibility of obtaining a maximum ratio of $Q/m \approx E/r\rho$, where r is the radius of the microparticle, ρ is the density of the microparticle material; and E is the electric field intensity on the particle surface.

With a negative charge, the electric field intensity of the microparticle is determined by the field emission from its surface. For a positive charge, the maximum electric field intensity is determined by the ion field emission and /344 depends on the strength of the particle material. In the case of a positive charge of the microparticle $E \approx 10^{10}$ V/m, and in the case of a negative charge, $E \approx 10^{9}$ V/m. Therefore, a positive potential is used for charging microparticles. The theoretical ratio for a diamond particle measuring ~1 micron is $Q/m \approx$ coulomb/kg. It is practically possible to obtain $Q/m \approx 100 - 400$ coulomb/kg.

A beam of positive ions may be employed for more effective charging of microparticles [28]. The particle in this case is retained in the vacuum space with the aid of a three-dimensional quadrupole variable electric field. This method is rather complex and has a very low efficiency; therefore, it is not widely used.

An electrostatic accelerator, used to obtain charged particle fluxes of carbonyl iron and carbon, is described in [17]. Particle flux intensity is 600 particles/min, particle diameter is 0.5 - 1 micron, and the velocity of the accelerated microparticles is 3 - 30 km/sec.

The principle of a linear accelerator with drift tubes (Figure 4.95) may be used to obtain higher velocities of charged microparticles. The linear accelerator has 10 acceleration gaps. Charged particles measuring 0.1 - 5 microns are first accelerated in an electrostatic accelerator with a potential difference of 430 kV. They are then injected into the linear accelerator. The frequency of the accelerating voltage, the linear dimensions of the accelerating tubes, and the gaps are

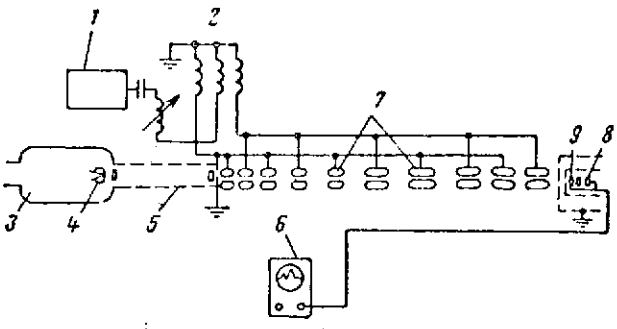

Figure 4.95. Diagram of linear accelerator with drift tubes for micrometeoric particles: 1 — high-frequency source of 36 kHz; 2 — high-voltage transformer, 300 kV; 3 — electrostatic accelerator; 4 — particle injector; 5 — drift tube; 6 — oscillograph for measuring particle velocity; 7 — acceleration electrodes; 8 — target; 9 — ring for measuring velocity.

selected such that particles with a specific charge of $Q/m \approx 30$ coulomb/kg may be accelerated in all cascades. Acceleration efficiency is low due to the large spread of Q/m and reaches ~50 particles/sec at $v \approx 10$ km/sec. When 90 acceleration cascades, supplied by a high-frequency source with variable frequency, are used in a linear accelerator, more intensive accelerated microparticle fluxes with an average velocity of micron particles of $v \approx 25$ km/sec may be obtained.

The principle of accelerating superconducting particles by a traveling magnetic wave permits microparticles to be obtained over the entire range of cosmic velocities. Acceleration to $v \approx 1000$ m/sec may be provided with the aid of new methods [183].

The fifth group of equipment is designed to simulate investigation of the complex effects of various types of solar corpuscular beams and electromagnetic radiation on the resistance of temperature controlling coverings and other elements, located on the external surface of the spacecraft [31, 240, 244]. /345

The principal characteristics of this simulator are presented in Table 44. The main purpose of the experimental chamber is to investigate the physicochemical processes on the surface of various materials and elements during simulation of the effects of the main factors of space. Charged particle accelerators permit proton and helium ion fluxes to be reproduced with a density up to $10^9 - 10^{11}$ ions/cm^2·sec. A micrometeoric particle accelerator with a potential of 3 MV accelerates microparticles of micron dimensions with a mass of $10^{-13} - 10^{-9}$ g at a specific density of 0.5 - 8 g/cm^3 to 10 - 30 km/sec. The accelerator provides a micrometeoric particle flux with a density of $10^3 - 10^4$ particles/m^2·sec.

The arrangement of the experimental facility provides simultaneous simulation of irradiation of test specimens of coverings and other materials by solar electromagnetic radiation, protons and micrometeoric particle fluxes in a vacuum (up to

TABLE 44

Space factors	Equipment and parameters of simulator
Vacuum, chamber dimensions	Experimental facility with pressure of $\sim 10^{-10}$ torr, diameter of 2.4 m and length of 3.3 m
Solar electromagnetic radiation	Arc lamp with an output of 32 kW with graphite electrodes
Corpuscular radiation	Proton electrostatic accelerator under pressure, 3 MeV
	Proton accelerator 200 keV
Micrometeoric particles	Electrostatic accelerator with potential of 3 MV

10^{-10} torr) over a wide temperature range. Different beams may be controlled individually and simultaneously. The equipment permits an experiment to be carried out over a period of months. The chamber contains equipment for automatic measurement throughout the experiment of the mechanical and optical properties of the materials being investigated. The walls of the experimental chamber are heated to 300° C. The chamber has a lock through which the specimens being investigated are loaded. Evacuation is accomplished by an oil-diffusion pump with an evacuation /346 rate of $5 \cdot 10^4$ l/sec. There are cryopanels cooled by liquid nitrogen and liquid helium. The panel on which the materials being investigated are located has dimensions of approximately 1 meter.

The solar radiation source is a 32-kilowatt arc lamp with graphite electrodes, which provides continuous operation over a period of several hundreds of hours. The lamp permits a target 0.6 m in diameter to be irradiated with a flux having an intensity exceeding by twofold the solar flux beyond the limits of the Earth's atmosphere.

Ultraviolet radiation is generated in an argon-plasma lamp with an output of 10 - 20 kW. The lamp provides a continuous spectrum in the range of 1500 - 7000 Å.

The proton accelerators are equipped with analyzing magnets. The scanning electrostatic devices permit irradiation of a target measuring 0.6 x 0.6 m^2.

The micrometeoric particle accelerator, like proton accelerators, provides uniform irradiation of a target 0.6 m in diameter and permits a higher flux density of micrometeoric particles compared to space.

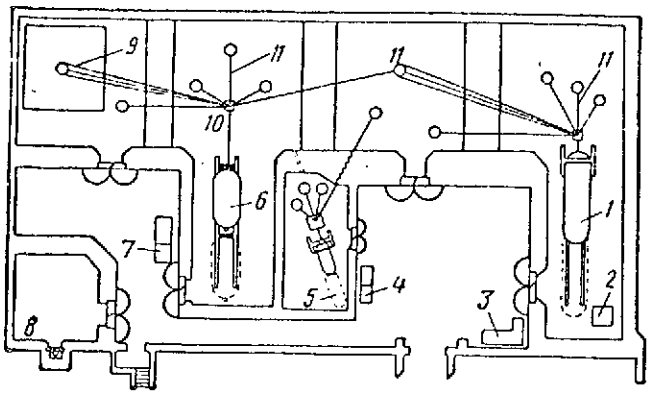

Figure 4.96. Diagram of the radiation laboratory of the Goddard Space Flight Center: 1 — electronic accelerator, 3 MeV; 2 — HF generator of electron accelerator; 3 — electron accelerator control console; 4 — injector control console; 5 — electron-proton injector, 1 MeV; 6 — proton accelerator, 4 MeV; 7 — proton accelerator control console; 8 — Co^{60} storage; 9 — neutron source; 10 — magnets; 11 — experimental chambers.

The Goddard Space Flight Center has constructed a radiation laboratory for investigating the complex effects of proton and electron beams on the materials and elements used in the equipment of artificial Earth satellites [244]. A diagram of the arrangement of the laboratory equipment is shown in Figure 4.96. The laboratory has three electron and proton accelerators and a cobalt gun with an activity of $3 \cdot 10^5$ curies. An electrostatic accelerator under pressure is used as an electron accelerator operating in the range of 0.5 - 3 MeV. Protons are accelerated in another similar accelerator to energies of 1 - 4 MeV.

The third type of accelerator, which has been developed especially for these purposes, permits simultaneous acceleration of electrons and protons in the range /347 of 0.1 - 1 MeV. The availability of several types of accelerators permits simulation of the radiation situation similar to the space environment over a specific energy range in a single chamber.

12. Facilities for Investigating the Effect of Weightlessness

A brief state of weightlessness may be achieved with the aid of a specially equipped aircraft, executing a maneuver along Keplerian trajectories. One of these trajectories, which permits total weightlessness to be achieved for a period of 12 - 15 sec, is shown in Figure 4.97. The length of the period of weightlessness may be increased by increasing the speed of the aircraft at the point where movement along the ascending segment begins. While the period of weightlessness comprises 12 - 15 sec at a flight speed of 465 km/hr, weightlessness lasts for ~34 sec at a speed of 800 km/hr, and this time is increased to approximately 4 minutes in the supersonic X-15 aircraft. The American astronaut, A. Sheppard, was in a state of /348 weightlessness for about 5 minutes during the suborbital flight of the Mercury spacecraft. A further sharp increase in the length of the state of weightlessness involves transition to orbital trajectories.

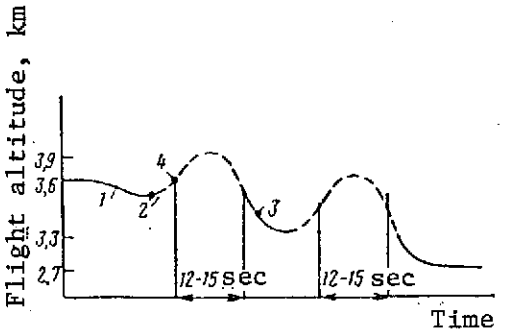

Figure 4.97. A maneuver executed in an aircraft to simulate the state of weightlessness: 1 — diving at an angle of 10°; 2 — speed of 465 km/hr; the ascending portion of the trajectory with g-force of 2.5 g begins at this moment; 3 — speed of 465 km/hr (beginning of overload); 4 — beginning of trajectory with 0 g-force (weightlessness).

Accurate experiments on investigation of vapor formation, boiling, condensation, behavior of fuel in tanks, processes of separation of small droplets from vapor, etc., require that the perturbing mechanical forces (for example, vibration) in flying laboratories be eliminated completely. "Floating" containers, inside which are placed the instruments and experimental equipment, are used for this purpose. During flight, the container is initially supported on flexible wires in the center of the aircraft cabin. The wires are separated from the container at the moment the aircraft begins to move through the ballistic trajectory. From this moment the container moves freely along an elliptical trajectory, which may also not coincide with the trajectory of aircraft motion, although both trajectories are similar to each other. Their divergence naturally ceases when the "floating" container comes into contact with the cabin wall. In this case, the time of "unperturbed" weightlessness is almost always much less than the time of motion of the aircraft along the ballistic curve.

The use of rockets and satellites to increase the time of the experiment is involves obvious increases in the cost of experiments and difficulties due to weight and size limitations.

Vertical towers, from which are dropped the containers with the instrument equipment, are used for fundamental physical investigations, when it is required that, prior to the period of weightlessness, a liquid be free of external perturbations for a prolonged period. If a vacuum is maintained inside the tower, a body moving freely in it will be in a state of weightlessness throughout the entire period of fall. The primary difficulty which must be encountered in the creation of such weightlessness simulators is the high speeds of the instrument container during the final segment of the fall. Thus, for example, a container, falling freely in a vacuum and increasing its speed by 9.8 m every second, reaches a speed of about 2100 km/hr within 1 minute. The second difficulty is that very high

towers must be erected to increase the length of the period of weightlessness. Thus, to obtain only 1 minute of weightlessness would require a tower 17.6 km high, inside which a vacuum would have to be maintained. For these and other technical reasons, towers are erected without a vacuumized shaft and of considerably smaller dimensions.

A streamlined body, having a comparatively low speed, undergoes very low deceleration during the first seconds of free fall. However, the overload factor $k = g/g_0$ subsequently increases very rapidly to unity. As was indicated in Section 6, Chapter 1, in order that the process inviestigated is similar to the process under conditions of weightlessness, it is necessary that the value of k of a falling container (for the force of aerodynamic deceleration related to the unit of weight) not exceed its critical value k_*: /349

$$k < k_* \approx \frac{\sigma}{\varrho g_0 L^2}. \tag{4.51}$$

On the other hand, the time of free fall t should be sufficiently high that there is a transition from the initial configuration of the liquid to that typical for the case of a total absence of an inertia field, i.e., it is necessary that the following inequality be fulfilled:

$$t > t_* \approx \sqrt{\frac{\varrho a^3}{\sigma}}. \tag{4.52}$$

The values k_* and t_* for water and mercury are presented in Table 45.

It follows from an analysis of the data in the table that the conditions of inequalitites (4.51) and (4.52) may be fulfilled only on models of very small dimensions. The value of $k = g/g_0$ may be decreased by increasing the weight of the container and by simultaneously decreasing its aerodynamic drag.

There is also another method of decreasing the value of k. The idea of this method, called the method of the encapsulated container, consists in the fact that the container with the instruments is placed inside the upper portion of a vacuumized capsule, which is dropped from the top of a tower in an ordinary atmosphere. The

TABLE 45

CRITICAL VALUES FOR WATER AND MERCURY (TYPICAL DIMENSIONS OF LIQUID VOLUME 5 cm AND 1 m)

Water			Mercury		
Parameters	L = 0.05 m	L = 1 m	Parameters	L = 0.05 m	L = 1 m
K_*	0.00297	$7.43 \cdot 10^{-6}$	k_*	0.00154	$3.85 \cdot 10^{-6}$
t_*	1.31 sec	117 sec	t_*	1.82 sec	163 sec

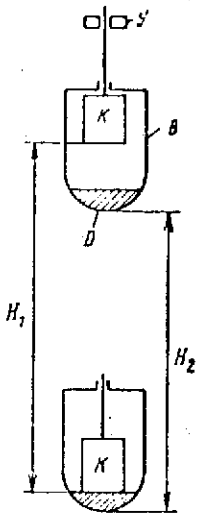

instrument container located inside it is released at the moment the capsule is dropped. According to the extent of deceleration of the capsule by the atmosphere, the internal container gradually approaches the forward end of the capsule, remaining the entire time in a state of free fall (Figure 4.98). This system may be used for drops of about 300 m, which simulates weightlessness for almost 8 seconds.

Figure 4.98. Diagram of falling encapsulated container to investigate processes of weightlessness: H_1 — height of fall of instrument container; H_2 — height of fall of vacuumized capsule; K — instrument container; B — vacuumized capsule; D — damper; Y — clamping device.

CHAPTER 5

/351

FOREIGN DEVELOPMENT OF SPACECRAFT GROUND TEST FACILITIES

Facilities have been created in England, France, Italy, Holland, West Germany, and Japan, but mainly in the United States, for the development and complex testing of spacecraft under conditions approximating real conditions.

Construction of simulators began in 1957 in the United States, but initially lagged behind practical requirements. This was obviously one of the reasons for the low reliability of the first American artificial Earth satellites.

During subsequent years, the deficiencies in ground test facilities were eliminated. At the present time, there is a well equipped experimental base in the United States, which permits testing not only of individual assemblies of spacecraft, but also complex preflight control tests of practically every spacecraft launched.

Rates of Development of the Experimental Base in the United States

Hundred of facilities, simulating space conditions, were created in the United States to carry out extensive investigations on development and testing of spacecraft or their assemblies. By 1968 more than 400 facilities were described with a total volume of the vacuum chambers exceeding 350,000 m^3.

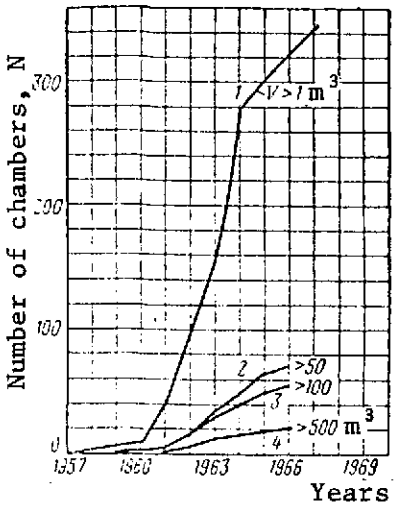

Figure 4.99. Growth of number of vacuum chambers in the United States by years: curve 1 — volume of chambers from 1 m^3 and higher; curve 2 — volume from 50 m^3 and higher; curve 3 — volume from 100 m^3 and higher; curve 4 — volume from 500 m^3 and higher.

We may assume that the actual number of facilities exceeds this figure. The rates of development of scientific research and test centers and creation of new facilities are not diminishing, but are at a very high level (Figure 4.99). Investigations on the creation of space simulation facilities are being conducted simultaneously in more than 50 organizations, as a result of which there is a wide diversity of facilities and variants on their technical design.

Data on simulators in the United States, put into operation during the past ten years, facilitate a statistical analysis to determine the main trends in the past and tendencies of future development. The experience of creation, adjustment and daily operation of a large number of facilities leads to a more rational approach to /352 solution of problems simulating the conditions of spacecraft operation.

The analysis presented below does not claim to have absolute quantitative reliability, because it was compiled only from the materials published in the open literature; however, the qualitative conclusions of the analysis are apparently accurate in reflecting the interrelationship between the principal characteristics of the facilities, their number, dimensions, cost, etc.

Characteristics of the Experimental Base in the United States

The characteristic feature of simulators in the United States is their narrow specialization. Many chambers were designed especially to test a certain specific spacecraft. Construction of a test facility usually coincided with beginning design of a spacecraft and ended prior to the beginning of flight test launches.

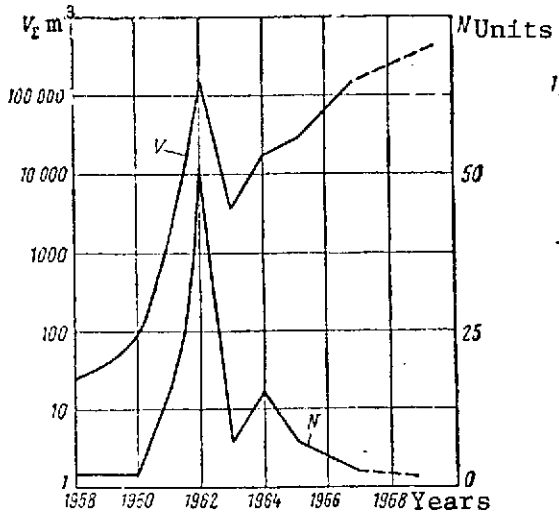

Figure 4.100. Total volume and number of simulation chambers for testing spacecraft, put into operation annually in the United States from 1958 through 1967.

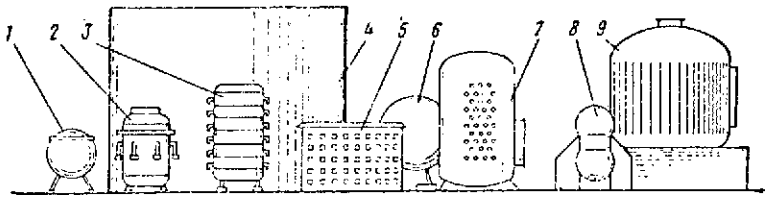

Figure 4.101. Comparative dimensions of some of the largest simulation chambers: 1 — one of three spherical chambers of the General Electric Company, V ≈ 840 m³; 2 — facility of the Goddard Space Flight Center (NASA), V = 1400 m³; 3 — Mark-1 facility of the Arnold Scientific Research Center, V = 1746 m³; 4 — facility of the Arnold Center, V = 134·365 m³; 5 — five-story apartment house; 6 — spherical chamber of the Langley Research Center (Langley Field, Virginia), V = 8060 m³; 7 — chamber of the NASA Manned Spacecraft Center for testing the Apollo spacecraft, V = 12,000 m³ (Houston, Texas); 8 — large chamber of the General Electric Company, V = 900 m³; 9 — chamber of the Lewis Research Center (NASA) for testing spacecraft with an atomic propulsion plant (Plum Brook, Ohio), V = 26·140 m³.

The Development of Simulators

If we follow the development of the experimental base in the United States from 1957, we may note that, beginning in 1962, the main attention was devoted to construction of large and superlarge chambers, required for testing spacecraft of large dimensions. The curves which reflect the change in the total volume and number of /353 vacuum simulation chambers, put into operation annually from 1957 through 1968, are presented in Figure 4.100. During the first four years of existence of the space program in the United States, the total volume V_Σ of chambers introduced annually increased from 50 m³ to 140,000 m³. During subsequent years, V_Σ increased gradually after a certain drop in 1963. Facilities with a volume greater than 10,000 m³ are being put into operation. The largest among them was constructed at the Arnold Scientific Research Center (Tullahoma, Tennessee) (Figure 4.101). The diameter of the chamber is 61 m, height is 46 m, volume is 135, 365 m³ and the proposed minimum pressure is up to 10^{-11} torr. Access to the chamber is accomplished through a top hatch 21 m in diameter. The chamber is designed for thermal tests of spacecraft, including spacecraft with nuclear propulsion plants.

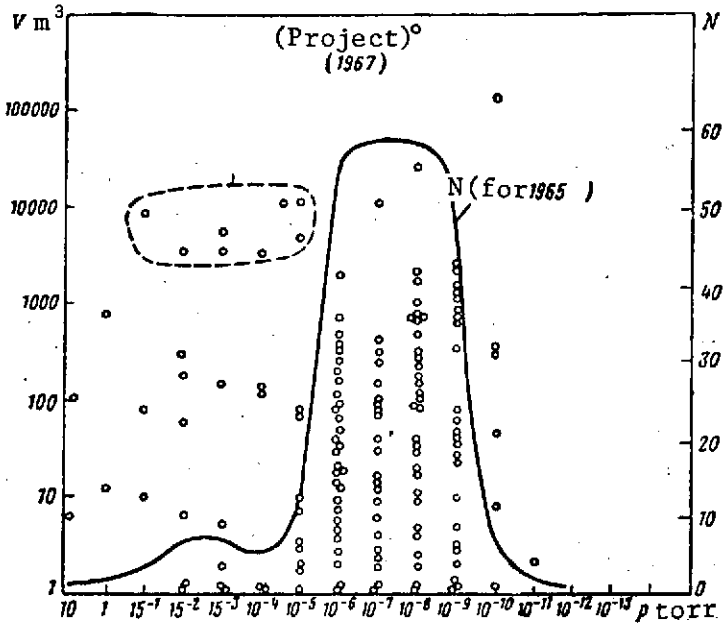

Figure 4.102. Relationship between the object of vacuum chambers in the United States and the working pressure in them according to data for 1965. The dependence of the number of chambers on working pressure is represented by the continuous curve. The dashed line denotes the range of service facilities.

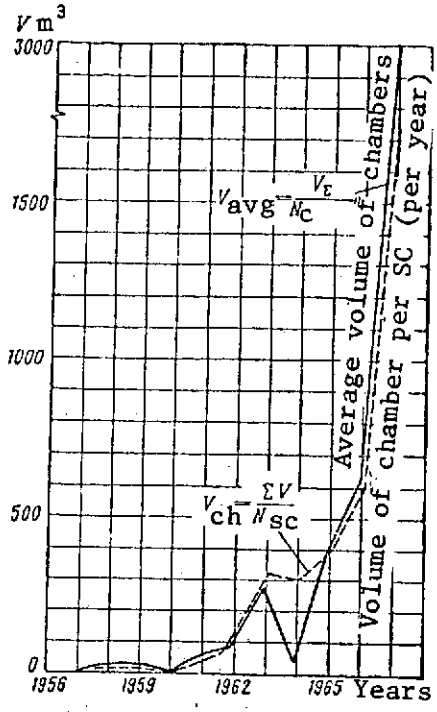

Figure 4.103. Average volume V_{av} of vacuum chambers created in the United States and their volume V_{ch} per spacecraft launched per year.

The Volume and Extent of the Vacuum

The overwhelming majority of chambers having a volume up to 1000 m^3 are designed for testing spacecraft thermal conditions at pressures from 10^{-5} to 10^{-9} torr (Figure 4.102). Chambers with a volume from 2000 to 10,000 m^3 are designed mainly for a pressure range from 10^{-1} to 10^{-5} torr. This group of chambers (denoted in Figure 4.102 by the dashed line) is usually intended for testing engines. A combination of large chamber dimensions and considerable gas flowrate at an average vacuum is typical for this group. There are comparatively few facilities for testing the physicochemical processes in an extremely high vacuum, i.e., in the pressure range from 10^{-10} to 10^{-14} torr. These are mainly facilities of small dimensions. The volume of the vacuum chamber in them is of the order of 1 cubic meter.

The Volume and Number of Chambers

Beginning in 1964, a sharp decrease is observed in the total number of chambers created during the year with a simultaneous increase in their total volume V_{Σ}. If V_{Σ} is divided by the number of chambers N_c, we can follow how the average volume of the chambers varied over the years (Figure 4.103).

The distribution of the number of chambers by volume is not a constant value, but varies with each year. This fact reflects the change in the dimensions of spacecraft tested. The data for 1967 on the number of chambers of different volumes in the United States, England, Holland, Italy, West Germany and Japan are presented /355
in Table 46.

TABLE 46

Country	Volume of Chambers in m^3								
	to 5	5-50	500-1000	1000-10^4	10^4-10^5	Above 10^5	Operating	Total	Under Construction
USA	215	91	46	6	17	5	1	380	24
England, Holland, Italy, West Germany Japan	9	7	3	-	-	-	-	12	7

The trend to change the number of vacuum chambers of a specific type by years may be followed in Figure 4.99.

Designation of Facilities /356

The overwhelming majority of all simulators in the United States (~90%) is intended for thermal vacuum tests of astronaut spacesuits, on-board power systems, structural elements, compartments, and the engines of spacecraft and rocket stages. An insignificant portion (about 5%) of the facilities is equipped with centrifuges and vibration benches, and approximately the same portion is comprised of facilities for investigating weightlessness, acoustical effects, and also for simulation of the different flight conditions and special materials tested.

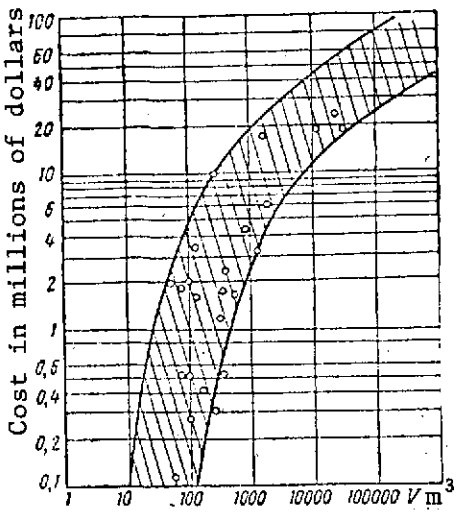

Figure 4.104. Cost of simulators as a function of the volume of the space chamber.

The Cost of Facilities

The cost of a facility is highly dependent on the complexity of its instrumentation and simulation equipment. In most cases, the cost of equipment greatly exceeds the cost of the vacuum chamber. Therefore, the dependence between the volume of the chamber and its cost may be established only approximately with a wide spread of experimental points (see Figure 4.104).

As an example, we may cite the vacuum chamber for testing a spacecraft with an atomic propulsion plant and atomic electric power sources, startup of which was planned for 1967. The vacuum chamber 30 m in diameter and 37 m long (volume of 26,114 m^3) cost \$2,743,900, and the total cost of the facility is estimated at approximately \$23 million. This difference in the cost of the chamber and the facility as a whole is not surprising, if certain typical details are presented which determine the complexity of creating such facilities. The entire chamber is surrounded by a concrete shell almost 2 meters thick for biological protection. The space between the chamber wall and the shell is evacuated to a low pressure. The door of the chamber measures 15 x 15 m and weighs 2000 tons. The powerful vacuum system must maintain a pressure in the chamber at a level of 10^{-6} torr for 90 days with an operating atomic electric power system. The entire /357 facility is located in a building whose dimensions comprise 80 x 155 x 43 m.

There is also another example when the cost of facilities, differing in volume by more than tenfold, is almost identical. This is the Mark-1 facility, with a chamber volume of 1746 m^3 and a cost of \$17.5 million and the complex of facilities for testing the Apollo spacecraft at Houston (NASA), which consists of two chambers of 11,293 m^3 each, with a total cost of \$19 million. Both facilities are equipped with solar simulators and have maximum pressures of 10^{-8} and 10^{-5} torr, respectively.

Despite the considerable spread of points in the graph of Figure 4.104, a general trend toward a decrease in cost as chamber volume increases is observed. This means that the unit volume of large chambers is cheaper than the unit volume of small chambers.

The total cost of the experimental base for developing Apollo spacecraft is estimated at approximately $1.5 billion.

Periods Required for Creation of Facilities and Cost of Their Operation

Designing the experimental equipment for the Apollo program occupied about 3 years. Construction was carried on for approximately 2 years. The operation of this base over a period of 5 years has cost $2.5 billion, i.e., an average of $500 million per year.

The cost of operating the large chambers of the complex is very high. One hour of operation of the large General Electric facility, 900 m^3 in volume, costs approximately $1000. The cycle of creating a chamber of average dimensions, including its designing and commissioning, usually does not exceed 1.5 - 2 years. As an example, we may cite the TRW chamber (United States), with a volume of 600 m^3, equipped with a solar simulator and evacuation system up to 10^{-6} torr. The time from beginning of design to commissioning of the chamber was 1.5 years. The cost of the facility is $3 million.

Ownership of Simulators

Most large and the largest facilities in the United States belong to the Manned Spacecraft Center (NASA), which includes: the Jet Propulsion Laboratory (JPL), the Lewis, Goddard, Langley and Ames research centers, the Marshall Space Flight Center, the Kennedy Space Center, the Manned Spaceflight Center, and other centers.

The United States Air Force also has large simulators in the Flight Test Center at Edwards Air Force Base and at the Arnold Scientific Research Center. /358

Many vacuum chambers equipped with space radiation simulators are at the disposal of Avio Corporation, Associated Testing Laboratory, Aerojet General Corporation, Bendix, Boeing, Bell Aerosystems, Beech Aircraft, Grumman, General Electric, Douglas Aircraft, etc., a total of about 40 companies. A certain number of facilities have been constructed at universities. The companies and universities own approximately twice as many facilities compared to government installations. However, these facilities are primarily of average and small dimensions. The total volume of chambers belonging to the companies is approximately 10 times less than the total volume of the chambers of government installations.

APPENDIX

/359

TABLE 1 *

MODEL OF MARTIAN ATMOSPHERE OF AVERAGE DENSITY [271]

(100% CO_2, p_s = 6.0 torr, T_s = 210° K)

H_0 km	n cm^{-3}	T °K	M	p torr	H_0 km	n cm^{-3}	T °K	M	p torr
0	$2,78\cdot10^{17}$	210	44	$6,0\cdot10^{0}$	250	$3,2\cdot10^{6}$	217,2	9,5	$7,2\cdot10^{-11}$
10	$1,232\cdot10^{17}$	160	44	$2,1\cdot10^{0}$	300	$1,55\cdot10^{6}$	303,5	7,8	$3,2\cdot10^{-11}$
20	$3,6\cdot10^{16}$	136,2	44	$5,1\cdot10^{-1}$	350	$4,93\cdot10^{5}$	402,9	6,8	$1,9\cdot10^{-11}$
30	$8,5\cdot10^{15}$	129,8	44	$1,1\cdot10^{-1}$	400	$2,83\cdot10^{5}$	514	5,7	$1,5\cdot10^{-11}$
40	$1,852\cdot10^{15}$	123,4	44	$2,4\cdot10^{-2}$	450	$1,83\cdot10^{5}$	639	5,2	$1,2\cdot10^{-11}$
50	$2,755\cdot10^{14}$	117	44	$4,6\cdot10^{-3}$	500	$1,29\cdot10^{5}$	776	4,7	$1,0\cdot10^{-11}$
60	$6,94\cdot10^{13}$	110,6	44	$0,8\cdot10^{-3}$	600	$7,38\cdot10^{4}$	1080	4,2	$0,8\cdot10^{-11}$
70	$1,352\cdot10^{13}$	104,2	38,1	$1,5\cdot10^{-4}$	700	$4,83\cdot10^{4}$	1440	3,6	$7,2\cdot10^{-12}$
80	$2,89\cdot10^{12}$	97,8	34,1	$2,9\cdot10^{-5}$	800	$3,42\cdot10^{4}$	1840	3,4	$6,5\cdot10^{-12}$
90	$6,69\cdot10^{11}$	91,4	30,7	$6,3\cdot10^{-6}$	900	$2,56\cdot10^{4}$	2280	3,2	$6,1\cdot10^{-12}$
100	$1,63\cdot10^{11}$	85	28,0	$1,4\cdot10^{-6}$	1000	$1,999\cdot10^{4}$	2770	3,0	$5,7\cdot10^{-12}$
110	$4,32\cdot10^{10}$	85	25,0	$3,8\cdot10^{-7}$	2000	$4,21\cdot10^{3}$	9890	2,8	$4,3\cdot10^{-12}$
120	$1,34\cdot10^{10}$	85	22,0	$1,3\cdot10^{-7}$	3000	$1,82\cdot10^{6}$	20800	2,7	$3,9\cdot10^{-12}$
130	$4,64\cdot10^{9}$	85	20,0	$3,9\cdot10^{-8}$	4000	$1,025\cdot10^{6}$	35300	2,5	$3,8\cdot10^{-12}$
140	$1,74\cdot10^{9}$	85	18,5	$1,5\cdot10^{-8}$	5000	$6,64\cdot10^{5}$	53200	2,3	$3,7\cdot10^{-12}$
150	$7,05\cdot10^{8}$	85	17,0	$6,2\cdot10^{-9}$	6000	$4,66\cdot10^{5}$	74400	2,2	$3,6\cdot10^{-12}$
160	$3,02\cdot10^{8}$	85	16,0	$2,6\cdot10^{-9}$	7000	$3,47\cdot10^{5}$	98700	2,0	$3,55\cdot10^{-12}$
170	$1,485\cdot10^{8}$	85	15,0	$1,3\cdot10^{-9}$	8000	$2,7\cdot10^{5}$	126000	1,8	$3,51\cdot10^{-12}$
180	$5,9\cdot10^{7}$	118,8	14	$7,2\cdot10^{-10}$	9000	$2,158\cdot10^{5}$	157000	1,7	$3,5\cdot10^{-12}$
190	$3,23\cdot10^{7}$	132,2	13	$4,4\cdot10^{-10}$	10000	$1,77\cdot10^{5}$	190000	1,5	$3,49\cdot10^{-12}$
200	$1,96\cdot10^{7}$	144,2	12	$2,9\cdot10^{-10}$					

*Commas represent decimal points.

TABLE 2*

CHARACTERISTICS OF PLANETS AND THEIR RADIATION

Characteristics	Mercury	Venus	Earth	Moon	Mars	Jupiter	Saturn	Uranus	Neptune	Pluto
Distance from Sun (average) in millions of km	58	108	150	150	228	778	1428	2872	4498	5910
Distance from Sun in astronomical units (average)	0,387	0,723	1,000	1,000	1,524	5,203	9,539	19,20	30,09	39,06
Average diameter in km	4860	12200	12700	3476	6780	140000	120000	49000	47000	6000
Orbital eccentricity	0,206	0,007	0,017	0,055	0,093	0,048	0,056	0,047	0,009	0,253
Period of rotation around Sun in years	0,24	0,62	1,00		1,88	11,9	29,46	84	165	250,6
Inclincation of equator to orbit	~7°	182°	23°27′	7°30′	24°	3°	26°45′	98°	151°	17°8′
Period of rotation around the axis in hours	1420±120	5850±12	23h56m4s	~656	~24	~10	~10	~108	16	6,4
Solar flux intensity (average) in W/m^2	9400	2700	1396	1396	620	52,8	15,7	3,88	1,57	0,94
Seasonal variations in W/m^2	±3160	±36	±49	±49	±117	—	—	—	—	±0,567
Albedo (average)	0,07÷0,06	0,73÷0,80	0,37÷0,39	0,073	0,15÷0,17	0,67÷0,51	0,69±0,42	0,93	0,84	0,16÷0,14
Average flux density of reflected radiation in W/m^2	330	940	265	49	50	14	5	1	0,55	0,07
Seasonal variations in W/m^2	±110	±13	±10	±16	±88					±0,42
Average flux density of self radiation in W/m^2	2200	170÷200	220	326	130	6,5	1,6	0,5	0,12	0,2
Maximum effective temperature in °C	+413 (irrad.)	—43,4	—21,1	+137	30	—	—	—	—	—
Minimum effective temperature in °C	—200÷130		—73	—155	—100	—	—	—	—	—
Average effective temperature in °C	+170	—43,4	—25	+7	—49	—138÷—171	—153÷—197	—180÷—224	—221÷—240	—229
Angle of non-parallelism of solar rays	1°22′30″	44′30″	32′	32′	21′	6′12″	3′16″	1′40″	1′04″	48″

*Commas represent decimal points.

TABLE 3

COMPONENTS OF NORMAL EQUATIONS

M			$-\dot{T}_1$			$-T_1^4$			(T_3-T_1)	(T_2-T_1)	X_1	$-\Phi$
	M			$-\dot{T}_2$			$-T_2^4$		(T_3-T_2)		(T_1-T_2)	X_2	$-\Phi_2$
		M			$-\dot{T}_3$			$-T_3^4$	(T_2-T_3)	(T_1-T_3)		X_3	$-\Phi_3$
$-\dot{T}_1$			$\dot{T}_1^2$			$\dot{T}_1T_1^4$				$-\dot{T}_1(T_3-T_1)$	$-\dot{T}(T_2-T_1)$	X_4	$\dot{T}_1\Phi_1$
	$-\dot{T}_2$			$\dot{T}_2^2$			$\dot{T}_2T_2^4$		$-\dot{T}_2(T_1-T_3)$		$-\dot{T}_2(T_1-T_2)$	X_5	$\dot{T}_2\Phi_2$
		$-\dot{T}_3$			$\dot{T}_3^2$			$\dot{T}_3T_3^4$	$-\dot{T}_3(T_2-T_3)$	$-\dot{T}_3(T_1-T_3)$		X_6	$\dot{T}_3\Phi_3$
$-T_1^4$			$\dot{T}_1T_1^4$			$(T_1^4)^2$				$-T_1^4(T_3-T_1)$	$-T_2^4(T_2-T_1)$	X_7	$T_1^4\Phi_1$
	$-T_2^4$			$\dot{T}_2T_2^4$			$(T_2^4)^2$		$-T_2^4(T_3-T_2)$		$-T_2^4(T_1-T_2)$	X_8	$T_2^4\Phi_2$
		$-T_3^4$			$\dot{T}_3T_3^4$			$(T_3^4)^2$	$-T_3^4(T_2-T_3)$	$-T_3^4(T_1-T_3)$		X_9	$T_3^4\Phi_3$
	(T_3-T_2)	(T_2-T_3)		$-\dot{T}_2(T_3-T_2)$	$-T_3(T_2-T_3)$		$-T_2^4(T_3-T_2)$	$-T_3^4(T_1-T_3)^2$	$(T_2-T_3)^2$	$(T_1-T_3)\times$ $\times(T_2-T_3)$	$(T_3-T_2)\times$ $\times(T_1-T_2)$	X_{10}	$(\Phi_2-\Phi_3)$ (T_2-T_3)
(T_3-T_1)		(T_1-T_3)	$-\dot{T}_1(T_3-T_1)$		$-\dot{T}_1(T_1-T_3)$	$-T_1^4(T_3-T_1)$		$-T_3^4(T_1-T_3)$	$(T_1-T_3)\times$ $\times(T_2-T_3)$	$2(T_3-T_1)^2$	$(T_2-T_1)\times$ $\times(T_3-T_1)$	X_{11}	$(\Phi_1-\Phi_3)$ (T_1-T_3)
(T_2-T_1)	(T_1-T_2)		$-\dot{T}_1(T_2-T_1)$	$-\dot{T}_2(T_1-T_2)$		$-T_1^4(T_1-T_2)$	$-T_2^4(T_1-T_2)$		$(T_3-T_2)\times$ $\times(T_1-T_2)$	$(T_2-T_1)\times$ $\times(T_3-T_1)$	$2(T_2-T_1)^2$	X_{12}	$(\Phi_2-\Phi_1)$ (T_2-T_1)

TABLE 4*

REFLECTIVITY OF LUNAR "SEAS" (THE REFLECTED BEAM IS LOCATED IN A PLANE NORMAL TO THE PLANE OF INCIDENCE

Angle of reflection δ, deg	Angle of incidence γ_s, deg							
	10	20	30	40	50	60	70	80
10	0,062	0,050	0,039	0,035	0,032	0,027	0,026	0,024
20	0,050	0,046	0,038	0,034	0,032	0,028	0,026	0,026
30	0,039	0,038	0,037	0,033	0,032	0,030	0,027	0,028
40	0,035	0,034	0,033	0,033	0,032	0,032	0,027	0,031
50	0,032	0,032	0,032	0,032	0,033	0,033	0,032	0,035
60	0,027	0,028	0,030	0,032	0,033	0,038	0,038	0,042
70	0,026	0,026	0,027	0,027	0,032	0,038	0,047	0,054
80	0,024	0,026	0,028	0,031	0,035	0,042	0,054	0,080

*Commas represent decimal points.

TABLE 5* /363

REFLECTIVITY OF LUNAR "CONTINENTS" (THE REFLECTED BEAM IS LOCATED IN A PLANE PERPENDICULAR TO THAT OF THE INCIDENT BEAM)

Angle of reflection δ, deg	Angle of incidence γ_s, deg							
	10	20	30	40	50	60	70	80
10	0,095	0,085	0,074	0,061	0,052	0,045	0,043	0,029
20	0,088	0,076	0,070	0,061	0,052	0,046	0,044	0,030
30	0,074	0,070	0,066	0,060	0,054	0,046	0,045	0,032
40	0,061	0,061	0,060	0,056	0,055	0,048	0,046	0,037
50	0,052	0,052	0,054	0,055	0,050	0,051	0,050	0,047
60	0,045	0,046	0,046	0,048	0,051	0,052	0,055	0,064
70	0,043	0,044	0,045	0,046	0,050	0,055	0,065	0,082
80	0,029	0,030	0,032	0,037	0,047	0,064	0,082	0,114

*Commas represent decimal points.

TABLE 6* /364

REFLECTIVITY OF LUNAR "CONTINENTS" (THE REFLECTED BEAM IS LOCATED IN THE SAME PLANE AS THE INCIDENT BEAM)

Angle of reflection δ, deg	Angle of incidence γ_s, deg							
	0	10	20	30	40	50	60	70
—80	0,028	—	0,045	0,062	0,075	0,102	—	—
—70	0,036	0,043	0,051	0,074	0,087	0,120	0,190	0,362
—60	0,043	0,052	0,058	0,087	0,100	0,150	0,248	0,243
—50	0,051	0,062	0,067	0,103	0,124	0,193	0,171	0,156
—40	0,061	0,072	0,081	0,124	0,161	0,144	0,117	0,112
—30	0,072	0,087	0,109	0,143	0,124	0,100	0,090	0,089
—20	0,085	0,104	0,131	0,120	0,092	0,079	0,072	0,073
—10	0,102	0,126	0,110	0,098	0,074	0,065	0,058	0,061
0	0,124	0,108	0,088	0,078	0,061	0,052	0,047	0,050

(Cont.)

TABLE 6 * (CONTINUED)

REFLECTIVITY OF LUNAR "CONTINENTS" (THE REFLECTED BEAM IS LOCATED IN THE SAME PLANE AS THE INCIDENT BEAM)

Angle of reflection δ, deg	Angle of incidence γ_s, deg							
	0	10	20	30	40	50	60	70
+10	0,102	0,084	0,072	0,064	0,053	0,045	0,040	0,045
+20	0,086	0,073	0,062	0,053	0,046	0,037	0,034	0,038
+30	0,072	0,060	0,053	0,042	0,037	0,032	0,030	0,035
+40	0,061	0,052	0,047	0,035	0,031	0,027	0,027	0,032
+50	0,051	0,042	0,037	0,030	0,027	0,025	0,026	0,030
+60	0,043	0,035	0,032	0,025	0,024	0,025	0,025	0,027
+70	0,036	0,025	0,025	0,022	0,022	0,025	0,025	0,027
+80	0,028	0,017	0,017	0,020	0,020	0,025	0,025	0,027

*Commas represent decimal points.

TABLE 7 *

REFLECTIVITY OF LUNAR "SEAS" (THE REFLECTED BEAM IS LOCATED IN THE SAME PLANE AS THE INCIDENT BEAM)

Angle of reflection δ, deg	Angle of incidence γ_s, deg							
	0	10	20	30	40	50	60	70
-80	0,024	0,034	0,032	0,034	0,039	0,049	—	—
—70	0,026	0,034	0,026	0,039	0,047	0,063	0,111	0,237
—60	0,027	0,035	0,040	0,046	0,057	0,086	0,162	0,128
—50	0,030	0,038	0,044	0,058	0,074	0,126	0,106	0,081
—40	0,034	0,042	0,053	0,075	0,106	0,089	0,069	0,057
—30	0,040	0,050	0,065	0,094	0,076	0,062	0,052	0,043
—20	0,049	0,063	0,086	0,071	0,058	0,048	0,039	0,035
—10	0,066	0,082	0,065	0,053	0,044	0,040	0,032	0,030
0	0,081	0,070	0,051	0,040	0,036	0,033	0,026	0,025
+10	0,066	0,053	0,042	0,033	0,030	0,028	0,022	0,021
+20	0,049	0,042	0,035	0,029	0,027	0,024	0,019	0,019
+30	0,040	0,034	0,031	0,026	0,024	0,020	0,018	0,017
+40	0,034	0,030	0,027	0,025	0,023	0,017	0,017	0,016
+50	0,030	0,028	0,025	0,023	0,020	0,016	0,016	0,015
+60	0,027	0,026	0,023	0,021	0,018	0,015	0,014	0,014
+70	0,026	0,024	0,023	0,020	0,016	0,013	—	—
+80	0,024	—	—	—	—	—	—	—

*Commas represent decimal points.

/365

TABLE 8 *

DATA ON THERMAL VACUUM TEST CHAMBERS IN THE UNITED STATES (for 1968)

Ownership	Number of organizations having chambers	Number of chambers	Total volume of chambers m^3	Number of chambers equipped with radiant Flux simulators	Type of radiation sources for solar simulators	
					Xenon, mercury-xenon, or carbon-arc	Infra-red radi-ators
Government	15	140 (34%)	300 000 (93%)	80	75 (94%)	9 (11%)
Companies and universities	40	280 (66%)	35 000 (7%)	190	180 (95%)	10 (5%)
Total	55 (100%)	420 (100%)	335 000 (100%)	270	255 (94,4%)	15 (5,9%)

*Commas represent decimal points.

REFERENCES

/368

1. Akishin, A. I. Ionnaya bombardirovka v vakuume (Ion Bombardment in a Vacuum), Energoizdat, Moscow, 1963.

2. Akishin, A. I., Ye. V. Blyudov, S. K. Guzhova, L. N. Isayev and G. G. Solov'yev. Interaction of a High-Frequency Discharge Plasma with Certain Dielectrics. Zhurnal prikladnoy spektroscopii (ZhPS), Vol. 12, No. 1, 1970.

3. Akishin, A. I., Yu. V. Bulgakov, S. S. Vasil'yev, S. N. Vernov, V. S. Nikolayev and I. B. Teplov. Simulation of the Radiation Effects of the Space Environment on the Materials and Elements of Spacecraft. Proceedings of the XVII Congress of JAF, North Holland Publishing Co., 1968.

4. Akishin, A. I., S. S. Vasil'yev and L. N. Isayev. Cathode Sputtering of Mica in Fused Quartz by Krypton Ions. Izvestiya AN SSSR, Ser. Fiz., Vol. 26, No. 11, 1962, p. 1356.

5. Akishin, A. I. and V. S. Zazulin. Controlling the Thickness of Films Obtained in a Vacuum by a Quartz Resonator. Pribory i tekhnika eksperimenta (PTE), No. 1, 1963, pp. 152-154.

6. Akashin, A. I., L. N. Isayev and Yu. I. Tyutrin. Sputtering of Alkali-Haloid Monocrystals by Argon Ions. Radiotekhnika i elektronika (RE), Vol. 9, No. 11, 1964, pp. 2065-2067.

7. Akishin, A. I., L. N. Isayev and Yu. I. Tyutrin. Sputtering of Polymers by Ar^+, He^+ and H^+ Ions with Energies up to 30 keV. Zhurnal fizicheskoy khimii (ZhFKh), Vol. 39, No. 12, 1965, pp. 3067-3069.

8. Allen, K. U. Astrophysical Units (translated from English). Foreign Languages Publishing House, Moscow, 1960.

9. Arifov, U. A. Vzaimodeystviye atomnykh chastits s poverkhnost'yu tverdogo tela (Interaction of Atomic Particles with a Solid Surface). "Nauka" Press, Moscow, 1968.

10. Bagrov, N. N., I. O. Kulik, A. A. Guslyakov and Ye. M. Lifshits. Investigating Certain Parameters of Cryogenic Vacuum Systems. CIVRES, Paris, 1964: 1st Int'l Congress on Vacuum Technology in Space Research.

11. Bagrov, N. N., A. M. Butenko, A. A. Guslyakov and I. O. Kulik. Investigating the Operation of a Cryogenic Pump in a Free Molecular Mode. Zhurnal tekhnicheskoy fiziki (ZhTF), Vol. 30, No. 6, 1967.

12. Bayeva, N. N., N. P. Danilova and A. I. Shal'nikov. Pribory i tekhnika eksperimenta, No. 6, 1966.

13. Bakulin, P. I., E. V. Kononovich and V. I. Moroz. Kurs obshchey astronomii (Course in General Astronomy). "Nauka" Press, Moscow, 1966.

14. Barabashov, N. P. Mars (Mars). Sovetskaya rossiya, Moscow, 1963.

15. Barabashov, N. P. Calculating the Earth's Albedo. Russkiy astronomicheskiy zhurnal (RAZh), Vol. 1, Nos. 3 and 4, 1924.

16. Barabashov, N. P., et al. Luna (The Moon), Fizmatgiz, Moscow, 1960.

17. Bekker, Fruyukhtenikht, Khamermesh and Longmyur. An Accelerator for Micrometeors. Pribory dlya nauchnykh issledovaniy, No. 10, 1965, p. 86.

18. Benedict, E. Weightlessness, Physical Phenomena and Biological Effects. (Translated from English). Mir, Moscow, 1965.

19. Baldwin, R. Chto my znayem o Lune? (What Do We Know about the Moon?). Mir, Moscow, 1967.

20. Borisenkov, Ye. P., Yu. P. Doronin and K. Ya. Kondrat'yev. Structural Characteristics of the Earth's Radiation Field as a Planet. Kosmicheskiye issledovaniya, Vol. 1, No. 1, 1963.

21. Borovik, Ye. S., F. I. Bussol and V. A. Kovalenko. ZhTF, Vol. 33, No. 1, 1963./369

22. Borovik, Ye. S., B. G. Lazarev and I. F. Mikhaylov. A Hydrogen Condensation Pump with an Autonomous Liquifier. Atomnaya energiya, Vol. 7, 1957.

23. Brauch, Douglas and Vance. The Effect of Electron Bombardment on the Optical Properties of Temperature Controlling Coverings of Space Apparatus. Raketnaya tekhnika i kosmonavtika, Vol. 3, No. 12, 1965, pp. 187-198.

24. Bulgakov, Yu. V. and T. I. Kolomenskaya. High Resistance Zones in Proton-Irradiated Silicon. Fizika i tekhnika poluprovodnikov, Vol. 1, No. 3, 1967, pp. 422-425.

25. Bukhartsev, N. G., M. V. Sokolov and O. P. Shchelkova. Industrial Instruments for Measuring Ultraviolet Radiation. Svetotekhnika, No. 7, 1961, pp. 18-23.

26. Byurganovskaya, G. V., V. V. Vargin, N. A. Leko and N. F. Orlov. Deystviye izlucheniy na neorganicheskiye stekla (The Effect of Radiation in Inorganic Glass). Atomizdat, Moscow, 1968.

27. Vanders, A. J. Fizicheskiye usloviya na planete Mars (Physical Conditions on the Planet Mars). Foreign Languages Publishing House, 1960.

28. Vedder. Charging and Acceleration of Macroparticles. Pribory dlya nauchnykh issledovaniy, No. 11, 1963, p. 3.

29. Veksler, V., L. Groshev and B. Isayev. Ionizatsionnyye metody issledovaniya izlucheniy (Ionization Methods of Investigating Radiation), Gostekhizdat, Moscow, 1950.

30. Vereshchenskiy, I. V. and A. K. Pikayev. Vvedeniye v radiatsionnuyu khimiyu (Introduction to Radiation Chemistry). Publishing House of the Academy of Sciences, USSR, Moscow, 1963.

30a. Verkhovtseva, E. T., V. P. Strel'nikov and B. I. Popov. A Source of Vacuum Ultraviolet Radiation, Based on Electron Beam Stimulation of a Supersonic Gas Jet. ZhPS, Vol. 7, No. 6, 1967.

31. Verkin, B. I., A. M. Markus, V. M. Suslo and N. A. Churikov. Using a Proton-Electron Injector to Investigate Radiation Effects in Solids. In the collection: Radiatsionnaya fizika nemetallicheskikh kristallov (Radiation Physics of Non-Metallic Crystals), Naukova Dumka, Kiev, 1967, pp. 437-443.

32. Vernov, S. N. and A. Ye. Chudakov. Investigating Cosmic Rays and Terrestrial Corpuscular Radiation during Flights of Rockets and Satellites. Uspekhi fizicheskikh nauk (UFN), Vol. 70, No. 4, 1960, p. 585.

33. Interaction of Gases with a Surface. Collection of translated articles. Mir, Moscow, 1965, p. 48.

34. Popov, B. I. A Source of Vacuum Ultraviolet Radiation, Based on Electron Beam Stimulation of a Supersonic Gas Jet. ZhPS, Vol. 7, No. 6, 1967, pp. 859-864.

35. Vinogradov, A. P., Yu. A. Surkov, K. P. Florenskiy and B. M. Andreychikov. Determination of the Chemical Composition of the Venusian Atmosphere by the Venera-4 Interplanetary Probe. Academy of Sciences USSR, Vol. 179, No. 1, 1968.

36. Vokuler, Zh. Fizika planety Mars (Physics of the Planet Mars). Foreign Languages Publishing House, Moscow, 1956.

37. Vinogradov, M. I., N. Ye. Biryukova and M. N. Yefimov. Nitrogen Sorption by Continuously Sputtering Titanium Films. Proceedings of the Fourth International Vacuum Congress, Manchester, 1968, p. 1.

38. Gennon, Lazlo, Lei and Wolnik. The Effect of Microparticle Bombardment on the Optical Properties of Metals. Raketnaya tekhnika i kosmonavtika (RTK), Vol. 3, No. 11, 1965, p. 148.

39. Hirschfelder, J., et al. Molekulyarnaya teoriya gazov i zhidkostey (The Molecular Theory of Gases and Liquids). Foreign Languages Publishing House, Moscow, 1961.

40. Groves, G. V. Probable Vacuum Conditions on the Moon, Preprint of Report at the Eighteenth International Astronautical Congress, Belgrad, 1967.

41. Gukhman, A. A. Vvedeniye v teoriyu podobiya (Introduction to Scaling Theory). Vysshaya Shkola, Moscow, 1963.

42. Danilova, N. G. and A. I. Shal'nikov. PTE, No. 6, 1967.

43. Deshman, S. Nauchnyye osnovy vakuumnoy tekhniki (Scientific Bases of Vacuum Technology). Mir, Miscow, 1965.

44. Dzhaff, L. D. and Zh. B. Rittenkhauz. Behavior of Materials Under Space Conditions. Raketnaya tekhnika, No. 3, 1962.

45. Zaydel', A. N. and Ye. Ya. Shreyder. Spektroskopiya vakuumnogo ul'trafioleta /370
(Spectroscopy of the Vacuum Ultraviolet). "Nauka" Press, Moscow, 1962.

46. Zarubin, V. S. Temperaturnyye polya v konstruktsiyakh letatel'nykh apparatov (Temperature Fields in Aircraft Structures). Mashinostroyeniye, Moscow, 1966.

47. Ivanov, A. P. Elektricheskiye istochniki sveta (Electrical Light Sources). Gosenergoizdat, Moscow, 1955.

48. Space Environment Simulation During Tests of Unmanned Spacecraft. Voprosy raketnoy tekhniki, Nos. 10 and 11, Mir, Moscow, 1966.

49. Ivanov, D. I. and A. I. Khromushkin. Sistemy zhizneobespecheniya cheloveka pri vysotnykh i kosmicheskikh poletakh (Human Life-Support Systems during High-Altitude and Space Flights). Mashinostroyeniye, Moscow, 1968.

50. The Use of Solar Energy in Space Investigations. Collection of Translated Articles. Mir, Moscow, 1964.

51. Jorgensen. Damage of Spacecraft Temperature Controlling Coverings by the Solar Wind. RTK, Vol. 5, No. 6, 1967, p. 212.

52. Kazachevskiy, V. M. Calculating the Earth's Albedo. Izvestiya astrofizicheskogo instituta AN kazakhskoy SSR, Vol. 1, No. 1, 1955.

53. Kalitin, N. N. The Solar Constant. Priroda, No. 2, 1948.

54. Kaminskiy, M. Atomnyye i ionnyye stolknoveniya na poverkhnosti metalla (Atomic and Ion Collisions on a Metal Surface). Mir, Moscow, 1967.

55. Cunningham, B. E. Calculating the Shadow Factor for Elliptical Orbits of Satellites. Raketnaya tekhnika, No. 9, 1962.

56. Karyakin, N. A. Svetovyye pribory prozhektornogo i proyektornogo tipov (Light Instruments of Searchlight and Projector Types). Vysshaya Shkola, Moscow, 1966.

57. Kellog, U. and C. Sagan. Atmosfera Marsa i Venery (The Atmosphere of Mars and Venus). Foreign Languages Publishing House, Moscow, 1962.

58. Kolotyrkin, V. M., A. B. Gil'man and A. K. Tsapuk. Obtaining Organic Films on Surfaces under the Effects of Electrons in the Ultraviolet and in a Glow Discharge. Uspekhi khimii, Vol. 36, No. 8, 1967.

59. Kondrat'yev, G. M. Teplovyye izmereniya (Thermal Measurements). Mashgiz, Moscow, 1957.

60. Kondrat'yev, K. Ya. Luchistaya energiya Solntsa (Solar Radiant Energy). Gidrometeoizdat, Moscow, 1954.

61. Kondrat'yev, K. Ya. Some Problems of Interpreting the Results of Measuring Retreating Radiation with the Aid of Meteorological Satellites. Kosmicheskiye issledovaniya, Vol. 1, No. 1, 1963.

62. Kondrat'yev, K. Ya., O. A. Avaste, M. P. Fedorova and K. Ye. Yakushevskaya. Pole izlucheniya Zemli kak planety (The Radiation Field of the Earth as a Planet). Gidrometeoizdat, Moscow, 1967.

63. Kondrat'yev, K. Ya. and M. P. Fedorova. Experience from Processing and Analysis of Certain Data on Measurement of the Components of the Radiation Balance of the "Earth's Surface-Atmosphere" System on the Tiros-2 Satellite. In the collection: Iskusstvennyye Sputniki Zemli (Artificial Earth Satellites). Publishing House of the Academy of Sciences USSR, No. 14, Moscow, pp. 95-105.

64. Kondrat'yev, K. Ya. and M. P. Fedorova. Retreating Radiant Fluxes toward Differently Oriented Surfaces at an Altitude of 300 Kilometers. Kosmicheskiye issledovaniya, Vol. 1, No. 3, 1963.

65. Kondrat'yev, K. Ya. and M. P. Fedorova. Retreating Long-Wave Radiant Fluxes toward Differently Oriented Surfaces. In the collection: Iskusstvennyye Sputniki Zemli (Artificial Earth Satellites). Publishing House of the Academy of Sciences USSR, Moscow, No. 14, 1962, pp. 133-137.

66. Kondrat'yev, K. Ya. and K. Ye. Yakushevskaya. The Angular Distribution of Retreating Thermal Radiation in Different Regions of the Spectrum. In the collection: Iskusstvennyye Sputniki Zemli (Artificial Earth Satellites). No. 14, Publishing House of the Academy of Sciences, USSR, Moscow, 1962, pp. 13-30.

67. Space Physics (translated from English). Collection of articles. Mir, Moscow, 1966.

68. Kroshkin, M. G. Fiziko-tekhnicheskiye osnovy kosmicheskikh issledovaniy (Physicotechnical Bases of Space Research). Mashinostroyeniye, Moscow, 1969.

69. Kressner, G. N. and J. Michaels. Vvedeniye v sistemy kosmicheskoy svyazi (Introduction to Space Communications Systems). Svyaz', Moscow, 1967.

70. Kruz, P., L. MacGloughlin and R. McKvistan. Fundamentals of Infrared Technology (translated from English). Voyenizdat, Moscow, 1964.

71. Laslo, T. Optical High-Temperature Furnaces (translated from English). Mir, Moscow, 1968. /371

72. Levin. Irradiation of an Earth Satellite by Reflected Solar Light. Raketnaya tekhnika, No. 9, 1962.

73. Link, F. Lunar Eclipses (translated from English). Foreign Languages Publishing House, Moscow, 1962.

74. Lekk, J. Izmereniye davleniya v vakuumnykh sistemakh (Measurement of Pressure in Vacuum Systems). Mir, Moscow, 1966.

75. Lawrence and Cox. Fundamental Investigations of the Resistance of Temperature Controlling Coverings. RTK, Vol. 4, No. 5, 1966, p. 174.

76. Luna (The Moon). Collection of articles, Znaniye, Moscow, 1964.

77. Malkov, M. P., I. B. Danilov, A. G. Zel'dovich and A. B. Fradkov. Spravochnik po fiziko-tekhnicheskim osnovam glubokogo okhlazhdeniya (Handbook on the Physicotechnical Bases of Deep Cooling). Gosenergoizdat, Moscow, 1963.

78. Malkovich, M. S. Angular and Spectral Distribution of Radiation Reflected by the Earth into Space. In the collection: Iskusstvennyye sputniki Zemli (Artificial Earth Satellites). No. 14, Publishing House of the Academy of Sciences USSR, Moscow, 1962, pp. 30-49.

79. Mark, Sotters and Mertich. The Effect of the Calibrated Effects of Micrometeorites on the Thermal Properties of a Surface. Raketnaya tekhnika, Vol. 4, No. 10, 1966, p. 148.

80. Mars (Mars). Collection of articles. Znaniye, Moscow, 1962.

81. Marov, M. Ya. New Data on the Moon and Planets. Zemlya i Vselennaya, No. 3, 1970.

82. Maslennikov, Ye. A., A. N. Nekrasov and Yu. M. Pustovoyt. PTE, No. 5, 1963.

83. Mezon'ye, Sh. Acceleration of Macroparticles and Thermonuclear Synthesis. Atomnaya tekhnika za rubezhom, No. 9, 1966.

84. Meshkov, V. V. Osnovy svetotekhniki (Fundamentals of Illumination Engineering). Part 1. Gosenergoizdat, Moscow, 1957.

85. Milliard, J. P. and S. B. Neal. Measuring the Earth's Albedo and Natural Radiation with the Aid of the Orbiting Solar Observatory OSO-1. RTK, No. 7, 1965, pp. 132-139.

86. Mishchenko, Ye. D. and G. P. Startsev. Phosphors for Recording the Vacuum Ultraviolet. Optiko-mekhanicheskaya promyshlennost', No. 8, 1967, pp. 7-10.

87. Moroz, V. I. Fizika planet (The Physics of the Planets). "Nauka" Press, Moscow, 1967.

88. New Data on the Moon. Reports of the Academy of Sciences USSR (DAN SSSR), 1963.

89. New Data on Mars and Venus. Collection of articles edited by V. I. Moroz. Mir, Moscow, 1968.

90. New Trends in Cryogenic Technology. Collection of translations from English, edited by Professor M. P. Malkov. Mir, Moscow, 1966.

91. Oiti, M. The Current State of Ultrahigh Vacuum Technology and Investigation of Surface Phenomena in the United States. Oyo Butsuri, Vol. 33, No. 8, 1964, pp. 571-582 (translation from Japanese, VINITI, No. 51393/5, 1966).

92. Circumterrestrial Space. Reference Data. (translated from English). Mir, Moscow, 1966, p. 191.

93. Operatsiya "Morskaya zvezda" (Operation Starfish). Atomizdat, Moscow, 1964.

94. Pleshivtsev, N. V. Katodnoye raspyleniye (Cathode Sputtering). Atomizdat, Moscow, 1968.

95. Pol, L. Evaporation Coefficients. Voprosy raketnoy tekhniki, No. 9, 1962.

96. Ponomarev, A. N. Pilotiruyemyye kosmicheskiye korabli (Manned Spacecraft). Voyenizdat, Moscow, 1968.

97. Prikladnaya gazovaya dinamika (Applied Gas Dynamics) (edited by S. A. Khristianovich). Central Aero-Hydrodynamic Institute (TsAGI), 1948.

98. Rabinovich, G. I. An Ultrahigh Pressure Metal Xenon Lamp-Luminaire with an Output of 40-50 kW. Svetotekhnika, No. 9, 1969.

99. Rodionov, B. N. Infrared Images of the Moon. Zemlya i Vselennaya, No. 6, 1967, pp. 63-65.

100. Rolstek. Crater Depth and Target Strength upon Impact at Hypersonic Speed. RTK, Vol. 3, No. 11, 1965, p. 213.

101. Rokhlin, G. N. Light Sources. Tekhnika kino i televideniya, December, 1965. /372

102. Santeller, D. Measuring Pressure in Unheated Ultrahigh Vacuum Systems. Pribory dlya nauchnykh izmereniy, No. 3, Mir, Moscow, 1962.

103. Simonov, V. A., G. F. Kleymenov, A. G. Mileshkin and V. A. Kochnev. Maintaining Ultralow Pressure of a Neutral Gas during Accumulation of a High-Temperature Plasma in Magnetic Injection Traps. Report No. 10/255. In the collection: Proceedings of the First International Conference on the Peaceful Uses of Atomic Energy, Salzburg, 1961.

104. Sinks, J. and R. Woods. Vvedeniye v radiatsionnuyu khimiyu (Introduction to Radiation Chemistry). Atomizdat, Moscow, 1967.

105. Slyusarev, G. G. O vozmozhnom i nevozmozhnom v optike (On the Possible and Impossible in Optics). Fizmatgiz, Moscow, 1960.

106. Handbook on Engineering Psychology for Engineers and Creative Designers (translation from English). Mir, Moscow, 1968.

107. Spravochnik po kosmonavtike (Handbook on Cosmonautics). (Edited by K. Ya. Kondrat'yev and V. A. Odintsov). Voyenizdat, Moscow, 1966.

108. Sternberg, S. and A. Shnapf. Characteristics of the Tiros-1 and Tiros-2 Satellites and Analysis of the Results of their Application. Raketnaya tekhnika, No. 11, 1961, p. 12.

109. Surinov, Yu. A. Methods of Calculating the Integral and Local Angular Radiation Coefficients. In the collection: Teploperedacha i teplovoye modelirovaniye (Heat Transfer and Thermal Simulation). Publishing House of the Academy of Sciences, USSR, Moscow, 1959.

110. Surkov, Yu. A. New Data on the Lunar Composition. Zemlya i Vselennaya, No. 6, 1967, pp. 57-66.

111. Sytinskaya, N. N. Luna i yeye nablyudeniye (The Moon and Its Observation). Gostekhizdat, Moscow, 1956.

112. Sytinskaya, N. N. Planeta Mars (The Planet Mars). Fizmatgiz, Moscow, 1962.

113. Sytinskaya, N. N. Priroda Luny (The Nature of the Moon). Fizmatgiz, Moscow, 1959.

114. Sytinskaya, N. N. Composite Catalog of the Visual Reflectivity of Lunar Objects. Astronomicheskiy zhurnal (AZh), Vol. 30, No. 3, 1953, p. 295.

115. Tverskoy, B. A. Dinamika radiatsionnykh poyasov Zemli (Dynamics of the Earth's Radiation Belts). "Nauka" Press, Moscow, 1968.

116. Troitskiy, V. S. Radio-Frequency Emission and the Nature of the Moon. Vestnik AN SSSR, No. 2, 1964, p. 33.

117. Solar Ultraviolet Radiation and the Interplanetary Medium. Collection of articles. Foreign Languages Publishing House, 1962.

118. Ursul, A. D. Osvoyeniye kosmosa (The Conquest of Space). Mysl', Moscow, 1967.

119. Favorskiy, O. N. and Ya. S. Kadaner. Voprosy teploobmena v kosmose (Problems of Heat Transfer in Space). Vysshaya shkola, Moscow, 1967.

120. Fastovskiy, V. G., Yu, V. Petrovskiy and A. Ye. Rovinskiy. Kriogennaya tekhnika (Cryogenic Technology). Energiya, Moscow, 1967.

121. Fedorova, M. F. Investigating Physical Adsorption. In the collection: Fizika i tekhnika sverkhvysokogo vakuuma (The Physics and Technology of Ultrahigh Vacuum). Mashinostroyeniye, Moscow, 1968.

122. Feyman, M. G. Selecting a Radiation Source for Laboratory Tests of Paint and Varnish Coverings for Atmospheric Resistance. Lakokrasochnyye materialy i ikh primeneniye, No. 5, 1964, p. 59.

123. Fesenkov, V. G. On the Periodicity of the Solar Constant in Relation to Weather Forecasting. Uspekhi astronomicheskikh nauk, Vol. 3, 1947.

124. Fizika i tekhnika sverkhvysokogo vakuuma (The Physics and Technology of Ultra-High Vacuum). Mashinostroyeniye, Moscow, 1968.

125. Fizika Luny i planet (The Physics of the Moon and Planets). Collection of articles. Naukova dumka, Kiyev, 1964.

126. Filatov, E. S. The Mechanism of the Elementary Act of a Combustion Reaction. Uspekhi khimii, Vol. 34, No. 9, 1965.

127. Fogel', M. Ya. Secondary Ion Emission. Uspekhi fizicheskikh nauk, Vol. 91, No. 1, 1967.

128. Frankel', Ya. I. On the Theory of the Phenomena of Accommodation and Condensation. Uspekhi fizicheskikh nauk, Vol. 20, No. 1, 1938.

129. Hall, Kemp and Selen. Using a Plasma Jet to Investigate the Interaction of a Plasma and Flying Vehicles. RTK, Vol. 2, No. 6, 1964, p. 71.

130. Hinteregger, H. Preliminary Results of Observing the Far Ultraviolet Spectrum of the Sun in the Upper Atmosphere. In the collection: Ul'trafioletovoye izlucheniye Solntsa i mezhplanetnaya sreda (Solar Ultraviolet Radiation and the Interplanetary Medium). Foreign Languages Publishing House, 1962. /373

131. Tseytlin, A. B. and L. V. Falaleyev. A "Cold" Diffusion Pump. In the collection: Fizika i tekhnika sverkhvysokogo vakuuma (The Physics and Technology of Ultrahigh Vacuum). Mashinostroyeniye, Moscow, 1968.

132. Sharonov, V. V. Priroda planet (The Nature of the Planets). Fizmatgiz, Moscow, 1958.

133. Sharonov, V. V. Planeta Venera (The Planet Venus). "Nauka" Press, Moscow, 1967.

134. Shvedchikov, A. P. The Chemistry of Hot Hydrogen Atoms with an Energy of 1 - 3 eV and of Excited Radicals. Uspekhi khimii, Vol. 36, No. 3, 1965.

135. Shchelkova, O. P., et al. Svetotekhnika, No. 3, 1963, pp. 11-16.

136. Shlykov, Yu. P. and Ye. A. Ganin. Kontaktnyy teploobmen (Contact Heat Exchange). Gosenergoizdat, Moscow, 1963.

137. Shuleykin, V. V. Behavior of Liquids in Weightlessness. DAN SSSR, Nos. 1 and 5, 1962; No. 152/5 and No. 153/6, 1963.

138. Shumskiy, K. P. Vakuumnyye apparaty i pribory khimicheskogo mashinostroyeniye (Vacuum Equipment and Instruments for Chemical Machine Building). Mashgiz, Moscow, 1963.

139. Shumskiy, K. P., A. I. Myalkin and I. S. Maksimovskaya. Osnovy rascheta vakuumnoy sublimatsionnoy apparatury (Fundamentals of Designing Vacuum Sublimation Equipment). Mashinostroyeniye, Moscow, 1967.

140. Edwards. Using the Directional Reflectivity of Solar Rays to Regulate the Temperature of Interplanetary Rockets. Raketnaya tekhnika, No. 11, 1961, pp. 82-88.

141. Edwards and Bivens. The Effect of Polarization on Heat Exchange by Irradiation of a Spacecraft. RTK, No. 7, 1965, pp. 139-149.

142. Yuferov, V. V., R. F. Bulatova, P. M. Kobsev, et al. Investigating the Mechanism of Hydrogen Sorption by Condensed Layers of CO_2. ZhTF, Vol. 38, No. 2, 1968, pp. 326-330.

143. Yuferov, V. V. and F. I. Bussol. Investigating Hydrogen and Neon Absorption by Layers of Condensed Solid Gases. In the collection: Fizika i tekhnika sverkhvysokogo vakuuma (The Physics and Technology of Ultrahigh Vacuum). Mashinostroyeniye, Moscow, 1968.

144. AIAA Space Simulation Testing Conference, 1964, 1966.

145. Anderson, D. L. and R. G. Dahms. Surface Blistering of Metals due to Low Energy Hydrogen Bombardment. J. Spacecraft and Rockets, Vol. 4, No. 3, 1967, p. 364.

146. Anderson, I. W., E. A. Lablane and H. Cohan. Experimental and Analytical Assessment of Space Thermal and Vacuum Environment Simulation Requirements. Journal of Spacecraft and Rockets, Vol. 3, No. 7, 1966, pp. 976-982.

147. Applied Optics, Vol. 2, No. 6, 1963, p. 591.

148. Arvesen, I. C. Spectral Dependence of Ultraviolet Induced Degradation of Coatings for Spacecraft Thermal Control. AIAA Paper, No. 67 - 340, 1967.

149. Astronautics and Aeronautics, Vol. XI, No. 11, 1964, pp. 98-99.

150. Balwanz, W. W. Cryogenic Vacuum Pumping. Adv. Cry. Eng., Vol. 9, 1964.

151. Beecher, Norman. Thermal Analysis of Space Simulation Chambers. Trans. of the Ninth Nat. Vac. Symp. of the Amer. Vac. Soc., 1962, pp. 253-259.

152. Babjak, S. J., C. P. Boebel and J. E. Scannapieco. Design Concepts for a Combined Space Environmental Effects Test Facility. Vacuum, Vol. 18, No. 2, 1968, pp. 57-62.

153. Bocarsly, S. I. Reflectory Metals for High Temperature Applications to Spacecraft and their Reactions with the Environment. Chemical Engineering Progress Symposium Series, Vol. 60, 1964.

154. Brackman, R. T. and W. L. Fite. J. Chem. Phys., Vol. 34, 1961, p. 1572.

155. Breuch, R.A. Exploratory Trapped-Particle and Trapped-Particle-Plus-Ultraviolet Effects on the Optical Properties of Spacecraft Thermal Control Coating. Thermophysics and Temperature Control of Spacecraft and Entry Vehicles. /374
Progress in Astronautics and Aeronautics, Vol. 18, 1966, p. 365-389. Ed. H. B. Heller, A. P., New York.

156. Breuch, R. A. and H. E. Pollard. Nuclear Environmental Effects on Spacecraft Thermal Control Coatings. Symposium on Thermal Radiation of Solids. Ed., NASA, 1965, p. 365.

157. Brauch, R. A. Studies in the Effects of the Interplanetary Space Environmental on Thermal-Control Coatings. AIAA Journal, Vol. 5, No. 9, 1967.

158. Brown, R. F. and E. S. J. Wang. Capture Coefficients of Gases at 77° K. Adv. Cry. Eng., Vol. 10, 1965.

159. Buffham, B. A., P. P. Henault and R. A. Flinn. A Theoretical Evaluation of the Sticking Coefficient in Criopumping. Ninth National Symposium on Vacuum Technology Transitions, 1962, pp. 205-211.

160. Burill, E. A. Simulating Space Radiation. Space/Aeronautics, Vol. 41, Nos. 5, 6, 1964.

161. Burnham, F. A. TRW Claims Major Gain in Test Capability with New Chamber. Aerospace Technology, May 6, 1968, pp. 48-49.

162. Chao, B. T. and G. L. Wedeking. Similarity Criteria for Thermal Modeling of Spacecraft. Journal of Spacecraft and Rockets, Vol. 2, No. 2, 1965, pp. 146-152.

163. Cheesman, C. E. J. Spacecraft and Rockets, Vol. 3, No. 8, 1966.

164. Cheever, P. R., I. K. Miles and I. Romanko. In Measurements of Spectral Reflectance of Thermal Control Coating Irradiated in Vacuo. AIAA Paper, No. 67, 1967, p. 342.

165. Chuan, R. L. Performance Rating of Space Vacuum Simulation Chambers. CIVRES, Paris, 1964.

166. Chubb, J. N. Performances of Cryopumping. Vacuum, Vol. 16, No. 12, 1966.

167. Clausing, R. E. Trans. 8th Nat. Vac. Symp., Vol. 1, 1961, p. 345.

168. Cospar International Reference Atmospheres (Cira-64, Cira-65), 1964, 1965.

169. Courtney, W. J., J. E. Zavelle, R. B. Britton and A. S. Denholm. Sealing Techniques for Rotation in Vacuum. Astronautics and Aeronautics, Vol. 2, No. 2, 1964.

170. Crosly, I. R. and M. A. Perlow. Snap-10A. Thermal Control Coatings. Thermophysics and Temperature Control of Spacecraft and Entry Vehicles. Progress in Astronautics and Aeronautics. Vol. 18, New York, 1966, pp. 473-494. Ed., G. B. and A. P. Heller.

171. Cunningham, B. E. and R. E. Eddy. Space Environmental Simulator for Studies of the Effect of the Space Environment on Materials. AAIA, IES, ASTM Space Simulation Conference. New York, 1966, p. 161-165.

172. Davidsen, P. D. Theory and Practice of RF Sputtering. Vacuum, Vol. 17, No. 3, 1967.

173. Dawson, J. P. Prediction of Cryopumping Speeds in Space Simulation Chamber. J. Spacecraft and Rockets, Vol. 6, 1965.

174. Dawson, J. P. and J. D. Haygood. Cryopumping, Cryogenics, Vol. 6, No. 14, 1965.

175. Dick and A. Sands. Coating Cryopumping Surfaces with Molecular Sieve Material. Vacuum, Vol. 16, No. 12, 1966.

176. Dingman, E. H. A Hypervelocity Microparticle Linear Accelerator for Use in Micrometeoritic Simulation. IEEE Transactions on Nuclear Sciences, Vol. NS-12, No. 3, 1965, p. 544.

177. Drechsler, M. Z. Electrochem, Vol. 58, 1964.

178. Environmental Quarterly, No. 3, 1963, pp. 16-31; No. 3, 1964; No. 3, 1961.

179. Dallas, E., Evans, Forrest, and G. Hall. Vacuum Environment in Space. AIAA, IES, ASTM Space Simulation Conference, Houston, Texas. Vols. 7-9, September 1966.

180. Francis and Johnson. Structure of the Upper Atmosphere. Satellite Environment Handbook. Stanford California University Press, 1965.

181. Fritz, S. The Albedo of the Planet Earth and of Clouds. Journal of Meteorology, Vol. 6, No. 4, 1949.

182. Fritz, S. Solar Radiant Energy and Its Modification by the Earth and its Atmosphere. Compendium of Meteorology, ed. by T. F. Malone, American Meteorological Society, Boston, 1951. /375

183. Harrison, E. H. The Problem of Producing Energetic Marcrous (Macroscopic Particles). Plasma Physics, Vol. 9, 1967, p. 183.

184. Haygood, J. D., J. E. Nichols and E. S. Wang. Cold Diffusion Pump. Adv. Cry. Eng., Vol. 7, 1962.

185. Heller, G. B. Problems and Research in Space Environment Effects. Symposium on Thermal Radiation of Solids, NASA, 1965, pp. 339-349.

186. Hengevoss, J. and E. Trendelenburg. Continuous Cryotrapping of Hydrogen by Argon in the Temperature Range between 4° K and 15° K. Vacuum, Vol. 17, No. 9, 1967.

187. Hengevoss, J. and E. Trendelenburg. Naturforshung, Vol. 18a, 1963, pp. 481-489.

188. Hess, W. N., G. D. Mead and M. P. Nakada. Low-Energy Charged Particle Environment of the Earth. Thermophysics and Temperature Control of Spacecraft and Entry Vehicles. Progress in Astronautics and Aeronautics, Vol. 18, 1966, Ed., G. B. Heller.

189. Hidle, R. A. Space Simulation. ASME Publication, N62-AV-34.

190. Hinteregger, H. Absolute Intensity Measurement in the Extreme Ultraviolet Spectrum of Solar Radiation. Space. Science Review, Vol. 4, 1965, pp. 461-470.

191. Hobson, J. P. Pumping at Solid Surfaces. Brit. J. Appl. Phys., Vol. 14, 1963; Hobson, J. P., P. A. Readhead and E. V. Kornelsen. The Physical Basis of Ultrahigh Vacuum. Barnes and Noble, Inc., New York, 1968.

192. Holland, D. L. Conference on Cryogenics in Relation to Vacuum. Brit. J. Appl. Phys., Vol. 16, 1965.

193. Honig, R. E. Vapor Pressure Data for the More Common Elements. RCA Review, Vol. XVIII, No. 2, 1957.

194. Haughton, H. G. An Annual Head Budget of the Northern Hemisphere. J. Met., Vol. 11, 1954.

195. Hunt, A. L., C. E. Taylor and J. E. Omohundro. Adv. Cry. Eng., Vol. 8, 1962, p. 100.

196. Hurlbut, F. C. and R. J. Mansfield. Calculated and Observed Pumping Speed of a Shielded Cryogenic Pumping Surface. Adv. Cry. Eng., Vol. 8, 1963.

197. Gardner, F. B. Cryogenic System for Space Simulation Chambers. CIVRES, Paris, 1964.

198. Garwin, E. L. Cryogenic Pumping and Space Simulation. Adv. Cry. Eng., Vol. 8, 1963.

199. Gelhard, J. C. and S. W. Meyer. Design Solution for a Space Environment Simulator. Paper JAS, N61-AV-52, Vol. I, 1963.

200. Gillette, R. B. Proton Radiation Effects on Solar Concentrator Reflective Surfaces, AIAA Paper, No. 67, 1967, p. 341.

201. Gillette, R. B., R. R. Brown, R. F. Seiler,and W. R. Sheldon. Effects of Protons and Alphas Particles on Thermal Properties and Temperature Control of Spacecraft and Entry Vehicles. Progress in Astronautics and Aeronautics. Ed. A. P. and G. B. Heller, Vol. 18, 1966, New York, pp. 423-440.

202. Gilligan, I. E. The Induced Optical Properties of Zinc Oxide. AIAA Paper, No. 67, 1967, p. 214.

203. Gilligan, I. E. and R. P. Caren. Some Fundamental Aspects of Nuclear Radiation Effects in Spacecraft Thermal Control Materials. Symposium on Thermal Radiation of Solids. San Francisco, California, 1964, 1965.

204. Goetz, D. and C. B. Grosh. Earth Emitted Infrared Radiation Incident upon a Satellite. Journal of Aerospace Sciences, 1962, pp. 521-524.

205. Grabner, H. and W. Pilz. High Pressure Discharge in Metal Halide Vapor with High Visual Efficiency. J. Met., Vol. 11, 1954.

206. Grabner, H. and M. Zauter. Indium Iodide High Pressure Lamps for Projection. Techn-Wiss. Abhandl, Osram, ges., 9, Berlin - Heidelberg - New York, 1967.

207. Jaffe, L. D. and J. B. Rittenhouse. Behavior of Materials in Space. ARS J., Vol. 32, No. 3, 1962. /376

208. Jenninson, R. C. and I. A. M. McDonnel. The Ariel II Micrometeoritic Penetration Measurements. Proc. Roy. Soc., A. 300, No. 1461, 1967, pp. 251-269.

209. Jerkes, J. W., et al. Conversion of Large Chamber to Sputter-Ion and Titanium Sublimation Pumping. Proceedings JES, 1967.

210. James, E. A. John. Cryogenic and Space Vacuum Simulation. The Journal of Environmental Sciences, Vol. 10, No. 3, 1967.

211. John, J. E. A. and W. F. Hardgrove. Design of an Ultrahigh Vacuum Space Simulator. J. Spacecraft and Rockets, Vol. 3, No. 3, 1966.

212. Johnson, F. S. The Solar Constant. J. Met., Vol. 11, 1954.

213. Journ. of Spacecraft and Rockets, Vol. 3, No. 3, 1966.

214. Journ. of Environmental Sciences, No. 2, 1964.

215. Katz, A. J. Thermal Testing. Space Astronautics, Technical Reference Series, Part 2, October, 1962.

216. Katzoff, S. Simulatude in Thermal Models of Spacecraft, NASA TN, D-1631, April, 1963.

217. Kingery, Marshall K. Electrical Power Transmission of Gimbal Mounts in High Vacuum. Inst. Env. Sci., Annual Techn. Meet. Proc., Chicago, 1965.

218. Klipping, G. and W. Mascher. Vacuum Production by Condensation of Highly Cooled Surfaces. Vacuum-Technic, Vol. 11, No. 3, 1962, IV.

219. Lavy. Use of Color Centers for Detection and Measurement Defects. Symp. on Chem. and Phys. Effects of High Energy Radiation in Inorganic Substances, 1964.

220. Lell, T., N. I. Kriedl and I. R. Hensler. Radiation Effects in Quartz Silica and Glasses. Progress in Ceramic Science, Ed., I. E. Burker, Ph.D., Vol. 4, 1966.

221. Lewis, D. W. and T. O. Thostesen. Mariner-Mars Absorptance Experiment Thermophysics and Temperature Control of Spacecraft and Entry Vehicles. Progress in Astronautics and Aeronautics, Ed., G. B. and A. P. Heller, Vol. 18, 1966, pp. 441-458.

222. Longmore, A. P. Simulation of Space Environment. Env. Eng. Quarterly, No. 7, 1963.

223. McMillan, H. F., A. F. Sklensky, and L. A. McKellar. Apparaturs for Spectral Bidirectional Reflectance Measurements during Ultraviolet Irradiation in Vacuum, Progress in Astro. and Aeron. Thermophysics and Temperature Control of Spacecraft and Entry Vehicles, Ed., G. B. and A. P. Heller, Vol. 18, New York, 1966.

224. Mandelstam, S. L. X-ray Emission of the Sun. Space Science Review, Vol. 4, No. 5/6, 1965.

225. Marchall and Sitting. Cryogenics, Research and Applications. London, P. P., 1964.

226. Mark, H. and R. D. Sommers. The Combined Use of Liquid and Gaseous Helium to Provide Near Actual Space Environment. Adv. Cry. Eng., Vol. 8, 1963.

227. Merrill, R. B. The Effects of Micrometeoroids on the Emittance of Solids, Symposium on Thermal Radiation of Solids, NASA, 1965, pp. 453-472.

228. Miller, R. A. and F. I. Campbell. Effects of Low Energy Protons on Thermal Control Coatings. Thermophysics and Temperature Control of Spacecraft and Entry Vehicles. Progress in Astronautics and Aeronautics, Eds. G. B. and A. P. Heller, Vol. 18, 1966, pp. 399-412.

229. Miller, W. E. and J. T. Bevans. Laboratory Simulation of Ultraviolet and Vacuum Effects of Solar Absorptance of Spacecraft Thermal Control Materials. Proc. of Inter. Sym. of Solar Radiation and Simulation, 1965.

230. Milo, Pelc Hnilicka and John Crankshaw Simons. High Vacuum Apparatus (NRC), Patent, FIN, No. 922457, 1965.

231. Mirtich, M. I. and H. Mark. Alteration on Surface Optical Properties by High-Speed Micron-Size Particles. Sym. on Thermal Radiation of Solids, NASA, 1965, pp. 473-481. /377

232. Missiles and Rockets, No. 3, Part I, No. 5, Part VII, No. 13, Part III, No. 8, Part II, No. 1, Part VII, 1962; No. 9, 1965; No. 2, 1961.

233. Moore, R. W. Cryopumping in the Free Molecular Flow Regime. 8th Nat. Symp. on Vacuum Tech. Trans., Vol. I, 1961, pp. 426-428.

234. Mori, L., T. Higashi, S. Nomura, J. Osawa, Yoko Tochiba and A. Lamp. Newly Developed Lamp with Maximum Color Rendering Property. Toshifa Rev., 1967, Sept., Oct.

235. Neel, C. B. Research on the Stability of Thermal Control Coating for Spacecraft. Proc. of 5th Intn'l. Symp. on Space Tech. and Science, 1963, Tokyo, Japan, 1964.

236. Neel, C. B. The Roll of Flight Experiments in the Study of Thermalcontrol Coating for Spacecraft. AIAA Paper, No. 67, 1967, p. 329.

237. Norman, A. E. Design and Testing of a Large Ultrahigh Vacuum Space Simulation Chamber. Inst. Env. Sci. Annual Tech. Meet. Proc., Vol. III, Ph Pa., Mt. Prospect, 1964.

238. Ornum, Van. Vortex Stabilized Radiation Sources for Improved Solar Simulation. Proc. of Inter. Symp. of Solar Radiation and Simulation, 1965.

239. Olson, R. L., L. A. McKellar and J. V. Stewart. The Effects of Ultraviolet Radiation on Law As/E Surfaces. Symp. on Thermal Radiation of Solids, NASA, 1965.

240. Outman, Vernon and E. S. J. Wang. Simulation Testing in a Space Environment, An Assessment. J. of Spacecraft and Rockets, Vol. 3, No. 12, 1966.

241. Pearson, B. D., Jr. Preliminary Results from the Ames Emissivity Experiment on OSO-II. Thermophysics and Temperature Control of Spacecraft and Entry Vehicles. Progress in Astronautics and Aeronautics. Ed., G. B. and A. P. Heller, Vol, 18, New York, 1966.

242. Pettit, E. and S. M. Nicolson. Astrophysics J., Vol. 12, No. 102, 1930.

243. Porter, R. W., et al. Thermal Simulation of Space. Le Vide, No. 11, 115, 1965.

244. Price, W. E. The Simulation of Space Radiation Damage to Spacecraft Systems. IEEE on Nuclear Sciences, Vol. NS 12, No. 6, 1965.

245. Proceedings Inst. of Env. Sciences, 13th Ann. Tech. Meeting, 1962, 1964, 1967, Washington, D. C.

246. Rausa, G. Ultraviolet Radiation Induced Effection Some Optical Materials. AIAA Paper, No. 67, 1967, p. 344.

247. Report Committee on Space Research. Established by the International Council of Scientific Unions, Los Angeles, California, April 7, 1961.

248. Roberts, J., L. Stern, and G. Richard. Stabilization of Space Vehicles by Means of Gas-Diffusion Surfaces. Adv. Astron. Sci., Vol. 9, 1966.

249. Roussel, J., J. Thibault and A. Nanaboff. Gen'l Study of Cryopumping. Le Vide, Vols. VII - VIII, No. 118, 1965.

250. Santeller, D. S., D. W. Jones, D. H. Holkeboer and F. Pagano. Vacuum Technology and Space Simulation. NASA, Washington, 1966.

251. Sawitzki, P. Simulation of Space in Terms of its Properties as a Radiation Sink. Linde, Berichte aus Technik and Wissenchaft, No. 21, 1966.

252. Schafer, C. F. Thermal Control Coating Degradation Data from the Pegasus Experiment Packages. AIAA Paper, No.67, 1967, p. 331.

253. Schafer, C. F. and T. C. Bannister. Pegasus Thermal Control Coating. AIAA Paper, No. 66, 1966, p. 419.

254. Sharp, C. C. and J. C. Stuart. Practical Solutions to some Space-Chamber Problems. Inst. Env. Sci. Annual Techn. Mett. Proc. Phil. Pa., 1964, Mt. Prospect, pp. 205-208.

255. Simmons, J.C., Jr. Simulations of Environmental Conditions in Near Space. Annual Meeting of ARS, 1959.

256. Sinton, W. M. Physics and Astronomy of the Moon. Acad. Press, New York and London, 1962. /378

257. Space Aeronautics, No. 7, 1961.

258. Space Research, COSPAR, Vol. VIII, Ed. Mitra, London, 1967, North-Holland Publ., Amsterdam, 1968.

259. Space Materials Handbook, Ed., Goetzel, 1965.

260. Stambler, I. Surface Effects in Space, Space/Facility Design. J. of Spacecraft and Rockets, Vol. 3, No. 16, 1966.

261. Stephens, J. B. Molecular Sink Res./Dev., Jub., 1967; Stephens, J. B., J. of Spacecraft and Rockets, Vol. 3, No. 6, 1966.

262. Streed, E. R. An Experimental Study of the Combined Space Environmental Effects on ZnO-Potassium-Silicate Coating. AIAA Paper, No. 67, 1967, p. 339.

263. Sutherland, G. S. and M. E. Mach. A Review of Microrocket Technology. J. of Spacecraft and Rockets, Vol. 3, No. 8, 1966, p. 1153.

264. Tibor, S. and J. Laszlo. Environmental Sci., Vol. 9, No. 6, 1966, p. 13.

265. Toussaint, M. Verficiation of the Thermal Mathematical Model for Artificial Satellites: A New Test Philosophy. AIAA Paper, No. 67, p. 304.

266. Le Vantine, A. D. Space Thermal Environment Simulation Facilities. 8th Nat'l. Sym. on Vacuum Tech. Trans., Vol. 2, 1961.

267. Vliet, van R. M. Passive Temperature Control in the Space Environment. The MacMillan Company, New York, 1965.

268. Wachman, H. X. ARS, J., Vol. 32, No. 2, 1962.

269. Wang, E. S. J., J. A. Collings, Jr., and J. D. Haygood. General Cryopumping Study. Adv. Cry. Eng., Vol. 7, 1962.

270. Wehner, G. K. Solar Wind, Bombardment of a Surface in Space. Symposium on Thermal Radiation of Solids, NASA, 1965, pp. 345-349.

271. West, G. S. and W. T. Roberts. The Atmosphere of Mars, A Derivation of Parameters for Engineering and Design Application. Proc. of the Inst. Env. Sci., 1967.

272. Wolfgang, R. Hot Atom Chemistry. Annual Rev. of Physical Chemistry, Vol. 16, 1965.

273. Zerlaut, G. A. and W. I. Courtney. Space-Simulation Facility for in Situ Reflectance Measurements. AIAA Paper, No. 67, 1967, p. 213.

274. Zerlaut, G. A., Y. Harada and E. H. Tomplins. Ultraviolet Irradiation of White Spacecraft Coatings in Vacuum Symposium on Thermal Radiation of Solids, NASA, 1965, p. 391.

*U.S. GOVERNMENT PRINTING OFFICE: 1973-739-154/60